Next-generation satellite gravimetry for measuring mass transport in the Earth system

Proefschrift

João Gregório DE TEIXEIRA DA ENCARNAÇÃO

Master of Science in Aerospace Engineering, Delft University of Technology

geboren te Funchal, Madeira, Portugal

To my ancestors.

Contents

Contents

Contents

Summary

The main objective of the thesis is to identify the optimal set-up for future satellite gravimetry missions aimed at monitoring mass transport in the Earth's system.

The recent variability of climatic patterns, the spread of arid regions and associated changes in the hydrological cycle, and vigorous modifications in the ice coverage at polar regions have been attributed to anthropogenic influence. As such, it is important to continue monitoring the Earth system in order to properly constrain and improve the geophysical and climatic models and to better interpret the causes and consequences of climate change. Satellite gravimetric data are also exploited to further the knowledge on other geophysical processes with high societal and scientific impact, such as megathrust earthquakes, drought monitoring and Glacial Isostatic Adjustment (GIA).

The primary focus of the study is to properly quantify the errors in the gravimetric data to be collected by future gravimetric satellites, in particular those related to the measurement of the temporal gravitational field variations.

One source of errors comes from the background force models describing rapid mass transport processes; another error source is related to the background static gravity field model. These models are used to complement geophysical signals that are missing or improperly represented in the gathered satellite gravity data. However, they are built on the basis of in situ data that lack global coverage and, therefore, suffer from a limited accuracy (particularly in remote areas). Although the fidelity of these models is constantly improving, the satellite data accuracy is also increasing with the on-going technological and methodological advances. Determining the net effect of these conflicting trends is the main driver to study the propagation of errors in background models into the estimated models.

Other sources of errors arise from imperfections of the on-board sensors, such as the ranging sensor or the Global Navigation Satellite System (GNSS) receiver. The influence of the sensors errors is divided into the major independent contributions, with the corresponding frequency description, and assembled into a detailed noise model. The model predicts the effects of i) the inaccurately known orbital positions, ii) the noise in the inter-satellite metrology system, iii) the noise in the on-board accelerometers, iv) the wrongly-estimated Line of Sight (LoS) frame accelerations resulting from errors in the radial orbital velocities, and v) errors in the orientation of the LoS vector. The model has been validated with the help of actual Gravity Recovery And Climate Experiment (GRACE) a posteriori residuals, which are compared to the output of the noise model considering a simulated GRACE mission. Therefore, once the assumptions describing sensor and model accuracies are modified to reflect those predicted for future gravimetric missions, it is reasonable to expected that this noise model reproduces realistic errors for those missions.

Also relevant is the analysis of the sensitivity of the data in terms of isotropy. As learned from the GRACE mission, the nearly-constant North-South alignment of the measurement direction makes the data less sensitive to gravitational changes along the East-West direction. Although formally not an error itself, the anisotropic data sensitivity amplifies the errors in the data.

The sensor and model errors are propagated firstly to the gravimetric data and further to the gravitational field, in full-scale simulations of the cartwheel, trailing and pendulum satellite formations. The results are analysed in terms of i) the observation error in the frequency domain and ii) the estimated gravity field model error in the frequency and spatial domains. The error budgets for these formations are also quantified. The results indicate that the pendulum formation with no along-track displacement is least sensitive to model and sensors errors, in particular to temporal aliasing. The conducted study reveals serious limitations in the cartwheel mission concept, since the orbit errors are considerably amplified by the diagonal components of the gravity gradient tensor, while the pendulum and trailing formations are only affected by (small) off-diagonal components. The spatial error patterns provide valuable clues on how to best combine the different formation geometries in order to produce minimum anisotropy in the sensitivity of collected data. The data from the pendulum formation show some anisotropic sensitivity but the combination of such data with those from a trailing formation, such as the GRACE Follow On (GFO), would eliminate this disadvantage (as well as the low accuracy near the poles of the pendulum formation). Unlike alternative proposals for dual-pair satellite missions, such as the *Bender* constellation, the dual trailing/pendulum constellation would provide global coverage in case of failure of one satellite pair and dense temporal sampling at high latitudes.

Furthermore, the data from gravimetric missions are shown to benefit greatly from the data gathered by numerous non-dedicated satellites. From the conducted simulations, it is predicted that the achievable temporal resolution is increased to a few days for the degrees below 10 and, crucially, with no significant level of temporal aliasing. Longer estimation periods allow for higher degrees to be estimated, with greatly reduced effects of temporal aliasing in the resulting gravity field models.

Summary

Samenvatting

Het hoofddoel van dit proefschrift is de identificatie van de optimale opstelling voor toekomstige gravimetrie-missies die als doel hebben het massatransport in het aardesysteem te meten.

De recente variabiliteit in klimaat patronen, de toename van droge gebieden en gerelateerde veranderingen in de hydrologische cyclus, en grote veranderingen in de ijsdekking van de poolgebieden hebben geleid tot de hypothese van antropogene invloed. In dit kader is het van belang de observatie van het aardesysteem te handhaven om zodoende de geofysische en klimaat modellen beter af te bakenen en te verbeteren alsook de oorzaken en gevolgen van klimaatverandering van verfijndere interpretaties te voorzien. Satelliet gravitatie data worden ook ingezet om de kennis van andere geofysische processen met een hoge maatschappelijk en wetenschappelijke impact, zoals megathrust aardbevingen, monitoring van droogte en postglaciale opheffing, verder uit te diepen.

Het primaire doel van dit onderzoek is om de fouten in gravimetrische data die door toekomstige gravimetrische satellieten verzameld zullen worden te quantificeren, in het bijzonder de data die gefocust zijn op het meten van de tijdsafhankelijke variaties van het gravitatieveld.

Één bron van fouten is de achtergrond krachtmodellen die snelle massatransportprocessen beschrijven; een andere bron van fouten heeft te maken met het achtergrond statische gravitatieveldmodel. Deze modellen worden gebruikt om geofysische signalen te completeren die ontbreken of onjuist vertegenwoordigd zijn in de verzamelde satelliet gravitatiedata. Echter, deze modellen zijn gebaseerd op in-situ data die geen wereldwijde dekking kennen en dus lijden onder beperkte nauwkeurigheid (in het bijzonder in afgelegen gebieden). Terwijl de waarheidsget-

rouwheid van deze modellen continu verbeterd wordt, wordt de nauwkeurigheid van satellietdata ook steeds hoger met de huidige technologische en methodologische vooruitgangen. Het bepalen van het netto effect van deze tegenstrijdige ontwikkelingen is de voornaamste impuls om de propagatie van fouten in achtergrondmodellen naar schattingsmodellen te bestuderen.

Andere foutenbronnen vloeien voort uit de imperfecties van de sensoren aan boord van de satelliet, bijvoorbeeld de ranging sensor of wel de Global Navigation Satellite System (GNSS) ontvanger. De invloed van de sensorafwijkingen kan onderverdeeld worden naar de voornaamste onafhankelijke bijdragen, met bijbehorende frequentiebeschrijving, en verzameld worden in een gedetailleerde ruismodel. Het model voorspelt de effecten van i) de onnauwkeurige maar bekende baanposities, ii) de ruis in het intersatelliet metrologiesysteem, iii) de ruis in de aan-boord versnellingsmeters, iv) de incorrect-geschatte "Line-of-Sight" (LoS) niet-inertiaal versnellingen als gevolg van de afwijkingen in de radiale baansnelheden, en v) afwijkingen in de oriëntatie van de LoS vector. Het model is gevalideerd met behulp van Gravity Recovery And Climate Experiment (GRACE) a posteriori residuen, die vergeleken zijn met de output van het ruismodel gegeven een gesimuleerde GRACE missie. Dus, als de aannames die de sensor en modelnauwkeurigheden beschrijven aangepast zijn om die weer te geven voor toekomstige gravimetrische missies, is het redelijk om te verwachten dat dit ruismodel realistische afwijkingen voor die missies reproduceert.

Ook relevant is de analyse van de sensitiviteit van de data in termen van isotropie. Van de GRACE missie is geleerd dat de haast constante Noord-Zuid collineairiteit van de metingsrichting de data minder gevoelig maakt voor gravitatieveranderingen in de Oost- West richting. Alhoewel dit zelf geen formele fout is, versterkt de anisotripische datasensitiviteit de afwijkingen in de data.

De sensor- en modelafwijkingen zijn eerst gepropageerd naar de gravimetrische data en verder naar het gravitatieveld, in volledige simulaties van de cartwheel, trailing en slinger satellietformaties. De resultaten zijn geanalyseerd in termen van i) de waargenomen afwijking in het frequentiedomein en ii) de geschatte gravitatieveld modelafwijking in de frequentie- en ruimtelijke domeinen. Het afwijkingsbudget voor deze formaties zijn ook gekwantificeerd. De resultaten geven aan dat de slingerformatie zonder along-track verplaatsing het minst gevoelig is voor model- en sensorafwijkingen, in het bijzonder voor tijdsgerelateerde aliasing. Dit onderzoek onthult belangrijke beperkingen in het cartwheel missieconcept omdat de baanafwijkingen significant versterkt zijn door de diagonale componenten van de gravitatiegradiënt tensor, terwijl de slinger en trailing formaties uitsluitend beïnvloed worden door (kleine) niet-diagonale componenten. De ruimtelijke afwijkingspatronen leveren waardevolle aanwijzingen hoe de verschillende formatieopstellingen het beste te combineren zijn om de minimale anisotropie in de sensitiviteit van de verzamelde data te

produceren. De data van de slingerformatie laten enige anisotropische sensitiviteit zien maar de combinatie van zulke data met die van de trailing formatie, zoals de GRACE Follow-On (GFO), zou dit voordeel opheffen (alsook de lage nauwkeurigheid dicht bij de polen van de slingerformatie). In tegenstelling tot andere voorstellen voor dual-pair satellietmissies, zoals de Bender constellatie, zou de dual- trailing/slinger constellatie wereldwijde dekking bieden in het geval van de mislukking van één satelliet-paar en dichte tijdsbemonstering op hoge breedtegraden.

Bovendien is gedemonstreerd dat de data van gravimetrische missies significant gebaat zijn bij de toevoeging van data verzameld door talrijke niet-toegespitste satellieten. Op basis van de uitgevoerde simulaties wordt voorspeld dat de haalbare tijdsresolutie verbeterd is naar enkele dagen onder graad 10 en, essentieel, zonder een significant niveau aan aliasing in het tijdsdomein. Schattingen over langere periodes maken schattingen voor hogere graden mogelijk, met sterk gereduceerde tijdsaliasing verschijnselen in de resulterende gravitatiemodellen.

Samenvatting

Acknowledgements

The work described in this book would not be possible without the guidance and encouragement of Prof. Klees. He has driven me to steadily and continuously improve of my skills, for which I am truly thankful. I also thank Pavel Ditmar for his supervision over the years, his extensive expertise and his acute, but always useful and positive criticism. We have also shared many heated exchanges of opinions, frequently slipping into the domain of philosophy. His views and arguments were always very tricky to contest, which was something I always found to be very appealing. I also thank him for his patience and perseverance in giving rigorous feedback, which greatly improved the quality of the thesis.

I also appreciated the time spent with fellow colleagues from the PSG group, which made my working hours very pleasant and the frequent discussion ensured my knowledge deepened and broadened: Bas, Brian, Cornelis, Elena, Erna, Hassan, Jasper, Mark-Willem, Pedro, Réne, Riccardo and Xianglin.

On the ASM group, I was welcomed by many people, with whom I have developed a close working relation in the office and enjoyed many happy hours outside of it: Bart, Boudewjin, Dominic, Eelco, EJO, Erwin, Gunter, Haiyang, Hermes, Jacco, Jeroen, Jinglang, Jose, Luke, Mao, Marc, Ron, Sowmini, Svenja, Taco, Tatiana, Tim and Wouter. Special thanks go to Pieter, who, in more than one way, made the final stretch of this work possible. Finally, I cherish the fortune of the ever-present support and availability of Relly, something I am sure many of my colleagues are jealous of, since I benefited from it in both PSG and ASM groups.

An important part of this work was only possible because of friends and family, to which I sincerely owe a lot. It started long, long ago. My parents Mónica and Mário taught me right from wrong, told me about God and the good, warned me

Acknowledgements

Introduction

<div style="text-align: right">**1**</div>

The accurate and continued measurement of the movement of mass on the Earth's surface is important for the understanding the on-going global climatic changes. The recent variability of climatic patterns, the spread of arid regions and associated changes in the hydrological cycle and vigorous modifications in the ice coverage at polar regions have prompted the hypothesis of likely anthropogenic influence. As such, it is important to continue monitoring the Earth system in order to properly constrain and improve the geophysical and climatic models, so that a better understanding of the causes and consequences of climate change is gained. These models provide, in turn, the fundamental tools that allow society to understand its role and act in the most efficient way towards an equilibrium with the environment. This can only be done with data collected over many years, if not many decades, at the global scale, for which satellites are well suited.

1.1 Background

The gravitational field of the Earth is for the most part constant in time. The temporal variability is less than 0.001 % of the long-term mean. In spite of this, much can be learned about the underlying geophysical processes by monitoring those variations. Measuring changes in the gravitational field is equivalent to quantifying how much mass is in motion, with the notable exception of buoyant mass, such as icebergs. To accomplish this with any other type of observation is more difficult, if not impossible. The problem is that non-gravimetric observations can only be indirectly related to mass by using additional measurements or models, which are needed in order to close the observation equations. One example is satellite altimetry,

which measures the height of polar ice sheets with high spatial resolution and centimetre accuracy. However, without knowing the density depth profile of the ice and the underlying bedrock topography, there is no accurate way of determining the amount of ice under the exposed surface. The major drawback of gravimetric data is that they cannot distinguish vertical mass distributions, without prior knowledge about the density profile with depth. In spite of this, gravimetric data can be used to pin-point the location of sharp density differences, such as underground cavities or the Mohorovičić discontinuity, the boundary separating the Earth's solid crust from the viscous mantle. If an ice sheet is melting but the bed rock underneath is uplifting due to Glacial Isostatic Adjustment (GIA), gravimetric data do not give information about the ice mass balance alone. They describe the net effect of mass change.

The gravitational field at the global scale is mostly determined by measuring accurately the motion of gravimetric satellites. It can be done in the absolute sense when taking advantage of a Global Navigation Satellite System (GNSS) to continuously track the position of the satellite. This constitutes the high-low Satellite-to-Satellite Tracking (hl-SST) measurement principle. It can also be done in the relative term when at least a pair of satellites fly in formation and track each other, collecting low-low Satellite-to-Satellite Tracking (ll-SST) data. The third alternative, which is exceptional in the sense that is does not depend heavily on the motion of the satellite, is to measure the differential motion of pairs of proof-masses in a gradiometer. The satellites dedicated to measuring small gravitational signals are remarkable in many respects. These satellites have a solid structure that does not vibrate nor bend significantly, they contain no external moving parts and are equipped with extremely accurate sensors that collect high quality data. They need to orbit the Earth as low as possible in order to be closer to the Earth's surface where the movement of mass takes place. Additionally, the monitoring role of these satellites demand that they work continuously for years.

The knowledge gained from gravimetric satellite data goes far beyond the innate curiosity for the natural world. The measurement of the hydrological cycle has enabled the better understanding of the water cycle and the quantification of the extremes associated with drought and flood conditions. The accurate measurement of mass variation on polar areas has quantified the effects of climate change in those regions, as well as globally. The integrated contribution of shrinking ice sheets and many other mass transport processes has increased the accuracy of the predictions of sea level rise.

1.1.1 A dynamic Earth

In the Earth system there is movement of mass on a wide range of temporal and spatial scales. The post-glacial rebound, associated with the uplift of the crust after the end of a glaciation age in response to the melting of ice, is an example of mass transport process that takes places over large temporal and long spatial scales, namely several hundred kilometres and thousands of years. The movement of mass in the atmosphere, on the other hand, is much faster, with cycles lasting from hours to a few years, over spatial scales from tens to several thousands of kilometres. Some of the processes have sufficiently large influence on the Earth system to be measured from space, see Table 1.1.

Geophysical Process	Amplitude [m/s^2]		Spatial Scale [km]		Temporal Scale [yrs]	
	Min	Max	Min	Max	Min	Max
Atmosphere and Ocean	3×10^{-10}	7×10^{-9}	20	10000	1×10^{-3}	2
Hydrology	3×10^{-9}	2×10^{-7}	≈ 0	10000	2×10^{-2}	10
Glaciology	4×10^{-9}	4×10^{-7}	≈ 0	1000	8×10^{-2}	100
GIA	4×10^{-10}	4×10^{-8}	500	10000	10000	100000
Solid Earth[a]	9×10^{-9}	4×10^{-6}	≈ 0	2000	≈ 0	0.5

[a]Specifically co- and post-seismic mass changes associated with large earthquakes.

Table 1.1 – Overview of typical values for the amplitude (in gravitational acceleration) and spatial and temporal scales for the most significant mass transport processes occurring at the surface of the Earth. Source: Rummel (2005); Ilk et al. (2005); Sneeuw et al. (2005); Panet et al. (2012).

To the casual observer, the most visible geophysical mass transport processes occur in the atmosphere. The free surface of the ocean reacts to the changes in atmospheric pressure and the shear force from winds, creating currents. Determining how much mass is being moved around by the atmosphere and respective oceanic response is not trivial. Measurements are taken at discrete locations at the Earth's surface and that may not be sufficient to accurately reconstruct the whole process. To an orbiting satellite, the frequency with which it revisits a particular location is much lower than the frequency with which the atmospheric mass variations take place, so all measurements include a component which is impossible to reconstruct unequivocally. For this reason, it is important to consider the effect of rapid-changing atmospheric mass on the data collected by future gravimetric mission.

Anthropogenic activity is believed to be accelerating the current de-glaciation cycle of the Earth. One tool to determine the driving factor behind climatic changes

is gravimetric data resulting from continued monitoring, in view of the fact that it is one of the few accurate ways of estimating the mass balance of ice sheets.

During the Last Glacial Maximum (LGM), ice covered the surface of the Earth to much lower latitudes that it does today. Large quantities of water were trapped as ice, which meant that the sea level was at a lower height, exposing large patches of land. Over the dry surface at high latitudes, most notably northern Europe and Canada, the thick ice sheets created sufficiently strong loading on the crust to induce a downwards deformation. As the ice receded with the onset of de-glaciation, the crust was no longer under the ice-loading and it slowly bounced upwards in response. As a consequence of this crustal adjustment, there is movement of material in Earth's interior to balance the changes in surface height, to which the term Glacial Isostatic Adjustment (GIA) refers to. From satellite gravimetric data, it is possible to observe the gravity changes corresponding to this mass movement. GIA modelling is an important ingredient in determining the extent of which the ice sheets are melting and the corresponding sea-level rise.

One geophysical process that moves large quantities of mass is the water cycle. Water is taken from the ocean through evaporation and is dumped on land as precipitation. The water collects in storage basins, percolates through soil, evaporates back to the atmosphere or runs off to the ocean. The combined effect of all these processes occurring in large hydrological basins are visible from space. The challenge is to distinguish the Terrestrial Water Storages (TWSs) from neighbouring hydrological system and to be able to derive frequent accurate estimates. Apart from the better understanding of the water cycle, gravimetric data can expose the location where the depletion of water resources is under way, enabling local authorities to produce plans in anticipation and handle the situation more effectively.

The earthquakes that are readily measurable by gravimetric missions are those where there is a strong vertical movement of the crust (Han, 2006). Resulting from this motion is the rearrangement of mass within the lithosphere, in addition to changes in its density. Unfortunately, only the largest earthquakes of this kind are measurable but the larger sensitivity of future missions will likely improve this situation.

1.1.2 Observing a planet

Measuring the minuscule gravitational accelerations resulting from the mass transport processes taking place at or in the immediate vicinity the surface of the Earth from an orbiting satellite requires three crucial ingredients: i) a stable observing platform to collect high quality data, ii) state-of-the-art models that make it possible for

innocuous signals to be removed from the data and iii) apt processing techniques to distil the data into usable representations of the phenomenon under analysis.

The orbit of the spacecraft is mainly determined by the gravitational forces. The way through which gravimetric data are collected is by determining the (relative) motion of the satellite(s) as accurately as possible, or by the on-board gradiometer. The collected data do not discriminate between the various effects to which the sensor is sensitive to. Often, it is necessary to predict some signals and remove them from the data. For example, the gravitational tidal force exerted by the Moon is clearly visible in the data but is of no interest if the objective is to study mass transport processes. The same can be said for the tidal effects of the ocean and solid Earth, polar motion and relativistic effects. To clean the data of these innocuous signals, appropriate models are used to quantify them at every data point to subtract them from the data.

The data distributed by the ground segment processing infrastructure is the result of a long sequence of actions. The gravimetric sensors on-board the satellite capture the geophysical process and transform it into an electrical signal. An analogue-to-digital converter discretises the signals voltage and records it in the on-board computer, so that it can be downloaded to the ground segments data storage systems. These data, often called Level 0 (L0), are decoded from the compressed telemetry format in which they are sent from the satellites and saved in the so-called Level 1A (L1A) data, which represent the original data, except they do not require dedicated software to understand the telemetry format. In turn, these data are decimated, calibrated, corrected and attributed quality descriptors, resulting in the so-called Level 1B (L1B) data. The purpose of this procedure is to reduce the data size, calibrate the data and clean them of measurement errors, making it easier for the users of these data to process them and extract the information of interest.

The main stage of data processing aims at estimating a number of parameters that describe the gravity field model. The data collected by the satellite is transformed into suitable *observations*, which are then connected to the parameters of the gravitational field by means of mathematical relationships called *functional model*.

1.2 Motivation

The continued global monitoring of the Earth system is of paramount importance to understanding the role of mankind in the climatic changes observed in recent decades. It provides valuable data used to constrain climatic models that predict the environment in which future generations will live. Additionally, it facilitates the accurate forecasting of changes in the distribution of water resources and the

determination of the locations under threatened by sea-level rise. Satellite gravimetric data are in the for-front of the means through which these objectives are met. The clear understanding of the difficulties in measuring mass transport processes with gravimetric satellites is critical to the design of mission concepts that are able to provide the most accurate data.

Although gravimetric satellite data has revolutionized the knowledge of the Earth's system, a number of priorities for future missions have been identified. For example, Panet et al. (2012) and Reubelt et al. (2014) prioritize the study of ice sheet mass balance (together with GIA), ocean and sea-level rise, hydrology and post-seismic deformation. In terms of the study of ice sheet mass balance, higher spatial resolution would make it possible to i) distinguish the effects of GIA; ii) compare gravimetric data with other data types, such as satellite altimetry and iii) assimilate gravimetric data into climatic models. The quantification of ocean bottom pressure with the purpose of monitoring deep ocean circulation and the associated global heat transport balance is limited by the current spatial resolution. The hydrological studies would benefit greatly from increased spatial resolution of the estimated models, since the signals from different drainage basins are often too close together to be distinguishable in currently available gravimetric data. Panet et al. (2012) indicates that the currently available models are only able to resolve 18 % of the main drainage basins, while a factor of two improvement in spatial resolution would include 75 %. Finally, the study of earthquakes is currently limited to the largest events, at Mw ~ 9 (Tanaka and Heki, 2014) and models with higher spatial resolution would extent it to earthquakes of smaller magnitude (Mw 7-8).

1.2.1 Limitations of GRACE

The data gathered by Gravity Recovery And Climate Experiment (GRACE) (Tapley et al. 1996; Tapley 2004b), although of sufficient high quality to permit the advancement of the knowledge of mass transport processes in an unprecedented way (refer to Section 2.3), is not free from limitations. The information content of the data decreases with smaller scales, as a result of the corresponding smaller signal amplitude in combination with the increasing noise amplitude (Swenson and Wahr, 2006). The most accurate monthly GRACE models predict a cumulative geoid height noise amplitude at mm level at degree 60 (e.g. Dahle et al., 2014, Figure 4.5).

The signals which are not properly described by these models are related to fast temporal variations, such as those present in the atmosphere and associated oceanic response, as well as fast changes associated with hydrology and glaciology. These fast movements of mass on Earth's surface contribute to temporal aliasing, as discussed in Section 2.1 and are one of the main challenges for future gravimetric missions. In

the spatial domain, the errors in the data make it impossible to determine features of the gravitational field smaller than 300 km. This constitutes a limitation in the study of hydrology and glaciology, since variations within many storage basins, lakes and glaciers cannot be determined. The last limitation of the GRACE models results from the anisotropic sensitivity of the data. It affects both temporal and spatial resolution and is also identified as an issue to be mitigated as much as possible in future gravimetric missions.

Temporal aliasing

Early simulations studies predicted that the cumulative degree geoid height error would be approximately 0.1 mm at degree 60 (Kim, 2000; Han, 2004b), often known as the "GRACE baseline". It was assumed that K-Band Ranging (KBR) measurement noise was the dominant factor limiting the accuracy of the monthly models. In reality, after the launch of the GRACE satellite, a number of studies have shown that the error in the estimated models (and also in the measurements) is as much as 5 to 15 times larger, e.g. Schmidt et al. (2008a); Horwath et al. (2010); Bandikova et al. (2012); Ditmar et al. (2012). It was quickly understood that temporal aliasing and error sources other than KBR measurement noise were underestimated in pre-launch studies. This is supported by numerical studies demonstrating that improved sensor accuracy results in higher than expected errors in the recovered gravity field models in the presence of temporal aliasing (Wiese et al., 2009; Loomis et al., 2011). The initial assumption was the effect of temporal aliasing was proportional to the signal intensity, i.e. decreasing in magnitude with increased degree (Velicogna et al., 2001), but many studies proved otherwise (Thompson et al., 2004; Han, 2004b; Ray and Luthcke, 2006; Schrama et al., 2007; Zenner et al., 2010). In spite of this, Zenner et al. (2012); Ditmar et al. (2012) have shown that model errors are not sufficient to explain the errors in GRACE data.

The only effective procedure to minimize the effect of temporal aliasing, assuming the de-aliasing models are not perfect, is to increase the temporal sampling of the gravitational field. In this way, the short-period variations are properly characterized in the data and these variations are reconstructed. In practice, such large number of measurement satellite systems make it economically impossible to accomplish the higher sampling rate with dedicated gravimetric satellites. Under this consideration, most research focuses on proposing a limited number of satellite formation pairs, which, if positioned in carefully selected orbits (usually with different inclinations and repeat periods), produce combined data that is less sensitive to temporal aliasing (Bender et al., 2008; Wiese et al., 2011a).

Limited spatial resolution

The attenuation of the gravitational field is increasingly severe for the smaller disturbances, so that their measurement is limited by the accuracy of the sensors. Although the sensors on-board GRACE provide high-quality data, several limitations have been identified. Horwath et al. (2010) have lowered the error in the CNES/GRGS 10-days gravity field models (CNES/GRGS-10d) (Lemoine et al. 2007b; Bruinsma et al. 2010; Lemoine et al. 2013b) model by as much as 60 % by co-estimating attitude bias along with the gravitational field and orbit parameters. This research looked into the RL01 of L1B data; meanwhile, processing improvements have resulted in the RL02 L1B data, which does not show these issues in such a significant way. Recently, Bandikova et al. (2012) has uncovered unexplained systematic errors in these corrections attributed to the magnetic torquer, star cameras and KBR antenna calibration. Bandikova and Flury (2014) have also combined the L1A attitude data from the two star-trackers on-board the GRACE satellites in an optimal way, reducing the noise by a factor of 3 to 4 when compared with the official RL02 attitude data. Inácio et al. (2014) have identified harmonic and random errors in the attitude data, which corrupt the KBR antennas phase centre correction. The harmonic errors component reaches 18 % of the total errors in the optimally-filtered gravity field models and are higher when there are numerous gap in the attitude data. Peterseim et al. (2014) have investigated non-geophysical signals present in the accelerometer data, the so-called *twangs*, caused mainly by the activation of magnetic torquers and heaters, indicating that correcting for them would improve the resulting gravity field models in a small but non-negligible manner.

The strategies that make it possible to increase the spatial resolution all depend on a higher quality of the sensors involved in collecting gravimetric data. For this reason, the planned GRACE Follow On (GFO) (Sheard et al. 2012; Larkin 2012; Zaragoza 2013) will measure the inter-satellite distance (in the form of a biased range) with a laser ranging sensor (Dehne et al., 2009) and many other proposal assume the same type of ranging sensor (cf. Table 1.2). Additionally, the design of the formation satellites with the ranging sensor placed at the Centre of Mass (CoM) makes the ranging data insensitive to attitude errors (Cesare et al., 2010b).

Anisotropic data sensitivity

The most prominent artefact of the GRACE solutions is a pronounced north-south striping error pattern (Ramillien et al., 2005; Chen, 2005), which is strong enough to be dominant over the small-scale features, making it difficult to determine

mass variations at regional scales. This pattern is associated with the lower quality of the sectorial and near-sectorial coefficients in the spherical harmonic expansion of these solutions (Tapley et al., 2005). The reason for the large errors in these coefficients results from the ranging data being collected always in the along-track direction, i.e. predominantly aligned with the meridional (i.e. North-South) direction. Consequently, the GRACE data lacks East-West sensitivity (except near the poles), therefore having anisotropic sensitivity.

The anisotropic sensitivity of the GRACE data, by itself, is not the cause of the errors in the data. It only amplifies them, predominantly along the direction it is least sensitive to, i.e. the East-West direction, introducing fluctuations which are not of a physical nature. The errors in the GRACE data originate from measurement and processing imperfections. The measurement error has its source in the various sensors that collect the data. The processing errors are mainly caused by the imperfect models used to describe the forces acting on the spacecraft, i.e. often being referred to as *model errors*. After the Gravity field and steady-state Ocean Circulation Explorer (GOCE) mission and the associated improvement of the static gravity field models, these errors are mainly the result of temporal aliasing in ocean and atmospheric mass transport models.

To address anisotropic sensitivity of the GRACE data, there are numerous strategies. Some models limit the maximum order (e.g. Meyer et al., 2012b). It is also possible to post-process the estimated gravity field models so as to mitigate this error, e.g by exploiting the error covariance information (Kusche, 2007; Klees et al., 2008), resorting to empirical orthogonal functions (Schrama et al., 2007; Schmidt et al., 2008b; Wouters and Schrama, 2007) or by employing Gaussian filtering (Wahr et al., 1998; Guo et al., 2010, 2014). In all cases, it is unavoidable to have as a side-effect the dampening and/or distortion of the signal of interest.

Regarding future gravimetric missions, the study of different satellite formations has demonstrated that other formation geometries reduce considerably the anisotropic sensitivity of the collected data. Refer to Table 1.2 for an overview of the research done in this subject and also refer to Chapter 8 for a description of the possible formation geometries.

1.2.2   Limitations of future gravimetric mission proposals

There have been many studies on the topic of future gravimetric missions simulation. The current section describes some points in those studies with room for improvement. In contrast, Section 2.6 aims at discussing the concepts and particularities of the most visible and concrete mission proposals and measurement principles.

The proposed solutions for future gravimetric missions have so far focused on increased sensor accuracy (e.g. Silvestrin et al., 2012), minimizing the effect of errors in the background force models with a limited number of satellites (e.g. Elsaka et al., 2012), the previous two issues simultaneously (e.g. Massotti et al., 2013; Reubelt et al., 2014; Panet et al., 2012) or the immediate continuation of monitoring (Zaragoza, 2013).

In the simulation of future missions, such as the ones listed in Table 1.2, the simulation of the error time series typically neglects or over-simplifies the dependency of the error amplitude on frequency. This is particularly the case for the simulation of positioning noise, which is exclusively done with uncorrelated time series (although Sharifi et al. (2007) considered a short correlation length). In what concerns the simulation of the ranging sensor errors, the number of studies that consider correlated errors is higher.

Furthermore, the list of error sources is usually trimmed down to those that are seen as the most dominant, determined on the basis of the knowledge provided by the GRACE mission. That might be a reasonable approximation for mission concepts which have produced actual data. For future concepts, e.g. novel satellite formations, such assumption might not be valid, e.g. there is no assurance that an insignificant error source in proven missions remains so in different mission configurations. Referring to Table 1.2, it is obvious that important error sources are missing, such as the non-inertial accelerations acting on the Line of Sight (LoS) vector and the accuracy with which the attitude of this vector is measured.

Last but not least, none of the mission proposals provides the means to measure with sufficiently high sampling rate the rapid temporal variations in order to significantly mitigate the effect of the errors in the background force models. Efforts in this direction are usually restricted to the simulation dual satellite pairs, which cannot resolve daily variations in spite of improving considerably the temporal sampling. The measurement of (bi) daily variations is needed in order to reduce the temporal aliasing caused by atmospheric and non-tidal oceanic mass transport.

Table 1.2 – Overview of the research conducted on gravimetric satellite formations.

formation type(s)	ranging noise [nm/s/$\sqrt{\text{Hz}}$]	accelerometer noise [nm/s^2/$\sqrt{\text{Hz}}$]	positioning noise [cm][a]	temporal aliasing	mis-modelled static signal	reference
GRACE-type pendulum cartwheel LISA-type[b]	1000 STD		0.6[c]			Sharifi et al. (2007)
single, dual[d] GRACE-type single, double[e] cartwheel	$f^{-1}+5$ nm/$\sqrt{\text{Hz}}$	4×10^{-4f}		based on AOD1B		Wiese et al. (2009)
GRACE-type pendulum[g] cartwheel T-formation[h]	10 μm STD		1 abs. 0.1 rel.			Encarnação et al. (2008)
single[i], dual[j], quadral[kl] GRACE-type	1000 and 10 STD		1	Δ(FES2004, TPXO)		Visser et al. (2010)
dual GRACE-type[m]	5 nm/$\sqrt{\text{Hz}}$	0.01[f]	1	[n]		Wiese et al. (2011a)
GRACE-type pendulum cartwheel LISA-type[b] pendulum-3S[o]	$50/(2\pi f)$ nm/$\sqrt{\text{Hz}}$		1	[p]		Elsaka et al. (2012)
single, dual ΔM[q], dual $\Delta\Omega$[l] GRACE-type				Δ(GLDAS, LaD)		Elsaka (2013)
single, dual[r] GRACE-type single[s], dual[t] pendulum cartwheel helix[u]	$f^{-1}+50$[v] nm/$\sqrt{\text{Hz}}$	9.8		10 % AOD1B	Δ(EGM96, EIGEN-GL04C)	Elsaka et al. (2013)
single, dual[r] GRACE-type pendulum[s] cartwheel helix[u]	$f^{-1}+50$[v] nm/$\sqrt{\text{Hz}}$	0.003[w]		10 % AOD1B + Δ(EOT08a, GOT4.7)	Δ(EGM96, EIGEN-GL04C)	Reubelt et al. (2014)
pendulum single, dual[r] GRACE-type		$f^{-2}+0.01$[x]		SST-AUX-2		Murböck and Pail (2014)
GRACE-type pendulum cartwheel	10000 and 10 STD		1	Δ(FES2004, EOT08a)	Δ(EGM96, EIGEN-5C)	Zhao et al. (2014)

[a]3D RMS

[b]A combination of cartwheel with pendulum, without along-track displacement.

[c]Correlation length of 3 minutes.

[d]In the same orbital plane.

[e]With a total of 4 satellites in the same formation.

[f]From a Drag-Free Attitude Control Systems (DFACS).

[g]Without any along-track displacement between the satellites.

[h]Combination of pendulum and GRACE-type, i.e. a total of four satellites and two sets of range measurements.

[i]One with 125 revolutions over 8 nodal days, another with 79 revolutions over 5 nodal days.

[j]One with both pairs in polar orbits, the other with one pair in a polar orbit and the other pair in an orbit with 117.4° inclination.

[k]All four pairs in polar orbits.

[l]In planes with different values of right ascension of the ascending node.

[m]Different orbital inclinations.

[n] Δ(FES2004,GOT00)(ocean tides)+Δ(ECMWF,NCEP)(atmosphere)+Δ(OMCT,MOG2D-G)(ocean)+GLDAS(hydrology)+van Dam et al. (2008)(ice)

[o]Composed of 3 satellites, 2 of which in a GRACE-type configuration.

[p] Δ(EOT08a,FES2004)(ocean tides)+Δ(ECMWF,NCEP)(atmosphere)+Δ(OMCT,PPHA)(ocean)

[q]In the same orbital plane.

[r]One pair at an orbit with 89.5° inclination and another pair at an orbit with 63° inclination.

[s]220 km and 96 km along-track displacement combined with 25 km and 43 km maximum cross-track displacement, respectively.

[t]Both pairs in a polar orbit, one with along-track and cross-track maximum displacement of 166 km and another with 83 km.

[u]Similar to the LISA-type formation but with a 100 km along-track displacement.

[v]50 nm/$\sqrt{\text{Hz}}$+100/f(0.355$\rho^{\text{(avg)}}$/100km) nm/$\sqrt{\text{Hz}}$

[w]U-shaped PSD, measurement bandwidth is [1,100] mHz

[x]$\sim f^{-2}$ for $f<1$ mHz, includes ranging errors.

[y]GOCE HPF non-tidal dealiasing product.

11

1.3   Objectives and methods

The objective of the dissertation is to predict the accuracy of future gravimetric missions to observe geophysical mass transport processes occurring at the surface of the Earth.   The focus is on how sensor errors, mission concepts and errors in the background force models propagate to the errors in the observations and corresponding gravity field models. The previous and current gravimetric missions, although unquestionably a success, have uncovered deficiencies in the observation systems and unexpected data corruption.   Understanding and modelling these deficiencies is critical to devise strategies to mitigate and circumvent them in future missions. The methodology of inverting observations into gravity field parameters is not the object of analysis, since proven procedures are exploited.

For this reason, the thesis largely focuses on the accurate modelling of the aforementioned errors, so that the reliable and meaningful prediction of the error budget of future gravimetric missions can be assessed. A few design options for future gravimetric satellite formations are analysed. It is also demonstrated that dedicated gravimetric missions can benefit considerably from a constellation of non-dedicated Low-Earth Orbit (LEO) satellites with an on-board geodetic-quality GNSS receiver, i.e. gathering data of comparable quality to those in dedicated missions.

The conducted research focuses on the following aspects of data quality:

i. Minimizing the detrimental effect of **temporal aliasing**, caused by the rapid mass transport processes that are too fast to be recovered by satellite gravimetry data.   This introduces errors in the data because, in reality, the models that describe these processes have deficiencies in remote regions where no measurements are available to constrain them. Consequently, the gravimetric data are not perfectly cleaned of signals associated with rapid mass changes, leaving a residual signal that deceases the accuracy of the estimated gravity field parameters. The use of numerous non-dedicated satellite systems, in view of providing independent data with a very high temporal sampling, makes it possible to minimize the effects of temporal aliasing, as described in Chapter 5. Additionally, sensitivity to temporal aliasing of the co-called *cartwheel*, *pendulum* and *trailing* formations is quantified in Chapter 8.

ii. Improving the **accuracy of the predictions of future gravimetric data quality**. The use of accurate sensor error models and the proper modelling of errors in the background force models are ways to accomplish this. In the thesis, these aspects are addressed by considering the realistic noise characteristics of future sensors as well as estimating the influence of errors in the force models. In Chapter 6 the GRACE data is analysed in order to make it possible to

validate the noise model. Chapter 7 is dedicated to studying the positioning noise, which may become significant in view of the increased accuracy of other sensors in comparison to GNSS. In Chapter 8, the noise model is updated to reflect future sensor accuracies and is applied in the simulation of future gravimetric satellite formations.

iii. Understanding the limitations and strengths of different satellite formation geometries, in what regards the **anisotropic sensitivity of the data** (caused by the nearly-constant direction along which measurement are taken) and the **sensitivity to different noise types** (namely those arising from the orbit position noise). The anisotropic sensitivity of the data is a well-known problem of the GRACE satellites since they collect data mainly along the North-South direction (particularly away from polar regions), causing artefacts in the estimated gravity field models and making it more difficult to derive a precise description of geophysical processes. The relative influence of different noise types is particular to each satellite formation geometry and requires full-scale simulations to be derived accurately. Other studies (cf. Table 1.2) often ignore noise types resulting from orbit position noise, mostly because they are not severe in case of GRACE (if the data is high-pass filtered, refer to Section 2.5.6). Different mission concepts and the respective orbit configuration result in different error magnitudes and data sensitivity, which is investigated in Chapter 8, considering the full-scale inversions of error time series produced on the basis of a realistic noise model. On the basis of this understanding, **propose the best candidate formation geometry for a future gravimetric mission**.

1.4 Outline

The thesis is divided into 9 chapters, with the first 4 chapters setting the stage for the original contribution presented in the remaining chapters.

In the Chapter 2, the general concepts of satellite geodesy are discussed, namely temporal aliasing, the techniques used to measure Earth's gravitational field, including the GRACE mission and the state-of-the-art of satellite gravimetry.

Chapter 3 looks into satellite formations, which are used in the context of ll-SST observations. Different types of formations and the methodology needed to compute their orbits are presented.

Chapter 4 describes the functional model, background force models and noise models used in the thesis. This is a fundamental chapter to understand the methodology used in the simulations.

Chapter 5 looks into the added value to gravity field recovery of dozens of non-dedicated LEO satellites equipped with GNSS receivers. The large number of satellites, though collecting much less accurate data, are suitable to remove the effect of temporal aliasing and improve the accuracy of the estimated models.

In Chapter 6, the data of the GRACE mission are exploited to better understand the errors in processing ll-SST data. The accuracy of the orbits used in the processing of actual data is estimated, the magnitude of errors found in the data is quantified and the considered noise model is evaluated.

Chapter 8 looks into three generic candidates for a future ll-SST mission, with the objective of identifying the strengths and weaknesses of each concept.

Finally, Chapter 9 discusses the conclusions of the conducted research and puts forward suggestions for future work on this research topic.

Section 6.2 contain excerpts from Ditmar et al. (2012), used in the thesis with permission. Chapter 5 contains excerpts from Gunter et al. (2009b), used with permission.

Satellite gravimetry for monitoring mass transport in the Earth system

2

The task of predicting the accuracy of future gravimetric missions invariably starts from understanding problems in monitoring global mass transport processes of geophysical origin and recognising limitations of existing missions. The reasons why it is non-trivial to measure the time-varying gravitational field are firstly explained in Section 2.1. The way in which gravimetric measurements are gathered is the issue addressed in Section 2.2, explaining the main types of such observations. The knowledge of time-varying gravitational field has benefited greatly from the Gravity Recovery And Climate Experiment (GRACE) mission. For this reason, Section 2.3 aims at giving a brief overview of this mission, the advances based on its data and, most importantly, its limitations (in Section 1.2.1). The main reasons for the studies presented in the thesis can be traced back to this section. The discussion proceeds by an overview of the state-of-the-art of satellite gravimetry. In particular, the accuracy of the orbits derived from Global Navigation Satellite System (GNSS) data reported in literature is summarized in Section 2.4. The overview of some processing strategies is presented Section 2.5. Finally, a few concepts for future gravimetric missions are described, along with the expected improvements of the estimated gravity field models inSection 2.6.

2.1 Temporal aliasing in measuring mass transport processes

When the objective is to measure Earth's gravitational field with an orbiting satellite, the observation system is unavoidably sensitive to signals at various spatial and

temporal scales. In general, the shortest observable spatial scales are limited by the sensor accuracy, while the shortest temporal periods are limited by the period the satellite revisits the vicinity of a geographical location. On top of this, there is no possibility to discern between the underlying causes. The satellite measures the gravitational acceleration as the summation of the signals resulting from all physical processes taking place at a certain location on surface of the Earth and at certain time. Each of these processes has a particular spatial and temporal scale. While the satellite is away from that location, the variations of short periods continue without being measured. Those mass transport processes contribute with a signal that cannot be reconstructed from the data. As such, these signals distort the observable mass transport processes and act as noise in the data. To refer to this distortion, the term *temporal aliasing* is usually used. The shorter the estimation periods, the lower the effect of the under-sampled mass transport processes and, consequentially, the lower the effect of temporal aliasing (Encarnação et al., 2008).

2.1.1 Spatio-temporal resolution

Evidently the orbit configuration plays a role in the severity to temporal aliasing. Particularly, its mitigation requires frequent revisits to the same geographic location. The direct consequence of this requirement is that the ground track pattern exhibits large gaps, which limits the recoverable spatial resolution, making it unsuitable to be represented by the spherical harmonic coefficients above a certain degree. Some authors refer to this fact as the *Heisenberg uncertainty principle of spatio-temporal sampling* (Reubelt et al., 2010; Elsaka, 2013; Pour, 2013).

The following analysis illustrates the limitation in measuring sub-weekly mass variations by a single satellite system. If the orbit is chosen so that the ground tracks are homogeneously distributed over the equator, the revisit period $T^{(\text{revisit})}$ is dependent on the maximum degree $L^{(\text{max})}$ and the orbital revolution period $T^{(\text{rev})}$ as (Reubelt et al., 2010)

$$T^{(\text{revisit})} = 2\,T^{(\text{rev})} L^{(\text{max})}. \qquad (2.1)$$

However, the relation described above is conservative. On one hand, as indicated by Visser et al. (2012), only the observations of the type collected by GRACE follow this rule; other observation types that collect information along perpendicular directions, such as those collected by CHallenging Mini-Satellite Payload (CHAMP) and Gravity field and steady-state Ocean Circulation Explorer (GOCE), allow the gravity field parameters to be estimated to comparatively higher degrees (if one ignores the noise in the data). On the other hand, Weigelt et al. (2013b) demonstrates

that it is the maximum order, not degree, that is the limiting factor and even for one-dimensional type of observations the most relevant consideration is the unique equator crossings, related to the parity of the difference between the number of complete revolutions of the corresponding number of nodal days.

In any case, the relation given by (Reubelt et al., 2010) has the advantage of being simple and useful if one is interested in the most conservative scenario. Considering that the $T^{(\text{rev})}$ of Low-Earth Orbit (LEO) satellites is around 5000 s, the complete globe could be sampled once up, for example, to degree 26 in 3 days. Mass changes at the spatial scale smaller than 770 km or that occur with a period smaller than 6 days are impossible to measure. In any practical situation, the case is made worse by the fact that the ground tracks are not homogeneously distributed over the equator, or that happens only after a large number of revolutions.

There is, therefore, a trade-off between temporal and spatial resolution. As a consequence, if both spatial and temporal resolutions are to be improved, multiple satellite systems should be used (Reubelt et al., 2010). This is a fundamental characteristic of the recovery of Earth's gravitational field by satellites and imposes severe limitations regarding the minimum resolvable spatial wavelength or the minimum observable temporal cycle.

2.1.2 Mitigating temporal aliasing

The usual strategy to mitigate the effect of temporal aliasing in satellite gravimetric data is to subtract from them the high-frequency mass variations computed on the basis of models that are constrained by measurements gathered from other sources. Such models are usually called a *de-aliasing product*, e.g. Atmosphere and Ocean De-aliasing Level 1B (AOD1B) product (Flechtner et al. 2006; Flechtner 2007, 2011), and the correction for rapid mass variations is called *temporal de-aliasing*.

Model-based de-aliasing is not perfect, as a result of model deficiencies, errors in the data exploited to estimate model parameters or even conversion from meteorological parameters to spherical harmonics representing gravitational disturbances (Engels et al., 2012). These imperfections are particularly significant for the models describing the motion of atmospheric mass along with the corresponding ocean inverse-barometer response and, to a lesser extent, the tidal displacement of the oceans due to lunar and solar gravitational pull (Zenner et al., 2010; Ray and Luthcke, 2006; Han, 2004a; Seo et al., 2008). The de-aliasing process will not completely remove the high-frequency signals. The effect of the de-aliasing model error in the estimated gravitational field solutions is also called *temporal aliasing*.

To mitigate the effects of temporal aliasing, several approaches are available. The so-called *Wiese-approach* (Wiese et al., 2011c) takes advantage of low degree

models estimated over short-periods (one or two days) to act as de-aliasing product for the estimation of gravity field models over longer periods (19 days in Wiese et al. (2011c)). Another possibility that is conceptually similar but more robust relies on the estimation of daily solutions constrained by temporal covariance derived from geophysical models (Kurtenbach et al., 2009; Mayer-Gürr et al., 2012; Kurtenbach et al., 2012). In other words, the daily solutions are not independent of each other; they are constrained to the way the gravitational field "usually" changes and updated on the locations where the observations of that day have been collected. An alternative techniques to mitigate temporal aliasing relies on a time-varying parametrisation of the gravity field parameters. This approach is very computationally expensive in view of a large number of parameters to be estimated. Furthermore, the number of time-related parameters is tied to the number of space-related parameters, so that it is only possible to describe smooth changes in the gravitational field if the resulting model describes spatial features small enough to represent interesting time-variable mass transport processes, cf. Table 1.1.

The isotropic sensitivity of the collected gradiometric data plays a role in temporal aliasing. Isotropic data sensitivity means that the associated errors are not more or less severe along a preferential direction, so that the resulting gravity field model errors are homogeneous along orthogonal directions in the spatial domain. Wiese et al. (2011c) demonstrates that anisotropic measurements are more sensitive to temporal aliasing. Consequentially, improving the isotropic sensitivity of the data, along with the direct benefits, also has the welcome advantage of decreasing the effects of temporal aliasing.

2.2 Measuring Earth's gravitational field from satellites

The study of the Earth's gravitational field with satellites emerged soon after the launch of the first artificial satellites in the end of the 1950's. The first data collected from these early satellites was either optical, using sensitive cameras, or the Doppler shift of the transmitted radio signals (Seeber, 2003), from which the lower degrees of the spherical harmonic coefficients representing Earth's static gravitational field could be estimated (Merson and King-Hele, 1958).

Presently, gravimetric satellites are equipped with dedicated sensors that provide data allowing their orbital position to be known with centimetre accuracy. The tracking data are either ground-based, as is the case of Satellite Laser Ranging (SLR) (Smith and Turcotte 1993; Combrinck 2010) and Doppler Orbit Determination and

Radio-positioning Integrated on Satellite (DORIS) (Dorrer et al. 1991; Barlier 2005; Willis et al. 2006) or space-based if exploiting a GNSS. In case of ground-based systems, the tracking information is only available close to the locations where a SLR station or a DORIS beacon is located and is generally not suitable for the estimation of Earth's gravity field parameters globally, except for the variations of the lower spherical harmonic degrees over long periods of time, e.g. Bianco et al. (1998) and Cox et al. (2004). In case of GNSS, a constellation of GNSS satellites continuously emits radio signals containing all necessary information for a receiver to determine its location, providing the opportunity for global coverage.

The high-low Satellite-to-Satellite Tracking (hl-SST) and low-low Satellite-to-Satellite Tracking (ll-SST) observation types are described in detail in the following sections. The Satellite Gravity Gradient (SGG) observations are also addressed for completeness although they are not relevant to the remaining chapters of the thesis. Together with the measurement principles, the main sensors associated with them, i.e. GNSS receivers, the ranging sensors and the accelerometers, respectively, are also discussed.

2.2.1 high-low Satellite-to-Satellite Tracking

The high-low Satellite-to-Satellite Tracking (hl-SST) measurement principle exploits the tracking signals being continuously emitted from GNSS constellation(s). The foremost example of a satellite gravimetric mission producing hl-SST observations is the CHallenging Mini-Satellite Payload (CHAMP) (Reigber et al. 1996, 2002) satellite.

Each GNSS satellite broadcasts its ephemerides, the accurate time of when the signals are sent and the necessary corrections for the receiver to be able to synchronise its clock to the Global Positioning System (GPS) time. With this information, the receiver is capable of determining its range to the GNSS satellite. In the field of GNSS data processing, this range is often called *pseudo-range*, owing to the fact that the range is calculated as the product of the speed of light with the time the signal took to reach the receiver and that there are timing errors. In conjunction with the pseudo-ranges of at least four GNSS satellites, the three-dimensional (3D) location of the receiver can be determined. These are called *code* measurements and provide a real-time estimate of the satellite's position, with a few meters accuracy. The more accurate *phase* measurements result from measuring the fraction of the phase of the carrier frequency of the code observations, after resolving for fractions of the wave-length (or, in some cases, integer wave-lengths), in a process called *ambiguity resolution*. The phase observations permit the distance between the receiver and the GPS satellites to be estimated with centimetre accuracy but their real-time

processing, although only needed for some applications, produces orbits that are roughly a factor of 10 less accurate that the orbits produced with traditional ground processing Montenbruck et al. (2012).

According to Newton's second law, it is possible to determine the total force acting on a satellite from its acceleration, which is inferred from the observed motion. The total force consists of gravitational and non-gravitational forces, also referred to as conservative and non-conservative forces. In LEO, the non-gravitational forces are composed mainly of atmospheric drag, solar radiation pressure, Earth albedo and infra-red radiation pressures. In order to consider the effect of non-gravitational forces, there are several options. The non-gravitational forces can be modelled and corrected; another possibility is to co-estimate drag and radiation pressure force coefficients along with the parameters defining the gravitational field. Another way is to measure the non-gravitational accelerations by means of an on-board accelerometer, as is the case with all gravimetric satellite missions.

Earlier investigations by Ditmar et al. (2007) into the refinement of (static) gravity field models from the CHAMP mission discovered that by properly accounting for the presence of correlated noise in the data, i.e., by using Frequency-Dependent Data Weighting (FDDW), the on-board accelerometers become essentially unnecessary. In short, the gravity field models computed from CHAMP could be derived entirely from the accelerations obtained from the on-board GNSS receiver. Further numerical studies (Ditmar et al., 2008) supported the conclusion that the effects of non-gravitational accelerations acting on the satellite are not the limiting factor in determining gravity field models. As a result, satellites that exploit hl-SST observations are not required to have an on-board accelerometer, only a GNSS receiver and an attitude determination/control system is needed. Note that the satellite attitude is required in order to derive the motion of the spacecraft's centre of mass, given the measured position of the GNSS receiver antenna.

Temporal variations of the gravitational field have been estimated solely from hl-SST data. For example:

- Zhu et al. (2004) have produced gravity field models up to degree 20 every 1.5 days based on hl-SST data from the GRACE and CHAMP missions, with the orbit accuracy improved with the addition of accelerometer and K-Band Ranging (KBR) data (the latter in case of GRACE and only for Precise Orbit Determination (POD));
- Hwang et al. (2008a) have produced a gravity field model up to degree 25 from one month of FORMOSAT-3/COSMIC (F3C) hl-SST data;
- Lin et al. (2012) has produced monthly gravitational field solutions up to degree 5 based on Kinematic Orbits (KOs) from the GRACE and F3C missions;

- Weigelt et al. (2013a) have computed monthly gravity field models from CHAMP data up to degree 10, from January 2002 to December 2009, and demonstrating that it is possible to estimate accurate mass-change trends in Greenland and
- Bezděk et al. (2014) computed satellite-specific monthly models up to degree 10 with hl-SST data gathered by CHAMP and GRACE.

It is unlikely that hl-SST data are sensitive degrees higher than $20 - 30$ since the associated gravitational disturbances have a lower amplitude than the errors of the orbits computed from GNSS data.

The largest advantage of the hl-SST measurement principle is that it requires a small set of sensors: a GNSS receiver and an attitude measurement system. Nowadays, this set of sensors is almost universal in LEO satellites. Examples are: FORMOSAT-3/COSMIC (F3C) (Kuo et al. 1999, 2005), FORMOSAT-7/COSMIC-2 (F7C2) (Ector et al. 2010; Cook et al. 2013), the Meteorological Operational satellite programme (MetOp) (Edwards and Pawlak 2000) satellites and Iridium Next (Gupta, 2008) (to name a few). As such, there is potentially a high density of hl-SST observations, both in the spatial and temporal sense, which make these large sets of hl-SST data less sensitive to temporal aliasing and particularly suitable to derive low-degree (up to degree 10 to 20) high-frequency (daily) gravity field models, see Chapter 5. These models are particularly suitable as de-aliasing products in the processing of more accurate data collected from dedicated gravimetric missions.

The disadvantage of hl-SST observations is their low accuracy, in comparison to other measurement principled. This limitation is associated with the quality of GNSS data, from which orbits are derived with an accuracy no better than a few centimetres (refer to Section 2.4 for more details on this issue), in spite of the millimetre-level precision of the carrier phase observations. Furthermore, accelerations derived from hl-SST data are corrupted with high-frequency noise. As a consequence, the gravity field models estimated from hl-SST data have typically a lower maximum degree than other observation techniques.

2.2.2 Satellite gradiometry

The Satellite Gravity Gradient (SGG) observation principles relies on the differential measurement of the gravitational acceleration at two distinct but neighbouring locations. To accomplish this, the gradiometer is composed of a rigid structures supporting (one or more) pairs of accelerometers, placed symmetrically with respect to the Centre of Mass (CoM) of the satellite. The accelerometers pairs are under the influence of the gravitational field in difference places and, as a result, their proof-

masses are under the influence of slightly different gravitational forces. Therefore, the data in the *differential mode* contain, in addition to centrifugal accelerations, the measured gravity gradients. The non-gravitational effects cancel out in this mode because the non-gravitational forces influence the motion of the spacecraft, to which both accelerometer are rigidly attached. In practice, however, the imperfect calibration of the gradiometer due to minute misalignments of the accelerometer axes during construction causes the non-gravitational accelerations to leak into the SGG differential mode data. The gradiometer is also delivers *common mode* data, in which case the accelerometer measurements in opposing pairs are averaged. Consequentially, the measured gravitational and centrifugal accelerations cancel each other since they are equal in absolute value and of opposite sign.

The main advantage of SGG data is that they have isotropic sensitivity. Additionally, the redundancy of the measurements, i.e. six 3D accelerometers measuring five independent components of the gravity gradient tensor, in conjunction with the isotropic nature of the measurements allows the gravity field model to be computed up to a higher degree at shorter estimation periods, in comparison to other measurement principles (Anselmi et al., 2010). This is because the five independent measurements increased the numerical stability of the gravity field parameters estimation, decreasing the influence of coverage gaps, e.g. on the poles due to a non-polar orbit or in the rest of the globe due to short repeat period of the orbit (Visser et al., 2012). For these reasons, SGG data are very attractive to estimate short-period (sub-weekly to daily) gravity field models, which are suitable for de-aliasing purposes.

High quality SGG data is technically demanding. GOCE's gradiometer contains extremely accurate accelerometers and a very stable structure to support them. It is encapsulated in a thermally-controlled environment, to ensure a high thermoelastic stability of the structure and to limit temperature-dependent variations on the accelerometer's measurements. Additionally, the attitude of the spacecraft needs to be measured with a very high accuracy, so that the angular accelerations can be removed from the differential acceleration measurements.

In addition, technical limitations in accelerometers make the gradiometer of GOCE unsuitable to measure the long-wavelength features of the gravitational field. According to Marque et al. (2008), the accelerometer that compose GOCE's gradiometer have an error spectra that is, in spite of the thermal control, dominated by the thermal sensitivity of the measurement bias at the low-frequencies. Additionally but to a lesser extent, the gold wire responsible for continuously maintaining the proof masses in neutral charge introduces damping in the proof-mass feedback control loop, decreasing the accuracy of the measurements at low-frequencies.

The accelerometers are also used in non-SGG gravimetric satellite missions. They typically contain a proof mass that is suspended at the centre of the device by means

of a restoring electrostatic force. This force is generated by electrodes on the sides of the proof mass cavity. In case of capacitive accelerometers, such as those on-board the CHAMP, GRACE and GOCE satellites, the capacitance between the proof mass and the electrodes provides the input necessary to control the voltage to be applied to the electrodes in order to create the restoring electrostatic force (Marque et al., 2008). As a results, the non-gravitational forces acting on the spacecraft are equal to the electrostatic force. The voltage applied to the electrodes constitutes the corresponding measurement exploited in gravimetric data processing.

The accuracy of the accelerometers used in gravimetric missions is often referred to as *resolution*. This is because the measurements have high internal accuracy (precision) but require calibration in order to derive observations with a useful physical meaning. The measured electrode voltages are translated into accelerations by a scale factor and a bias, with the largest variations occurring in the latter, although slowly with time (Helleputte et al., 2009). In addition, the assembly of the accelerometers and their integration in the spacecraft is not perfect, resulting in errors from the non-orthogonality of their axes and misalignments with respect to a pre-defined reference frame. These errors are measured after launch, since the accelerometers can only operate accurately in a micro-gravity environment, resulting in the so-called *inverse calibration matrices* in case of the GOCE satellite Siemes et al. (2012). The calibration of accelerometers is a vast research topic, see e.g. Bruinsma et al. (2004); Tianhe and Yuanxi (2005); Bezděk (2010). Recently, Lenoir et al. (2013a,b) proposed to mitigate the accelerometer bias by mounting the accelerometer on a rotating platform, the so-called *Bias Rejection System*. It rotates with a modulated (i.e. pre-defined time-varying) angular velocity, so that the centrifugal acceleration can be exploited to calibrate the accelerometer.

The capacitive accelerometers on-board gravimetric missions are very sensitive instruments. According to Touboul et al. (2012) and Marque et al. (2008), the STAR accelerometer of CHAMP has an error STandard Deviation (STD) equal to 3×10^{-9} m/s^2, the SuperSTAR accelerometers of GRACE produce measurements with 10^{-10} m/s^2 error STD (although Frommknecht et al. (2006) reports 3×10^{-10} m/s^2 and Flury et al. (2008) specifies less than 10^{-10} m/s^2) and GOCE's GRADIO accelerometers introduce noise in the data with a STD equal to 3×10^{-12} m/s^2 over the measurement bandwidth from 0.5 mHz to 100 mHz (Christophe et al., 2010).

2.2.3   low-low Satellite-to-Satellite Tracking

The low-low Satellite-to-Satellite Tracking (ll-SST) measurements require that the involved satellites fly in formation, which is to say that they remain close to each other at all times. Under these conditions, on-board tracking sensors have the opportunity

to continuously measure the distance between the satellites very accurately. This is the measurement principle of the Gravity Recovery And Climate Experiment (GRACE) (Tapley et al. 1996; Tapley 2004b) mission.

The same type of sensors is not suitable for hl-SST because they are generally highly directional. The GNSS satellites that make it possible to gather hl-SST data are placed at a high altitude orbit. There two main reasons for this choice: the gravitational and non-gravitational accelerations are more predictable at those altitude and, important to the current discussion, the tracking signals can be directed to the complete globe and LEO with the limited view angle of roughly 45 degrees. In comparison, the instruments responsible for ll-SST have an angular beam width of a few degrees. The narrow tracking beam makes it possible to exploit high-frequency electromagnetic signals for ranging purposes. In general terms, higher signal frequency produces more accurate data but more power is required to emit the signal. In case of GRACE, the gravimetric mission that first exploited ll-SST data, the ranging sensor emits signal in the K-band, at 24 and 32 GHz. The GPS tracking signals, on the hand, operate in the L-band, at 1.2 and 1.5 GHz. Future ll-SST gravimetric mission have been proposed to use LASER in infra-red band, at around 200THz (Sheard et al., 2012).

The success of the GRACE mission is the direct result of the extremely accurate K-Band Ranging system and the resulting high quality ll-SST data. It makes it possible to measure the distance between the satellites with an accuracy of around $1\,\mu$m (Biancale et al., 2005; Frommknecht et al., 2006). This remarkable accomplishment, considering that the satellites are travelling at 7.5 km/s at the distance of around 200 km from each other, resorts to the Dual One-Way Ranging (DOWR) concept. Each one-way ranging sensor measures the carrier phase of the other instrument and subtracts it from the internal reference phase, resulting in two so-called *one-way phases* measurements. The *dual one-way phase* measurement is the sum of the two one-way phases, which benefits from the fact that the phase noise in the one-way phases has not changed significantly over the time of signal propagation, less than 1 ms, thus mostly cancelling it. Evidently, high-frequency phase noise occurring at periods less than 1 ms is still present in the measurements but does not play a significant role. Another source of measurement error results form the ionospheric signal propagation delay, which is mitigated by using two carrier frequencies, much in the same way as the ionosphere-free combination of double-frequency GPS observations (Kim and Lee, 2009). The internal oscillator of both satellites is disciplined by the GPS clock corrections, effectively keeping the clocks in both satellites within 10^{-10} s of each other. A feature of this concept is that the range measurements are known up to an unknown bias, which changes when the carrier phase lock is lost, as a result of (e.g.) sudden changes in the attitude of the

spacecraft or obfuscation by direct sunlight. On the other hand, the range-rates, i.e. the time derivative of the ranges, are measured directly and do not require such pre-processing

The accuracy of the KBR system does not translate directly into the accuracy of the measured distance between the GRACE satellites. The microwave horn antennas are located on the front and rear surfaces of the trailing and leading satellites, respectively. Consequently, they measure the distance between these two surface. In order to derive the distance between the CoM of the two satellites, the *antenna phase centre correction* has to be applied. This correction is mostly related to the attitude of the satellites, which can be such that the CoM is not exactly aligned with the direction connecting the two microwave antennas.

Unlike hl-SST where multiple GNSS satellites provide opportunity for multiple segmented range measurements, there is only one range measurement. The main consequence is that the measurements are taken along one single Line of Sight (LoS) direction and, depending on the geometry of the formation, this direction may be roughly constant in the Local Orbital Reference Frame (LORF, Section A.4). Therefore, the resulting gravimetric measurement is taken strictly along the LoS direction and is, therefore, insensitive to changes in the gravitational potential along perpendicular directions. This lack of sensitivity along all directions is referred to as *anisotropic sensitivity of the data*. In case of GRACE, this issue is further discussed in Section 1.2.1.

Another disadvantage of the ll-SST concept is that the tracking signal has to be emitted with a constant frequency and the received signals need to be compared with the stable internal oscillator, increasing the technical complexity. Additionally, it is mandatory to include an accurate accelerometer in order to measure the non-gravitational forces which would otherwise be indistinguishable from the gravitational ones.

As for advantages, the ll-SST data allows for the gravity field models to be determined with very high accuracy; in case of GRACE the mid to long wavelengths (below degree 70). Unlike the SGG data, the ll-SST data depicts accurately the long wavelength features of the gravitational field, making it possible to measure the temporal variations of the gravitational field with very high accuracy. The small features of the gravitational field, however, are limited by the accuracy of the ranging sensor, since these errors are dominant at the high frequencies.

2.3   The GRACE mission

Since its launch in 2002, the Gravity Recovery And Climate Experiment (GRACE) (Tapley et al. 1996; Tapley 2004b) has been measuring the temporal variations of Earth's gravitational field with extremely high accuracy. The two twin satellites that constitute the measuring system fly in a leader/follower formation, also known as a *trailing* formation. The two near-polar orbits have nearly the same orbital planes and the satellites fly with a nearly-constant 200 km along-track distance between them, at 500 km altitude. The KBR system makes it possible to measure the distance between the satellites with an accuracy estimated to be of a few micrometers. The satellites are also equipped with accelerometers to measure non-gravitational forces, making it possible to accurately remove them from the measured inter-satellite acceleration at the stage of data processing.

   Prior to the launch of the GOCE satellite, the GRACE data was the preferential source of data for static gravity field recovery. On the basis of these data, many models were computed, namely the ones listed i.a. in Table 2.1.

2.3.1   Contribution of GRACE to the advances in modelling the time-variable gravitational field

The high quality data gathered by the GRACE satellites makes it possible to measure the movement of mass on the surface of the Earth described in Section 2.1, down to spatial scales of a few hundred kilometres and temporal scales of sub-monthly to monthly. The temporal gravity field models produced from GRACE data are listed i.a. in Table 2.2, which in combination with Table 1.1 illustrates the observable geophysical signals. The most important signals present in the GRACE data are related to hydrological and glaciological processes, as well as Glacial Isostatic Adjustment (GIA).

   It is possible with GRACE models to monitor hydrological processes and determine the availability of water as resource. The large number of publications illustrated in Table 2.3 attests not only the importance of gaining a better understanding of the water cycle but also the fruitfulness of the GRACE data to this purpose.

   The understanding of other geophysical processes has also benefited from GRACE data. The data is also used to study the processes shown in Table 2.4, most notably the determination of the depletion of ice mass at high latitudes and the application of these data to sea-level rise studies.

   The publications listed in Tables 2.2, 2.3 and 2.4 intends to summarise the contributions of the GRACE mission to the understanding of mass transport processes

Model name	Max. Deg.	SLR[a]	CHAMP hl-SST[a]	GRACE ll-SST[a]	GOCE grad.[a]	Other Data	Reference(s)
GGM02	360	–	–	0.99	–	high-frequency information from EGM96	Tapley et al. (2005)
EIGEN-CG03C	360	–	2.36	1.05	–	altimetry, terrestrial gravimetry	Förste et al. (2005)
GGM03	360	–	–	4.00	–	altimetric mean sea surface, terrestrial gravimetry	Tapley et al. (2007)
EIGEN-GL04C	360	3	–	3.41	–	altimetry, terrestrial gravimetry	Förste et al. (2008b)
EGM2008	2190[b]	–	–	4.5	–	altimetry, terrestrial gravimetry	Pavlis et al. (2008)
EIGEN-5C	360	6	–	5.33	–	altimetry, terrestrial gravimetry	Förste et al. (2008a)
ITG-GRACE2010s	180	–	–	7.0	–	–	Mayer-Gürr et al. (2010)
AIUB-GRACE03S	160	–	–	6.25	–	–	Jäggi et al. (2011a)
GOCO02S	250	5	8	7.5	0.66	–	Goiginger et al. (2011)
DGM-1S	250	0	0	6.83	0.83	–	Farahani et al. (2013b)
GOCO03S	250	5	8	7.5	1.5	–	Mayer-Gürr (2012)
EIGEN-6C	1420	6.5	–	6.5	0.55	high-frequency information from DTU10 (Andersen, 2010)	Shako et al. (2014)
EIGEN-6C2	1949	15	–	7.75	0.96	high-frequency information from DTU12 and EGM2008	Förste et al. (2012)
EIGEN-6C4	1949	15	6.5	9.6	3.5	high-frequency information from DTU12 and EGM2008	Förste et al. (2014)

[a]Data period in years, not necessarily contiguous.
[b]The maximum order is 2159.

Table 2.1 – Overview of the main static gravity field models derived from GRACE data.

at the Earth's surface. It is not a complete list; for that the interested reader is directed to the web page grace.jpl.nasa.gov/publications.

In spite of the revolutionary and numerous advances in the understanding of mass transport processes at Earth's surface, the GRACE data has some critical limitation, as discussed in Section 1.2.1, that constitute one of the main motivations for the

Model name	Max. Deg.	Period	Validity		Particularities	Reference(s)
GSFC-mfs	60	monthly	Jul 2003	Jul 2004[a]	More accurate than contemporary official L2 products	Luthcke et al. (2006a)
ITG-GRACE2010	40[b], 120[c]	daily and monthly	Aug 2002	Aug 2009	Modelled temporal correlations constrain the daily solutions [d]	Kurtenbach et al. (2009)
JPL-R05	60, 90	monthly	Apr 2002	present	Formulated as MasCons[e], official GRACE L2 product	Watkins and Yuan (2012)
AIUB	60[f]	monthly	Jul 2003	Dec 2009[g]	–	Meyer et al. (2012b)
CNES/GRGS-10d	80	10 daily and monthly	Jan 2003	Dec 2012[h]	–	Lemoine et al. (2007b); Bruinsma et al. (2010); Lemoine et al. (2013b)
DMT	120	monthly	Feb 2003	2011	Available as both unconstrained and optimally filtered solutions	Liu et al. (2010); Ditmar et al. (2013)
GFZ-R05	90	weekly and monthly	Jan 2003	present[i]	Official GRACE L2 product	Dahle et al. (2013)
CSR-R05	96	monthly	Apr 2002	present	Official GRACE L2 product	Kruizinga (2014)

[a]Except January 2004.
[b]Daily solutions
[c]Monthly solutions
[d]Monthly solutions use daily solutions for de-aliasing, in addition to the AOD1B model.
[e]Mass Concentration (MasCon) approach (Rowlands et al. 2005; Lemoine et al. 2007a)
[f]Maximum order is 45.
[g]Except November 2003, January and November 2004
[h]Except June 2003, January 2011 and October 2012.
[i]Except June 2003, January 2011, June 2011, May 2012, October 2012 and March 2013.

Table 2.2 – Overview of the main temporal gravity field models derived from GRACE data.

research described in the thesis.

Geographical location	Research subject[a]	Reference(s)
South-western India	anthropogenic ground water depletion	Rodell et al. (2009)
Bengal Basin		Shamsudduha et al. (2012)
South-western China	drought events	Tang et al. (2014)
China		Zhao et al. (2010b)
Yangtze River basin	modelling, evapo-transpiration estimation	Corbari et al. (2014)
Siberia		Vey et al. (2012)
Aral Sea, Central Asia		Singh et al. (2013)
Central Asia		Dapeng et al. (2014)
Asia Minor		Lenk (2013)
Middle-East	anthropogenic ground water depletion	Joodaki et al. (2014)
Tigris-Euphrates and Lower Nile basins		Longuevergne et al. (2013)
Europe	modelling, drought monitoring	Li et al. (2012)
North America and Scandinavia		Wang et al. (2012a)
Great Lakes, North America		Huang et al. (2012)
North America	modelling, drought detection	Houborg et al. (2012); Sun (2013)
North America		Swenson (2003)
Great Plains, USA		Longuevergne et al. (2010)
Western Kansas, USA		Wang et al. (2013)
Mississippi River basin, USA		Rodell et al. (2006)
Southern USA	drought events	Long et al. (2013)
South America		Ramillien et al. (2012)
Amazon river basin	drought events	Chen et al. (2009b)
Amazon river basin		Papa et al. (2013)
Nile Basin		Awange et al. (2014)
Africa		Hassan and Jin (2014)
West Africa	modelling, ground water storage prediction	Forootan et al. (2014)
East Africa		Becker et al. (2010)
Zambezi river basin		Winsemius et al. (2006); Klees et al. (2007)
Southern Mali, Africa		Henry et al. (2011)
Lake Naivasha, Kenya		Awange et al. (2013)
Australia		Seoane et al. (2013)

[a]An empty entry means ground water monitoring.

Table 2.3 – Overview of the application of GRACE data in hydrological studies.

Geographical location	Geophysical process	Reference(s)
Sumatra-Andaman earthquake	Seismology	Han (2006); Li and Shen (2012); Wang et al. (2012b)
Tohoku-Oki earthquake	Seismology	Yong-zhi et al. (2011); Fuchser and Ward (2013)
Okhotsk earthquake[a]	Seismology	Tanaka et al. (2015)
Maule earthquake	Seismology	Heki and Matsuo (2010); Han et al. (2010)
Large earthquakes[b]	Seismology	Tanaka and Heki (2014)
Antarctica and Greenland	Glaciology	Cazenave (2006); Velicogna (2009); Ramillien et al. (2006); Groh et al. (2014); Velicogna et al. (2014)
Greenland	Glaciology	Baur et al. (2009); Harig and Simons (2012); Schrama et al. (2011); Svendsen et al. (2013); Luthcke et al. (2006b); Slobbe et al. (2009); Siemes et al. (2012); Chen et al. (2011); Chen (2006); Baur et al. (2012); Wouters et al. (2008); Schrama and Wouters (2011); van Angelen et al. (2013)
Antarctica	Glaciology	Chen et al. (2008a); Sasgen et al. (2007); Földváry (2012); Chen et al. (2009a); Gunter et al. (2009a); Bouman et al. (2014); Horwath and Dietrich (2009)
Canada	GIA	Tamisiea et al. (2007)
Fennoscandia	GIA	Steffen et al. (2008)
Antarctica and Greenland	GIA	Barletta et al. (2008)
Canada and Fennoscandia	GIA	van der Wal et al. (2011)
Western Antarctica	GIA	Groh et al. (2012)
Tibetan Plateau	GIA	Zhang and Jin (2013)
Global	GIA	Wu and Wang (2008); Wu et al. (2010)
Global	Geo-centre motion	Argus (2012); Roy and Peltier (2011); Swenson et al. (2008); Kang et al. (2009)
Global	Ocean circulation	Chambers and Schröter (2011)
Global	Sea-level rise	Jacob et al. (2012); Riva et al. (2010); Wouters et al. (2011); Baur et al. (2013); Ivins et al. (2013); Spada and Galassi (2012); Spada et al. (2013); Cazenave et al. (2009); Llovel et al. (2010); Woodworth et al. (2011); Vergos et al. (2012); Lombard et al. (2007); Garcia et al. (2007); Piecuch et al. (2013)
Global	Land-ocean mass balance	Boening et al. (2012)

[a]The first deep-focus earthquake to be observed by satellite gravimetric data.
[b]The 2004 Sumatra-Andaman, 2010 Chile (Maule), and 2011 Tohoku-Oki earthquakes

Table 2.4 – Overview of the application of GRACE data in geophysical studies other than hydrology.

2.4   Orbit accuracy of LEO satellites

One important ingredient in computing gravity field models is the orbits of the satellites. They result from measurements collected by the GNSS receiver. Unlike the accelerometers and ranging sensors discussed in Section 2.2, the accuracy of the measurements collected by the GNSS receiver are not of immediate interest to geodetic applications. Much more relevant is the result of processing these measurements into a set of orbital positions and velocities. For this reason, the characteristics of the GNSS receiver not discussed and more attention is devoted to the accuracy of the resulting orbits.

With the exception of the SGG type of observation, the accuracy in which orbital positions and velocities are estimated is of critical importance. In case of hl-SST, the orbits are themselves the main gravimetric observations, and their errors propagate directly to the estimated gravity field parameters. In case of ll-SST, in addition to the obvious geo-location information, the orbit is needed in order to characterize the direction of the ll-SST gravimetric observation. In case of SGG observations, the orbits are only used to geo-locate the gradiometric measurements and their error has a small impact on the quality of the final gravity field model.

A proper characterisation of the current LEO orbit errors is needed to quantify their role in the total noise budget of a future gravimetric mission. The information gathered in this analysis is a realistic estimate of the amplitude of the relative and absolute orbit errors.

2.4.1   Orbit determination methods

The procedure that transforms the GPS pseudo-ranges into a useful and congruent set of position and velocity data is referred to as Precise Orbit Determination (POD). There are three types of orbits that result from the respective POD methods:

1. Kinematic Orbit (KO)
2. Reduced Dynamic Orbit (RDO) and
3. Purely Dynamic Orbit (PDO).

The first type of orbit is the result of purely kinematic positioning, i.e. fundamentally of a geometric nature, produced without any knowledge of the dynamics of motion. The last type of orbit is produced by the unconstrained integration of the equations of motion on the basis of an assumed force model. The role of geometrical information is restricted to the computation of the initial state vectors, needed to initiate the integration. The RDO is somewhere in-between the previous two types, in the sense

that orbit integration takes both geometrical and dynamic information into account. More precisely, the pseudo-ranges derived from GPS measurements are processed with the additional constraint that the resulting orbit obeys to a predefined dynamic model.

The KOs do not contain any information related to a force model. They are estimated solely from the GPS measurements. Since they are determined epoch-wise and the accuracy of data point is dependent on the number of the visible GPS satellites, KOs are characteristically less smooth than the orbits of other types. Additionally, KOs are plagued with frequent data gaps, which can result from e.g. a low quality of GPS observations which have to be removed as outliers or from a small number of satellites in view, see e.g. Götzelmann et al. (2006). To illustrate this argument, Hwang et al. (2009) reports that as many as 70 % percent of kinematic orbit arcs were unsuitable for gravity field recovery during the POD of the F3C orbits. This number can be seen as a worst-case scenario in view of the fact that the F3C satellites gather radio occultation data, for which the GPS antenna placement on the satellite is not optimal for POD.

The RDOs are the result of the integration of the equations of motion constrained by GPS data (Yunck et al., 1994). Orbits of this type are not subject to data gaps because at those times when GPS measurements are unavailable or erroneous, the orbit follows the assumed dynamic model. On the other hand, RDOs require the estimation of empirical parameters or the co-estimation of force parameters to compensate for errors in the (often simplified) force model (Švehla and Rothacher, 2005). These errors might be of gravitational or non-gravitational origin, of static or time-varying nature. More critical is the fact that the computed RDOs tend to reflect deficiencies in the assumed force model, particularly if the number of estimated empirical parameters is low. On the other hand, setting a large number of empirical parameters tends to absorb most unmodelled signals, making the co-estimation of gravity field parameters less accurate. On this topic, van den IJssel and Visser (2007) has exploited linear-piecewise empirical accelerations to estimate the non-gravitational accelerations solely based on GNSS data.

Since integrated solely from the equations of motion and on the basis of an assumed force model, the PDOs require only six parameters (the initial state vector) to be completely defined for each orbit arc. The length of each arc is usually long enough to decrease the frequency of the arc boundary discontinuities and short enough to limit the build-up of integration errors; orbits arcs are often computed with daily periods, or fractions thereof. The initial state vectors can be derived from a KO or, in the case of simulation studies, determined analytically.

Each orbit type has different roles and purposes. The lack of any a priori information regarding the dynamic model makes the KOs suitable to estimate

Earth's gravitational field, if care is taken to mitigate the large high-frequency noise resulting from the differentiation of the kinematic positions. For the same reason, the KO is also exploited to estimate the initial state vectors used for the integration of PDO, since they are not biased towards any background force model. The PDOs describe the unconstrained motion of a satellite under the influence of a background force model, which means that the computed velocities tend to have lower differentiation errors than the KOs, provided that the background force model is adequately complete. This fact is advantageous in some ll-SST data processing strategies, when the centrifugal accelerations of the reference frame fixed to the LoS vector need to be removed from the data, refer to Section 4.3.3. Since the GRACE satellites have their LoS vector constantly aligned with the along-track direction, this vector rotates in inertial space. Associated with this motion are frame rotation accelerations which are not related to the gravitational field and need to be cleaned from the data. In those processing strategies, the PDOs provides a more accurate estimation of the frame accelerations than other orbit types, improving the accuracy of the final gravitational field solutions. The RDOs are typically "rapid" orbits, used in the preliminary data processing stages, since they can be computed very quickly and do not suffer from data gaps. Another application particular to the RDOs is associated with the co-estimation of parameters which are not known accurately, such as non-gravitational force parameters (e.g. the drag or lift coefficients and surface reflectivity parameters).

2.4.2 Absolute LEO orbit positioning accuracy

In this section, a literature study concerning the absolute orbit accuracy of LEO is presented. There are numerous studies on POD of LEO satellites, so the analysis is limited to a few representative and important Earth Observation (EO) missions: TOPEX/Poseidon, CHAMP, Jason-1, GRACE, first satellite of the Meteorological Operational satellite programme (MetOp-A), GOCE and F3C. The type of GPS observation is either Zero-differenced (ZD), Single-Differenced (SD) – either Single-Differenced phase measurements between GPS Satellites (SD-S) or Single-Differenced phase measurements between Epochs (SD-E) – or Double-differenced (DD). The study covers GPS data from 1997 to 2007 and considers data periods from one day to nearly one year.

The accuracy of the POD scheme is estimated using one of the following validation methods: overlap analysis, RDO - KO difference, comparison with an independently-computed orbit and comparison with independent measurements, such as SLR and/or DORIS.

The overlap analysis is done by computing the difference between the overlapping extremities of successive arcs, since generally the POD procedure is done independently over arcs of limited length (normally 1 day) that start/end (generally a few hours) before/after the staring/ending date of previous/following arcs, respectively.

It is also possible to gain some insight into the accuracy of the POD procedure if the difference between the RDO and KO is computed. The drawback is that it is impossible to discern between the deficiencies of the assumed force model considered in the RDO computation from the errors in processing GNSS data, in particular because the latter originates in different ways in RDO and KO processing.

The most obvious validation method is to compare the computed orbit with another that is obtained independently. The disadvantage is that it is not possible to say which of the two is more accurate, when the reported accuracies are of a few centimetres.

Ideally, the comparison should be made with respect to independent and accurate measurements of the satellite motion. To that end, SLR and DORIS data can be used. The accuracy of SLR is highly dependent on the elevation angle because of the difficulties in modelling the effects of the troposphere on the path of the LASER beam at low elevation angles. Along the zenith direction, the SLR data is accurate within a few millimetres and a few centimetres at low elevation angles (Wijaya and Brunner, 2011). DORIS boast similar accuracy, reportedly at centimetre-level along the radial direction (Luthcke et al., 2003). As a consequence, misfits of comparable magnitudes to SLR and/or DORIS data cannot be solely attributed to orbit determination error.

Referring to Table 2.5, the lowest absolute error of GPS-derived orbits refers to RDOs and can be as little as 2 cm (Jäggi et al., 2007), if considering validation with SLR data. If the validation is done by comparing two independently-computed orbits, without making use of any measurement principles other than GPS, the precision is as high as 1 cm (Hwang et al., 2009). Considering a simulated environment, Visser et al. (2009) reports a 1.34 cm error for the GOCE mission.

Comparing the accuracies of the kinematic and reduced-dynamic processing strategies, the most obvious finding is that KOs are systematically less accurate than RDOs. This is an expected outcome, since the force model used in the RDO provides additional information which is not available in the KO processing. This is true because over typical integration periods, the accumulation of integration and model errors is small enough to be negligible. However, the difference in accuracy of KOs vs. RDOs is not large, e.g. 3.4 cm vs. 2.8 cm (Zhao et al., 2010a), 3.8 cm vs. 2.4 cm (Jäggi et al., 2007) and 2.8 cm vs. 2.7 cm (Švehla and Rothacher, 2005). One explanation to this fact is that the independent validation techniques for absolute positioning, i.e. SLR and DORIS, have limited accuracy, which might obscure the

comparison.

Of the satellites in Table 2.5, one can identify *dedicated mission*, which rely heavily on accurate positioning: gravimetric satellites (CHAMP, GRACE and GOCE) and altimetry satellites (TOPEX/Poseidon and JASON-1); and the *non-dedicated missions* F3C and MetOp-A, which are launched for the purpose of atmospheric research and meteorology, respectively. Although the number of satellites under analysis is not sufficient to draw definitive conclusions, this distinction is nonetheless illustrative of the higher orbital positioning accuracy of the dedicated satellites. Notice that Hwang et al. (2009) reports $1 \sim 3$ cm accuracy but using *internal* validation methods, such as overlap analysis and the difference between KOs and RDOs, thus making the comparison with other references not possible. The reason for the higher accuracy of the orbits of dedicated satellites is due to a number of factors, namely GPS receiver performance, a large number of receiver channels (i.e. the maximum number of trackable GPS satellites), wide field-of-view, optimal (zenith-pointing) direction, absence of multi-path effects caused by moving appendices, e.g. solar panels, and the shape of the satellite body that does not cause signal blockage (Hwang et al., 2008b, 2009). Taking as examples the GRACE and F3C satellites, the former has no moving solar panels and the placement of the GPS antenna is optimal, unlike in the latter. The ratio between the number of visible and tracked GPS satellites is on average 37 % lower for F3C than for GRACE and the multipath effect is 40 cm larger; over a period of 300 days, the average number of observations per day for satellites FM2 and FM4 of the F3C constellation is 30000, while for GRACE it is 60000 (Hwang et al., 2009).

It is also worth mentioning that in the study performed by Zhu et al. (2004) on GRACE RDOs, the inclusion of accelerometer data has lowered the error Root Mean Squared (RMS) from 6.5 cm to 3.2 cm, thus increasing the accuracy of the estimated orbit by a factor of two. Additionally to the accelerometer data, the inclusion of KBR data has further improved the accuracy to 2.9 cm.

From Table 2.5 it is possible to infer that the absolute accuracy of orbits from LEO satellites is around 2 cm (Jäggi et al., 2007; Qile et al., 2006; Švehla and Rothacher, 2005).

3D[a] RMS (cm)	Mission	Orbit type	Meas. type	Validation method	Analysis period (days)	Starting date	Author
2.8	GRACE	RDO	ZD	SLR	101	DoY 101, 2003	Zhao et al. (2010a)
3.3		KO					
3	F3C	RDO	ZD	Overlap analysis	300	DoY 100, 2007	Hwang et al. (2009)
1	GRACE						
1	F3C	RDO /KO		RDO - KO difference			
2	GRACE						
4.0	F3C	RDO	ZD	Overlap analysis	25	DoY 214, 2006	Hwang et al. (2008b)
4.6		KO					
1.34	GOCE[b]	RDO	ZD	Comparison w/ E2E[c] simulation	55	DoY 86, 2008	Visser et al. (2009)
1.62		KO					
5	MetOp-A	RDO	varies	Inter-agency comparison	3	DoY 360, 2006	Montenbruck et al. (2008)
10		RDO /KO		RDO - KO difference			
2.44/ 2.47	GRACE A/B	RDO	ZD	SLR	335	DoY 31, 2003	Jäggi et al. (2007)
3.08/ 2.88		KO					
2.03/ 1.81		RDO	DD				
10.2	CHAMP	RDO	ZD	Comparison w/ PSO of GFZ	6	DoY 126, 2002	Qile et al. (2006)
2.2				SLR			
2.67	CHAMP	RDO	ZD	SLR	8	DoY 195, 2002	Švehla and Rothacher (2005)
2.77		KO					
2.69		RDO	DD				
2.56		KO					
4.7	JASON-1	RDO	ZD	Orbit independently estimated from GPS and SLR	1	DoY 97, 2002	Colombo and Luthcke (2004)
6.5	GRACE	RDO	ZD	SLR	4	DoY 121, 2002	Zhu et al. (2004)
3.2		RDO[d]	ZD				
2.9		RDO[e]	ZD				
4.9	CHAMP	RDO	ZD[f]	SLR	11	DoY 139, 2001	Svehla et al. (2003)
5.0		RDO	DD[g]				
5.6		KO	DD[h]				
4.9		RDO	DD[i]				
4.4		RDO	DD[j]				
2.8	TOPEX/ Poseidon	RDO	SD-E	SLR and DORIS	8	DoY 54, 1997	Bock et al. (2002)

[a]Notice that validations with SLR are relative to station-to-satellite uni-dimensional (1D) distance RMS.

[b]Simulated

[c]End-to-End

[d]Considering accelerometer data.

[e]Considering accelerometer and KBR data.

[f]Acceleration pulses every 15 minutes.

[g]Float ambiguity resolution, acceleration pulses every 15 minutes.

[h]Integer ambiguity resolution.

[i]Integer ambiguity resolution, acceleration pulses every 15 minutes.

[j]Float ambiguity resolution, acceleration pulses every 9 minutes.

Table 2.5 – Summary of the absolute POD accuracy reported in literature.

2.4.3 Relative LEO orbit positioning accuracy

In addition to absolute POD errors, it is possible also to consider how accurate are the relative positions of LEO satellites that fly in formation. This section presents a short literature study that illustrates the state-of-the-art accuracy of relative positioning. The reported sources deal exclusively with the GRACE mission, exploiting the opportunity to use the KBR system for validation. This system only provides observation of changes in the inter-satellite LoS vector length and is unable to derive any information along the orthogonal directions. The motivation for studying the relative positioning accuracy is that errors in the attitude of the LoS vector, particularly the vertical component, may significantly deteriorate the estimated gravity field model. Additionally, Ditmar et al. (2012) showed analytically that gravity field models derived from GRACE KBR data show more sensitivity to relative than to absolute positioning errors.

Relative positioning accuracy is inherently different to absolute positioning accuracy. The close proximity of the satellites in the formation greatly facilitates the integer ambiguity fixing of the carrier phase (Kroes, 2006; van Barneveld, 2012). As a consequence, the relative positioning accuracy is higher than the absolute one, in particular the low-frequency errors that dominate the latter.

The relative accuracy of RDOs is higher than that of KOs. For example, Zhao et al. (2010a) shows a two-fold improvement in the accuracy of the RDO relative to the KO. The computation of RDOs takes into account the constraint that both orbits follow the same pre-defined force model, which effectively restricts the solution.

Table 2.6 relays the message that relative accuracy of the POD of GRACE can reach 1 mm in the along-track direction (Kroes et al., 2005; Jäggi et al., 2007). For this reason, white-noise with amplitude of 1 mm is assumed in the thesis as the near-future relative orbit error for the simulation of next-generation gravimetric missions in Chapter 5. The analysis done in Section 6.1 confirms that this is a reasonable assumption.

RMS (cm)	Orbit type	Meas. type	Analysis period (days)	Starting date	Author
0.22	RDO	ZD	101	DoY 190, 2003	Zhao et al. (2010a)
0.46	KO				
1.25	RDO	ZD	335	DoY 31, 2003	Jäggi et al. (2007)
1.14					
2.05	KO		55	DoY 243, 2007	
0.31	RDO	DD			
0.09		DD[a]			
0.09	RDO	ZD	101	DoY 190, 2003	Kroes et al. (2005)
4.15	KO				

[a]Along- and cross-track relative acceleration constrained to 1.4μm/s

Table 2.6 – Summary of relative POD accuracy of GRACE reported in literature.

2.5 Processing strategies

The methodologies used to retrieve the relevant information from gravimetric data and condense it in the form of a gravity field model are numerous. In this section, a brief description of gravimetric processing strategies is presented, pointing out the respective strengths and weaknesses.

2.5.1 Variational equations approach

The variational equations approach (Reigber, 1989) connects the measured distances from the GPS satellites (or other GNSS measurements, SLR observations, KO data or ll-SST tracking data) and a set of unknown parameters which may include Stokes coefficients, initial state vectors, empirical accelerations, drag coefficients, instrument calibration parameters (e.g. accelerometer or inter-satellite metrology system) and other parameters which play a role in the dynamic equations of motion of the satellite. This is accomplished by linearising the mathematical model describing the motion of the satellite when considering a priori reference gravity field model and remaining *a priori* assumptions (such analytically-derived initial state vectors, initial guess for drag coefficients, calibration parameters provided by instruments manufacturer, etc.). The linearisation is performed (usually numerically) around the reference model response, i.e. the values of the unknown parameters computed from the reference model when considering the *a priori* assumptions.

As a disadvantage, the reference model needs to be iteratively updated with the newly-computed model corrections, thereby explicitly assembling the the normal equations in every iteration.

The advantage of this approach is that it is flexible enough to contemplate a wide range of observation types as well as different types of unknown parameters, such as demonstrated by Reigber et al. (2005) and Tapley (2004a) when processing GRACE KBR data. Additionally, the estimation of initial state vectors ensures that there is agreement between the orbital positions and the estimated gravity field model, making this approach relatively robust to positioning errors.

There are numerous gravity field models produced using the classical variational equations approach, such as AIUB GRACE-only model, version 2 (AIUB-GRACE02S) (Jäggi et al. 2012), CNES/GRGS 10-days gravity field models (CNES/GRGS-10d) (Lemoine et al. 2007b; Bruinsma et al. 2010; Lemoine et al. 2013b) and the official time-variable gravity field solutions of the GRACE mission: JPL-R05 (Watkins and Yuan, 2012), GFZ-R05 Dahle et al. (2013) and CSR-R05 Kruizinga (2014). Additionally, this approach has been used to retrieve the gravity field of the moon using Gravity Recovery and Interior Laboratory (GRAIL) data (Lemoine et al., 2013a; Konopliv et al., 2013; Arnold et al., 2015).

2.5.2 Energy balance approach

The energy balance approach (also known as *energy integral approach*) is based on the energy conservation principle (O'Keefe, 1957; Jekeli, 1999; Gerlach, 2003; Gerlach et al., 2003). This principle states that the variations in kinetic energy of the satellite are equal to the work done by the all forces directed parallel to the velocity vector. Furthermore, conservative forces, such as gravity, can be related to their potential, providing a direct connection to the unknown spherical harmonics coefficients. Consequentially, the application of this methodology to ll-SST data connects the range-rates (which in the case of GRACE are directly given as unbiased quantities, unlike the ranges) to gravitational potential differences; Han et al. (2003) uses the term *potential difference observables* to refer to this method.

The advantage of this approach is its numerical efficiency.

As for disadvantages, the satellite velocities need to be computed from kinematic positions (in case of hl-SST data), requiring numerical differentiation that amplifies the noise at high-frequencies even if dedicated numerical integration schemes are employed (Ilk and Löcher, 2005; Reubelt et al., 2012). An additional disadvantage is related to the intrinsic scalar formulation of the energy balance approach, which leads to the loss of information perpendicular to the velocity direction (Ditmar and Sluijs, 2004; Baur et al., 2014). This disadvantage is addressed by defining

energy integrals for all directions and integrals of motions following the linear and angular momentum conservations (Ilk, 2007). A number of gravity field models were estimated considering this approach, such as the TUG CHAMP 2004 (TUG-CHAMP04) gravity field model (Badura et al. 2006) and the TUM 2Sp (TUM-2Sp) gravity field model (Földváry et al. 2004), to name a few.

2.5.3 Boundary value problem for short arcs

The boundary value problem for short arcs, or *short arcs approach* in short, considers the double-integration of Newton's equation of motion, resulting in a boundary value problem in the time domain (Mayer-Guerr et al., 2005; Mayer-Gürr et al., 2005; Mayer-Gürr, 2006). The relation between the unknowns parameters and the observations, i.e. the satellite trajectory in case of hl-SST data and the range in the case of ll-SST data, is not linear, requiring linearisation (much like the variational equations approach). The unknown parameters are the Stokes coefficients; the observations are defined by the orbit and additionally by the range if ll-SST data is also available. It is also possible to consider as unknowns the boundary state vectors of each orbit arc, as is done in case of the data processing from the GRAIL mission, as described by Klinger et al. (2013).

As a consequence the linearisation, this method should have the disadvantage of requiring iterative parameter estimation but in practice it is shown that convergence is reached after the first iteration (Klinger et al., 2013). As an advantage, the iterative parameter estimation in conjunction with the co-estimation of the arc-boundary state vectors make the approach very insensitive to orbit position errors. This is the case because the orbit is automatically kept consistent with the estimated gravity field parameters. Furthermore, since the orbital positions are treated without any form of differentiation, there is no amplification of high-frequency noise. Another advantage is that the short arc approach makes it easy to use any kind of positioning data, such as SLR, hl-SST and ll-SST. A number of models have been derived on the basis of the short arcs approach, namely ITG CHAMP-only model, version 1 (ITG-CHAMP01) (Mayer-Gürr et al. 2005), ITG GRACE-only model, version 2 (ITG-GRACE02s) (Mayer-Gürr et al. 2007) and ITG GRACE-only model, 2010 (ITG-GRACE2010) (Mayer-Gürr et al. 2010; Kurtenbach et al. 2009).

It has also been applied to the determination of the gravitational field of the Moon (Klinger et al., 2013).

The integral nature of the method has some undesirable consequences: localized errors, e.g. those associated with the temporal aliasing at one geographical location, are accumulated over the whole arc (which is no longer than 30 min for this reason), propagating these errors to other geographical locations. This disadvantage is

addressed i) by exploiting spherical splines as local base functions, thus restricting the error propagation to small geographical regions (Mayer-Gürr et al., 2006), and ii) by estimating daily snapshots of the gravitational field which are then used as an improved de-aliasing product (Kurtenbach et al., 2012).

2.5.4 Acceleration approach

The acceleration approach exploits Newton's equation of motion directly (Rummel, 1979). The method connects the double-differentiated orbital positions (or double-differentiated range) to the (relative) forces acting on the satellite. This is regarded as an elegant formulation because i) it avoids numerical integration operations characteristic of other approaches, using instead the numerically efficient differentiation operator, and ii) uses the force model directly. The observations are usually transformed to the (quasi-) inertial reference frame before differentiation to avoid frame accelerations. The differentiation of noisy observations leads to the amplification of the high-frequency noise; however, it is possible to handle the high-frequency noise with a decorrelation procedure, such as FDDW.

There are two sub-categories of the acceleration approach: the *point-wise* (Austen et al., 2002; Reubelt et al., 2003; Chen et al., 2008b) and *averaged* (Ditmar and Sluijs, 2004; Liu, 2008; Bezděk et al., 2014). The point-wise acceleration approach differentiates interpolating functions fitted to the observations instead of the observations themselves, while the averaged acceleration approach differentiates the observations directly.

There are numerous advantages in using the acceleration approach, in addition to the already mentioned elegance of the formulation, which results in a comparatively high numerical efficiency. Foremost is that the observations are local quantities, since they do not suffer any numerical integration (unlike in the variational equations and short arcs approaches). In addition, the measured or modelled nuisance forces (i.e. those not related to the gravitational field, such as non-gravitational forces and known gravitational forces, e.g. tidal) also retain the localized nature. As a result, errors located in one section of the data period (and/or a certain geographical location) do not propagate far. This is particularly beneficial when errors associated with temporal aliasing are present, which means that the acceleration approach is not particularly sensitive to them (Ditmar et al., 2012).

As a major drawback, the orbital positions are treated as pre-existing quantities and are not co-estimated, see Section 2.5.6. Another disadvantage of the point-wise acceleration approach is that it does not handle gaps efficiently, since the warm-up behaviour of the double differentiation operator unavoidably discards the observations at the vicinity of gaps. For data with numerous gaps, this can lead to

a substantial loss of observations. In case of the averaged acceleration approach, the differentiation only consider three consecutive epochs, making it very efficient in this respect. As an example of the application of the acceleration approach, the Delft Mass Transport (DMT) model (Liu et al. 2010; Ditmar et al. 2013) and Delft Gravity Model (DGM-1S) (Farahani et al. 2013b) models are derived considering this methodology.

2.5.5 Classification

Ilk et al. (2008) classifies some of the methods above in three categories. The short arcs approach falls into the *analysis level 1* category, since the orbital positions are used directly in conjunction with a double integration of the force model. The energy balance approach is classified as *analysis level 2* because there is the need to differentiate the orbits and integrate the force model. The *analysis level 3* includes the acceleration approach, since the orbital positions are double-differentiated, while the force model is used directly.

2.5.6 Correlated noise in gravimetric data

Gravimetric data are invariably corrupted by correlated noise. A particular source of correlated noise are the errors in the orbital position and velocity data (Švehla and Rothacher, 2005; Švehla and Földváry, 2006), which appear as low-frequency noise in gravimetric data, as demonstrated by Ditmar et al. (2012). The accuracy of the GNSS is limited, resulting in orbits with errors of a few centimetres, cf. Section 2.4.2, The orbit errors are dominant at low-frequencies, particular close to those frequencies associated with 1 and 2 Cycles Per Revolution (CPRs) (Jäggi et al., 2011b). This is the case for KOs, RDOs and PDOs, as shown by Reubelt et al. (2006) and in Section 6.1. Liu (2008) refers to the effect of these errors in the observations as *resonance effects*. Another source of correlated noise particular to the GRACE data is the KBR instrument, which manifests as high-frequency noise as a result of the double-differentiation of the ranges. All processing strategies are affected by correlated noise, since it is a property of the data, not of the exploited methodology.

The low-frequency noise corrupts the gravity field parameters considerably, since its effect are not restricted to low degrees. The slowly-changing amplitude of the noise maps mainly to sectorial and near-sectorial coefficients because of the polar orbit of the satellites. Over the course of the data period, there is the accumulation of numerous ascending and descending tracks with observations that produce a spatial pattern that is characterised by i) a slowly changing mean values along the latitudinal direction and ii) rapidly changing values over the longitudinal

direction. Consequentially, the error in sectorial and near-sectorial coefficients becomes dominant over the error in zonal and tesseral coefficients and significant up to a high degree. Although manifesting in a similar way to the anisotropic sensitivity of ll-SST data (refer to Section 2.2.3 and Section 1.2.1), the low-frequency noise is of a different nature.

Some processing strategies are not significantly affected by the low-frequency noise. The short arc approach, by means of initially estimating the gravity field parameters up to a modest degree (Mayer-Gürr et al., 2006), naturally averages the strong longitudinal variations in the spatial pattern of the accumulated ascending and descending tracks. In variational equations approach, there are co-estimated empirical parameters that absorb the low-frequency errors in the data. On the other hand, the acceleration approach applied to ll-SST data is comparatively sensitive to the low-frequency noise. It regards the orbits as pre-existing quantities, i.e. none of the estimated parameters relate to them explicitly. Furthermore, this functional model requires the derivation of parameters from the orbits, which are themselves not errors free. As a result, the errors in the orbits propagate directly to the range combinations and ultimately to the estimated gravity field parameters.

In practice, it is necessary to apply some form of filtering to the data before the inversion to handle the low-frequency noise, even when FDDW is used (as is the case of the DMT model). One immediate way to do that is to filter the observation vector, with the purpose of suppressing the frequencies where the correlations are most dominant. The result is, however, that not only the noise will be damped but also the geophysical signal of interest present at those frequencies, which may otherwise be recoverable. It is also possible to subtract from the observations an analytical function with a period close to the orbital period (and optionally a few multiples). The set of parameters that describe the analytical function are estimated by least-squares fitting. This approach is used in the production of the DMT model and the data is effectively cleaned from these errors (Ditmar et al., 2012).

Frequency-Dependent Data Weighting (FDDW) is the process of assigning weights to the observation data in the frequency domain, so that the temporal correlations present in the data noise, assumed to be stationary, are taken into account (Klees et al., 2003; Klees and Ditmar, 2004). Some gravitational field modelling approaches employ FDDW implicitly; an example of that are the empirical parameters used in the variational equations. FDDW is accomplished by building a suitable noise covariance matrix, usually considering the a posteriori residuals. To improve numerical efficiency, the stochastic models of noise can be produced in the form of an Auto-Regressive Moving-Average (ARMA) model. The ARMA model representation of noise is computationally efficient for the purpose of multiplying the noise covariance matrix to the vectors of observation which is needed for proper

data weighting. If the order of ARMA model is not sufficiently high, peaks in the error spectrum may not be effectively suppressed and, for this reason, the analytical approach described above is complementary. FDDW has been applied to CHAMP data (Ditmar et al., 2007), GRACE data (Liu et al., 2010) and GOCE data (Farahani et al., 2013b).

It is also possible to consider a decorrelation filter applied to the data before inversion, as used by Bezděk et al. (2014), but the disadvantage is that data is lost near gaps due to the filter warm-up behaviour.

In the context of future gravimetric missions, there is the possibility that the low-frequency noise affects a wider frequency range in comparison the case of GRACE. The reason is that accuracy improvement of future gravimetric sensors is probably higher than that of future (multi) GNSS receivers. As a consequence, the influence of the errors in the orbital position and velocity data are not restricted to the frequencies associated with 1 and 2 CPRs. It is, therefore, not assured that the measures used currently on GRACE data are equally successful in future missions. This argument provides the motivation to consider the errors in position and velocity data in the simulation of future missions.

2.6   Future gravimetric missions

With the experience gained from the recent gravimetric satellite missions, particularly CHAMP, GRACE and GOCE, the geodetic community has learned that the next-generation gravimetric mission needs to address issues other than a higher sensor accuracy. The consensus is that the main improvements to be included in future missions are a) lower sensitivity to temporal aliasing, b) higher measurement isotropic sensitivity and, most importantly, c) continuation of the monitoring of Earth's mass transport processes, particularly those pertaining to climate change.

Of the three main observation principles, hl-SST, SGG and ll-SST, the latter is the most promising one for monitoring mass transport processes in the near future. The reasons are unavoidably related to the accuracy of the sensor systems as compared to the measured signal. In case of hl-SST, the quality of GNSS tracking data is not sufficient to provide accurate measurements that enable the mid to high frequency features of Earth's gravitational field to be resolved, although for low-frequency features this can be done, refer to Section 2.2.1. In what regards SGG data, current technology level does not allow temporal gravitational field variations to be observed with a sufficiently high accuracy. This is largely because temperature variations introduce slowly-changing accelerometer bias that increase dramatically the error magnitude at low frequencies, decreasing the sensitivity of the gradiometer to

low-degrees, where most of the temporal gravitational field variations is concentrated. Consequentially, the ll-SST observation principle, particularly after the success of the GRACE mission, is favoured as most promising.

One promising concept for increased accuracy of acceleration measurements comes from atomic interferometry (Peters et al., 1999). Silvestrin et al. (2012) conservatively predicts a flat error spectrum that is one order of magnitude lower error at the measurement bandwidth of GOCE's accelerometers and several orders of magnitude at low frequencies. Considering that the GOCE cannot observe temporal gravitational field variations because of high accelerometer errors at low frequencies, such development would effectively enable the collected SGG data to be sensitive to those variations.

One research direction that promises significant improvements in terms of the sensitivity and isotropy of ll-SST data is the investigation of different configurations of satellite formations, refer to Chapter 3. In case of GRACE, the LoS direction is nearly aligned with the meridional direction. The constant alignment of the LoS direction constitutes the worst case scenario in what regards anisotropy. The only way to minimise anisotropic data sensitivity, without resorting to other measurement principles, is to design a formation that causes the LoS direction to change as the satellites go around the Earth, in the case of a single measurement system. Table 1.2 summarizes the formation types that have recently been under investigation, considering full-scale simulations.

Future gravimetric formations are envisioned to exploit laser interferometry (Nerem et al., 2004; Cesare et al., 2008; Pierce et al., 2008), with an expected improvement in the accuracy of the inter-satellite metrology system by 2 to 3 orders of magnitude (Bender et al., 2003). Simulations have shown that a GRACE-type formation equipped with a interferometric ranging sensor with an accuracy of 5 nm is capable of resolving the gravitational field with an accuracy 2.5 times higher than GRACE (Wiese et al., 2009). The proposed inter-satellite metrology system have the advantage of being insensitive to pointing errors (Sheard et al., 2012) or of being able to measure the attitude of the satellites relatively to the LoS direction (the so-called *Angle Metrology* and *Lateral Displacement Metrology*) to provide feedback control to the Attitude Control System (ACS) (Cesare et al., 2010a). Since the errors in laser interferometry increase with the distance between the satellites, it is expected that the future gravimetric ll-SST missions will fly in a much tighter formation than GRACE (e.g. as close as 10 km in case of the study done by Cesare et al. (2010a)).

As a consequence of the requirement to continue monitoring the Earth system, the GRACE Follow On (GFO) (Sheard et al. 2012; Larkin 2012; Zaragoza 2013) mission is set to replace GRACE, albeit no sooner than in 2017. It will consist

of a pair of satellites nearly identical to GRACE, with an identical micro-wave ranging sensor. An innovative component is a laser ranging sensor (Dehne et al., 2009; Sheard et al., 2012), included for the purpose of technology demonstration. Schültze et al. (2012) reports that it is an adapted version of the one on-board the Laser Interferometer Space Antenna (LISA) (Merkowitz 2003) satellites. The distance between the GFO satellites will be known with an accuracy of 80 nm at the measurement bandwidth of 1 to 100 mHz (Schültze et al., 2012). In spite of these improvements, Loomis et al. (2011) have concluded that the added accuracy of the laser interferometry will not improve significantly the quality of the estimated gravity field models due to temporal aliasing. This conclusion has been confirmed by other studies (Visser et al., 2010; Wiese et al., 2011c).

A similar proposals has been put forth but exploiting laser interferometry exclusively (Cesare et al., 2010b). In this proposal, a GRACE-like formation equipped with a drag-free system flies at 325 km altitude in a Sun-Synchronous Orbit (SSO), with 10 km inter-satellite separation. The satellites are equipped with identical laser ranging sensors, although only one operates at a given time; the ranging sensor on-board of the other satellites acts as backup. The laser signal emitted by one satellite is reflected on the Corner-Cube Retroreflector (CCR) located at the CoM of the other satellite, permitting the distance to be measured with an error magnitude of 50 nm between 10 and 1000 mHz. The placement of the CCR at the CoM intends to minimise ranging errors arising from attitude uncertainty but creates a problem regarding the placement of the accelerometer. Unless placed at the CoM, the accelerometer will register angular acceleration in addition to linear accelerations. The solution is to include a cross-track gradiometer arm, with two accelerometers placed in a rigid bench along with the laser ranging sensor. As a benefit, the cross-track gravity gradient is measured, which can be used for improving the accuracy of gravity field models describing short-period mass changes (Anselmi et al., 2010).

It is most likely that the GRACE satellites will cease operation before the launch of the GFO mission. Between these two events, there will be no gravimetric mission monitoring the mass transport processes at the surface of the Earth. Under these conditions, there is the need to resort to alternative satellites that can provide data to mitigate the monitoring gap, such as The Earth's Magnetic Field and Environment Explorers (Swarm) (Friis-Christensen et al. 2006). Although this mission's primary object is to monitor Earth's magnetic field, it is equipped with a dual-frequency GPS receiver and accurate star cameras. Wang et al. (2012c) demonstrates through simulations that the Swarm satellites are capable of measuring hydrological cycle at monthly intervals up to degree 5 to 10.

The so-called *e.motion* proposal (Panet et al., 2012) is in many ways similar to the previous one, namely one satellite pair, 370 km altitude, laser ranging sensor and

a drag-free control system. The novel component is related to the configuration of the formation, employing the pendulum formation with a maximum inter-satellite distance of 207 km. The pendulum formation requires the two satellites to be placed in orbits with different right ascension of the ascending node. Consequently, there is a cross-track component in the LoS vector, which is maximum at the equator and zero at the poles. The formation has been designed in such a way that the azimuth of the LoS vector is 15° when the satellites are close to the equator. The complete coverage of the Earth is reached every 10 days, with a claimed spatial resolution of 200 km.

The widely accepted feasible solution to mitigate the effect of temporal aliasing in the near future considers two GRACE-type formations (Wiese et al., 2011a), also known as the *Bender constellation* after Bender et al. (2008), in which each GRACE-type satellite pair is placed in orbits with different inclinations. Through simulations and the use of empirical orthogonal functions, Wiese et al. (2011b) has shown, for example, up to 80 % lower error level in the recovered hydrological signals at some basins, leading to the possibility to measure mass variations in small basins, which are invisible to one satellite pair. Unfortunately, the number of formations needed to reduce the temporal aliasing significantly, in particular that resulting from high-frequency gravitational field variations, would be too many to make this option practical.

On the topic of constellations, one promising option is to utilise a large number of LEO satellites to measure high-frequency long wavelength features of Earth's gravitational field. One possibility is to use non-dedicated satellites, see Chapter 5; another option is to use nano-satellites such as *CubeSats*, used in the *QB50* initiative (Gill et al., 2013). These small satellites have tight constraints in what concerns the power or mass budget, so all components have to be miniaturised. Virgili and Roberts (2013) proposed to equip one of such CubeSats with a GPS receiver in order to derive thermospheric density variations. Recently, Pesyna et al. (2014) have demonstrated that phase measurements can be acquired with smartphone-type GNSS antennas, instead of bulkier survey-grade antennas (which are also part of gravimetric satellites, albeit in a compact form), if the signal is processed by a Software Defined Radio (SDR). In other words, the higher weight and mechanical complexity of traditional GNSS antennas are replaced by higher power and software complexity of an SDR, which are more suitable for miniaturization. Dubovskoi et al. (2012) reports developments in the production of micro-accelerometers that enables the measurement of accelerations with 10^{-8} m/s^2 accuracy. CubeSats are routinely equipped with capable ACS. Including these technologies into one CubeSat effectively demonstrates that the CHAMP satellite (in what concerns the geodetic payload and assuming comparable performance of the ACS) is very close to being

scaled down from 4 m and 500 kg to 30 cm and 3 kg, with marginal decrease in performance (although formally the accelerometer is not mandatory for gravimetric purposes, according to Ditmar et al. (2007, 2008)). This remarkable accomplishment in miniaturisation is noteworthy and should be taken seriously in the design of future gravimetric missions, particularly those intended to tackle the measurement of fast mass transport processes.

Beyond the traditional gravimetric measurements, efforts have been taken to exploit the relativistic effects associated with the curvature of the space-time domain under the influence of the gravitational attraction of a planet. The sensitivity of such measurements is inherently homogeneous and isotropic. Mayrhofer and Pail (2012) conducted a (simplified) feasibility study on this type of observation, which is referred to as the *Post-Newtonian Method*. The conclusions where that the lower to medium spherical harmonic degrees (below degree 120) are recoverable as long as the on-board clock stability is better than 10^{-18} s and the orbital velocity error is lower than 10^{-6} m/s. In what regards the requirement on orbital velocity error, Section 2.4.3 shows a *relative* orbit accuracy of a few μm/s (in case of the PDOs of GRACE). Although the *absolute* orbit accuracy is lower, better dynamic modelling, more stable on-board clocks and more GNSSs, mean that the required orbital velocity accuracy is certainly attainable in the near future. Regarding the clock accuracy, Hinkley et al. (2013) has developed in laboratory two so-called *optical lattice clocks* that deviate from each other less by than 1.6×10^{-18} s after 7 hours. It should be noted that the required clock stability for the Post-Newtonian method is related to *short-term* periods, i.e. a few minutes, and that the clock stability increases as the averaging period increases (up to a minimum, after which *random walk* make the errors increase with longer periods). Fortunately, Bloom et al. (2014) has reached a comparable level of accuracy but with a two-order of magnitude decrease in the measurement time. In conclusion, the relativistic frequency shift measurement exploited by the Post-Newtonian Method is an attractive and emerging development.

2.7 Summary

Satellite gravimetry is a technique by which data collected by LEO satellites is used to estimate the gravitational field. Three types of gravimetric data exist: high-low Satellite-to-Satellite Tracking (hl-SST), low-low Satellite-to-Satellite Tracking (ll-SST) and Satellite Gravity Gradient (SGG). Of the three types, the Gravity Recovery And Climate Experiment (GRACE) mission has shown that ll-SST data provides the most accurate data to estimate the temporal variations of Earth's gravitational field. For this reason, it is generally regarded as the preferential

measurement concept to be used in future satellite missions to monitor mass transport processes. The understanding the of the limitation of ll-SST data is of utmost importance, so that future gravimetric missions effectively circumvent those limitations and deliver the highest quality data.

Temporal aliasing errors corrupt the models produced on the basis of gravimetric data gathered by satellites. The limited temporal resolution in which a geographical location is sampled by satellites in combination with the errors in the models describing fast mass transport processes, also know as de-aliasing products, is the main cause for temporal aliasing. Satellite observations, albeit inherently global, are unsuitable to be used in the production of the de-aliasing products because of the limited temporal resolution. Ground observations, which have sufficiently high temporal sampling, lack in terms of spacial coverage. In this context, the challenge is to find ways to minimize the influence of temporal aliasing in the accuracy of gravity field models produced by data collected by future gravimetric satellite missions.

Also of relevance is to understand the state-of-the-art in what regards the sensors on-board gravimetric satellites. The knowledge of the way these instruments collect data and the associated errors are crucial in deriving credible and realistic simulation results.

Much research has been done on the topic of future gravimetric missions. The most proposals aim at legitimate incremental improvements over the GRACE concept. However, there are ideas that step out of this paradigm. Most notable are the use of inexpensive CubeSats, potentially in large numbers and suitable to be developed at University level, equipped with miniaturized technology sufficiently advanced to make them competitive in terms of data quality with previous dedicated missions, such as CHAMP. Another exciting proposal is to place highly accurate clocks on a satellite and in this way collect data that is sensitive to the relativistic effects of the motion on LEO. These measurements are appealing since they are homogeneous and isotropic. The current technological level is not quite up to the task but near future advances may motivate a more dedicated development of this idea.

In spite of the recent research on satellite gravimetry, many issues still remain. In the following chapters, some of these open issues are addressed, namely the mitigation of temporal aliasing and the proper modelling of data errors. In Chapter 5, it is proposed to use numerous non-dedicated LEO satellites to measure the long wavelength features of the temporal changes of the gravitational field, effectively decreasing the detrimental effects of temporal aliasing in dedicated gravimetric missions. At the same time, the data collected by the non-dedicated satellites may provide valuable global measurements on the fast movement of mass on Earth's surface, potentially improving the understanding of weather patterns and other applications in Atmospheric studies. In Chapter 6, the knowledge gained from the

GRACE mission is used to validate an accurate noise model, which is exploited in Chapter 8 to study the errors in the gravity field models estimated by a number of satellite formations.

Satellite formations for gravity field recovery

3

The major goal of future gravimetric satellite missions is to determine the time-varying gravitational field, with the purpose of better understanding of the processes of mass transport in the Earth's system. A much higher accuracy and spatial resolution than what is currently available would be highly beneficial for this goal.

One of the most promising observation concepts of satellite gravimetry is based on satellite formations.

A satellite formation is defined as a group of satellites flying close together in such a way that they passively, or with minimal active orbit corrections, remain in relative proximity. Active formations, i.e. those require (near-) continuous thruster firing are not suitable for gravimetric applications because the fuel requirements tend to limit the mission lifetime. Particularly to passive formations with significant altitude difference or with a large maximum range, the motion of the satellites can be affected differently due to disturbances, such as atmospheric drag, solar radiation or gravitational forces, requiring frequent orbit maintenance manoeuvres and consequently lowering the mission's lifetime. There is, therefore, a small subset of satellite formations that are suitable to gravimetric purposes.

The distinction should be made between a formation and a constellation. The latter is composed of a large number of satellites, generally evenly spaced around the Earth to provide global coverage and performing independent tasks. Satellite telephone communication services, for example, require a satellite constellation to operate.

Satellite formations are characterised by the relative motion between the individual constituent satellites. Three satellite formations can be devised that exhibit totally different motion along the along-track, cross-track and vertical directions. These

are the trailing, pendulum and cartwheel formations, respectively. This section looks into their particularities, such as the relative orbital elements for each formation and qualitative considerations on the dependence of the attitude of the Line of Sight (LoS) vector, altitude and range on latitude. To simplify the analysis, it is assumed that the formation is orbiting a spherically-symmetric planet, so that the orbits are purely Keplerian.

3.1 Orbital elements

The orbital position of satellite j in the formation is adequately represented by the orbital elements $\boldsymbol{o}$:

$$\boldsymbol{o}^{(j)} = \left[a^{(j)}, e^{(j)}, i^{(j)}, \Omega^{(j)}, \omega^{(j)}, M^{(j)} \right]^{\mathrm{T}}, \tag{3.1}$$

called semi-major axis a, eccentricity e, inclination i, right ascension of the ascending node Ω, argument of perigee ω and mean anomaly M. These parameters are suitable to describe orbits because they remain constant, with the exception of mean anomaly, if the gravitational field is spherically symmetric. The semi-major axis determines the size of the orbit. The shape of a closed orbit is described by eccentricity, which ranges from zero (circular orbit) a value less than one (elliptical orbits). In case of an open orbit, e has a value from one (parabolic orbit) to infinity (hyperbolic orbits). The three angles (inclination, right ascension of the ascending node and argument of perigee) define the orientation of the orbit in 3D space. Finally, the mean anomaly defines the position of the satellite along the orbit relative to a reference epoch.

In the context of satellite formation orbits, the term relative orbital elements of satellite 1 relatively to satellite 2 $\boldsymbol{o}^{(12)}$ is introduced, which is simply the difference between the orbital elements of the satellites that compose the formation:

$$\boldsymbol{o}^{(12)} = \boldsymbol{o}^{(1)} - \boldsymbol{o}^{(2)} = \left[a^{(12)}, e^{(12)}, i^{(12)}, \Omega^{(12)}, \omega^{(12)}, M^{(12)} \right]^{\mathrm{T}}. \tag{3.2}$$

3.2 Orbit stability

For the formation to be stable, there is the obvious constraint that the semi-major axis of the orbits must be similar, i.e. $a^{(12)} \approx 0$. If not, the orbits have different periods and the satellites tend to travel away from each other. It could be considered that a formation-like motion occurs at those epochs when the satellites are in close

proximity but such type of intermittent formations, i.e. not maintained during the whole orbital period, is not considered.

The equality of the semi-major axes is the fundamental criteria for formation stability. It is only applicable when the motion is under the influence of purely spherically-symmetric gravitational fields; in realistic gravitational fields, this simplistic requirement is not sufficient. This is due to cross-track disturbances associated with the asymmetry of the gravitational field.

3.3 The trailing formation

In this formation both satellites follow exactly the same orbit, with the trailing satellite lagging at a distance behind the leading satellite. The LoS vector is nearly co-linear with the orbital track at all times.

If the eccentricity of both orbits is not zero, there is a relative motion in the vertical plane, as seen in Figure 3.1. In the top left-hand plot, one of the satellites is placed at the zero-coordinate and the relative motion of the other satellite is represented in the orbital plane, in the plane that contains the radial and cross-track vectors, also known as the Cross-track plane, and in the horizontal plane, which is perpendicular to the radial direction.

Alignment of the LoS vector :

- along-track
- radial, if $e^{(1)}$ or $e^{(2)}$ or $e^{(12)} \neq 0$

Inter-satellite motion :

- static, if $e^{(1)} = e^{(2)} = e^{(12)} = 0$
- cyclic non-zero-crossing, if $e^{(1)}$ or $e^{(2)}$ or $e^{(12)} \neq 0$

Formation characteristics :

- range: proportional to $M^{(12)}$
- relative motion: cyclic vertical component if $e^{(1)}$ or $e^{(2)}$ or $e^{(12)} \neq 0$

The eccentricity, when equal and non-zero in both orbits, introduces a circular relative motion in the orbital plane, refer to Figure 3.1, top left. Increasing the common eccentricity of the orbits leads to a larger amplitude of the circular motion, Figure 3.1, top right. In contrast, if the eccentricity is not the same for both orbits, then the relative motion is elliptical instead of circular, as shown in Figure 3.1, bottom left. Increasing the difference in eccentricity between both orbits results in a larger amplitude of the elliptical motion. In addition to the larger along-track

Figure 3.1 – The relative motion of the eccentric trailing formation, with one of the satellites located at the point with zero-coordinates. The top left-hand plot shows the relative motion of the satellites in the cross-track, orbital and horizontal planes, with $\boldsymbol{o}^{(1)}=[9000\text{km}, 0.20, 90^\circ, 0^\circ, 0^\circ, 0.00^\circ]$ and $\boldsymbol{o}^{(12)}=[0\text{km}, 0.00, 0^\circ, 0^\circ, 0^\circ, -2.00^\circ]$. The cross-track plane is defined as the plane that contains the radial and cross-track vectors, with the DoF perpendicular to the paper. The horizontal plane is perpendicular to the radial direction. On the top right-hand plot, the effect of different values for the eccentricity common to both orbits is depicted, with $\boldsymbol{o}^{(1)}=[9000\text{km}, e, 90^\circ, 0^\circ, 0^\circ, 0.00^\circ]$ and $\boldsymbol{o}^{(12)}=[0\text{km}, 0.00, 0^\circ, 0^\circ, 0^\circ, -2.00^\circ]$. The bottom left-hand plot shows the effect of different values of eccentricity of satellite 1 relatively to satellite 2, with $\boldsymbol{o}^{(1)}=[9000\text{km}, 0.20, 90^\circ, 0^\circ, 0^\circ, 0.00^\circ]$ and $\boldsymbol{o}^{(12)}=[0\text{km}, e^{(12)}, 0^\circ, 0^\circ, 0^\circ, -114.59^\circ]$. The bottom right-hand plot shows the effect of different values of the mean anomaly of satellite 1 relatively to satellite 2, with $\boldsymbol{o}^{(1)}=[9000\text{km}, 0.20, 90^\circ, 0^\circ, 0^\circ, 0.00^\circ]$ and $\boldsymbol{o}^{(12)}=[0\text{km}, 0.00, 0^\circ, 0^\circ, 0^\circ, M^{(12)}]$.

distance, increasing the value of the $M^{(12)}$ introduces a small eccentricity and larger amplitude in the relative motion, as illustrated in Figure 3.1, bottom right. Larger values of the $M^{(12)}$ accentuate the eccentricity of the relative motion. As the eccentricity approaches zero, the relative motion converges to a point. In all cases, such formations are still regarded as a trailing formation, as long as the along-track distance is larger than the amplitude of the elliptical or circular motion.

For the purpose of Earth Observation, circular orbits are more desirable simply because the altitude is always at the minimum. On the other hand, truly circular orbits, i.e. when the eccentricity is formally zero, are a theoretical idealization without any practical application because they are impossible due to the Earth's non-spherical gravitational field. The trailing formation has, therefore, limited relative motion in the vertical direction.

3.4 The pendulum formation

The pendulum formation is characterised by a cross-track cyclic motion. Term *pendulum* can be traced to Sharifi et al. (2007), although Sneeuw and Schaub (2005) already considers formations with cross-track displacements in the context of gravity field parameter estimation. Bezděk et al. (2014) shows that the East-West sensitivity of the data reduces the errors in the estimated sectorial coefficients and mitigates the effects of a large polar gap, in the likely case that the satellites fly in a sun-synchronous orbit to meet the power requirements of a drag-free control system.

As shown in Figure 3.2, top left, the cyclic motion of this particular pendulum formation is restricted to the cross-track and horizontal planes. The amplitude of the cross-track motion is controlled by the inclination of satellite 1 relatively to satellite 2, $i^{(12)}$, as shown in the top right of Figure 3.2, or by the right ascension of the ascending node of satellite 1 relatively to satellite 2, $\Omega^{(12)}$, shown in the bottom right (notice the scales of the axes is not the same). The eccentricity of both orbits distorts the symmetric pattern of the cross-track motion, as shown in Figure 3.2, bottom left. The orbits of gravimetric satellites are usually (nearly) circular; the dependency of the relative motion of the pendulum formation on eccentricity is reported here to illustrate the possibilities within the limitations of orbital mechanics.

The formations are identical in their relative motion, as long as one of $i^{(12)}$ or $\Omega^{(12)}$ is zero. Figure 3.2, top right, is identical if $\Omega^{(12)} = 0 \wedge i^{(12)} \neq 0$ or $\Omega^{(12)} \neq 0 \wedge i^{(12)} = 0$. The difference between considering these two cases is that the minimum range is located at the equator or at the poles, respectively. The terms *Equatorial* and *Polar* pendulum formations are henceforth respectively associated with these cases. In practice, the Equatorial pendulum is not stable because the different inclinations of
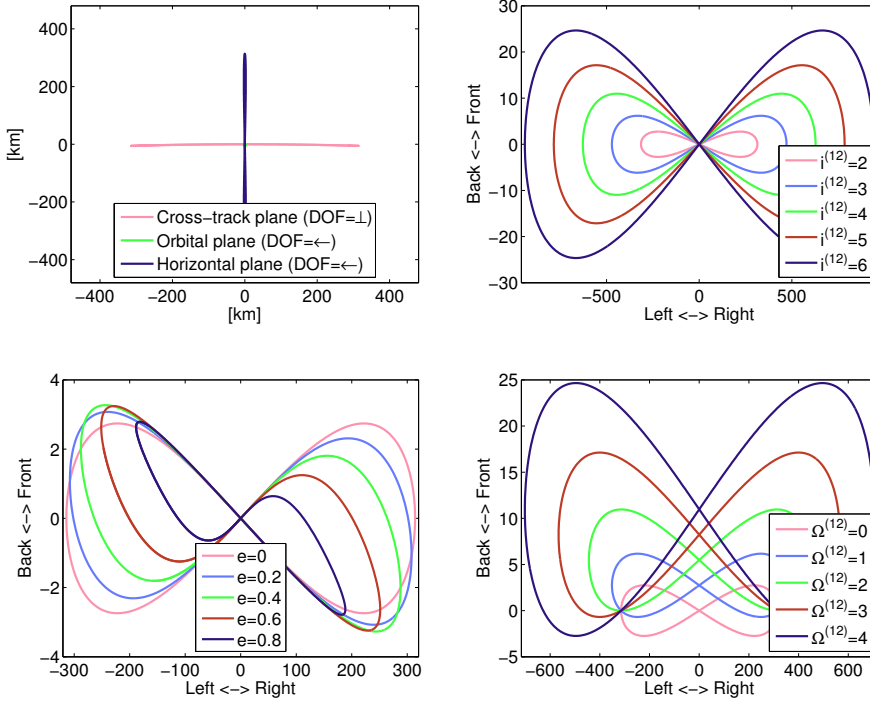
Figure 3.2 – The relative motion of the pendulum formation, with one of the satellites located at the zero-coordinate. The top left-hand plot shows the relative motion of the satellites in the cross-track, orbital and horizontal planes, with $\boldsymbol{o}^{(1)}$=[9000km, 0.00, 90º, 0º, 0º, 0.00º] and $\boldsymbol{o}^{(12)}$=[0km, 0.00, 2º, 0º, 0º, 0.00º]. The cross-track plane is defined as the plane that contains the radial and cross-track vectors, with the DoF perpendicular to the paper. The horizontal plane is perpendicular to the radial direction. The top right-hand plot shows the effect of different values of the inclination of satellite 1 relatively to satellite 2, with $\boldsymbol{o}^{(1)}$=[9000km, 0.00, 90º, 0º, 0º, 0.00º] and $\boldsymbol{o}^{(12)}$=[0km, 0.00, $i^{(12)}$, 0º, 0º, 0.00º]. The bottom left-hand plot depicts the relative motion when changing the eccentricity of both orbits, $\boldsymbol{o}^{(1)}$=[9000km, e, 90º, 0º, 0º, 0.00º] and $\boldsymbol{o}^{(12)}$=[0km, 0.00, 2º, 0º, 0º, 0.00º]. The bottom right-hand plot illustrates the effect of increasing the right ascension of the ascending node of satellite 1 relatively to satellite 2, with $\boldsymbol{o}^{(1)}$=[9000km, 0.00, 90º, 0º, 0º, 0.00º] and $\boldsymbol{o}^{(12)}$=[0km, 0.00, 2º, $\Omega^{(12)}$, 0º, 0.00º].

the orbits lead to different precession rates, changing $\Omega^{(12)}$ over time. Nevertheless, the discussion includes this case for completeness.

It is possible to set the location of the intersection of the ground-tracks of both satellties, *the cross-over point*, at a designated latitude, different from 0° or 90°, by combining the relative polar and equatorial rotations, $i^{(12)}$ and $\Omega^{(12)}$ respectively, of the orbital planes of the satellites. The latitude of the cross-over point is:

$$\lambda = \tan^{-1}\left(\frac{\Omega^{(12)}}{i^{(12)}}\right). \tag{3.3}$$

In this way, the range is more homogeneously distributed over latitude. For example, if $i^{(12)} = \Omega^{(12)}$, then both the cross-over and maximum range points are located at latitudes $\pm 45°$ and the formation exhibits an intermediate range at the poles and equator. The rotation of the Earth carries the cross-over points to different longitudes, alternating the geographical locations under larger and small ranges. This is in contrast to the equatorial and polar pendulum formations that lead to a distribution of range constant with latitude. In practice, a satellite formation with $i^{(12)} \neq 0$ is unstable; only if $i^{(12)}$ is very small and $i^{(1)} \approx i^{(2)} \approx 90°$, is there any reason to consider this case. Under these conditions, the latitude of the cross-over point will be close to the poles. It should be noted that setting the cross-over point a few degrees away from the poles might be beneficial to avoid having the minimum range consistently at the same location. If the location of minimum range is always at the poles, there is a detrimental effect on the accuracy of the estimated gravity field model at those locations (Encarnação et al., 2008).

Figure 3.2, bottom right, shows the pendulum formation with cross-over latitudes of 0°, 26.6°, 45°, 56.3° and 63.4°, for $\Omega^{(12)}$ equal to 0°, 1°, 2°, 3° and 4°, respectively. The along-track displacement becomes larger with increasing $\Omega^{(12)}$ because the orbital plane of the second satellite is rotated relative to the orbital plane of the first satellite by two rotations, i.e. by $i^{(12)}$, which does not change the along-track displacement, and consequentially by $\Omega^{(12)}$, which does. This effect can be compensated with the adequate choice of $M^{(12)}$.

3.4.1 The pendulum formation with along-track displacement

It is also possible to define the pendulum formation so that there is a combination of the along- and cross-track offsets. Some authors (e.g. Sharifi et al., 2007; Elsaka et al., 2013; Massotti et al., 2013; Reubelt et al., 2014) restrict the definition of the pendulum formation to this case. Formally, no distinction is made in this text between the pendulum formation with or without along-track displacement.
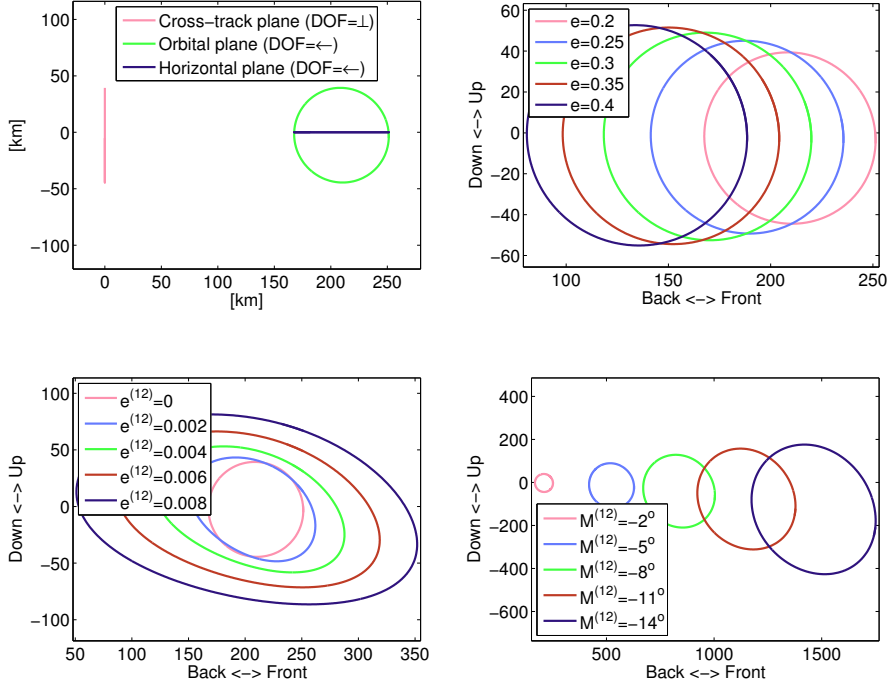
Figure 3.3 – The relative motion of the trailing-pendulum formation, with one of the satellites located at the point with zero-coordinates. The left-hand plot shows the relative motion of the satellites in the cross-track, orbital and horizontal planes, with $\boldsymbol{o}^{(1)}$=[9000km, 0.00, 90°, 0°, 0°, 0.00°] and $\boldsymbol{o}^{(12)}$=[0km, 0.00, 2°, 0°, 0°, −2.00°]. The cross-track plane is defined as the plane that contains the radial and cross-track vectors, with the DoF perpendicular to the paper. The horizontal plane is perpendicular to the radial direction. The top right-hand plot shows the effect of different values of the inclination of satellite 1 relatively to satellite 2, with $\boldsymbol{o}^{(1)}$=[9000km, 0.00, 90°, 0°, 0°, 0.00°] and $\boldsymbol{o}^{(12)}$=[0km, 0.00, $i^{(12)}$, 0°, 0°, −2.00°].

It is possible to add an along-track displacement by setting $M^{(12)} \neq 0$, as illustrated in Figure 3.3, left-hand side (cf. with Figure 3.2, top left). It should be noted that in this type of pendulum formation, the LoS vector is never orientated along the cross-track direction, since there is always an along-track component. The relative motion is identical, compare Figure 3.3 right-hand plot with Figure 3.2 top-right-hand plot, only differing in the along-track distance between the two satellites as shown by the values on the ordinate axes.

Additionally, it is possible to introduce vertical in-plane relative motion by setting $e^{(12)} \neq 0$ (not shown) or $e^{(1)} = e^{(2)} \neq 0$, refer to Figure 3.4 left-hand plot. Increasing the value of eccentricity leads to a larger amplitude of the vertical and along-track relative motion, as shown in Figure 3.4 right-hand plot. The relative motion in the orbital plane is equal to that of the trailing formation with $i^{(12)} = 0$, cf. with Figure 3.1 bottom right-hand plot.

Alignment of the LoS vector :

- cross-track
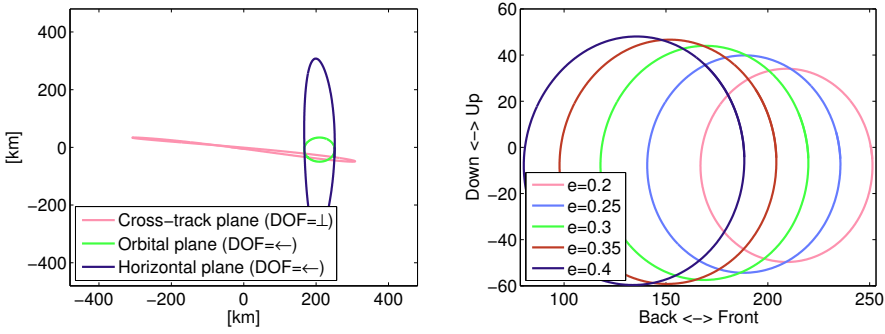
Figure 3.4 – The relative motion of the eccentric trailing-pendulum formation, with one of the satellites located at the zero-coordinate. The left-hand plot shows the relative motion of the satellites in the cross-track, orbital and horizontal planes, with $\boldsymbol{o}^{(1)}$=[9000km, 0.20, 90°, 0°, 0°, 0.00°] and $\boldsymbol{o}^{(12)}$=[0km, 0.00, 2°, 0°, 0°, −2.00°]. The cross-track plane is defined as the plane that contains the radial and cross-track vectors, with the DoF perpendicular to the paper. The horizontal plane is perpendicular to the radial direction. The right-hand plot shows the relative motion in the orbital plane for different values of the eccentricity, with $\boldsymbol{o}^{(1)}$=[9000km, e, 90°, 0°, 0°, 0.00°] and $\boldsymbol{o}^{(12)}$=[0km, 0.00, 2°, 0°, 0°, −2.00°].

- along track, if $M^{(12)} \neq 0$
- radial, if $e^{(1)} \neq 0$ or $e^{(2)} \neq 0$

Inter-satellite motion :

- absent in the along track direction, if $e^{(1)} = e^{(2)} = e^{(12)} = 0$
- cyclic

Formation characteristics :

- maximum range: function of $i^{(12)}$, $\Omega^{(12)}$ (cross-track), $M^{(12)}$ (along-track) and $e^{(1)}$ or $e^{(2)}$ or $e^{(12)}$ (radial)
- latitude of cross-over: function of $\Omega^{(12)}/i^{(12)}$

3.5   The cartwheel formation

The cartwheel formation makes it is possible to measure the range along the radial direction, which is an advantage because the sensitivity of such measurements is more isotropic. This can be understood from the fact that the spherical harmonics representing a gravitational field are dependent on the radial direction for all degrees and orders. On the other hand, the zonal and sectorial spherical harmonic coefficients do not depend on the longitudinal and latitudinal directions, respectively. As a consequence, measuring the range along the longitudinal or latitudinal directions, as happens in the case of the polar pendulum ($M^{(12)} = 0$) or trailing formations (both non-eccentric), leads to the inaccurate estimation of zonal or sectorial coefficients, respectively. The cartwheel formation, since it samples the gravitational field along the vertical direction, is less sensitive to this limitation. The cartwheel formation is mentioned conceptually by Rummel et al. (1978), although the term is later used in the context of gravity field recovery by Sneeuw et al. (2005).

Due to orbital dynamics, the radial motion is always coupled with the along-track motion, so that the satellites follow a relative elliptical motion in the common orbital plane. For this to happen, the eccentricity and argument of perigee of satellite 1 relatively to satellite 2 must be different from zero, in addition to a proper choice of the relative mean anomaly. The major axis of this ellipse is aligned with the horizontal plane, so that the along-track maximum range is twice as large as the vertical maximum range.

The simplest form of cartwheel formation is one where both orbits have their argument of perigee in opposite sides, i.e. 180° apart. In Figure 3.5 left-hand plot, the relative motion of this formation is represented in green. This curve is not exactly an ellipse because the relative motion is plotted in the Local Horizontally-aligned Reference Frame (LHRF), which does not follow the curvature of the orbit. Therefore,
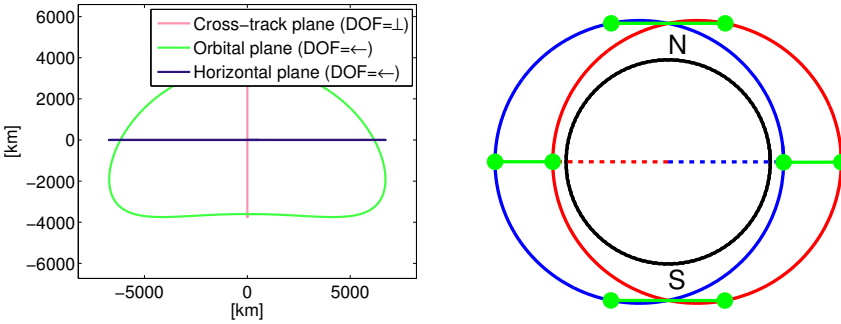
Figure 3.5 – The relative motion of the cartwheel formation, with vertical orientation of the LoS vector at the equator and horizontal on the poles. One of the satellites located at the point with zero-coordinates. The left-hand plot shows the relative motion of the satellites in the cross-track, orbital and horizontal planes, with $\boldsymbol{o}^{(1)}$=[9000km, 0.20, 90º, 0º, 0º, 0.00º] and $\boldsymbol{o}^{(12)}$=[0km, 0.00, 0º, 0º, 180º, 180.00º]. The cross-track plane is defined as the plane that contains the radial and cross-track vectors, with the DoF perpendicular to the paper. The horizontal plane is perpendicular to the radial direction. The right-hand plot illustrates the orbits (in blue and red) of the satellites in the formation (green dots) and the LoS vector (green lines) at horizontal and vertical orientation. The Earth is represented by the black circle. The dotted line connects the centre of the Earth to the perigee of each orbit.

a distant object at the same altitude appears to be below the local horizontal plane. The elliptical relative motion of the cartwheel formation is visible when plotted in the LHRF only for small values of the maximum ranges.

It is interesting to note that the LoS vector is in the horizontal plane on the full and half-period, while being vertical on the quarter and three-quarter period. This means that an argument of perigee of 0° and 180° produces a formation with vertical orientation of the LoS vector at the equator and horizontal on the poles, refer to Figure 3.5, right-hand plot.

On the other hand, considering an argument of perigee of 45° and 225° forces the attitude of the formation to be more homogeneous with latitude, since both vertical and horizontal orientations are over latitude ±45°, refer to Figure 3.6, right-hand plot. At the poles and equators, this formation has the LoS vector with an attitude of 45°. The relative motion shown in Figure 3.6 left-hand plot, is the same as in the cartwheel formation with vertical orientation of the LoS vector at the equator, cf. with Figure 3.5, left-hand plot.

If $\omega^{(12)}$ is not 180°, the satellites are closer at a certain latitude (centred around
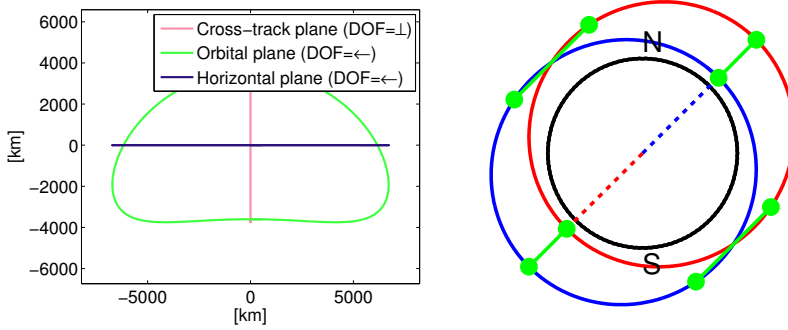
Figure 3.6 – The relative motion of the cartwheel formation, with vertical orientation of the LoS vector at the latitude ±45°. One of the satellites is located at the point with zero-coordinates. The left-hand plot shows the relative motion of the satellites in the cross-track, orbital and horizontal planes, with $o^{(1)}$=[9000km, 0.20, 90°, 0°, 45°, 0.00°] and $o^{(12)}$=[0km, 0.00, 0°, 0°, 180°, 180.00°]. The cross-track plane is defined as the plane that contains the radial and cross-track vectors, with the DoF perpendicular to the paper. The horizontal plane is perpendicular to the radial direction. The right-hand plot illustrates the orbits (in blue and red) of the satellites in the formation (green dots) and the LoS vector (green lines) at horizontal and vertical orientation. The Earth is represented by the black circle. The dotted line connects the centre of the Earth to the perigee of each orbit.
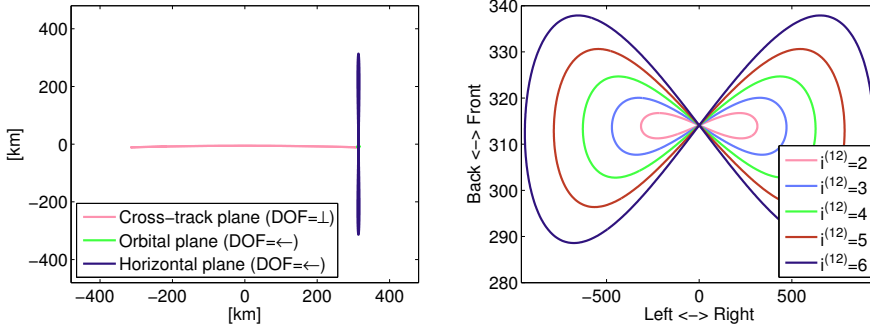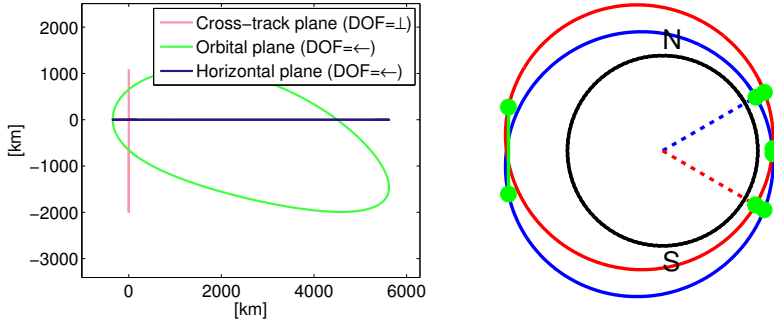
Figure 3.7 – The relative motion of the off-centred cartwheel formation, with one of the satellites is located at the point with zero-coordinates. The left-hand plot shows the relative motion of the satellites in the cross-track, orbital and horizontal planes, with $\mathbf{o}^{(1)}$=[9000km, 0.20, 90°, 0°, 30°, 0.00°] and $\mathbf{o}^{(12)}$=[0km, 0.00, 0°, 0°, 300°, 60.00°]. The cross-track plane is defined as the plane that contains the radial and cross-track vectors, with the DoF perpendicular to the paper. The horizontal plane is perpendicular to the radial direction. The right-hand plot illustrates the orbits (in blue and red) of the satellites in the formation (green dots) and the LoS vector (green lines) at horizontal and vertical orientation. The Earth is represented by the black circle. The dotted line connects the centre of the Earth to the perigee of each orbit.

the angular mean of both arguments of perigee) and further apart on the other side of the globe (at the symmetric latitude). In this case the ellipse is not centred, as shown in Figure 3.7, left-hand plot. The orientation of the LoS vector of the off-centred cartwheel formation is rotating slowly close to the horizontal direction when $M \approx 180°$ and changing rapidly between the vertical, horizontal and back to the vertical direction when $M \approx 0°$. This motion is illustrated in Figure 3.7, right-hand plot, by the close location of the points of vertical attitude of the LoS vector, identified by the dashed lines connecting to the centre of the Earth, and the point of horizontal attitude of the LoS vector, situated in-between.

A cartwheel formation with $\omega^{(12)}$=180° maintains the orientation of the LoS vector constant relative to the inertial frame, as seen in Figure 3.5 and Figure 3.6, right-hand plots. In principle, this is technically favourable, since it relieves the Attitude Control System (ACS) of one satellite from actively tracking the other satellite. On closer inspection, however, it is possible that the differential drag experienced by the satellites, particularly at Low-Earth Orbit (LEO), requires frequent active

thrust control in order to maintain the formation, introducing black-out periods and increasing the demand on the ACS.

Alignment of the LoS vector :

- along-track
- vertical

Inter-satellite motion :

- cyclic, non-zero-crossing

Formation characteristics :

- maximum range: function of $\omega^{(12)}$, $M^{(12)}$, $e^{(1)}$, $e^{(2)}$ or $e^{(12)}$
- latitude of vertical/horizontal LoS: function of $\omega^{(1)}$, $\omega^{(12)}$
- centred/off-centred elliptical relative motion: function of $\omega^{(12)}$

3.6 Relative orbital elements

Table 3.1 summarises the relative orbital elements required to define a particular formation considered in the thesis.

	trailing	pendulum	cartwheel
$a^{(12)}$	0	0	0
$e^{(12)}$	0^a	0^a	$e^{(1)} \neq 0 \vee e^{(2)} \neq 0 \vee e^{(12)} \neq 0$
$i^{(12)}$	0	$\neq 0^b$	0
$\Omega^{(12)}$	0	$\neq 0^c$	0
$\omega^{(12)}$	0	0	$\neq 0$
$M^{(12)}$	$\neq 0$	0^d	$\neq 0$

^{a}Optionally, vertical motion if $e^{(1)} \neq 0 \vee e^{(2)} \neq 0 \vee e^{(12)} \neq 0$
^{b}or 0 if $\Omega^{(12)} \neq 0$
^{c}or 0 if $i^{(12)} \neq 0$
^{d}Optionally, along-track displacement if $M^{(12)} \neq 0$

Table 3.1 – Orbital elements difference for basic formations

3.7 Distinction between similar formations

In Section 3.3, Section 3.4 and Section 3.5, the trailing, pendulum and cartwheel formations were presented. It is possible to come up with a formation in such a way

that it can be defined in more than one of above-mentioned types. For example, the trailing formation can be composed of satellites following an eccentric orbit, so as to introduce vertical relative motion. In that case it can be argued that such formation can also be regarded as a cartwheel formation. This section separates formation types from each other unambiguously. The definitions presented in this section are valid for the thesis, although they are not in conflict with the terminology found in literature.

3.7.1   Distinction between the pendulum and all other formations

The pendulum formation always has cross-track relative motion. The trailing and cartwheel formations, on the other hand, exhibit only in-plane relative motions. In this case, the distinction is immediate: as long as there is cross-track motion, such formation will be associated with the pendulum type.

   The pendulum formation always has non-zero relative inclination and/or relative right ascension of the ascending node, in contrast with the trailing cartwheel formations, which, due to their in-plane requirement, have these two relative orbital elements equal to zero.

3.7.2   Distinction between trailing and cartwheel formations

The trailing formation always has along-track displacement, while the cartwheel formation always shows vertical relative motion. The distinction is made when the relative motion is such that the satellites revolve around each other, in which case it is referred to as a cartwheel formation. If the ellipse that defines the motion of one satellite relative to the other does not enclose the latter, then such formation is defined as the trailing formation.

   With this in mind, Figure 3.7 represents the motion of a cartwheel formation, since the zero-coordinate is located inside the ellipse that defines the relative motion. On the other hand, Figure 3.1 clearly depicts an example of the Trailing formation.

3.8   Orbit simulation of Satellite Formations

With the purpose of simulating the motion of satellite formations in the context of studying future gravimetric satellite missions, there is the need to derive the orbital elements of formations with a pre-defined relative motion. This section presents the

methodology that allows for the relative orbital elements $\boldsymbol{o}^{(12)}$ to be computed, given the required relative motion $\mathbf{x}^{(12)}$ and the orbital elements of satellite 2, $\boldsymbol{o}^{(2)}$.

3.8.1 The Hill equations

The Hill equations (Hill, 1878), also known as the Clohessy-Wiltshire equations (Clohessy and Wiltshire, 1960), describe the relative motion of two satellites in close proximity, around a circular Keplerian orbit in the Hill Reference Frame (HRF, Section A.8). The solution to this linearised system of differential equations, after inverse linear mapping, determines unambiguously the orbital elements of a given formation. This approach is accurate if used to calculate the orbital elements of a close formation (i.e. with a range of less than a few hundred meters) and around a circular reference orbit. Nevertheless, as it will be shown later, it is still applicable to formations with a large maximum range, i.e. up to hundreds of kilometres, and to eccentric reference orbits.

The Hill equations describe in the HRF the linearised relative motion of the satellites flying in a circular orbit (Schaub and Junkins, 2003). Let the orbit position of satellite 1 relatively to satellite 2 be represented by $\mathbf{x}^{(12)} = [x, y, z, \dot{x}, \dot{y}, \dot{z}]^{\mathrm{T}}$, the Hill equations are:

$$\begin{aligned}
\ddot{x} - 2n\dot{y} - 3n^2 x &= 0 \\
\ddot{y} + 2n\dot{x} &= 0 \\
\ddot{z} + n^2 z &= 0.
\end{aligned} \tag{3.4}$$

The HRF, centred on the chief satellite is defined as follows (refer to Figure 3.8):

x-axis : parallel to the radial vector, perpendicular to the horizontal plane;
z-axis : parallel to the orbital angular momentum vector, perpendicular to the orbital plane;
y-axis : right-hand perpendicular to the x- and z-axis, parallel to the DoF if circular orbit.

The mean angular orbital rate n is:

$$n = \sqrt{\frac{G_0 M_\oplus}{r_c^3}}, \tag{3.5}$$

with r_c the radius of the circular orbit of the chief satellite and $G_0 M_\oplus$ the geocentric gravitational constant.
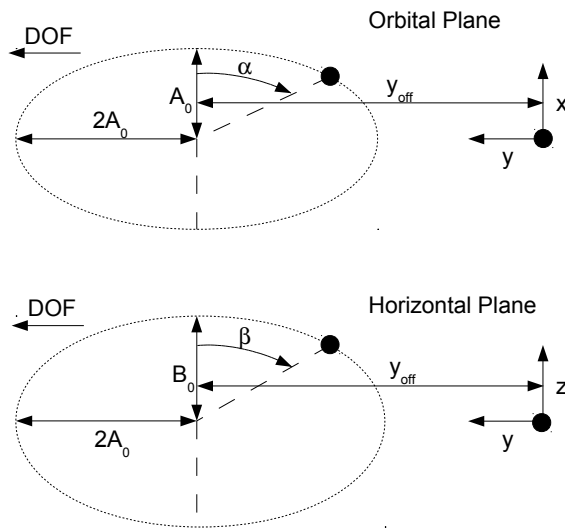
Figure 3.8 – Hill Reference Frame with the boundary conditions of the Hill equations

3.8.2 The formation parameters

The set of ordinary differential equations has the explicit solution given by Schaub and Junkins (2003):

$$
\begin{aligned}
x &= A_0 \cos(n t + \alpha) + x_{\text{off}} \\
y &= -2\,A_0 \sin(n t + \alpha) + y_{\text{off}} \\
z &= B_0 \cos\big(n t + \beta\big).
\end{aligned}
\tag{3.6}
$$

The following boundary conditions are relevant, refer to Figure 3.8:

x_{off}: radial offset between the two satellites;

y_{off}: along-track offset between the two satellites;

A_0: amplitude of the elliptical relative motion on the orbital plane. Due to orbital mechanics, it is always an ellipse with the major axis twice as large as the minor axis. Therefore, the horizontal amplitude is twice that of the vertical amplitude.

B_0: amplitude of the motion perpendicular to the orbital plane;

α: initial phase angle of the deputy satellite in the orbital plane, relative to the x-axis;

β: initial phase angle of the deputy satellite in the horizontal plane, relative to the z-axis.

These parameters also define the initial position of the deputy satellite relatively to the chief satellite:

$$
\begin{aligned}
x_0 &= A_0 \cos(\alpha) + x_{\text{off}} \\
y_0 &= -2\,A_0 \sin(\alpha) + y_{\text{off}} \\
z_0 &= B_0 \cos\big(\beta\big).
\end{aligned}
\tag{3.7}
$$

The first requirement for a stable formation is that the semi-major axis of satellite 1 relatively to satellite 2 is zero. Consequently, Eq. (3.6) meets this requirement if the radial offset x_{off} is set to zero:

$$
x_{\text{off}} \equiv \frac{2}{n}\big(\dot{y}_0 + 2 n x_0\big) = 0 \Rightarrow \dot{y}_0 = -2 n x_0.
\tag{3.8}
$$

The importance of these parameters is that they inherently provide a way to describe a feasible formation within the constraints of orbital mechanics. Their definition forbids impossible formations such as, for example, formations with constant cross-track or radial offset. These parameters are henceforth referred to as *formation parameters*.

As an example, Table 3.2 shows the typical values of the formation parameters of some formations. The vertical and horizontal phases are not included since they are free parameters that define the initial position of the deputy satellite relative to the chief satellite within the relative motion defined by the other three parameters.

Parameter	symbol	trailing	pendulum	cartwheel
along-track offset	y_{off}	$\neq 0$	$(\neq 0^a)$	0
radial amplitude	A_0	$(\neq 0^b)$	$(\neq 0^b)$	$\neq 0$
cross-track amplitude	B_0	0	$\neq 0$	0

[a]Optional, to introduce along-track displacement.
[b]Optional, to introduce vertical motion.

Table 3.2 – Formation parameters

3.8.3   Formations in elliptical mean orbits

So far, the requirement that the mean orbit is circular has been maintained. This section looks at relaxing this limitation, so that elliptical orbits can be considered. Although circular mean orbits are most desirable to Earth Observation satellite missions, orbits with near-zero eccentricity are not to be disregarded, should other requirements dictate so, e.g. orbit repeat period or orbit stability under a realistic gravitational field.

In Sharifi et al. (2007), the formation parameters are expressed as function of the initial conditions in the Hill reference frame, i.e. substituting $t = 0$ in Eq. (3.6) and solving for the formation parameters:

$$
\begin{aligned}
A_0 &= \frac{1}{n}\sqrt{\dot{x}_0^2 + \left(2\dot{y}_0 + 3n x_0\right)^2} \\
B_0 &= \frac{1}{n}\sqrt{\dot{z}_0^2 + n^2 z_0^2} \\
\alpha &= \arctan\left(\frac{\dot{x}_0}{3n x_0 + 2\dot{y}_0}\right) \\
\beta &= \arctan\left(-\frac{\dot{z}_0}{n z_0}\right) \\
y_{\text{off}} &= y_0 - \frac{2}{n}\dot{x}_0.
\end{aligned}
\tag{3.9}
$$

In Schaub and Junkins (2003), a more general constraint than that in Eq. (3.8) is derived, in which eccentric orbits are contemplated ($e > 0$):

$$
x_{\text{off}} = \dot{y}_0 + n x_0 \frac{2 - e}{\sqrt{(1 + e)(1 - e)^3}} = 0.
\tag{3.10}
$$

For a given set of formation parameters $\left[\,y_{\mathrm{off}}, A_0, B_0, \alpha, \beta\,\right]^{\mathrm{T}}$, the system of equations given by Eq. (3.9) and Eq. (3.10) can be solved for $\mathbf{x}^{(12)}{}_0 = \left[\,x_0, y_0, z_0, \dot{x}_0, \dot{y}_0, \dot{z}_0\,\right]^{\mathrm{T}}$, using a non-linear Least-Squares (LS) solver, for example.

The motivation to consider Eq. (3.10) instead of Eq. (3.8) is that the computations of the $\mathbf{x}^{(12)}$ initial state vector are more robust. The Hill equations are valid under strict conditions which are not particularly useful to simulation of gravimetric satellite formations. With the improvement of the procedure with the inclusion of Eq. (3.10), the requirements are more relaxed and the resulting $\mathbf{x}^{(12)}$ is associated with orbits of more stable formations.

3.8.4 Inverse linear mapping

Although it is interesting to know the relative motion of the satellites in the HRF, it is much more useful to know their absolute motion so that their orbits can be used for the simulation of gravimetric satellite missions.

One possibility is to add the orbit position of satellite 1 relatively to satellite 2 given by Eq. (3.6) to the orbit position of satellite 2, after appropriate coordinate transformations so that both quantities are in the same reference frame. However, the resulting orbit positions of satellite 1 have physical meaning only when the maximum range is small, since only in that case Eq. (3.4) is accurate. For a large maximum range, the resulting orbit violates the laws of motion.

The solution is to calculate the relative orbital elements $\boldsymbol{o}^{(12)}$ using the so-called *inverse linear mapping* procedure. Since the result are two sets of orbital elements, the corresponding orbits comply with the laws of motion. The relative motion $\mathbf{x}^{(12)}$ is connected to the relative orbital elements via the matrix $\boldsymbol{A}\big(\boldsymbol{o}^{(2)}\big)^{-1}$, which is function of the orbital elements of satellite 2, $\boldsymbol{o}^{(2)}$:

$$\boldsymbol{o}^{(12)} = \boldsymbol{A}\big(\boldsymbol{o}^{(2)}\big)^{-1}\mathbf{x}^{(12)}. \tag{3.11}$$

The inverse mapping matrix $\boldsymbol{A}\big(\boldsymbol{o}^{(2)}\big)^{-1}$ is given in Schaub and Junkins (2003, pp. 697–698) and duplicated in Appendix B.

It should be noted that only one epoch of $\mathbf{x}^{(12)}$ is needed to derive $\boldsymbol{o}^{(12)}$. The current analysis is done strictly under the assumption that the motion is governed by Keplerian dynamics; consequently, $\boldsymbol{o}^{(2)}$ and $\boldsymbol{o}^{(12)}$ are constant in time, with the exception of the mean anomaly, which changes in time according to Kepler's equation (see e.g. Weisstein, 2015). For this reason it is easier to consider $\mathbf{x}^{(12)}$ at $t = 0$.

Having computed $\boldsymbol{o}^{(12)}$ (and given $\boldsymbol{o}^{(2)}$), the Keplerian reference orbits of the first satellite are derived from $\boldsymbol{o}^{(2)} + \boldsymbol{o}^{(12)}$, from which the orbital positions in Cartesian

coordinates in the Celestial Reference Frame (CRF) can be computed (see e.g. Cornelisse et al., 1979, p. 381).

The computation of the Keplerian reference orbits is simple and efficient but evidently do not accurately represent the motion of spacecraft orbiting the Earth. They are used when the accuracy of the orbital positions is not required to be high, such as the cases of high-low Satellite-to-Satellite Tracking and Satellite Gravity Gradient simulations.

The Keplerian reference orbits are used directly in the simulation of high-low Satellite-to-Satellite Tracking (hl-SST) observations, since the accuracy of the orbital positions (for simulation purposes) is not required to be high. In case of low-low Satellite-to-Satellite Tracking simulations, where there is the need to derive realistic range observations, the Keplerian reference orbits serve as a reference for the computation of Modelled orbits, which are integrated on the basis of a high-degree gravity field model.

The inverse linear mapping procedure is validated in Section B.1.

3.8.5 Orbits of satellites formations under an aspherical gravitational field

In the numerical analysis done in the thesis, two types of orbits are considered: *Keplerian reference orbits* and non-Keplerian orbits, henceforth called *Modelled orbits*. The former are needed in order to compute the latter, which results in a two-step procedure. In the first step, the Keplerian reference orbits are produced according to the procedure presented in Section 3.8.3. These orbits serve as basis for the estimation of the initial state-vector of the Modelled orbits in the second step. The Modelled orbits are the result of highly-accurate numerical integration on the basis of a realistic gravity field model and the estimated initial state vectors.

Keplerian reference orbits

The Keplerian reference orbits are computed by exploiting the procedure described in Section 3.8, summarized in Figure 3.9. The formation is defined by a set of formation parameters, refer to Section 3.8.2 and by the orbit position of satellite 2, described by the respective orbital elements, $\boldsymbol{o}^{(2)}$. The corresponding position at $t = 0$ in the Hill reference frame $\mathbf{x}^{(12)}{}_0$ is determined by solving the system of equations given by Eq. (3.9) and Eq. (3.10), considering the known $\boldsymbol{o}^{(2)}$, Section 3.8.3. Using linear mapping between the Hill frame coordinates and orbital elements differences, as described in Section 3.8.4, the relative orbital elements of satellite 1 relatively to

satellite 2, $\boldsymbol{o}^{(12)}$ are determined from which the orbital elements of satellite 1, $\boldsymbol{o}^{(1)}$ are readily computed. Consequentially, the orbits of the satellites that compose the formation are described by $\boldsymbol{o}^{(1)}$ and $\boldsymbol{o}^{(2)}$, which are treated as mean orbital elements, i.e. constant throughout the simulation (with the obvious exception of the mean anomaly, which is function of time as defined by Kepler's equation).

The motivation to start with Keplerian reference orbits is that it is simpler to determine the stable relative motion of the satellites that compose a formation without the influence of the higher degree terms gravitational disturbances. The motion of a satellite integrated on the basis of a high-order gravity field model suffers from many gravitational disturbances that make it impossible to use the available analytical tools, such as the linearised Hill equations (Section 3.8.1).

Modelled orbits

The Keplerian reference orbit serves as input for the second step, the computation of the Modelled orbit. This orbit is a collection of successive 6-hours arcs, each of which is integrated considering the initial state vector that minimises its distance to the Keplerian reference orbit. As a result of this procedure, there are discontinuities at the extremities of arcs and the bordering data is discarded. The estimation of the initial state vectors and the orbit integration is done with the Position And Navigation Data Analyst (PANDA) software (Zhao 2004).
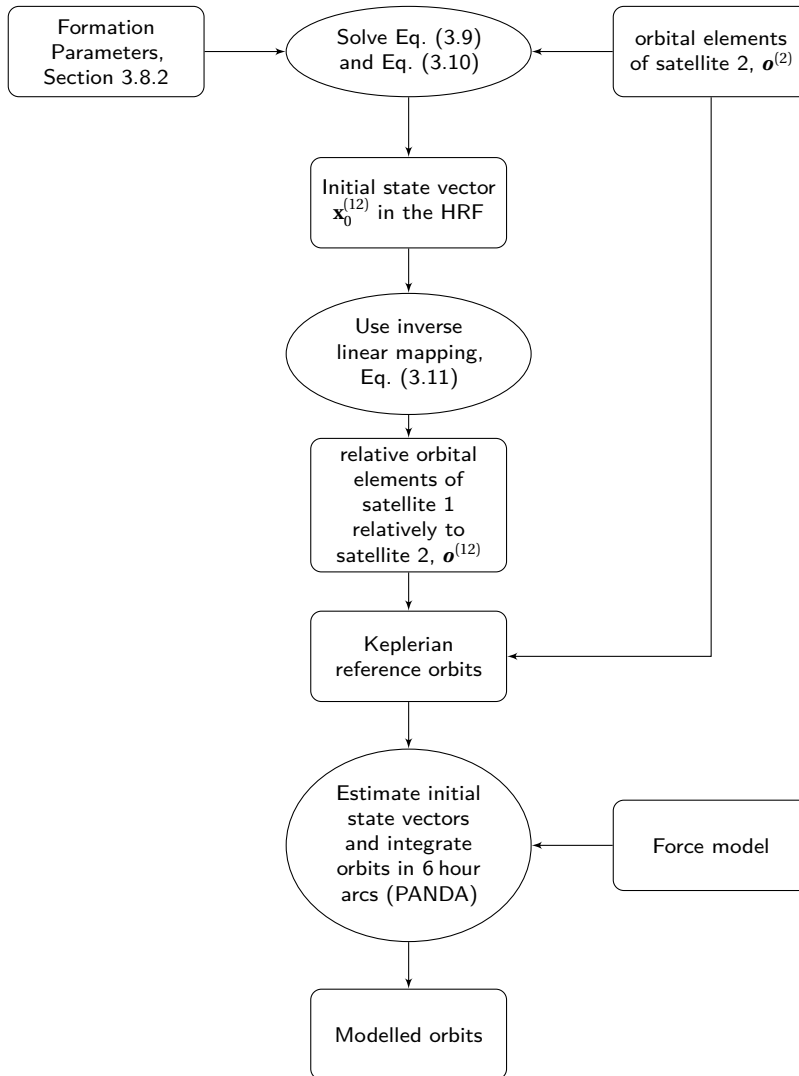
Figure 3.9 – Diagram illustrating the procedure used to simulate *Keplerian reference orbits* and *Modelled orbits*.

3.9   Summary

Satellite formations are promising for future gravimetric because they make it possible to use dedicated instruments to derive extremely accurate ranging data. In addition, the concept has been proven by the Gravity Recovery And Climate Experiment (GRACE) satellites and the high quality data they have produced. In spite of the accomplishments of the GRACE mission, the trailing formation is not the most optimal formation for measuring the gravitational field of the Earth and its variations in time. The nearly constant alignment of the LoS vector with the meridional direction amplifies errors in the data, in particular decreasing the accuracy of the sectorial and near-sectorial coefficients of the estimated gravity field models. For this reason, the research on the topic of satellite formations for gravimetric applications is an on-going topic of debate.

   The formations of interest to gravimetric applications are a small subset of all possible satellite formations. Active formations, those where frequent or continuous thrusters firing are required to maintain the close proximity of the satellites, are not desirable because of the possible addition of errors and gaps in the data. This requirement also excludes formations with orbital planes with different inclinations, in order to keep the precession rate of the orbital plane the same. Additionally, the differential drag of formation with large altitude differences also requires frequent orbit maintenance manurers, which decreases the lifetime of the mission.

   In this chapter, the definition of *trailing*, *pendulum* and *cartwheel* formations is provided in Section 3.3, Section 3.4 and Section 3.5, respectively. The reason to classify the formation into these three types is related to that fact that they exhibit totally different motion along the along-track, cross-track and vertical directions. It was also clarified how to distinguish between formations that have similar characteristic (Section 3.7). The chapter ends with the presentation of the methodology used in the simulation of the orbits of satellite formations, in Section 3.8. This procedure is used in throughout the thesis. It is relevant for the production of the orbits of the GRACE-type formation considered in Chapter 5 and Section 6.3, and in the simulation of the formations analysed in Chapter 8.

Modelling Satellite Gravimetry

<div style="text-align: right; font-size: large;">4</div>

The simulation of future gravimetric satellite missions relies on mathematical models that describe the gravitational signal to be observed, the strategy to exploit this signal in order to estimate the underlying gravitational field and the appropriate representation of the errors in the data. These mathematical models are the signal, functional and noise models, respectively.

The first aspect to be mentioned is what *signal* is, since there is the need to define what is going to be simulated. The signal is represented by measurements, which need to be synthesised on the basis a representative gravity field model. They possibly result from the sum of a number of different components, each related to a particular geophysical processes of a static or time-varying nature. This defines the *signal model*.

The second step is to extract information about the gravitational field from the measurements. For that to be done, the *observation equation* relates the measurements of the gravitational signal to a set of parameters that describe the gravitational field. In the thesis, the gravitational field is parameterised by a set of Stokes coefficients and the associated spherical harmonics. The estimated gravitational field is given by the set of Stokes coefficients, on the basis of which results a gravitational signal that best fits to the measured signal, in the Least-Squares (LS) sense. The *functional model* is composed by the observation equations and parametrisation.

Finally, the simulations are useless unless they are somehow infused with some degree of realism. For that purpose, there is the need to define the *noise model*. The accurate simulation of the errors in the measurements is of utmost importance for the analysis of future gravimetric missions. Without it, there is no assurance

that the results are realistic and the conclusions drawn from them are valid. The simulated noise requires three ingredients: i) a stochastic model, ii) a procedure to generate noise realizations, and iii) a data weighting scheme to mitigate data noise appropriately during the computation of the gravity field model.

In this chapter the functional, signal and noise models are presented in Section 4.1, Section 4.2 and Section 4.3, respectively, for the two measurement principles under discussion in the thesis (Section 2.2): high-low Satellite-to-Satellite Tracking (hl-SST) and low-low Satellite-to-Satellite Tracking (ll-SST). The discussion goes deep into technical details in order to facilitate the reproducibility of the results and to better identify the limitations of the conducted study.

4.1 Functional Model

The objective of this section is to present the processing algorithms used in satellite geodesy, covering the two main types of observations: hl-SST in Section 4.1.1 and ll-SST in Section 4.1.2. The details of the simulation procedure is given for each type of observations. The set-up of the simulations is meant to replicate real-data processing, even though the latter is not the main topic of the dissertation.

According to Ditmar (2009b), the functional model $\boldsymbol{\Phi}$ defines the numerical relation between a set of unknown model parameters $\mathbf{m}$ and the observed data $\mathbf{y}^{(obs)}$. In view of $\mathbf{y}^{(obs)}$ generally being corrupted with noise, this relation is not exact:

$$\mathbf{y}^{(obs)} \approx \boldsymbol{\Phi}(\mathbf{m}). \tag{4.1}$$

The unknown model parameters $\mathbf{m}$ are a collection of parameters that define the model unambiguously, such as the Stokes coefficients $\overline{C}$ of Earth's gravity field model, plus any additional unknown parameters such as data biases or empirical parameters. The observed data $\mathbf{y}^{(obs)}$ are the measurements obtained by the sensors, which take the form of either ll-SST or hl-SST observations. In the simulation environment, $\mathbf{m}$ is exclusively the set of coefficients $\overline{C}$ and the observed data $\mathbf{y}^{(obs)}$ are synthetic signals corrupted by synthetic noise.

In order to cope with a possible non-linearity of the functional model and improve the quality of the results at the data inversion stage, it is advisable to consider the best possible reference model parameters $\mathbf{m}^{(ref)}$, generally representing the state-of-the-art knowledge of Earth's gravitational field. On its basis the forecasted data $\mathbf{y}^{(for)}$ are computed considering the functional model $\boldsymbol{\Phi}$:

$$\mathbf{y}^{(for)} = \boldsymbol{\Phi}\left(\mathbf{m}^{(ref)}\right). \tag{4.2}$$

Making use of the zero and first order terms of the Taylor expansion of $\mathbf{\Phi}$ at vicinity of $\mathbf{m}^{(\mathrm{ref})}$, Eq. (4.1) can be approximated by

$$\mathbf{y}^{(\mathrm{obs})} = \mathbf{y}^{(\mathrm{for})} + \mathbf{A}\big(\mathbf{m} - \mathbf{m}^{(\mathrm{ref})}\big). \tag{4.3}$$

The design matrix $\mathbf{A}$ is the matrix of partial derivatives of $\mathbf{\Phi}$ over $\mathbf{m}$, taken at $\mathbf{m} = \mathbf{m}^{(\mathrm{ref})}$:

$$A_{ij} = \left.\frac{\partial \Phi_i}{\partial m_j}\right|_{\mathbf{m}=\mathbf{m}^{(\mathrm{ref})}}. \tag{4.4}$$

Considering that the residual data $\mathbf{y}^{(\mathrm{res})}$ is $\mathbf{y}^{(\mathrm{obs})} - \mathbf{y}^{(\mathrm{for})}$ and that the model correction $\hat{\mathbf{m}}^{(\mathrm{res})}$ is $\mathbf{m} - \mathbf{m}^{(\mathrm{ref})}$, Eq. (4.3) leads to a linearised functional model

$$\mathbf{y}^{(\mathrm{res})} = \mathbf{A}\hat{\mathbf{m}}^{(\mathrm{res})}. \tag{4.5}$$

The statistically optimal solution to the linear system, minimizing the squares of $\mathbf{y}^{(\mathrm{res})}$, requires the data noise covariance matrix $\mathbf{C}^{(\mathrm{res})}$ and the reference model noise covariance matrix $\mathbf{C}^{(\mathrm{ref})}$:

$$\hat{\mathbf{m}}^{(\mathrm{res})} = \mathbf{N}^{-1}\mathbf{A}^{\mathrm{T}}\mathbf{C}^{(\mathrm{res})-1}\mathbf{y}^{(\mathrm{res})}, \quad \text{where} \quad \mathbf{N} = \mathbf{A}^{\mathrm{T}}\mathbf{C}^{(\mathrm{res})-1}\mathbf{A} + \mathbf{C}^{(\mathrm{ref})-1}. \tag{4.6}$$

The inverse of the reference model noise covariance matrix $\mathbf{C}^{(\mathrm{ref})-1}$ can also be interpreted as a regularization matrix.

The reference model noise covariance matrix $\mathbf{C}^{(\mathrm{ref})}$ describes the error of $\mathbf{m}^{(\mathrm{ref})}$. If $\mathbf{m}^{(\mathrm{ref})}$ is very inaccurate, $\mathbf{C}^{(\mathrm{ref})-1}$ is small relatively to $\mathbf{A}^{\mathrm{T}}\mathbf{C}^{(\mathrm{res})-1}\mathbf{A}$ and will not contribute significantly to $\hat{\mathbf{m}}^{(\mathrm{res})}$, the latter being therefore largely driven by the information in $\mathbf{y}^{(\mathrm{res})}$. The simulations conducted in the thesis are not regularized, i.e. $\mathbf{C}^{(\mathrm{ref})-1}$ is zero and no other matrix is added to $\mathbf{N}$.

In this formulation, the estimated model $\hat{\mathbf{m}}$ is the sum of the model correction $\hat{\mathbf{m}}^{(\mathrm{res})}$ and the reference model parameters $\mathbf{m}^{(\mathrm{ref})}$. This is the origin of the terminology used in Section 4.2, so that the estimated "true" gravitational potential $\hat{V}^{(\mathrm{true})}$, is the sum of the residual gravitational potential $V^{(\mathrm{res})}$ and the reference gravitational potential $V^{(\mathrm{ref})}$. Notice that in case of the data, the terminology is slightly different: the observed data $\mathbf{y}^{(\mathrm{obs})}$ is the sum of the residual data $\mathbf{y}^{(\mathrm{res})}$ and the forecasted data $\mathbf{y}^{(\mathrm{for})}$.

4.1.1 Processing of hl-SST observations

The working principle behind the use of hl-SST observations for gravity field determination relies on the ability to compute accurate accelerations from precise Kinematic

Orbit (KO) provided by Global Positioning System (GPS) tracking data. In actual data processing, the correction for the GPS antenna offset relative to the Centre of Mass (CoM) with the satellite attitude information is needed. In the study of future gravimetric missions, this correction is ignored under the assumption that it is done with sufficient accuracy.

The link between the Stokes coefficients of the gravity field model and a point-wise acceleration is straightforward, and starts with the relationship between the acceleration $\mathbf{a}$, and the gravitational potential V

$$\mathbf{a} = \boldsymbol{\nabla} V + \mathbf{a}^{(\text{ng})}, \tag{4.7}$$

where $\mathbf{a}^{(\text{ng})}$ represents the non-gravitational acceleration of the satellite measured by the on-board accelerometer.

Theoretically, the observations associated with the instantaneous acceleration $\mathbf{a}$ can be obtained by the double-differentiation of the estimated orbital positions $\mathbf{x}$

$$\mathbf{a} = \frac{d^2 \mathbf{x}}{d t^2}. \tag{4.8}$$

In practice, the double-differentiation is conducted in the thesis with a 3-point double differentiation scheme, applied to the positions $\mathbf{x}_{i-1}$, $\mathbf{x}_i$ and $\mathbf{x}_{i+1}$ at three consecutive epochs, considering a constant sampling rate Δt (Ditmar and Sluijs, 2004):

$$\bar{\mathbf{a}}_i = \frac{\mathbf{x}_{i-1} - 2\mathbf{x}_i + \mathbf{x}_{i+1}}{\Delta t^2}. \tag{4.9}$$

The distinction between the instantaneous acceleration $\mathbf{a}$ and the averaged acceleration $\bar{\mathbf{a}}$ is that the former is valid for one particular epoch, while the latter contains information that spans 3 epochs.

In an inertial frame, an averaged acceleration at epoch i, $\bar{\mathbf{a}}_i$, is related to the point-wise accelerations, $\mathbf{a}_j = \left[a_j^{(\text{x})}, a_j^{(\text{y})}, a_j^{(\text{z})} \right]^T, \left(i - n \le j \le i + n \right)$ by the expression

$$\bar{\mathbf{a}}_i = \begin{bmatrix} a_{i-n:i+n}^{(\text{x})} \cdot \mathbf{w}_{-n:n} \\ a_{i-n:i+n}^{(\text{y})} \cdot \mathbf{w}_{-n:n} \\ a_{i-n:i+n}^{(\text{z})} \cdot \mathbf{w}_{-n:n} \end{bmatrix}, \tag{4.10}$$

where the vector $\mathbf{w}$ defines the averaging filter of length $2n+1$ and is composed of constant (pre-defined) coefficients (Ditmar and Sluijs, 2004). The number $2n$ is called the order of the averaging filter. For instance, for the second-order averaging

filter, it holds: $\mathbf{w} = (1/12; 5/6; 1/12)^T$, i.e. the x-component of Eq. (4.10) can be explicitly represented as follows

$$a^{(\mathrm{x})}{}_i = \frac{1}{12}\left(a^{(\mathrm{x})}{}_{i-1} + 10a^{(\mathrm{x})}{}_i + a^{(\mathrm{x})}{}_{i+1}\right). \qquad (4.11)$$

In other words, a time-series of averaged accelerations can be interpreted as a slightly smoothed time-series of point-wise accelerations. At low frequencies, average and point-wise accelerations are almost identical.

Eq. (4.10) can be represented shorter as

$$\bar{\mathbf{a}}_i = \mathbf{a}_i * \mathbf{w}, \qquad (4.12)$$

where $*$ is the convolution operation, $\mathbf{a}$ is the point-wise acceleration, $\mathbf{w}$ is the averaging filter and $\bar{\mathbf{a}}$ is the averaged acceleration.

Simulation of accelerations derived from hl-SST observations

The total accelerations are computed as the sum of the "observed" gravitational accelerations $\mathbf{g}^{(\mathrm{obs})}$ and non-gravitational accelerations $\mathbf{a}^{(\mathrm{ng})}$

$$\mathbf{a} = \mathbf{g}^{(\mathrm{obs})} + \mathbf{a}^{(\mathrm{ng})}. \qquad (4.13)$$

As pointed out in Section 2.2.1, the use of non-gravitational acceleration measurements does not contribute significantly to the improvement of the accuracy of the estimated gravity field parameters, as long as proper Frequency-Dependent Data Weighting (FDDW) is considered (refer to Section 2.5.6 for more details on FDDW). As a consequence, tracking data from non-dedicated satellites, i.e. those without an on-board accelerometer, can be used for gravimetric purposes. In case of dedicated satellites, evidently, the accelerometer measurements can be used to correct the "observed" gravitational acceleration. The error introduced by neglecting this correction, in case of non-dedicated satellites, is not significant because the correction modifies the data in frequencies to which hl-SST data is not sensitive to the gravitational field (Ditmar et al., 2007). Therefore, non-gravitational accelerations are not considered in the simulation environment, i.e. it is assumed that $\mathbf{a}^{(\mathrm{ng})} = 0$.

The "observed" gravitational accelerations $\mathbf{g}^{(\mathrm{obs})}$ are synthesised at each epoch using the "true" gravitational potential model $V^{(\mathrm{true})}$, represented by the Stokes coefficients $\overline{\mathbf{C}}^{(\mathrm{true})}$ and the orbit position of the satellite, $\mathbf{x}$:

$$\bar{\mathbf{g}}^{(\mathrm{obs})} = \boldsymbol{\nabla}V\left(\mathbf{x}, \overline{\mathbf{C}}^{(\mathrm{true})}\right) * \mathbf{w}. \qquad (4.14)$$

The orbit positions $\mathbf{x}$, which are assumed to be know perfectly in order to avoid the introduction of positioning errors, are simulated for the satellite by integrating the equations of motion considering simple Keplerian dynamics. The choice of Keplerian orbits is motivated by the need to keep the constellation geometry unchanged.

As usual, the observations of interest are of a residual nature, since they are better suited for the LS inversion:

$$\bar{\mathbf{g}}^{(\text{res})} = \bar{\mathbf{g}}^{(\text{obs})} - \bar{\mathbf{g}}^{(\text{for})}. \qquad (4.15)$$

The forecasted quantities represent the state-of-the-art knowledge of the gravitational field, in order to minimize the effect of errors on older models (in particular related to temporal variation), and are computed on the basis of the reference gravitational potential $V^{(\text{ref})}$:

$$\bar{\mathbf{g}}^{(\text{for})} = \boldsymbol{\nabla} V\left(\mathbf{x}, \overline{\boldsymbol{C}}^{(\text{ref})}\right) * \mathbf{w}. \qquad (4.16)$$

When considering the Keplerian orbit $\mathbf{x}$ to generated the residual average gravitational acceleration $\bar{\mathbf{g}}^{(\text{res})}$, there is discrepancy between force model originating $\mathbf{x}$ and $V^{(\text{true})}$. The error associated with this discrepancy is, fortunately, not significant. The orbit positions are merely used as locations where the gravity field model is (accurately) synthesized. Whether or not those positions agree with the dynamic motion resulting from said gravity field model is not critical in what concerns for the computation of $\bar{\mathbf{g}}^{(\text{obs})}$ or $\bar{\mathbf{g}}^{(\text{for})}$. It also does not influence the estimation of the residual gravity field model from the set of observations $\bar{\mathbf{g}}^{(\text{res})}$, since the Keplerian orbit $\mathbf{x}$ is considered when building the associated design matrix.

Evidently, it is desirable to keep the discrepancy limited to no more than a few kilometres (which is a representative value of the Root Mean Squared (RMS) difference between a Keplerian and an orbit integrated on the basis of a high-degree gravity field model). The resulting set of $\bar{\mathbf{g}}^{(\text{res})}$ represents the gravitational accelerations acting on the satellite under study. In fact, the differences between $\bar{\mathbf{g}}^{(\text{res})}$ generated on the basis of a Keplerian orbit and one integrated on the basis of a high-degree gravity field model is not significant. In Figure 4.1, the difference between two sets of $\bar{\mathbf{g}}^{(\text{res})}$ computed from the same pair of gravity field models evaluated at two orbits, one Keplerian and another integrated from a completed gravity field model, is shown to be on average a factor of 30 smaller than either set of $\bar{\mathbf{g}}^{(\text{res})}$.

To emulate the numerical differentiation of the orbit positions in the simulated GPS observations, the series of "observed" and forecasted point-wise accelerations, represented by the terms $\boldsymbol{\nabla} V\left(\mathbf{x}, \overline{\boldsymbol{C}}^{(\text{true})}\right)$ and $\boldsymbol{\nabla} V\left(\mathbf{x}, \overline{\boldsymbol{C}}^{(\text{ref})}\right)$ in Eq. (4.14) and Eq. (4.16), respectively, require the use of the averaging filter $\mathbf{w}$ defined in Eq. (4.10). In
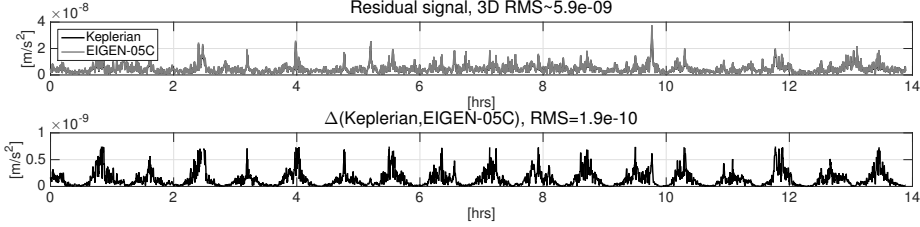
Figure 4.1 – Example of the residual average gravitational acceleration $\bar{\mathbf{g}}^{(\text{res})}$ computed from the difference of the "observed" average gravitational acceleration $\bar{\mathbf{g}}^{(\text{obs})}$ generated on the basis of EIGEN-5C and the forecasted average gravitational acceleration $\bar{\mathbf{g}}^{(\text{for})}$ generated on the basis of EIGEN-CG03C. On the top, two lines are plotted, corresponding to different orbit positions $\mathbf{x}$, where the gravity field models are synthesized: a Keplerian and an orbit integrated on the basis of EIGEN-5C. On the bottom, their difference is shown.

practice, the application of the averaging filter is performed in the Celestial Reference Frame (CRF) in order to prevent that frame accelerations are averaged over the $2n+1$ epochs spanning the filter length. With that in mind and in the context of hl-SST data, e.g. Eq. (4.14) and Eq. (4.16), the convolution operation $*$ implicitly represent the following:

$$\bar{\mathbf{g}}_i = \boldsymbol{R}_i^{(\text{LHRF})\leftarrow(\text{CRF})}\left(\left(\boldsymbol{R}_i^{(\text{CRF})\leftarrow(\text{LHRF})}\boldsymbol{\nabla}V\left(\mathbf{x}_i,\overline{\boldsymbol{C}}\right)\right)*\mathbf{w}\right). \tag{4.17}$$

4.1.2 Processing of ll-SST observations

The Gravity Recovery And Climate Experiment (GRACE) mission has proven that ll-SST data provide accurate information about the Earth's gravitational field and its changes in time. The success of this mission prompts that any investigation into future gravimetric missions should take this measurement principle into consideration.

The procedure that is considered in the thesis is the *range combination approach* (Liu et al., 2007), which is a variant of the acceleration approach (Rummel, 1979), It is based on the so-called range combinations $\bar{a}$, each of which is formed as a linear combination of three successive range measurements ρ_{i-1}, ρ_i, and ρ_{i+1}

$$\bar{a}_i = \frac{\cos\theta_{i-}\cdot\rho_{i-1}-2\rho_i+\cos\theta_{i+}\cdot\rho_{i+1}}{(\Delta t)^2}, \tag{4.18}$$

where θ_{i-} is the angle between the Line of Sight (LoS) vector at epoch i and that at the previous epoch and θ_{i+} is the angle between the LoS vector at epoch i and that at the following epoch.
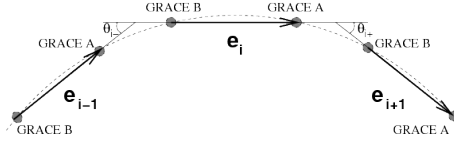
Figure 4.2 – Direction of line-of-sight vectors at three successive epochs and the angles between them. This information is used for computing range combinations, Eq. (4.18).

The angles θ_{i-} and θ_{i+} are derived from the precise dynamic orbits $\mathbf{x}^{(1)}$ and $\mathbf{x}^{(2)}$ of the leading and trailing satellite, respectively. In addition to permitting the computation of θ_{i-} and θ_{i+}, $\mathbf{x}^{(1)}$ and $\mathbf{x}^{(2)}$ accurately relate the observed range combinations to particular positions above the surface of the Earth.

In real-data processing, the orbits are integrated on the basis of the reference gravitational potential $V^{(\mathrm{ref})}$ and non-gravitational accelerations measured by the on-board accelerometers, minimising the distance to the KOs. The reference gravitational potential $V^{(\mathrm{ref})}$ is composed of a number of state-of-the-art force models that accurately describe the gravitational forces acting on the satellites.

Simulation of ll-SST observations

Having identified the functional model used in real data processing, the way in which it is applied to the simulation of ll-SST observations is described in detail.

The "observed" range combinations $\overline{a}^{(\mathrm{obs})}$ are the equivalent of the observations in real-data processing. They are computed on the basis of the observation equation, Eq. (4.18). The forecasted range combinations $\overline{a}^{(\mathrm{for})}$ represent the observations as predicted by the reference gravitational potential model. These two types of range combinations are scalars and represent time-averaged inter-satellite accelerations projected onto the LoS direction. Their difference is the residual range combinations $\overline{a}^{(\mathrm{res})}$, which is used to estimate the model correction, see Eq. (4.6).

In the following paragraphs, the simulation procedure used to generate the observed range combinations $\overline{a}^{(\mathrm{obs})}$ and forecasted range combinations $\overline{a}^{(\mathrm{for})}$ is presented.

Observed range combinations

The simulation of observed range combinations requires the computation of the range observations ρ. Unlike in real-data processing where these quantities are measured by the ranging data, these have to be generated from the orbits of the

two satellites in the formation $\mathbf{x}^{(j)}$, $j = 1,2$. These orbits are the result of numerical integration on the basis of the "true" gravitational potential $V^{\text{(true)}}$ and following the initial conditions specific to the formation given by the orbital elements of satellite j, $\boldsymbol{o}^{(j)}$:

$$\mathbf{x}^{(j)} = \mathrm{f}(V^{\text{(true)}}, \boldsymbol{o}^{(j)}). \tag{4.19}$$

The quantities $\boldsymbol{o}^{(j)}$ are adequate to this context because they can be easily associated with the required relative motion of the satellites (see Section 3.8). The integration of the orbits on the basis of $V^{\text{(true)}}$, even assuming the initial conditions given by $\boldsymbol{o}^{(j)}$, results in a relative motion that diverges after a few days. For this reason, the integration is re-started periodically, usually every 6 hr, each time exploiting the Keplerian orbit $\boldsymbol{o}^{(j)}$ to derive the new initial conditions.

From the simulated orbits, the range observations are derived as:

$$\rho_i = \left| \mathbf{x}_i^{(1)} - \mathbf{x}_i^{(2)} \right|. \tag{4.20}$$

After this point, there is no further use for $\mathbf{x}^{(j)}$ since these quantities are not known with sufficient accuracy in real data processing. The orbital positions of the satellites used in that context are by definition *forecasted* quantities. The forecasted orbit positions $\mathbf{x}^{\text{(for)}(j)}$ are integrated on the basis of the reference gravitational potential $V^{\text{(ref)}}$, also taking as initial conditions the orbital elements of satellite j:

$$\mathbf{x}^{\text{(for)}(j)} = \mathrm{f}(V^{\text{(ref)}}, \boldsymbol{o}^{(j)}). \tag{4.21}$$

The orbital elements of satellite j, $\boldsymbol{o}^{(j)}$ should not be associated with $V^{\text{(true)}}$ or $V^{\text{(ref)}}$; they are only used to provide the means to compute the orbit of satellite formations with a bounded relative motion. Although $\mathbf{x}^{(j)}$ and $\mathbf{x}^{\text{(for)}(j)}$ have the same initial conditions, they follow different paths, as imposed by $V^{\text{(true)}}$ and $V^{\text{(ref)}}$, respectively.

The forecasted orbit positions provide the necessary information to compute the quantities $\theta_{i,k}$, defined as the angle between the LoS vector at the k-th epoch before (k is negative) or after (k is positive) epoch i:

$$\theta_{i,k} = \cos^{-1} \frac{\left(\mathbf{x}_{i+k}^{\text{(for)}(1)} - \mathbf{x}_{i+k}^{\text{(for)}(2)} \right)}{\rho_{i+k}^{\text{(for)}}} \cdot \frac{\left(\mathbf{x}_i^{\text{(for)}(2)} - \mathbf{x}_i^{\text{(for)}(2)} \right)}{\rho_i^{\text{(for)}}}. \tag{4.22}$$

Following Eq. (4.18) and the notation of Eq. (4.22), the observed range combinations $\bar{a}^{\text{(obs)}}$ are:

$$\overline{a}_i^{(\text{obs})} = \frac{\cos\theta_{i,-1}\cdot\rho_{i-1} - 2\rho_i + \cos\theta_{i,+1}\cdot\rho_{i+1}}{(\Delta t)^2}. \tag{4.23}$$

Forecasted range combinations

The forecasted range combinations can be computed in two ways: either from Eq. (4.18) or by averaging of point-wise inter-satellite accelerations. In the former procedure, the forecasted range $\rho^{(\text{for})}$ is considered in the functional model:

$$\overline{a}_i^{(\text{for})} = \frac{\cos\theta_{i-1}\cdot\rho_{i-1}^{(\text{for})} - 2\rho_i^{(\text{for})} + \cos\theta_{i,+1}\cdot\rho_{i+1}^{(\text{for})}}{(\Delta t)^2}. \tag{4.24}$$

The forecasted range $\rho^{(\text{for})}$ is computed in the same way as the "observed" range ρ, with Eq. (4.20), but considering the forecasted orbit position $\mathbf{x}^{(\text{for})}$.

The latter procedure is based on the fact that the resulting quantity of Eq. (4.24), $\overline{a}_i^{(\text{for})}$, can be interpreted as a weighted average of the inter-satellite accelerations in the time interval $[t_i - \Delta t; t_i + \Delta t]$ projected onto the LoS at the epoch i. Consequently, the average accelerations $\overline{a}_i$ can be produced from a time-series of point-wise inter-satellite accelerations $\mathbf{a}^{(12)}$ by applying the averaging filter $\mathbf{w}$, mentioned in Section 4.1.1. The detailed description of this procedure follows.

At each epochs i, the forecasted gravitational acceleration $\mathbf{g}^{(\text{for})}$ is computed on the basis of the reference gravitational potential $V^{(\text{ref})}$, represented by the Stokes coefficients $\overline{\mathbf{C}}^{(\text{ref})}$, at the forecasted orbit positions of the satellites:

$$\mathbf{g}^{(\text{for})(j)} = \boldsymbol{\nabla}V\left(\mathbf{x}^{(\text{for})(j)}, \overline{\mathbf{C}}^{(\text{ref})}\right). \tag{4.25}$$

The difference between the gravitational accelerations of the two satellites are the point-wise inter-satellite accelerations $\mathbf{a}^{(12)}$

$$\mathbf{a}^{(12)} = \mathbf{g}^{(\text{for})(1)} - \mathbf{g}^{(\text{for})(2)}. \tag{4.26}$$

The point-wise inter-satellite accelerations need to be averaged in order to be compared at the same level with the range combinations; that is done as shown in Eq. (4.10):

$$\overline{\mathbf{a}}_i^{(12)} = \mathbf{a}_i^{(12)} * \mathbf{w}. \tag{4.27}$$

The averaged inter-satellite acceleration $\overline{\mathbf{a}}^{(12)}$ is projected onto the forecasted unit vector defining the LoS direction $\mathbf{e}^{(\text{LoS})(\text{for})}$, resulting in the scalar forecasted range combinations $\overline{a}^{(\text{for})}$:

$$\overline{a}^{(\text{for})} = \overline{\mathbf{a}}^{(12)} \cdot \mathbf{e}^{(\text{LoS})(\text{for})}. \tag{4.28}$$

In practice, there is the need to perform average filtering in the inertial frame, otherwise the frame accelerations associated with the rotation of the Local Horizontally-aligned Reference Frame (LHRF) will be averaged over the $2n+1$ epochs where the filter is valid. For this reason, the point-wise inter-satellite accelerations $\mathbf{a}^{(12)}$ are first rotated to the CRF where filtering operation is performed, rotated to the Terrestrial Reference Frame (TRF) and only then is the projection onto the LoS direction conducted:

$$\overline{a}_i^{(\text{for})} = \left(\mathbf{R}_i^{(\text{TRF})\leftarrow(\text{CRF})} \left(\left(\mathbf{R}_i^{(\text{CRF})\leftarrow(\text{LHRF})} \mathbf{a}_i^{(12)} \right) * \mathbf{w} \right) \right) \cdot \mathbf{e}_i^{(\text{LoS})}. \tag{4.29}$$

Implied in Eq. (4.29) is that $\mathbf{e}^{(\text{LoS})}$ is defined in the TRF. This is usually the case since $\overline{a}_i^{(\text{for})}$ are computed from the forecasted orbit positions. The $\mathbf{x}^{(\text{for})}$ are needed in that reference frame in order to perform the Spheric Harmonic synthesis shown in Eq. (4.25). Evidently the transformation $\mathbf{R}^{(\text{TRF})\leftarrow(\text{CRF})}$ can be skipped if $\mathbf{e}^{(\text{LoS})}$ are derived from $\mathbf{x}^{(\text{for})}$ defined in the CRF.

For the sake of brevity, the procedure depicted by Eq. (4.29) is represented as:

$$\overline{a}^{(\text{for})} = \mathbf{a}^{(12)} * \mathbf{w} \cdot \mathbf{e}^{(\text{LoS})}. \tag{4.30}$$

According to Ditmar and Sluijs (2004), the approach of Eq. (4.24) and the one leading to Eq. (4.30) are equivalent as long as the force model used to compute the forecasted orbit position $\mathbf{x}^{(\text{for})}$, Eq. (4.21), is the same as the one used to compute the forecasted gravitational acceleration $\mathbf{g}^{(\text{for})}$, Eq. (4.25). It has been verified that the results obtained with the two approaches coincide (within numerical round-off errors).

The forecasted range combinations $\overline{a}^{(\text{for})}$ are subtracted from the observed range combinations $\overline{a}^{(\text{obs})}$, producing the residual range combinations $\overline{a}^{(\text{res})}$:

$$\overline{a}^{(\text{res})} = \overline{a}^{(\text{obs})} - \overline{a}^{(\text{for})}. \tag{4.31}$$

The residual range combinations define the observation vector that is the input to the LS estimation. As a result, the estimated residual gravitational potential $\hat{V}^{(\text{res})}$ is the update to the reference gravitational potential, so that the estimated "true" gravitational potential $\hat{V}^{(\text{true})}$ is recovered as

$$\hat{V}^{(\text{true})} = \hat{V}^{(\text{res})} + V^{(\text{ref})}. \tag{4.32}$$

4.2 Signal Model

In the simulation environment, the gravitational signal has to be simulated on the basis of numerical models related to different geophysical processes such as ocean tides, solid-earth tides, hydrological and glaciological processes, atmospheric mass transport process, post-glacial rebound, etc., in addition to the long-term mean (i.e. static) gravitational field. Each component contains a characteristic period, ranging from a few hours for the rapidly moving atmospheric masses to thousands of years for post-glacial rebound.

Generally, global gravity field models take the form of a collection of Stokes coefficients. The relationship between a set of Stokes coefficients $\overline{C}$ and the gravitational potential V at a point defined by the spherical coordinates $\mathbf{x} = [r, \vartheta, \lambda]^{\mathrm{T}}$, with r the radius, ϑ the co-latitude and λ the longitude, is described as

$$V(\mathbf{x}, \overline{C}) = V([r, \vartheta, \lambda]^{\mathrm{T}}, \overline{C}) = \frac{G_0 M_\oplus}{R} \sum_{\ell, m=0}^{L^{(\mathrm{max})}} \overline{C}_{\ell m} \left(\frac{R}{r} \right)^{\ell+1} \overline{Y}_{\ell m}(\vartheta, \lambda), \qquad (4.33)$$

with R the semi-major axis of a reference ellipsoid, $L^{(\mathrm{max})}$ the maximum degree contemplated in the gravity field model, $M_\oplus$ the mass of the Earth, G_0 the universal gravitational constant and $\overline{Y}$ the 4π-normalised surface spherical harmonic function, given as function of $P_{\ell|m|}$, the associated Legendre functions (e.g. Hofmann-Wellenhof and Moritz, 2006, Eq. 1-91):

$$\overline{Y}_{\ell m}(\vartheta, \lambda) = \begin{cases} \sqrt{(2\ell+1)} & P_{\ell 0}(\cos(\vartheta)) & \text{if } m = 0 \\ \sqrt{2(2\ell+1)\frac{(\ell-m)!}{(\ell+m)!}} & P_{\ell|m|}(\cos(\vartheta)) & \begin{cases} \cos(m\vartheta), & \text{if } m > 0 \\ \sin(|m|\vartheta), & \text{if } m < 0 \end{cases} \end{cases} . \quad (4.34)$$

The summation in Eq. (4.33) has the following meaning:

$$\sum_{\ell, m=0}^{L^{(\mathrm{max})}} = \sum_{\ell=0}^{L^{(\mathrm{max})}} \sum_{m=-l}^{\ell} . \qquad (4.35)$$

In case of a time-varying model, each spherical harmonic coefficient is a function of time.

4.2.1 The "true" and reference force models

Every simulation begins by choosing representative "true" and reference gravitational potentials, $V^{(\mathrm{true})}$ and $V^{(\mathrm{ref})}$, respectively. The "true" gravitational potential

represents the gravitational potential of a fictious Earth, chosen to be close to the most up-to-date knowledge about the gravitational field to provide realistic simulation results. The reference gravitational potential represents the state-of-the-art knowledge of the gravitational potential.

This set-up is designed to mimic the actual data processing of gravimetric satellite data (Section 4.1). The purpose of the estimation process is to determine the update to be added to the reference gravitational potential in order to represent accurately the actual one. This update is called residual gravitational potential $V^{(\text{res})}$.

The choice of "true" and reference gravitational potentials is defined by the purpose of the simulation. Should the sensitivity of a certain satellite formation to the static gravitational field be studied, then the observations measured by the satellite would be simulated on the basis of one static gravity field model, for example the Gravity Observation COmbination release 03 satellite-only gravity field model (GOCO03S), which is taken as the "true" model, and the reference observations would be computed on the basis of another static gravity field model, e.g. NGA's Earth Gravitational Model 2008 (EGM2008). In order to determine how sensitive a satellite mission would be to the atmospheric de-alliasing model error, the "true" gravitational field is simulated on the basis of a time-variable representation of the atmospheric model error plus a suitable static gravity field model and the reference gravitational field taken as the same static gravity field model plus the time average, e.g. monthly averages, of said model error (refer to Section 4.3.1 for details).

In addition to an overview of static gravity field models in Section 4.2.2, this section discusses the Atmosphere and Ocean De-aliasing Level 1B (AOD1B) in section Section 4.2.3 and the Delft Mass Transport (DMT) in Section 4.2.4. The latter models decribe, respectively, daily and monthly temporal gravitational field variations. They are considered in the conducted studies because the signals they describe play the largest role in the temporal aliasing.

4.2.2 Static gravity field models

Earth's global static gravity field models are produced from long periods of gravimetric satellite data, optionally augmented by terrestrial gravimetric surveying, altimeter satellite data and Satellite Laser Ranging (SLR) data. Modern gravity field models are estimated up to a high degree, up to 250 if only SLR and gravimetric satellite data are used and up to 2190 if altimetry and terrestrial data are involved as well. As implied, the satellite data typically dominate the lower range of degrees, below spheric harmonic degree 150 − 200, while the terrestrial data dominate the higher degrees, above degree 250.

The models relevant to this thesis are. cf. Table 2.1:

- GFZ/GRGS EIGEN, version 3 (EIGEN-CG03C) (Förste et al. 2005),
- GFZ/GRGS EIGEN, version 4 (EIGEN-GL04C) (Förste et al. 2008b),
- GFZ/GRGS EIGEN, version 5 (EIGEN-5C) (Förste et al. 2008a) and
- Gravity Observation COmbination release 02 satellite-only gravity field model (GOCO02S) (Goiginger et al. 2011).

The EIGEN-CG03C model is estimated on the basis of hl-SST data from the CHallenging Mini-Satellite Payload (CHAMP) satellite mission, hl-SST and ll-SST data from GRACE, as well as altimetry and terrestrial gravimetry data from various sources. The GRACE ll-SST data set is 376 days long and the CHAMP hl-SST data set covers 860 days.

The EIGEN-GL04C model is the update to EIGEN-CG03C and is estimated on the basis of data from the same sources. The exceptions are that CHAMP data are not considered and LAser GEOdynamics Satellite (LAGEOS) SLR data are. The GRACE ll-SST data cover a period of 3 years and 5 months and the LAGEOS data span 3 years. Compared to EIGEN-CG03C, an updated ocean model was used for temporal de-aliasing of the satellite data and the altimetry data include an updated mean sea-level height model.

The EIGEN-5C model is the update to EIGEN-GL04C and estimated on the basis of data from the same sources but using more satellite data: 5 years and 4 months of GRACE ll-SST data and 6 years of LAGEOS data. Additionally, the airborne, maritime and terrestrial gravity data for Europe, Australia and the Arctic region were updated.

The GOCO02S model is based solely on satellite data, namely Satellite Laser Ranging tracking data and data from the missions CHAMP, GRACE, and Gravity field and steady-state Ocean Circulation Explorer (GOCE). It exploits 8 months of GOCE gradiometric data, 12 months of GOCE hl-SST data, 7.5 years of GRACE data, 8 years of CHAMP hl-SST data and 5 years of SLR tracking data.

4.2.3 The Atmosphere and Ocean De-aliasing Level 1B product

The Atmosphere and Ocean De-aliasing Level 1B (AOD1B) product (Flechtner et al. 2006; Flechtner 2007, 2011), produced by Helmholtz-Zentrum Potsdam Deutsches GeoForschungsZentrum (GFZ), is computed from the European Centre for Medium-Range Weather Forecasts (ECMWF) atmospheric data and from the Ocean Model for Circulation and Tides (OMCT). In satellite data processing, it is frequently used as correction for non-tidal high frequency mass variations associated with the atmospheric pressure changes and corresponding oceanic response.

It is a time series of Stokes coefficients from degree and order 0 to 100, with a 6 hour time step, from 1976 to today. Starting from release 04, four models are provided at each epoch: global atmosphere and ocean combination (codename "GLO"), global atmosphere (codename "ATM"), ocean area (codename "OCN") and ocean bottom pressure analysis (codename "OBA").

This product can be used to simulate rapid mass transport processes occurring at the surface of the Earth, in order to derive the level of temporal aliasing in the estimated gravity field models. More interesting and relevant would be to have an estimation of the errors in the AOD1B product, but unfortunately that is not available.

4.2.4 The Delft Mass Transport model

The Delft Mass Transport (DMT) model (Liu et al. 2010; Ditmar et al. 2013) is a collection of Stokes coefficient defined in the degree range from 2 to 120, describing the monthly variation of Earth's gravitational field derived from GRACE data. Relevant to the numerical studies conducted in the thesis is the version 1 of this model. The temporal gravitational field variations are relative to the EIGEN-GL04C model, corrected for the linear trends in low-degree coefficients that are a part of this static model. The rapid changes in surface mass are corrected with the release 2004 of the Finite Element Solution (FES2004) global tide model (Lyard et al. 2006) and the AOD1B product. A statistically optimal Wiener-type filter that takes into account the full covariance matrices of signal and noise is used to reduce the influence of noise (Klees et al., 2008; Liu et al., 2010).

This model is used to simulate the temporal gravitational variations with a characteristic time of a month and longer. It is somewhat complementary to the AOD1B product, since the latter is associated with mass transport processes with much shorter characteristic times. Additionally, the signal associated with rapid atmospheric and ocean mass transport processes is nearly absent in the DMT model, since the AOD1B signal was removed from the data.

4.3 Noise Model

Conceptually, defining noise is not a trivial task. Consider a collection of ideal observations $\xi^{(obs)}$ describing a given phenomenon. They can also be predicted based on an ideal physical model of said phenomenon, thus producing a collection of forecasts $\xi^{(for)}$. Under these conditions, the model completely describes the observations so that

$$\xi^{(\text{obs})} = \xi^{(\text{for})}. \tag{4.36}$$

In reality, neither are the observations perfect, since all sensors have certain amount of uncertainty $\boldsymbol{\delta}^{(\text{obs})}$, nor does the physical model perfectly describe the phenomenon, mis-representing it by $\boldsymbol{\delta}^{(\text{for})}$, i.e.

$$\hat{\xi}^{(\text{obs})} = \xi^{(\text{obs})} + \boldsymbol{\delta}^{(\text{obs})} = \xi^{(\text{for})} + \boldsymbol{\delta}^{(\text{for})}. \tag{4.37}$$

The forecast noise $\delta^{(\text{for})}$ comprehends the errors in the background models. They are composed of residual signals which result from errors in the background force model, i.e. discrepancies between the signal predicted by the background force models and the actual signal. These errors take the form of the mis-modelled time-variable signal $\delta^{(\text{tv})}$, the omission signal $\delta^{(\text{sp})}$ and the mis-modelled static signal $\delta^{(\text{st})}$. Particular to the context of ll-SST measurements, the forecast noise is additionally composed of the positioning noise $\delta^{(\text{P})}$ and the orientation noise $\delta^{(\text{L})}$, as well as the term associated with non-inertial frame accelerations called correction noise $\delta^{(\text{C})}$.

The observation noise has a different origin, depending on the instrument providing the ll-SST and hl-SST measurements. It is the ranging sensor and accelerometer in case of ll-SST observations and the GPS receiver for hl-SST observations.

This section presents the details needed to properly simulate noise of various types, which are divided into two categories: model and measurement errors. The model errors are conceptually common to hl-SST and ll-SST observations, while the measurement errors are only applicable to the respective type of observation.

The model errors are addressed in Section 4.3.1 and comprise:

- the mis-modelled time-variable signal,
- the omission signal and
- the mis-modelled static signal.

The measurement errors relevant to hl-SST data are explained in Section 4.3.2. The measurement errors in ll-SST data are described in Section 4.3.3 and include:

- the accelerometer noise,
- the ranging noise,
- the positioning noise,
- the orientation noise and
- the correction noise.

Table 4.1 summarizes the distinction between observed/forecasted and measurement/model categories of all noise types.

symbol	name	noise model	observation type	observed/ forecasted	measurement/ model
$\delta^{(\mathrm{tv})}$	mis-modelled time-variable signal	both	both	forecasted	model
$\delta^{(\mathrm{sp})}$	omission signal	both	both	forecasted	model
$\delta^{(\mathrm{st})}$	mis-modelled static signal	both	both	forecasted	model
$\delta^{(\mathrm{C})}$	correction noise	advanced	ll-SST	forecasted	measurement
$\delta^{(\mathrm{L})}$	orientation noise	advanced	ll-SST	forecasted	measurement
$\delta^{(\mathrm{P})}$	positioning noise	advanced	ll-SST	forecasted	measurement
$\delta^{(\mathrm{acc})}$	accelerometer noise	advanced	ll-SST	observed	measurement
$\delta^{(\mathrm{R})}$	ranging noise	both[a]	ll-SST	observed	measurement
$\delta^{(\mathrm{rP})}$	relative position noise	simplistic	ll-SST	observed	measurement
$\delta^{(\mathrm{aP})}$	absolute position noise	simplistic	ll-SST	observed	measurement
$\delta^{(\mathrm{obs})(\mathrm{hl\text{-}SST})}$	hl-SST observation noise	N/A	hl-SST	observed	measurement

[a]The ranging noise $\delta^{(\mathrm{R})}$ is simulated differently for the simplistic and advanced noise models but both cases are conceptually equivalent, refer to Section 4.3.3 and Section 4.3.3.

Table 4.1 – Overview of the categories of all noise types.

4.3.1 Model errors

Model errors refer to limitations in existing background force models that result in an erroneous description of Earth's gravitational field and corresponding forecasted quantities. Relevant to the thesis is the simulation of:

- temporal aliasing associated with the mis-modelled time-variable signal,
- omission signal and
- mis-modelled static signal.

The definition of these model errors is given in the following sections; before that, the motivation to consider model errors is explained.

Determining how sensitive future gravimetric missions are to model errors may be seen as a academic exercise, in view of the fact that the knowledge of Earth's gravitational field is improving as more data from satellites, aircraft, ships and surface surveying is gathered. Nevertheless, there still remains, albeit increasingly smaller, a level of errors in the state-of-the-art models. In parallel, the data accuracy is also increasing with the technological and methodological advances. Better sensors and processing strategies become available and, consequently, a higher sensitivity to modelling errors. Determining the net effect of these conflicting trends is the main reason to study the sensitivity of future gravimetric missions to model errors.

Although the analysis of model errors does not offer a procedure that mitigates them, it provides an accurate quantification of how significant one error type is

relative to the other. Additionally, the analysis also permits determining which mission configuration is more sensitive to a particular error type, since the latter propagates differently to the gravity field parameters depending on the gravimetric mission.

Mis-modelled time-variable signal

In the course of processing gravimetric data, the use of the models describing the motion of mass in the Earth system is mandatory in order to correct the observations for signals which have a temporal time scale shorter than what is measurable by the satellite system, i.e. in the order of days or less. The surface transport processes responsible for the high-frequency changes in Earth's gravitational field are mainly associated with changes in atmospheric pressure, the corresponding oceanic response and tides. If this model-based correction is not done, the resulting gravity field models will be heavily corrupted by temporal aliasing.

To make matters worse, the level of uncertainty in these models is not known but certainly not zero. This error is responsible for the mis-modelling of the high-frequency temporal gravitational field variations, which manifests itself as temporal aliasing in gravimetric data.

However, there is another aliasing contribution present in the data, associated with all mass transport processes that are not described by any model during the processing of gravimetric data. The most significant process that contributes to temporal aliasing is due to hydrology and, to a lesser extent, due to glaciological changes.

Omission signal

The omission error, also known as *spatial aliasing*, is associated with the truncation of the spherical harmonic series summation, Eq. (4.33). Formally, in order to describe Earth's gravitational field, an infinite number of coefficients is required. In practice, the series is truncated at a maximum degree $L^{(\text{max})}$, negating the high-frequency signal associated with degrees above $L^{(\text{max})}$.

In real data processing, the omission error is introduced into the estimated gravity field models through two distinct ways:

In the first way, the omission error is incurred when the forecasted signal fails to represent the high-frequency features of the actual gravitational field because the reference background force model is of limited degree. This constitutes a problem with a trivial solution: one simply increases the maximum degree of the reference gravity field model. There is no problem in doing so, since it is possible to represent

the static gravitational field of the Earth up to a very high degree and order, namely 2159 as is the case of the EGM2008 model.

The second form of omission error has its origin in the truncation of the spherical harmonic series at the stage of data inversion. As a consequence, the associated residual high frequency signal (i.e. the update to the forecasted data given by the high-frequency content of the measurements) is mis-represented by the estimated parameters because their degree is not sufficiently high. The lack of high-degree coefficients in the model to be estimated becomes a problem when the satellite gravimetric measurements are sensitive to signals represented by those coefficients, unless filtered out prior to the data inversion. If the choice of $L^{(\mathrm{max})}$ is unsuitable, the mis-represented high-frequency signals map onto the set of Stokes coefficients with degrees lower than $L^{(\mathrm{max})}$, which may lead to noticeable distortions, such as Gibbs artefacts. This form of omission signal is present even when the reference model forecasts the signal up to sufficiently high-frequency (but does so imperfectly, otherwise there is nothing to be estimated).

Mis-modelled static signal

Although the long-term mean of the Earth's gravitational field, also known as the static gravitational field, is known to an unprecedented level of accuracy, particularly after the GRACE and GOCE satellite missions, there is room for further improvement. In the context of satellite-only static gravitational field modelling, with increasing number of GRACE and GOCE data, increasing quality of gravimetric data and better data combination strategies, the following trend is observed: every new static model released supersedes the predecessors. This is an indication that the current state-of-the-art satellite-based gravity field models contain errors, although progressively in lesser magnitude and towards the highest degrees and orders.

The accuracy of the small-features described by the high degrees of models is not homogeneous in all geographical locations. The information that is used to estimate the high degrees comes largely from terrestrial, aerial and ship-born data, which are limited to certain geographical areas. Consequentially, the locations not covered by gravimetric measurement campaigns are described poorly by the high degrees of any model. It is, therefore, unavoidable that some level of static commission error is present in the gravitational field solutions derived from satellite data, particularly at high degrees.

The mis-modelled static signal is particularly relevant when the ground-track of the satellite's orbits changes significantly over time. This does not happens when there is active maintenance of the ground-track pattern, which is very costly in terms of fuel, if one considers the whole lifetime of a satellite mission. The

change in ground track pattern results in different spacial coverage of the data and also different orbital repeat periods. When the repeat period is smaller, the satellite revisits the same locations more often but the spatial gaps are larger. This unfavourable situation limits the sensitivity of the data to the high-frequency features of the gravitational field and amplifies the errors in the static background force model at the high degrees.

Simulation of model errors

Irrespectively of the measuring principle, simulating model errors follows consistently the same procedure. To explain the idea better, the following abstraction is made in this section and summarised in Table 4.2: the symbol η represents either the range combinations $\bar{a}$ from a satellite formation or the average gravitational accelerations $\bar{\mathbf{g}}$ of a single satellite. Recall that these quantities are relevant for the simulation of ll-SST (Section 4.1.2) and hl-SST (Section 4.1.1) observations, respectively. The symbol η represents a scalar quantity in case of range combinations or a vector quantity in case of average gravitational accelerations.

Additionally, let the symbol $\tilde{\nabla}$ define the following operators: ∇' for the scalar/ll-SST case or gradient $\boldsymbol{\nabla}'$ for the vector/hl-SST case.

The operator $\boldsymbol{\nabla}'$ assumes the usual form of the gradient $\boldsymbol{\nabla}$ (refer to Eq. (4.33) for the meaning of $V\left(\mathbf{x}, \overline{\boldsymbol{C}}\right)$), with the addition of the averaging operation described in Eq. (4.10) and Eq. (4.17):

$$\boldsymbol{\nabla}'V\left(\mathbf{x}, \overline{\boldsymbol{C}}\right) = \bar{\mathbf{g}} \tag{4.38}$$
$$= \mathbf{g} * \mathbf{w}$$
$$= \boldsymbol{\nabla}V\left(\mathbf{x}, \overline{\boldsymbol{C}}\right) * \mathbf{w}.$$

The operator ∇' applies the averaging filter $\mathbf{w}$ (see Eq. (4.10) and Eq. (4.27)) to the difference between the three-dimensional (3D) accelerations at $\mathbf{x}^{(1)}$ and $\mathbf{x}^{(2)}$ (see Eq. (4.25) and Eq. (4.26)) and projects the result onto the LoS vector $\mathbf{e}^{(\text{LoS})}$ as shown in Eq. (4.28) and Eq. (4.29).

$$\nabla'V\left(\mathbf{x}, \overline{\boldsymbol{C}}, \mathbf{e}^{(\text{LoS})}\right) = \bar{a} \tag{4.39}$$
$$= \bar{\mathbf{a}}^{(12)} \cdot \mathbf{e}^{(\text{LoS})}$$
$$= \mathbf{a}^{(12)} * \mathbf{w} \cdot \mathbf{e}^{(\text{LoS})}$$
$$= \left(\boldsymbol{\nabla}V\left(\mathbf{x}^{(1)}, \overline{\boldsymbol{C}}\right) - \boldsymbol{\nabla}V\left(\mathbf{x}^{(2)}, \overline{\boldsymbol{C}}\right)\right) * \mathbf{w} \cdot \mathbf{e}^{(\text{LoS})}.$$

The symbol $\mathbf{x}$ always refers to a single orbit for the hl-SST case. For the case of ll-SST and if no superscript is indicated, it refers to two orbits, one for each satellite that composes the formation.

Table 4.2 summarizes the meaning of the symbols $\boldsymbol{\eta}$ and $\tilde{\nabla}$.

measurement principle	physical quantity	$\boldsymbol{\eta}$	$\tilde{\nabla}$	dimension
hl-SST	average gravitational acceleration	$\bar{\mathbf{g}}$	∇'	vector
ll-SST	range combination	$\bar{a}$	∇'	scalar

Table 4.2 – Meaning of the symbols $\boldsymbol{\eta}$ and $\tilde{\nabla}$ for different measurement principles.

Simulation of temporal aliasing

The time-variable signal that is used to study temporal aliasing in the estimated gravity field model is simulated by synthesising the observations $\boldsymbol{\eta}^{(tv)}$ on the basis of a set of Stokes coefficients representing the error in the time-variable gravity field model $\overline{\boldsymbol{C}}^{(tv)}$. In order to model a time variable signal with zero mean, i.e. unbiased towards a static signal, the synthesis is made considering $\overline{\boldsymbol{C}}^{(tv)}$ corrected for its mean over the period under analysis, $\overline{\overline{\boldsymbol{C}}}^{(tv)}$, which is typically one month:

$$\boldsymbol{\eta}^{(tv)} = \tilde{\nabla} V\left(\mathbf{x}, \overline{\boldsymbol{C}}^{(tv)} - \overline{\overline{\boldsymbol{C}}}^{(tv)}\right). \tag{4.40}$$

The model $\overline{\boldsymbol{C}}^{(tv)}$ represents the error in the modelled gravitational acceleration due to rapid mass changes in the atmosphere and oceans (as is considered in Chapter 5, Section 6.2 and Chapter 8), as well as due to monthly changes associated with hydrological and glaciological processes (as is considered in Section 6.2). This error is not known accurately, so it is a reasonable assumption to define it as a fraction of the total signal (e.g Ditmar et al., 2012; van Dam et al., 2008; Visser, 2010; Reubelt et al., 2014; Gunter et al., 2010).

Simulation of omission errors

In the simulation environment, the omission error is represented as a discrepancy in the maximum spatial frequency of observed and forecasted quantities (Gunter et al.,

2006). As such, the "true" gravitational potential $V^{(\text{true})}$ and reference gravitational potential $V^{(\text{ref})}$ are given by the same model $\overline{\boldsymbol{C}}$ with the exception that the maximum degree in the reference model, $L^{(\text{max})(\text{for})}$, is lower than that in the "true" model, $L^{(\text{max})(\text{obs})}$:

$$\boldsymbol{\eta}^{(\text{obs})} = \tilde{\nabla} V\left(\mathbf{x}, \left[\overline{C}_{\ell m}\right]\right), \quad l = 2 \dots L^{(\text{max})(\text{obs})}$$
$$\boldsymbol{\eta}^{(\text{for})} = \tilde{\nabla} V\left(\mathbf{x}, \left[\overline{C}_{\ell m}\right]\right), \quad l = 2 \dots L^{(\text{max})(\text{for})}$$
$$L^{(\text{max})(\text{for})} < L^{(\text{max})(\text{obs})}.$$

Assuming that the link between the Stokes coefficients and the observations is linear, the omission signal $\boldsymbol{\eta}^{(\text{sp})}$ can also be represented as

$$\begin{aligned} \boldsymbol{\eta}^{(\text{sp})} &= \boldsymbol{\eta}^{(\text{obs})} - \boldsymbol{\eta}^{(\text{for})} \\ &= \tilde{\nabla} V\left(\mathbf{x}, \left[\overline{C}_{\ell m}\right]\right), \quad l = L^{(\text{max})(\text{for})} + 1 \dots L^{(\text{max})(\text{obs})}. \end{aligned} \tag{4.41}$$

Crucially, $\boldsymbol{\eta}^{(\text{sp})}$ is propagated into the gravity field parameters, considering the maximum degree of the LS estimation to be $L^{(\text{max})(\text{for})}$.

For Earth observation satellites, the maximum degree that is possible to estimate is given by the largest ground-track gap, usually located at or at the vicinity of the equator. By considering a larger data set, it is possible to decrease the equatorial gap sufficiently so that the maximum degree is large enough for the omission errors to be insignificant. Nevertheless, the orbit configuration must be such that there is no ground track repeat pattern or the associated repeat period is sufficiently long, as is the case of GOCE. This satellite had a repeat period of 2 months, resulting in a ground-track separation of less that 40 km at the end of this period (Balmino et al., 1999). A repeat orbit is avoided by allowing the orbit to naturally decay due to atmospheric drag over the course of time, with periodic orbit-maintenance manoeuvres to extend the life-time of the mission, as is the case with CHAMP and GRACE. However, this strategy does not avoid occasional short repeat periods occurring over the course of a few weeks (Weigelt et al., 2009).

Simulation of static gravity field model errors

The simulation of static gravity field model errors considers two different static gravity field models for the observed and forecasted quantities. It is assumed that one of them is an improvement over the other, so their difference mainly depicts the error of the less accurate one. If two independent models of similar accuracy

are considered, such as those derived from data of similar origin and period, their difference is limited mainly to discrepancies in the processing strategies, which is not the objective of the analysis.

As an example, let it be assumed that the observed quantities are generated on the basis of the EIGEN-5C and the forecasted quantities on the basis of the EIGEN-CG03C:

$$\boldsymbol{\eta}^{(\text{obs})} = \tilde{\nabla} V\left(\mathbf{x}, \overline{\boldsymbol{C}}^{(\text{EIGEN-5C})}\right)$$
$$\boldsymbol{\eta}^{(\text{for})} = \tilde{\nabla} V\left(\mathbf{x}, \overline{\boldsymbol{C}}^{(\text{EIGEN-CG03C})}\right).$$

Recognising the linearity of the Spherical Harmonic Synthesis and the linearity of the considered functional model, the mis-modelled static signal $\delta^{(\text{st})}$ can be represented as

$$\begin{aligned}
\delta^{(\text{st})} &= \boldsymbol{\eta}^{(\text{obs})} - \boldsymbol{\eta}^{(\text{for})} \\
&= \tilde{\nabla} V\left(\mathbf{x}, \overline{\boldsymbol{C}}^{(\text{EIGEN-5C})} - \overline{\boldsymbol{C}}^{(\text{EIGEN-CG03C})}\right).
\end{aligned} \tag{4.42}$$

The maximum degree of the estimated gravity field parameters resulting from $\delta^{(\text{st})}$ should be in agreement with the maximum degree considered in the simulation, so as to avoid the additional spatial aliasing effect.

4.3.2 Modelling hl-SST noise

In the following sections, the errors associated with random noise in hl-SST and ll-SST data are presented. These errors differ from the modelling errors in the sense that they arise due to imperfect sensors, instead of deficient knowledge of the geophysical processes that are not comprehensively observable by the gravimetric satellite mission.

Measurement noise in the satellite accelerations derived from GPS observations is simulated by generating coloured noise which realistically reproduces the uncertainty associated with GPS positioning, as determined by experiments with CHAMP mission data conducted by Ditmar et al. (2007). The Amplitude Spectral Density (ASD) of the noise along each component (along-track, cross-track and radial) is shown in Figure 4.3. The analytical representation of the curves in Figure 4.3 is given as function of frequency f by

$$\sqrt{u(f)} = \frac{2\sigma}{\Delta t^{\frac{3}{2}}}\left(1 - \cos\left(2\pi f \Delta t\right) + \left(\frac{\Delta t}{4\tau}\right)^2\right). \tag{4.43}$$
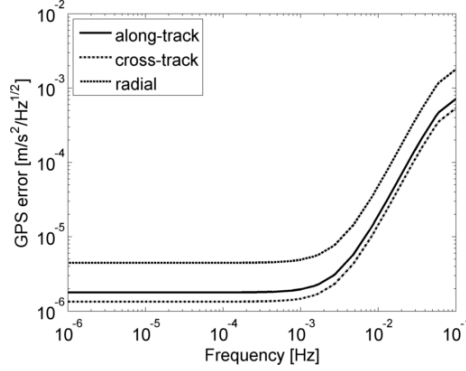
Figure 4.3 – ASD of the orbit errors, in terms of absolute accelerations used in the simulation of hl-SST errors.

The parameter σ is associated with the amplitude of the GPS positioning error and takes the values of 2, 1.5 an 5 mm for the along-track, cross-track and radial directions, respectively. The empirical parameter τ, controls the amplitude of noise at low frequencies and is typically set to 180 s.

A realization of this noise $\delta^{(obs)(hl\text{-}SST)}$, with the frequency description represented by Eq. (4.43) is added directly to the averaged accelerations generated on the basis of the "true" gravitational potential.

4.3.3 Modelling ll-SST noise

The errors in ll-SST data are the less understood in comparison to those in hl-SST data. There is a large number of publications dedicated to the study of errors in the data (Frommknecht et al., 2003, 2006; Gerlach et al., 2004; Flury et al., 2008; Horwath et al., 2010; Meyer et al., 2012a; Touboul et al., 2012; Bandikova et al., 2012), many of which focus on a dedicated instrument or on how errors of a particular instrument propagate to the gravity field parameters. It is rare to find an analysis of the a posteriori residuals, where the sources of noise are clearly identified. Even when that is done, as presented in Section 6.2.2, it is difficult to fully understand the origin of noise in GRACE data.

In this section, two noise models are presented: the *simplistic* and *advanced* noise model. The simplistic noise model was implemented at an earlier study stage. With the progress of the research, it became evident that the simplistic model was not contemplating all the errors in the ll-SST measurement principle. In order to

overcome this limitation, the advanced noise model was developed. The reason to present the simplistic noise model is to describe the initial naive attempts undertaken to model the errors in the GRACE data and in this way to justify the complexity of the advanced noise model.

The simplistic noise model considers white noise in the orbit positions and ranges. The assumption is that the added noise realisations propagate through the functional model to re-create the most significant errors in the range combinations. The advanced noise model, on the other hand, realistically describes a number of types of errors explicitly at the level of the range combinations. For those noise types where this approach is not possible, care is taken to produce error time series considering a realistic simulation process. Such is the case of orbit position errors, where orbits are integrated from force models which differ in a way representative of the gravity field model errors.

Both simplistic and advanced noise models are the sum of several *noise types*. In the simplistic model, they are:

- ranging noise $\delta^{(R)}$,
- relative position noise $\delta^{(rP)}$ and
- absolute position noise $\delta^{(aP)}$.

The advanced noise model is composed of:

- ranging noise $\delta^{(R)}$,
- accelerometer noise $\delta^{(acc)}$,
- positioning noise $\delta^{(P)}$,
- correction noise $\delta^{(C)}$ and
- orientation noise $\delta^{(L)}$.

Simplistic noise model

The simplistic noise model is based on the super-imposition of uncorrelated noise with a pre-defined magnitude. The noise time series are added at the level of ll-SST range data and satellite's orbit positions. The errors in the ranges are represented by the ranging noise $\delta^{(R)}$. The error in the orbit positions is further divided into two constituents: 1) the relative position noise $\delta^{(rP)}$ representing the uncertainty of the position of one satellite relative to the other and 2) the uncertainty in the position of the satellites relative to the centre of the Earth, which makes up the absolute position noise $\delta^{(aP)}$.

The noise in accelerometer data has not been included in the simplistic noise modelling, because their error is negligible in comparison to other error components (Frommknecht et al., 2006; Flury et al., 2008).

Table 4.3 summarises the noise types that form the simplistic noise model.

name	symbol	description
ranging noise	$\delta^{(R)}$	ranging sensor noise propagated to the range combinations
relative position noise	$\delta^{(rP)}$	noise in the orientation of the LoS vector and relative orbit positions
absolute position noise	$\delta^{(aP)}$	noise in the orbit positions

Table 4.3 – Summary of the noise types in the simplistic noise model.

Simulating ranging noise   The ranging noise represents the errors in measuring the inter-satellite range. Inaccuracies in the ranging data of a ll-SST satellite system are simulated as a time series of uncorrelated ranging sensor noise $\delta^{(\rho)}$. It is added to the computed ranges ρ, as obtained with Eq. (4.20), resulting in the estimated ranges $\hat{\rho}$

$$\hat{\rho} = \rho + \delta^{(\rho)}. \tag{4.44}$$

The estimated range combination $\hat{\bar{a}}$ are computed from $\hat{\rho}$, making use of Eq. (4.23), thus propagating $\delta^{(\rho)}$ to those quantities. Note that $\hat{\bar{a}}$ is linear with $\hat{\rho}$ and $\cos\theta_{i,\pm1} \approx 1$. Consequently, from the ranging sensor noise $\delta^{(\rho)}$, it is possible to explicitly derive the propagated $\delta^{(\rho)}$ on the average accelerations, henceforth called ranging noise $\delta^{(R)}$:

$$
\begin{aligned}
\hat{\bar{a}}_i &= \frac{\cos\theta_{i,-1}^{(\text{obs})} \cdot \left(\rho_{i-1}^{(\text{obs})} + \delta_{i-1}^{(\rho)}\right) - 2\left(\rho_i^{(\text{obs})} + \delta_i^{(\rho)}\right) + \cos\theta_{i,+1}^{(\text{obs})} \cdot \left(\rho_{i+1}^{(\text{obs})} + \delta_{i+1}^{(\rho)}\right)}{(\Delta t)^2} \\
&= \bar{a}_i^{(\text{obs})} + \frac{\cos\theta_{i,-1}^{(\text{obs})}\delta_{i-1}^{(\rho)} - 2\delta_i^{(\rho)} + \cos\theta_{i,+1}^{(\text{obs})}\delta_{i+1}^{(\rho)}}{(\Delta t)^2} \\
&\approx \bar{a}_i^{(\text{obs})} + \frac{\delta_{i-1}^{(\rho)} - 2\delta_i^{(\rho)} + \delta_{i+1}^{(\rho)}}{(\Delta t)^2}, \quad \cos\theta_{i,\pm1}^{(\text{obs})} \cdot \delta_{i\pm1}^{(\rho)} \approx \delta_{i\pm1}^{(\rho)} \\
&\equiv \bar{a}_i^{(\text{obs})} + \delta_i^{(R)}.
\end{aligned} \tag{4.45}
$$

As illustrated in Eq. (4.45) and relevant to the simplistic noise model, the ranging noise $\delta^{(\mathrm{R})}$ at time t_i depends only on the K-Band Ranging (KBR) sensor errors $\delta_{i-1}^{(\rho)}$, $\delta_i^{(\rho)}$, and $\delta_{i+1}^{(\rho)}$.

Simulating relative position noise   The relative position noise $\delta^{(\mathrm{rP})}$ is the relative orbit position noise $\boldsymbol{\delta}^{(\Delta\mathbf{x})}$ propagated to the range combinations. The relative orbit position noise is function of the error in the orientation of the LoS direction vector. The middle point between the positions of the two satellites does not depend on the magnitude of $\boldsymbol{\delta}^{(\Delta\mathbf{x})}$. Uncorrelated relative orbit position noise $\boldsymbol{\delta}^{(\Delta\mathbf{x})}$ is added in a symmetric way to the positions of both satellites:

$$
\begin{cases}
\mathbf{x}^{(\mathrm{for})(1)} = \mathbf{x}^{(\mathrm{obs})(1)} + \boldsymbol{\delta}^{(\Delta\mathbf{x})}/2 \\
\mathbf{x}^{(\mathrm{for})(2)} = \mathbf{x}^{(\mathrm{obs})(2)} - \boldsymbol{\delta}^{(\Delta\mathbf{x})}/2.
\end{cases}
\tag{4.46}
$$

The relative orbit position noise $\boldsymbol{\delta}^{(\Delta\mathbf{x})}$ is a 3D random variable without a cross-correlation between different components: it represents the errors of $\mathbf{x}^{(1)}$ relative to $\mathbf{x}^{(2)}$. It should not be confused with the relative position noise $\delta^{(\mathrm{rP})}$, which has units of $[\mathrm{m/s}^2]$.

The relative orbit position noise $\boldsymbol{\delta}^{(\Delta\mathbf{x})}$ is propagated to the relative position noise $\delta^{(\mathrm{rP})}$ by computing the difference between the noise-free and noisy observations. Eq. (4.23) is used to derive the two types of observations, i.e. considering the noise-free $\theta^{(\mathrm{obs})}$ and noisy $\theta^{(\mathrm{for})}$:

$$
\delta_i^{(\mathrm{rP})} = \frac{\cos\theta_{i,-1}^{(\mathrm{obs})} \cdot \rho_{i-1}^{(\mathrm{obs})} - 2\rho_i^{(\mathrm{obs})} + \cos\theta_{i,+1}^{(\mathrm{obs})} \cdot \rho_{i+1}^{(\mathrm{obs})}}{(\Delta t)^2}
$$
$$
- \frac{\cos\theta_{i,-1}^{(\mathrm{for})} \cdot \rho_{i-1}^{(\mathrm{obs})} - 2\rho_i^{(\mathrm{obs})} + \cos\theta_{i,+1}^{(\mathrm{for})} \cdot \rho_{i+1}^{(\mathrm{obs})}}{(\Delta t)^2}.
\tag{4.47}
$$

The angles $\theta^{(\mathrm{for})}$ and $\theta^{(\mathrm{obs})}$ are computed using Eq. (4.22) from the noise-free and noisy orbits, the $\mathbf{x}^{(\mathrm{for})}$ and $\mathbf{x}^{(\mathrm{obs})}$, respectively.

One could argue the same could be done considering Eq. (4.39), i.e.:

$$
\delta^{(\mathrm{rP})} \overset{?}{=} \nabla' V\left(\mathbf{x}^{(\mathrm{obs})}, \overline{\boldsymbol{C}}^{(\mathrm{ref})}, \mathbf{e}^{(\mathrm{LoS})(\mathrm{for})}\right) - \nabla' V\left(\mathbf{x}^{(\mathrm{obs})}, \overline{\boldsymbol{C}}^{(\mathrm{ref})}, \mathbf{e}^{(\mathrm{LoS})(\mathrm{obs})}\right).
\tag{4.48}
$$

However, that is not the case. Eq. (4.47) projects the preceding and following LoS vectors along the direction of the current LoS vector (before the double differentiation

is done), as indicated by the terms $\theta_{i,\pm 1}^{(\text{obs})}$. As a consequence, the consecutive differences between the errors over three epochs play a role. On the other hand, Eq. (4.48) projects point-wise inter-satellite accelerations along error-free and noisy unit vectors defining the LoS direction and only the error of the LoS vector at the current epoch is relevant. The type of noise depicted by Eq. (4.48) is considered in the advanced noise model, cf. Section 4.3.3.

Simulating absolute position noise   The absolute position noise $\delta^{(\text{aP})}$ represents the noise in the observations resulting from the identical error in the orbital positions of the two satellites. To simulate it, the same realization of uncorrelated absolute orbit position noise $\boldsymbol{\delta}^{(\mathbf{x})}$ is added to the position of both satellites, independently along each of the orthogonal coordinate directions:

$$\begin{cases} \mathbf{x}^{(\text{for})(1)} = \mathbf{x}^{(\text{obs})(1)} + \boldsymbol{\delta}^{(\mathbf{x})} \\ \mathbf{x}^{(\text{for})(2)} = \mathbf{x}^{(\text{obs})(2)} + \boldsymbol{\delta}^{(\mathbf{x})}. \end{cases} \tag{4.49}$$

Unlike the relative position noise, the LoS vector is not modified, i.e.:

$$\mathbf{e}^{(\text{LoS})(\text{for})} = \mathbf{e}^{(\text{LoS})(\text{obs})} \equiv \mathbf{e}^{(\text{LoS})}.$$

As a consequence, absolute position noise does not propagate to the observations if computed with Eq. (4.23). It is necessary to use Eq. (4.39) to complete its propagation to the level of the observations. The difference between the uncorrupted and corrupted observations, is the absolute position noise $\delta^{(\text{aP})}$ (the meaning of the ∇' operator is defined in Eq. (4.39)):

$$\delta^{(\text{aP})} = \nabla' V \left(\mathbf{x}^{(\text{for})}, \overline{\boldsymbol{C}}^{(\text{ref})}, \mathbf{e}^{(\text{LoS})} \right) - \nabla' V \left(\mathbf{x}^{(\text{obs})}, \overline{\boldsymbol{C}}^{(\text{ref})}, \mathbf{e}^{(\text{LoS})} \right). \tag{4.50}$$

Advanced noise model

The advanced noise model, originally proposed by Ditmar et al. (2012), describes explicitly a number of noise types at range combinations level, which are not accurately represented by considering noise in the orbit positions and propagating it to the range combinations. The motivation is to gain deeper understanding of the error budget in ll-SST data by implementing explicitly all the conceivable noise types.

Another development associated with the advanced noise model, as compared to the simplistic noise model, concerns an accurate description of the noise in the frequency domain. Recall that in the simplistic noise model, the ranging sensor noise

$\delta^{(\rho)}$, absolute orbit position noise $\boldsymbol{\delta}^{(\mathbf{x})}$ and relative orbit position noise $\boldsymbol{\delta}^{(\Delta\mathbf{x})}$, are all assumed to be white, i.e. only described by the standard deviation. A detailed characterization of the noise in the frequency domain further makes the simulations more representative of the actual noise.

Table 4.4 summarises the noise types that are part of the advanced noise model and Appendix D presents the analytical derivation of the noise model, as well as of the formulas describing the positioning noise, orientation noise, correction noise.

name	symbol	description
accelerometer noise	$\delta^{(\mathrm{acc})}$	noise in measuring non-gravitational accelerations
correction noise	$\delta^{(\mathrm{C})}$	noise resulting from the inaccurately known relative radial velocity
orientation noise	$\delta^{(\mathrm{L})}$	noise in the orientation of the LoS vector
positioning noise	$\delta^{(\mathrm{P})}$	noise in the orbit positions
ranging noise	$\delta^{(\mathrm{R})}$	noise in the ranging sensor

Table 4.4 – Summary of the noise types in the advanced noise model.

Simulating accelerometer noise The accelerometer noise is directly related to the inaccuracies in the data gathered by the on-board accelerometer. These data are needed to take into account the non-gravitational accelerations, without having to rely on radiation pressure and aerodynamic models, thus avoiding the associated modelling errors. This error component is not part of the simplistic noise model because it is known to be insignificant in comparison to other errors. However, keeping in mind that future gravimetric missions are to be analysed, it is important to understand at which point other noise types become comparable with the accelerometer noise.

Simulating accelerometer noise is a matter of using the ASD of the accelerometer's noise to generate the random time-series $\boldsymbol{\delta}^{(\mathrm{acc})(j)}$ for each satellite j. The quantities $\boldsymbol{\delta}^{(\mathrm{acc})(j)}$ represent the accuracy of the accelerometer in 3D space. The accelerometer noise $\delta^{(\mathrm{acc})}$ is computed from the difference between accelerometer noise of satellite 1, $\boldsymbol{\delta}^{(\mathrm{acc})(1)}$ and accelerometer noise of satellite 2, $\boldsymbol{\delta}^{(\mathrm{acc})(2)}$. Considering that both accelerometers are identical, i.e. $\mathrm{ASD}\big(\boldsymbol{\delta}^{(\mathrm{acc})(1)}\big)=\mathrm{ASD}\big(\boldsymbol{\delta}^{(\mathrm{acc})(2)}\big)=\mathrm{ASD}\big(\boldsymbol{\delta}^{(\mathrm{acc})(\mathrm{pw})}\big)$, the total accelerometer noise is $\sqrt{2}\boldsymbol{\delta}^{(\mathrm{acc})(\mathrm{pw})}$.

The point-wise accelerometer noise $\boldsymbol{\delta}^{(\mathrm{acc})(\mathrm{pw})}$ cannot be added directly to the range combinations, which are averaged over three epochs. To correct for this, the averaging filter must be applied, which can only be done in the inertial frame. Additionally, $\boldsymbol{\delta}^{(\mathrm{acc})(\mathrm{pw})}$ are vector quantities that need to be projected onto the forecasted unit vector defining the LoS direction $\mathbf{e}^{(\mathrm{LoS})(\mathrm{for})}$, as described by Eq. (4.29):

$$\delta^{(\mathrm{acc})} = \sqrt{2}\,\boldsymbol{\delta}^{(\mathrm{acc})(\mathrm{pw})} * \mathbf{w} \cdot \mathbf{e}^{(\mathrm{LoS})}. \tag{4.51}$$

Under the assumption that the accelerometer noise is isotropic in magnitude, i.e. one accelerometer axis is not more accurate than the other, it is possible to skip the rotation $R^{(\mathrm{CRF})\leftarrow(\mathrm{LoSRF})}$ and define the accelerometer noise directly in the CRF. The stochastic properties of a normally-distributed isotropic random vector do not change if transformed into another reference frame, as long as the determinant of that transformation is one. The same is not true in case the accelerometer axes have different accuracies, in which case Eq. (4.51), with the meaning of the $* \mathbf{w} \cdot \mathbf{e}^{(\mathrm{LoS})}$ operations defined by Eq. (4.29), represents this general case.

The simulated range combinations $\bar{a}$ are corrupted by accelerometer noise $\delta^{(\mathrm{acc})}$ in order to produce the estimated range combinations $\hat{\bar{a}}$:

$$\hat{\bar{a}} = \bar{a} + \delta^{(\mathrm{acc})}. \tag{4.52}$$

Simulating advanced ranging noise   Unlike the simplistic noise model, the time series of $\delta^{(\rho)}$ in the advanced noise model is generated on the basis of a suitable ASD, characteristic of a particular inter-satellite metrology system. For example, the estimated ASD of the ranging noise in GRACE is shown in Figure 6.12b and what is assumed in the simulation of future gravimetric missions is shown in Figure 8.7a.

Unlike the ranging noise in the simplistic noise model, cf. Eq. (4.45), the ranging noise in the advanced noise model is computed accurately, i.e. without the assumption that $\theta^{(\mathrm{obs})}$ is small:

$$\cos\theta_{i,\pm1}^{(\mathrm{obs})} \cdot \delta_{i\pm1}^{(\rho)} \not\approx \delta_{i\pm1}^{(\rho)}.$$

As a consequence, the ranging noise is given by:

$$\delta_i^{(\mathrm{R})} = \frac{\cos\theta_{i,-1}^{(\mathrm{obs})}\delta_{i-1}^{(\rho)} - 2\delta_i^{(\rho)} + \cos\theta_{i,+1}^{(\mathrm{obs})}\delta_{i+1}^{(\rho)}}{(\Delta t)^2}. \tag{4.53}$$

The approximation incurred in the simplistic noise model does not modify substantially the produced range combinations as long as consecutive changes in the

attitude of the LoS direction are not too large. This is the case in most satellite formations. Nevertheless, it was decided to model the propagation of the ranging sensor noise $\delta^{(\rho)}$ without any approximation, so that a more general and accurate procedure is considered. As demonstrated in Section 8.2.1, the approximation may modify the resulting range combinations in some particular cases but only at the low frequencies.

Simulating correction noise The correction noise can be interpreted as inaccuracies in the estimated centrifugal accelerations. The orbital positions provide the means to reconstruct the accelerations associated with the rotation of the LoS vector. In practice, this reconstruction is imperfect because of the errors in the orbital positions.

Neglecting the out-of-plane motion, the point-wise inter-satellite centrifugal acceleration $a^{(12)(\text{cent})}$ is mainly a function of the orbit velocity of satellite 1 relatively to satellite 2 projected onto the plane perpendicular to the LoS direction $\dot{\mathbf{x}}^{(12)\perp}$ (Rummel, 1979):

$$a^{(12)(\text{cent})} \approx -\frac{1}{\rho}\big(\dot{\mathbf{x}}^{(12)\perp}\big)^2. \tag{4.54}$$

This means that the correction noise, or the inaccuracies in the estimated centrifugal accelerations, can be represented approximately as

$$\delta^{(\text{C})} = -2\frac{\dot{\mathbf{x}}^{(12)\perp}}{\rho}\delta^{\big(\dot{x}^{(12)\perp}\big)} + \left(\frac{\dot{\mathbf{x}}^{(12)\perp}}{\rho}\right)^2 \delta^{(\rho)}. \tag{4.55}$$

The derivation of this equation is shown in Section D.3.3.

Thus, the correction noise depends on i) errors in the estimated orbit velocity of satellite 1 relatively to satellite 2 projected onto the plane perpendicular to the LoS direction (the first term in the expression above) and ii) on KBR sensor errors (the second term). Notice that Eq. (4.54) represents a continuous function, while the functional model used in the study is a finite difference. Ditmar et al. (2012) shows that in practice it is possible to use Eq. (4.55) to model the errors in the estimated centrifugal accelerations without a significant loss of accuracy.

Simulating orientation noise The orientation noise $\delta^{(\text{L})}$ represents the error of the LoS orientation in the computation of the forecasted point-wise inter-satellite accelerations. The inter-satellite accelerations are computed accurately but projected onto the wrongly-estimated unit vectors defining the LoS direction $\mathbf{e}^{(\text{LoS})(\text{for})}$, instead of the correct $\mathbf{e}^{(\text{LoS})(\text{obs})}$.

105

In the Line-of-sight Reference Frame (LoSRF), the forecasted LoS vector $\mathbf{d}^{\text{(for)}}$ differs from the observed LoS vector $\mathbf{d}^{\text{(obs)}}$ by $\left[0, \delta_y^{(\Delta\mathbf{x})}, \delta_z^{(\Delta\mathbf{x})}\right]^{\text{T}}$, where $\delta^{(\Delta\mathbf{x})}$ is the relative orbit position noise. This means that, relative to $\mathbf{d}^{\text{(obs)}}$, the $\mathbf{d}^{\text{(for)}}$ is slightly rotated along the axes perpendicular to the LoS vector. In terms of unit vectors, the $\mathbf{e}^{\text{(LoS)(for)}}$ differs from $\mathbf{e}^{\text{(LoS)(obs)}}$ by the noise in the orientation of the LoS vector $\boldsymbol{\delta}^{\text{(LoS)}}$:

$$\boldsymbol{\delta}^{\text{(LoS)(LoSRF)}} = \frac{1}{\rho^{\text{(for)}}} \begin{bmatrix} 0 \\ \delta_y^{(\Delta\mathbf{x})\text{(LoSRF)}} \\ \delta_z^{(\Delta\mathbf{x})\text{(LoSRF)}} \end{bmatrix}. \tag{4.56}$$

Note that, by definition, $\mathbf{e}^{\text{(LoS)}} \equiv \mathbf{d}/\rho$.

In other reference frames, the x-component is not necessarily zero and $\boldsymbol{\delta}^{\text{(LoS)}}$ is given by the more general expression:

$$\boldsymbol{\delta}^{\text{(LoS)}} = \frac{1}{\rho^{\text{(for)}}} \begin{bmatrix} \delta_x^{(\Delta\mathbf{x})} \\ \delta_y^{(\Delta\mathbf{x})} \\ \delta_z^{(\Delta\mathbf{x})} \end{bmatrix} = \frac{\boldsymbol{\delta}^{(\Delta\mathbf{x})}}{\rho^{\text{(for)}}}. \tag{4.57}$$

The orientation noise is simulated as the difference between the gravitational accelerations $\boldsymbol{\nabla} V$, generated on the basis of the force model $\overline{\boldsymbol{C}}^{\text{(ref)}}$, at the orbital positions $\mathbf{x}^{\text{(for)}(j)}$, scaled by $\boldsymbol{\delta}^{\text{(LoS)}}$:

$$\delta^{\text{(L)(pw)}} = \delta^{\text{(L)(1)(pw)}} - \delta^{\text{(L)(2)(pw)}}$$
$$\text{with} \quad \delta^{\text{(L)(j)(pw)}} = \boldsymbol{\nabla} V\left(\mathbf{x}^{(j)}, \overline{\boldsymbol{C}}^{\text{(ref)}}\right) \cdot \boldsymbol{\delta}^{\text{(LoS)}} \quad \text{and} \quad j = 1, 2. \tag{4.58}$$

The derivation of this equation can be found in Section D.3.2.

The point-wise orientation noise $\delta^{\text{(L)(pw)}}$ cannot be added directly to the range combinations. In the same way as the accelerometer noise and as shown in Eq. (4.29), the averaging filter and the projection onto the forecasted LoS direction need to be considered in order to derive the averaged orientation noise.

Simulating positioning noise The positioning noise represents the error associated with the forecasted inter-satellite gravitational accelerations taken at inaccurately known orbit position $\mathbf{x}$. In other words, the forecasted gravitational accelerations are computed on the basis of a pre-defined force model accurately but at the wrong locations. Unlike the orientation noise, the positioning noise assumes there is no error in the LoS vector. This means that the point-wise inter-satellite accelerations

computed at the inconsistent observed and forecasted orbital positions are projected onto the same observed and forecasted LoS vector. This is in contrast to the orientation noise, which projects the point-wise inter-satellite accelerations computed at consistent observed and forecasted positions along the different observed and forecasted LoS vectors. This distinction is also described in Appendix D, Eq. (D.2) and Eq. (D.3).

The simulation of the positioning noise requires two sets of orbit positions, the first integrated on the basis of the "true" gravitational potential $V^{\text{(true)}}$, called observed orbit positions $\mathbf{x}^{\text{(obs)}}$ and the second one integrated on the basis of the reference gravitational potential $V^{\text{(ref)}}$, called forecasted orbit positions $\mathbf{x}^{\text{(for)}}$. The difference between $\mathbf{x}^{\text{(obs)}}$ and $\mathbf{x}^{\text{(for)}}$ represents the uncertainty of the orbital positions of the satellites, since it is predicted that they are located at $\mathbf{x}^{\text{(for)}}$ but in reality they are at $\mathbf{x}^{\text{(obs)}}$.

The simulation of positioning noise requires the explicit integration of two sets of orbits in order to ensure that both the absolute and relative positioning error propagate to the positioning noise. Corrupting $\mathbf{x}^{\text{(obs)}}$ with only the relative orbit position noise $\boldsymbol{\delta}^{(\Delta\mathbf{x})}$ (in the way described by Eq. (4.46)) does not change the middle-point of the orbit and, therefore, ignores the effects of the absolute positioning error. Contrary to the positioning noise, the absolute positioning error is irrelevant to the simulation of the orientation noise because these errors, which are of equal amplitude in the positions of both satellites, do not change the attitude of the LoS vector. In that case, there is no strong reason to explicitly integrate two sets of orbits, particularly when a suitable estimation of $\boldsymbol{\delta}^{(\Delta\mathbf{x})}$ is possible to derive from actual GRACE data, cf. Section 6.1.

The point-wise positioning noise $\boldsymbol{\delta}^{\text{(P)(pw)}}$ is given by:

$$\boldsymbol{\delta}^{\text{(P)(pw)}} = \boldsymbol{\nabla} V\left(\mathbf{x}^{\text{(obs)}}, \overline{\boldsymbol{C}}^{\text{(ref)}}\right) - \boldsymbol{\nabla} V\left(\mathbf{x}^{\text{(for)}\left(\text{adj}\right)}, \overline{\boldsymbol{C}}^{\text{(ref)}}\right). \tag{4.59}$$

The derivation of this equation is shown in Section D.3.1.

The adjusted forecasted orbit positions $\mathbf{x}^{\text{(for)}\left(\text{adj}\right)}$ are the result of forcing the ranges described by the forecasted orbit positions to be equal to those described by the observed orbit positions:

$$\mathbf{x}^{\text{(for)}\left(\text{adj}\right)} = \mathbf{x}^{\text{(for)}\left(\overline{12}\right)} \pm \mathbf{e}^{\text{(LoS)(for)}} \frac{\left|\mathbf{x}^{\text{(obs)(1)}} - \mathbf{x}^{\text{(obs)(2)}}\right|}{2}. \tag{4.60}$$

The purpose of this procedure, used in actual data processing, is to increase the accuracy of the forecasted orbit, by assimilating the accurate measurements provided by the ranging sensor.

For the production of the time series of $\boldsymbol{\delta}^{(P)(pw)}$, $V^{(true)}$ and $V^{(ref)}$ describe no mass transport processes because the resulting indirect effect associated with residual temporal aliasing would be small in comparison to the effect of the full static signal. For the same reason, the maximum degree of $V^{(true)}$ and $V^{(ref)}$ are the same in the simulation of $\boldsymbol{\delta}^{(P)(pw)}$, in order to avoid the inclusion of an omission signal (Section 4.3.1).

Additionally, the difference between the observed and forecasted orbits depends on parameters that are relevant to the integration of the orbits. These parameters are the length of the orbit arc where the integration is uninterrupted, the number of empirical accelerations and the frequency in which they are estimated and how the accelerometer calibration parameters are handled. In the case of simulations conducted in the thesis, the only parameter that is relevant is the arc length, since the no empirical accelerations nor calibration parameters are estimated. The arc length considered in the simulations is 6 hrs, which in agreement with that used to process actual GRACE data in the production of the DMT model.

In the same way as the orientation noise, the point-wise positioning noise $\boldsymbol{\delta}^{(P)(pw)}$ cannot be added directly to the range combinations. For that reason, the same sequence of operations shown in Eq. (4.29) has to be performed in order to derive the averaged positioning noise.

4.3.4 Summary of the Noise types

With the purpose of facilitating the overview of the various noise types, Table 4.5 and Table 4.6 provide the connection between the symbols, names and the noise model, where relevant, of the considered noise types as well as the page where the they are defined.

The noise types associated with model errors, introduced in Section 4.3.1 are summarised in Table 4.5.

symbol	name	page nr.
$\delta^{(tv)}$	mis-modelled time-variable signal	95
$\delta^{(sp)}$	omission signal	95
$\delta^{(st)}$	mis-modelled static signal	96

Table 4.5 – Summary of the symbols and names of the model errors.

Table 4.6 summarises the hl-SST and ll-SST noise types, identifying the simplistic and advanced noise models in case of the ll-SST observation principle.

symbol	name	noise model	observation type	noise magnitude	page nr.
$\delta^{(obs)}(hl\text{-}SST)$	hl-SST observation noise	N/A	hl-SST	Figure 4.3	97
$\delta^{(R)a}$	ranging noise	simplistic	ll-SST	$10\,\mu m$	100
$\delta^{(rP)}$	relative position noise	simplistic	ll-SST	$1\,mm$	101
$\delta^{(aP)}$	absolute position noise	simplistic	ll-SST	$1\,cm$	102
$\delta^{(acc)}$	accelerometer noise	advanced	ll-SST	Figure 6.20a	103
$\delta^{(R)a}$	ranging noise	advanced	ll-SST	Figure 6.22a	104
$\delta^{(C)}$	correction noise	advanced	ll-SST	Figure 6.24a	105
$\delta^{(L)}$	orientation noise	advanced	ll-SST	Figure 6.25a	105
$\delta^{(P)}$	positioning noise	advanced	ll-SST	Figure 6.28a	106

[a]The ranging noise $\delta^{(R)}$ is simulated differently for the simplistic and advanced noise models but both cases are conceptually equivalent, refer to Section 4.3.3 and Section 4.3.3.

Table 4.6 – Summary of the symbols and names of the noise types relevant to the ll-SST and ll-SST observation principles.

4.4   Summary

Modelling satellite gravimetry requires the definition of the function, signal and noise models. The functional model (Section 4.1) defines the mathematical relation between the set of model parameters and the measurements taken by the satellite system. The signal model (Section 4.2) is the a priori knowledge of Earth's gravitational field and is necessary in order to reduce the measurements to residual quantities where the functional model is linear. The noise model (Section 4.3) is introduced to properly quantify the observation and model uncertainties in order to introduce a level of realism in the simulations.

The total error is divided into model and measurement errors. The model errors are common in the case of hl-SST and ll-SST data, differing only in the simulation procedure, refer to Section 4.3.1. In contrast, the measurement errors are specific to each observation principle. The model and measurement errors are simulated concurrently, as is the case of Chapter 5 and Chapter 8, in order to predict the effect of model and sensor-related uncertainties.

The two observations principles, high-low Satellite-to-Satellite Tracking (hl-SST) and low-low Satellite-to-Satellite Tracking (ll-SST), each have particular contributors regarding the noise model. The noise in the hl-SST data (Section 4.3.2) is the most simple to model in view of the fact that the errors in the Global Navigation Satellite System (GNSS) receiver are dominant enough to justify neglecting all the errors

in other sensors. The error in the ll-SST measurements (Section 4.3.3) required the most attention when modelling the data noise. The ranging sensor noise is not the only relevant error source, but also the errors in determining the LoS direction, further requiring information about the accuracy of the computed satellite orbits. Two measurement noise models are defined; the simplistic noise model being the one initially used, as is the case with the combined inversion in Chapter 5; and the advanced noise model, validated in Section 6.2 and later used to conduct a numerical study on satellite formations in Chapter 8.

Although great effort was made to include every imaginable noise type, it is possible that further research uncovers new error that have not been so far considered. In any case, it is assumed that the (possibly incomplete) set of noise types analysed in the thesis is sufficiently broad and substantial to produce results that are sufficiently general and do not have to be significantly modified after the inclusion of new noise types.

Added Value of non-Dedicated GPS-Equipped Constellations

<div style="text-align: right">**5**</div>

The spatio-temporal resolution of the time-variable gravity field models derived from dedicated gravimetric satellite missions is inherently limited by their ground track coverage. Those models are subject to aliasing effects caused by sub-monthly mass transport signals, such as atmospheric and ocean processes. To address these issues, this chapter explores the feasibility of using non-dedicated satellite constellations, namely those from commercial communication networks or a low-cost array of custom-built micro-satellites, as a complementary data source. The positioning receivers on-board the constellation's satellites would ideally provide a high density of observations in the form of derived accelerations which, while much less accurate than those obtained from dedicated gravimetric missions, may still be sufficient to observe the longest wavelengths at even sub-daily intervals. Using a series of simulated mission scenarios it is shown that such constellations, acting either independently or when combined with dedicated gravimetric missions, may offer a noticeable improvement in the recovery of the large scale ($> 1000\,\text{km}$), high frequency ($< 1\,\text{month}$) components of the time-varying gravitational field.

5.1 Introduction

The Gravity Recovery And Climate Experiment (GRACE) mission constitutes only a single instrument pair, a fact that has implications on the temporal resolution of the resulting gravity field models. As a general rule of thumb, it takes approximately one month of GRACE data to produce a gravity field model of relatively high spatial resolution and quality, i.e., spherical harmonic degree and order 60 (this translates into a half-wavelength distance of roughly 330 km at the equator) or higher (up

to degree 120 in particularly well covered regions) with standard deviations less than 2 cm Equivalent Water Height (EWH) (Schmidt et al., 2008a; Liu et al., 2010). The reason is that the ground track coverage needs to be dense enough to adequately observe small features. Furthermore, Earth's gravitational field is itself changing during the chosen time interval, as there are many mass transport processes (e.g., atmospheres, continental hydrology, tides, etc.) that have cycles much shorter than one month. The high-frequency (i.e., < 1 month) signals created from these short-term processes introduce aliasing error into the monthly gravity field models. The current approach for dealing with these errors is to use modelled estimates for these short-period signals and adjust the K-Band Ranging (KBR) measurements accordingly. Such an approach is naturally limited by the accuracy of the models used, and introduces another potentially large error source into the GRACE gravity field models. In order to measure rapid mass transport processes themselves with satellite data, one has to get higher temporal resolution and, therefore, sacrifice spatial resolution; the only way to improve both is to increase the number of satellites involved.

One option is to fly multiple pairs of satellites equipped with ranging sensors in different orbit planes, as proposed by Bender et al. (2008) and others (Sneeuw et al., 2005; Sharifi et al., 2007; Encarnação et al., 2008; Wiese et al., 2009). The number of GRACE-like pairs that would need to be flown depends on the accuracy desired, but assuming more and more pairs are flown, the set of satellites would begin to resemble a constellation. While the concept is intriguing, the resources required to build, launch, and support more than one or two GRACE-like satellite pairs is significant, making such proposals academically interesting, but not very realistic in the near future. Another option is to fly gradiometer-equipped satellites but the same type problems are not avoided. Recognising this, the focus of this study is to explore alternative ideas that still involve constellations, but use satellites from other missions that are not dedicated to gravitational field monitoring (i.e., non-dedicated satellites). The general concept is to utilise any available satellite that is, at a minimum, equipped with a high-precision Global Positioning System (GPS) receiver and an attitude determination system. The forces acting on the satellite can be derived from the GPS positioning information, in essence providing low accuracy acceleration measurements. While the measurements would have a lower level of accuracy, the benefit is that there is a constant, high-volume stream of globally distributed observations collected, especially in the case where tens or hundreds of satellites are involved. In short, the high density of observations may permit the observation of Earth's time-variable gravitational field at much shorter time scales than currently possible, i.e., at daily or sub-weekly intervals. The information from these measurements can then be used as either an independent data set, or

in combination with a dedicated gravimetric mission (e.g., a GRACE follow-on) to help reducing the effects of aliasing and improving the overall accuracy of models generated from such dedicated missions. Such constellations are expected to become a reality in the near future. Foust (2015) reports that OneWeb (`www.oneweb.world`) plans to build 900 micro-satellites for global communications, BlackSky Global (`www.blacksky.com`) plans to launch 60 satellites for Earth imagery, UrtheCast (`www.urthecast.com`) plans to launch 16 optical and Synthetic Aperture Radar (SAR) imagery satellites. In addition, Iridium NEXT (`www.iridium.com`, Gupta, 2008) is soon to launch 66 global communication satellites, the FORMOSAT-3/ COSMIC (F3C) (Kuo et al. 1999, 2005) and FORMOSAT-7/COSMIC-2 (F7C2) (Ector et al. 2010; Cook et al. 2013) constellations will add 12 radio occulation satellites and the Community Initiative for Continuing Earth Radio Occultation (CICERO, `geooptics.com`) project proposes to launch 24 or more satellites for severe weather monitoring. Hsu (2015) also reports that SpaceX (`www.spacex.com`), with support form Google (`www.google.com/about`), plans to provide Internet access to developing regions of the world through a constellation of 4000 satellites.

This study will focus on the determination of the high-frequency gravitational variations, i.e. those which change at time-scales less than one month, using the proposed Iridium NEXT constellation as the primary case study. Announced in late 2007, Iridium NEXT is the next generation of the well-known satellite communication network, with the added benefit that each satellite is expected to carry a secondary scientific payload on-board. While the development of the constellation and associated payloads are still in progress, the current plan is to launch 66 satellites (in six orbit planes, at 780 km altitude, and with an inclination of 86.4°) beginning in 2015 de Selding (2015), with a scheduled mission lifetime of more than 15 years. Many of these satellites (currently estimated at a minimum of 24) will fly geodetic quality GPS receivers, which could be used for gravity field recoverys. As will be seen in this chapterdesc, the case study into the Iridium NEXT constellation nicely demonstrates the feasibility of using non-dedicated satellites in the context of time-variable gravity field recovery.

Additionally, the smaller F3C constellation is considered in the simulation study in order to gain insight into the immediate benefit of exploiting current constellations for the purpose of augmenting dedicated gravimetric missions. The F3C mission is a GPS occultation mission launched in 2006 as part of a joint US-Taiwan collaboration, and consists of six satellites at an orbit inclination of 72° and an altitude of 800 km. The CHallenging Mini-Satellite Payload (CHAMP) satellite is added to the F3C in order to increased the measurement rate, resulting in the F3C/CHAMP constellation.

5.2 Methodology

One of the obvious benefits of using constellations is that the high number of satellites generates a large number of globally distributed measurements. For example, using simulated orbits for the proposed Iridium NEXT (24 satellite case) constellation, it takes GRACE data approximately 21 days to generate the same density of observations as the constellation generates in about 21 hours (Figure 5.1). While the observations would be much less accurate than those from dedicated gravimetric missions such as GRACE, errors due to temporal aliasing would be significantly reduced. The degree of spatial aliasing would be greatly reduced as well, up to the maximum degree described in the data. The data of non-dedicated missions describes mainly the long wavelength features of Earth's gravitational field. Nonetheless, there is a minimum coverage needed to allow the complete frequency content of the data to be recovered. The constellations' nearly homogeneous global ground-track coverage minimizes the time needed to reach this coverage.

To examine whether this higher density of observations is sufficient to overcome the lower accuracy of the GPS-derived accelerations, a series of simulations are developed in which the GRACE Atmosphere and Ocean De-aliasing Level 1B (AOD1B) product (Flechtner et al. 2006; Flechtner 2007, 2011) is used as a realistic time-variable gravitational input signal. It should be noted that the AOD1B product does not account for all short-term mass transport processes, such as tides and continental hydrology; however, the AOD1B product does represent the primary signals of interest at the daily to weekly time-frames. Neglecting the influence of ocean tidal aliasing is justified, since these variations are fairly well understood (Ray and Luthcke, 2006), although ocean tide models keep improving (Stammer et al., 2014). Therefore, it is assumed that those models are of sufficiently high quality by the time the proposed gravimetric mission is launched, in view of i) the current and planned large number of altimetric satellite missions, ii) the errors in those models are mainly restricted to the polar regions (resulting from little or poor altimetry data) and areas covered with shallow seas (caused by frictional effects, enhanced tidal motion and the presence of coastlines) (Schrama and Visser, 2006; Ray et al., 2009; Visser et al., 2010; Müller et al., 2014). Furthermore, Thompson et al. (2004), Visser (2010) and Reubelt et al. (2014) have demonstrated through numerical simulations that the effects on the gravity field parameters of temporal aliasing originating from the non-tidal atmosphere and ocean variations are comparable to those originating from ocean tides. If high-frequency atmospheric temporal variations can be measured, it is reasonable to assume the same can be said for ocean tides. The influence of continental hydrology is uncertain, as this occurs across a range of spatial and temporal scales; however, for the purposes of the
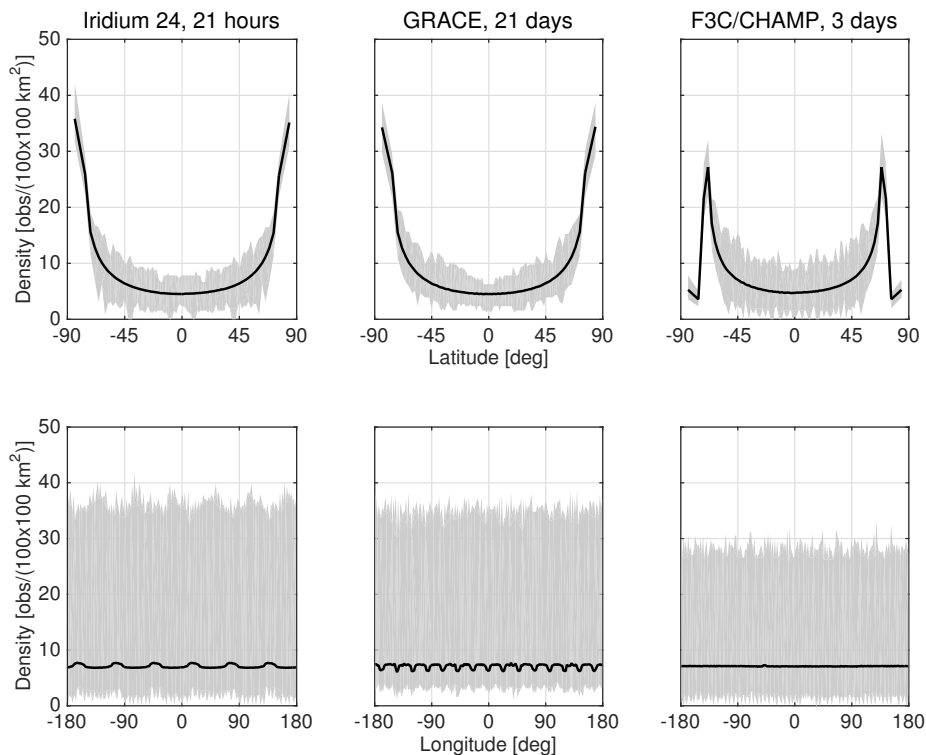
Figure 5.1 – Mean (solid line) and maximum/minimum (grey) ground track densities by latitude (top row) and longitude (bottom row) for the 24–satellite Iridium Next constellation (21 hours, left-hand column), the GRACE mission (21 days, centre column), and the F3C/CHAMP constellation (3 days, right-hand column).

simulations presented here, precise knowledge of hydrology is not required. This is because the amplitude of the temporal aliasing associated with the AOD1B product is of comparable amplitude as the temporal aliasing associated with hydrology, cf. Section 6.2.2 as well as Figures 6.18 and 6.19).

The amplitude of the AOD1B signal, in terms of the Amplitude Spectral Density (ASD) of geoid height variations, across a range of spatial and temporal scales is shown in Figure 5.2. Shown is the degree amplitude of the per-coefficient ASD of the 6 hourly AOD1B product. This is made possible by the assumptions that the temporal variation of each Stokes coefficient are stationary. The data considered Figure 5.2 covers the months of August and September in 2002. The figure highlights the fact that the AOD1B signals have the largest amplitudes at the lower degrees (i.e., less than degree 20, which translates into spatial wavelengths larger than 1000 km), but that these amplitudes can span across all time scales within a month (i.e., from sub-daily to 31 days). The signal shown in Figure 5.2 is in fact the signal that GRACE cannot observe, and which must be removed in the data pre-processing. The AOD1B product is naturally subject to inaccuracies, as they are produced from climate data of varying quality and global distribution. Recent studies (Zenner et al., 2010, 2012) have shown that, for a mission such as a GRACE follow-on, or even the current GRACE mission operating at the originally projected baseline performance level, uncertainties in the AOD models could be one of the dominant error sources. If such signals can be observed by the constellations examined in this study, this would translate into improved gravity field models.

Accelerations are derived for each satellite in the Iridium NEXT or F3C/CHAMP constellations from absolute position data, representative of what might be expected from a GPS receiver, using a realistic coloured noise spectrum (refer to Figure 4.3) derived from the earlier studies of CHAMP mission data (Ditmar et al., 2007). A GRACE-like formation is also simulated, with accuracies similar to those of the actual mission, considering the simplistic noise model described in Section 4.3.3. A series of gravity field models are then computed over time spans ranging from 1 to 31 days, for both the individual (i.e., Iridium 24-satellite or GRACE) and combined (i.e., Iridium 24-satellite and GRACE) scenarios. These models are then compared to the actual time-varying AOD1B signal (i.e., the truth input signal), averaged over the corresponding time interval. By using only the AOD1B product in the force model, the results highlight what contributions such a constellation might make towards resolving those short-term signals, which are not recoverable from GRACE data alone.
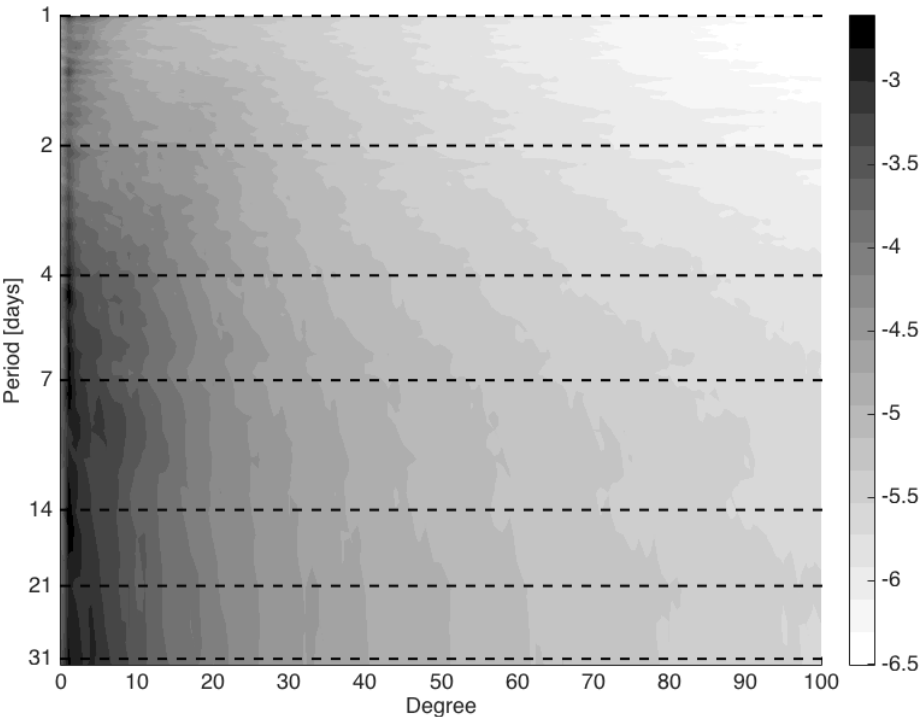
Figure 5.2 – ASD of the AOD1B model, across varying time-frames (1 to 31 days), in decimal orders of magnitude of geoid height ($\log^{10}(m/\sqrt{Hz})$).

5.2.1 Simulation Setup

To evaluate the influence of spatial and temporal aliasing errors for a given constellation scenario, the development of a robust simulation environment is required.

The errors associated with inaccuracies in the instruments are introduced by corrupting the simulated observations with noise (i.e., measurement noise). Temporal aliasing is evaluated by examining the noise-free residual between a time-varying gravitational field (the "true" force model) and a static one (the reference), refer to Section 4.3.1. The maximum degree of the force models in the simulations is set to 100, which is the maximum degree of the AOD1B product. At the data inversion step, spherical harmonic coefficients are estimated only up to degree 45 due to restrictions caused by the polar gap of the Iridium constellation (45 is the maximum degree allowable with a 4 degree polar gap) and degree 20 for the F3C/CHAMP constellation. An additional error component is present in the simulations in the form of spatial aliasing, already presented in Section 4.3.1.

An inversion of observations created using either measurement noise, spatial aliasing or temporal aliasing results in a gravity field model which differs from the time average of the true dynamic model, thereby providing an indication of the magnitude of each error type. The assumption made in this study is that the measurement error, spatial and temporal aliasing are independent, and can therefore be computed separately and later combined. The validity of this assumption was confirmed numerically (not shown). Note that since the AOD1B product is produced in 6 hour time intervals, a linear piecewise interpolation scheme is used to compute the time-varying gravitational signal during these intervals. The choice of the static field used is essentially arbitrary, but for this study the GFZ/GRGS EIGEN, version 3 (EIGEN-CG03C) (Förste et al. 2005) is used.

In the simulation of the observations related to the constellations, use is made of the functional model described in Section 4.1.1. Measurement noise is simulated as realistic coloured noise, as described in Section 4.3.2. In other words, it is assumed that the orbit position accuracies are essentially of the same level as in case of CHAMP, or approximately $2-3$ cm. In a study conducted by Iridium to determine the requirements for the altimetry payload expected for the Iridium NEXT constellation (Richard et al., 2008), the non time-critical orbit products (i.e., latencies >1 month) are listed as having expected accuracies of <2 cm, which fits well with the measurement noise levels assumed in this study.

To generate simulated GRACE-like observations, the functional model presented in Section 4.1.2 is considered. The inclusion of measurement noise is done according to the simplistic noise model described in Section 4.3.3. The assumed noise magnitudes are absolute position noise $\delta^{(\mathrm{aP})}$ equal to 1 cm, relative position

noise $\delta^{(\mathrm{rP})}$ is 1 mm and ranging noise $\delta^{(\mathrm{R})}$ is 10 μm, which constitute a reasonable approximation.

Measurement Noise Scenarios

To better understand the influence of the measurement noise onto the resulting gravity field parameters, two different cases are examined. The first case, called the *high-noise* case, represents what is believed to be the accuracy of current space-borne GPS receivers and the GRACE KBR system. For GRACE, this translates into absolute position errors with standard deviations on the order of 1 cm, relative positioning errors of about 1 mm, and ranging sensor noise of 10 μm. For the constellations, errors in the accelerations are implemented using the ASD shown in Figure 4.3.

While the high-noise case represents the current state-of-the-art, there are many advances expected in the future within the Global Navigation Satellite System (GNSS) and geodesy communities that will likely improve upon the current accuracies, as discussed in Section 6.1.7. As such, a second case called *low-noise* is considered, in which it is assumed that there will be an order of magnitude improvement in the accuracy of GPS-derived accelerations and ranging data in the near future (i.e., the high-noise errors are simply reduced by a factor of 10). While it is recognised that this degree of improvement is likely optimistic, the goal of this low-noise case is to establish a reasonable upper-bound of the performance that might be achieved through future technological advancements. As expected, the influence of the measurement noise on the final solution depends on the type and number of observations collected.

Figure 5.3 shows the high and low measurement noise propagated to the gravity field parameters for the three mission scenarios simulated in this study (Iridium, GRACE, and F3C/CHAMP), over two different time spans (1 day and 31 days). The figure also illustrates the level of the measurement noise with respect to other sources of error present in the simulations, namely spatial and temporal aliasing error. Note that the measurement noise for the constellations stays approximately the same for both time-frames, meaning that the constellations achieve essentially the same level of accuracy at 1 day that they do at 31 days (apart from the $\sqrt{31}$ times lower noise amplitude in the latter case resulting from the larger number of observations). In contrast, the GRACE-type formation is more sensitive to measurement noise at the 1 day interval, with errors a factor 10 larger than in case of the constellations. Notice that as more observations are collected, this error becomes significantly lower than in case of the constellations, cf. bottom row of Figure 5.3.

In what concerns the error due to spatial aliasing, it is essentially negligible when compared with the other error sources (temporal aliasing and measurement noise) for the constellations. However, for GRACE, the spatial aliasing is much more significant and can exceed the measurement noise in some instances. Note that for the experiments involving temporal aliasing described below, the solutions are also estimated up to degree 20 or 45, but the observations are generated using a time-varying (non-static) gravity field model. For these cases, the calculation of the temporal aliasing error by nature includes a component due to spatial aliasing error.
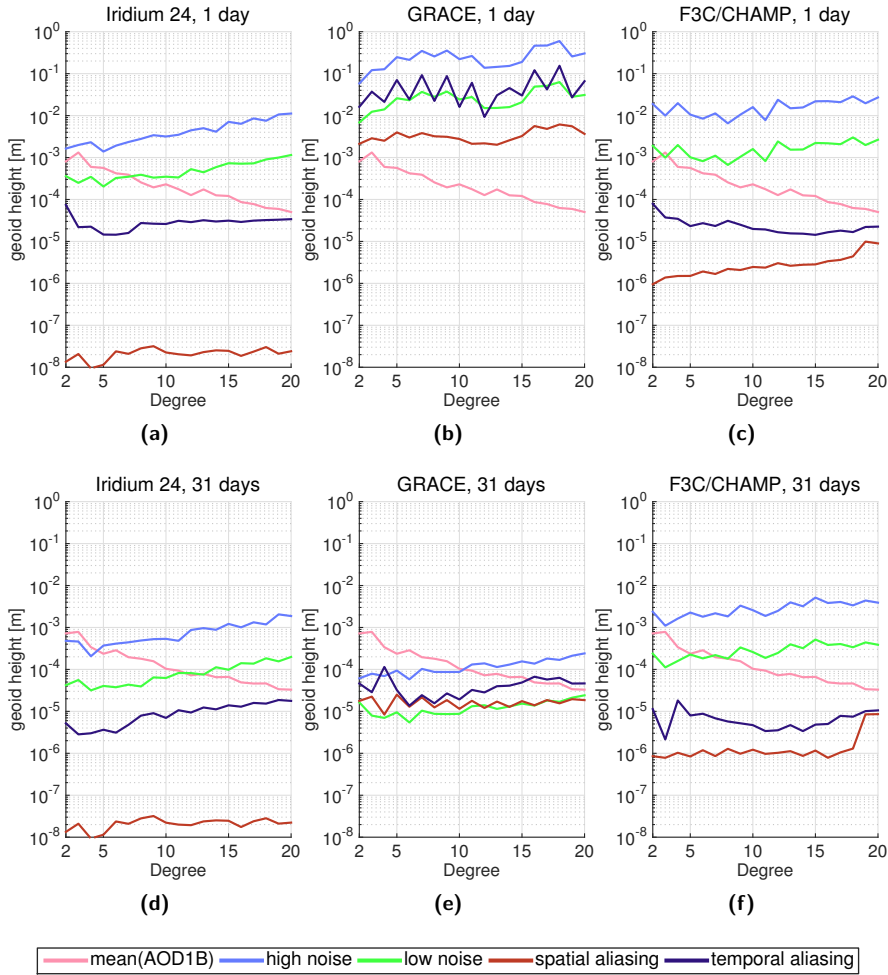
Figure 5.3 – Degree variance plots of the various noise types propagated to the gravity field parameters. The considered scenarios are: Iridium 24–satellite (a,d), GRACE (b,e), and F3C/CHAMP (c,f) over the 1 day (a-c) and 31 day (d-f) time intervals.

5.3   Simulation Results

Focusing first on the performance of the constellation alone, Figure 5.4 shows the error degree variances of the estimated gravity field parameters for the high and low noise cases for a hypothetical Iridium 24 and 66 satellite constellation over a 31 day time span. As already illustrated in Figure 5.3, the error from temporal and spatial aliasing is quite small in both cases, so the error levels shown are almost entirely influenced by the performance of the GPS receivers. For comparison, the 31 day average of the AOD1B product is also shown. The figure demonstrates that at least for the 31 day case, the 24 and 66 satellite constellation is able to observe some of the AOD1B signal spectrum (up to degree 15 for the low-noise, 66-satellite case). Naturally, more signal is observed as more satellites are added, and as the accuracy of the GPS measurements improve. Many other time-frames are evaluated in addition to the 31 day case. The left panel of Figure 5.5 shows a more complete picture of the constellations' performance for the Iridium 24-satellite, low-noise case. The plot shows the solutions expressed in terms of signal-to-noise ratio, created by comparing the computed solution in terms of geoid height for each time-frame with the time averaged AOD1B product (i.e., the "truth"). The plot demonstrates the spatio-temporal accuracy, with the vertical (log-scale) axis representing the duration of the solution (i.e., 1 day, 2 day, etc.), and the horizontal axis the spatial resolution in units of spherical harmonic degree. A ratio of 1.0 (delineated by a white line in the plot) or higher implies that the gravitational signal can be observed at the given time and spatial resolution, and corresponds to the point at which the AOD1B and Iridium curves cross in Figure 5.4. In Figure 5.5b, the spatio-temporal accuracy of the GRACE data is depicted, clearly illustrating its limited temporal sampling for periods below 7 to 2 days.

The next step is to compare the performance of the combined mission scenarios, i.e., using both GRACE and the constellation. The results are shown in Figure 5.5c, and represent the combination of the Iridium 24 satellite low-noise case with the GRACE high-noise case (with both spatial and temporal aliasing error also included). Two important conclusions can be made from this figure. First, the Iridium constellation observes the AOD1B time-variable signal up to degree 7 for all time scales, where as a GRACE-like mission is limited to signals with time scales of approximately 4 days and longer. Secondly, the combined solution can observe a larger part of the AOD1B spectrum than a solution based on the data from only one mission. This indicates that of the constellation data are able to reduce the amount of aliasing present in the GRACE-only solution.

The results of Figure 5.5 demonstrate a fairly realistic scenario. The GRACE measurements represent those of the current GRACE mission. The low noise Iridium
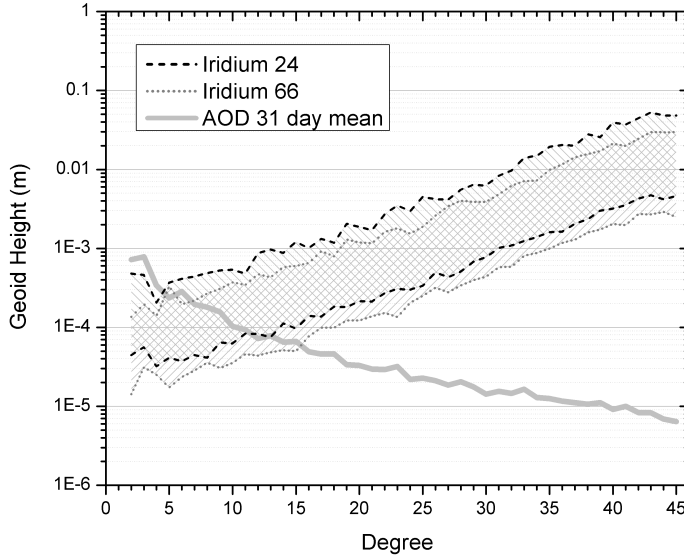
Figure 5.4 – Degree variances of the GPS high and low error, represented in shadowed bands, for the 31 day Iridium 24 and 66 satellite constellation simulations using assumptions of high and low measurement noise.
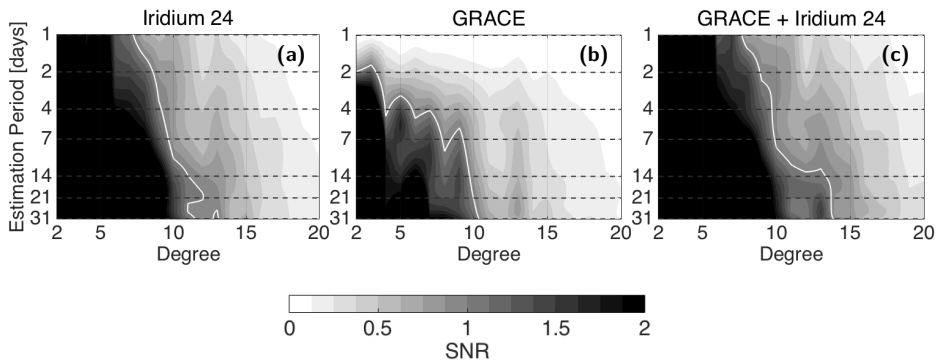
Figure 5.5 – Signal-to-noise ratios for a) the Iridium 24 satellite low-noise cases, b) the GRACE high-noise cases, and c) the resulting combined solutions for a range of spatial (spherical harmonic degree) and temporal values.

24 constellation is also an intermediate option on the side of the constellation, because there are options that are better, such as the low noise Iridium 66 solution. In fact, the low noise Iridium 24 constellation, when considering Figure 5.4 again, could also represent a 48 satellite constellation (twice as many observations) with, (e.g.) only a factor 7 improvement in errors, (i.e the original factor 10 divided by $\sqrt{2}$), relative to the current GNSS accuracy; or it could represent any other permutation of number of satellites (assuming this number exceeds 24) and a level of improvement, e.g., 66 satellites with a factor 6 improvement in GPS error.

This is done to maintain consistency of the orbit products used for the constellation, even though dynamic orbit estimation techniques have been shown to achieve more precise orbits for CHAMP.

The simulated results of the F3C/CHAMP constellation are shown in Figure 5.6, where a series of high-noise (Figure 5.6a-c) and low-noise (Figure 5.6d-f) solutions are created over time spans that varied from one day to one month. For each noise case, a corresponding set of GRACE-like measurements is created, and a combined F3C/CHAMP/GRACE solution generated. It is important to note again that the only gravitational signal used in the simulations is that introduced by the AOD1B product for August 2006.

The first observation that can be made from Figure 5.6 is that in the high-noise case (top row), F3C/CHAMP is not able to clearly observe any of the AOD1B signal, as the signal-to-noise ratio is much less than one at all degrees and time-frames. The high-noise, GRACE-only case is sensitive to some signal up to approximately degree 7-8, but only at periods greater than four days. The combined F3C/CHAMP/ GRACE solution for the high-noise case shows little difference from the GRACE-only case, again confirming that at current positioning accuracies, the F3C/CHAMP constellation is not able to sense the time-variable AOD1B signal.

The low-noise case is much different (bottom row), however, and shows that the F3C/CHAMP constellation is able to observe some of the AOD1B signal. The GRACE-only solution also benefits from the low noise level, as seen in the lower-middle plot. Most importantly, the F3C/CHAMP/GRACE combination shows a noticeable improvement over the GRACE-only case, indicating that the F3C/CHAMP constellation data has a stabilising effect on the solution and allows the higher degrees to be estimated with greater certainty. The results indicate that a combined low-noise solution should be able to resolve time-variable features up to degree 15 at temporal scales of two days and longer, and daily/sub-daily variations at spatial scales up to degree 7-8.
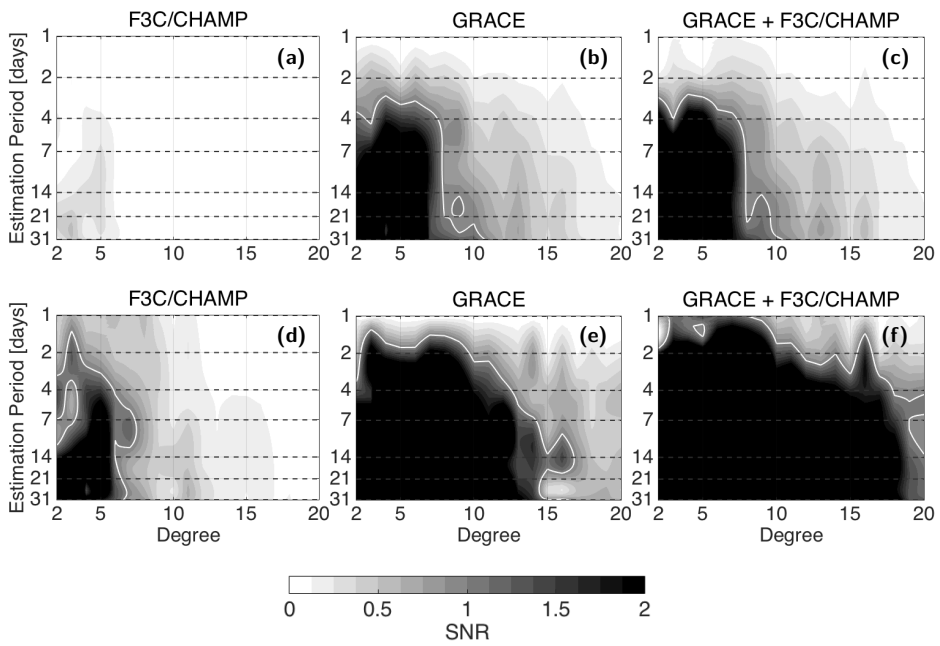
Figure 5.6 – Signal-to-noise ratios for the simulated F3C/CHAMP (a,d), GRACE (b,e) and combined (c,f) solutions, using both high-noise (a-c) and low-noise (d-f) scenarios.

5.4   Conclusions

Several important conclusions can be drawn from this study. The first one addresses the question of whether a constellation of non-dedicated satellites (i.e., satellites not specifically designed for collecting gravimetric data) can improve the knowledge of Earth's time-variable gravitational field. The simulations performed using the proposed Iridium NEXT constellation demonstrated that such non-dedicated satellite constellations should be able to observe the large scale ($> 1000\,\mathrm{km}$), short-term (i.e., < 1 month) gravitational signals accurately. Such a constellation would observe a part of the spectrum of the gravitational field to which GRACE and the likely GRACE Follow On (GFO) (Sheard et al. 2012; Larkin 2012; Zaragoza 2013) is inherently insensitive. Furthermore, the incorporation of the constellation data would improve the overall quality of the time-variable gravity field models as compared to a GRACE-only solution, by reducing temporal aliasing. This option is especially attractive considering that the constellation approach could potentially rely entirely on existing (or future planned) satellites, making such improvements available for a relatively small amount of extra cost, and would not impose any restrictions to the development of a potential GRACE follow-on mission. Furthermore, these constellations may be the only source of continuous global time-variable gravimetric data if there is a gap between the GRACE and GRACE follow-on missions, in addition to Satellite Laser Ranging (SLR) data.

Should the Iridium NEXT project fail to materialise, other suitable constellations are currently under development, cf. Section 5.1 Independent of these, a similar constellation could conceivably be developed through the use of low-cost mini- or micro-satellites equipped with a GPS receiver and an attitude determination system. All that is required is a series of small cannonball style satellites that could periodically be launched in support of a much more complex and expensive dedicated GRACE follow-on mission. These small satellites would ideally be inexpensive to build and launch (no dedicated launchers required) and would likely have short lifetimes, enabling replacements with improved technology.

The simulations that support these conclusions included error sources representative of the current GRACE mission. The analysis also made clear that the extent to which the constellations can help depends largely on the quality of the computed orbits. High orbit quality will require, in addition to accurate GPS receivers, also precise satellite attitude data, the reduction of GPS errors caused by multi-path, as well as accurate determination of time-varying shifts in the satellite's centre of mass (e.g., due to rotating solar panels). In spite of this, the predicted accuracy of the Iridium NEXT orbits is of the order of a few centimetres (Richard et al., 2008). As such, the results of the simulations presented here are encouraging, and highlight the

notion that a GRACE follow-on mission could potentially benefit from a supporting constellation of non-dedicated satellites.

Lessons learned from GRACE 6

Analysing future gravimetric missions that exploit low-low Satellite-to-Satellite Tracking (ll-SST) measurements unavoidably requires accurate predictions of errors in the data. Fortunately, the Gravity Recovery And Climate Experiment (GRACE) (Tapley et al. 1996; Tapley 2004b) mission has provided high-quality data for over a decade. Consequently, it is the primary source of information regarding the accuracy of ll-SST measurements. Any attempt to predict the accuracy of a future gravimetric mission demands a close analysis of the GRACE data, in order to learn as much as possible and build accurate error models.

The current chapter groups all the analyses that exploit actual GRACE data for the purpose of estimating the accuracy of the ll-SST measurement principle. The chapter is divided into three sections. In Section 6.1, the K-Band Ranging (KBR) is exploited to estimate errors in the orbits of GRACE in the Line of Sight (LoS) direction. In Section 6.2, the estimated errors in the GRACE data are used to obtain a better understanding of the error sources that are dominant. In Section 6.3, the ll-SST noise models are considered in the simulation of noise in data from a GRACE-like formation and the simulation results are compared with the GRACE a posteriori residuals, for the purpose of validation.

The actual GRACE data used in this chapter were kindly provided by Dr. Hassan Hashemi Farahani.

6.1 Relative orbit accuracy of GRACE

The Amplitude Spectral Density (ASD) of noise in the relative positions and velocities of GRACE is computed and analysed in this section. With this information, it is

possible to better quantify the errors present in the GRACE observations and consequently predict more precisely the accuracy of future gravimetric satellite missions. The noise types that depend on the orbit accuracy, apart from positioning noise, are the correction noise, which depends explicitly on the accuracy of the relative radial velocity and the orientation noise which is function of the relative orbit position noise (refer to Section 4.3.3, particularly Eq. (4.55) and Eq. (4.58), respectively). The positioning noise, although it represents the uncertainty in the orbit positions themselves, refer to Eq. (4.59), does not depend on the ASDs derived in this section. Those errors, as demonstrated in Chapter 7, are the result of a combination of both absolute and relative orbit position noise. Simulating positioning noise only on the basis of relative orbit position errors would omit the important contribution of the absolute orbit position errors. The analysis results are exploited in Section 6.3 when the noise models are validated and in Chapter 8 to quantify the error budget of a number of formations.

It is noted that the frequency description of the orbital errors is restricted to relative quantities, i.e. of one satellite with respect to the other. It is possible to compute the relative accuracy of GRACE orbits because there are accurate independent measurements to serve as the reference: the KBR observations. The same cannot be said about the absolute accuracy of any satellite orbit, since relevant independent measurement techniques, such as Satellite Laser Ranging (SLR) or Doppler Orbit Determination and Radio-positioning Integrated on Satellite (DORIS), lack the required accuracy. Furthermore, the data provided by those techniques are only available above discrete locations on the surface of the globe, where SLR stations or DORIS beacons are located. These sparse measurements are insufficient to properly estimate the dependence of noise on frequency. Comparing orbits estimated from Global Positioning System (GPS) measurements at different research centres is also inadequate, since the same data are used to produce the orbits. Any such analysis would only illustrate differences in the processing strategies. Nevertheless, Chapter 7 illustrates that reasonable estimates of absolute orbit accuracy can be derived from orbits integrated on the basis of difference background force models.

As a rule, the relative accuracy of GRACE's orbits is provided by various authors as a single Root Mean Squared (RMS) value, cf. Table 2.6, p. 38. Although this representation gives a general idea of the orbit determination accuracy, it provides no information concerning the dependency of error amplitude on frequency. The frequency description of the error is important because the estimated gravity field parameters have a different sensitivity to errors at different frequencies, therefore motivating the study described in this section. As notable exception, Jäggi et al. (2009) illustrates the Allan variances (variances of differences over a range of periods) of the error in kinematic baselines.

6.1.1   Considered orbits

The purpose of the analysis is not to determine the best possible orbit determination accuracy. Although that is certainly the best measure to predict the accuracy of the orbits to be used in future gravimetric missions, it would be an insurmountable effort, requiring the analysis of orbits derived on the basis of a representative number of processing strategies and/or from different sources. In face of the difficulty of that task and considering the unavoidable time constraints, the analysis is restricted to orbits relevant to the actual data processing in producing the Delft Mass Transport (DMT) model. These orbits are assumed to be representative of the state-of-the-art orbit accuracy, as demonstrated by Zhao et al. (2010a). The orbits are kindly provided by Dr. Qile Zhao, Wuhan University, China.

Two distinct sets of orbits are considered: the Kinematic Orbit (KO) and the Purely Dynamic Orbit (PDO), both already discussed in Section 2.4.1. The KOs are similar to those presented by Zhao et al. (2010a) and are solely function of GPS tracking data. The PDOs, described in Liu (2008, pp. 105 − 107), are computed in the form of 6-hour arcs on the basis of the reference force model considered for the computation of the DMT model, described in Section 4.2.4. In the course of the computation of the PDOs, the initial state vectors, as well as accelerometer calibration parameters, are estimated per arc, in order to ensure the best fit to the kinematic positions. The computations are carried out with the Position And Navigation Data Analyst (PANDA) software (Zhao 2004) software. The same algorithm and software are used for the computation of GRACE orbits in the production of the DMT model.

It should be noted that the background force model used in the orbit integration lacks the temporal gravitational field variations captured by the DMT model. Nevertheless, these variations are not significant to the current analysis because they are at the level of $30\,\mu\mathrm{m}$ if derived from double-integration of the time series related to the green line in Figure 6.14. Note that this level of range variability corresponds to the temporal aliasing caused by the mass transport processes described by the DMT model, not by the corresponding total signal. In spite of this, the total signal is unlikely to be two orders of magnitude larger than the corresponding temporal aliasing; this would be needed to bring the level of $30\,\mu$m up to mm level and modify significantly the current analysis. On the other hand, the range variations associated with the (total) Atmosphere and Ocean De-aliasing Level 1B (AOD1B) signal, if estimated by the same process, are at the level of $2\,\mathrm{mm}$ and, therefore, cannot be ignored (and are not, cf. Section 4.2.4).

The PDO is relevant because it is the most accurate type of orbit, refer to Section 2.4.2, in the sense that it allows for highest accuracy when computing the angle between the LoS vectors at successive epochs and limits the error in the radial

velocity between the satellites, resulting in a lower correction noise. The motivation to analyse the KO is of less practical application than what is the case with the PDO. It is nevertheless an interesting academic exercise, particularly in the context of replacing PDOs with KOs in the actual processing of ll-SST data. Additionally, the accuracy of the PDO is connected to the accuracy of the KO, since the latter is used to derive initial state vectors for the integration of the former.

The various data sets are provided with different sampling intervals. The KOs have 30 second sampling interval, the PDOs and KBR observations are defined every 5 seconds. As a consequence, the KBR data are down-sampled to synchronise their time stamps with those of the KOs but unchanged when compared to the PDO. The data after synchronisation are called the *input data* in Figure 6.1. The KOs are provided as position information only. The velocity data are computed by numerical differentiation of the position data, using an 11-point central differentiation scheme (e.g. Abramowitz and Stegun, 1964, Section 25.1.2). It should be noted that the KBR data are not used in any way to produce the considered KO or PDO. The KBR data considered in this analysis are the same as in the production of the DMT model, release 1. The unknown bias in the range data (refer to Section 2.2.2) was estimated in the Least Square sense, as explained in Liu (2008, pp. 102 and 103). The processing is done on a monthly basis, considering the complete year of 2006. An exception is 8 days at the end of December, which are also discarded in the computation of the DMT model.

6.1.2 Analysis set-up

The relative orbit accuracy is determined by comparing epoch by epoch the length of the inter-satellite vector derived from the estimated GRACE satellite orbits with the KBR observations. The analysis of orbit-derived relative velocities is also done, for which purpose KBR range-rate data are used.

The precision of KBR measurements, estimated to be of a few μm (Kim, 2000; Kim and Tapley, 2002; Frommknecht et al., 2006; Frommknecht, 2007; Kim and Lee, 2009), is much higher than that of inter-satellite relative positioning, which is at millimetre-level, refer to Section 2.4.3. With the exception of the high frequencies, the amplitude of KBR errors in the frequency domain is lower than that of the relative positioning. The same assumption is also made for the KBR-rate and relative velocity accuracy. This validity of these assumptions is verified at a later stage. Under this condition, the computed discrepancy between the orbit-derived ranges and the KBR measurements mainly reflects the error in the relative orbits.

Computation of the forecasted range

Consider the orbit positions of the GRACE satellites, represented by $\mathbf{x}^{(1)}$ and $\mathbf{x}^{(2)}$ and their orbit velocities, $\dot{\mathbf{x}}^{(1)}$ and $\dot{\mathbf{x}}^{(2)}$. The relative position vector is

$$\mathbf{x}^{(12)} = \mathbf{x}^{(1)} - \mathbf{x}^{(2)}, \tag{6.1}$$

and the relative velocity vector is

$$\dot{\mathbf{x}}^{(12)} = \dot{\mathbf{x}}^{(1)} - \dot{\mathbf{x}}^{(2)}. \tag{6.2}$$

The range ρ is compared to the inter-satellite distance $\|\mathbf{x}^{(12)}\|$, whereas the range-rate $\dot{\rho}$ is compared to the projection of the relative velocity vector $\dot{\mathbf{x}}^{(12)}$, onto the unit vector defining the LoS direction $\mathbf{e}^{(\mathrm{LoS})}$. This results in the following representation of relative orbit position noise $\delta^{(\Delta\mathbf{x})}$ and relative orbit velocity noise $\delta^{(\Delta\dot{\mathbf{x}})}$, respectively:

$$\delta^{(\Delta\mathbf{x})} = \rho - \|\mathbf{x}^{(12)}\|, \tag{6.3}$$

$$\delta^{(\Delta\dot{\mathbf{x}})} = \dot{\rho} - \left(\dot{\mathbf{x}}^{(12)}\right)^{\mathrm{T}} . \mathbf{e}^{(\mathrm{LoS})}. \tag{6.4}$$

The quantities $\delta^{(\Delta\mathbf{x})}$ and $\delta^{(\Delta\dot{\mathbf{x}})}$ are henceforth referred together as *residuals*, or specifically *position residuals* and *velocity residuals*, respectively. The residuals are a quantification of the relative orbit errors.

6.1.3   Data screening

The original data need to be processed in order to remove the epochs associated with erroneous observations. There are a number of reasons for selectively discarding data, all of which are addressed in this section.

The KBR observations are provided with information about the Signal-to-Noise Ratio (SNR) at each epoch (Case et al., 2010). The observations flagged with low SNR are discarded. Additionally, there are occasional gaps in the KBR data associated with so-called *phase break* events, cf. Case et al. (2010, p. 14).

The orbits also contain invalid data. The KOs contain frequent data gaps associated with those epochs when the number of GPS observations is not sufficient to derive an accurate kinematic position. The PDOs are defined in arcs of 6 hours duration, with discontinuities at the beginning and end of each arc. The epochs at the beginning and at the end of each arc are discarded.

There is also a need to address the residuals which are too large in comparison to the RMS, identified as *outliers* in Figure 6.1. A simple iterative $n-\sigma$ rule is used to

identify them: the STandard Deviation (STD) of the data set is computed and the epochs with residuals larger than n times the computed STD are discarded. This step is repeated, with a new value for the data set STD being computed at each iteration, until the difference between STD values in successive iterations is less than a factor of 10^{-5} of the STD of the current iteration. The outliers-removal procedure is applied independently to each monthly set of range and range-rate data.

The analysis was repeated for three values of n: 3, 4 and 5, consistently applied to all orbit types and months under consideration. When n is equal to 5, it was observed that a large number of outliers were left in the month of May for the KO (not shown). The RMS in that month is a factor of two larger than in the remaining months. The difference between the analyses conducted with n equal to 3 and 4 is not significant. Therefore, the results shown in this section are related to $n = 4$.

The preliminary analysis of the PDO data detected some months with unrealistically large RMS. Looking at the time series of the position residuals, those months show extremely large values in several 6 hr arcs (not shown), occasionally reaching several meters in magnitude. The large residuals in these arcs are attributed to imperfectly-estimated initial state vector that are used in the orbit integration within each 6 hrs arc. In view of this, it was decided to regard the months of March to June and October to December of the PDOs residuals as outliers for the remainder of the analysis. Alternatively, these inaccurate arcs could be manually signalled as outliers and explicitly removed from the analysis. This course of action was not taken because a) it would be a very impractical and time consuming activity to perform, b) it is not done in the routine computation of the DMT solutions and nor in other models, as far as reported in literature, c) there is enough remaining data to warrant that the results are statistically representative.

Table 6.1 gives a summary of the amount of data considered after all data removal steps and Figure 6.1 presents a summary of the data quality for each month.

The total number of epochs is the sum of the values in the Table 6.1a and Table 6.1b , i.e. 1028160 and 6168960 for KO and PDO, respectively. Considering a sampling period of 30 and 5 seconds, the total number of epochs related to a total of 357 days. This value corresponds to the number of days in one year minus the 8 days at the end of December, which were removed from the data set at the stage of computing the DMT model.

6.1.4 Monthly RMS residuals

The RMS residuals computed on a monthly basis are shown in this section. This statistics gives an overview of the general accuracy of the analysed KOs and PDOs and show how it changes over the considered months, refer to Figure 6.2.
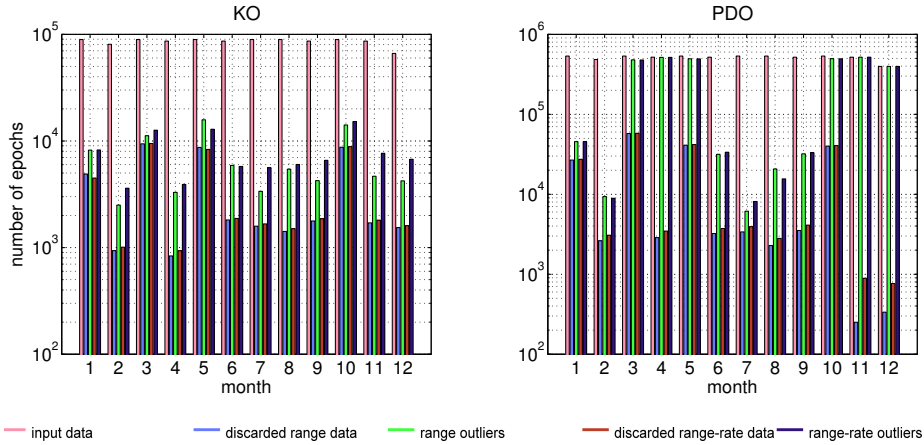
Figure 6.1 – Summary of data quality for the 12 months of 2006. *Input data* are the common data between the orbits and KBR, *discarded data* relates to data removed due to low SNR of KBR data or orbit data gaps, *outliers* are data removed based on large residuals.

	KO	PDO
position	901897	2940553
velocity	889950	2937814

(a) number of valid data

	KO	PDO
position	126263 (12.28%)	3228407 (52.33%)
velocity	138210 (13.44%)	3231146 (52.38%)

(b) number of discarded data

Table 6.1 – Number of valid epochs (top) and sum of discarded data and outliers (bottom) of all data sets. The data periods are: KO, the year of 2006; PDO, the months of January, February, and June to September of 2006.

A number of immediate observations can be made. The velocity RMS residual of the KO is at least one order of magnitude larger than the one of PDOs. This is an expected outcome because the position data are much smoother in the latter orbit type. Also expected, is that the accuracy of the PDOs in terms of positions is higher than that of the KOs, in view of additional information provided by the
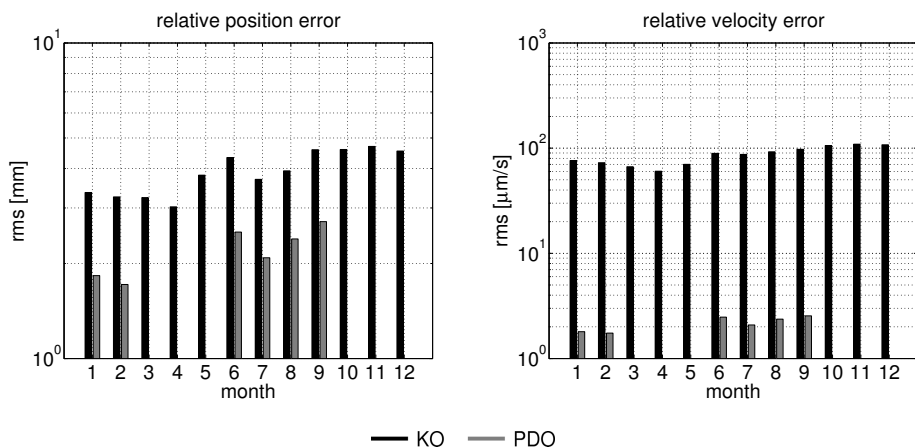
Figure 6.2 – Monthly RMS of the position (left) and velocity (right) residuals over 2006. The data periods are: KO, the year of 2006; PDO, the months of January, February, and June to September of 2006.

dynamic model exploited to estimate the PDOs.

6.1.5 Total RMS residuals

The RMS difference between positions or velocities derived from the orbits and KBR data contain integrated information about the accuracy of the different types of orbits. This information is presented in Table 6.2.

It is opportune to compare the relative positioning accuracy results shown in Table 6.2 with the data shown in Table 2.6.

The Double-differenced (DD) Reduced Dynamic Orbit (RDO) of Jäggi et al. (2007) (3.1 mm, 38 % larger relative to the estimated error in the PDO, 2.24 mm) is in fair agreement with the analysed PDO. Nevertheless, RDOs are typically more accurate than PDOs if a background model of similar complexity is considered in both cases. Jäggi et al. (2007) considered only a static-only background force model, EIGEN-CG03C, while empirical accelerations estimated every 6 min absorb to some extent the remaining mis-modelling. In comparison, the PDOs under analysis in this section are integrated on the basis of a more complete background force model in addition to exploiting accelerometer data of GRACE; these factors lead to a higher relative orbit accuracy in spite of lacking the co-estimation of empirical accelerations.

The RDO of Zhao et al. (2010a) (RMS error of 2.2 mm) is computed considering a very comprehensive force model, which considered the GFZ/GRGS EIGEN, version 3 (EIGEN-CG03C) static gravitational field, astronomical tides, relativistic effects, ocean tides, atmospheric drag and lift forces, solar radiation pressure and empirical accelerations and drag coefficients estimated for every orbital period. The accuracy of the RDO estimated by Zhao et al. (2010a) is close to that of the analysed PDO, indicating that exploiting an exhaustive force model leads to good results.

The KO of Zhao et al. (2010a) (RMS error of 4.6 mm) is less accurate than the analysed KO by +18 %. The difference is attributed to different GPS data used in the processing of the orbits: 100 days from 2003 in Zhao et al. (2010a) vs. the year of 2006 used in the production of the KOs under analysis.

	KO	PDO
position [mm]	3.94	2.24
velocity [μm/s]	87.18	2.19

Table 6.2 – Position and velocity RMS residual, derived from a comparison with KBR data, for the following periods: KO, the year of 2006; PDO, the months of January, February, and June to September of 2006.

6.1.6 Spectra

The frequency representation of the difference between the relative orbit and KBR data is computed using the Lomb-Scargle periodogram method (Scargle, 1982), which is suitable for the analysis of time series with gaps. The ASD of the residuals for all data considered is shown in Figure 6.3. The interpretation of this figure is given in the following paragraphs.

In the bandwidth from 0.01 to 0.23 mHz, the relative positions from the KO are more accurate than those from the PDO. This bandwidth is associated with the periods from 1.2 Cycles Per Revolution (CPRs) to 1.2 days. Contained in this bandwidth is the frequency of 0.046 mHz, which is marked in the ASD of the PDOs by a distinct local maximum. The period associated with this frequency is 6 hrs, which is the length of one interrupted integration arc. It is suggested that the imperfectly-estimated initial state vectors are responsible for the decreased accuracy of the PDOs relative to the KO in the 0.01 mHz to 0.23 mHz bandwidth.

A larger amplitude of the discrepancies between KBR data and the KO orbit above 0.23 mHz is indication that kinematic positioning is unable to provide a sequence of orbital positions that are as "smooth", as a dynamic orbit over periods
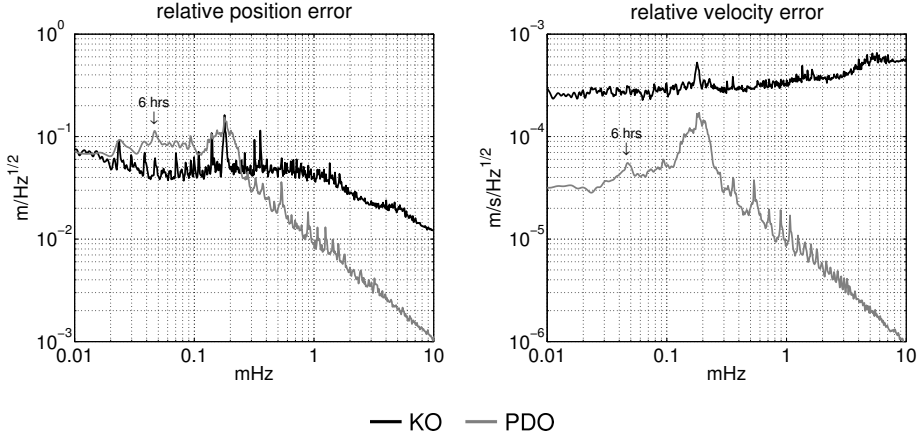
Figure 6.3 – Spectra of relative position (left) and velocity (right) residuals.

smaller than roughly 1 hour. For this reason, the estimation of initial state vectors on the basis of KOs would be less accurate if done considering shorter lengths of time. The error at high frequencies is of significant amplitude in case of the KO. When the kinematic velocities are computed through numerical differentiation, the orbit error is also differentiated, increasing the discrepancy with the KBR data at high frequencies. In case of the PDO, the dynamic model ensures that the velocity vector is mainly the derivative of the position vector and not of the positioning error. For this reason, the amplitude of the relative kinematic velocities does not decrease with increasing frequency, cf. right-hand side of Figure 6.3.

The assumption that the KBR data are more accurate than the estimated orbit error amplitude across the complete frequency spectrum (at least up to 10 mHz) is now proven correct. The error of these measurements is of a few tens of $\mu m/\sqrt{Hz}$, as shown in Figure 6.12, which makes them at least two orders of magnitude more accurate than the computed position residuals, which represent the relative positioning accuracy of the PDOs or KOs. In case of the velocities, the error in terms of the KBR range-rates is predicted to be around 10^{-7} m/s$\sqrt{Hz}$ at 10 mHz, cf. Gerlach et al. (2004, Figure 2), which is one order of magnitude lower than the relative velocity errors derived for the PDO.

Velocity and differentiated position spectra

One unexpected result is that the spectra of the velocity residuals of the KO and PDO are not equal to the corresponding spectra of the position residuals multiplied by the angular frequency, as predicted by the analytical differentiation in the frequency domain.

To gain a better insight into this issue, the velocity residuals spectra for the KO and PDO are plotted along side the spectra of the 11-points central-stencil numerically-differentiated position residuals and the spectra of the position residuals multiplied by the angular frequency, i.e. $2\pi f$, see Figure 6.4.
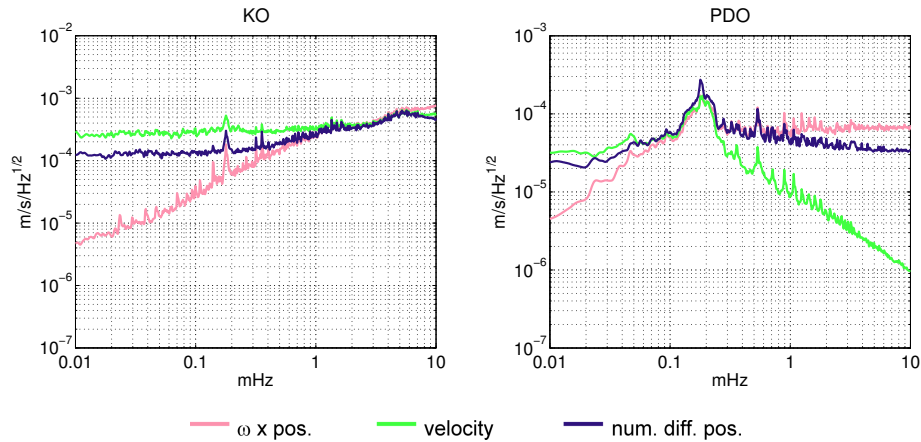
Figure 6.4 – Spectra of the velocity residuals (green) for the KO (left) and PDO (right) compared with the numerically differentiated position residuals (blue) and the position residuals multiplied by the angular frequency (pink).

The spectra of the numerically differentiated position residuals (blue) and of the position residuals multiplied by the angular frequency (pink) derived from the KO (left-hand plot) are, above 1 mHz, very similar to the velocity residuals (green). Below this frequency, the amplitude of the numerically differentiated position residuals (blue) is lower than the velocity residuals (green) by no more than a factor of 3. This discrepancy is attributed to different gaps in the position and velocity data, which can change significantly the maximum length of the contiguous segments and, therefore, modify the spectrum at low frequencies. The spectrum of the position residuals multiplied by the angular frequency (pink), which is two orders of magnitude below the numerically differentiated position residuals (blue) at 0.01 mHz, is completely

insensitive to this effect. As a consequence, it shows the theoretical spectrum as if it were computed without any impact of gaps.

In what concerns the PDO, the same argumentation is applicable below 0.2 mHz. However, the largest differences are above this frequency, particularly between the velocity residuals (green) and the other two spectra. This is an indication that the direct differentiation shown in the numerically differentiated position residuals (blue) and position residuals multiplied by the angular frequency (pink) suffer from worse numeric conditioning in comparison to the dedicated numerical integration scheme used in producing the velocity residuals (green). In other words, the input errors, which are of equal magnitude in all procedures, are amplified more significantly by the direct differentiation (either in the time or frequency domains) into larger output errors. This effect is usually caused by poor numerical stability, e.g. due to the rapid accumulation of round-off errors.

6.1.7 Future relative position and velocity accuracy

In the course of the conducted analysis, position and velocity residuals were produced, which are a realistic representation of the relative position and velocity errors in the KO and PDOs, projected onto the LoS direction.

The ASD of the KO allowed for deficiencies in the processing of the PDO to be identified, which are mainly associated with the higher noise in the bandwidth of 0.01 to 0.23 mHz resulting from imperfectly-estimated initial state vectors.

In the context of future gravimetric missions, it is expected that these limitations are mitigated. With this in mind, the ASD of the relative orbit accuracies in terms of position and velocity considered in the advanced noise model (Section 4.3.3) for the simulation of future gravimetric satellite missions is the curve that minimises the ASDs of the KO and PDOs, refer to Figure 6.5.

The assumption reflected in Figure 6.5 does not suggest that information in the KO and PDO orbits is to be combined. In view of the fact that the KOs serve as input for the processing of the PDOs, any information in the KOs that is lost at the stage of producing the PDOs, as is the case with the analysed dynamic orbits, is indicative of the opportunity to improve the orbit processing algorithms. Once such improvements are implemented, it is reasonable to assume that the residuals in the computed PDO will look similarly to the residuals in the KOs below 0.23 mHz and similarly to the current PDO residuals above this frequency.

Furthermore, there are good reasons to believe that the orbit determination accuracy will improve in the future. The number of GNSSs is increasing and the American GPS is no longer the sole provider of global positioning service. The Russian Globalnaya Navigatsionnaya Sputnikovaya Sistema (GloNaSS) (Polischuk and
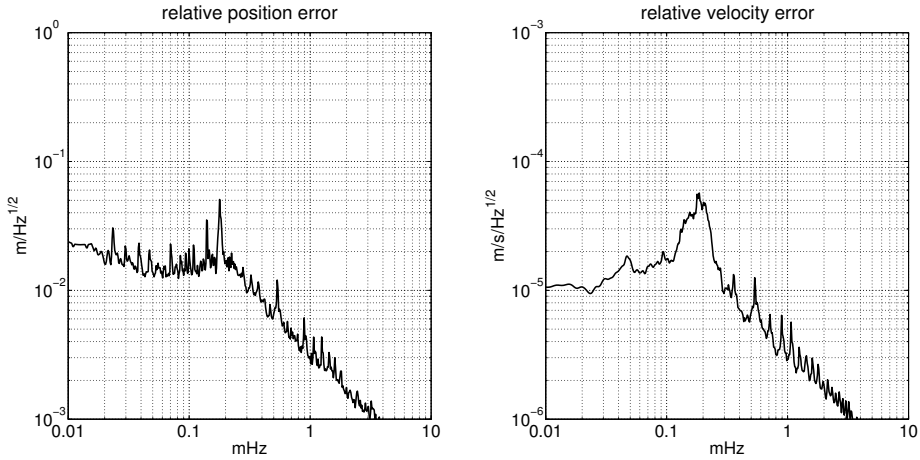
Figure 6.5 – Spectra of relative position (left) and velocity (right) errors in the orbit for the purpose of simulating future gravimetric satellite missions, determined from the spectra in Figure 6.3, after downscaling by the factor of 3, attributed to the improved accuracy of the combination of future GNSSs.

Revnivykh 2004), the European Galileo satellites and the Chinese BeiDou/Compass Navigation Satellite System (BDNSS) (Chengzhi 2013) are quickly reaching a level of maturity, which enables them to actively contribute to positioning. When fully operational, these GNSS systems will have a total of 115 satellites; 32 GPS, 24 GloNaSS, 27 Galileo and 32 BDNSS satellites, excluding spares. All these systems plan to take advantage of at least three-frequency measurements for an improved mitigation of ionospheric delay errors and as much as four in case of Galileo (Li et al., 2013). In addition to global navigation systems, there are also the regional systems, such as Japan's Quasi Zenith Satellite System (QZSS) (Inaba et al. 2009) and the Indian Regional Navigation Satellite System (IRNSS) (Ganeshan et al. 2005). A future gravimetric mission would gain significantly from taking advantage of the variety of GNSS systems, by being equipped with a combined GNSS receiver, such as the one proposed by Roselló et al. (2012). In combination with the state-of-the-art GNSS tracking data, the methodology of Precise Orbit Determination (POD) is continuously advancing, leading to more accurate KOs. In parallel, more accurate PDOs will be computed taking advantage of more accurate KOs and the higher accuracy of the dynamic models.

  If it is possible to exploit all GNSS systems, once fully operational, the number

of satellites visible to a Low-Earth Orbit (LEO) satellite increases roughly four times. The additional third frequency means that on average six times more observations are available. Statistical theory predicts that the accuracy of the computed KO would improve by a factor of $\sqrt{6} \approx 2.5$. This number can be safely rounded to a factor of 3 in view of the advances in the POD methodology. Assuming the PDOs are able to benefit from this improvement and remembering the expected improvement in the force models, it is reasonable to attribute the same accuracy improvement factor to the PDOs. In conclusion, the simulation of future gravimetric missions is carried out under the assumption that the relative position and velocity error is represented by the ASDs shown in Figure 6.5 (already scaled down by the factor of 3 to represent future GNSS positioning accuracy).

6.2   Knowledge gained from GRACE data

The major objective of this section is to carry out an in-depth analysis of noise in GRACE KBR data and, ideally, identify other noise sources than sensors and inaccuracies in background models. The motivation of such research is two-fold. Firstly, it may result in a further improvement of GRACE data processing techniques. Secondly, it might be very helpful in designing GRACE follow-on missions. Investigations of the optimal design of such a mission started a few years ago, cf. Table 1.2, and have become the focus of research efforts of numerous groups worldwide. The key element of such researches is assessing the performance of various mission scenarios. However, this is only possible if all the major contributors to the noise budget are well understood and can be reliably reproduced in the course of simulations. The GRACE mission can be considered as a unique source of such knowledge.

In order to reach the study goals, noise in GRACE Level-1B data is analysed in the spectral domain. In different frequency bands, the properties of actually observed noise level are compared with those of synthetic noise of various origins. In this way, most probable sources of noise in GRACE data are identified.

6.2.1   Production of noise realisations in GRACE data

The realisations of noise considered for the numerical study are produced following the procedures described in this section. For the most part, the text mostly references previous sections where the basic concepts are introduced. The section starts with the methodology, where the functional and signal models are identified, the details of the production of GRACE data noise realisations are explained, and the inventory

of the relevant noise types is presented in order to define the noise model. The GRACE data considered for the study are described next, followed by a preliminary analysis of the data.

Methodology

The conducted analysis relies heavily on the methods and algorithms used in the DMT model processing, namely making use of the functional model generally referred to as *range combinations approach*, refer to Section 4.1.2, and the force model described in Section 4.2.4. The DMT model itself is added to the exploited force model as a source of information about mass re-distribution at a monthly and longer time scales. The orbits considered are the ones used in the production of DMT and are presented in Section 6.1.1.

Computation of data noise   In the conducted study, realisations of total GRACE data noise are obtained by computing the difference between the observed and forecasted range combinations. The observed range combinations are computed directly with Eq. (4.18) on the basis of real GRACE data, which are provided with 5 second sampling period. These data are supplied with information about the LoS direction, which is derived from the produced dynamic orbits. As far as the forecasted range combinations are concerned, two approaches can be applied, as presented in Section 4.1.2. In the analytical analysis of forecast errors presented in further sections, the second approach, which relies on computed three-dimensional (3D) point-wise accelerations, is exploited as more straightforward.

Noise in forecasted range combinations can occur due to several factors. One of these is errors in the orbits, which result in an inaccurate definition of the positions at which the force model is estimated. In addition, noise of this type leads to an inaccurate estimation of the angles θ_{i-} and θ_{i+}. The second factor is inaccuracies in the considered "ideal" force model itself.

As it was already pointed out, range combinations are close to the conventional (point-wise) inter-satellite accelerations. This means that the errors in the force model directly propagate into the data at the vicinity of the locations where the force model is inaccurate. In other words, the functional model is local in this sense (this is in contrast to ranges or range-rates, which depend on the forces not only at the vicinity of the current point, but also at the points visited by the satellites in the past). Such a feature, in principle, might help to identify more precisely the origin of errors in the force model.

Inventory of potential sources of noise in range combinations   The advanced noise model, refer to Section 4.3.3, is the grounds in which the inventory of noise type is based. It describes the errors in the GRACE data as the combination of ranging noise $\delta^{(\mathrm{R})}$ (Eq. (4.45)), correction noise $\delta^{(\mathrm{C})}$ (Eq. (4.55)), accelerometer noise $\delta^{(\mathrm{acc})}$ (Eq. (4.51)), positioning noise $\delta^{(\mathrm{P})}$ (Eq. (4.59)) and orientation noise $\delta^{(\mathrm{L})}$ (Eq. (4.58)). The first two add up to the observation noise $\delta^{(\mathrm{obs})}$, since the observations, i.e. the range combinations, can be represented as the sum of (finite-difference approximation of) range-accelerations and a correction for centrifugal accelerations (Ditmar et al., 2012):

$$\delta^{(\mathrm{obs})} = \delta^{(\mathrm{R})} + \delta^{(\mathrm{C})}. \tag{6.5}$$

The last three enumerated noise types add up to the model errors given by the mis-modelled static signal $\delta^{(\mathrm{st})}$ (Eq. (4.42)) and mis-modelled time-variable signal $\delta^{(\mathrm{tv})}$ (Eq. (4.40)) to compose the forecast noise $\delta^{(\mathrm{for})}$:

$$\delta^{(\mathrm{for})} = \mathbf{w} * \left(\delta^{(\mathrm{st})} + \delta^{(\mathrm{tv})} + \delta^{(\mathrm{acc})} + \delta^{(\mathrm{P})} + \delta^{(\mathrm{L})} \right). \tag{6.6}$$

The observation noise and the forecast noise, in turn define the total data noise δ.

It is noted that in the conducted analysis, there is no distinction between the mis-modelled static signal $\delta^{(\mathrm{st})}$ and the omission signal $\delta^{(\mathrm{sp})}$, since the latter is implicitly included in the former.

Considered GRACE data and preliminary analysis of actual data noise

The methodology presented above was applied to produce realisations of noise in the GRACE data for 11 months in 2006: from January to November (the month of December was removed from the analysis because of a low data quality in the last 8 days of the month). Each monthly noise realisation is obtained by differencing the corresponding sets of the observed and forecasted range combinations. Later on, these realisations are referred to as "actual noise realisations", in order to distinguish them from the synthetic noise realisations that reflect the individual contributions of the hypothetical sources to the overall noise budget. The actual noise realisations reflect inaccuracies both the in the observations and in the predictions.

Spectra of the produced noise realisations are shown in Figure 6.6 in terms of the ASD. One can see that all the monthly ASDs share a number of common features. First of all, the plot reveals an increased noise level below the frequency of 1 mHz. This level shows large variations from month to month and, therefore, can hardly be explained by sensor noise. In Ditmar et al. (2012) and Farahani (2013), this feature
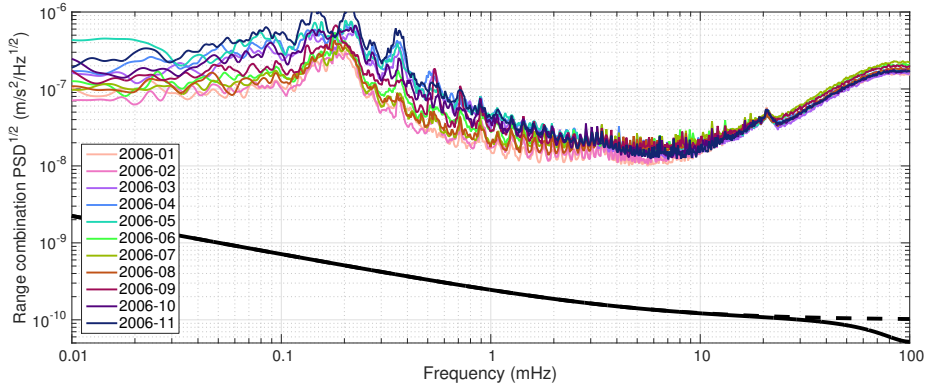
Figure 6.6 – ASDs of the actual realisations of noise in the GRACE-based range combinations for January-November 2006, as well as a theoretical ASD of accelerometer noise directly reproduced from Kim (2000) (thick black dashed line) and the same ASD transformed into range combinations by multiplying with the averaging filter gain (thick black solid line).

is explained by relative errors in the estimated GRACE orbits. Errors of this type are not further analysed since they were extensively discussed in Section 6.1. Secondly, all the ASDs show a peak between 10 and 20 mHz. Later in Section 6.2.2, it is demonstrated that the origin of this feature is an imperfectness of the exploited static gravity field model (EIGEN-GL04C, cf. Section 4.2.4). Thirdly, all the ASDs show a rapid increase above the frequency of 10 mHz, being practically independent on the month. The likely cause of this feature is KBR sensor noise (Frommknecht et al., 2006; Flury et al., 2008). Noise of this type is further discussed in Section 6.2.2.

Finally, Figure 6.6 shows the theoretical ASD of accelerometer noise (Kim, 2000) (thick black dashed line). Strictly speaking, this curve is not directly comparable with the actual noise ASDs, since the latter ones are shown in terms of range combinations, which can be interpreted as averaged inter-satellite accelerations. In order to eliminate this inconsistency, the theoretical ASD of accelerometer noise has been scaled in Figure 6.6 with the averaging filter gain; the result being shown as the thick black solid line. At low and intermediate frequencies, the application of the averaging filter does not have a visible influence, but at the highest frequencies it reduces the ASD about two times. It is worth adding that, according to Flury et al. (2008), actual accelerometer noise fits the theoretical expectations only within a few time intervals when the on-board heaters are de-activated. In the rest of the

time, the actual accelerometer noise can exceed the theoretical one by an order of magnitude (Frommknecht et al., 2006). Even in that case, accelerometer noise would be much lower than actually observed noise at all frequencies (Figure 6.6b). This means that the on-board GRACE accelerometers provide, most probably, only a minor contribution to the GRACE noise budget. For this reason, the accelerometer noise is not discussed further in the current study.

6.2.2 Sources of noise in GRACE data

In the following sections the sources of data noise that play (or may play) a role at the intermediate and high frequencies are investigated. In doing so, the actual noise is compared with synthetic noise realisations associated with various hypothetical sources.

Three sources of noise are addressed:

- errors in the static gravity field model, which is a part of the set of background force models,
- ranging sensor noise and
- possible inaccuracies in the models of temporal gravitational field variations (associated with mass transport at processes the Earth's surface)

In addition, a hypothesis is considered that the dominant noise in the frequency range $1-9\,\text{mHz}$ is just random stationary noise (of an undefined origin).

As it was already demonstrated in the previous section, spectral analysis is a powerful tool for comparing noise realisations. Unfortunately, such a comparison may not be sufficiently informative if a noise is associated with a process or feature at the Earth surface, so that the resulting noise variations manifest themselves in the spatial rather than in the time or frequency domain. This is the reason why the second way was also followed: to propagate noise into gravity field parameters (spherical harmonic coefficients) and then to analyse it in the spatial domain. In doing so, band-pass filtering is (optionally) applied to noise time-series in order to highlight the frequency band where a certain noise source is presumably dominant. Technically, filtering is performed with the 7th order Butterworth band-pass filter, for which purpose the MATLAB function *butterworth* is exploited. The filter is applied twice, in the forward and reverse direction, which is equivalent to applying a zero-phase filter (of a different order), so that filtered signal is not subject to any time shift. The Butterworth filter is selected due to having a maximally flat magnitude frequency response at the bandwidth of interest.

For each epoch i, the filtered time series y is computed from the original time series x as:
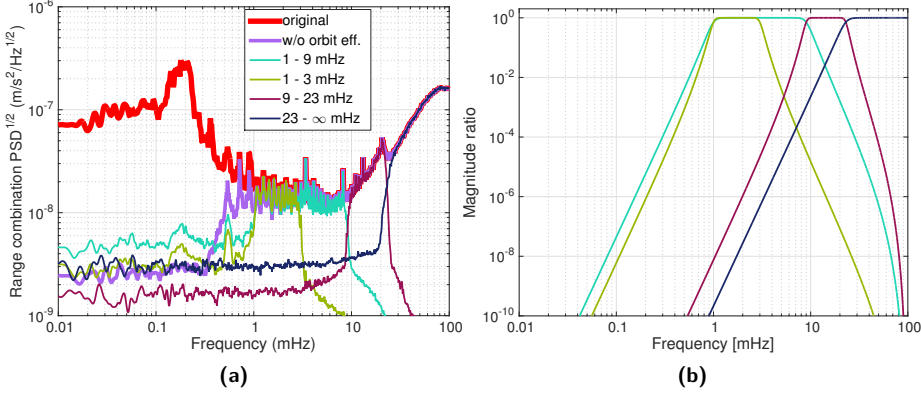
Figure 6.7 – a) ASDs of actual GRACE data noise obtained after band-pass filtering applied in order to highlight noise in one of the four frequency bands considered. ASDs of the original noise (red curve) and of noise cleaned from the orbit inaccuracies (purple curve) are also shown. The considered month is February, 2006. b) Amplitude response of the considered Butterworth filters used to obtain the band-pass filtered noise time series.

$$y_i = \sum_{k=0}^{n} b_k x_{i-k} + \sum_{k=1}^{n} a_k y_{i-k}, \tag{6.7}$$

with the $a_1...a_n$ the feedback filter coefficients, $b_0...b_n$ the feed-forward filter coefficients and, considering that m is the filter order, $n = m$ in case of the high-pass filter and $n = 2m$ in case of the band-pass filters. The values of the filter coefficients are shown in Table 6.3.

In the frequency domain, the transfer function $H(z)$ of the filter is

$$H(z) = \frac{\sum_{k=0}^{n} b_k z^{-k}}{1 + \sum_{k=1}^{n} a_k z^{-k}}. \tag{6.8}$$

ASDs of actual noise obtained after band-pass filtering are shown in Figure 6.7a and the amplitude response of the respective Butterworth filters in Figure 6.7b.

Computation of gravity field parameters without a band-pass filtering is considered as well, so that the results can be interpreted as a reproduction of noise that is present in actual GRACE-based gravitational field solutions. In that case, the realisations

147

k	$1-9\,\text{mHz}$ b_k	a_k	$1-3\,\text{mHz}$ b_k	a_k	$9-23\,\text{mHz}$ b_k	a_k	$23-\infty\,\text{mHz}$ b_k	a_k
0	3.094×10^{-7}		-8.946×10^{-7}		1.027×10^{-5}		0.18809	
1		-12.813		-13.697		-10.798	-1.3166	-3.7616
2	-2.166×10^{-6}	76.314	6.262×10^{-6}	87.130	-7.189×10^{-5}	55.167	3.9498	6.5246
3		-280.01		-341.16		-176.66	-6.5831	-6.6013
4	6.498×10^{-6}	707.18	-1.878×10^{-5}	918.62	2.156×10^{-4}	396.02	6.5831	4.1640
5		-1300.4		-1799.4		-657.18	-3.9498	-1.6260
6	-1.083×10^{-5}	1795.6	3.131×10^{-5}	2644.2	-3.594×10^{-4}	832.41	1.3166	0.36220
7		-1891.2		-2961.2		-817.45	-0.1880	-0.0035377
8	1.083×10^{-5}	1527.0	-3.131×10^{-5}	2539.6	3.594×10^{-4}	625.41		
9		-940.44		-1659.9		-370.98		
10	-6.498×10^{-6}	434.94	1.878×10^{-5}	813.90	-2.156×10^{-4}	167.98		
11		-146.47		-290.31		-56.318		
12	2.166×10^{-6}	33.952	-6.262×10^{-6}	71.213	7.189×10^{-5}	13.221		
13		-4.8493		-10.752		-1.9464		
14	-3.094×10^{-7}	0.3219	8.946×10^{-7}	0.7539	-1.027×10^{-5}	0.1356		

Table 6.3 – Filter coefficients.

of actual noise are cleaned from the effects of inaccurately known orbits, which manifest themselves as an increased noise at low frequencies. To that end, the same scheme is used as was applied by Liu et al. (2010) in producing the DMT model.

The inversion procedure used to propagate noise time series into gravity field parameters is also somewhat similar to that designed for the production of the DMT model (Liu et al., 2010). The gravity field parameters are estimated by solving the corresponding system of linear equations. The minimum spherical harmonic degree is set equal to 2, the maximum one is typically set equal to 120. Unlike Liu et al. (2010), the Frequency-Dependent Data Weighting (FDDW) is applied (Klees et al., 2003; Klees and Ditmar, 2004) based on the actual data noise ASD (red curve in Figure 6.7). This is consistent with the statistically optimal approach to the inversion of actual data.

The usage of the pre-conditioned conjugate-gradient scheme (Hestenes and Stiefel, 1952) allows the inversion to be carried out with a high numerical efficiency. The exploited pre-conditioner is based on the assumption that the input data are defined as the xx-component of gravity gradient matrix (Ditmar and Klees, 2002) scaled with the average range.

Finally, the integrated effect of the errors of all the considered types onto the recovered gravity field parameters is presented and compared with that of the actual noise.
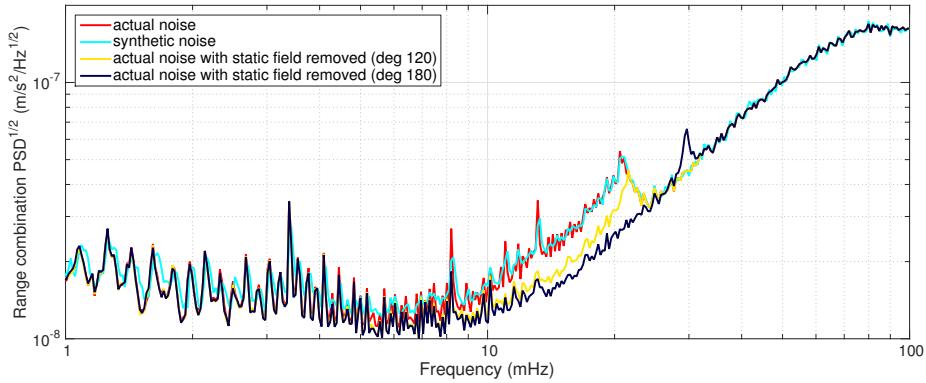
Figure 6.8 – ASD computed on the basis of the following noise types: actual noise (red line); synthetic stationary noise (blue line); actual noise corrected for the contribution of the residual static gravity field parameters estimated up to degree 120 (yellow line); and the same, but for the maximum degree 180 (dark blue line). The month under consideration is February, 2006.

Contribution of errors in the static gravity field model

In this section, the contribution of errors in the static gravity field model to the produced data noise is analysed. As it will become clear later, those errors manifest themselves mostly in the frequency band between 9 and 23 mHz. This band, therefore, in the subject of the discussion.

To begin with, the hypothesis is considered that actual noise in the aforementioned frequency band is purely random. Monthly realisations of a synthetic random stationary noise are synthesised in such as way that the ASD of a particular realisation coincides with the ASD of the actual noise in the corresponding month (see the blue and red curves in Figure 6.8, respectively). It is important to mention that actual noise realisations contain gaps due to, e.g., the elimination of outliers from the data (Liu et al., 2010). All such gaps are fully reproduced in the realisations of simulated stationary noise.

Noise realisations of both types – actual and synthetic – are band-pass filtered (band $9 - 23\,\mathrm{mHz}$) and propagated into gravity field parameters. It turns out that the resulting RMS geoid height error in case of the actually observed noise is more than 2 times larger than in case of the synthetic noise for all the months (see the red and light blue curve in Figure 6.9, respectively). This observation is interpreted as an evidence that the actually observed noise is characterised by correlations in
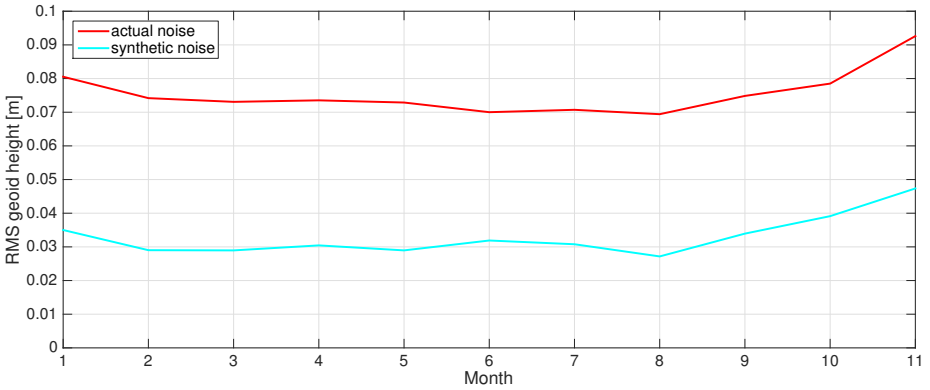
Figure 6.9 – RMS geoid height error computed after the propagation of monthly noise realisations into gravity field parameters (as a function of month). Considered noise types: actual noise (red line) and synthetic stationary noise (light blue line).

the spatial domain, which cannot be described by the ASD and, therefore, are not reproduced by the synthetic noise. To reveal the nature of those spatial correlations, the mean value of the gravity field parameters are computed over the considered 11 months. It turns out that the resulting RMS geoid height is 6.9 cm, i.e. close to the mean monthly RMS value, 7.5 cm (the mean level of the red curve in Figure 6.9). This is in contrast to the case of the synthetic noise, when the RMS geoid height of the mean field is only 1 cm, which is about $\sqrt{11}$ times smaller than the mean monthly RMS value, 3.3 cm (the mean level of the light blue curve in Figure 6.9). This is fully consistent with the statistical theory. It is suggested that the observed phenomenon is nothing but an evidence of a residual signal left in the noise realisations due to inaccuracies in the exploited static gravity model (namely EIGEN-GL04C).

In order to verify this hypothesis, the procedure described above is repeated without applying a band-pass filter. The mean gravity field parameters estimated in this way up to degree 120 is used as a correction to the EIGEN-GL04C model. More specifically, the residual average accelerations are computed on the basis of the obtained mean field using Eq. (4.30) and the produced time series are subtracted from the original realisations of actual noise. The ASD of the corrected noise realisations is shown in Figure 6.8 in yellow. One can see that the updated noise is indeed noticeably lower in the frequency band $9 - 23$ mHz. Thus, inaccuracies of the exploited static gravity field model are one of the dominant contributors to the total error budget in the aforementioned frequency range. In other words, the observed

noise, which is rapidly increasing above 9 mHz, is partly explained by the presence of residual gravitational signal in the data, which is left after the subtraction of the imperfectly forecasted range combinations.

At the first glance, such a conclusion is counter-intuitive. It is well-known that gravitational signal observed at the satellite altitude decreases as the frequency increases due to the upward continuation effect. One should keep in mind, however, that the residual signal in this case is the signal caused by the difference between the true mean gravitational field and the one described by the EIGEN-GL04C model, i.e. the residual signal that is equal to the errors in the latter model. Those errors increase with spherical harmonic degree, and so does the residual signal, which apparently compensates the upward continuation effect.

It is also interesting to see that the corrected noise ASD still contains a peak near the frequency of 20 mHz or 120 CPR. This peak is explained by the presence of residual signals above degree 120. In order to demonstrate that, the noise correction procedure is repeated with the mean field recomputed up to degree 180. The resulting ASD is shown in Figure 6.8 in dark blue. One can see that the peak at 20 mHz has vanished, but a new (though smaller) peak around the frequency of 33 mHz (or 180 CPR) has appeared. Thus, even a gravity field model complete to degree 180 cannot fully explain all the signal present in GRACE data.

Finally, it is analysed whether the computed correction may be considered as an actual improvement of model EIGEN-GL04C (in other words, whether this correction is close to the difference between the true field and the one described by the EIGEN-GL04C model. To this end, the computed correction is compared with the residual field defined as the difference between the state-of-the-art Gravity Observation COmbination release 02 satellite-only gravity field model (GOCO02S) (Goiginger et al. 2011) and the EIGEN-GL04C model, with the truncation at degree 120 being applied. In order to clean the computed correction from noise and nuisance signals, the correction procedure presented above is used (maximum degree is set equal to 120; band-pass filter is applied to the actual noise realisation in order to highlight the $9-23$ mHz bandwidth). After that, a visual comparison of the two residual fields shows that some similarity between them indeed exists, but only in the polar areas (see e.g. Figure 6.10).

In order to make a more objective comparison of the two residual fields, the correlation between them is estimated as a function of latitude and longitude. The procedure is the following. The two functions to be compared are computed on the equiangular $1.5°×1.5°$ grid. Then, a fragment of the grid of a certain size $2k+1$ by $2k+1$ grid-points is selected, the correlation coefficient between the two functions within the selected fragment is computed, and then assigned to the node at the centre of the fragment. The procedure is repeated until a global grid
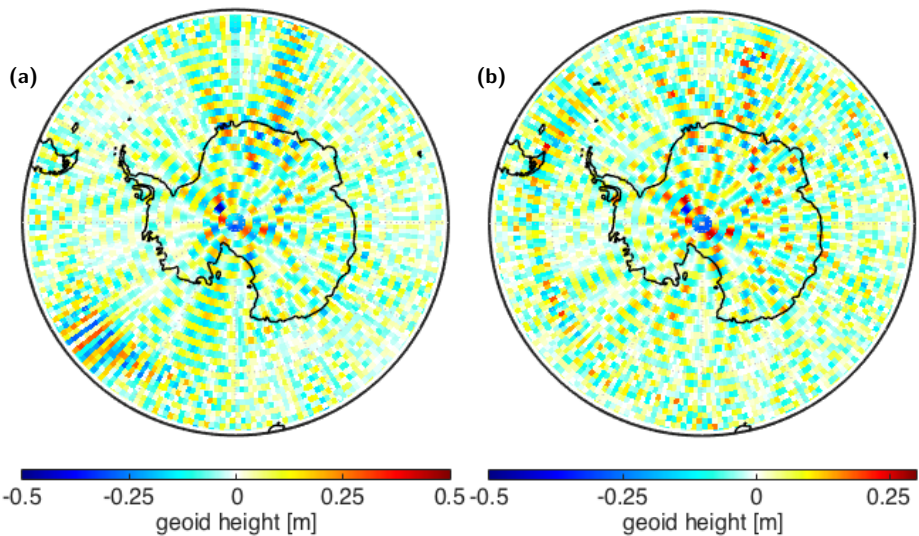
Figure 6.10 – Static gravitational correction computed up to degree 120 from 11 months of (a) actual noise (after the band-pass filtering to highlight the range $9-23\,\mathrm{mHz}$ and (b) difference between GOCO02S and EIGEN-GL04C static gravity field models truncated at degree 120, in terms of geoid height [m]. The colour bar scale in the two plots is purposely different in order to make the error patterns in both cases more evident.

of correlation coefficients is obtained. Unfortunately, it turns out that the spatial pattern shown in this grid is very dependent on the parameter k. The produced spatial correlation map is strongly dominated by features of the size of k cells, i.e., in general, not sufficiently representative. In order to eliminate a dependence on a pre-defined fragment size, multiple correlation coefficient grids are produced, changing the parameter k uniformly from 1 to 30 (i.e. each grid computed on the basis of fragments of sizes between 3 by 3 and 61 by 61 cells), and then the mean of all of these grids is computed. The obtained result is shown in Figure 6.11. This map confirms a relatively high correlation between the two residual fields in the polar regions and a much lower correlation at low latitudes.

This outcome is explained by the fact that the difference between the azimuths of the ascending and descending tracks in the polar areas is large. This makes the sensitivity of the GRACE mission to gravitational signals more isotropic and, therefore, reduces the non-uniqueness of the gravity field recovery. An additional factor, which also plays a role, is a relatively high density of measurements in the polar areas. Thanks to the combination of these two factors, the computed correction to the original static gravity field model allows that model to be improved near the poles. As far as low-latitude areas are concerned, the intrinsic non-uniqueness of the GRACE mission, which is caused by its anisotropic sensitivity, leads to the situation that the computed correction is only one of many possible options. It can explain the residual signal in the GRACE data, but cannot be treated as an actual improvement of the static model of the Earth's gravitational field.

It is worth adding that the actual noise corrected for the residual static field up to degree 180 is called hereafter "corrected actual noise". Only this type of actual noise is considered in the analysis in the following sections.

Contribution of ranging sensor errors

The relatively strong noise at high frequencies, which is observed even after the subtraction of the residual static field contribution, is attributed to the imperfectness of the KBR sensor. In order to provide a further support of this statement, synthetic realisations of the ranging noise $\delta^{(R)}$ are generated. As input, noise ASD is defined in terms of ranges. It is assumed that the ASD of the ranging sensor noise is represented by a linear function in the logarithmic scale. On this basis, realisations of noise in the ranges are computed, transformed into range-combinations with Eq. (4.45), and then modified by introducing the appropriate data gaps. It is found that the best fit to the corrected actual noise in the range $14-80$ mHz is obtained if the noise in terms of ranges decreases with a rate of -6.4 dB per decade (see Figure 6.12a). This parameter remained unchanged in the scaling procedure that
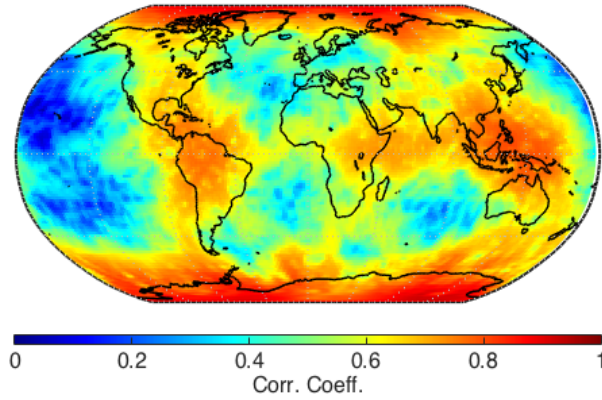
Figure 6.11 – Spatial correlation between: (i) computed correction to the static gravity field model EIGEN-GL04C and (ii) the difference between the state-of-the-art GOCO02S model and EIGEN-GL04C (truncation at degree 120 is applied). Notice that there are no negative correlation coefficients, this is the reason why the colour bar covers only positive values.

fitted the synthetic noise realisations to the real noise data within each month. It turns out that the ranging sensor noise STD varies between 0.72 and 0.94 μm (in average, 0.81 μm). The estimated parameters of the ranging sensor noise are, in general, consistent with those known from literature (Kim and Tapley, 2002; Frommknecht et al., 2006; Kim and Lee, 2009).

The ASDs of the corrected actual noise and of the synthetic noise transformed into range-combinations are presented for one of the months in Figure 6.12b. As one can see, these two ASDs are very close to each other above the frequency of ~ 14 mHz. The other months also show a good consistency between the synthetic and corrected actual noise in this frequency range (not shown). The peak at the frequency of 30 mHz observed in the corrected actual noise ASD can be explained by a residual static field signal, as it is explained in the previous section. At the frequencies below ~ 14 mHz, an increasing discrepancy between the synthetic noise and the corrected actual one is observed. This suggests that some other contributors to the noise budget start to play a role there.

A comparison of the synthetic and corrected actual noise is also performed in terms of gravity field parameters. To achieve this, the noise time series of both types are, first of all, subject to a high-pass filtering, so that the contribution of frequencies below 23 mHz is suppressed. After that, the noise realisations of both
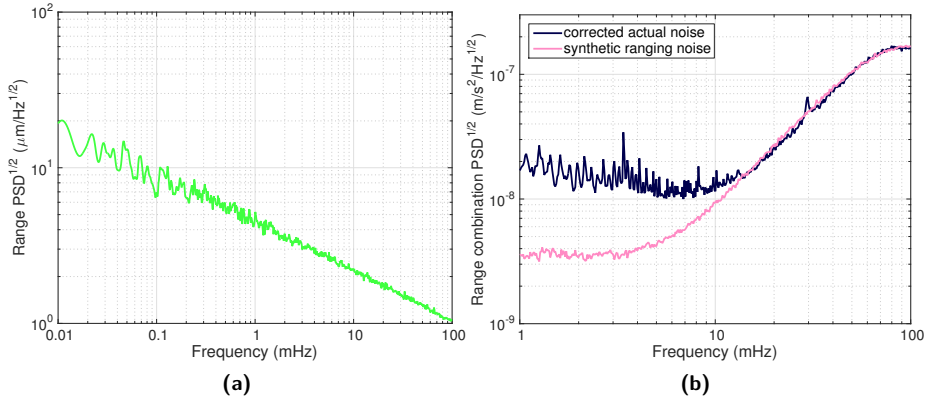
Figure 6.12 – a) ASD of synthetic ranging sensor errors; b) ASD of the synthetic ranging noise obtained by the propagation of ranging sensor errors (in pink) and ASD of the corrected actual noise (in dark blue). The month under consideration is February, 2006.

types are inverted into gravity field parameters as described above. It is worth mentioning that the FDDW in this particular case is switched off in order to prevent down-weighting of the high frequencies, which are the major focus of the conducted comparison. The computed gravity field parameters are represented in terms of geoid heights. It turns out that the spatial patterns of noise of the two considered types are sufficiently similar to each other (see e.g., Figure 6.13). In both cases, the noise forms along-track stripes, which vanish near the poles and reach maximum near the equator. Otherwise, the regions with relatively low and high noise are randomly distributed over the globe. It is necessary to add that the total RMS error averaged over 11 months is somewhat larger in case of the corrected actual noise than in case of the synthetic one: 9.2 m and 5.2 m, respectively. This discrepancy can be attributed to the fact that corrected actual noise still contains a residual gravitational signal, as indicated by the peak at degree 180. This signal is hardly visible in the frequency domain, but apparently overwhelms noise of other types in the spatial domain: it does not average out as the length of the time series increases.

Potential contribution of inaccuracies in models of temporal gravitational variations

In the present section, it is analysed whether errors in the exploited background models of mass transport can (at least, partly) explain the observed data noise. Two
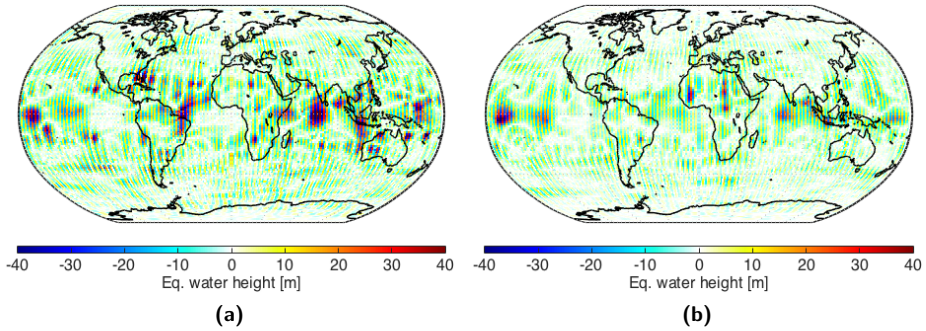
Figure 6.13 – High-pass filtered noise propagated into gravity field parameters and represented in terms of equivalent water layer thickness (m): (a) corrected actual noise (RMS=8.1 m) and (b) synthetic ranging noise (RMS=5.2 m). The month under consideration is February, 2006. The average RMS for the 11 months considered is (a) 9.2 m and (b) 5.2 m.

potential sources of errors are considered: (i) inaccuracies in the models of non-tidal mass transport in the atmosphere and ocean; and (ii) an insufficiently accurate description of slow mass transport given by the DMT model. Although the scope of the conducted analysis is very limited, it still allows some general conclusions to be drawn regarding the potential effect of errors in mass transport models.

There are a few possibilities to quantify errors in models of non-tidal mass transport in the atmosphere and ocean. One of the possible approaches is to consider the difference between two alternative meteorological models describing atmospheric pressure variations, which are the major contributor to non-tidal mass transport in the atmosphere and ocean (Velicogna et al., 2001; Thompson et al., 2004; Han, 2004a). Another possible approach is to make use of the error estimations provided by a meteorological model itself (Zenner et al., 2010). In the analysis of the current section, errors in a model of non-tidal mass transport in the atmosphere and ocean are defined as 10% of residual signal, which is derived as the difference between the instantaneous signal and the monthly mean. In view of previous researches of errors in mass transport models, such an assumption can be considered as sufficiently reasonable (see, e.g., Thompson et al., 2004).

Of course, non-tidal mass re-distribution in the atmosphere and ocean is only one of the on-going mass transport processes; an inaccurate description of other processes contributes to the noise budget as well. Therefore, it was decided to
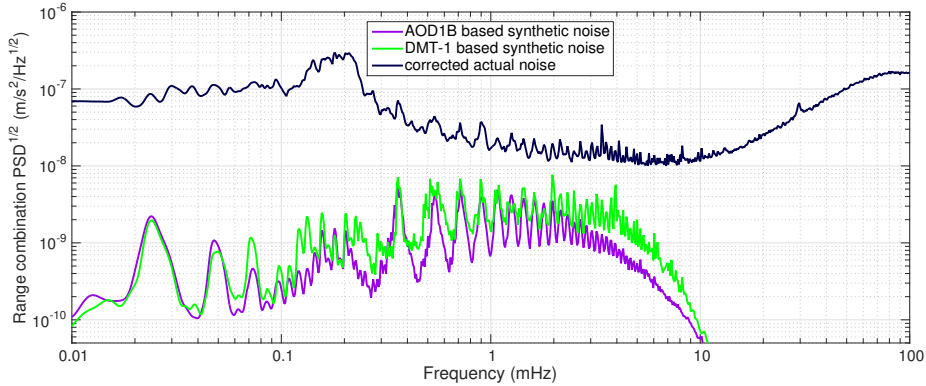
Figure 6.14 – ASDs of synthetic noise caused by potential errors in background time-varying gravity field models: based on the AOD1B product (purple line), and based on the DMT model (green line). ASD of corrected actual data noise (dark blue line) is shown as a reference. The month under consideration is February, 2006.

consider also the DMT model as a potential source of inaccuracies. This model is based on GRACE data themselves and, therefore, describes the total mass transport independently of its geophysical origin. An obvious limitation of the DMT model stems from its limited temporal resolution. Like most of other GRACE-based models, it consists of monthly solutions, so that a mass anomaly within each particular month is assumed to be constant. The difference between the actual mass anomaly at a certain moment and the mean monthly value is a source of additional errors. In order to estimate their potential effect, an alternative scheme is used to derive mass variations in the time domain from the DMT model. Instead of assuming that mass variations are piece-wise constant, a quadratic spline approximation is applied in such a way that the monthly mean computed on the basis of the spline is equal to the original value from the DMT model (implementation by Christian Siemes). The difference between the two representations in the time domain is taken as the residual signal and used in the analysis.

The residual mass transport signals of both types (associated with the AOD1B product and with the DMT model) are propagated into range combinations, as discussed in Section 6.2.1. The result is interpreted as synthetic noise of $\delta^{(tv)}$ type (noise caused by the mis-modelled time-variable signal). The ASDs computed on the basis of the obtained time-series for February 2006 are shown in Figure 6.14 (the results for other months look similar).

From a comparison of the presented ASD curves, one can conclude that synthetic noise of both types is at least one order of magnitude smaller than the corrected actual noise. Errors in time-varying gravity field models may contribute to the noise budget substantially only if their level is about 10 times larger. In the AOD1B case, this means that the errors must be comparable with the signal itself, which is likely an overly pessimistic assumption. Furthermore, even in that case the contribution of the errors under consideration would be limited to the frequency band $1-3$ mHz. At higher frequencies, the ASDs of the synthetic noise of both types decay rapidly, which can be explained by the upward continuation effect.

One may argue that residual mass transport signals may not be stationary, so that an attempt to quantify them in terms of ASD might be misleading. In order to make the analysis more comprehensive, the forecasted range combinations based on the residual mass transport signals, as well as corrected actual data noise, are propagated into gravity field parameters. To isolate the frequency range where the residual mass transport signals are mostly significant, the band-pass filtering (band $1-3$ mHz) is consistently applied to the time series of data noise and residual signal. The results obtained in this way for February 2006 are shown in terms of equivalent water layer thickness in Figure 6.15. One can see that in the spatial domain, the corrected actual noise also shows a different behaviour than the synthetic noise. The corrected actual noise reaches maximum near the equator; the RMS value averaged over 11 months being equal to 42.7 m. On the contrary, synthetic noise based on the AOD1B product is maximal at the intermediate latitudes and is much smaller at the equator. Furthermore, the RMS value of noise of this type (average over 11 months) is only 0.5 m. One may argue that in reality noise in the AOD1B product may not be proportional to signal and, therefore, may result in a very different spatial pattern. Nevertheless, in order to explain the level of the corrected actual noise near the equator, it would be needed to assume that the noise in AOD1B product in the equatorial area exceeds the signal by orders of magnitude, which is very unlikely. As far as synthetic noise based on the DMT model is concerned, the resulting spatial pattern is much closer to that in case of the corrected actual noise. Nevertheless, the level of synthetic noise is still too low. The RMS value of this noise averaged over 11 months is equal to 7.0 m, which is an order of magnitude smaller than in the case of corrected actual noise.

In conclusion, the inaccuracies in the AOD1B product as well as the limited temporal resolution of the DMT model are, most probably, not the dominant source of noise in the GRACE data, including the frequency range $1-3$ mHz. Furthermore, it is unlikely that errors in the other background mass transport models significantly exceed the residual signals considered in the analysis. Thus, no evidence is found that GRACE-based models significantly suffer from errors in background mass transport
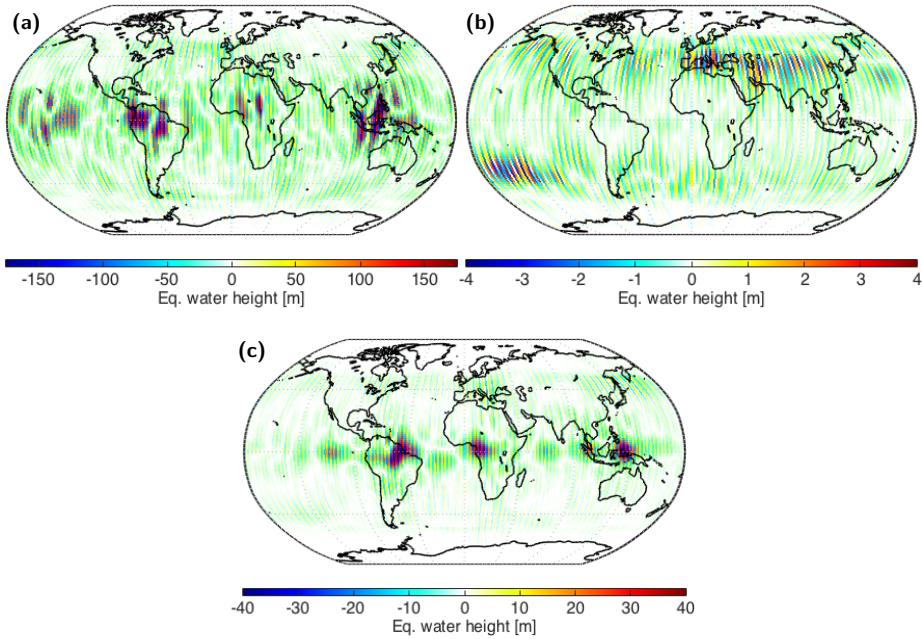
Figure 6.15 – Corrected actual noise and synthetic noise due to errors in models of temporal gravitational variations, propagated into gravity field parameters after band-pass filtering (band $1-3$ mHz) and represented in terms of equivalent water layer thickness (m): (a) case of corrected actual noise (RMS=31.6 m); (b) case of synthetic noise based on the AOD1B product (RMS=0.6 m); and (c) case of synthetic noise based on the DMT model (RMS=4.8 m). The month under consideration is February, 2006. The average RMS for the 11 months considered is (a) 42.7 m, (b) 0.5 m and (c) 7.0 m.
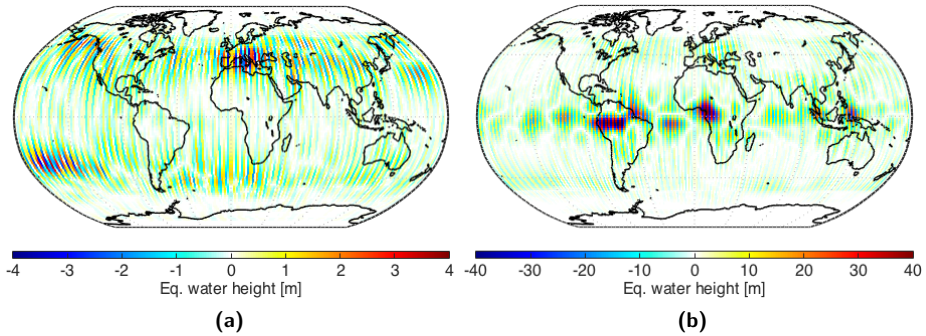
**Figure 6.16** – Synthetic noise due to errors in models of temporal gravitational variations, propagated into gravity field parameters represented in terms of equivalent water layer thickness (m): (a) case of synthetic noise based on the AOD1B product (RMS=0.6 m); and (b) case of synthetic noise based on the DMT model (RMS= 5.1m). The month under consideration is February, 2006. The average RMS for the 11 months considered is (a) 0.5 m and (b) 7.3 m.

models used for temporal de-aliasing. This does not exclude the option, however, that such errors still play a role locally, i.e. in limited regions where their level significantly exceeds the average one.

A realisation of synthetic noise $\delta^{(tv)}$ is also propagated into gravity field parameters without a band-pass filtering in order to demonstrate the total effect of those signals. The obtained results turn out to be very similar to those obtained with the band-pass filtering, as shown for February 2006 in Figure 6.17 in terms of equivalent water layer thickness. One can see that the resulting spatial patterns are close to those already observed in the case of bandpass-filtered residual signals. The RMS of the propagated unfiltered residual signals is nearly identical to the filtered cases, only 1.9% higher for the AOD1B product and 4.2% higher for the DMT model, considering the mean RMS for the 11 months. This proves that the temporal aliasing of natural mass transport processes originates mainly from the signals within the $1-3$ mHz bandwidth.

Contribution of random noise of unknown origin

After the analysis presented in the previous sections, the origin of data noise in the frequency band $1-9$ mHz remains unclear. However, it is at least possible to investigate whether the impact of this noise is similar to that of random stationary
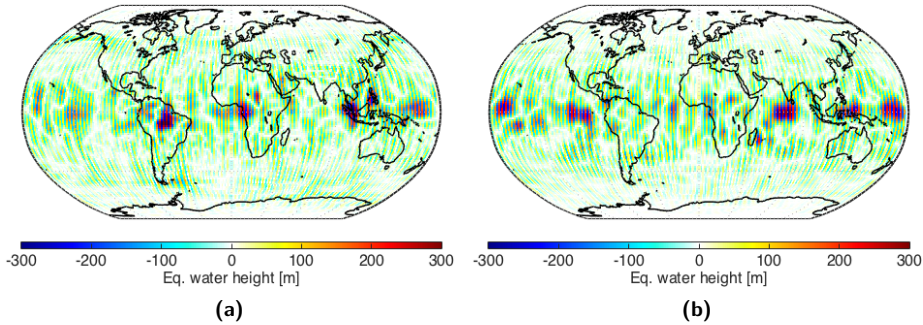
Figure 6.17 – Corrected actual and empirically defined synthetic random noise propagated into gravity field parameters after a band-pass filtering (band $1-9$ mHz), in terms of equivalent water layer thickness (m): (a) case of corrected actual data noise (RMS = 51.8 cm); (b) case of synthetic random noise (RMS = 53.3 m). The month under consideration is February, 2006. The average RMS for the 11 months considered is (a) 61.4 m and (b) 59.1 m.

noise characterized by the same ASD. To that end, realisations of stationary random noise are generated using the ASDs of actual data noise. A band-pass filtering (band $1-9$ mHz) is consistently applied to the corrected actual and synthetic noise realisations in order to suppress the contribution of the content in the irrelevant frequency bands. A comparison of ASDs of the computed noise realisations in the target band demonstrates that they may differ by as much as 20%, which can be explained as the effect of filtering and the gaps introduced into the synthetic noise. Therefore, the synthetic noise is scaled in order to make its ASD close to that of the corrected actual noise in the target frequency band. Finally, the corrected actual and synthetic noise realisations are propagated into gravity field parameters. The results obtained for February 2006 are shown in terms of equivalent water layer thickness in Figure 6.17.

One can see that the spatial patterns of the propagated noise as well as the RMS geoid height errors over the globe are very similar for the corrected actual and the synthetic noise realisations in February 2006. The same result is obtained also for other months (the RMS values averaged over 11 months are equal to 61.4 m and 59.1 m, respectively). Thus, the assumption that the data noise in the frequency band $1-9$ mHz is stationary cannot be proven false. This is an additional evidence that the origin of this noise is not related to errors in the background models describing the Earth's static or time-varying gravitational field.
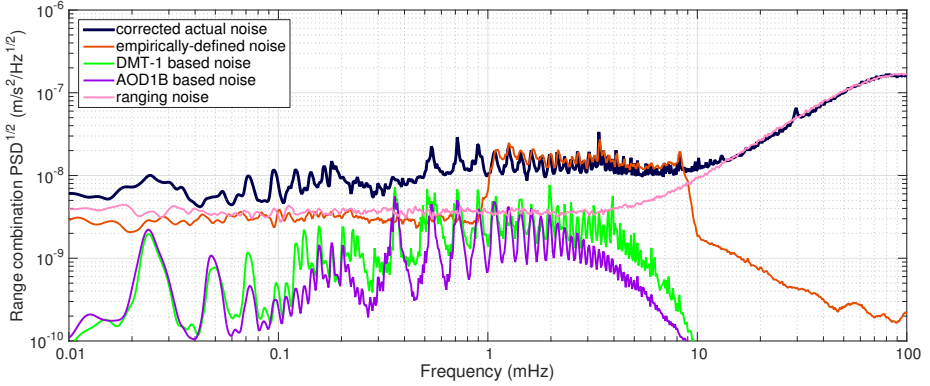
Figure 6.18 – ASDs of the considered realisations of synthetic noise associated with middle- and high-frequencies (February 2006). The considered types of synthetic noise are: ranging noise in pink; noise $\delta^{(tv)}$ caused by errors in the AOD1B product (in purple); noise $\delta^{(tv)}$ caused by errors in the DMT model (in green); empirically defined stationary random noise occupying the frequency bad $1-9\,\mathrm{mHz}$ (in brown). Results based on the corrected actual data noise are shown as well (dark blue lines).

Integrated effect of noise of different origin

To conclude this analysis, the integrated effect of synthetic noise of four different types considered in this section is estimated. This concerns:

1. ranging noise $\delta^{(R)}$;
2. noise $\delta^{(tv)}$ caused by the assumed errors in the AOD1B-derived product;
3. noise $\delta^{(tv)}$ caused by a limited temporal resolution of the DMT model;
4. Empirically defined stationary random noise occupying the frequency band $1-9\,\mathrm{mHz}$.

ASDs of noise of the considered types, as well as of the corrected actual noise, are shown in Figure 6.18.

The considered realisations of synthetic noise are propagated into gravity field parameters. It is important to point out that band-pass filtering is not applied in the context of this analysis (except for the case of empirically defined random noise, which is the result of a band-pass filtering by definition). For a comparison, corrected actual noise is also propagated into gravity field parameters, the low-frequency contents being suppressed with the procedure explained in Ditmar et al. (2012, Section 4, Eq. 52). The obtained results are presented in terms of RMS geoid height
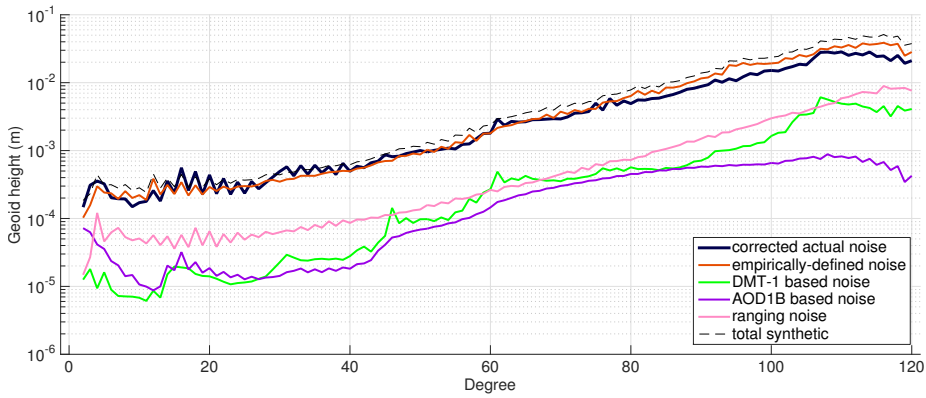
Figure 6.19 – Results of propagating the noise realisations show in Figure 6.18 into gravity field parameters and shown in terms of RMS geoid heights per degree (average over the 11 months). The considered types of synthetic noise are: ranging noise in pink; noise $\delta^{(tv)}$ caused by errors in the AOD1B product (in purple); noise $\delta^{(tv)}$ caused by errors in the DMT model (in green); empirically defined stationary random noise occupying the frequency bad $1-9$ mHz (in brown); sum of all 4 synthetic noise types (dashed grey line). Results based on the corrected actual data noise are shown as well (dark blue lines).

per degree (averaged over 11 months) in Figure 6.19. The effects of synthetic noise of various types are shown both separately and after the summation. From this figure, it is obvious that random noise of unknown origin in the frequency band $1-9$ mHz is the dominant contributor to the errors in GRACE-based gravity field models. The contribution of middle- and high-frequency noise of other types (due to ranging errors and errors in background models of time-varying gravitational field) is an order of magnitude lower. Such a high impact of random noise of the unknown origin can be explained by the fact that it spans the frequency band from 5.4 to 49 cycles per revolution, i.e. overlaps with that containing the major part of the gravitational spectrum. It is also remarkable that this noise remains dominant up to the maximum considered degree (120). Most probably, this is because this noise manifests itself in the form of along-track stripes in the spatial domain (see Figure 6.17b). Thus, even high-degree coefficients are severely distorted, if they are sectorial and nearly-sectorial. It is worth adding that the observed impact of ranging noise alone is close to the baseline errors (Kim, 2000), which reflect the pre-launch expectations regarding the GRACE mission performance.

6.2.3 Discussion and conclusions

The analysis presented in Section 6.2.2 leads to a better understanding of noise in the data acquired by the GRACE satellite mission. Unfortunately, the dominant source of noise in the range of intermediate frequencies $(1-9$ mHz) is still not fully understood. In spite of that, the conducted analysis has led to a number of important findings.

Firstly, the analysed realisations of data noise contains a residual static field signal. It is shown that the inversion of produced noise realisations into a static field update allows this signal to be reduced. On the other hand, it is important to realise that the implementation of this update does not necessarily improve the static field model. In the considered example, the update was somewhat meaningful in the polar areas and fully unsuccessful at low latitudes. Most probably, this can be explained by the intrinsic non-uniqueness of the GRACE mission caused by its anisotropic sensitivity: different updates can explain the residual signal in the GRACE data equally well. In other words, the situation is somewhat similar to that already existed in pre-GRACE era, when the available data allowed "tailored" gravity field models to be produced that perfectly explained those data. However, those tailored models could be rather different from the real field, which became clear as soon as new data became available.

Secondly, it has been demonstrated that the contribution of ranging errors becomes dominant only at high frequencies (above 9 mHz). After a propagation of

such high-frequency noise in gravity field parameters, the resulting effect is about one order of magnitude lower than that of the actual noise. It is worth adding that errors in gravity field models caused by ranging noise are very close to the baseline errors (Kim, 2000), which reflect the pre-launch expectations regarding the GRACE mission performance.

It is also shown that errors in background models of time-varying gravitational field cannot play a significant role in the observed noise spectrum. In addition, it is demonstrated that those errors cannot, in general, explain noise in gravity field models obtained by inversion of GRACE data.

It is now discussed whether the conclusions drawn on the basis of the conducted study can be considered as sufficiently general. As it is explained in Ditmar et al. (2012), the range combinations can be considered as a finite-difference approximation of inter-satellite accelerations. On the one hand, those data can be directly related to the forces acting on the satellites (including the Earth's gravitational attraction). On the other hand, they can be derived from double-differentiated ranges corrected for the contribution of centrifugal accelerations. Let us assume for a moment that the latter correction can be made exactly. In this case, the exploited functional model would provide a unique link between the unknown parameters and the double-differentiated observations (namely, ranges). As it was shown by (Ditmar and Sluijs, 2004), the solution based on this functional model coincides with the solution obtained by the inversion of the original observations (i.e., ranges) themselves or their first-order derivatives (i.e., range-rates), provided that a statistically optimal gravity field parameter estimation procedure is followed. In reality, the correction for centrifugal accelerations is not error-free. However, the corresponding noise manifests itself at low degrees (below $1\,\text{mHz}$) only. Therefore, all obtained results for the intermediate and high frequencies (the focus of Section 6.2.2) should be considered as applicable to optimal estimation procedures in general, no matter whether ranges, range-rates, or range-accelerations are used as input. Of course, the conducted study does not allow anything to be said about non-optimal procedures (e.g., lacking a proper data weighting). For instance, a non-optimal procedure might show a much stronger influence of the ranging sensor noise than is observed in the current study. However, all such problems of non-optimal procedures must be considered as procedure-specific ones and should be treated on a case-by-case basis.

In the context of GRACE follow-on missions, a point of attention is the definition of the static field in mass transport monitoring. Inaccuracies in the exploited static field model can manifest themselves as a residual signal in the input data. One may argue that this issue is not critical because the presence of such a signal simply causes a static bias in the time-varying gravitational field solutions. It is, however, not impossible that this residual signal propagates into different solutions differently

due to a changing ground-track pattern and the intrinsic non-uniqueness of gravity field recovery from GRACE follow-on mission data (particularly, at high degrees). Then, a fictitious time-varying signal can be produced. A possible solution to this problem is to start mass transport recovery from computing a static gravity field model up to a very high spherical harmonic degree (in any case, above degree 180), so that all static field signal in the data is absorbed as completely as possible. It is important to stress that the static model produced in this way must be treated as a tailored model, which can be far from reality. One may argue that compiling such a tailored static field model is not needed if a state-of-the-art model is exploited (e.g., the one produced by a combined inversion of GRACE and GOCE data). It is important to realise, however, that future GRACE follow-on missions may be even more sensitive than GRACE. Therefore it can happen that residual static field signal is still present in the data, whereas the spherical harmonic degrees involved are too high to benefit from GOCE data.

Another aspect tackled in the conducted analysis is the accuracy of the background force models (e.g., the AOD1B product). One might interpret the fact that it is not possible to observe a significant influence of those errors as a recommendation not to care about a further improvement of those models. Such interpretation would be totally wrong. First of all, it is possible that those errors still play a role in limited geographical areas (revealing such an effect would require a more detailed analysis of errors in background force models, which is beyond the scope of the presented analysis). Secondly, improvement of background force models is definitely needed in the context of GRACE follow-on missions, as one of the necessary prerequisites to improve the accuracy of mass transport models to be produced.

Finally, investigation of the remaining sources of noise in GRACE data must be continued (in particular those responsible for the noise observable in the frequency range $1-9$ mHz). For instance, the inaccuracies in satellite attitude data revealed by Horwath et al. (2010) can be considered as a potential source of such noise. It goes without saying that complete understanding of the noise budget would be important not only for GRACE data processing, but also in designing GRACE follow-on missions.

6.3 Validation and fine-tuning of the advanced noise model

This section analyses the advanced noise model of ll-SST data, with the purpose of validation. The noise model should be understood as the simulation procedure used

to generate realistic error time series. In the current section, a set of assumptions is considered with the aim at reproducing the actual GRACE errors as closely as possible, refer to Table 6.4. In Chapter 8, a different set of assumptions intends to reproduce the predicted error amplitudes relevant to future gravimetric mission. In both cases, the same *advanced noise model* is relevant, i.e. the simulation procedure is identical; the difference is only in what concerns the set of assumptions that define the amplitude of the individual noise types.

Table 6.4 provides an overview of the assumptions made for the simulation of the ll-SST noise type and quick reference to the page number where the corresponding noise type is introduced. All noise types rely explicitly on the complete frequency description of the underlying time series of noise (except for the positioning noise $\delta^{(\mathrm{P})}$, where that is done implicitly).

name	symbol	assumptions	description	page nr.
accelerometer noise	$\delta^{(\mathrm{acc})}$	$\mathrm{ASD}\big(\delta^{(\mathrm{acc})}\big)$ grey line in Figure 6.20a	error in the accelerometer measurements	103
ranging noise	$\delta^{(\mathrm{R})}$	$\mathrm{ASD}\big(\delta^{(\rho)}\big)$ in Figure 6.21	error in the measured ranges	104
correction noise	$\delta^{(\mathrm{C})}$	$\mathrm{ASD}\big(\delta^{(\dot{x}^{(12)\perp})}\big)$ in right-hand side plot of Figure 6.5, $\mathrm{ASD}\big(\delta^{(\rho)}\big)$ in Figure 6.21	error from the inaccurately known relative vertical velocity	105
orientation noise	$\delta^{(\mathrm{L})}$	$\mathrm{ASD}\big(\delta^{(\Delta x)}{}_y\big) = \mathrm{ASD}\big(\delta^{(\Delta x)}{}_z\big)$ in left-hand side plot of Figure 6.5	error in the inaccurately known LoS direction	105
positioning noise	$\delta^{(\mathrm{P})}$	$\mathbf{x}^{(\mathrm{for})}$ integrated on the basis of EIGEN-CG03C and $\mathbf{x}^{(\mathrm{obs})}$ integrated on the basis of EIGEN-5C	error in the orbital positions	106

Table 6.4 – Summary of the assumptions considered for the simulation of the ll-SST noise type of the advanced noise model.

The purpose of the conducted analysis is to demonstrate that the simulated errors are representative of the errors present in actual GRACE data. The validation is fundamental in gaining confidence in the exploited noise model. The simulated errors in the trailing formation data are compared with the GRACE a posteriori residuals, which were produced in a similar way to those considered in Section 6.2.

The comparison is made in terms of the ASD of range combinations and gravity field parameters.

The assumptions listed in Table 6.4 are representative of the GRACE mission. However, the simulations do not use actual GRACE data directly. The contribution of actual data is restricted to the production of the GRACE a posteriori residuals, which serves as validation reference. A formation consisting of a pair of satellites in the same orbit 200 km apart, at the height of 500 km, is considered. The choice of orbital altitude intends to be representative of the altitude of the GRACE mission, not to accurately duplicate it. Unlike the GRACE formation, the formation considered in the numerical analysis has a strictly polar orbit, i.e. the inclination is set equal to 90 degrees. No data gaps are added artificially to the simulated time series, apart from those naturally arising from the orbit simulation procedure, cf. Section 3.8.5. The discrepancy in the gap distribution does not influence significantly the results, as explained in Section 6.3.2. The relative orbit position noise derived in Section 6.1.7 is considered in the current analysis without scaling, because a scaling is only relevant for future gravimetric missions.

The range combinations errors of various types are propagated to the gravity field parameters considering FDDW, with the stochastic model derived from the GRACE a posteriori residuals (see Section 2.5.6). The same stochastic model is considered consistently in the computation of all gravity field model error models describing the respective noise types. This makes it is possible to compare them directly with each other.

It is assumed that no model errors are present in the GRACE a posteriori residuals used to the derive the stochastic model for the FDDW. In other words, it is assumed that the GRACE data residuals are not corrupted significantly by mis-modelled static signal, mis-modelled time-variable signal or omission signal. In view of this assumption, the error introduced by the static gravity field model has been mitigated, as discussed in Section 6.2.2.

In most plots shown in this section, the simulation results are compared with the ASDs computed from the GRACE a posteriori residuals for the complete year of 2006 (with the exception of the month of December).

The time series of GRACE a posteriori residuals is propagated to the gravity field parameters and the resulting RMS geoid height error per degree, i.e. the GRACE-derived error Degree Amplitude Spectrum (DAS), is shown. Any other month could have been considered without a significant change in the degree amplitudes presented in the figures and without any change in the conclusions drawn from this study. Alternatively, a month-long time series of synthetic GRACE a posteriori residuals could have been generated on the basis of the ASD derived from actual data, but the resulting geoid height error would not be significantly difference from the considered

one. The GRACE-derived error DAS are consistently represented by dark curves in the plots.

The validation of the noise model starts by presenting the simulation results, since the simulation procedure is already introduced in Section 4.3.2. The results pertaining to different noise types are shown in Sections 6.3.1 to 6.3.5, with a brief interpretation of the associated ASD and DAS. An integrated interpretation of the results is postponed until Section 6.3.6, where the comparison with the GRACE a posteriori residuals is discussed. In Figure 6.3.6, the results are summarised and conclusions are drawn.

6.3.1   Accelerometer noise

In the case of GRACE, the accelerometers have the noise ASD as depicted by Kim (2000, fig. 5.12). In the thesis, the accelerometer noise is assumed to be a linear function in the logarithmic domain, i.e. showing a log-linear dependency with frequency. It approximates the noise model from Kim (Figure 5.12 2000) in the frequencies between 0.1 and 10 mHz, having the amplitudes of 10^{-9} and 10^{-10} m/s^2/$\sqrt{\text{Hz}}$ respectively, see Figure 6.20. Outside this frequency band, the accelerometer noise deviates from the adopted model: it is under-estimated above 10 mHz (by at most a factor of 3 at 100 mHz, before applying the averaging filter) and over-estimated below 0.1 mHz (by not more than 40 %). In comparison to the model simulated by Frommknecht et al. (2003), the noise assumed in the thesis is under-estimated below 0.1 mHz by a factor of 2. In view of these discrepancies, the assumed log-linear function was chosen to lie in-between. Above 40 mHz, the curve slightly slopes downwards, as the result of the averaging filter $\mathbf{w}$, as already pointed out in Figure 6.6.

In view of the fact that the accelerometer noise $\delta^{(\text{acc})}$ is at least two orders of magnitude lower than the GRACE a posteriori residuals, cf. Figure 6.20a, it is not surprising that in terms of gravity field parameters, it is 140 times smaller than the actual GRACE gravity field model error, cf. Figure 6.20b. The accelerometers are sufficiently accurate to measure the non-gravitational forces acting on the GRACE satellites and it is safe to say that these errors do not contribute significantly to the gravity field model error.
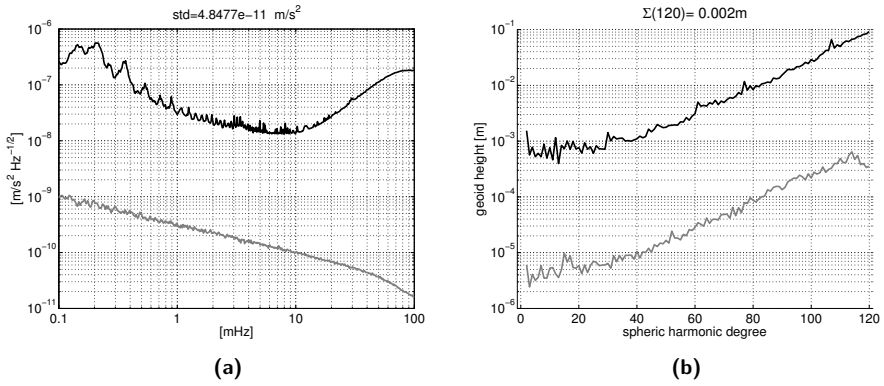
Figure 6.20 – a) ASD of simulated accelerometer noise $\delta^{(\mathrm{acc})}$, assumed to be linear in the logarithmic scale between the points $(0.1\,\mathrm{mHz}, 10^{-9}\,\mathrm{m/s}^2)$ and $(10\,\mathrm{mHz}, 10^{-10}\,\mathrm{m/s}^2)$ and valid the whole frequency domain; adapted from Kim (2000); b) DAS of the error in the gravity field parameters resulting from the propagation of the simulated accelerometer noise $\delta^{(\mathrm{acc})}$. The black curves in both plots represent the actual data and the grey curves represent the simulation results. The data period is 1 month for the simulation results. For the actual data, the data period of the ASD is the year of 2006. For the DAS, it is the month of February 2006.

6.3.2 Ranging noise

As discussed in Section 6.2.2, the ASD of the ranging sensor noise $\delta^{(\rho)}$ is assumed to decrease with frequency at a constant rate per decade, i.e. it is represented by a straight line in the logarithmic plot. Under this assumption, it is possible to find the best fit between the amplitudes above 20 mHz of the actual GRACE data noise and the ranging noise $\delta^{(R)}$ generated on the basis of the assumed ASD of $\delta^{(\rho)}$, refer to Figure 6.22. Figure 6.21 presents the analytic ASD considered in the simulation of $\delta^{(\rho)}$. The assumed ranging sensor noise ASD agrees well with the simulations of Kim and Lee (2009, Fig. 4).

The analytical double differentiation of white noise in the frequency domain results in a ASD equal to the original noise multiplied by the square of the angular frequency. At first sight, the shape of the ASD of the ranging noise is in contradiction with the analytical theory since the grey line becomes horizontal at the low frequencies. In reality, the representation of the time series in the frequency domain by the ASD is not perfect, giving rise to the low-frequency artefact. The low frequency representation of a time series is less accurate in view of the fact that it is computed on the basis of a lower number of complete cycles. This fact becomes increasingly important for the lowest frequencies, since those signals span periods close to the length of time over which the data is defined. This artefact is particularly severe for the case of the ranging noise because that time series is dominated by the high-frequencies, limiting the accuracy with which the (very low-amplitude) low frequencies coefficients are represented in the ASD. In contrast, the high frequencies are more accurately described, because there is a large number of cycles corresponding to those frequencies. In Eq. (4.43), the parameter τ accounts for the low-frequency artefact, since it influences the amplitude of $\delta^{(R)}$ at those frequencies. The analytical theory is reproduced by Eq. (4.43) if $\tau = \infty$.

When fitting a ASD of a $\delta^{(R)}$ time series resulting from double differentiation of the ranging sensor noise $\delta^{(\rho)}$, the estimated value of τ is heavily dependent on the maximum length of uninterrupted sequences in $\delta^{(R)}$. To illustrate this effect, gaps were introduced into several time series by applying an $n-\sigma$ iterative outlier removal procedure (this procedure is also exploited in Section 6.1.3), with the factor n ranging from 5 (the least data removed) to 2 (the most data removed).

In addition the time series without gaps is considered (when the factor n is equal to infinity). The resulting ASDs are shown in Figure 6.23. The empirically-estimated values of τ, determined by fitting Eq. (4.43) to the each curve, have values ranging from 5.5 s to 81.6 s. Notice that it is only possible to reproduce the theoretical ASD of double-differentiated white noise if the $\delta^{(R)}$ time series has infinite length and no gaps.
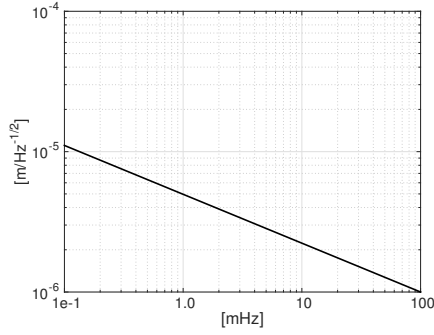
Figure 6.21 – Assumed ASD of the ranging sensor noise $\delta^{(\rho)}$; $\mathrm{std}\left(\delta^{(\rho)}\right)=8.0\times10^{-7}$ m.

(a)

(b)
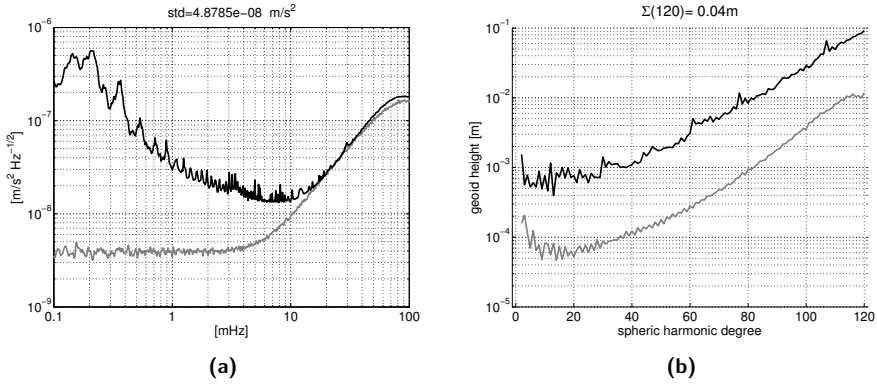
Figure 6.22 – a) ASD of simulated ranging noise $\delta^{(\mathrm{R})}$ considering $\delta^{(\rho)}$ with the ASD show in Figure 6.21; b) DAS of the error in the gravity field parameters resulting from the propagation of the simulated $\delta^{(\mathrm{R})}$. The black curves in both plots represent the actual data and the grey curves represent the simulation results. The data period is 1 month for the simulation results. For the actual data, the data period of the ASD is the year of 2006. For the DAS, it is the month of February 2006.
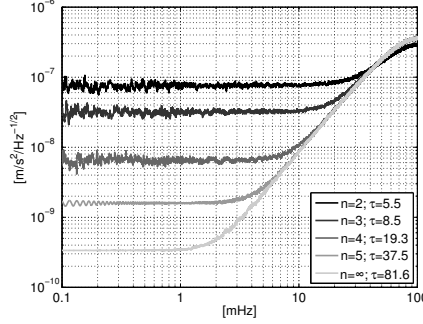
Figure 6.23 – Effect of the $n\sigma$ iterative outlier removal procedure on the low-frequency amplitude of the simulated ranging noise.

The conducted simulations do not maintain the same gap distribution as the real data. On one hand, it is not the purpose of the simulations to duplicate exactly of the errors in GRACE data but only to show that the noise model predicts those errors in a representative way. On the other hand, the low amplitude and low frequency ranging noise plays no significant role in the total error, since it is one to two orders of magnitude smaller (below 1 mHz). Any efforts to ensure the highest fidelity of the low frequency ranging noise are inconsequential to the analysis. Notice also that the ranging noise is the only noise type where changing the gap distribution could have a visible effect. All other noise types are insensitive to it, since in those cases the amplitude at the low-frequencies is higher than at the high-frequencies and, therefore, are well determined irrespective of the gap distribution.

The gravity field model error associated with the ranging noise $\delta^{(R)}$ is 7.2 times smaller than the propagated GRACE a posteriori residuals, see Figure 6.22. This result supports the pre-launch error analysis of GRACE, which only addressed errors in the accelerometers and ranging sensor (Kim, 2000) and, as a consequence, underestimated the actual errors by roughly one order of magnitude (Tapley, 2004a; Schmidt et al., 2008a).

6.3.3   Correction noise

One ingredient needed to simulate the correction noise $\delta^{(C)}$ is the ranging sensor noise $\delta^{(\rho)}$, as demonstrated by Eq. (4.55). For the conducted validation analysis, the ranging sensor noise $\delta^{(\rho)}$ is a random time series generated on the basis of the
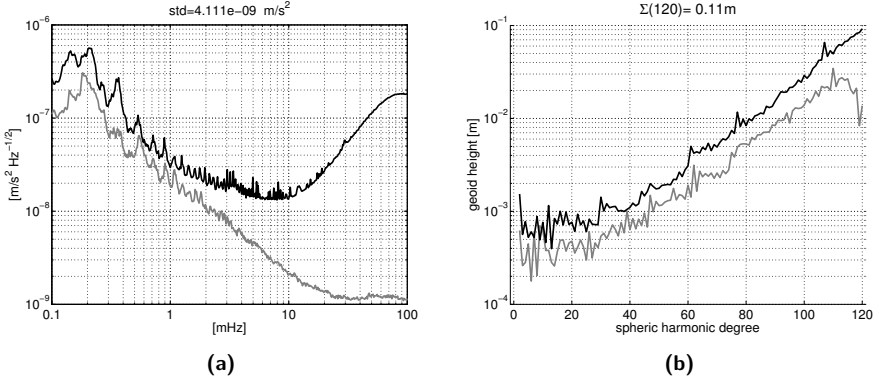
Figure 6.24 – a) ASD of simulated correction noise, $\delta^{(C)}$; b) DAS of the error in the gravity field parameters resulting from the propagation of the simulated correction noise, $\delta^{(C)}$. The black curves in both plots represent the actual data and the grey curves represent the simulation results. The data period is 1 month for the simulation results. For the actual data, the data period of the ASD is the year of 2006. For the DAS, it is the month of February 2006.

pre-defined ASD used to simulate the ranging noise, see Figure 6.21.

The second ingredient is the noise in the orbit velocity of satellite 1 relatively to satellite 2 projected onto the plane perpendicular to the LoS direction, $\delta^{(\dot{x}^{(12)\perp})}$, which is generated on the basis of the ASD shown in Figure 6.5, right-hand side, up-scaling it by a factor of three in order to reflect the current level of orbital velocity accuracy (relevant to GRACE, not the future level as depicted in that figure). Recall that Figure 6.5 shows the estimated noise in the relative positions and velocities projected on the LoS direction. The assumption is made, in view of the lack of any further information, that the ASD of the noise in the orbit velocity of satellite 1 relatively to satellite 2 projected onto the plane perpendicular to the LoS direction is equal to that of the noise in the x-component.

Figure 6.24 shows that the simulated correction noise closely matches that of Ditmar et al. (2012, Fig. 5). The main difference is a slight under-estimation of the noise below 2 mHz, but never by more than a factor of 2.4. The reason for this discrepancy is that the amplitude of the correction noise varies from month to month. Ditmar et al. (2012) considered July 2006, whereas the whole year of 2006 in considered in the thesis. With increasing frequency, the difference grows to roughly one order of magnitude at 10 mHz. These two frequencies, 2 mHz and 10 mHz,

correspond roughly to degrees 11 and 57. The explanation for the different behaviour of the ASD and DAS is found in the way how low-frequency noise propagates to the gravity field parameters, as explained in Section 2.5.6.

6.3.4   Orientation noise

The ASD of the relative orbit position noise $\boldsymbol{\delta}^{(\Delta \mathbf{x})}$ is known accurately for the x-component of the Line-of-sight Reference Frame (LoSRF), as depicted in Figure 6.5, left-hand plot, after up-scaling it by the factor of 3 to represent the current orbital positioning accuracy. As a first approximation in view of the lack of any other information, the y and z-components are assumed to have the same ASD. Figure 6.25 presents the ASD of simulated orientation noise, calculated using Eq. (4.58).

Figure 6.25b shows that orientation noise is 3 orders of magnitude smaller (a factor of 2.0×10^3) than the GRACE a posteriori residuals, i.e. not significant as was also predicted by Ditmar et al. (2012).
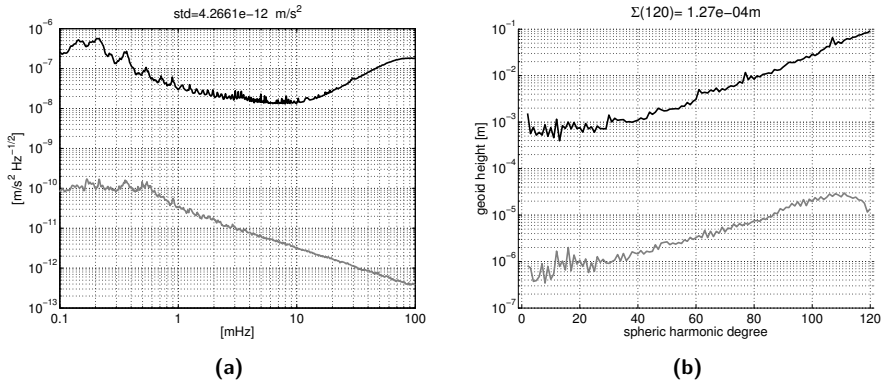
Figure 6.25 – a) ASD of simulated orientation noise with the ASD of $\delta^{(\Delta \mathbf{x})}{}_y$ and $\delta^{(\Delta \mathbf{x})}{}_z$ equal to Figure 6.5, left-hand sided plot, up-scaled by a factor of 3; b) DAS of the error in the gravity field parameters resulting from the propagation of the simulated orientation noise $\delta^{(\mathrm{L})}$. The black curves in both plots represent the actual data and the grey curves represent the simulation results. The data period is 1 month for the simulation results. For the actual data, the data period of the ASD is the year of 2006. For the DAS, it is the month of February 2006.

6.3.5 Positioning noise

In the current section, the analysis of the positioning noise $\delta^{(P)}$ is conducted. The positioning noise derived from actual GRACE data is first used to calibrate the simulated positioning noise resulting from the relative orbit position noise along the LoS direction $\delta^{(P)(\mathrm{LoS})}$. The need for this calibration is identified. The positioning noise defined in Section 4.3.3, where the orbits are adjusted by exploiting range data, is compared with $\delta^{(P)(\mathrm{LoS})}$. After the calibration, the simulated positioning noise is compared with the GRACE a posteriori residuals.

Referring to Eq. (4.59), the positioning noise requires two sets of orbits: the observed orbit position $\mathbf{x}^{(\mathrm{obs})}$ and the forecasted orbit position $\mathbf{x}^{(\mathrm{for})}$. In the presented analysis below, they are integrated on the basis of EIGEN-5C and EIGEN-CG03C, respectively. This choice of models is intended to ensure that the results are conservative. The orbit integration in uninterrupted over 6-hour arcs, as is the case in actual data processing.

Comparison with positioning noise estimated from actual GRACE data

The definition of the positioning noise is given by Eq. (4.59), ensures that there is no contribution from the discrepancy (in the relative sense) between $\mathbf{x}^{(\mathrm{obs})}$ and $\mathbf{x}^{(\mathrm{for})}$ along the LoS direction. This is accomplished by the adjustment of the forecasted orbit position considering the highly accurate range data (Eq. (4.60)). However, the difference between $\mathbf{x}^{(\mathrm{obs})}$ and $\mathbf{x}^{(\mathrm{for})}$ along the LoS direction provides important clues about the (relative) positioning noise. In Section 6.1, the relative positioning noise along the LoS direction is quantified on the basis of actual GRACE data, i.e. KBR data and PDOs used in real data processing. The results of that analysis are a suitable verification criterion for the simulation of positioning noise. With the purpose of reproducing those results in the simulation environment, the positioning noise resulting from the relative orbit position noise along the LoS direction $\delta^{(P)(\mathrm{LoS})}$ is considered, which has the corresponding point-wise quantities defined as:

$$\delta^{(P)(\mathrm{LoS})(\mathrm{pw})} = \left(\boldsymbol{\nabla} V \left(\mathbf{x}^{(\mathrm{for})}, \overline{\boldsymbol{C}}^{(\mathrm{ref})} \right) - \boldsymbol{\nabla} V \left(\mathbf{x}^{(\mathrm{for})(\mathrm{adj})(\mathrm{LoS})}, \overline{\boldsymbol{C}}^{(\mathrm{ref})} \right) \right) \cdot \mathbf{e}^{(\mathrm{LoS})(\mathrm{for})}, \qquad (6.9)$$

where the forecasted orbit positions adjusteds with range data along the LoS direction $\mathbf{x}^{(\mathrm{for})(\mathrm{adj})(\mathrm{LoS})}$ is:

$$\mathbf{x}^{(\mathrm{for})(\mathrm{adj})(\mathrm{LoS})} = \mathbf{x}^{(\mathrm{for})(\overline{12})} \pm \mathbf{e}^{(\mathrm{LoS})(\mathrm{for})} \frac{\rho^{(\mathrm{for})} + s^{(\rho)} \left(\rho^{(\mathrm{obs})} - \rho^{(\mathrm{for})} \right)}{2}. \qquad (6.10)$$

The parameter $s^{(\rho)}$ in Eq. (6.10) controls the level of adjustment. The case $s^{(\rho)} = 1$ corresponds to the nominal adjustment procedure, when the inter-satellite distances in the adjusted orbits are set equal to the true ones (i.e., taken over from the "observed" orbits). In the extreme case when $s^{(\rho)} = 0$, the adjustment vanishes, so that the output of the adjustment procedure is identical to the original unadjusted orbits.

From the simulated orbits $\mathbf{x}^{(obs)}$ and $\mathbf{x}^{(for)}$, it is possible to compute the observed and forecasted ranges. The difference between these quantities has a STD of 0.36 mm, cf. Section 7.3. Comparing this value with real-data analysis results, i.e. 2.24 mm (Section 6.1.5), it is observed that it is 6.22 times lower than expected. The observed discrepancy is attributed to way the initial state vectors of $\mathbf{x}^{(for)}$ and $\mathbf{x}^{(obs)}$ are estimated in the thesis. In both cases, i.e. for the forecasted and observed orbits, they are derived from the same Keplerian reference orbit and, as a result, there is good agreement between them. In contrast, the orbit used to derive the initial state vectors in real data processing is the KO (with the help of dynamic orbit fitting). The KO is characterised by noise with STD of a few centimetres, as determined from the optimally-fit RDO integrated on the basis of a complete force model, cf. Section 2.4. The uncertainties in the KO results in the mis-representation of the actual orbit and corresponding imperfectly-estimated initial state vectors. This mis-representation is not present in the simulated orbits; their discrepancy is solely driven by the differences in the gravity field models.

Alternatively, the error in the KO used in real data processing could be simulated by adding noise to the Keplerian reference orbit, thus producing a synthetic KO. Such orbit could then be considered when estimating the initial state vectors relevant to the integration of $\mathbf{x}^{(for)}$. However, the statistics and spectral properties of this noise are unknown, so a number of assumptions would have to be made. Such assumptions, in particular those pertaining to the spectral properties of the absolute orbit position noise, are not well supported by observations or physical evidence.

Instead, it was decided to consider the following simple scaling procedure. As discussed before, the difference between the observed and forecasted ranges resulting from the simulations is a factor of 6.22 lower than that derived from actual GRACE data. For that reason, the parameter $s^{(\rho)}$ is set equal to 6.22 in order to bring the simulation of the positioning noise up to a representative level. It might seem strange to "adjust" $\mathbf{x}^{(for)}$ to produce $\mathbf{x}^{(for)(adj)(LoS)}$ with a larger disparity relative to the observed orbit positions $\mathbf{x}^{(obs)}$. However, the purpose of the parameter $s^{(\rho)}$, in this context, is not to produce adjusted orbits but to calibrate the simulated positioning noise in order to produce a realistic level of positioning uncertainty.

As it is shown in Figure 6.26, the positioning noise simulated in this way (grey line) matches well the one derived from real data (black line), traced from Ditmar
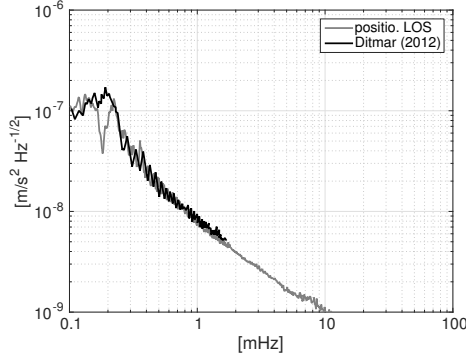
Figure 6.26 – ASD of positioning noise resulting from the relative orbit position noise along the LoS direction $\delta^{(P)(LoS)}$, considering $\mathbf{x}^{(for)}$ integrated on the basis of EIGEN-CG03C, $\rho^{(obs)}$ derived from $\mathbf{x}^{(obs)}$ integrated on the basis of EIGEN-5C (in both cases up to degree 120) and according to Eq. (6.9) and Eq. (6.10), considering $s^{(\rho)} = 6.22$. The black curve represents the actual data and the grey curve represents the simulation results. The data period is 1 month for the simulation results. For the actual data, the data period of the ASD is the year of 2006.

et al. (2012, blue curve of Fig. 5). There are a few discrepancies in narrow frequency bands, namely 0.2 mHz, which are attributed to the differences between the simulated and actual GRACE orbits.

It is also possible to apply the calibration scaling factor of 6.22 to the positioning noise resulting from the relative orbit position noise along the LoS direction $\delta^{(P)(LoS)}$ directly, instead of adjusting $\mathbf{x}^{(for)}$ to produce $\mathbf{x}^{(for)(adj)(LoS)}$, as indicated in Eq. (6.10). The small adjustments described by this calibration parameter are well within the linear regime of Eq. (4.59). This fact was tested numerically in the simulation environment (now shown).

Comparison between $\delta^{(P)(LoS)}$ and $\delta^{(P)}$

So far, the analysis of the positioning noise only considered the positioning noise resulting from the relative orbit position noise along the LoS direction $\delta^{(P)(LoS)}$. This makes the comparison of the simulations results with actual data possible and the subsequent calibration described in the previous section. Nevertheless, the positioning noise that is relevant for the simulation of future gravimetric missions mitigates the discrepancy between forecasted and observed range (cf. Eq. (4.59)
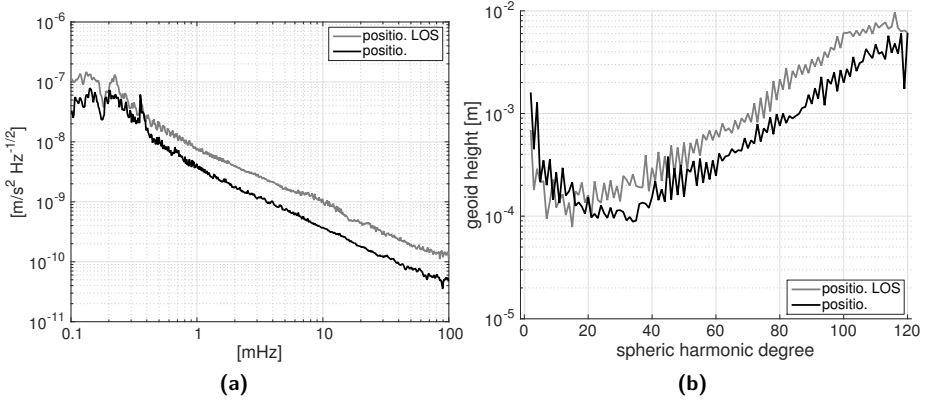
Figure 6.27 – a) ASDs of the positioning noise resulting from the relative orbit position noise along the LoS direction $\delta^{(P)(LoS)}$ and the positioning noise $\delta^{(P)}$, the former considering $s^{(\rho)} = 6.22$ and the latter up-scaled by a factor of 6.22; b) DAS of the error in the gravity field parameters resulting from the propagation of the respective variants of the simulated positioning noise. The data are sampled every 5 s. The simulation scenario is a GRACE-like formation at a polar orbit of 500 km altitude.

and Eq. (4.60)), which is represented by the symbol $\delta^{(P)}$. Note that $\delta^{(P)}$ is the sum of the contributions of the absolute positioning noise and positioning noise resulting from the relative orbit position noise perpendicular to the LoS direction, since the positioning noise resulting from the relative orbit position noise along the LoS direction is eliminated when considering range data.

The comparison between $\delta^{(P)}$ and $\delta^{(P)(LoS)}$ is shown in Figure 6.27. The calibration scale factor of 6.22 is applied to the results shown in this section.

What the simulations indicates is that, for a GRACE-type formation, the impact on the positioning noise resulting from the relative orbit position noise along the LoS direction is twice as large as the sum of the absolute positioning noise and positioning noise resulting from the relative orbit position noise perpendicular to the LoS direction. In other words, Figure 6.27 indicates that exploiting range data to adjust the forecasted orbits reduces the amplitude of the errors related to mis-positioning of the forecasted positions by half.

In terms of geoid heights per degree, the variant $\delta^{(P)(LoS)}$ of the positioning noise is lower for degree 16 and below, as shown in Figure 6.27b. This is in contradiction to the fact that the amplitude in terms of residual range combination ASD, this
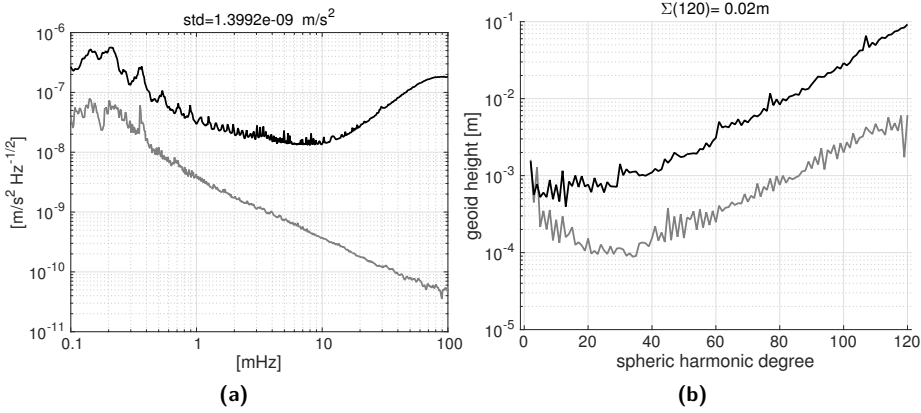
Figure 6.28 – a) ASD of the simulated positioning noise $\delta^{(P)}$, considering $\mathbf{x}^{(for)}$ integrated on the basis of EIGEN-CG03C, adjusted considering $\rho^{(obs)}$ derived from $\mathbf{x}^{(obs)}$ integrated on the basis of EIGEN-5C (in both cases up to degree 120) and according to Eq. (4.59) and Eq. (4.60), considering the calibration factor of 6.22; b) DAS of the error in the gravity field parameters resulting from the propagation of the simulated $\delta^{(P)}$. The black curves in both plots represent the actual data and the grey curves represent the simulation results. The data period is 1 month for the simulation results. For the actual data, the data period of the ASD is the year of 2006. For the DAS, it is the month of February 2006.

error is always higher (except for the small peak at 0.33 mHz), cf. Figure 6.27a. This results illustrates the different ways in which the two noise variants propagate to the gravity field parameters.

In Chapter 7 a more detailed analysis of the contributions of each component of the positioning noise is conducted.

Simulated positioning noise

The previous sections illustrated how the simulated positioning noise resulting from the relative orbit position noise along the LoS direction $\delta^{(P)(LoS)}$ and actual GRACE data are exploited to scale the positioning noise $\delta^{(P)}$ in order to make its level realistic. The current section compares the simulated $\delta^{(P)}$ with the GRACE a posteriori residuals, in the same way as it is done for the remaining noise types.

Referring to Figure 6.28, the ASD of the simulated positioning noise is 5 to 10 times less intense than the GRACE a posteriori residuals, below 1 mHz. The

difference increases above this frequency, since the amplitude of the positioning noise decreases exponentially with increasing frequencies (roughly at the rate of one order of magnitude per decade).

The propagated positioning noise $\delta^{(\mathrm{P})}$ is 18 times smaller than the gravity field model error from the GRACE a posteriori residuals. Between degrees 15 and 100, the difference to the propagated GRACE a posteriori residuals remains relatively constant, in spite of the ASDs diverging considerably in the range between 2.6 and 17 mHz, which is roughly associated with the respective degrees. The explanation for this disagreement is the same as in Section 6.3.3 for the correction noise.

6.3.6   Summary

Referring to Figure 6.29a, the advanced noise model is dominated by the ranging noise above 5 mHz and by the correction noise below 5 mHz. The positioning noise is roughly a factor of 5 smaller than the correction noise. The accelerometer noise and orientation noise are at least one to two orders of magnitude below the actual data noise. Importantly, the shape is remarkably consistent between the total error and the actual data error. The discrepancy is at most a factor of 2 at around 6 mHz, which falls within the frequency band of the actual data noise that is least understood, see Section 6.2.2.

In terms of the gravity field model error, refer to Figure 6.29b, the advanced noise model under-determines the actual data noise by a factor of 2.4, on average. This discrepancy results mainly from the lower simulated noise in the frequency band between 1 and 13mHz , relatively to the GRACE a posteriori residuals. The accelerometer noise, ranging noise and orientation noise are not significant in the total error budget. The error budget is consequentially driven by the correction noise and by the positioning noise below degree 10.

The positioning noise and the correction noise, which dominate the low frequencies at the level of range combinations, map mainly to the sectorial or nearly-sectorial coefficients over a wide degree range; there are, nevertheless, ways to mitigate it, as discussed in Section 2.5.6. The contribution of the ranging noise is not particular significant in the conducted simulations, being a factor of 7.2 lower than the GRACE a posteriori residuals. However, in view of the advances in data processing, improved POD and the possibility to co-estimate orbit parameters in the data processing, the ranging noise cannot be totally ignored.

To summarise, the STD of the range combination noise time series and the corresponding geoid heights error per degree at degrees 60 and 100 are presented in Table 6.5.
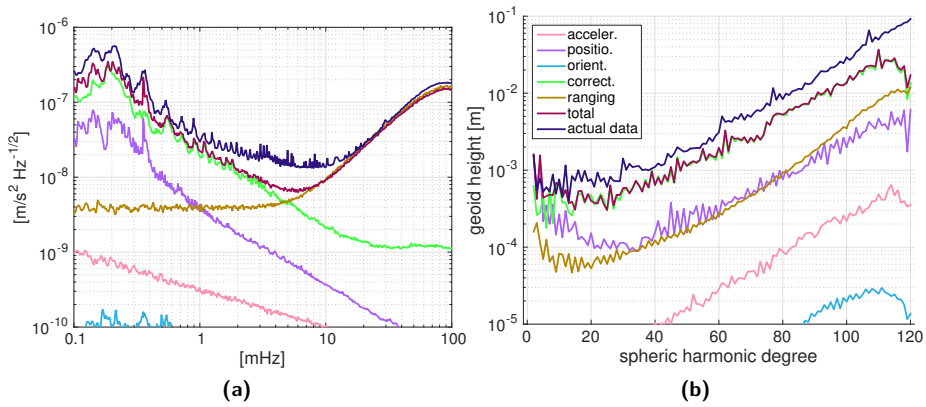
Figure 6.29 – a) ASD of simulated noise from the advanced noise model and their total contribution; b) DAS of the errors in the gravity field parameters resulting from the propagation of the corresponding simulated noise. The dark-blue curves in both plots represent the actual GRACE data noise for the year of 2006. The data period is 1 month for the simulation results. For the actual data, the data period of the ASD is the year of 2006. For the DAS, it is the month of February 2006.

noise type	symbol	STD [m/s^2]	geoid error [mm]		
			per degree		cumulative
			degree 60	degree 100	degree 120
advanced noise model					
accelerometer noise	$\delta^{(\text{acc})}$	4.8×10^{-11}	0.028	0.22	2.0
correction noise	$\delta^{(\text{C})}$	4.1×10^{-9}	1.9	14	110
orientation noise	$\delta^{(\text{L})}$	4.3×10^{-12}	3.3×10^{-3}	0.020	0.13
positioning noise	$\delta^{(\text{P})}$	1.4×10^{-9}	0.25	2.0	20
ranging noise	$\delta^{(\text{R})}$	4.9×10^{-8}	0.28	3.5	39
total		4.9×10^{-8}	1.9	14	110
actual data					
		5.6×10^{-8}	3.1	29	280

Table 6.5 – Summary of the advanced noise model, showing the STD of the time series of range combination error and the geoid height error per degree at degrees 60 and 100, as well as the cumulative geoid height error at degree 120. The statistics of the actual data noise refer to the year of 2006 in case of the STD and to the February 2006 in case of the geoid height errors.

The advanced noise model is built on a detailed modelling of all foreseeable sources of error. Not included in the numerical analyses were the model errors, since it is assumed that the GRACE data residuals are not corrupted significantly by them. This assumption is shown to be reasonable in Section 6.2.2, considering that the error introduced by the static gravity field model has been mitigated, as discussed in Section 6.2.2. The noise model is yet to include the elusive error that is dominant in the bandwidth between 1 and 13 mHz, which leads to an optimistic estimate of the errors in the error in the gravity field models. In any case, less than a factor of two is hardly enough argument to question the simulation results in the context of future gravimetric missions.

6.4   Conclusions

The current chapter groups all the analyses that exploit actual GRACE data for the purpose of estimating the accuracy of the ll-SST measurement principle.

The analysis conducted in Section 6.1 produces position and velocity residuals of the considered KOs and PDOs, which are a realistic representation of the relative position and velocity errors, projected onto the LoS direction. The ASDs of these errors are estimated and exploited in order to model more accurately the errors in future ll-SST gravimetric data, refer to Figure 6.5. It is assumed that, if all predicted future GNSS systems as well as the additional frequency measurements are exploited, the accuracy of the KOs and PDOs of future gravimetric missions will be a factor of 3 higher. The reasoning behind this assumptions is presented in Section 6.1.7.

In Section 6.2, spectral analysis of data noise is performed in the context of gravity field recovery from ranging data acquired by the satellite gravimetric mission GRACE. The motivation of the study is to understand the primary contributions of the error budget of real GRACE data. The analysed noise realisations are produced as the difference between actual GRACE observations and predictions based on state-of-the-art force models. It is demonstrated that the major contributors to the noise budget at high frequencies (above 9 mHz) are: (i) ranging sensor noise and (ii) limited knowledge of the Earth's static gravitational field at high degrees. Importantly, it is shown that updating the model of the static field on the basis of the available data must be performed with caution, as the result may not be physical due to a non-unique recovery of high-degree coefficients. The source of noise in the range of intermediate frequencies $(1-9\,\mathrm{mHz})$, which is particularly critical for an accurate gravitational field recovery, is still not fully understood. It is shown, however, that it cannot be explained by inaccuracies in background models of mass transport. The conducted analysis also leads to a more general recommendation: it is worth to design GRACE follow-on mission in such a way that the non-uniqueness of gravity field recovery is minimised. In particular, an isotropic sensitivity of the future mission would be a highly desirable feature, as it will reduce static field signals that cannot be uniquely explained by the models produced on the basis of the collected data. Another potential benefit of such a mission design is that it will presumably reduce the impact of data noise in general. Consequentially, lower noise in gravity field models can be achieved compared to the GRACE-type design, even if noise in the Level-1B data is similar.

Section 6.3 analyses the advanced noise model of ll-SST data, by comparing the simulation of the errors in the data of a GRACE-like formation with the GRACE a posteriori residuals. The comparison is made in terms of range combination ASD and geoid height per degree. In this way, a noise model is established that realistically describes the accuracy of GRACE data. The accelerometer noise and orientation noise are not significant in the total error budget. The error budget, as derived from the analysis, is driven by the correction noise and positioning noise (the latter exclusively below degree 10). However, as explained in Section 2.5.6, these errors

are not dominant in actual data processing because appropriate measures are taken to surpress it by high-pass filtering the data. The high-pass filtering procedure was not considered in Section 6.3 because the purpose of the conducted analysis is to determine the effect of the various noise sources and not to find ways to mitigate them (refer to the discussion in Section 2.5.6). There is also a good match between the sum of the noise types simulated on the basis of the advanced noise model and the actual GRACE data errors.

The validation has demonstrated that the simulated noise is under-determined by a factor of 2.4 relatively to the actual data noise. It would be instructive to clarify the exact meaning of this number. This discrepancy results from the fact that the noise dominant in the frequency band between 1 and 13 mHz has not been modelled properly because its cause has not been fully identified.

In Chapter 8, the advanced model is applied to predict errors in the measurements to be collected by future satellite gravimetric missions. In those chapter, the assumptions regarding orbit position and velocity errors (already discussed in Section 6.1.7), as well as the amplitudes of accelerometer noise and ranging sensor noise are modified to reflect the corresponding (expected) accuracy improvements (cf. Section 8.1.4).

Positioning noise

7

The current chapter presents an in-depth analysis of the positioning noise. The purpose of this analysis is to gain a deeper understanding on this noise, so that the results of the simulations in the context of future gravimetric formations (discussed in Chapter 8) can be better interpreted. The simulation of positioning noise is done for the cartwheel, pendulum and trailing formations.

One important consideration in the current chapter is that the positioning noise (which is defined at the level of range combinations) is best described as the combination of its relative and absolute components. In this way, these components can be related to the equivalent components in terms of orbital positioning noise.

The formations that are relevant here are presented and motivated in Section 7.1. Section 7.2 discusses the simulation of the orbits. Section 7.3 looks into the relative and absolute orbit position noise given by the difference between the positions of two sets of orbits integrated from different force models. The analytical derivation of the components of the positioning noise is presented in Section 7.4, so that their amplitude is properly predicted. Finally, in Section 7.5, the simulation of individual components of the positioning noise is presented and discussed.

7.1 Formation scenarios

The formations considered in the numerical study are the trailing, pendulum and cartwheel formations. These formations are introduced in Section 3.3, Section 3.4 and Section 3.5, respectively. The motivation for choosing this set of formations is mostly driven by the dominant orientation of the Line of Sight (LoS) vector, relatively to the Local Horizontally-aligned Reference Frame (LHRF). Given the

polar orbits of the formations, the LoS vector is mainly aligned with the North-South direction in the trailing formation, with the East-West direction in the pendulum formation and contains a radial component in the cartwheel formation (except at the vicinity of the poles). This means that the orientation of the LoS vector is different for each formation and perpendicular to those of the other formations. The only exception is an overlap of the cartwheel and trailing formations in what regards the alignment of the LoS vector along the North-South direction, particularly near the poles. This is a requirement of orbital dynamics that cannot be circumvented. Concerning the pendulum formation, there is a choice to include an along-track offset (y_{off} in Table 7.1), but that would make the observations non-orthogonal to the other formations. In the current set-up of the trailing and pendulum formations, it is possible to quantify the contribution of collecting gravimetric data sampled along the North-South and East-West directions separately, which would not be possible if the pendulum formation's y_{off} were different from zero.

The formation parameters relevant for the conducted numerical analysis are presented in Table 7.1 (refer to Section 3.8.2 and Figure 3.8). These parameters are expressed as functions of the maximum range $\rho^{(max)}$, which is 200 km in the analysis presented in this chapter. The maximum range is approximately equal to the amplitude of the cross-track motion in the pendulum formation (the B_0 parameter is the half cross-track amplitude), the relative distance between the satellites in the trailing formation and twice the maximum altitude difference in the cartwheel formation (the A_0 parameter is the half maximum altitude difference).

formation parameter	cartwheel	pendulum	trailing
A_0	$\rho^{(max)}/4$	0	0
B_0	0	$\rho^{(max)}/2$	0
α	0°, 180	0	N/A
β	0	0°, 180°	N/A
y_{off}	0	0	$\rho^{(max)}$

Table 7.1 – Formation parameters of the cartwheel, pendulum and trailing formations, as function of the maximum range, $\rho^{(max)}$. The meaning of the formation parameters is explained in Section 3.8.2.

The phase angles α and β define the initial position of the satellites in the ellipse describing the relative motion. In case of the pendulum and cartwheel formations, these angles are opposite in phase. In case of the trailing formation, there is no (significant) relative motion and the phase angles are not relevant.

To simplify referring to a particular formation, the cartwheel, pendulum and trailing formations are identified by the letters **k**, **p** and **t**, respectively. To refer to

a particular formation with a particular $\rho^{(\text{max})}$, the letter identifying the formation is followed by $\rho^{(\text{max})}$, e.g. **k200** or **p200** (in Chapter 8, other values of $\rho^{(\text{max})}$ are considered and this notation is maintained).

7.2 Orbit simulation

The numerical analysis makes use of the Keplerian reference orbits and orbits simulated on the basis of a realistic gravity field model, called *Modelled orbits*, according to the definitions introduced in Section 3.8.5. The Keplerian reference orbits are exploited to derive the initial state vectors from which the Modelled orbits are integrated under a realistic force model.

The simulations span a period of one month, with a sampling rate of 5 seconds. In case of the trailing and pendulum formations, the mean orbital elements are those of a polar circular orbit at 500 km altitude above the Earth's equator; in case of the cartwheel formation, the mean orbit is at 550 km altitude, so that there is agreement between all formations regarding the minimum altitude. This altitude was chosen because it is a proven compromise, as demonstrated by Gravity Recovery And Climate Experiment (GRACE), between the increased signal strength at lower altitudes and a long mission lifetime at higher altitudes. In any case, the value of this parameter is relatively arbitrary when comparing the results of different formations, since the increase in the signal amplitude associated with a lower orbital altitude would be the same for all formations.

7.2.1 Keplerian reference orbits

For the conducted analysis, the relevant sets of formation parameters are presented in Table 7.1. These parameters permit the orbital elements of the formation satellites to be computed, refer to Section 3.8.4. The resulting orbital elements are reported in Table 7.2.

7.2.2 Modelled orbits

The statistics about the length and attitude of the LoS vector for the case of the Modelled orbits are now presented.

In Table 7.3, the statistics of the ranges are shown. From this table, it is seen that the actual maximum range slightly differs from designated maximum ranges, equal to 200 km. The reason is that the procedure used to derive the Keplerian reference orbit, described in Section 3.8, is accurate for small maximum ranges, where the Hill

formation	sat. nr	h_{min} [km]	h_{max} [km]	a [km]	e []	i [°]	Ω [°]	ω [°]	M [°]
k200	1	491	588	6918.14	0.007	90	0	180.00	182.94
k200	2			6918.13				352.30	10.75
p200	1	500	500	6878.14	1.2×10^{-10}	90	359.17	82.1	244.87
p200	2						0.83		
t200	1	500	500	6878.14	1.2×10^{-10}	90	0	82.9	262.16
t200	2							89.5	257.16

Table 7.2 – Orbital elements of the Keplerian reference orbits. The minimum altitude h_{min} and maximum altitude h_{max} are computed considering the equatorial radius of 6378.137 km.

equations, Eq. (3.4), are valid. It turns out that although the exploited procedure is also applicable to larger maximum ranges, at least up to 200 km (Table 8.3 demonstrates that this is true up to 1000 km), the resulting relative motion is not exactly the same as the one dictated by the original set of formation parameters. Fortunately, the discrepancy is limited to a few percent. Noteworthy is that the minimum range for the pendulum formation is of a few meters, which occurs over the poles, when the orbits of the two satellites cross each other. This result is expected, since the analytical Keplerian reference orbits predict zero range at the poles. It also confirms that the Modelled orbits remain close to the idealization represented by the Keplerian reference orbits, in spite of the aspherical gravity field model used in the integration of those orbits.

orbit	min(ρ)	mean(ρ)	max(ρ)	std(ρ)
k200	97.0	150.0	207.0	34.3
p200	1.9×10^{-3}	127.3	200.0	61.6
t200	199.8	199.9	200.1	6.9×10^{-2}

Table 7.3 – Statistics of the ranges (in km).

In Table 7.4 and Table 7.5, the statistics of the inertial attitude are shown. The first table refers to inertial elevation, defined as the angle between the LoS vector and the Earth's equatorial plane. The latter table shows the inertial azimuth angle, the angle between the LoS vector and the (mean) orbital plane. These tables show how the orientation of the LoS vector differs between the formations.

In the pendulum formation, the LoS vector has zero inertial elevation most of the time, as shown by the low values of the mean and the standard deviation in Table 7.4. Consequentially, the LoS vector is nearly-parallel to the equatorial plane. The inertial

orbit	min(Elev)	mean(Elev)	max(Elev)	std(Elev)
k200	-19.0	3.9	26.7	13.8
p200	-7.8×10^{-1}	-6.8×10^{-5}	7.7×10^{-1}	2.7×10^{-2}
t200	-90.0	-5.1×10^{-3}	90.0	51.9

Table 7.4 – Statistics of the inertial elevation in degrees. The inertial elevation is the angle between the LoS vector and the Earth's equatorial plane.

orbit	min(Azim)	mean(Azim)	max(Azim)	std(abs(Azim))
k200	-4.6×10^{-3}	-2.5×10^{-6}	4.6×10^{-3}	7.2×10^{-4}
p200	-90.0	-1.9×10^{-2}	90.0	1.2
t200	-6.8×10^{-3}	-5.7×10^{-8}	1.3×10^{-2}	1.2×10^{-4}

Table 7.5 – Statistics of the inertial azimuth in degrees. The inertial azimuth is the angle between the LoS vector and the (mean) orbital plane.

elevation of the LoS vector of the trailing formation changes between -90 and 90°, since the LoS vector continuously rotates in inertial space. The variations of the LoS vector inertial elevation of the cartwheel formation are much lower, between -19 and 27°. The elevation angle oscillates between these extreme values every half orbital period.

The small values of the mean and the standard deviation of the inertial azimuth (Table 7.5) for the cartwheel and trailing formations confirm that the LoS vector remains parallel to the orbital plane. In case of the pendulum formation, the standard deviation of the absolute azimuth is close to 1°, in spite of large maximum and minimum values, ±90°. This means that, in combination with the nearly-constant zero inertial elevation, the transition between the extreme values occurs rapidly (and at the poles). This happens in such a way that the LoS vector is most of the time (nearly) orthogonal to the mean orbital plane.

7.3   Orbital noise

The current section explains how the orbit errors are simulated. These quantities are defined at the level of orbit position errors, unlike the positioning noise, which is defined at the level of range combinations.

In the context of the simplistic noise model, these errors are regarded as instrument errors and, therefore, added to the observations, cf. Table 4.1. On the other hand, the positioning noise is defined as errors in the forecasted quantities and, for that

reason, the orbits corrupted by noise are regarded as the forecasted orbits, while the original noiseless orbits are regarded as the observed orbits.

In the context of the positioning noise, the observed and forecasted orbits are integrated explicitly from different gravity field models. In Section 4.3.3, relative to the simplistic noise model, Eq. (4.46) and Eq. (4.49) demonstrate how the relative and absolute orbit position errors, respectively, are added to a simulated orbit. In that case, the errors were generated independently from the orbits and the noisy orbits were computed as the sum of noiseless orbits and orbit errors. In case of the simulation of the orbits errors relevant to the positioning noise, the orbits are already available and the orbit errors are computed from them.

The relative orbit position noise $\boldsymbol{\delta}^{(\Delta\mathbf{x})}$ and absolute orbit position noise $\boldsymbol{\delta}^{(\mathbf{x})}$ can be determined from the observed and forecasted orbits considering the following operations:

$$\boldsymbol{\delta}^{(\Delta\mathbf{x})} = \mathbf{d}^{(\text{obs})} - \mathbf{d}^{(\text{for})}, \quad \text{with} \quad \mathbf{d} = \mathbf{x}^{(1)} - \mathbf{x}^{(2)}, \tag{7.1}$$

and

$$\boldsymbol{\delta}^{(\mathbf{x})} = \mathbf{x}^{(\text{obs})(\overline{12})} - \mathbf{x}^{(\text{for})(\overline{12})}, \quad \text{with} \quad \mathbf{x}^{(\overline{12})} = \left(\mathbf{x}^{(1)} + \mathbf{x}^{(2)}\right)/2, \tag{7.2}$$

respectively.

The noise amplitudes given by Eq. (7.1) and Eq. (7.2) can only be derived from simulated orbits. From actual data, a possibility is to compute the relative orbit position noise along the LoS direction $\delta^{(\Delta\mathbf{x})(\text{LoS})}$ from the Purely Dynamic Orbits (PDOs), as extensively described in Section 6.1 and Section 6.3.5. The same can be said about the Kinematic Orbits (KOs), although these are observed orbits and not forecasted orbits, as is the case with PDOs, relevant to the current section. Another source for this information, which follows the same approach of comparing K-Band Ranging (KBR) data with orbit differences, is briefly mentioned in Ditmar et al. (2012, Section 3.2).

Figure 7.1 shows the Amplitude Spectral Densitys (ASDs) of the relative and absolute orbit position noise (column-wise), for the cartwheel, pendulum and trailing formations (row-wise), estimated as the difference between the orbits integrated on the basis of the EIGEN-5C and EIGEN-CG03C gravity field models. The plots show the orbit differences in the Line-of-sight Reference Frame (LoSRF), i.e. the x-component is always aligned with the LoS direction. Table 7.6 summarizes the corresponding values of Root Mean Squared (RMS), as well as $\delta^{(\Delta\mathbf{x})(\text{LoS})}$ derived from actual data of the GRACE satellites (relevant only to the trailing formation).

The second column of Figure 7.1 shows the ASDs of the components of the absolute orbit position noise. Its shape is fairly consistent for all components and
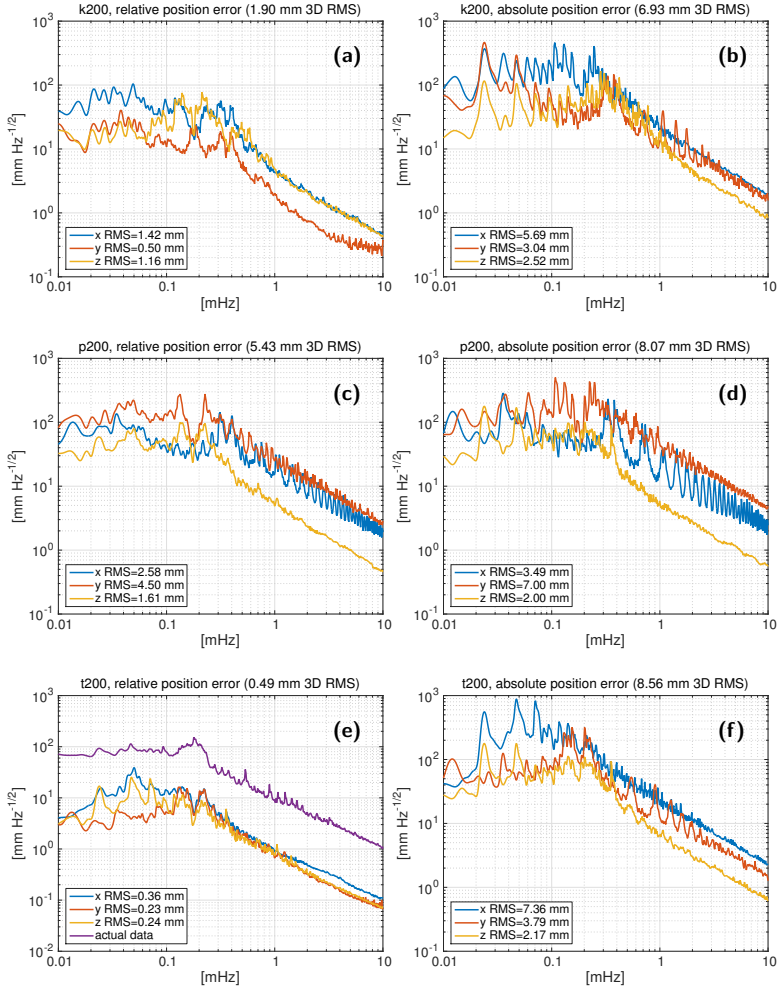
Figure 7.1 – ASD of the relative (first column) and absolute (second column) orbit position errors in the LoSRF (i.e. $\delta_x^{(\Delta \mathbf{x})} = \delta^{(\Delta \mathbf{x})(\mathrm{LoS})}$), for the cartwheel (top row), pendulum (middle row) and trailing (bottom row) formations. The orbit errors are simulated as the difference between two sets of orbits integrated on the basis of the EIGEN-5C and EIGEN-CG03C gravity field models. The relative orbit position noise curve labelled *actual data* in Figure (e) refers to the difference between the range derived from actual KBR data and the PDO of the GRACE satellites (cf. Section 6.1).

	simulated data	
	$\delta^{(\Delta \mathbf{x})(\mathrm{LoS})}$ RMS [mm]	$\boldsymbol{\delta}^{(\mathbf{x})}$ 3D RMS [mm]
cartwheel	1.42	6.93
pendulum	2.58	8.07
trailing	0.36	8.56

	actual data
	$\delta^{(\Delta \mathbf{x})(\mathrm{LoS})}$ RMS [mm]
trailing, Section 6.1	2.24
trailing, Ditmar et al. (2012)	3.7

Table 7.6 – RMS of the absolute orbit position noise $\delta^{(\mathbf{x})}$ and the relative orbit position noise along the LoS direction $\delta^{(\Delta \mathbf{x})(\mathrm{LoS})}$ in the LoSRF , simulated as the difference between two sets of orbits integrated on the basis of the EIGEN-5C and EIGEN-CG03C gravity field models (top). RMS of the difference between the ranges derived from actual KBR data and the PDOs of the GRACE satellites, according to Section 6.1 and Ditmar et al. (2012) (bottom).

all formations: large amplitude below 0.2 mHz and logarithmic decrease above this frequency. Among the components of the absolute orbit position noise, the x-component is the one with the largest amplitude for the cartwheel and trailing formations; for the pendulum formation, the y-component is the component with the largest amplitude. The three-dimensional (3D) RMS of the absolute orbit position noise is similar for all formations, between 7 and 8.5 mm, see Table 7.6. The lowest value is for the cartwheel formation, which is caused by the higher average altitude of the satellites for this formation (resulting from a larger value of eccentricity e, cf. Table 7.2).

Referring to the first column of Figure 7.1, all components of the relative orbit position noise are of comparable magnitude for all formations, particularly above 0.2 mHz. This observation supports the assumption that the components of the relative orbit position noise orthogonal to the LoS vector can also be estimated with the help of range data (see Section 6.1).

In spite of a similar amplitude of the components of the relative orbit position noise, the following exceptions are noteworthy: i) the y-component of the relative orbit position noise of the cartwheel formation is of lower amplitude and ii) the x-component and y-component of the relative orbit position noise of the pendulum

formation are of larger amplitude in comparison to the z-component. This seems to suggest that the directions with lowest relative motion amplitude, i.e. the y-component in case of the cartwheel formation and the z-component in case of the pendulum formation, are the ones least corrupted by relative orbit position noise. The fact that the trailing formation shows similar amplitude for all components supports this argument; recall that the relative motion in case of the trailing formation is small along all directions. This argument is further supported by the 3D amplitude of the relative orbit position noise between formations, refer to Table 7.6: the noise for the trailing formation is seven times lower than for the pendulum formation and 4 times lower than for the cartwheel formation.

As a consequence of the exceptions discussed above, it can be expected that the assumption of equal amplitude of the relative orbit position noise along all orthogonal directions is conservative for the y-component of the cartwheel formation and for the z-component of the pendulum formation. Notwithstanding, exploiting range data (from hypothetical future pendulum and/or cartwheel formations) to estimate the relative orbit position noise and assuming equal amplitude along all directions is the only accurate option. Figure 7.1 shows that incurred over-estimation is, at most, a factor of three, which is acceptable in the context of the simulation of future gravimetric missions.

As discussed in Section 6.3.5, Figure 7.1e illustrates that the x-component of the relative orbit position noise derived from actual data has a ASD with a similar shape to the relative orbit position noise derived from the simulated orbits, with some exceptions below 0.2 mHz.

7.3.1 Calibration of the positioning noise

This section discusses the calibration procedure that is conducted in the simulation of the positioning noise. A similar issue was discussed in Section 6.3.5, where the need for the calibration procedure is identified when the simulation results are confronted with actual GRACE data. In that section, the focus was exclusively to the trailing formation. In the current section, the calibration of the positioning noise is put in the context of the pendulum and cartwheel formations.

The positioning noise is calibrated in Section 6.3.5 so that influence of the imperfectly-estimated initial state vectors is incorporated into the simulation environment. Figure 7.1e and Table 7.6 motivate this calibration procedure, since the RMS of the relative orbit position noise derived from real data is 2.24 mm, while the relative orbit position noise computed from the simulated orbits is 0.36 mm. Considering these values for RMS, the resulting scale factor is 6.22.

The RMS of the relative orbit position noise derived from real data is 2.24 mm in case of the analysis conducted in Section 6.1 and 3.7 mm in case of Ditmar et al. (2012). The discrepancy between these two values, which were obtained from the same orbits, is attributed to the outlier removal scheme, which is much stricter in Section 6.1 (recall that over 50 % of the data is discarded, cf. Table 6.1). The RMS derived in Section 6.1 is favoured since it is most likely less affected by the imperfectly-estimated initial state vectors, as discussed in Section 6.1.3.

As mentioned in Section 6.3.5, the calibration is done at the level of the residual range combinations, not at the level of the relative orbit position noise. In this way, both the relative orbit position noise and the absolute orbit position noise are effectively calibrated. If the calibration factor of 6.22 is applied to the simulated 3D error amplitudes shown in Table 7.6, the absolute orbit position noise amplitude becomes 5.3 cm. This value is in agreement with the 3D RMS values reported in literature (albeit in a conservative way), cf. Table 2.5. Consequently, imperfectly-estimated initial state vectors affect both relative and absolute components of the orbit position noise.

In the context of the cartwheel and pendulum formations, there are two possibilities for the calibration of the simulated positioning noise:

1. Consider the RMS values of the relative orbit position noise along the LoS direction $\delta^{(\Delta \mathbf{x})(\mathrm{LoS})}$ of each formation and derive from them individual calibration factors;
2. Consider the calibration factor derived for the trailing formation to be common to all formations.

The first option assumes that the actual relative orbit position noise estimated on the basis of real GRACE data (with amplitude 2.24 mm) is independent of the formation geometry, while the second option assumes that the amplitudes of the simulated relative orbit position noise are proportional to the real ones. Unfortunately, there is no range data from a pendulum of cartwheel formation to determine which assumption is correct. Nevertheless, there are other clues which make it possible to make an educated guess. The first option would mean that the calibration factor for the pendulum formation is close to unity. If that is the case, the absolute orbit position noise would remain at sub-centimetre level for this formation, which is unrealistic. Furthermore, the RMS of the absolute orbit position noise is comparable across all formations; this is expected since the common differences introduced by different force models on the orbits integrated with the same initial state vector is not sensitive to the formation geometry. These arguments support the second option as the most likely to be realistic. Consequently, the scale factor of 6.22 is applied

consistently in the simulation of positioning noise of all formations. Note that this scale factor addressed the issue of imperfectly-estimated initial state vectors; there is an additional scale factor of $1/3$, which predicts the improvement of the accuracy of Global Navigation Satellite Systems (GNSSs), processing strategies and force models, as discussed in Section 6.1.7. The latter scale factor concerns future gravimetric missions, to be addressed in Chapter 8, and is not relevant in the current chapter.

7.4 Analytical derivation of the components of the positioning noise

The current section derives analytical representations, particular to the trailing, cartwheel and pendulum formations, of the relative and absolute positioning noise. For the sake of simplicity, the averaging filter $\mathbf{w}$ described in Eq. (4.29) is ignored, i.e. the discrepancy between point-wise and averaged quantities is assumed to be negligible. This assumption is supported by Figure 6.6, which shows that the point-wise and averaged accelerometer noise only differs at the highest frequencies by no more than a factor of two. Starting from Eq. (4.59), the aforementioned simplification allows the point-wise positioning noise $\boldsymbol{\delta}^{(\mathrm{P})(\mathrm{pw})}$ to be projected onto the forecasted unit vector defining the LoS direction $\mathbf{e}^{(\mathrm{LoS})(\mathrm{for})}$ directly:

$$\delta^{(\mathrm{P})(\mathrm{pw})} = \boldsymbol{\delta}^{(\mathrm{P})(\mathrm{pw})} \cdot \mathbf{e}^{(\mathrm{LoS})(\mathrm{for})} = \left(\boldsymbol{\nabla} V\left(\mathbf{x}^{(\mathrm{obs})}, \overline{\boldsymbol{C}}^{(\mathrm{ref})} \right) - \boldsymbol{\nabla} V\left(\mathbf{x}^{(\mathrm{for})(\mathrm{adj})}, \overline{\boldsymbol{C}}^{(\mathrm{ref})} \right) \right) \cdot \mathbf{e}^{(\mathrm{LoS})(\mathrm{for})}.$$

Let $\mathbf{G}$ be the gravity gradient tensor computed on the basis of $\overline{\boldsymbol{C}}^{(\mathrm{ref})}$, which mainly describes features at spatial scales larger that the length of the LoS vector $\mathbf{d}$, and $\mathbf{G}(\mathbf{x})$ represents this tensor evaluated at the orbit positions $\mathbf{x}$. Under these assumptions, $\boldsymbol{\nabla} V(\mathbf{x}) \approx \mathbf{G}(\mathbf{x})\mathbf{d}$, so that:

$$\delta^{(\mathrm{P})(\mathrm{pw})} \approx \left(\mathbf{G}\left(\mathbf{x}^{(\mathrm{obs})(\overline{12})} \right) \mathbf{d}^{(\mathrm{obs})} - \mathbf{G}\left(\mathbf{x}^{(\mathrm{for})(\overline{12})} \right) \mathbf{d}^{(\mathrm{for})(\mathrm{adj})} \right) \cdot \mathbf{e}^{(\mathrm{LoS})(\mathrm{for})}. \tag{7.3}$$

7.4.1 Relative positioning noise

In the context of deriving the contribution of the relative point-wise positioning noise, it is assumed that $\mathbf{G}\left(\mathbf{x}^{(\mathrm{for})(\overline{12})} \right) \approx \mathbf{G}\left(\mathbf{x}^{(\mathrm{obs})(\overline{12})} \right) \equiv \mathbf{G}\left(\mathbf{x}^{(\overline{12})} \right)$. From Eq. (7.3), this assumption means that the relative point-wise positioning noise is:

$$\delta^{(\mathrm{P})(\mathrm{pw})(\mathrm{rel})} \approx \left(\mathbf{G}\left(\mathbf{x}^{(\overline{12})} \right) \left(\mathbf{d}^{(\mathrm{obs})} - \mathbf{d}^{(\mathrm{for})(\mathrm{adj})} \right) \right) \cdot \mathbf{e}^{(\mathrm{LoS})(\mathrm{for})}. \tag{7.4}$$

The relative point-wise positioning noise is now divided into the relative point-wise positioning noise resulting from the relative orbit position noise perpendicular to the LoS direction $\delta^{(\mathrm{P})(\mathrm{pw})(\mathrm{rel})\perp}$ and relative point-wise positioning noise resulting from the relative orbit position noise parallel to the LoS direction $\delta^{(\mathrm{P})(\mathrm{pw})(\mathrm{rel})\|}$. The contribution of $\delta^{(\mathrm{P})(\mathrm{pw})(\mathrm{rel})\|}$ could be ignored since the range data makes it possible to reduce the orbit errors several orders of magnitude (from mm to μm in case of GRACE). For completeness, this terms is not ignored in the derivation below.

In the case of $\delta^{(\mathrm{P})(\mathrm{pw})(\mathrm{rel})\perp}$, recalling that the adjustment given by Eq. (4.60) ensures that $\left|\mathbf{d}^{(\mathrm{obs})}\right| = \left|\mathbf{d}^{(\mathrm{for})\left(\mathrm{adj}\right)}\right| = \rho$:

$$\delta^{(\mathrm{P})(\mathrm{pw})(\mathrm{rel})\perp} \approx \rho\left(\mathbf{G}\left(\mathbf{x}^{(\overline{12})}\right)\left(\mathbf{e}^{(\mathrm{LoS})(\mathrm{obs})} - \mathbf{e}^{(\mathrm{LoS})(\mathrm{for})\left(\mathrm{adj}\right)}\right)\right) \cdot \mathbf{e}^{(\mathrm{LoS})(\mathrm{for})}.$$

From Eq. (D.4), the difference between observed and forecasted unit vectors defining the LoS direction is the noise in the orientation of the LoS vector $\boldsymbol{\delta}^{(\mathrm{LoS})}$, which is a function of the relative orbit position noise perpendicular to the LoS direction $\boldsymbol{\delta}^{(\Delta\mathbf{x})\perp}$:

$$\mathbf{e}^{(\mathrm{LoS})(\mathrm{obs})} - \mathbf{e}^{(\mathrm{LoS})(\mathrm{for})\left(\mathrm{adj}\right)} = \boldsymbol{\delta}^{(\mathrm{LoS})} = \frac{\boldsymbol{\delta}^{(\Delta\mathbf{x})\perp}}{\rho};$$

so that:

$$\delta^{(\mathrm{P})(\mathrm{pw})(\mathrm{rel})\perp} \approx \left(\mathbf{G}\left(\mathbf{x}^{(\overline{12})}\right)\boldsymbol{\delta}^{(\Delta\mathbf{x})\perp}\right) \cdot \mathbf{e}^{(\mathrm{LoS})}. \tag{7.5}$$

In the case of $\delta^{(\mathrm{P})(\mathrm{pw})(\mathrm{rel})\|}$, the conditions are that $\mathbf{e}^{(\mathrm{LoS})(\mathrm{obs})} = \mathbf{e}^{(\mathrm{LoS})(\mathrm{for})\left(\mathrm{adj}\right)} \equiv \mathbf{e}^{(\mathrm{LoS})}$ and $\rho^{(\mathrm{obs})} - \rho^{(\mathrm{for})} \equiv \delta^{(\Delta\mathbf{x})(\mathrm{LoS})}$. Under these conditions:

$$\delta^{(\mathrm{P})(\mathrm{pw})(\mathrm{rel})\|} \approx \delta^{(\Delta\mathbf{x})(\mathrm{LoS})}\left(\mathbf{G}\left(\mathbf{x}^{(\overline{12})}\right)\mathbf{e}^{(\mathrm{LoS})}\right) \cdot \mathbf{e}^{(\mathrm{LoS})}. \tag{7.6}$$

7.4.2 Absolute positioning noise

In case of the absolute point-wise positioning noise $\delta^{(\mathrm{P})(\mathrm{pw})(\mathrm{abs})}$, $\mathbf{d}^{(\mathrm{obs})} = \mathbf{d}^{(\mathrm{for})\left(\mathrm{adj}\right)} = \mathbf{d}$, so that Eq. (7.3) simplifies to:

$$\delta^{(\mathrm{P})(\mathrm{pw})(\mathrm{abs})} \approx \left(\mathbf{G}\left(\mathbf{x}^{(\mathrm{obs})(\overline{12})}\right) - \mathbf{G}\left(\mathbf{x}^{(\mathrm{for})(\overline{12})}\right)\right)\mathbf{d} \cdot \mathbf{e}^{(\mathrm{LoS})}.$$

Since $\mathbf{d} = \rho\mathbf{e}^{(\mathrm{LoS})}$:

$$\delta^{(\mathrm{P})(\mathrm{pw})(\mathrm{abs})} \approx \rho\left(\left(\mathbf{G}\left(\mathbf{x}^{(\mathrm{obs})(\overline{12})}\right) - \mathbf{G}\left(\mathbf{x}^{(\mathrm{for})(\overline{12})}\right)\right)\mathbf{e}^{(\mathrm{LoS})}\right) \cdot \mathbf{e}^{(\mathrm{LoS})}.$$

For brevity and only in the context of the absolute positioning noise, the equation above henceforth represented as:

$$\delta^{(P)(pw)(abs)} \approx \rho \left(\left(\mathbf{G}^{(obs)} - \mathbf{G}^{(for)} \right) \mathbf{e}^{(LoS)} \right) \cdot \mathbf{e}^{(LoS)}. \tag{7.7}$$

7.4.3 Positioning noise magnitudes

In the Local Orbital Reference Frame (LORF) and for the formations considered in the thesis, it holds that:

for the trailing formation, $\mathbf{e}^{(LoS)} \approx [1,0,0]^T$, i.e. the unit vector defining the LoS direction is oriented mainly in the along-track direction, which means that:

- $\boldsymbol{\delta}^{(\Delta\mathbf{x})\perp} \approx \left[0, \delta_y^{(\Delta\mathbf{x})\perp}, \delta_z^{(\Delta\mathbf{x})\perp} \right]^T$;
- $\mathbf{Ge}^{(LoS)} \approx \left[G_{xx}, G_{yx}, G_{zx} \right]^T$;

for the pendulum formation, $\mathbf{e}^{(LoS)} \approx [0,1,0]^T$, i.e. the unit vector defining the LoS direction is oriented mainly in the cross-track direction, which has as a consequence:

- $\boldsymbol{\delta}^{(\Delta\mathbf{x})\perp} \approx \left[\delta_x^{(\Delta\mathbf{x})\perp}, 0, \delta_z^{(\Delta\mathbf{x})\perp} \right]^T$;
- $\mathbf{Ge}^{(LoS)} \approx \left[G_{xy}, G_{yy}, G_{zy} \right]^T$;

Implied in this analysis is that the change in the attitude of $\mathbf{e}^{(LoS)}$ near the poles, when the orbits of the satellites converge, happens quickly and localized enough to have negligible influence on the stochastic properties of $\delta^{(P)}$

for the cartwheel formation, $\mathbf{e}^{(LoS)} \approx \left[e_x^{(LoS)}, 0, e_z^{(LoS)} \right]^T$, i.e. the unit vector defining the LoS direction has neglibigle cross-track direction, producing:

- $\boldsymbol{\delta}^{(\Delta\mathbf{x})\perp} = \left[\delta_x^{(\Delta\mathbf{x})\perp}, \delta_y^{(\Delta\mathbf{x})\perp}, \delta_z^{(\Delta\mathbf{x})\perp} \right]^T$ (no neligible component in the relative orbit position noise);
- $\mathbf{Ge}^{(LoS)} \approx e_x^{(LoS)} \left[G_{xx}, G_{yx}, G_{zx} \right]^T + e_z^{(LoS)} \left[G_{xz}, G_{yz}, G_{zz} \right]^T$.

Assuming a polar circular orbit, the LORF is very similar to the LHRF, where $\mathbf{G}\left(\mathbf{x}^{(\overline{12})} \right)$ is easily computed. During the ascending tracks, the two reference frames nearly match; during the descending tracks, the x and y-axes have opposite directions. The derived equations deal with random variables, which means that the change in the direction of these two axes does not influence the magnitude of the resulting positioning noise. On the other hand, this change in direction modifies the stochastic properties of the positioning noise; this is not critical for the current analysis since only the noise amplitude is relevant. It is also assumed that

for the trailing and pendulum formations: $\quad \mathbf{G}_{ii} \gg \mathbf{G}_{ij}$
and for the cartwheel formation: $\quad \mathbf{G}_{ij} \gg \mathbf{G}_{iy}$.

Under these considerations and noting that G_{ij} are the entries of the tensor $\boldsymbol{\nabla}\boldsymbol{\nabla} V\left(\mathbf{x}^{(\overline{12})}, \overline{\boldsymbol{C}}^{(\mathrm{ref})}\right)$, Table 7.7 presents approximate analytic expressions for the amplitudes of different variants of the positioning noise $\delta^{(\mathrm{P})}$.

$\delta^{(\mathrm{P})(\mathrm{pw})}$ variant	cartwheel	pendulum[a]	trailing
$\delta^{(\mathrm{P})(\mathrm{pw})(\mathrm{rel})\perp}$	$G_{xx}\delta_x^{(\Delta\mathbf{x})\perp}\mathrm{e}_x^{(\mathrm{LoS})} + G_{zz}\delta_z^{(\Delta\mathbf{x})\perp}\mathrm{e}_z^{(\mathrm{LoS})}$	$G_{yx}\delta_x^{(\Delta\mathbf{x})\perp} + G_{yz}\delta_z^{(\Delta\mathbf{x})\perp}$	$G_{xy}\delta_y^{(\Delta\mathbf{x})\perp} + G_{xz}\delta_z^{(\Delta\mathbf{x})\perp}$
$\delta^{(\mathrm{P})(\mathrm{pw})(\mathrm{rel})\|}$	$\delta^{(\Delta\mathbf{x})(\mathrm{LoS})}\left(G_{xx}\left(\mathrm{e}_x^{(\mathrm{LoS})}\right)^2 + G_{zz}\left(\mathrm{e}_z^{(\mathrm{LoS})}\right)^2\right)$	$\delta^{(\Delta\mathbf{x})(\mathrm{LoS})}G_{yy}$	$\delta^{(\Delta\mathbf{x})(\mathrm{LoS})}G_{xx}$
$\delta^{(\mathrm{P})(\mathrm{pw})(\mathrm{abs})}$	$\rho\left(\left(\mathrm{e}_x^{(\mathrm{LoS})}\right)^2 G_{xx}^{(\mathrm{res})} + \left(\mathrm{e}_z^{(\mathrm{LoS})}\right)^2 G_{zz}^{(\mathrm{res})} + 2\mathrm{e}_z^{(\mathrm{LoS})}\mathrm{e}_x^{(\mathrm{LoS})}G_{zx}^{(\mathrm{res})}\right)$	$\rho G_{yy}^{(\mathrm{res})}$	$\rho G_{xx}^{(\mathrm{res})}$

[a]It is assumed that the attitude of $\mathbf{e}^{(\mathrm{LoS})}$ remains constant, i.e. the rapid changes around the poles do not play a significant role in the stochastic properties of $\delta^{(\mathrm{P})}$.

Table 7.7 – Amplitude of the relative point-wise positioning noise resulting from the relative orbit position noise perpendicular to the LoS direction $\delta^{(\mathrm{P})(\mathrm{pw})(\mathrm{rel})\perp}$, relative point-wise positioning noise resulting from the relative orbit position noise parallel to the LoS direction $\delta^{(\mathrm{P})(\mathrm{pw})(\mathrm{rel})\|}$ and absolute point-wise positioning noise $\delta^{(\mathrm{P})(\mathrm{pw})(\mathrm{abs})}$, for the cartwheel, pendulum and trailing formations, as derived analytically on the basis of Eq. (7.5), Eq. (7.6) and Eq. (7.7). Note that $G_{ij}^{(\mathrm{res})} \equiv G_{ij}^{(\mathrm{obs})} - G_{ij}^{(\mathrm{for})}$ and $G_{ij}^{(\mathrm{obs})}$ and $G_{ij}^{(\mathrm{for})}$ are the entries of the tensors $\boldsymbol{\nabla}\boldsymbol{\nabla} V\left(\mathbf{x}^{(\mathrm{obs})(\overline{12})}, \overline{\boldsymbol{C}}^{(\mathrm{ref})}\right)$ and $\boldsymbol{\nabla}\boldsymbol{\nabla} V\left(\mathbf{x}^{(\mathrm{for})(\overline{12})}, \overline{\boldsymbol{C}}^{(\mathrm{ref})}\right)$, respectively. Relevant to $\delta^{(\mathrm{P})(\mathrm{pw})(\mathrm{rel})\perp}$ and $\delta^{(\mathrm{P})(\mathrm{pw})(\mathrm{rel})\|}$ components, the term G_{ij} refers to $\boldsymbol{\nabla}\boldsymbol{\nabla} V\left(\mathbf{x}^{(\overline{12})}, \overline{\boldsymbol{C}}^{(\mathrm{ref})}\right)$, in which case there is no distinction between $\mathbf{x}^{(\mathrm{obs})(\overline{12})}$ and $\mathbf{x}^{(\mathrm{for})(\overline{12})}$.

Comparing the variants of the positioning noise and assuming that the components of relative orbit position noise $\boldsymbol{\delta}^{(\Delta\mathbf{x})}$ are of equal magnitude, it is possible to say that $\delta^{(\mathrm{P})(\mathrm{pw})(\mathrm{rel})\|}$ is of larger amplitude compared to $\delta^{(\mathrm{P})(\mathrm{pw})(\mathrm{rel})\perp}$ for the pendulum and trailing formations. This is because the relative orbit position noise is scaled by diagonal elements of the gravity gradient tensor in case of $\delta^{(\mathrm{P})(\mathrm{pw})(\mathrm{rel})\|}$ (G_{yy} for the pendulum formation and G_{xx} for the trailing formation) and by off-diagonal elements in case of $\delta^{(\mathrm{P})(\mathrm{pw})(\mathrm{rel})\perp}$ (G_{yx} and G_{yz} for the pendulum formation and G_{xy} and G_{xz} for the trailing formation). In case of the cartwheel formation, the

difference in amplitude between $\delta^{(P)(pw)(rel)\perp}$ and $\delta^{(P)(pw)(rel)\|}$ is not as large as for the other two formations. These two noise variants differ only in the factors $\mathbf{e}_i^{(LoS)}$ and $\left(\mathbf{e}_i^{(LoS)}\right)^2$ (if $\delta_x^{(\Delta\mathbf{x})\perp} = \delta_z^{(\Delta\mathbf{x})\perp} = \delta^{(\Delta\mathbf{x})(LoS)}$). The comparison between $\delta^{(P)(pw)(abs)}$ and the other two positioning noise variants is not straightforward. The amplitude of the terms $G_{ii}^{(res)}$ cannot be determined analytically because it depends largely on the discrepancy between $\mathbf{x}^{(obs)(\overline{12})}$ and $\mathbf{x}^{(for)(\overline{12})}$.

Table 7.7 makes it possible to predict that $\delta^{(P)(pw)(rel)\perp}$ are of comparable magnitudes for the trailing and pendulum formations, as long as the relative orbit position noise perpendicular to the LoS direction $\boldsymbol{\delta}^{(\Delta\mathbf{x})\perp}$ is of comparable amplitude. The analytic expressions for the two formations are nearly identical, only the x-component and y-component are swapped. For the cartwheel formation, on the other hand, this noise variant contains the contribution of diagonal terms of the gravity gradient tensor and is, therefore, of larger amplitude. The amplitude of $\delta^{(P)(pw)(abs)}$ is of comparable amplitude for all formations, in view of the fact that diagonal elements of the gravity gradient tensor play a role (in case of the cartwheel formation, there is additionally the contribution of some off-diagonal elements).

7.5 Simulation of relative and absolute positioning noise

Considering the observed orbit positions $\mathbf{x}^{(obs)}$ and forecasted orbit positions $\mathbf{x}^{(for)}$, simulated with the procedure discussed in Section 7.1 and Section 7.2 on the basis of the EIGEN-5C and EIGEN-CG03C gravity field models, respectively, it is possible to simulate the individual contribution of the relative and absolute positioning noise. In order to do that, the forecasted orbit position needs to be adjusted in order to match its relative or absolute components to the observed orbit position. In this context, the term *adjustment* is slightly different than in Section 6.3.5: the adjustment does not aim to correct the orbit along the LoS direction with range data but eliminate the differences in observed and forecasted orbital positions and, consequently, mitigate the corresponding variant of the positioning noise. Each relative and absolute positioning noise variant (k), either (abs), (rel)$\perp$ or (rel)$\|$, requires a different adjustment of the forecasted orbit position:

$$\boldsymbol{\delta}^{(P)(pw)(k)} = \boldsymbol{\nabla}V\left(\mathbf{x}^{(obs)}, \overline{\boldsymbol{C}}^{(ref)}\right) - \boldsymbol{\nabla}V\left(\mathbf{x}^{(for)(adj)(k)}, \overline{\boldsymbol{C}}^{(ref)}\right). \tag{7.8}$$

When simulating the absolute positioning noise $\delta^{(P)(abs)}$, the forecasted LoS vector $\mathbf{d}^{(for)}$ is adjusted to be equal to the observed LoS vector $\mathbf{d}^{(obs)}$:

$$\mathbf{x}^{(\text{for})(\text{adj})(\text{abs})} = \mathbf{x}^{(\text{for})(\overline{12})} \pm \mathbf{d}^{(\text{obs})}. \tag{7.9}$$

Eq. (7.9) ensures that $\mathbf{x}^{(\text{for})(\text{adj})(\text{abs})}$ differs from $\mathbf{x}^{(\text{obs})}$ only in what concerns the middle-point between satellite 1 and satellite 2.

For the case of the relative positioning noise, two variants are relevant: the positioning noise resulting from the relative orbit position noise along the LoS direction $\delta^{(\text{P})(\text{rel})\|}$ and the positioning noise resulting from the relative orbit position noise perpendicular to the LoS direction $\delta^{(\text{P})(\text{rel})\perp}$. In both cases, the forecasted orbit positions require adjusting the middle-point between satellite 1 and satellite 2 so that it matches the observed counterpart $\mathbf{x}^{(\text{obs})(\overline{12})}$. In addition to that, the adjustment needed to simulated $\delta^{(\text{P})(\text{rel})\|}$ as to ensure that the forecasted unit vector defining the LoS direction is equal to $\mathbf{e}^{(\text{LoS})(\text{obs})}$:

$$\mathbf{x}^{(\text{for})(\text{adj})(\text{rel})\|} = \mathbf{x}^{(\text{obs})(\overline{12})} \pm \mathbf{e}^{(\text{LoS})(\text{obs})} \rho^{(\text{for})}. \tag{7.10}$$

In practice, $\mathbf{x}^{(\text{for})(\text{adj})(\text{rel})\|}$ is easily mitigated by exploiting range measurements, in the way described by Eq. (4.60). The current analysis is only relevant to illustrate its influence if the range data are not used for the orbit adjustment.

In case of the forecasted orbit positions adjusted to simulate positioning noise resulting from the relative orbit position noise perpendicular to the LoS direction $\mathbf{x}^{(\text{for})(\text{adj})(\text{rel})\perp}$, the forecasted range is replaced by the observed range $\rho^{(\text{obs})}$:

$$\mathbf{x}^{(\text{for})(\text{adj})(\text{rel})\perp} = \mathbf{x}^{(\text{obs})(\overline{12})} \pm \mathbf{e}^{(\text{LoS})(\text{for})} \rho^{(\text{obs})}. \tag{7.11}$$

Table 7.8 summarizes the adjustment procedures applied in the thesis.

adjusted orbit	$\mathbf{x}^{(\text{for})(\overline{12})}$	$\mathbf{e}^{(\text{LoS})(\text{for})}$	$\rho^{(\text{for})}$	equation
$\mathbf{x}^{(\text{for})(\text{adj})(\text{abs})}$	$=$	$\mathbf{e}^{(\text{LoS})(\text{obs})}$	$\rho^{(\text{obs})}$	(7.9)
$\mathbf{x}^{(\text{for})(\text{adj})(\text{rel})\|}$	$\mathbf{x}^{(\text{obs})(\overline{12})}$	$\mathbf{e}^{(\text{LoS})(\text{obs})}$	$=$	(7.10)
$\mathbf{x}^{(\text{for})(\text{adj})(\text{rel})\perp}$	$\mathbf{x}^{(\text{obs})(\overline{12})}$	$=$	$\rho^{(\text{obs})}$	(7.11)
$\mathbf{x}^{(\text{for})(\text{adj})}$	$=$	$=$	$\rho^{(\text{obs})}$	(4.60)

Table 7.8 – Summary of the adjusted forecasted orbits considered in the thesis, in the context of simulating positioning noise and its relative and absolute components.

After conducting the aforementioned adjustments of the forecasted orbit positions, all three variants of the positioning noise are simulated. This is done for the cartwheel, pendulum and trailing formations, see Figures 7.2 and 7.3.

Referring to Figure 7.2a, the positioning noise resulting from the relative orbit position noise perpendicular to the LoS direction is significantly more intense for the cartwheel formation. In case of the trailing and pendulum formations, this variant of the positioning noise is of similar amplitude (particularly above 1 mHz). These characteristics are predicted by the analytical analysis presented in Section 7.4.3, in particular the first row of Table 7.7. The analytical analysis indicates that, for the cartwheel formation, the positioning noise resulting from the relative orbit position noise perpendicular to the LoS direction is contaminated by the diagonal components of the gravity gradient tensor and, therefore, its amplitude is much larger than for the other formations. The differences below 1 mHz for the pendulum and trailing formations are likely the result of the different average range, being smaller for the pendulum formation.

In what concerns the positioning noise resulting from the relative orbit position noise along the LoS direction shown in Figure 7.2b, the ASDs is mainly driven by the amplitude of the relative orbit position noise parallel to the LoS vector. Referring to Table 7.6, the relative amplitudes of the relative orbit position noise in the orbits of the three formations is reproduced in Figure 7.2b: relative to the pendulum formation, i) it is almost one order of magnitude smaller than for the trailing formation and ii) it is 1.8 times smaller than for the cartwheel formation. This is because the positioning noise resulting from the relative orbit position noise along the LoS direction depends linearly on the diagonal components of the gravity gradient tensor (and additional off-diagonal elements in case of the cartwheel formation), which have similar amplitudes. Note that the positioning noise resulting from the relative orbit position noise perpendicular to the LoS direction is effectively mitigated by taking advantage of the range data collected by the ranging sensor (microwave or interferometer).

Figure 7.2c illustrates that the ASDs of the simulated absolute positioning noise are of similar amplitude. As an exception, the amplitude of the positioning noise variant for the cartwheel formation is higher than for the other two formation between 0.3 and 3 mHz. The reason is likely associated with the contribution of the G_{zz} and the $2G_{zx}$ terms; G_{zz} alone is of higher amplitude (roughly twice) than G_{yy} and G_{xx} components that play a role in the pendulum and trailing formations, respectively (cf. the last row of Table 7.7).

Figure 7.2 – ASDs of the a) positioning noise resulting from the relative orbit position noise perpendicular to the LoS direction, b) positioning noise resulting from the relative orbit position noise along the LoS direction (which can be effectively mitigated with range data) and c) absolute positioning noise variants, for the cartwheel (pink), pendulum (green) and trailing (blue) formations.

Figure 7.3 shows the same curves but now arranged such that the variants of the positioning noise are compared for individual formations.

In case of the cartwheel formation, shown in Figure 7.3a, the amplitude of the positioning noise resulting from the relative orbit position noise perpendicular to the LoS direction is up to a factor of 5 larger than the amplitude of the positioning noise resulting from the relative orbit position noise along the LoS direction. This is a highly unfavourable situation, since it effectively means that adjusting the orbits of the cartwheel formation with range data is futile for the purpose of limiting the effect of the positioning noise.

Figure 7.3b shows the amplitude of the variants of the positioning noise for the pendulum formation. Unlike for the cartwheel formation, the amplitude of the positioning noise resulting from the relative orbit position noise along the LoS direction is over one order of magnitude larger than the next significant variant, the absolute positioning noise. In this case, the use of range data to suppress the positioning noise is essential.

Finally, Figure 7.3c shows that the trailing formation may also benefits from exploiting range data. Unlike for the pendulum formation, the improvement is more modest, only decreasing the positioning noise by roughly a factor of two. Since the absolute positioning noise is of comparable amplitude for the trailing and pendulum formations, the use of range data reduces the amplitude of their positioning noise to comparable levels. In the case of these formations, the positioning noise resulting from the relative orbit position noise perpendicular to the LoS direction can safely be ignored since its amplitude is two orders of magnitude below the absolute positioning noise.

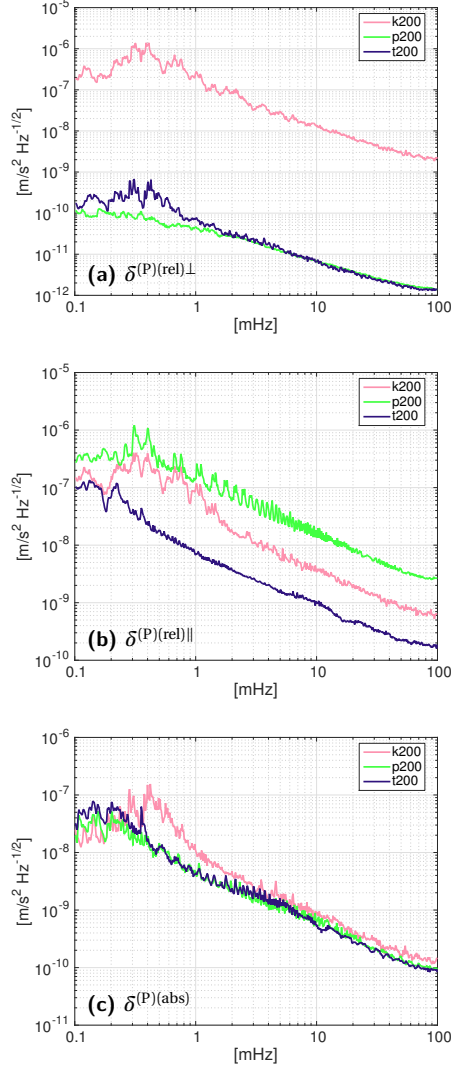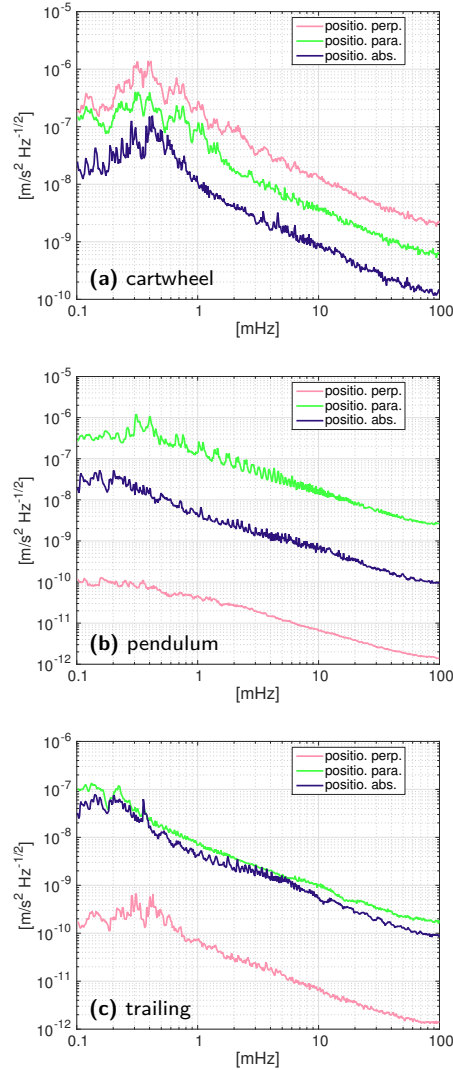**Figure 7.3** – ASDs of the positioning noise resulting from the relative orbit position noise perpendicular to the LoS direction (pink), positioning noise resulting from the relative orbit position noise along the LoS direction (green, which can be effectively mitigated with range data) and absolute positioning noise (blue) variants, for the a) cartwheel formation, b) pendulum formation and c) trailing formation.

7.6 Conclusions

In this chapter, the absolute and relative components of the orbit position noise are analysed for the cartwheel, pendulum and trailing formations. In the same way as the orbit noise, the positioning noise is decomposed in its relative and absolute components, with the latter further split into the components resulting from the relative orbit position noise parallel and perpendicular to the LoS direction. The influence of these components of the orbit position noise (i.e. distance error) on the positioning noise (i.e. range combinations errors) is quantified both analytically and through numerical simulations. The motivation for choosing this set of formations is mostly driven by the dominant orientation of the LoS vector, relatively to the LHRF.

In contrast, the analysis of the positioning noise in Section 6.3.5 focuses on the trailing formation and how the simulation of the positioning noise compares with the GRACE a posteriori residuals and the positioning noise estimated from actual data. In fact, the simulation of the trailing formation is consistent between Section 6.3.5 and the current chapter. In what regards future gravimetric missions, that analysis is done exclusively in Chapter 8, although the orbits are the same.

The orbit noise is estimated as the difference between two sets of orbits integrated on the basis of the EIGEN-5C and EIGEN-CG03C gravity field models, as defined in Section 4.3.3. In Section 7.3, it is shown that the absolute orbit position noise is of comparable magnitude for all formations, while the amplitude of the relative orbit position noise changes considerably. It is expected that the amplitude of the absolute orbit position noise remains relatively constant irrespective of the formation because this component of the orbit error is insensitive to the formation geometry.

As discussed in Section 6.3.5, the simulation environment differs from actual data processing, since the imperfectly-estimated initial state vectors considered in actual data processing have a much larger variability than the initial state vectors derived from the Keplerian reference orbits. This motivates the use of the calibration factor of 6.22, derived with the help of GRACE range data. Given the fact that the relative orbit position noise derived from the integrated orbits of the three formations differs considerably, the most reasonable approach is to apply the calibration factor derived for the trailing formation to the other two formations as it is. In this way, it is assured that the magnitude of the relative orbit position noise duplicates that of actual data in case of the trailing formation (cf. Section 6.3.5) and the amplitude of the calibrated absolute orbit position noise is in agreement with other studies, e.g. those listed in Table 2.5.

It is shown in Section 7.4 that the cartwheel formation suffers from a very high sensitivity to the positioning noise resulting from the relative orbit position noise perpendicular to the LoS direction. This is a fundamental characteristic of this

formation that results from the amplification of the relative orbit position noise by diagonal components of the gravity gradient tensor, while the pendulum and trailing formations are only affected by off-diagonal components (which are small in their case).

The pendulum formation, in spite of the higher amplitude of relative orbit position noise, produces a lower level of positioning noise resulting from the relative orbit position noise perpendicular to the LoS direction in comparison to the cartwheel formation, cf. Section 7.5. In fact, the amplification effect in the cartwheel formation is so severe that, in spite of the lower relative orbit position noise amplitude, the positioning noise resulting from the relative orbit position noise perpendicular to the LoS direction is 3 orders of magnitude larger than that of pendulum formation. This means that any implementation of the cartwheel formation, e.g. those listed in Table 1.2, will most likely produce data with relatively low quality, in particular for future gravimetric missions, which are equipped with highly accurate ranging sensors.

The simulations show that the adjustment of the orbit errors along the LoS direction is futile in case of the cartwheel formation, owing to the high amplitude of the positioning noise resulting from the relative orbit position noise perpendicular to the LoS direction. In fact, the orbit adjustment is most effective in case of the pendulum formation, with an improvement of around one order of magnitude, since this formation is more sensitive to the positioning noise resulting from the relative orbit position noise along the LoS direction than the trailing formation. In case of the trailing formation, the orbit adjustment decreases the level of positioning noise by a factor of two, as discussed in Section 6.3.5.

Satellite Formations

<div style="text-align: right">

8

</div>

The purpose of this chapter is to compare the performance of different types of satellite formations exploiting low-low Satellite-to-Satellite Tracking (ll-SST) data. In the course of a numerical study, the accuracy of the gravity field recovery is quantified as function of the type of formation and maximum range. The main purpose of the analysis is to deliver a realistic noise budget of the considered satellite formations.

The formations considered are the trailing, pendulum and cartwheel formation, presented in Chapter 3, their orbit simulation is described in Section 7.1 and further detailed in Section 8.1.1. These formations are chosen because they sample the gravitational field along different directions, resulting in the largest differences between their sensitivity to various gravitational field features. The numerical study does not take into account the technical complexity of each of the formations under analysis. The purpose is to study the gravimetric measurement system concepts associated with the considered scenarios. Nevertheless, in Section 8.1.1 the issue of technical complexity is briefly addressed, in order to illustrate the technical challenges of each formation concept.

In Section 8.1.2, the force model considered in the simulation of the orbits and the relevant noise types are presented.

In Section 8.1.3, the details of the orbit integration step are presented. Three scenarios of different maximum range are contemplated: 200, 400 and 1000 km. The objective of extending the simulations to different values of maximum range is to gain insight into the benefits of a larger maximum range and into how the estimated gravity field model error correlates with this parameter.

The simulation of noise of different types is addressed in Section 8.1.4. This

section starts with describing the procedure used to simulate the noise, while the paragraph *Assumptions in the simulation of noise of different types* presents the underlying assumptions. Two types of errors are considered: measurement and model errors. The measurement error is associated with the performance of various sensors on-board the spacecraft, as well as with orbit determination accuracies. The model errors describe how inaccuracies in the background force models corrupt the estimated gravity field models. The measurement errors considered in the numerical study are the accelerometer noise, correction noise, orientation noise, positioning noise and ranging noise. These are the noise types that make up the *advanced noise model* presented in Section 4.3.3 and validated in Section 6.3. The only considered model error is the mis-modelled time-variable signal, refer to Section 4.3.1 for the definition of this noise type. The errors resulting from the omission signal and from the mis-modelled static signal (Section 4.3.1) are not considered in the context of this numerical study but are addressed in Appendix E. The reason to ignore these model errors is associated with the underlying assumptions considered in their simulations. In the case of errors resulting from the omission signal, the reference gravitational field can be forecasted up to a sufficiently large degree, effectively eliminating this error. In what concerns the signals described by the coefficients above that degree, it is reasonable to assume that satellite formations for monitoring the temporal gravitational field variations are not sensitive to them. In case of the errors caused by the mis-modelled static signal, the Gravity field and steady-state Ocean Circulation Explorer (GOCE) mission has improved considerably the knowledge of the static field. For this reason, most research into future gravimetric formations ignores the effects of the mis-modelled static signal and omission signal, cf. Table 1.2. Including these model errors in the noise budget would be artificially unfavourable to the remaining noise types, if over-conservative assumptions are considered in their production. The question of which formations is most sensitive to these two model errors is nevertheless analysed in Appendix E.

The measurement and model errors are propagated to the gravity field parameters to quantify the sensitivity of the formations to each noise type. The methodology considered in the numerical study consists of two major steps: (i) data simulation (already mentioned) and (ii) data inversion, detailed in Section 8.1.5. Results of the noise propagation are presented in Section 8.2.

The discussion in Section 8.3 applies the results of the numerical study to the practical aspects of a possible future gravimetric mission. The proposed mission makes use of a polar pendulum formation, therefore taking advantage of this formation's low sensitivity to temporal aliasing and orbital errors. This formation is particularly favourable in conjunction with a polar trailing formation, thus resulting in a dual gravimetric mission.

The summary and concluding remarks can be found in Section 8.4.

8.1 Simulation set-up

The numerical analysis intends to follow as close as possible the procedure used for the production of the Delft Mass Transport (DMT) model (Liu et al. 2010; Ditmar et al. 2013), introduced in Section 4.1.2.

The range observations are computed from a pair of orbits, with the distance between the satellites at each epoch being considered as the range observation. The force model used in the orbit integration defines the signal in the range measurements. The force model exploited in the step of orbit integration is not necessarily the same as the one used for purpose of simulating some noise types, as described in Section 8.1.2.

In the production of the DMT model, the influence of the low-frequency noise in the Gravity Recovery And Climate Experiment (GRACE) data, resulting from errors in the orbital positions and velocities (cf. Section 2.5.6), is minimized by estimating the parameters of an empirical analytical function, cf. Ditmar et al. (2012, eq. 52) and Farahani et al. (2013a). This procedure unequivocally results in more accurate estimated models but it is not considered in the conducted study. There is no reason to assume that this particular procedure would be beneficial in the processing of data from other formations. Irrespective of the fact that it is suitable to suppress the low-frequency noise in the GRACE data, it may be inadequate or sub-optimal for the pendulum or cartwheel formations. In that case, the analysis results would be biased towards the trailing formation. Consequentially, an appropriate low-frequency noise suppression methodology would have to be developed for the pendulum and cartwheel formations, which is outside the scope of the conducted study. The comparison between the formations is done strictly on the basis of simulated errors without any further processing.

Another difference between the numerical analysis in the thesis and the production of the DMT model concerns the post-processing with a statistically optimal Wiener-type filter based on full covariance matrices of signal and noise (Klees et al., 2008; Liu et al., 2010). The DMT model takes advantage of this filtering technique, which down-weights the sectorial and near-sectorial spherical harmonic coefficients poorly estimated by GRACE, thus minimizing the North-South stripes in the resulting gravity field models. This technique has not been employed in the analysis, because the purpose of this section is to determine the sensitivity of each formations to different noise types. One important aspect is to assess the level of isotropy in the

data sensitivity for each satellite formation type. Such assessment could not be done after applying the aforementioned filtering.

8.1.1 Formation scenarios

The formations considered in the numerical study are the trailing, pendulum and cartwheel formations. These formations were introduced in Section 3.3, Section 3.4 and Section 3.5, respectively. Section 7.1 described the orbit simulation of these formations. The maximum range $\rho^{(\mathrm{max})}$ considered in the current chapter, referred in Table 7.1 is 200, 400 and 1000 km.

The trailing formation is a proven concept for measuring Earth's gravitational field, as demonstrated by the GRACE mission. It is the simplest formation and also the easiest to achieve technically. The angle between the velocity vector and the Line of Sight (LoS) vector is nearly constant and equals a few degrees. Unlike for the other formations, this permits the ranging sensor to be mounted rigidly on the body of the satellites and use the Attitude Control System (ACS) to point it towards the other satellite. The disadvantage is that the collected data have anisotropic sensitivity, they are insensitive to variations of the gravitational field along the cross-track (predominantly East-West) direction.

The pendulum formation is characterized by a cross-track cyclic motion, with a nearly zero along-track component. The amplitude of the cross-track motion is controlled by the right ascension of the ascending node of satellite 1 relatively to satellite 2 provided that the orbits cross at the poles and have maximum range at the equator. The chosen distribution of range with latitude produces a higher sensitivity to the gravitational field in equatorial regions, particularly the large wavelength features. The increased localized sensitivity is beneficial to compensate for the larger distance between neighbouring equator crossings. Near the poles, the large density of observations compensates the small range. The pendulum formation, as considered in the numerical study, has the same disadvantage as the trailing formation, i.e. anisotropic sensitivity, with the difference that the data are more sensitive along the cross-track direction. Furthermore, it is technically more challenging in view of the fact that the angular difference between the LoS vector and the velocity vector is in the -90 to 90° range. It is considered in the numerical study because it samples the gravitational field along the direction orthogonal to the other two formations. Any practical and technically feasible implementation of the pendulum formation, such as the one suggested by Panet et al. (2012), includes a non-zero along-track offset so that the largest angular difference between the velocity and LoS vectors is reduced while the formation still benefits from sensing the East-West gravitational component. Unfortunately, such configurations do not benefit from the

inertially-frozen attitude of the LoS vector of the pendulum formation considered in the present study, which considerably mitigates the effects of some noise types, see Section 8.2.

The cartwheel formation is a promising configuration for future gravimetric missions. Of the three formations considered, it is the only one capable of measuring the relative acceleration in the radial direction. The gravitational field can be unambiguously reconstructed if measurements are taken in the radial direction, while that is not so if only one horizontal direction is sampled. As a result, the data gathered with the cartwheel formation are expected to have more isotropic sensitivity, at least while the attitude of the LoS vector contains a significant radial component. Unfortunately, the ability of the cartwheel formation to sample the gravitational field along the radial direction turns out to make it highly sensitivity to orbit errors, as discussed in Chapter 7. This is a severe limitation of any formation with a significant radial relative motion, which can only be mitigated with (much) more accurate orbits. Another disadvantage of the cartwheel formation is related to the technical difficulty in implementing it, namely the complete 360° angular difference between the LoS vector and the velocity vector. Additionally, the differential drag associated with the different altitudes of the satellites (except near the poles) introduces complexity in formation control, unlike for the pendulum and trailing formations. The cartwheel formation considered in the numerical study assumes a horizontal LoS vector over the poles and radial over the equator. This choice aims at ensuring that the data sensitivity is highly isotropic over the equator where the inter-track distance is the largest. Over the poles, the anisotropic sensitivity is mitigated by different directions in which the range is measured at the converging ground-tracks.

8.1.2   Force model

In the numerical studies of future satellite gravimetric missions, two gravity field models are typically used. The "true" model, representing the real gravitational field of the Earth, is used for the integration of the orbits and, from them, the computation of the observed data. The reference model representing the current knowledge of the Earth's gravitational field is used to compute the forecasted data, refer to Section 4.1.2.

In contrast, the purpose of the conducted numerical experiment described in this chapter is to study the propagation of the noise, not signal, for different types of formations. Consequently, the "true" and reference gravitational potentials are often the same and the resulting residual quantities are equal to zero. In that case, the errors are not influenced by the gravitational potentials. The exception are the simulations concerning the positioning noise (Section 4.3.3) and mis-modelled

time-variable signal (Section 4.3.1). In those sections, the difference between the "true" and reference gravity field models is explained.

The temporal aliasing is assumed to be caused solely by the time-varying component of the Earth's gravitational field associated with the high-frequency processes described by the Atmosphere and Ocean De-aliasing Level 1B (AOD1B) product, namely non-tidal mass re-distribution in the atmosphere and oceans. The force model components associated with the N-body perturbations and tides (both ocean and solid-Earth), as well as the relativistic effects, are assumed to be forecasted accurately enough and, therefore, not considered. Neglecting the influence of ocean tidal aliasing is justified, since these variations are fairly well understood (Ray and Luthcke, 2006), although ocean tide models keep improving (Stammer et al., 2014). Therefore, it is assumed that those models are of sufficiently high quality by the time the proposed gravimetric mission is launched, in view of i) the current and planned large number of altimetric satellite missions, ii) the errors in those models are mainly restricted to the polar regions (resulting from little or poor altimetry data) and areas covered with shallow seas (caused by frictional effects, enhanced tidal motion and the presence of coastlines) (Schrama and Visser, 2006; Ray et al., 2009; Visser et al., 2010; Müller et al., 2014). Furthermore, Thompson et al. (2004), Visser (2010) and Reubelt et al. (2014) have demonstrated through numerical simulations that the effects on the gravity field parameters of temporal aliasing originating from the non-tidal atmosphere and ocean variations are comparable to those originating from ocean tides. Importantly, the mitigation of the effects of errors in tidal models is best done at the level of careful orbit design to avoid aliasing periods. In other words, this analysis cannot done without regard to the repeat periods of the orbits; the results may be biased since these orbits may have repeat periods close to the aliasing periods of the tide constituents. For this reason, the fair comparison of the result of all formations must be based on orbits with similar repeat periods. This consideration makes the production of those orbits much more complex and outside the initial objectives of the study. The influence of continental hydrology is uncertain, as this occurs across a range of spatial and temporal scales; however, for the purposes of the simulations presented here, precise knowledge of hydrology is not required. This is because the amplitude of the temporal aliasing associated with the AOD1B product is of comparable amplitude as the temporal aliasing associated with hydrology, cf. Section 6.2.2 as well as Figures 6.18 and 6.19). Low-frequency temporal variations associated with glaciology are also not considered, since they introduce a comparable or less significant level of temporal aliasing. In other words, is assumed that considering components other than AOD1B would not change the simulation results significantly.

The static gravity field models used in the numerical study are listed in Table 8.1

and are henceforth identified by the number shown in the first column.

model nr	gravity field model
0	point-mass
1	EIGEN-5C + AOD1B
2	EIGEN-CG03C
3	EIGEN-5C

Table 8.1 – Definition of the background force models. The *point-mass* gravity field model is described by the $\overline{C}_{00}$ coefficient only.

8.1.3 Orbit simulation

The orbits considered in the current study are the same as to those discussed in Section 7.2. In addition to the orbits with maximum range equal to 200 km, similar orbits with maximum range equal to 400 and 1000 km are considered. The corresponding orbital elements are presented in Table 8.2.

Similarly to Tables 7.3, 7.4 and 7.5 in Section 7.2, Tables 8.3, 8.4 and 8.5 present, for completeness, the statistics about the length and attitude of the LoS vector for the orbits with maximum range equal to 400 and 1000 km. These orbits are integrated on the basis of a complete force model, specifically the sum of the EIGEN-5C and AOD1B models (force model number 1 in Table 8.1). The statistics related to other force models are very similar.

The interpretation of the statistics presented in Section 7.2 is the same for the values of maximum range equal to 400 and 1000 km.

8.1.4 Data simulation

The simulation of various noise components follows the procedure presented in Section 4.3.3. There are, however, a number of details particular to the current analysis that need clarification.

Table 8.6 shows which "true" and reference background force model is used to integrate the observed orbit positions $\mathbf{x}^{(obs)}$ and forecasted orbit positions $\mathbf{x}^{(for)}$, respectively, for each simulated noise type. Referring to the distinction between Keplerian reference orbit and Modelled orbit introduced in Section 3.8.5, the orbits integrated on the basis of force model number 0 (the spherical gravity field model) are Keplerians, while the remaining orbits are integrated on the basis of the force models 1 to 3 (refer to Table 8.1 for the definition of the force models).

formation	sat. nr	h_{min} [km]	h_{max} [km]	a [km]	e []	i [°]	Ω [°]	ω [°]	M [°]
k200	1	491	588	6918.14	0.007	90	0	180.00	182.94
k200	2			6918.13				352.30	10.75
k400	1	505	700	6980.64	0.014	90	0	180.00	182.86
k400	2							358.20	4.89
k1000	1	503	1002	7130.64	0.035	90	0	180.00	182.66
k1000	2			7130.63			0	357.10	6.00
p200	1	500	500	6878.14	1.2×10^{-10}	90	359.17	82.1	244.87
p200	2						0.83		
p400	1	500	500	6878.14	1.2×10^{-10}	90	358.33	82.8	262.22
p400	2						1.66		
p1000	1	500	500	6878.14	1.2×10^{-10}	90	355.83	82.1	244.87
p1000	2						4.16	82.9	262.16
t200	1	500	500	6878.14	1.2×10^{-10}	90	0	82.9	262.16
t200	2							89.5	257.16
t400	1	500	500	6878.14	1.2×10^{-10}	90	0	82.9	262.16
t400	2				1.9×10^{-10}			89.8	258.53
t1000	1	500	500	6878.14	1.2×10^{-10}	90	0	82.9	262.16
t1000	2				4.8×10^{-10}			95.4	275.97

Table 8.2 – Orbital elements of the Keplerian reference orbits. The minimum altitude h_{min} and maximum altitude h_{max} are computed considering the equatorial radius of 6378.137 km.

orbit	$\min(\rho)$	$\text{mean}(\rho)$	$\max(\rho)$	$\text{std}(\rho)$
k200	97.0	150.0	207.0	34.3
k400	205.0	316.0	416.7	71.6
k1000	504.5	778.4	1035.7	176.7
p200	1.9×10^{-3}	127.3	200.0	61.6
p400	4.4×10^{-3}	254.5	400.0	123.1
p1000	2.0×10^{-2}	635.8	999.2	307.5
t200	199.8	199.9	200.1	6.9×10^{-2}
t400	399.6	399.8	400.2	1.4×10^{-1}
t1000	998.2	998.9	999.7	3.4×10^{-1}

Table 8.3 – Statistics of the ranges (in km) for the case of the force model number 1.

The ranging noise $\delta^{(R)}$ and accelerometer noise $\delta^{(acc)}$ do not dependent significantly on the orbits. The choice of orbits used for their simulation is not critical, as long as a representative orbit is considered. For that reason, these noise types are

orbit	min(Elev)	mean(Elev)	max(Elev)	std(Elev)
k200	−19.0	3.9	26.7	13.8
k400	−19.7	9.3×10^{-1}	21.5	13.7
k1000	−19.5	1.5	22.5	13.7
p200	-7.8×10^{-1}	-6.8×10^{-5}	7.7×10^{-1}	2.7×10^{-2}
p400	-7.6×10^{-1}	-6.4×10^{-5}	7.7×10^{-1}	2.7×10^{-2}
p1000	-7.2×10^{-1}	-4.4×10^{-5}	7.2×10^{-1}	2.5×10^{-2}
t200	−90.0	-5.1×10^{-3}	90.0	51.9
t400	−90.0	-1.6×10^{-2}	90.0	51.9
t1000	−90.0	-6.2×10^{-3}	90.0	51.9

Table 8.4 – Statistics of the inertial elevation in degrees for the case of the force model number 1. The inertial elevation is the angle between the LoS vector and the Earth's equatorial plane.

orbit	min(Azim)	mean(Azim)	max(Azim)	std(abs(Azim))
k200	-4.6×10^{-3}	-2.5×10^{-6}	4.6×10^{-3}	7.2×10^{-4}
k400	−1.8	3.4×10^{-7}	1.7	7.1×10^{-3}
k1000	−1.5	4.1×10^{-6}	1.6	6.0×10^{-3}
p200	−90.0	-1.9×10^{-2}	90.0	1.2
p400	−90.0	-1.9×10^{-2}	90.0	1.2
p1000	−90.0	-1.9×10^{-2}	90.0	1.2
t200	-6.8×10^{-3}	-5.7×10^{-8}	1.3×10^{-2}	1.2×10^{-4}
t400	-1.8×10^{-2}	-9.8×10^{-8}	1.4×10^{-2}	1.3×10^{-4}
t1000	-1.0×10^{-2}	-5.6×10^{-8}	1.2×10^{-2}	1.3×10^{-4}

Table 8.5 – Statistics of the inertial azimuth in degrees for the case of the force model number 1. The inertial azimuth is the angle between the LoS vector and the (mean) orbital plane.

computed with the simplifying assumption that the motion of the satellites is under the influence of a spherical gravitational field. The orbits simulated in this was are favoured because they do not contain the gaps associated with the arc-boundary discontinuities of the Modelled orbits. In case of $\delta^{(R)}$, the noise at the level of the range combinations is derived directly from ranging sensor noise $\delta^{(\rho)}$, as indicated in Eq. (4.53), so that ρ plays no role. The parameters $\theta_{i,\pm 1}$ do not change significantly between Keplerian and Modelled orbits, so it is not important from which orbit they are derived. The accelerometer noise $\delta^{(\mathrm{acc})}$ is also computed explicitly, since it is generated using Eq. (4.51). Although the correction noise $\delta^{(C)}$ is inherently associated with errors in the orbital velocity, it is simulated explicitly with Eq. (4.55).

noise type	symbol	$\mathbf{x}^{\text{(obs)}}$	$\mathbf{x}^{\text{(for)}}$
accelerometer noise	$\delta^{\text{(acc)}}$	0	0
correction noise	$\delta^{\text{(C)}}$	0	0
orientation noise	$\delta^{\text{(L)}}$	3	3
positioning noise	$\delta^{\text{(P)}}$	3	2
ranging noise	$\delta^{\text{(R)}}$	0	0
mis-modelled time-variable signal	$\delta^{\text{(tv)}a}$	1	3

[a]The resulting gravity field model error should be scaled by the factor 0.1, as discussed in Section 4.3.1.

Table 8.6 – For each noise type, the force model (listed in Table 8.1) used for the integration of the observed orbit position $\mathbf{x}^{\text{(obs)}}$ and forecasted orbit position $\mathbf{x}^{\text{(for)}}$ is identified.

Recall that the $\delta^{\left(\dot{x}^{(12)\perp}\right)}$ term, associated with the noise in the orbit velocity of satellite 1 relatively to satellite 2 projected onto the plane perpendicular to the LoS direction, is determined in Section 6.1 and its Amplitude Spectral Density (ASD) is shown in Figure 6.4, right-hand side. For the same reasons as for $\delta^{\text{(R)}}$ and $\delta^{\text{(acc)}}$, the simulation of the correction noise is done considering Keplerian orbits.

Assumptions in the simulation of noise of different types

The assumed noise amplitudes, as functions of frequency, are taken from literature or another section of the thesis. The following list describes the assumptions of the noise amplitudes needed to simulate the various noise type presented in Table 8.7.

accelerometer noise: representative of the current SuperSTAR accelerometer noise amplitude, on-board the GRACE satellites, with ASD shown in Figure 6.20;

relative orbit velocity noise: (relevant to the **correction noise**): relative velocity errors given by the ASD in Figure 6.5, right;

relative orbit position noise: (relevant to the **orientation noise**): relative positioning errors given by the ASD in Figure 6.5, left;

ranging sensor noise: noise amplitude adapted from Cesare et al. (2008, Fig. 2B), Silvestrin et al. (2012, Fig. 27.3) and Pierce et al. (2008, Fig. 3), with ASD shown in Figure 8.1;

positioning noise: considering the discussion in Section 6.1.7 related to the accuracy of future Global Navigation Satellite Systems (GNSSs), the positioning noise shown in in Figure 7.3 (excluding the positioning noise resulting from the relative orbit position noise along the LoS direction, green lines) is down-scaled by a factor of 3.
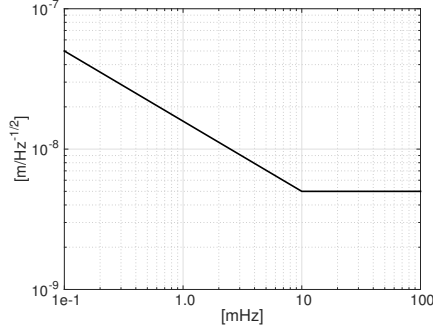
Figure 8.1 – ASD of the assumed ranging sensor noise $\delta^{(\rho)}$, adapted from Cesare et al. (2008); Silvestrin et al. (2012); Pierce et al. (2008).

Except for the assumptions listed above, the simulation procedure is identical to the validation conducted in Section 6.3.

The accuracy of the accelerometer measurements is in-line with the current characteristics of the accelerometers of GRACE. It can be argued that the noise amplitude of the accelerometer considered in the thesis is too conservative, particularly in comparison to the accuracy of the GOCE accelerometers, reportedly at the level of 10^{-12} m/s^2 (Christophe et al., 2010). However, those instruments are exceptional and produced specifically to meet the strict accuracy requirements of the GOCE mission. It is not assured that future gravimetric missions will benefit from comparable accuracy in the accelerometers, considering that these instruments are not the most dominant source of errors in the data.

The relative orbit velocity noise and relative orbit position noise are determined experimentally from the comparison of K-Band Ranging (KBR) data with the range derived from the Purely Dynamic Orbits (PDOs) used in the production of the DMT model, as presented in Section 6.1, particularly in Figure 6.5.

The ranging noise is assumed to reflect the predicted accuracy of the laser ranging sensor proposed by Cesare et al. (2008); Silvestrin et al. (2012); Pierce et al. (2008), cf. Figure 8.1. Alternatively, the ranging sensor proposed for the GRACE Follow On (GFO) (Sheard et al. 2012; Larkin 2012; Zaragoza 2013) mission, shown in Sheard et al. (2012, Fig. 2), could have been considered. However, this was not done since that system is a technology demonstrator and its expected accuracy is low relatively to other proposed future inter-satellite metrology system.

The positioning noise is considered to decrease by a factor of 3 in the near

future, as discussed in Section 6.1.7. In Section 6.3.5 it is demonstrated that the simulated positioning noise needs to be up-scaled by a factor of 6.22 in order to represent the actual positioning noise, as a consequence of imperfectly-estimated initial state vectors in actual data processing. Consequently, the simulation of future positioning noise assumes that the imperfectly-estimated initial state vectors corrupt the positioning noise by a factor of 2.07, relative to the case of perfectly estimating them.

Unlike the other noise types, the mis-modelled time-variable signal does not depend on the sensor accuracy. It is simulated by computing the difference between i) the range combinations generated on the basis of the sum of the EIGEN-5C and the AOD1B models (scaled down by a factor of 10); and ii) the range combinations generated on the basis of the EIGEN-5C model alone.

name	symbol	assumptions
accelerometer noise	$\delta^{(acc)}$	$\mathrm{ASD}\big(\delta^{(acc)(pw)}\big)$ in Figure 6.20, grey line
correction noise	$\delta^{(C)}$	$\mathrm{ASD}\big(\delta^{(\rho)}\big)$ in Figure 6.21; $\mathrm{ASD}\big(\delta^{(\dot{x}^{(12)\perp})}\big)$ in Figure 6.5, right
orientation noise	$\delta^{(L)}$	$\mathrm{ASD}\big(\delta^{(\Delta\mathbf{x})}{}_{y}\big) = \mathrm{ASD}\big(\delta^{(\Delta\mathbf{x})}{}_{z}\big)$ in Figure 6.5, left
positioning noise	$\delta^{(P)}$	Eq. (4.59) considering EIGEN-5C and EIGEN-CG03C
ranging noise	$\delta^{(R)}$	$\mathrm{ASD}\big(\delta^{(\rho)}\big)$ in Figure 8.1, adapted from Silvestrin et al. (2012, Fig. 27.3, bottom) and Pierce et al. (2008, Fig. 3)
mis-modelled time-variable signal	$\delta^{(tv)}$	10 % of AOD1B

Table 8.7 – Summary of the assumptions used to simulate the relevant noise types.

8.1.5 Data inversion

The Stokes coefficients $\overline{C}$ of the estimated gravitational field are the result of a linear Least-Squares (LS) adjustment. The input observations are the residual range combinations. The design matrix is built considering Eq. (4.33) evaluated at the forecasted orbital positions of the satellites.

The noise at the level of range combinations is coloured, as shown in Figure 6.29a. As a consequence, the statistically optimal solution can only be computed with Frequency-Dependent Data Weighting (FDDW), based on the appropriate stochastic model of noise. At the level of implementation, the FDDW is performed with the use of an Auto-Regressive Moving-Average (ARMA) model, according to Klees et al. (2003) (see also Section 2.5.6).

The stochastic model considered in the FDDW is derived from the sum of all measurement noise types, within each formation. In view of the fact that the propagation of noise time series into gravity field model error is a linear operation, it is possible in this way to determine individual contributions to the total noise at the level of estimated gravity field parameters.

An iterative Pre-Conditioned Conjugate Gradient (PCCG) method (Hestenes and Stiefel 1952) is used for the inversion of the noise types of the trailing formations because efficient pre-conditioners have been developed for those cases (Liu et al., 2010). For the remaining formations, explicit inversion of the normal matrix is needed. Typically, the inversion procedure takes around 20 min when the iterative PCCG method is used (on 4 Central Processing Units (CPUs)) and, in contrast, 19 hrs otherwise (on 32 CPUs). The solutions are obtained without any form of regularisation.

The inversion is done up to degree 120. The value of the maximum degree intends to be a balance between minimizing the use of computational resources and conducting the analysis over the widest degree range. It is important to consider a sufficiently high degree so that the estimated errors at the level of the gravity field model represent features small enough to be comparable with the signals that can be retrieved with such formations.

8.2 Results

The major findings of the numerical study are presented in this section. In Section 8.2.1, the various noise types are compared between the considered formations with maximum range equal to 200 km. These comparisons aim at determining which formation configuration is least sensitive to each noise type. In Section 8.2.2,

the error budget of each formation is quantified, making it possible to determine which noise type is most significant. In Section 8.2.3, the effect of the maximum range is considered. Finally, selected spatial patterns are presented and discussed in Section 8.2.4.

8.2.1 Noise types

The analysis of the noise types shows their impact in the gravity field parameters estimated with the data collected with the pendulum, cartwheel and trailing formations, making it possible to compare the noise sensitivity of these formations. The comparison is done considering the ASDs of the residual range combinations and the propagated gravity field model error is the spectral domain (represented by Degree Amplitude Spectra (DASs)):

    i. the accelerometer noise (p. 222),
   ii. the correction noise (p. 223),
  iii. the orientation noise (p. 225),
  iv. the positioning noise (p. 227),
   v. the ranging noise (p. 229) and
  vi. the mis-modelled time-variable signal (p. 232).

Accelerometer noise

The ASD of the accelerometer noise is the same for all formations, as shown in Figure 8.2a, because it is generated explicitly as a random time series at the level of residual range combinations. The accelerometer noise is dominated by the low frequencies, since it is assumed to be a logarithmic function between the points $(0.1\,\mathrm{mHz}, 10^{-9}\,\mathrm{m/s^2}/\sqrt{(\mathrm{Hz})})$ and $(10\,\mathrm{mHz}, 10^{-10}\,\mathrm{m/s^2}/\sqrt{(\mathrm{Hz})})$.

The accelerometer noise propagates more intensively to the gravity field parameters in the case of the trailing formation and the least for the pendulum formation below degree 55. The degree error amplitude increases with degree with the smallest rate for the cartwheel formation. The data gathered by the cartwheel formations are, as a result, least sensitive to accelerometer noise at high degrees, particularly above degree 80. The reason for the different way in which the accelerometer noise propagates to the gravity field is solely associated with the formation geometry, since all other simulations parameters (noise amplitude, altitude, data length, etc.) are the same.

Table 8.8 reports some key numeric values shown in Figure 8.2 and additionally the geoid cumulative errors at the degree 120.

(a) (b)

Figure 8.2 – a) ASD of the simulated accelerometer noise $\delta^{(\mathrm{acc})}$ and b) the corresponding gravity field model error, for the cartwheel, pendulum and trailing formations with maximum range equal to 200 km.

formation	range combination error STD $[\,\mathrm{m/s^2}]$	geoid height error [mm]		
		degree 60	degree 100	cum @ deg 120
cartwheel	4.7×10^{-11}	8.7×10^{-3}	0.056	0.43
pendulum	4.6×10^{-11}	9.6×10^{-3}	0.068	0.89
trailing	4.7×10^{-11}	0.028	0.33	2.2

Table 8.8 – Summary of the accelerometer noise, showing the STD of the time series of range combinations error and the resulting gravity field model error quantified in terms of the geoid height error at degrees 60 and 100 and cumulative geoid height error at degree 120.

Correction noise

The correction noise is the result of an inaccurate reconstruction of the centrifugal accelerations projected onto the LoS vector and is a direct function of the accuracy with which the orbital velocity is measured. As a consequence, it is expected that those formations that rotate the associated LoS vector the least in inertial space will be less sensitive to this noise type.

A correction noise time series is generated on the basis of Eq. (4.55). The results are shown in Figure 8.3, and Table 8.9 reports some important values.

The magnitude of the correction noise in the simulation of the pendulum formation

Figure 8.3 – a) ASD of the simulated correction noise $\delta^{(C)}$ and b) the corresponding gravity field model error, for the cartwheel and trailing formations with maximum range equal to 200 km. The curve for the pendulum formation is not shown because it is 10 orders of magnitude below the other two curves, cf. Table 8.9.

is very low, resulting from the nearly frozen inertial attitude of this formation. Referring to Table 8.4, the LoS vector of the pendulum formation generally remains at zero inertial elevation angle, as indicated by the small value of the STD and mean. The inertial azimuth angle alternates between ±90°, except for rapid variations near the poles, as described by the low value of STD of the absolute value of this angle. The curves related to the pendulum formation are not shown in Figure 8.3 because they are 9 to 10 orders of magnitude below the presented results.

Referring to Figure 8.3a, the cartwheel formation is less sensitive to the correction noise below 0.6 mHz in comparison to the trailing formation. This is the result of its inertial elevation angle being limited to the range from −19° to 27°. The LoS vector in the cartwheel formation oscillates between these extremes at a rate of 2 CPRs, consequently eliminating the peak at 0.2 mHz (1 CPR), which is pronounced in the residual range combinations ASD of the trailing formation. The LoS vector of the trailing formation, on the other hand, makes a complete revolution in the inertial frame each orbital period. The inertial azimuth angle is always small in these two formations, so that the rotation of the LoS vector is mainly driven by the variations in the inertial elevation angle.

The amplitude of the variations of the inertial attitude per orbit revolution is an important parameter controlling this noise type. Larger variations of this parameter lead to a larger value of the orbit velocity of satellite 1 relatively to

satellite 2 projected onto the plane perpendicular to the LoS direction, $\dot{\mathbf{x}}^{(12)\perp}$ and consequentially a larger scaling of the associated error $\delta^{(\dot{x}^{(12)\perp})}$, as described by in Eq. (4.55). It is, therefore, not surprising to see that the propagated correction noise is largest in the trailing formation and negligible in the pendulum formation, refer to Figure 8.3b.

formation	range combination error STD [m/s^2]	geoid height error [mm]		
		degree 60	degree 100	cum @ deg 120
cartwheel	6.5×10^{-10}	0.083	0.42	4.6
pendulum	7.9×10^{-19}	3.5×10^{-11}	3.5×10^{-10}	4.9×10^{-9}
trailing	1.4×10^{-9}	0.64	4.8	31

Table 8.9 – Summary of the correction noise, showing the STD of the time series of range combinations error and the resulting gravity field model error quantified in terms of the geoid height error at degrees 60 and 100 and cumulative geoid height error at degree 120.

Orientation noise

The orientation noise represents the inaccurate knowledge of the attitude of the LoS vector. Similarly to the correction noise, this noise type is directly related to the accuracy with which the attitude of the LoS vector is known, as derived from the orbits of the two satellites. Unlike the correction noise, where the errors in the orbital velocities play a role, the orientation noise is the result of the errors in the orbital positions. The data noise is simulated on the basis of Eq. (4.58), considering EIGEN-5C as the background force model.

The results are shown in Figure 8.4. Table 8.10 provides further numeric details.

In addition to the orbital position noise, the orientation noise is proportional to the difference between the gravitational acceleration at the orbit position of the two satellites, refer to Eq. (4.58). The cartwheel formation is most sensitive to this noise, in view of the fact that the two satellites are generally at different altitudes, up to 100 km altitude difference. The amplitude of the difference in gravitational acceleration is much larger than when they are at equal altitudes. The satellites in the pendulum and trailing formations have an altitude that never differs by more than 3 km. Considering only the $\overline{C}_{00}$ coefficient, the difference between the terms $\boldsymbol{\nabla} V\left(\mathbf{x}^{(j)}, \overline{\boldsymbol{C}}^{(\mathrm{ref})}\right)$, for $j = 1, 2$, in Eq. (4.58) is, at most

$$\frac{1/(r_{\mathrm{Earth}} + h_{\mathrm{orb}} + 100\,\mathrm{km})^2 - 1/(r_{\mathrm{Earth}} + h_{\mathrm{orb}})^2}{1/(r_{\mathrm{Earth}} + h_{\mathrm{orb}} + 3\,\mathrm{km})^2 - 1/(r_{\mathrm{Earth}} + h_{\mathrm{orb}})^2} \approx 32$$
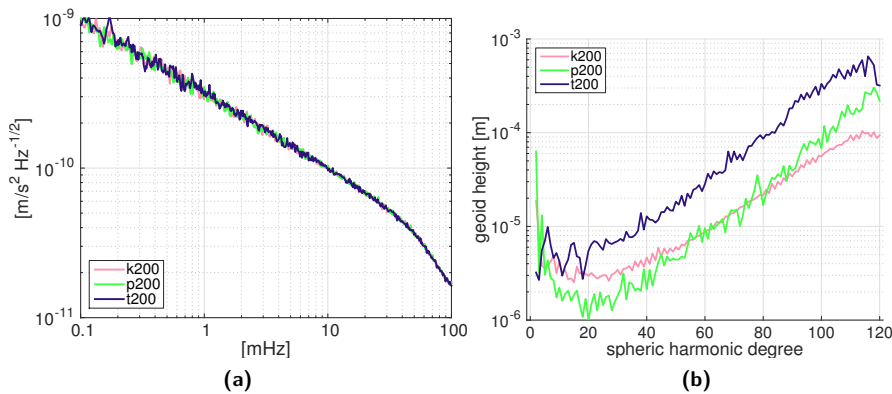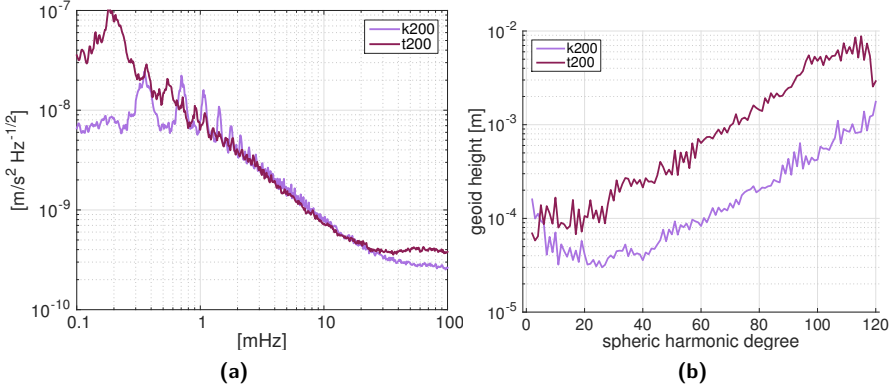
Figure 8.4 – a) ASD of the simulated orientation noise $\delta^{(L)}$ and b) the corresponding gravity field model error, for the cartwheel, pendulum and trailing formations with maximum range equal to 200 km.

times larger for the cartwheel formation than for the other two formations, considering an orbital altitude h_{orb} of 500 km.

The pendulum formation is least sensitive to the orientation noise because the gravitational differences between the satellites along the East-West direction (at equal altitude) is smaller than the gravitational differences between the two satellites in the trailing formation along the North-South direction, recalling that the $\overline{C}_{20}$ coefficient is the second largest coefficient.

formation	range combination error STD [m/s^2]	geoid height error [mm]		
		degree 60	degree 100	cum @ deg 120
cartwheel	3.9×10^{-10}	0.055	0.27	2.0
pendulum	7.1×10^{-14}	5.7×10^{-6}	3.0×10^{-5}	5.0×10^{-4}
trailing	1.4×10^{-12}	8.4×10^{-4}	6.7×10^{-3}	0.037

Table 8.10 – Summary of the orientation noise, showing the STD of the time series of range combinations error and the resulting gravity field model error quantified in terms of the geoid height error at degrees 60 and 100 and cumulative geoid height error at degree 120.

Positioning noise

As the result of the incomplete knowledge of the Earth's gravitational field, the forecasted orbit positions are not exactly equal to the actual orbit positions, giving raise to the discrepancy between the forecasted gravitational accelerations and those that are actually acting on the satellite. This discrepancy is called positioning noise. The simulation of the positioning noise conducted in the numerical study considers two sets of orbits, computed on the basis of the EIGEN-5C and EIGEN-CG03C models, from which the observed and forecasted range combinations are computed, respectively. The procedure is described by Eq. (4.59) and Eq. (4.29). In view of:

- the **calibration factor of 6.22** described in Section 6.3.5 and Section 7.3.1, which is needed to reproduce the effect of the imperfectly-estimated initial state vectors in the simulation environment, and
- the considerations in Section 6.1.7 regarding the accuracy of future GNSSs, which is assumed to be **3 more accurate than currently**,

the simulation of positioning noise in the context of future gravimetric missions considers the **scaling factor of 2.07**.

Chapter 7 is important for understanding of the results described below, in particular i) Section 7.4.3, where the amplitude of the positioning noise is predicted analytically and ii) Section 7.5, where the analytical results are confirmed with a numerical study of the positioning noise. Those findings support the results shown in Figure 8.5a. The trailing and pendulum formations are affected mainly by the absolute orbit position noise, which is of comparable magnitude. For these formations, the relative orbit position noise, after adjusting the orbits with range data, is not dominant. The cartwheel formation, on the other hand, is highly sensitive to the relative orbit position noise and the absolute orbit position noise does not play a role.

In terms of the propagated gravity field model error, shown in Figure 8.5b, the cartwheel formation has unsurprisingly the largest degree amplitude. Unexpectedly, the pendulum formation has much lower amplitude than the trailing formation, particularly above degree 10. One explanation for this result is in the different ways the high-amplitude low-frequency positioning noise propagates to the gravity field parameters in case of the trailing and pendulum formations. In both cases, the positioning noise is largest at the low frequencies, below 1 mHz. In the case of the trailing formation, the contamination of near-sectorial coefficients by the positioning noise is present up to high degrees. The pendulum formation, being able to sample high-order coefficients, is much better equipped to limit the effects of the positioning noise to low degrees. This advantageous characteristic of the pendulum formation is

Figure 8.5 – a) ASD of the simulated positioning noise $\delta^{(\mathrm{p})}$ and b) the corresponding gravity field model error, for the cartwheel, pendulum and trailing formations with maximum range equal to 200 km.
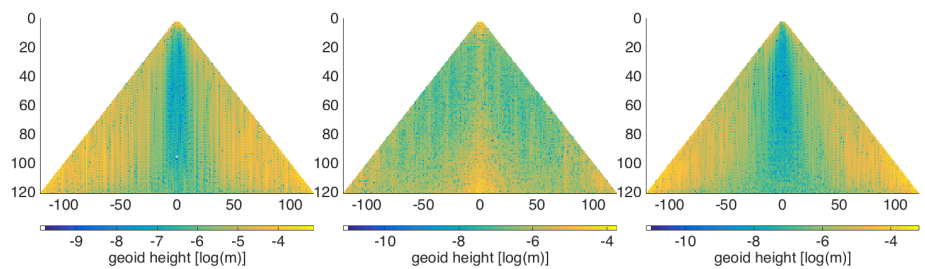
Figure 8.6 – Geoid height amplitude of the coefficients of the positioning noise for the a) cartwheel, b) pendulum and c) trailing formations with maximum range equal to 200 km.

visible in Figure 8.6, showing the amplitude of the gravity field parameters of the positioning noise. Consequentially for this formation, the mitigation of this noise type by high-pass filtering of the data, as mentioned in Section 2.5.6, should be particularly effective.

Table 8.11 includes a selection of values to support the interpretation of Figure 8.5.

formation	range combination error STD $[\,m/s^2\,]$	geoid height error [mm]		
		degree 60	degree 100	cum @ deg 120
cartwheel	8.3×10^{-9}	0.57	1.3	9.3
pendulum	3.2×10^{-10}	0.012	0.078	0.91
trailing	4.7×10^{-10}	0.081	0.66	5.8

Table 8.11 – Summary of the positioning noise, showing the STD of the time series of range combinations error and the resulting gravity field model error quantified in terms of the geoid height error at degrees 60 and 100 and cumulative geoid height error at degree 120.

Ranging noise

The ranging noise represents the errors in measuring the distance between the satellites by means of a dedicated ranging sensor. The noise is simulated by double differentiating the coloured ranging sensor noise with the ASD shown in Figure 8.1, following Eq. (4.53). The approximation assumed in the simplistic noise model (cf. Eq. (4.45)) is not considered in the conducted simulations. This modification intends to simulate accurately the pendulum formation as it moves over the poles, when the attitude of the LoS direction changes rapidly and $\cos\theta_{i,\pm1}$ is no longer ≈ 1. The results of the simulations are shown in Figure 8.7. Table 8.12 show some relevant values.

Since the gravimetric observations are the result of the double differentiation of the range, the noise in the ranges propagates to the range combinations as noise dominant at the higher frequencies. This property, as well as additional details specific to the shape of the ASD of the ranging noise, is analysed in detail in Section 6.3.2.

In case of the the pendulum formation, however, the ranging noise below $10\,\text{mHz}$ has an amplitude that is at least two times larger than for the other formations and with peaks at multiples of 2 CPR, or 0.35 mHz. Unlike for the trailing and cartwheel formations, the range of the pendulum formation varies sinusoidally with time between maximum range and (nearly) zero. The period of these oscillations
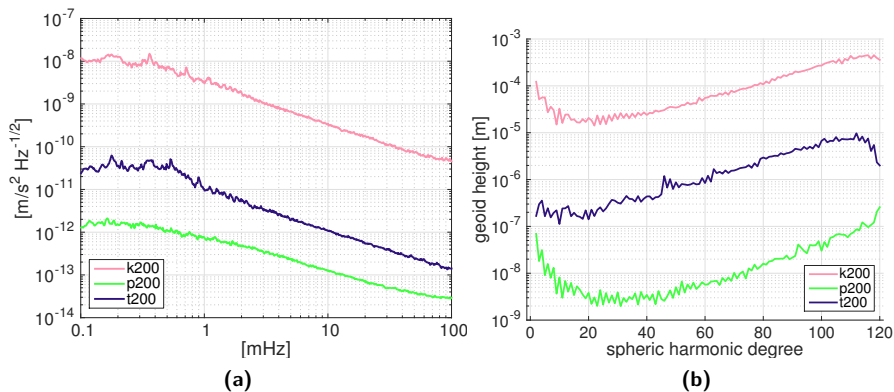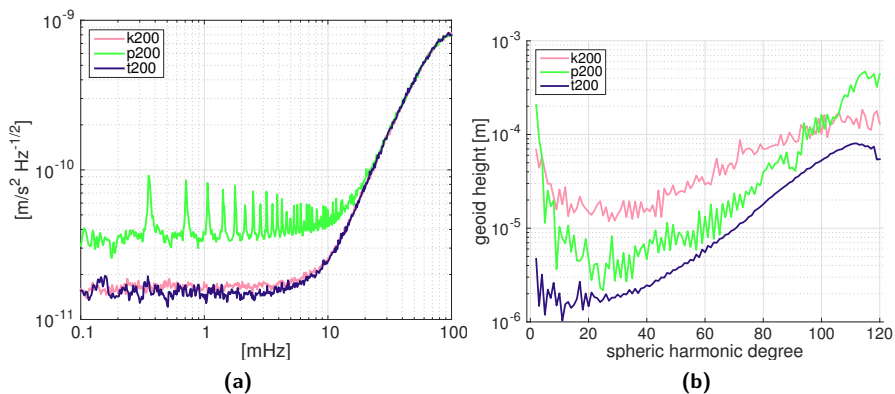
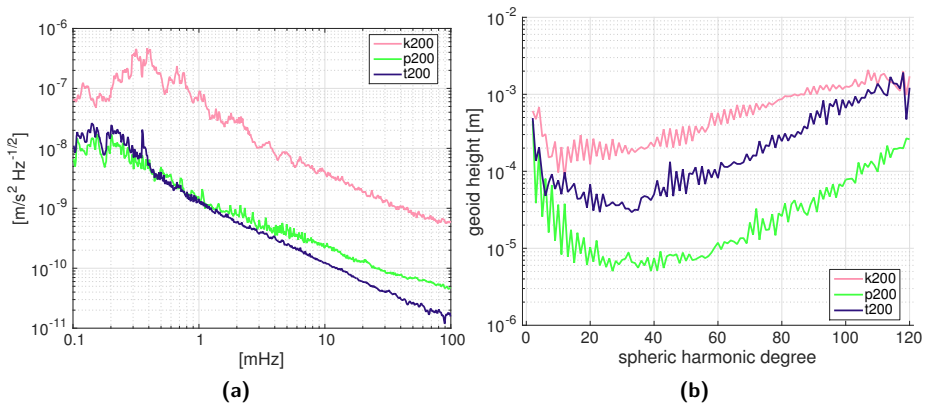**Figure 8.7** – a) ASD of the simulated ranging noise $\delta^{(R)}$ and b) the corresponding gravity field model error, for the cartwheel, pendulum and trailing formations with maximum range equal to 200 km.
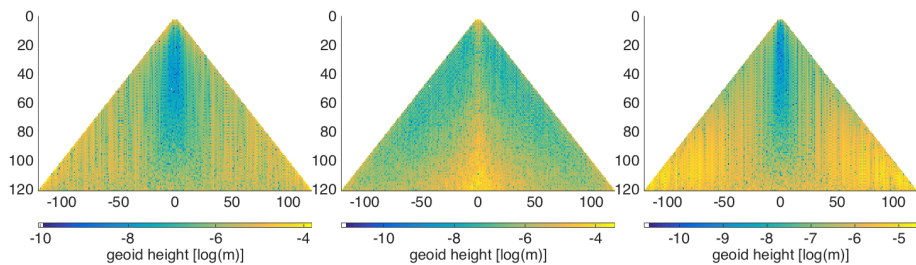
Figure 8.8 – Geoid height amplitude of the coefficients of the positioning noise for the a) cartwheel, b) pendulum and c) trailing formations with maximum range equal to 200 km.

is half of the orbital period, since the maximum range is reached at the ascending and descending equator crossings and the minimum range is reached at both poles. The distance between the satellites, which varies over five orders of magnitude, cf. the minimum and maximum range in Table 8.3, propagates the ranging sensor noise more heavily into those frequencies that are multiples of 0.35 mHz. In the estimated gravity field model error, the high amplitude of the 0.35 mHz harmonics propagates to the degrees below 20, as seen in their large amplitude relative the remaining degrees, also visible in Figure 8.8 as a bright region at the low degrees.

If the procedure used for the simulation of the simplistic ranging noise was considered, i.e. Eq. (4.45) instead of Eq. (4.53), the noise ASD for the pendulum formation would be exactly the same as for the other two formations. In case of the cartwheel and trailing formations, there are no sudden changes in the direction of the LoS vector and the approximation incurred in the simplistic ranging noise, cf. Eq. (4.45), would be sufficiently accurate (although it is not considered in the current study).

In spite of the lower noise in the range combinations, the cartwheel formation shows a larger propagated ranging noise than the trailing formation. The same is true when compared to the pendulum formation in most of the degree range (between degrees 3 and 100); i.e. the cartwheel formation is more sensitive to the ranging noise. In spite of this, the rate in which the amplitude of the ranging noise increases with degree for the cartwheel formation is lower than for the other two formations (there is consistency in the minimum orbital altitude for all formations). The high amplitude of the sectorial and near-sectorial coefficients are the reason for the large degree amplitude of the ranging noise for the cartwheel formation, cf. Figure 8.8. This is enough to make the cartwheel formation is less sensitive to the ranging noise at high degrees (above degree 100) than the pendulum formation. The trailing formation is least sensitive to this noise type, as a result of the comparatively higher Signal-to-Noise Ratio (SNR) associated with the larger range. The low sensitive of the pendulum formation to the gravitational field at the poles increases the amplitude of the zonal and near-zonal coefficients, as shown in Figure 8.8.

formation	range combination error STD $[\,\mathrm{m/s^2}]$	geoid height error [mm]		
		degree 60	degree 100	cum @ deg 120
cartwheel	2.2×10^{-10}	0.029	0.10	0.85
pendulum	2.2×10^{-10}	0.013	0.16	1.5
trailing	2.2×10^{-10}	5.5×10^{-3}	0.053	0.36

Table 8.12 – Summary of the ranging noise, showing the STD of the time series of range combinations error and the resulting gravity field model error quantified in terms of the geoid height error at degrees 60 and 100 and cumulative geoid height error at degree 120.

Mis-modelled time-variable signal

The presence of temporal aliasing in gravity data processing is unavoidable as a result of errors in de-aliasing models. The mis-modelled time-variable signal propagates to the gravity field parameters with a non-zero value, even if it is generated on the basis of a gravitational field error model with zero mean over the estimation period. This is the result of an insufficient temporal sampling to capture the complete evolution of the changes in the original gravitational field over time.

The ASDs shown in Figure 8.9a illustrate the characteristic drop in amplitude above 3 mHz of the mis-modelled time-variable signal. This is the result of the upward continuation effect, which suppresses short wave-length signals. On top of this, the physical processes occurring in sub-daily time scales in the Earth's atmosphere (and associated oceanic response), as modelled by the AOD1B product, in which the motion of masses of small size, and consequentially small mass, does not generate a significant gravitational signal.

The ASD of the mis-modelled time-variable signal is similar in all formations, with the exception of the pendulum formation, which has a lower amplitude between 2 and 10 mHz. Additionally, the pendulum formation also produces less pronounced "spikes" below 2 mHz, which are clearly seen in the mis-modelled time-variable signal of the other two formations.

In what concerns the propagated noise, refer to Figure 8.9b, the degree amplitude spectra are similar below degree 10 for all formations, as a result of the fact that below 1 mHz the ASDs have comparable amplitudes. Above degree 10, the pendulum formation shows an error degree amplitude that is lower by over one order of magnitude in comparison to the cartwheel and trailing formations. This result suggests that the larger width of the ground-track strip sensed by the pendulum formation combined with the higher sensitivity to mass variations outside this strip (as a result of the cross-track orientation of the LoS vector), favours the averaging of the high-frequency mass transport processes. The cartwheel and trailing formation,
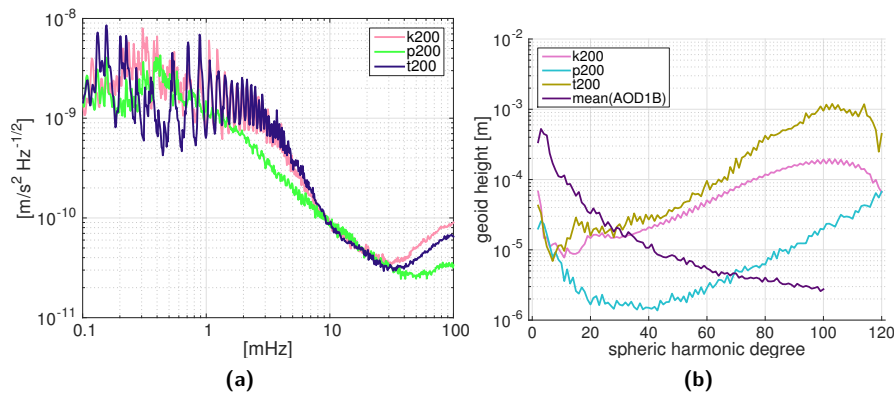
Figure 8.9 – a) ASD of the simulated mis-modelled time-variable signal $\delta^{(tv)}$ and b) the corresponding gravity field model error, for the cartwheel, pendulum and trailing formations with maximum range equal to 200 km.

on the other hand, have nearly zero cross-track separation, so the strip of surface to which they are sensitive to is narrower.

The error in the gravity field parameters is more significant at higher degrees in spite of the sudden amplitude decrease above 4 mHz (roughly degree 23) of the mis-modelled time-variable signal. This is indication that the strong low-frequency signal, which cannot be unambiguously reconstructed from the data collected by the formations, is captured by the gravity field parameters of higher degrees.

Some values are presented in Table 8.13 to support the interpretation of Figure 8.9.

formation	range combination error STD [m/s^2]	geoid height error [mm]		
		degree 60	degree 100	cum @ deg 120
cartwheel	1.7×10^{-10}	0.051	0.19	1.4
pendulum	10^{-10}	5.5×10^{-3}	0.019	0.92
trailing	1.6×10^{-10}	0.096	0.95	5.3

Table 8.13 – Summary of the mis-modelled time-variable signal, showing the STD of the time series of range combinations error and the resulting gravity field model error quantified in terms of the geoid height error at degrees 60 and 100 and cumulative geoid height error at degree 120.

8.2.2 Noise budgets

The spectra of all noise types, in the frequency and degree domain, are analysed for each formation. The results show which noise types dominate in different frequency bands and at different spherical harmonic degrees. If a noise of a certain type is negligible, it is not shown to make a plot more readable.

Cartwheel formation

Referring to Figure 8.10a, the error budget in terms of residual range combinations associated with the cartwheel formation is dominated by the positioning noise. The exception is the ranging noise, which is dominant only above 70 mHz but never by more than 30 %. For the frequencies below 20 mHz, the magnitude of the ranging noise is at least three orders of magnitude lower than the positioning noise. The correction noise, orientation noise and accelerometer noise are between a factor of 5 and two orders of magnitude below the positioning noise. The model error associated with the mis-modelled time-variable signal is also negligible, as shown in Figure 8.10a, since its amplitude is at least one order of magnitude smaller. Consequentially, the orbit position errors, the driving factor behind the positioning noise, are the dominant source of errors in the data collected by the cartwheel formation. The high-pass filtering of the data to mitigate the resonance effect (see Section 2.5.6) would be, in this case, probably not very successful, since the effects of positioning noise are present at almost all frequencies.

The errors propagated to the gravity field parameters produce the DASs shown in Figure 8.10b. The DASs are in line with the Amplitude Spectral Densitys of errors in residual range combinations: the positioning noise is the largest error source, while the accelerometer noise is the least significant at all degrees. Between these two extremes are the orientation noise, ranging noise and mis-modelled time-variable signal, clustered together with comparable amplitudes, while the correction noise is a factor of two larger. This observation bring into evidence that the improvement of the accuracy of the ranging sensor will likely not lead to a higher data quality. Even if the effects of the positioning noise, correction noise and orientation noise are effectively removed with the high-pass filtering discussed in Section 2.5.6 (which is not likely, since the positioning noise is dominant over all frequencies below 70 mHz), the data is still significantly corrupted by the mis-modelled time-variable signal.

Figure 8.10 – Simulation of the cartwheel formation with maximum range equal to 200 km, showing a) the ASDs of the simulated noise types and b) the corresponding errors at the level of the estimated gravity field model. The curve labelled *alias* refers to the mis-modelled time-variable signal (from the term *temporal aliasing*).

noise type	range combination error STD [m/s²]	geoid height error [mm]		
		degree 60	degree 100	cum @ deg 120
accelerometer noise	4.7×10^{-11}	8.7×10^{-3}	0.056	0.43
correction noise	6.5×10^{-10}	0.083	0.42	4.6
orientation noise	3.9×10^{-10}	0.055	0.27	2.0
positioning noise	8.3×10^{-9}	0.57	1.3	9.3
ranging noise	2.2×10^{-10}	0.029	0.10	0.85
mis-modelled time-variable signal	1.7×10^{-10}	0.051	0.19	1.4
total	8.4×10^{-9}	0.59	1.4	11

Table 8.14 – Noise budget of the cartwheel formation, showing the STD of the time series of range combinations error and the resulting gravity field model error quantified in terms of the geoid height error at degrees 60 and 100 and cumulative geoid height error at degree 120.

Pendulum formation

The noise in the data of the simulated pendulum formation is dominated by the positioning noise below 20 mHz and by the ranging noise above, as shown in Figure 8.11a. Compared to the positioning noise, the mis-modelled time-variable signal is one order of magnitude smaller at 0.2 mHz, of comparable magnitude between 0.4 and 2 mHz and a factor of 2 or more smaller above 10 mHz. The accelerometer noise is of comparable magnitude to the mis-modelled time-variable signal, being of less amplitude by at most a factor of 3 between the frequencies of 0.1 mHz and 8 mHz. The orientation noise and correction noise are negligible in comparison to the above-mentioned noise types and have a noise amplitude that is between 1 and 7 orders lower than the other noise type, respectively (not shown).

Roughly the same error amplitudes are present in terms of the gravity field model error (Figure 8.11b). The positioning noise is the dominant noise type below degree 40, followed by the ranging noise, which is roughly a factor of two less intense. The positioning noise, ranging noise and accelerometer noise are of comparable amplitude above degree 60, with the ranging noise slightly higher than the other two above degree 80. Below degree 55, the accelerometer noise is less intense than the positioning noise and ranging noise, up to an order of magnitude relative to the positioning noise at degree 20. The mis-modelled time-variable signal shows a lower amplitude than the other noise types above degree 30, but never by a factor larger than 5. The amplitude of the propagated orientation noise is at least 2 orders of magnitude lower than the accelerometer noise and the orientation noise is 8 orders of magnitude lower (not shown).

The methods that handle the resonance effects (refer to Section 2.5.6) should reduce the effects of positioning noise (albeit not completely since these errors are dominant up to 20 mHz), making the ranging sensor and, to a lesser extent, the accelerometer accuracy more important to the quality of the models estimated from gravimetric data collected by the pendulum formation (Figure 8.11b). Below degree 30, the effects of mis-modelled time-variable signal are of similar amplitude as the ranging noise, which means that the measures that reduce the effects of temporal aliasing described in Section 2.1.2 are important.

Under the assumption that the positioning noise and the effects of the mis-modelled time-variable signal can be effectively mitigated, e.g. with the help of low-pass filtering, advanced Precise Orbit Determination (POD) techniques, future GNSS data and numerous non-dedicated missions (Chapter 5), the quality of the data collected by the pendulum formation would benefit from a more accurate ranging sensor. Any improvement in the ranging sensor would have to be met with a comparatively equal improvement in the accelerometer accuracy, as a result of
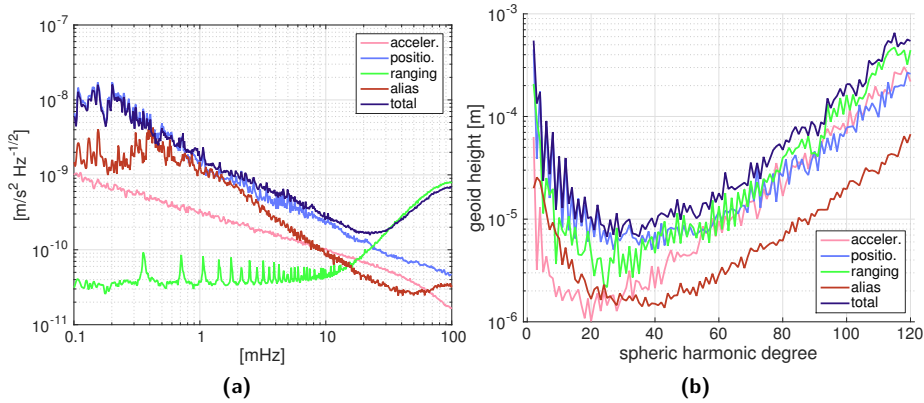
Figure 8.11 – Simulation of the pendulum formation with maximum range equal to 200 km, showing a) the ASDs of the simulated noise types and b) the corresponding errors at the level of the estimated gravity field model. The orientation noise and correction noise are not shown in (a) because they are 1 and 7 orders below and in (b) because they are 2 and 8 orders of magnitude below the other noise types. The curve labelled *alias* refers to the mis-modelled time-variable signal (from the term *temporal aliasing*).

the fact that the two noise types have nearly equal amplitudes across the whole degree range. This situation would be the most beneficial, since the data quality, particularly at high degrees, would be a direct function of the accuracy of its geodetic instruments. Although this is an optimistic assumption, there is no room to make a comparable prediction in the context of the trailing and cartwheel formations.

noise type	range combination error STD $[\mathrm{m/s^2}]$	geoid height error [mm]		
		degree 60	degree 100	cum @ deg 120
accelerometer noise	4.6×10^{-11}	9.6×10^{-3}	0.068	0.89
correction noise	7.9×10^{-19}	3.5×10^{-11}	3.5×10^{-10}	4.9×10^{-9}
orientation noise	7.1×10^{-14}	5.7×10^{-6}	3.0×10^{-5}	5.0×10^{-4}
positioning noise	3.2×10^{-10}	0.012	0.078	0.91
ranging noise	2.2×10^{-10}	0.013	0.16	1.5
mis-modelled time-variable signal	10^{-10}	5.5×10^{-3}	0.019	0.92
total	4.1×10^{-10}	0.021	0.19	2.2

Table 8.15 – Noise budget of the pendulum formation, showing the STD of the time series of range combinations error and the resulting gravity field model error quantified in terms of the geoid height error at degrees 60 and 100 and cumulative geoid height error at degree 120.

Trailing formation

The correction noise is dominant for the trailing formation, except for the frequencies above 50 mHz, where the ranging noise is the largest, (Figure 8.12a). Relative to the total noise, the accelerometer noise is always (nearly) one order of magnitude lower and the amplitude of the mis-modelled time-variable signal is between a factor of 2 and one order of magnitude below. The orientation noise is at least two orders of magnitude smaller. As a consequence, the errors in the relative velocity of the spacecraft are the dominant source of errors in the trailing formation under analysis.

In terms of the gravity field parameters, it is confirmed that the gravity field model error resulting from the correction noise is dominant at all degrees, with the exception of the degrees lower than 4 where the positioning noise is of larger amplitude. Above degree 35, the positioning noise is almost an order of magnitude lower than the correction noise. The degree amplitude of the mis-modelled time-variable signal is comparable to the positioning noise above degree 60; below this degree, the mis-modelled time-variable signal has a lower amplitude by roughly a factor of two until degree 15 and up to an order of magnitude below this degree. The accelerometer noise and ranging noise are at least a factor of 3 and 10 below the mis-modelled time-variable signal, respectively. In other words, the high accuracy
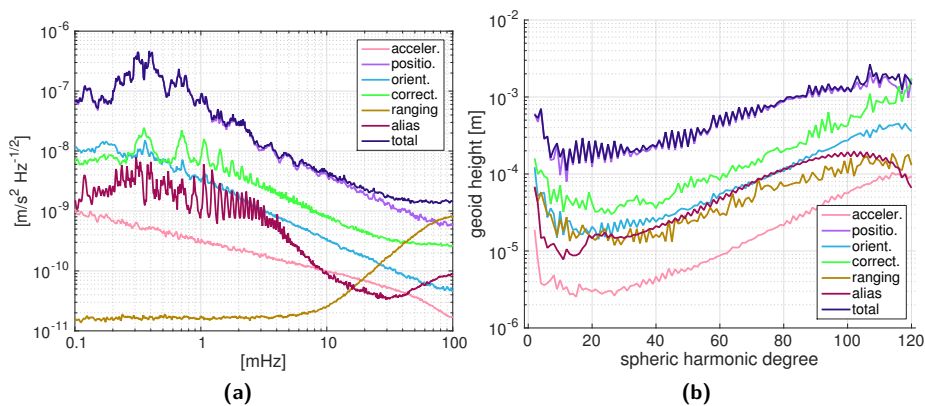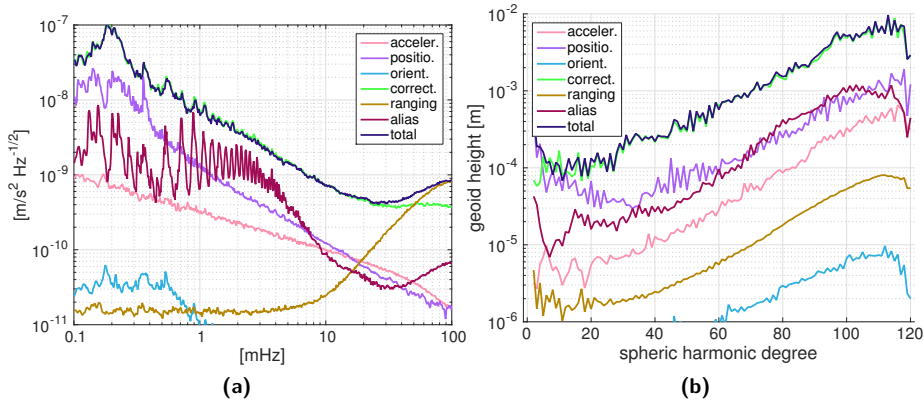
Figure 8.12 – Simulation of the trailing formation with maximum range equal to 200 km, showing a) the ASDs of the simulated noise types and b) the corresponding errors at the level of the estimated gravity field model. The curve labelled *alias* refers to the mis-modelled time-variable signal (from the term *temporal aliasing*).

of the accelerometers and ranging sensor is wasted in the trailing formation. This is true unless i) an effective high-pass filtering of the data (recall Section 2.5.6) is able to mitigate the effect of the positioning noise and correction noise across the whole frequency range (which is unlikely; the procedure currently done on GRACE data addresses a narrow low-frequency band) ii) the errors in the de-aliasing models are much lower than the 10% of the original signal that is currently assumed.

noise type	range combination error STD [m/s^2]	geoid height error [mm]		
		degree 60	degree 100	cum @ deg 120
accelerometer noise	4.7×10^{-11}	0.028	0.33	2.2
correction noise	1.4×10^{-9}	0.64	4.8	31
orientation noise	1.4×10^{-12}	8.4×10^{-4}	6.7×10^{-3}	0.037
positioning noise	4.7×10^{-10}	0.081	0.66	5.8
ranging noise	2.2×10^{-10}	5.5×10^{-3}	0.053	0.36
mis-modelled time-variable signal	1.6×10^{-10}	0.096	0.95	5.3
total	1.5×10^{-9}	0.65	4.9	32

Table 8.16 – Noise budget of the trailing formation, showing the STD of the time series of range combinations error and the resulting gravity field model error quantified in terms of the geoid height error at degrees 60 and 100 and cumulative geoid height error at degree 120.

Summary

Table 8.17 provides an overview of the impact of the various noise types in terms of residual range combinations. For the dominant noise types, the bandwidths in which that is the case are reported. In case a noise type is not dominant at any frequency, the largest ratio of its amplitude to the total errors is shown.

The ranging noise is always dominant at the high-end of the frequency domain in all formations. Consequently, the ranging sensor is the limiting factor for the accurate estimation of small spatial features of Earth's gravitational field, starting at degree 170 for the pendulum formation, degree 283 for the trailing formation and degree 567 for the cartwheel formation, as deduced from the frequencies at which the ranging noise becomes dominant (30, 50 and 100 mHz, respectively).

At the low degrees, the most significant error source is the positioning noise for the cartwheel and pendulum formations (originating from the relative and absolute orbit position noise, respectively, cf. Section 7.5 and Figure 7.3) and the correction noise for the trailing formation. The orientation noise is never the dominant source of error, since it is always at least one order of magnitude lower than the total noise. Likewise, the accelerometer noise is not significant in any formation scenario considered in the numerical study. The mis-modelled time-variable signal does not

play a role in the cartwheel formation due to the high level of positioning noise; in case of the other formations, in spite of not being dominant at any frequency range, it cannot be ignored because its amplitude reaches 90 % and 60 % of the total noise in case of the pendulum and trailing formations, respectively. In conclusion, the orbit errors play a significant role in the error budget of all formations: for the cartwheel and pendulum formations, the discrepancy between modelled and actual orbital positions dominates, while the accuracy of the orbit velocity of satellite 1 relatively to satellite 2 projected onto the plane perpendicular to the LoS direction $\dot{\mathbf{x}}^{(12)\perp}$ plays the most important role in case of the trailing formation.

noise type	cartwheel	pendulum	trailing
accelerometer noise	0.03	0.33	0.15
correction noise	0.2	10^{-8}	below 50 mHz
orientation noise	0.1	10^{-3}	10^{-3}
positioning noise	below 70 mHz	below 20 mHz	0.5
ranging noise	above 70 mHz	above 20 mHz	above 50 mHz
mis-modelled time-variable signal	0.1	0.9	0.6

Table 8.17 – Frequency ranges where the noise types in terms of residual range combinations are dominant; if noise is not dominant, the largest ratio to the total noise is reported.

While Table 8.17 summarises the dominant noise types in terms of range combinations, Table 8.18 gives an overview of the contribution of each noise type in terms of cumulative geoid height error. The contribution $f^{(i)}$ of the noise type i, with $i = \mathrm{acc, P, L, C, R, tv}$ (referring to $\delta^{(\mathrm{acc})}$, $\delta^{(\mathrm{P})}$, $\delta^{(\mathrm{L})}$, $\delta^{(\mathrm{C})}$, $\delta^{(\mathrm{R})}$ and $\delta^{(\mathrm{tv})}$, respectively), is computed as the ratio between the square of the corresponding cumulative geoid height error at degree 120, $\delta_{120}^{(i)}$, and the square of the total noise, $\delta_{120}^{(\mathrm{tot})}$:

$$f^{(i)} = \frac{\left(\delta_{120}^{(i)}\right)^2}{\left(\delta_{120}^{\mathrm{tot}}\right)^2}, \quad i = \mathrm{acc, P, L, C, R, tv}.$$

In this way, the sum of all contributions is approximately equal to one, resulting from the fact that the total noise variance is approximately equal to the variances of

the squares of all noise types if none of them are correlated with each other:

$$\sum_{i=\text{acc,P,L,C,R,tv}} f^{(i)} = 1.$$

In the cartwheel formation, the positioning noise accounts for 76 % of the errors in estimated gravity field model. The remaining noise types that originate from orbital errors (i.e. the correction noise and orientation noise) are the second and third most significant. Together, they are responsible for 98 % of the errors in the estimated gravity field model. The high-pass filtering mentioned in Section 2.5.6 is probably not a practical solution to deal with the high orbit noises in the cartwheel formation, since these errors are present over a wide frequency range.

In the trailing formation, the correction noise accounts for nearly 93 % and the positioning noise with 3.4 %. The remaining 3.3 % are distributed over the mis-modelled time-variable signal (with 2.8 %) and accelerometer noise (with 0.50 %).

The correction noise and orientation noise play no role in the simulated pendulum formation while the ranging noise contributes with 48 %. The remaining of the noise budget of the pendulum formation is evenly split between the mis-modelled time-variable signal, positioning noise and accelerometer noise, with 18 %, 17 % and 17 %, respectively.

noise type	cartwheel	pendulum	trailing
accelerometer noise	0.16 %	17 %	0.50 %
correction noise	19 %	5.0×10^{-16} %	93 %
positioning noise	76 %	17 %	3.4 %
ranging noise	0.62 %	48 %	0.013 %
orientation noise	3.4 %	5.3×10^{-6} %	1.4×10^{-4} %
mis-modelled time-variable signal	1.7 %	18 %	2.8 %
total [m]	11	2.2	32

Table 8.18 – Contribution of different noise types, in terms of % of cumulative geoid height error variance at degree 120.

8.2.3   Effect of the maximum range

The numerical study has focused so far exclusively on the formations with a maximum range equal to 200 km. The current section looks into how the propagated noise types changes when the maximum range is increased to 400 and 1000 km. The analysis is done for all formations and noise types but without discussing in detail each combination of the two. For that reason, it is useful to have a broad view of the error per degree of all formations and noise types, refer to Figure 8.13 and Figure 8.14.

In general, a larger maximum range results in a lower propagated noise, particularly for the lower degrees, with a number of exceptions, to be discussed below. This is an expected result: larger maximum ranges lead to larger inter-satellite gravitational accelerations. At the same time, the magnitude of the coefficients in the design and normal matrix is also larger and, therefore, the estimation of the associated unknown parameters is more accurate; in other words, the SNR is larger.

It is possible to identify two types of exceptions to the general rule explained above. The first type of exception is those formations and noise types that are associated with gravity field parameters distorted by degree-localised spikes. The second type are those that are insensitive to the maximum range.

Resonance artefacts in the gravity field model error

There are patterns in the degree amplitude spectra of some noise types that are repeated for different maximum ranges. These patterns are identified as a local increase of the error amplitude at consistently the same degree, resulting from disturbances with a certain wavelength influencing the satellites in the same way. They are referred to as *resonance artefacts* (not to be confused with the *resonance effect* resulting from errors in satellite orbits, discussed in Section 2.5.6). Sneeuw et al. (2005) has studied this issue with the semi-analytical approach (Sneeuw, 2000), and refers to these artefacts as *attenuation bands*. They result from the lack of sensitivity of the formation to particular wavelengths, identified below. In other words, features that change in space with a particular wavelength do not produce a significant differential signal, since they affect the two satellites in the formation in a very similar way. As a consequence, it is not possible to recover those features accurately.

Table 8.19 summarises the formations and noise types which result in a error in the gravity field models distorted by resonance artefacts. That tables reports the factor between the amplitude of the degrees immediately below and above the localized jump. For example, for the pendulum formation with 1000 km maximum

(a) accelerometer noise, cartwheel formation

(b) accelerometer noise, pendulum formation

(c) accelerometer noise, trailing formation

(d) correction noise, cartwheel formation

(e) correction noise, pendulum formation

(f) correction noise, trailing formation

(g) orientation noise, cartwheel formation

(h) orientation noise, pendulum formation

(i) orientation noise, trailing formation

Figure 8.13 – Comparison of the effects of the maximum range on the geoid error per degree of the accelerometer noise, correction noise and orientation noise (per row, respectively) for the cartwheel, pendulum and trailing formations (per column, respectively).

(a) positioning noise, cartwheel formation

(b) positioning noise, pendulum formation

(c) positioning noise, trailing formation

(d) ranging noise, cartwheel formation

(e) ranging noise, pendulum formation

(f) ranging noise, trailing formation

(g) mis-modelled time-variable signal, cartwheel formation

(h) mis-modelled time-variable signal, pendulum formation

(i) mis-modelled time-variable signal, trailing formation
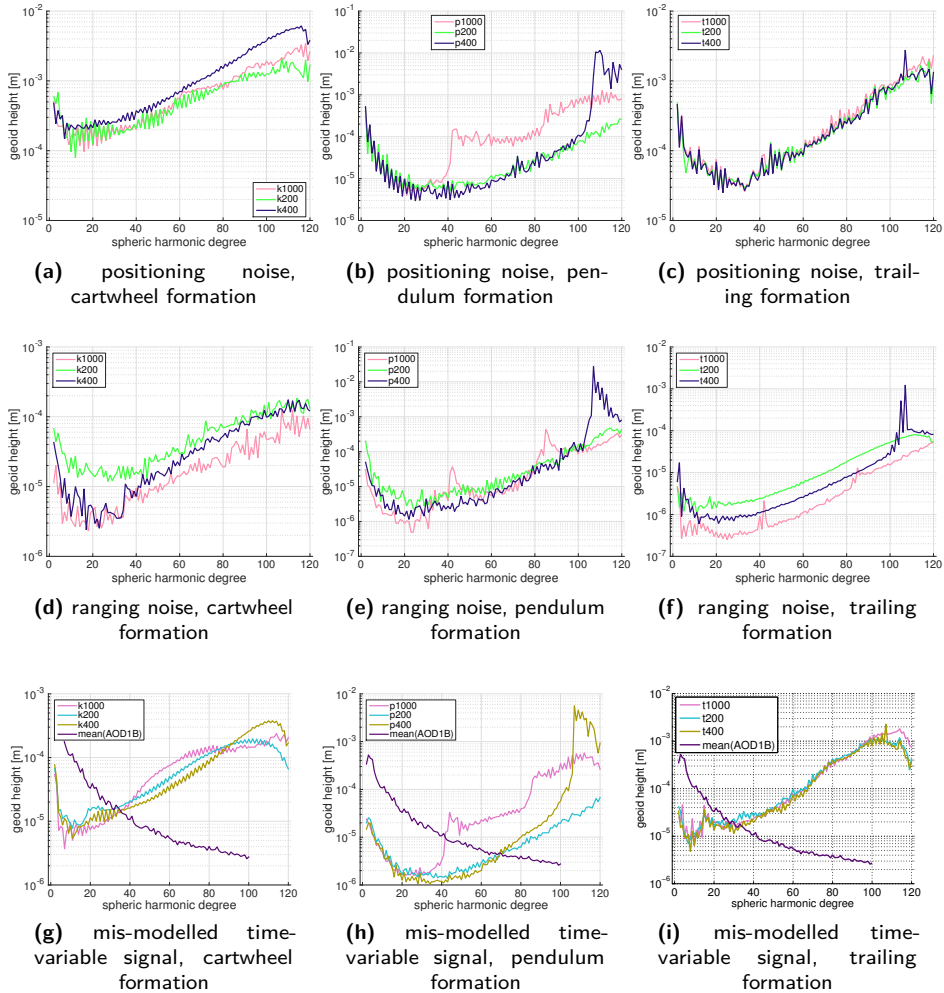
Figure 8.14 – Comparison of the effects of the maximum range on the geoid error per degree of the positioning noise, ranging noise and mis-modelled time-variable signal (per row, respectively) for the cartwheel, pendulum and trailing formations (per column, respectively).

range, there are sudden jumps in the geoid height amplitude at degree 41 for all
noise types. Degree 41 is related a wavelength of 976 km, which is approximately
the maximum range. These jumps increase the degree error amplitude by a factor
of 5 to 10. Empty cells mean that there is no visible artefact.

formation	k1000	p400	p1000		t400	t1000	
degree	60	108	41	86	107	42	85
spatial wavelength [km]	333	185	487	232	187	476	236
accelerometer noise	4	100	6	2	2.5		
correction noise		60	5	2.5	2		
orientation noise	1.5	75	6	3	1.5		
positioning noise		100	8	2.5			
ranging noise		300	8	6	25	5	1.5
mis-modelled time-variable signal	2	70	10	5	2		

Table 8.19 – Factor of the degree-localized amplitude increase in the error of the estimated
error in the gravity field models, associated with the resonance artefacts.

The resonance artefacts in the gravity field model error for the pendulum and
trailing formations are located at the degrees approximately associated with the
multiples of the half maximum range, i.e. degrees 41-42 and 85-86 for the maximum
range equal to 1000 km and degrees 107-108 when the maximum range is 400 km.
The shape of the resonance artefacts for these formations tends to be very sharp. In
case of the pendulum formation with maximum range equal to 400 and 1000 km,
resonance artefacts are visible in the degree amplitude spectra of all noise types.
They introduce large errors in the solutions for the **p400** formation, decreasing the
accuracy of the estimated models by a factor of 30 to 300. The resonance artefacts
present in the solutions of the **p1000** formation are less severe. For the trailing
formation with maximum range equal to 400 km, the resonance artefacts are of
limited magnitude, with the exception of the gravity field model error associated with
the ranging noise. The trailing formation with maximum range equal to 1000 km
shows no significant resonance artefacts.

The propagated noise resulting from the simulations of the cartwheel formation
indicates that the resonance artefacts are located at the degrees that correspond to
the spatial wavelengths approximately equal to the average range. The resonance
artefacts are characteristically spread over a range of degrees; they are not of a
sharp and localized nature and increase the error amplitude by only a modest factor,
from 1.5 to 4. Only the propagated accelerometer noise and orientation noise show
resonance artefacts, in addition to the mis-modelled time-variable signal.

On the basis of Table 8.19, assuming that the degrees at which the resonance

artefact are visible can be extracted from the maximum range $\rho^{(\text{max})}$, and recalling that a is the semi-major axis, the following applies:

$$L^{(\text{resonance})} \approx \text{round}\left(n\,\frac{2\pi a}{\rho'}\right), \tag{8.1}$$

$$n = 1, 2, \dots$$

$$\rho' = \left\{ \begin{array}{ll} \rho^{(\text{max})}, & \text{trailing and pendulum} \\ \rho^{(\text{avg})}, & \text{cartwheel} \end{array} \right. .$$

Eq. (8.1) is only valid for near-circular orbits, since the orbit circumference $2\pi a$ is computed without considering the orbit eccentricity. For the orbits under consideration, this is a reasonable approximation. It should be noted that these equations are accurate to within a few degrees; given the available information, Eq. (8.1) computes degree 58 instead of degree 60 for the cartwheel formation. For the trailing formation it yields one degree above those reported in Table 8.19. Nonetheless, Eq. (8.1) makes it possible to predict $L^{(\text{resonance})}$ from the orbit geometry (given by a) and the formation geometry (given by $\rho^{(\text{max})}$ or $\rho^{(\text{avg})}$).

The analysis of the resonance artefacts is important because it allows one to predict at which degrees the resonance artefacts will decrease the accuracy of the estimated gravity field models. It makes it possible to suggest that the GRACE solutions would be locally inaccurate at around degree 216 (considering $\rho^{(\text{max})} = 200\,\text{km}$ and $a = 6871\,\text{km}$), if it were possible to exploit the data up to that degree.

This knowledge is crucial when designing future gravimetric missions. Figures 8.13 and 8.14 indicate that the increase in propagated error amplitude associated with the resonance artefacts outweighs the gains in accuracy associated with larger maximum range, particularly for the cartwheel and pendulum formations. Only at degrees below the resonance artefacts, there is an improvement in the accuracy of the estimated gravity field parameters. As a result, the maximum range can be chosen so as to circumvent the decrease in accuracy associated with the resonance artefacts. For example, for a future pendulum formation flying at 325 km (this was the altitude proposed by Cesare et al. (2010b)) that is sensitive to the gravitational field up to degree 180, the maximum range should not exceed 234 km.

Insensitivity to the maximum range

The positioning noise (top row of Figure 8.14) and mis-modelled time-variable signal (bottom row of Figure 8.14) of the trailing formation do not show a significant

variation of the geoid height error per degree for different maximum ranges. The propagated positioning noise and mis-modelled time-variable signal for the cartwheel and pendulum would be equally insensitive to the maximum range if the corresponding amplitude spectra were not distorted by the resonance artefacts. This result suggests that the errors associated with the positioning noise and mis-modelled time-variable signal are not sensitive to the maximum range. The exception is the cartwheel formation, where some differences are observed for different maximum range.

In the case of the mis-modelled time-variable signal, larger maximum range results in larger sensitivity to the underlying time-varying signal, recall that spatial variations with long wavelength (below degree 20 or around 4 mHz) have much large power than otherwise (cf. Figure 5.2 and Figure 8.9a). Any values of maximum range up to 1000 km (associated with degree 20), make the gathered data sensitive to the majority of the signal power. Since the error is defined as a fraction of the total signal, any increase in signal sensitivity leads to a proportional increase in error sensitivity. As a result, the SNR remains constant and the DASs do not change significantly with different maximum range.

In case of the positioning noise, the reason for the insensitivity to maximum range is equivalent. In Section 7.4 it is shown that the relative point-wise positioning noise resulting from the relative orbit position noise perpendicular to the LoS direction $\delta^{(P)(pw)(rel)\perp}$ does not depend on the range ρ, cf. Eq. (7.5), the absolute point-wise positioning noise $\delta^{(P)(pw)(abs)}$ is dependent on ρ, cf. Eq. (7.7). In case of the trailing and pendulum formation, $\delta^{(P)(pw)(abs)}$ is largest, cf. Figure 7.3b and c (the green lines related to the relative point-wise positioning noise resulting from the relative orbit position noise parallel to the LoS direction $\delta^{(P)(pw)(rel)\|}$ are not relevant to the current discussion). Therefore, the higher signal sensitivity of a trailing or pendulum formation with larger maximum range compensates the higher positioning noise (in other words, the elements of the normal matrix are proportional to the so-called right-hand side vector). For the cartwheel formation, the $\delta^{(P)(pw)(rel)\perp}$ is largest, cf. Eq. (7.7)a, producing different DASs for different maximum ranges.

8.2.4 Spatial error patterns

Results of the numerical simulations have been presented so far only as degree amplitude spectra. That type of visualization describes how each degree contributes to the estimated error in the gravity field models and is, therefore, suitable to quantify the influence of different error sources in general. What the degree amplitude spectra fail to depict is the spatial pattern of the error, which is the object of analysis in this section.

Not all estimated errors in the gravity field models are analysed; there are 6 noise types for each of the three formations under consideration, resulting in 18 spatial plots, many of which are not significantly different from the others. The analysis focuses on particularities that are relevant. Firstly, the issue of anisotropy is discussed. The spatial patterns of the error in the gravity field models associated with the mis-modelled time-variable signal are subsequently analysed.

Anisotropy

Anisotropy is identified in the spatial plots of the estimated error in the gravity field models as the alignment of spatial error features along a certain direction, also known as *striping pattern*. If the data have anisotropic sensitivity, some Stokes coefficients are estimated with relatively large errors, decreasing the quality of the resulting gravity field models. Fortunately, there are a number of techniques that weight down the erroneous coefficients and minimize the striping patterns (e.g. Swenson and Wahr, 2006; Klees et al., 2008). Notwithstanding, these procedures may suppress elongated geophysical features, such as the signature of an earthquake, because those features are not distinguishable from the striping error pattern when the two have similar spatial orientation. For this reason, a future gravimetric mission should have isotropic sensitivity of the measurements so that the resulting gravity field models are free of striping artefacts.

Figure 8.15, showing the spatial plots of the total measurement noise, presents the typical striping patterns associated with the pendulum and trailing formations: East-West stripping and North-South stripping, respectively. The considered pendulum and trailing formations sample the gravitational field differences exclusively along one direction which is (mainly) oriented along the East-West and North-South directions, respectively, and the collected data are insensitive to variations along the orthogonal direction, resulting in the respective stripping pattern. The spatial pattern of the cartwheel formation shows long and narrow stripes that are often interrupted at the equatorial regions. At low latitudes, the considered cartwheel formation measures the inter-satellite accelerations along (mainly) the radial direction and the gravitational field can be accurately reconstructed. Outside the equatorial belt, the striping pattern emerges, as a result of the lower ratio between the radial and horizontal directions of these inter-satellite baseline vector and by the high-amplitude positioning noise. Recall that the errors in the data of the cartwheel formation are dominated by the positioning noise, so the patterns that are most evident in the spatial domain are those associated with this noise type.

It is also opportune to address the amplitude of the stripping patterns. The amplitude of the geoid height error in case of the trailing formation, 32 mm, is larger

than the one of the cartwheel formation, 11 mm. The pendulum formation produces the errors with the lowest amplitude, 2.2 mm. Notice that the colour bars in the plots are different.

The cartwheel and trailing formations produce error in the gravity field models that contain similar stripping length. In contrast, the stripes in the case of the pendulum formation are (on average) shorter in length and superimposed over a larger-scale (of relatively) isotropic error pattern. This is an advantageous characteristic since the anisotropic sensitivity is limited to shorter distances and the required a posteriori filtering is less intrusive.

The region with largest errors in case of the trailing formation is restricted to the low latitudes, while is extends up to higher latitudes in case of the cartwheel formation and all over the globe for the pendulum formation. The study of mass transport processes, in particular those related to the hydrological cycle, are, in comparison to the pendulum and cartwheel formations, hampered by the large errors that are consistently located at equatorial regions.

It should be noted that the spatial plots of the cartwheel and trailing formations do not exhibit any anisotropy at the poles, resulting from successive polar crossings at different orientations. The pendulum formation also samples the poles at different orientations but, in spite of this, the spatial plot of the pendulum formation depicts East-West stripes at all latitudes. The reason is that the distance between the satellites of the pendulum formation at near-polar locations is consistently very small, resulting in a (comparatively) poor estimation of the gravity field parameters.

In conclusion, the striping pattern in the data gathered by the pendulum formation is of less amplitude and with shorter stripes than in case of the other formations, indicating a more isotropic data sensitivity. Therefore, it is expected that post-processing filtering techniques are less critical to the production of gravity field models from the data collected by the pendulum formation.

Mis-modelled time-variable signal

Future dedicated gravimetric missions have as a main objective the accurate measurement of the time-variable gravitational field, down to the weekly and sub-weekly periods. One important error source, even at such short estimation periods, is associated with the mis-modelled time-variable signal. The number of measuring satellite systems to be launched in the near future will not be sufficient to completely mitigate the effects of temporal aliasing. Therefore, future gravimetric missions are to be insensitive to those effects as much as possible. In this section, the spatial pattern of the mis-modelled time-variable signal is analysed, with the purpose of

(a) cartwheel

(b) pendulum
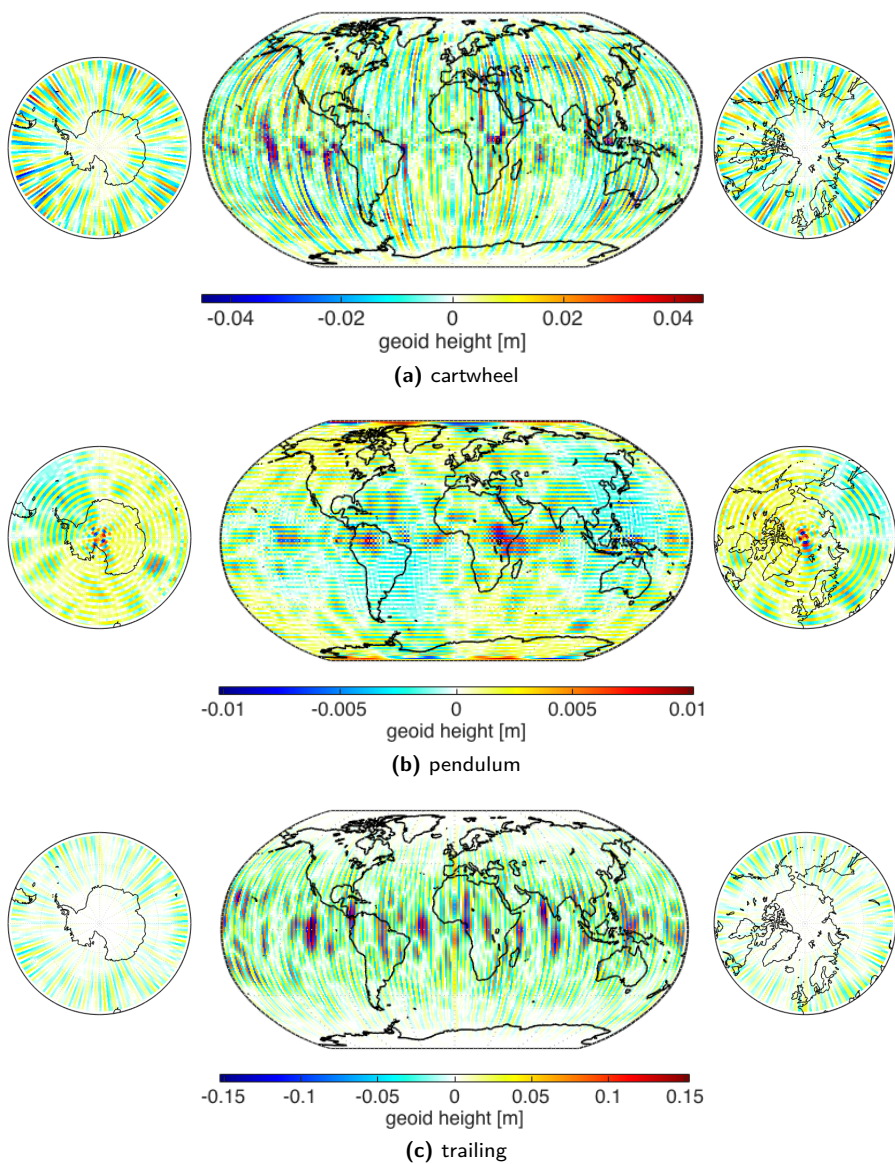
(c) trailing

Figure 8.15 – Spatial maps of the geoid height error due to the total noise for the a) cartwheel, b) pendulum and c) trailing formations with maximum range equal to 200 km.

making a qualitative assessment of the distribution of the errors resulting from temporal aliasing.

Referring to Figure 8.16, the immediate observation is that the spatial patterns of the propagated mis-modelled time-variable signal are vastly different between the considered formations. The latitude range over which the error amplitude is largest is:

- for the cartwheel formation, at the 40° to 80° and −40° to −80° bands,
- for the pendulum formation, fairly homogeneous across all latitudes and
- for the trailing formation, between ±50°.

Moreover, the striping pattern is visible in the North-South direction for the cartwheel and trailing formations and along the East-West direction for the pendulum formation, in the latter case with less amplitude.

The radial attitude of the LoS vector of the cartwheel formation effectively suppresses the detrimental effect of the mis-modelled time-variable signal at latitudes close to the equator. It suggests that a gravimetric satellite mission that measures the inter-satellite acceleration along the radial direction continuously, e.g. a cartwheel formation with three or more satellites, is effective at mitigating temporal aliasing.

The spatial error pattern due to the propagated mis-modelled time-variable signal in the pendulum formation is surprisingly homogeneous with latitude, with the exception of small-scale East-West stripping and restricted regions in the immediate vicinity of the poles where the large errors are concentrated. This result indicates that the pendulum formation is very effective when it comes to minimizing the effects of temporal aliasing. A number of possible reasons for this effectiveness are proposed in Section 8.2.1. The low quality of data at the polar regions can be compensated with other data sources, such as a trailing formation.

The trailing formation is, among the considered formations, the most sensitive to temporal aliasing. The associated gravity field model error is corrupted over the widest latitude band. On the positive side, it shows very little error in the polar regions, from which glaciological studies may benefit.

(a) cartwheel

(b) pendulum
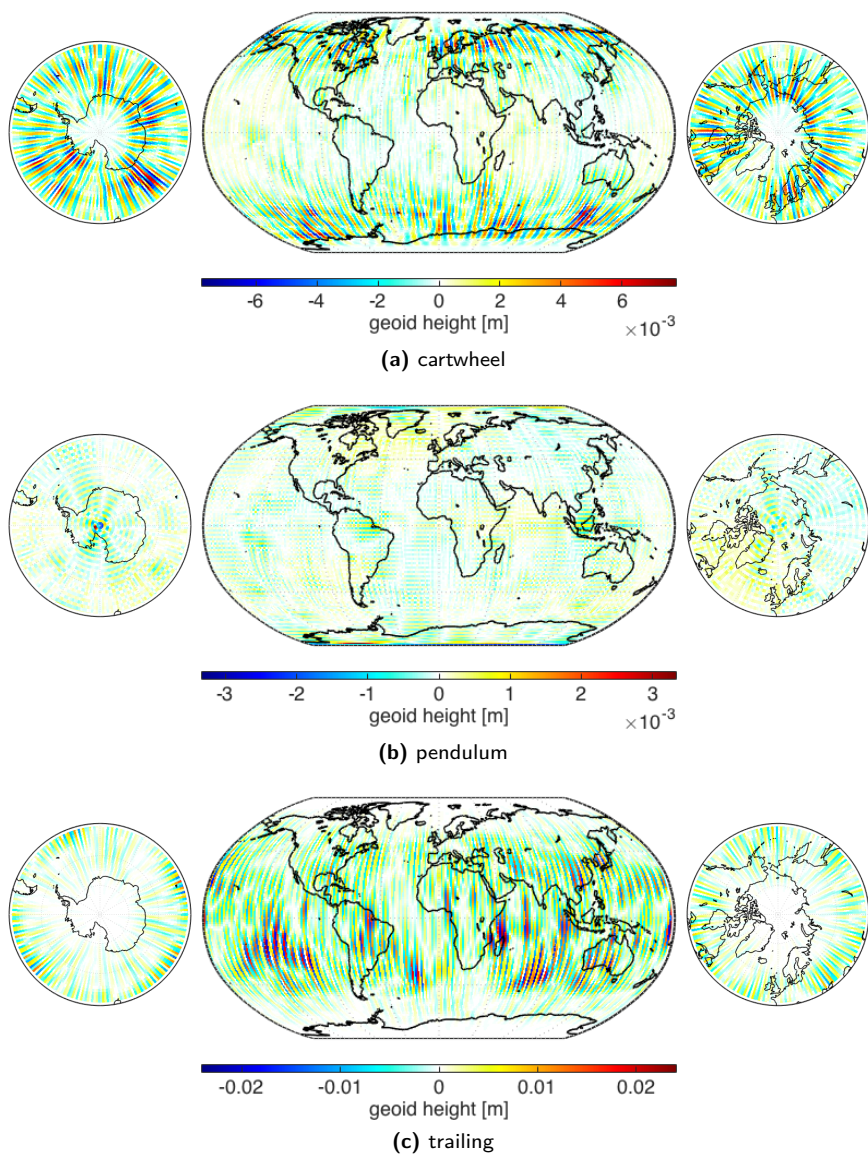
(c) trailing

Figure 8.16 – Spatial maps of the geoid height error due the mis-modelled time-variable signal for the a) cartwheel, b) pendulum and c) trailing formations with maximum range equal to 200 km.

253

8.3   Technical aspects of future gravimetric missions

One aspect of the formations that has been hitherto ignored is the technical complexity and difficulty in reaching a practical and functional design of each of the proposed formations. Addressing this issue was never the purpose of the numerical study but when discussing a concept for a future mission, there is no way to avoid it.

Without any doubt, the trailing formation is the most accessible concept in technical terms, as the GRACE mission proves it. Between the pendulum and cartwheel formation, the former is the easiest to implement. The pendulum formation has been the object of research, e.g. Cesare et al. (2010a); Panet et al. (2012), while there are no such complete studies and design proposals involving the cartwheel formation. Furthermore, the two satellites in the pendulum formation fly at the same altitude, unlike in the cartwheel formation. The problem with having the satellites in the same formation flying at different altitudes comes from the different magnitude of the aerodynamic force acting on them. Consequently, the Attitude and Orbital Control System (AOCS) needs to actively and frequently make corrections in order to keep the range within the nominal values. It should be said that if the satellites are equipped with a Drag-Free Attitude Control Systems (DFACS), this problem becomes an argument in favour of the cartwheel formation, since the higher orbital eccentricity means that the average drag is lower and the required propellant mass is less (or the mission life time is longer).

The largest problem of the cartwheel formation, however, is the wide range of the angular difference between the velocity vector and the LoS vector. This angular difference is of importance because the velocity vector defines the attitude of the body of the satellites, so that it is aligned with the aerodynamic flow to minimize the drag force or, if applicable, to efficiently deliver the thrust commanded by the DFACS. In case of the cartwheel formation, this angular difference is described (to a large extent) by the relative elevation angle (recall that the elevation angle is the angular distance between the local horizontal plane and LoS vector). This angle varies from 0° at one pole, through 90° at the first equator crossing, 180° at the other pole, 270° at the second equator crossing and 360° at the first pole. The resulting difficulties in keeping the beam of the ranging sensor illuminating the other satellite are significant. One possibility would be to assign two quadrants to the ranging sensor in each satellite, so that one satellite is responsible for emitting the tracking signal to be reflected from the other satellite in one hemisphere and the roles are switched every time the satellites cross over the poles. Still, the ranging sensor needs to swivel 180° – the least, to avoid measurement gaps – while the satellite body remains aligned with the incoming aerodynamic flow. One can think of one additional iteration on this idea, by equipping each satellite with two ranging

sensors, each assigned to one quadrant, thus restricting the swivelling system to operate over a 90° range. In any case, the complexity of each satellite is considerable, particularly in comparison to the GRACE satellites.

In case of the pendulum formation, the largest angular difference between the velocity vector and the LoS vector takes place in the horizontal plane, so the relative azimuth angle is relevant (recall that the azimuth angle is the angular distance between the local Northerly direction and horizontal projection of the LoS vector). In case of the pendulum formation considered in the numerical study, the relative azimuth angle is very close to ±90°. As a result of the minimum range of only a few meters, cf. Table 8.3, the relative azimuth angle remains nearly constant during the ascending and descending arcs, switching almost instantly at the poles. A pendulum formation under these conditions is not particularly difficult to implement: each satellite would be equipped with two ranging sensor, each one facing opposite cross-track directions. Each ranging sensor would be responsible for taking measurements at either the ascending or descending arcs. At the poles, one ranging sensor would be turned off, while the other would be turned on, as the satellites paths intersect. As a drawback, it is unavoidable to have measurement gaps consistently at the poles, because the relative azimuth angle is too low to permit the operation of the inter-satellite metrology system at those locations. Furthermore, the simulated formation is not practical because of the high risk of collision. The minimum range has to be at least a few hundred meters but this distance should preferably be kept as small as possible to limit the measurement gap occurring near the cross-over point. Another consideration to be addressed regards the redundancy of the crucial inter-satellite metrology system. Unlike the trailing formation, the pendulum formation would require multiple systems in each satellite.

In conclusion, the least technically feasible formation concept is the cartwheel. The pendulum formation does not present significant technical hurdles. The trailing formation, although the least complex in technical terms, should not be favoured since it is characterized by large measurement errors, significant sensitivity to model errors and considerable data anisotropy.

8.4 Summary and conclusions

In the current chapter, a numerical study on future gravimetric satellite formations is conducted. The simulations considered three formation types, the cartwheel, pendulum and trailing formations. This choice of formations is motivated by the respective orientation of the LoS vector. The cartwheel formation permits the inter-satellite acceleration to be (occasionally) measured along the vertical direction, the

pendulum formation samples the gravitational field along the cross-track direction and the trailing formation collects gravimetric data in the along-track direction.

For each formation, six noise types are considered: i) the accelerometer noise, ii) the correction noise which is proportional to the error in the relative orbital velocity perpendicular to the LoS vector, iii) the orientation noise which quantifies the uncertainty in the orientation of the LoS direction, iv) the positioning noise describing the contribution of the orbital positioning errors, v) the ranging noise that describes the uncertainty in measuring the distance between the satellites and vi) the mis-modelled time-variable signal that depicts the effects of temporal aliasing. Summarized in Table 8.20 are the sensitivity of the formations to different noise types.

The trailing formation is, of the three formations considered in the numerical study, the most sensitive to the accelerometer noise, correction noise and mis-modelled time-variable signal. The cartwheel formation is most sensitive to the orientation noise and positioning noise, while the pendulum formation is most sensitive to the ranging noise.

The trailing formation shows a measurement error in terms of cumulative geoid height at degree 120 equal to 32 mm, the cartwheel formation 11 mm and the pendulum formation, 2.2 mm. The errors of the cartwheel formation are dominated by the positioning noise, which amounts to 76 %. In case of the pendulum formation, the ranging noise dominates, with 48 %. The correction noise dominates the trailing formation with 93 %. The pendulum formation is the least sensitive to temporal aliasing and the trailing formation is the most sensitive.

Recall that the numerical study did not consider the removal of the resonance effect (see Section 2.5.6), which increases significantly the accuracy of the estimated gravity field parameters by mitigating low-frequency errors, i.e. particularly those associated with positioning noise, correction noise and orientation noise. Assuming that these effects effectively mitigated, the results predict a much higher level of accuracy, i.e. the cartwheel and pendulum formations would determine Earth's gravitational field with a cumulative geoid height error at degree 120 of 1.7 mm and 2.0 mm, respectively, the former mainly driven by the mis-modelled time-variable signal and the latter by the ranging noise. The trailing formation error would be at the level of 5.7 mm, mainly as the result of the mis-modelled time-variable signal and accelerometer noise.

The analysis considered a maximum range equal to 200 km. With the purpose of gaining insight into the way this parameter affects the accuracy of the estimated gravity field parameters, two additional values of maximum range are considered: 400 km and 1000 km. As expected, larger maximum ranges lead to a more accurate estimation of the gravity field parameters, particularly in the trailing and cartwheel

noise type	cartwheel	pendulum	trailing
accelerometer noise	0.43	0.89	<u>2.2</u>
correction noise	4.6	4.9×10^{-9}	<u>31</u>
orientation noise	<u>2.0</u>	5.0×10^{-4}	0.037
positioning noise	<u>9.3</u>	0.91	5.8
ranging noise	0.85	<u>1.5</u>	0.36
mis-modelled time-variable signal	1.4	0.92	<u>5.3</u>
total measurement noise	11	2.2	<u>32</u>
contribution of dominant noise type	positioning noise: 76 %	ranging noise: 48 %	correction noise: 93 %
advantages	Potentially very accurate, if correction noise, orientation noise positioning noise are mitigated.	Insensitive to correction noise and orientation noise; low sensitivity to positioning noise and mis-modelled time-variable signal.	Low sensitivity to orientation noise.
disadvantages	Extremely sensitive to positioning noise; North-South stripes away from equator and poles.	East-West stripes at all latitudes; high mis-modelled time-variable signal at the poles.	High sensitivity to correction noise and mis-modelled time-variable signal; North-South stripes away from poles; low level of isotropy.

Table 8.20 – Overview of the simulation results in terms of cumulative geoid height errors at degree 120 (in millimetres) and summary of the advantages and disadvantages of each formation. The underlined values indicate the formation with the highest error magnitude for each noise type.

formation, although the benefit is limited to the low degrees in the latter. The degree amplitude spectra showed patterns of localized error increase, to which the term *resonance artefacts* is attributed. They limit the benefits of the larger maximum range and predictably occur at the degrees equal to the multiples of the ratio between the orbit perimeter (i.e. $2\pi a$, with a being the semi-major axis) and the maximum range for the trailing and pendulum formations or the average range for the cartwheel formation.

Concerning the spatial error patterns, the pendulum formation produces data with the highest level of isotropic sensitivity, while the trailing formation the lowest. The stripping pattern in the trailing and cartwheel formation is aligned with the North-South direction and in case of the pendulum formation with the East-West direction. The pendulum formation shows stripes at all latitudes but of less amplitude and length than the other formations. The error pattern of the cartwheel formation does not show stripes close to the equator and at the vicinity of the poles. The trailing formation shows stripes at all latitudes except at the polar areas.

In summary, the pendulum formation produces the most accurate data; is the least corrupted by the mis-modelled time-variable signal and positioning noise. It is remarkable that the inertially-frozen attitude of the LoS direction of the pendulum formation effectively mitigates the correction noise. The spatial pattern of the estimated error in the gravity field models indicates some data anisotropy, although not as severe as for the trailing formation. All these characteristics make the pendulum formation the prime candidate for a future gravimetric mission.

Conclusion and recommendations

<div style="text-align: right">9</div>

The research described in the thesis has the objective of gaining a better understanding of how to measure Earth's temporal gravitational field variations with gravimetric satellite formations, optionally augmented by non-dedicated satellites.

As discussed in Section 1.2.2, the need for this research line is justified by a number of limitations in similar studies, cf. Table 1.2:

  i. the lack of frequency description of the noise time series (with the exception of the ranging noise), in particular those resulting from orbit position noise;
 ii. often ignored noise types, such as as positioning noise, and the assumption that if a noise type is not significant in Gravity Recovery And Climate Experiment (GRACE) data, is will remain so in other formations;
iii. the focus on dedicated gravimetric satellites, which due to their high production and operation costs, are necessarily limited in number and, therefore, limited in the temporal sampling of the gravitational field.

The following areas are studied in detail, in order to tackle the aforementioned limitations:

  i. improving the accuracy of the predictions of future gravimetric data quality, which is addressed by considering a validated realistic noise model as well as estimating the influence of errors in the gravity field parameters;
 ii. determining the anisotropic sensitivity of the data and the influence of different noise types, which is investigated in the simulation of the cartwheel, pendulum and trailing formations, considering full-scale inversions of error time series produced on the basis of a realistic noise model;

   iii. minimizing the effect of temporal aliasing, by exploiting non-dedicated satellite missions to improve the temporal sampling of the gravitational field and by finding formation geometries which are least sensitive to temporal aliasing.

A number of points can be highlighted in the research presented in the thesis. The use of non-dedicated missions to augment the dedicated missions constitutes a distinctive approach to reduce the effect of temporal aliasing on the accuracy of the estimated gravity field models. The simulation of all foreseeable errors is compared with the errors estimated from GRACE data and shown to accurately represent them. On the basis of the error simulations, it is demonstrated that the cartwheel formation is highly sensitive to orbit errors. Finally, the numerical simulations have shown that the cross-track pendulum formation is virtually insensitive to some noise types and significantly less sensitive to temporal aliasing, when compared to other formation geometries.

Section 9.1 lists the major findings of the thesis. Section 9.2 provides further discussion based on new knowledge gained in the thesis research. The recommendations for future research are tackled in Section 9.3. The chapter concludes with some final remarks in Section 9.4.

9.1 Summary

The presentation of the results is divided into four major parts:

   i. the added value of non-dedicated satellites to decrease the effects of temporal aliasing is studied in **Chapter 5**, particularly at long wavelengths where temporal aliasing is most influential;

   ii. the analysis and validation of the noise model is presented in **Chapter 6**, demonstrating that it represents accurately the errors in gravimetric satellite measurements;

   iii. the components of the positioning noise are investigated analytically and numerically in **Chapter 7**; and

   iv. the numerical analysis of three different gravimetric formations – trailing, pendulum, and cartwheel – is the subject of **Chapter 8**, with the purpose of identifying the advantages and disadvantages of each concept.

In **Chapter 5**, the effects of temporal aliasing associated with mis-modelled time-variable signal are shown to be effectively minimized at low spatial frequencies by augmenting future gravimetric missions with a constellation of non-dedicated satellites carrying on-board geodetic-quality Global Navigation Satellite System (GNSS)

receivers. The lower accuracy of the data gathered by the non-dedicated satellites can be counter-acted by large spatial and temporal density of the measurements. It is shown that those data contribute to resolve large-scale and short-term gravitational signals, such as those with wavelengths larger than 1000 km and periods shorter than 1 month (even down to a few days).

In order to predict the future error levels, there must be an understanding of how they contaminate data from existing satellite missions. Chapter 6 is a collection of studies that analyse and quantify the errors in the data acquired by the GRACE mission. These studies are based on the noise model proposed by Ditmar et al. (2012), or, in case of Section 6.1, intend to quantify its important ingredients. The noise types that compose it are, cf. Section 4.3.3:

- accelerometer noise, describing the errors in measuring non-gravitational accelerations;
- correction noise, resulting from the inaccurately known relative velocity perpendicular to the Line of Sight (LoS) vector and associated errors in reconstructing the frame accelerations of the rotating LoS direction;
- orientation noise, which is the inaccurate representation of the orientation of the LoS vector;
- positioning noise, associated with in the errors in the orbit positions;
- ranging noise, related to the errors in measuring the range; and
- mis-modelled time-variable signal, representing the effects of the errors in the models describing the rapid mass changes in the atmosphere and oceans.

The first step, described in **Section 6.1**, is to take advantage of the K-Band Ranging (KBR) data collected by GRACE and determine the spectra of the relative position and velocity errors, projected onto the LoS direction. They dominate at the frequencies below 0.2 mHz and quickly decrease at higher frequencies, see Figure 6.5.

The second step of analysing actual GRACE data, discussed in **Section 6.2**, focuses on comparing the a posteriori residuals with synthetic noise representing different noise types at different frequency bands, so that it is possible to identify the dominant source in each band. As a result, the understanding of the data gathered by the GRACE mission is improved with the associated benefits for the prediction of the accuracy of future missions. A mis-modelled static signal was uncovered in the data, illustrating that: i) the GRACE data are sensitive to the gravitational signal up to degrees in excess of degree 180 and ii) the background force model needs to be extended to a such degree to eliminate the errors introduced by the omission signal. Furthermore, it was confirmed that the ranging noise is only significant at frequencies above 9 mHz, which leads to an amplitude of the errors in the estimated gravity field model coefficients one order of magnitude lower than the actual data

noise. The effect of the errors associated with the mis-modelled time-variable signal is not substantial enough to explain the magnitude of the errors in the data. One reason is that the amplitude of the mis-modelled time-variable signal is restricted to low frequencies.

In **Section 6.3**, GRACE a posteriori residuals are exploited to validate the noise model adopted in this study. The simulated errors are compared to the GRACE a posteriori residuals in terms of the range combination error and in terms of the gravity field model error. The range combinations represent time-averaged inter-satellite accelerations projected onto the LoS direction. The simulated positioning noise is calibrated with help of actual data (up-scaled by a factor of 6.22), in order to incorporate in the simulation environment the effects of the imperfectly-estimated initial state vectors, which originate from errors in GNSS observations. The amplitude of the error in the gravity field models is under-estimated by a factor of two, considering the cumulative amplitude at degree 120, because it is yet to describe the error source in the $1-9\,\mathrm{mHz}$ bandwidth (see Section 6.2). However, this discrepancy is sufficiently small to allow the utilization of the noise model in the study of future gravimetric missions, after considering a 3-fold improvement in the orbit accuracy resulting from a new generation of GNSSs and a laser ranging sensor (refer to Table 8.7 for more details).

In **Chapter 7**, the absolute and relative components of the positioning noise are quantified for the cartwheel, pendulum and trailing formations. Although the positioning noise is a scalar quantity at the level of range combinations, it originates from the absolute and relative components of the orbit position noise. It is shown that the cartwheel formation suffers from a very high sensitivity to the positioning noise resulting from the relative orbit position noise perpendicular to the LoS direction. This is a fundamental characteristic of this formation that results from the amplification of the relative orbit position noise by diagonal components of the gravity gradient tensor (defined in the Local Horizontally-aligned Reference Frame (LHRF, Section A.3)), while the pendulum and trailing formations are only affected by off-diagonal components, which are small in their case. The simulations also show that the elimination of the orbit errors along the LoS direction, by exploiting data collected by the ranging sensor, is futile in case of the cartwheel formation. The orbit adjustment is most effective in case of the pendulum formation, with an improvement of around one order of magnitude.

The objective of **Chapter 8** is to conduct a numerical study of all noise types for the same three satellite formations as in Chapter 7. The analysis is done in terms of range combinations, degree amplitude spectra and per-coefficient plots up to degree 120, so that the mission configuration that produces the most accurate results can be identified. The considered noise types are those defined in the noise model,

described in Section 4.3.3. In terms of cumulative geoid height degree amplitude at degree 120, the trailing formation shows an error (32 mm) 3 times higher than the cartwheel formation (11 mm), which in turn is 5 times less accurate than the pendulum formation (2.2 mm).

The errors of the cartwheel formation are dominated by the positioning noise, which amounts to 76 %. The correction noise dominates in the data from the trailing formation with 93 %. The ranging noise is the largest in the pendulum formation, accounting for 48 %. The correction noise is the second most intense noise type in the cartwheel formation (19 %), while it is the positioning noise and mis-modelled time-variable signal in the trailing formation, respectively 3.4 % and 2.8 %. In case of the pendulum formation, the mis-modelled time-variable signal, positioning noise and accelerometer noise are comparable in terms of contribution to the total noise with 18 %, 17 % and 17 %, respectively.

In what concerns the mis-modelled time-variable signal, the pendulum formation stands out as being most insensitive to it. The simulations show that the degree RMS of the gravity field model error at degree 120 is 0.92 mm. In comparison, these errors are 1.4 mm for the cartwheel formation and 5.3 mm for the trailing formation.

Note that the numerical study does not remove the resonance effect (see Section 2.5.6), which increases significantly the inaccuracy of the estimated gravity field parameters by propagating the low-frequency errors, particularly orbital errors (i.e. those associated with positioning noise, correction noise and orientation noise). In case the effects of the orbital errors are ignored, the cartwheel and pendulum formations would determine Earth's gravitational field with a cumulative geoid height error at degree 120 of 1.7 mm and 2.0 mm, respectively, the former mainly driven by the mis-modelled time-variable signal and the latter by the ranging noise. The trailing formation error would be at the level of 5.7 mm, mainly as the result of the mis-modelled time-variable signal and accelerometer noise.

In Section 8.2.3, in addition to the maximum range equal to 200 km considered so far, two additional values are of maximum range considered: 400 km and 1000 km, permitting the identification of patterns of localized increase in error-per-degree, called *resonance artefacts*, at the degrees inversely proportional to maximum range in case of the trailing and pendulum formations and average range in case of the cartwheel formation.

In what concerns the errors in the spatial domain, described in Section 8.2.4, the considered pendulum and trailing formations produce errors in the gravity field models with striping patterns (mainly) oriented along the East-West and North-South directions, respectively. This is a result of the (nearly) constant orientation of the LoS vector, parallel to the respective directions. The spatial pattern of the cartwheel formation shows long and narrow stripes aligned with the North-South

direction, since the errors in the data collected by this formation are dominated by the positioning noise. At low latitudes the strips are interrupted since the inter-satellite accelerations are measured along (mainly) the radial direction and the positioning noise is of less amplitude. The amplitude of the stripping patterns is lowest in the pendulum formation and highest in the trailing formation. Furthermore, the stripes in the case of the pendulum formation are (on average) shorter in length and superimposed over a larger-scale (of relatively) isotropic error pattern. From these findings, it is possible to say that the data sensitivity of the pendulum formation is most isotropic, while that of the trailing formation is the least isotropic. The region with largest errors in case of the trailing formation is restricted to the low latitudes, while those errors are visible up to higher latitudes in case of the cartwheel formation and at any latitude for the pendulum formation. The successive polar crossings at different orientations ensures that the errors are of low amplitude at the poles for the cartwheel and trailing formations. The errors in the data collected by pendulum formation are not of less amplitude at the poles because the distance between the satellites is very small at those regions.

9.2   Conclusions

In **Chapter 5**, is was shown that non-dedicated satellites help resolving the high-frequency temporal gravitational field variations, in spite of the fact that this can only be achieved with a few dozens of satellites. Non-dedicated satellites with a GNSS receiver are a resource that will likely be available in the near future. Foust (2015) reports that OneWeb (`www.oneweb.world`) plans to build 900 micro-satellites for global communications, BlackSky Global (`www.blacksky.com`) plans to launch 60 satellites for Earth imagery, UrtheCast (`www.urthecast.com`) plans to launch 16 optical and Synthetic Aperture Radar (SAR) imagery satellites. In addition, Iridium NEXT (`www.iridium.com`, Gupta, 2008) is soon to launch 66 global communication satellites, the FORMOSAT-3/COSMIC (F3C) (Kuo et al. 1999, 2005) and FORMOSAT-7/COSMIC-2 (F7C2) (Ector et al. 2010; Cook et al. 2013) constellations will add 12 radio occulation satellites and the Community Initiative for Continuing Earth Radio Occultation (CICERO, `geooptics.com`) project proposes to launch 24 or more satellites for severe weather monitoring. Hsu (2015) also reports that SpaceX (`www.spacex.com`), with support form Google (`www.google.com/about`), plans to provide Internet access to developing regions of the world through a constellation of 4000 satellites. All these satellites can easily be equipped with miniaturized GNSS receivers (Virgili and Roberts, 2013) and antennas (Pesyna et al., 2014), as well as accelerometers (Dubovskoi et al., 2012) (although

the latter are not strictly needed). In what regards attitude determination systems, those are already routinely flow in CubeSat satellites with accuracies $\approx 0.1°$ (which results in sub-millimetre accuracy for satellite sizes in the order of 0.1 m). These data come at virtually no additional cost, especially when compared with *flagship* missions, and has the potential of having extremely high temporal resolution. In case the commercial satellite operators are not willing to cooperate, the cost of launching small CubeSats or mass-produced cannonball-style satellites is not particularly high.

The analysis presented in **Chapter 6** did not succeed in identifying the dominant source of noise in the range of intermediate frequencies, at $1-9$ mHz. Nevertheless, it was uncovered that the errors on this frequency band are stationary, indicating that they possibly originate in the instrumentation of the GRACE satellites. A possible source for these errors is the attitude determination system (Bandikova and Flury, 2014; Inácio et al., 2014) and/or the accelerometers (Peterseim et al., 2014). The former errors are effectively mitigated by a laser interferometry system with the Corner-Cube Retroreflector (CCR) positioned at the Centre of Mass (CoM) (such as the one proposed by Cesare et al., 2010b) The latter errors can be reduced by incorporating in future gravimetric missions the accelerometers, rigid spacecraft structure and thermal control capabilities similar to those developed for the Gravity field and steady-state Ocean Circulation Explorer (GOCE) mission.

As discussed in Section 6.2 and in the context of GRACE follow-on missions, the errors in the static field used in the background force model may propagate to the time-varying gravitational field solutions in a different way for each new solution (i.e. as a fictitious time-varying signal) as a result of the changing ground-track pattern and the non-uniqueness of the gravity field recovery. Although the GOCE mission has made it possible to compute accurate static gravity field models up to a high spherical harmonic degree, the highly accurate sensors of future missions may produce data that are sensitive to even higher degrees than those covered by GOCE. The solution to this problem is to produce a static model (i.e. considering a long period of data, such as one year) up to a high degree (above the maximum degree of the time-varying solutions). This tailored static model does not represent the actual static gravity field but depicts the systematic errors with which it is observed by the future gravimetric satellite mission, possibly as a result of the non-uniqueness of the gravity field recovery. Nevertheless, it would be able to capture all static signal, preventing it from appearing in the time-varying solutions.

The findings made in Section 6.3.5 tell that the high amplitude of the positioning noise simulated as the difference between EIGEN-5C and EIGEN-CG03C is mainly the result of the imperfectly-estimated initial state vectors. This is because a calibration factor of 6.22 is needed in order to reproduce the positioning noise estimated from actual GRACE data. Had the analysis been done with a more recent pair of models,

e.g. GOCO03S and EIGEN-6C4, the calibration factor would have been larger as a result of the smaller difference between these models than the models considered in the production of the positioning noise (EIGEN-5C and EIGEN-CG03C). It is, therefore, more advantageous for the mitigation of the positioning noise to improve the accuracy of the estimation of the initial state vectors than to increase the accuracy of the background force model. This can only be achieved by more accurate GNSS measurements and methodological advances in producing Kinematic Orbits (KOs).

In **Chapter 7**, the amplitude of the positioning noise is quantified for the considered formations. The results presented in this section are derived with the acceleration approach used in the production of the Delft Mass Transport (DMT) model. Nevertheless, the positioning noise is also present in other approaches because these errors results from imperfections in background force models used to integrate the orbits. In some approaches, such as those based on variational equations or short arcs, the orbits are inherently kept in agreement with the estimated gravity field parameters. Nevertheless, that characteristic does not ensure that the computed orbits are error free since the produced gravity field models are not error-free themselves. An additional consideration is that the estimation of the initial state vectors in other approaches may be more robust than in the case of the orbits used in the production of the DMT model. In spite of this, it is unlikely that the calibration factor is much lower in value (certainly not close to one). In general, the results of Chapter 7 should be understood in relative terms between the formations and the quantitative results can be somewhat different in case of other approaches used for the inversion of gravity data into gravity field parameters.

One of the most important results of Chapter 7 is that the cartwheel formation is extremely sensitive to positioning noise. Since the positioning noise is mainly the result of errors in GNSS observations (through the imperfectly-estimated initial state vectors), the expected improvement in accuracy of these observations is modest (cf. Section 6.1.7), in particular when compared to technological improvements in inter-satellite metrology systems. In practice, this means that the cartwheel formation is probably, of the considered formations, the one to benefit the least from technological advances.

An important finding presented in **Chapter 8** is that the correction noise is practically non-existing in the pendulum formation. This is the result of the nearly constant attitude of the LoS vector in inertial space. In comparison, the cartwheel formation, which also shows a fairly stable attitude of the LoS vector (inertial elevation between $-19°$ and $27°$, cf. Table 8.4), is under the influence of correction noise which is nine orders of magnitude more intense. It should be noted that the orbits of the cartwheel formation maybe be fine-tuned to reduce the amplitude of the variations of the inertial elevation of the LoS vector, thus decreasing the amplitude

of the correction noise. In contrast, there is no such option in case of the trailing formation. One possibility to reduce the correction noise is to measure the attitude of the LoS vector, which has been accomplished so far by exploiting the orbits of the satellites. In a similar idea to a star-tracker, both satellites could be equipped with high-definition cameras that record the position of the other satellite relative to the background stars, with very angular resolution if suitable optics are employed. These measurements would directly provide the inertial attitude of the satellites. Unfortunately, the Sun glare and the Earth surface (the latter relevant in case of the cartwheel formation) might reduce the periods when these data can be collected, limiting their usefulness.

The analysis of the positioning noise in Section 8.2.1 demonstrated that the models based on the trailing formation are affected by this noise type up to a high degree. In this case, the slowly-changing amplitude of the long-wavelength errors accumulate as numerous ascending and descending tracks because there is little East-West sensitivity in the data, resulting in large errors in to sectorial and near-sectorial coefficients. In contrast, the pendulum formation effectively limits the impact of the positioning noise to low degrees because it is able to sample near-sectorial coefficients, given the East-West orientation of the LoS direction most of the time. As a consequence, the mitigation of this noise type by high-pass filtering (refer to Section 2.5.6) in case of the pendulum formation should be particularly effective.

In Section 8.2.4, it is shown that the region with largest errors in case of the trailing formation is restricted to the low latitudes, while it is located at higher latitudes in case of the cartwheel formation and at all latitudes for the pendulum formation. This observation is of interest to hydrological studies, since some areas of the globe are retrieved less accurately than others, except in case of the pendulum formation. The stripes in the case of the pendulum formation are (on average) shorter in length and superimposed over a larger-scale (of relatively) isotropic error pattern. This is an advantageous characteristic since the anisotropic sensitivity is limited to shorter distances and the required a posteriori filtering is expected to be less intrusive.

In addition to the spatial error patterns of the total noise, those associated with temporal aliasing were also analysed in Section 8.2.4. The trailing formation is, among the considered formations, the most sensitive to temporal aliasing; furthermore the associated gravity field model error affects the widest latitude band. On the positive side, it shows very little error in the polar regions, from which glaciological studies may benefit. The radial attitude of the LoS vector of the cartwheel formation effectively suppresses the detrimental effect of the mis-modelled time-variable signal at latitudes close to the equator. This suggests that a gravimetric satellite mission that measures

the inter-satellite acceleration along the radial direction continuously, e.g. a cartwheel formation with three or more satellites, Wiese et al. (2009), might be effective in mitigating temporal aliasing. The spatial error pattern of the propagated mis-modelled time-variable signal in the pendulum formation is surprisingly homogeneous with latitude, with the exception of small-scale East-West stripping and restricted regions in the immediate vicinity of the poles where the large errors are concentrated. This result indicates that the pendulum formation is very effective when it comes to minimizing the effects of temporal aliasing. A possible reason for this effectiveness is that the larger width of the ground-track strip sensed by the pendulum formation combined with the higher sensitivity to mass variations outside this strip (as a result of the cross-track orientation of the LoS vector), favours the averaging of the high-frequency mass transport processes. The cartwheel and trailing formation, on the other hand, have nearly zero cross-track separation, so the strip of surface to which they are sensitive to is narrower.

The findings reported in the thesis support the pendulum formation as the best option for a future gravimetric satellite missions. This formation is accurate and technically feasible. The reasons for that are as follows:

- compared with the trailing and cartwheel formations, the pendulum formation is the **least sensitive to the mis-modelled time-variable signal**;
- the pendulum formation is highly insensitive to correction noise, orientation noise and, of the simulated formations, is the least sensitive to positioning noise, i.e. **least affected by orbit errors** – this is noteworthy since the accuracy of GNSS is not predicted to improve significantly in the foreseeable future;
- the pendulum formation collects data with **more isotropic sensitivity** because the striping pattern is of less amplitude and with shorter stripes than the other formations;
- in combination with a polar trailing formation, such as the planned GRACE Follow On (GFO) (Sheard et al. 2012; Larkin 2012; Zaragoza 2013), there would be **multiple synergistic advantages**:
    i. the resulting data would have a high isotropic sensitivity in view of the combined orthogonal sampling directions;
    ii. the accurate data gathered by the trailing/pendulum formation at the polar/equatorial locations would compensate the lower data quality gathered by the counterpart formation at those locations;
    iii. the failure of either formation in the constellation does not result in the loss of global coverage, as is the case of other proposals, such as the *Bender* formation.

9.3 Recommendations

As a result of the lack of understanding of noise in the intermediate frequency range, $1-9$ mHz, it is very difficult to derive an appropriate noise model to describe it. Possibly, this error is particular to the GRACE mission, since it may be caused by deficiencies in the processing of attitude data (e.g. Bandikova and Flury, 2014). It is important to complete the noise model with the missing noise types, in order to predict their role in future gravimetric missions.

The simulation of the low-low Satellite-to-Satellite Tracking (ll-SST) observations done in the context of the added value of a constellation of non-dedicated satellites was conducted under the *simplistic noise model*. At the time this study was conducted, the *advanced noise model* (considered in the remainder of the thesis) was not yet developed. Although the qualitative results would not change significantly, it would be useful to upgrade the noise model in that study. In addition, knowledge gained from the simulation of future gravimetric satellite formations has identified the pendulum formation as particular insensitive to the effects of temporal aliasing resulting from errors in the Atmosphere and Ocean De-aliasing Level 1B (AOD1B) product. The question that follows is to what extent the data from a non-dedicated satellite constellation provide an added value to the pendulum formation. On the other hand, it might be the case that the lower sensitivity of the pendulum formation to temporal aliasing in combinations with the densely sampled data from the non-dedicated constellation improves the estimation of the high-frequency time-variable gravitational field much more than described in Chapter 5.

One assumption in the thesis is that the temporal aliasing results from errors in the AOD1B product, which are set equal to 10 % of signal. This is may be an overly simplistic assumption. A more accurate simulation of the effects of temporal aliasing would not only improve the prediction of the accuracy of future missions but also provide clues to understand the effects of temporal aliasing better. One of the possible approaches is to consider the difference between two alternative meteorological models describing atmospheric pressure variations, which are the major contributor to non-tidal mass transport in the atmosphere and ocean (Velicogna et al., 2001; Thompson et al., 2004; Han, 2004a). Another possible approach is to make use of the error estimations provided by a meteorological model itself (Zenner et al., 2010). Yet another possibility is to consider a long time series of de-aliasing models and apply a Principal Component Analisys (PCA), discarding the most significant principal components and reconstructing the model errors as the sum of the least significant components. In this way, the temporal correlations are maintained and the spatial distribution is that of the orthogonal components that captures the lowest amount of variance in the original signal.

Other sources of temporal aliasing, in particular ocean tide model errors, should be considered. This type of temporal aliasing was not considered because the focus of the analyses was on the effects of atmospheric mass transport model errors (and corresponding ocean response). Although it is reasonable to consider the simplistic assumption that the errors in the AOD1B model are 10 % of the signal, that would not be the case in ocean tide models; the errors in these models are much more geographically restricted. They are located mainly at polar regions and areas covered with shallow seas (Schrama and Visser, 2006; Ray et al., 2009; Müller et al., 2014). Another important difference is related to the propagation of the respective aliasing signals to the gravity field parameters; Murböck et al. (2013, Figure 12) shows that the tidal signal aliases strongly into particular degrees, while the temporal aliasing caused by non-tidal signals in the atmosphere is smoother and spreading over wider degree ranges. Furthermore, the repeat periods of the orbits considered in the analysis of tidal model errors must be selected in such a way that the aliasing periods of all tidal constituents are avoided or, if that is not possible, affect all formation geometries in a similar way. Failing to do so would introduce a disproportionate effect of temporal aliasing associated with tide model errors among the formation geometries. These particularities are sufficient motivation to investigate the effects of ocean tide model errors in the proposed pendulum formation, in spite of other studies demonstrating that the effects of aliasing caused by tidal and non-tidal signals are of similar amplitude (Visser, 2010; Reubelt et al., 2014, which consider pendulum formations with non-zero along-track offset).

It is of importance to extend the simulation of the pendulum formations by considering different latitudes of the cross-over point, which should be close to 90° to limit relative drift of the right ascension of the ascending node. Additionally, it is important to investigate the effect of non-zero along-track offset in the pendulum formation to the correction noise and orientation noise. It might be the case that small increments of along-track offset increase significantly the effects of these noise types, severely limiting the advantages of the cross-track pendulum formation.

Since the pendulum formation stands out as a promising configuration for a future gravimetric mission, the positioning noise, one of the most significant noise types, should be better understood. In Section 7.5, the positioning noise in the pendulum formation was determined to arise mainly from the absolute orbit position noise. Decomposing the influence of the radial, along-track and cross-track components of the absolute orbit position noise would give further insight into how to best mitigate the positioning noise. The Precise Orbit Determination (POD) strategies could be fine-tuned to increase the accuracy of the orbits in the direction where positioning noise is affected the most.

The analysis is focused on single satellite pairs. In reality, usage of multiple pair

would improve the temporal sampling, particularly by combining different orbit repeat cycles (Wiese et al., 2011b; Elsaka, 2013; Murböck and Pail, 2014). In addition to the benefits in terms of temporal sampling, the combination of the proposed pendulum formation with a trailing formation should provide models with very high quality. This is a promising aspect that should be further investigated, since the weaknesses of one formation are optimally compensated by the other formation. The research into multiple formations is currently of particular importance, given the fact that the GFO mission (consortium between NASA/JPL, CSR, DLR and GFZ) is to be launched in the near future (Sheard et al., 2012; Larkin, 2012; Zaragoza, 2013) and other institutions, such as the European Space Agency (ESA) (e.g. Anselmi et al., 2010) and the Chinese Academy of Sciences (CAS) (Ye et al., 2009) are planning their own gravimetric satellite missions. The identification and quantification of the potential synergies between multiple dedicated missions is a significant consideration in the design of those missions. This consideration is particularly relevant to parameters that can be changed without many consequences, such as the orbit repeat period.

The intrinsic sensitivity of a formation to temporal aliasing is an important factor in selecting the optimal measurement system. However, those considerations do not reflect the latest developments in processing strategies that mitigate the effects of temporal aliasing (e.g. Kurtenbach et al., 2009; Wiese et al., 2011c). Future studies should consider these strategies so that they are incorporated into the error budget and a more accurate prediction of the effect of temporal aliasing can be derived. This is particularly relevant when the technical difficulty of implementing a particular formation is addressed.

The spatial pattern of the error in the gravity field models based on the pendulum formation indicates some data anisotropy (although not as severe as for the trailing formation). One possible solution to this problem is to complement the suggested pendulum formation with a polar trailing formation, such as the GRACE Follow On (GFO) (Sheard et al. 2012; Larkin 2012; Zaragoza 2013). The proposed polar pendulum/trailing constellation can be seen as a modification to the *Bender* formation, where the inclined trailing formation is replaced by the polar pendulum formation. The combined data would have a highly isotropic sensitivity in view of the orthogonal sampling directions. Furthermore, the low-quality measurements gathered by the pendulum formation close to the poles (because of persistently small range) are effectively redeemed by the isotropic and high-quality data of the trailing formation (as a result of the converging orbits and high ground-track density). The proposed modification, in addition to the discussed advantages of the pendulum formation and the aforementioned synergistic effect of the pendulum/trailing formations, ensures that the failure of either formation in the constellation does not result in the loss of global coverage.

One of the difficulties identified in the prediction of the quality of the data in future missions is the combination of model and measurement errors. Unlike the measurement errors, the model errors are not constrained by technical characteristics, such as instrument noise amplitude and spectra. Model errors rely exclusively on assumptions, e.g. how to simulate the errors caused by mis-modelled static signal. The simulated errors produced as the difference between two existing gravity field models should be carefully scaled down to reflect the accuracy of future models. Without such scaling, adding these simulation results to the noise budget of a formation would distort the analysis of the results. A more suitable approach would be to analyse a large number of increasingly accurate models (starting from models from the pre-CHallenging Mini-Satellite Payload (CHAMP) era, up to models from the GOCE era) and derive a trend describing the accuracy of those models over "time", or rather, over the semi-continuous increase in data quality and processing advances. This would make it possible to extrapolate the accuracy of the static errors in the context of future missions, under the assumption that the trend is maintained.

9.4   Final remarks

With the purpose of measuring Earth's temporal gravitational field variations, the thesis tackles the objectives of i) minimizing the detrimental effect of temporal aliasing, ii) improving the accuracy of the predictions of future gravimetric data quality and iii) finding the best formation geometry for a future gravimetric mission. The proposed means to reach these objectives are to i) exploit constellations of non-dedicated satellites, equipped with miniaturized GNSS instruments and attitude control systems, ii) consider the *advanced* noise model, which is as descriptive as possible of all foreseeable errors in gravimetric data and iii) sample the gravitational field with a purely cross-track pendulum formation. As demonstrated in the thesis, the aforementioned measures constitute a significant and noteworthy advance towards collecting high quality gravimetric satellite data.

Reference frames

A

The reference frames relevant to the thesis are briefly described in this chapter. The purpose is mainly the disambiguation, since the same reference frame is often referred to with different names in various publications.

A.1 Celestial Reference Frame

The Celestial Reference Frame (CRF), also known as Earth-Centred Inertial reference frame (ECI), Conventional Inertial Frame (CIF) and Inertial Reference Frame (IRF), is the quasi-inertial reference frame defined with the x-axis pointing towards the direction of the mean equinox at J2000.0 epoch (12:00 on 1st of January, 2000, Terrestrial Time (TT)), the z-axis points to the North pole at that epoch (formally, orthogonal to the plane defined by the mean equator at J2000.0) and the y-axis closes the right-handed set of orthogonal axes. The origin of the CRF is located at the Centre of Mass (CoM) of the Earth. The quasi-inertial property of this reference frame makes it suitable to represent the motion of a spacecraft.

A.2 Terrestrial Reference Frame

The Terrestrial Reference Frame (TRF), also known as Earth-Centred, Earth-Fixed reference frame (ECEF), Earth Centred Fixed reference frame (ECF), Conventional Terrestrial Frame (CTF) and Earth-Fixed Reference Frame (EFRF), is centred at the CoM of the Earth. The x-axis points towards longitude 0° and is parallel to the equatorial plane. The y-axis, also parallel to the equatorial plane, points towards

90° longitude. The z-axis points towards the North pole. The TRF is suitable to represent geophysical processes in the Earth system.

A.3   Local Horizontally-aligned Reference Frame

The Local Horizontally-aligned Reference Frame (LHRF), also known as Local North-Oriented Frame (LNOF) and Geographical Reference Frame is centred at the CoM of the orbiting satellite. The z-axis is parallel to the radial direction and points away from the CoM of the Earth. The x-axis is perpendicular to the z-axis and points to the geographic North. The y-axis, also perpendicular to the z-axis, points towards West. This reference frame is preferential to represent physical forces acting on the satellite, in particular the gravitational force.

A.4   Local Orbital Reference Frame

The Local Orbital Reference Frame (LORF) is centred at the CoM of the satellite. The x-axis is parallel to and pointing towards the same direction as the velocity vector. The y-axis is parallel to the orbital angular velocity vector and pointing towards the same direction, which also means that the y-axis is perpendicular to the radial direction. The z-axis is the complementary right-handed orthogonal axis. In a circular orbit, the z-axis is parallel to the radial direction.

A.5   Line-of-sight Reference Frame

The Line-of-sight Reference Frame (LoSRF), centred at the trailing satellite, is defined at every epoch as the reference frame with the x-axis parallel to the Line of Sight (LoS) vector, the y-axis perpendicular to the radial direction and the z-axis orthogonal to the other two in a right-handed axes arrangement. This reference frame needs a second satellite so that the LoS vector can be defined as the vector difference between the orbital position vectors of the two satellites. In the context of gravimetric satellite formations, this is the reference frame in which the low-low Satellite-to-Satellite Tracking (ll-SST) observations are defined.

A.6   Satellite Reference Frame

The Satellite Reference Frame (SRF) is used to define the geometry of the spacecraft. The axes are connected to the body of the spacecraft in a predefined (but otherwise arbitrary) way. The attitude determination system provides measurements that connect the CRF to this reference frame. The pressure forces due to Solar and Earth radiation as well as of aerodynamic nature are most suitably defined in this reference frame since the orientation of the satellite exterior panels is constant. This reference frame also serves as basis to define the reference frame of the various sensors and actuators on-board the satellites, such as the accelerometer(s), the star-tracker(s), magneto torquers, propulsion, etc.

A.7   Gradiometer Reference Frame

The Gradiometer Reference Frame (GRF) is an example of a sensor reference frame. The axes of this reference frame are parallel to the gradiometer arms and define the directions of the accelerations measured by the accelerometers. The need to define different reference frames for critical sensors on-board gravimetric satellites results from the minute mis-alignments introduced during assembly of the satellite, which need to be estimated during flight.

A.8   Hill Reference Frame

The Hill Reference Frame (HRF) is relevant when two satellites in a formation are considered. It is centred at one of the satellites and defines the x-axis parallel to the radial direction, the z-axis parallel to the orbital angular momentum vector (i.e. perpendicular to the orbital plane and consequentially perpendicular to the radial direction) and the y-axis closing the right-handed set of axes. The satellite located at the origin of the axes can be called *leader*, *sheriff* or *Tom*, while the other satellite can be called *follower*, *deputy* or *Jerry*, usually in only one of the respective forms. It should be noted that this reference frame implies an idealisation. The satellites in the trailing formation, for example, have null x and z coordinates. In reality, the curvature of the orbit will dictate that the deputy satellite has negative x coordinate. The longer the inter-satellite range, the more the actual satellite positions deviate from the idealised ones.

The HRF and the LORF are very similar in a circular orbit but the names of the axes are different. For the HRF, the z-axis is where the y-axis can be found in the

LORF (usually referred to as the *cross-track* direction), the x-axis in the former is in place of the z-axis (the *radial* direction) and the y-axis corresponds to the x-axis in the LORF (the *along-track* direction).

Inverse linear mapping of formation parameter to orbital elements

<div style="text-align:right">

B

</div>

In Chapter 3, in particular Section 3.8.4, the link between the relative orbit positions and the relative orbital elements of satellite 1 relatively to satellite 2 are referred to as *inverse linear mapping*. In this section, the elements of the inverse mapping matrix $A\big(o^{(2)}\big)^{-1}$ are listed. Section B.1 presents a numerical expriment that exposes the conditions under which the inverse linear mapping method is valid.

Given the formation parameters $\mathbf{X_0} = \big[y_{\text{off}}, A_0, B_0, \alpha, \beta\big]$, the initial conditions of the relative motion $\mathbf{x_0} = \big[x_0, y_0, z_0, \dot{x}_0, \dot{y}_0, \dot{z}_0\big]$ in the Hill Reference Frame (HRF) are computed using Eq. (B.1).

$$
\begin{aligned}
x_0 &= A_0 \cos(\alpha) \\
y_0 &= -2 A_0 \sin(\alpha) + y_{\text{off}} \\
z_0 &= B_0 \cos(\beta) \\
\dot{x}_0 &= -n A_0 \sin(\alpha) \\
\dot{y}_0 &= -2n A_0 \cos(\alpha) \\
\dot{z}_0 &= -n B_0 \sin(\beta).
\end{aligned}
\tag{B.1}
$$

Given the orbital elements of satellite 2 $o^{(2)}$

$$
o^{(2)} = \big[a^{(2)}, e^{(2)}, i^{(2)}, \Omega^{(2)}, \omega^{(2)}, M^{(2)}\big]^{\text{T}},
$$

the relative orbital elements of satellite 1 relatively to satellite 2 $o^{(12)}$

$$
o^{(12)} = \big[a^{(12)}, e^{(12)}, i^{(12)}, \Omega^{(12)}, \omega^{(12)}, M^{(12)}\big]^{\text{T}},
$$

are computed from initial conditions of the relative motion $\mathbf{x_0}$ using *inverse linear mapping* procedure represented by Eq. (B.2).

$$\boldsymbol{o}^{(12)} = \boldsymbol{A}\big(\boldsymbol{o}^{(2)}\big)^{-1}\mathbf{x_0}. \tag{B.2}$$

The non-zero elements of the inverse mapping matrix $\boldsymbol{A}\big(\boldsymbol{o}^{(2)}\big)^{-1}$ are given by Schaub and Junkins (2003, pp. 697–698) and corrected according to Schaub and Junkins (2009):

$$\alpha = \frac{a}{R}$$

$$\nu = \frac{V_r}{V_t}$$

$$\rho = \frac{R}{p}$$

$$\kappa_1 = \alpha\left(\frac{1}{\rho} - 1\right)$$

$$\kappa_2 = \nu^2 \frac{1}{\rho}\alpha$$

$$q_1 = e\cos\omega$$

$$q_2 = e\sin\omega$$

$$A_{11}^{-1} = 2\alpha(2 + 3\kappa_1 + 2\kappa_2)$$

$$A_{12}^{-1} = -2\alpha(1 + 2\kappa_1 + \kappa_2)\nu$$

$$A_{14}^{-1} = \frac{2\alpha^2\nu p}{V_t}$$

$$A_{15}^{-1} = \frac{2a}{V_t}(1 + 2\kappa_1 + \kappa_2)$$

$$A_{22}^{-1} = \frac{1}{R}$$

$$A_{23}^{-1} = \frac{\cot i}{R}(\cos\theta + \nu\sin\theta)$$

$$A_{26}^{-1} = -\frac{\sin\theta\cot i}{V_t}$$

$$A_{33}^{-1} = \frac{\sin\theta - \nu\cos\theta}{R}$$

$$A_{36}^{-1} = \frac{\cos\theta}{V_t}$$

$$A_{41}^{-1} = \frac{1}{\rho R}(3\cos\theta + 2\nu\sin\theta)$$

$$A_{42}^{-1} = -\frac{1}{R}\left(\frac{\nu^2\sin\theta}{\rho} + q_1\sin 2\theta - q_2\cos 2\theta\right)$$

$$A_{43}^{-1} = -\frac{q_2\cot i}{R}(\cos\theta + \nu\sin\theta)$$

$$A_{44}^{-1} = \frac{\sin\theta}{\rho V_t}$$

$$A_{45}^{-1} = \frac{1}{\rho V_t}(2\cos\theta + \nu\sin\theta)$$

$$A_{46}^{-1} = \frac{q_2\cot i\sin\theta}{V_t}$$

$$A_{51}^{-1} = \frac{1}{\rho R}(3\sin\theta - 2\nu\cos\theta)$$

$$A_{52}^{-1} = \frac{1}{R}\left(\frac{\nu^2\cos\theta}{\rho} + q_2\sin 2\theta + q_1\cos 2\theta\right)$$

$$A_{53}^{-1} = \frac{q_1\cot i}{R}(\cos\theta + \nu\sin\theta)$$

$$A_{54}^{-1} = -\frac{\cos\theta}{\rho V_t}$$

$$A_{55}^{-1} = \frac{1}{\rho V_t}(2\sin\theta - \nu\cos\theta)$$

$$A_{56}^{-1} = -q_1\frac{\cot i\sin\theta}{V_t}$$

$$A_{63}^{-1} = -\frac{\cos\theta + \nu\sin\theta}{R\sin i}$$

$$A_{66}^{-1} = \frac{1}{V_t}\frac{\sin\theta}{\sin i}.$$

The symbols used in the formulas above are only applicable to this section and are defined as:

R radial coordinate, instantaneous distance to the center of the Earth
V_t transverse velocity $(V_t = \dot{R})$
V_r radial velocity $(V_r = R\dot{\theta})$
p semilatus rectum $(p = a(1 - e^2))$
θ true latitude $(\theta = \omega + \nu)$

B.1 Validation

This section presents the conditions under which the analytical linear mapping given by Eq. (B.2) is accurate. To that end, the orbits of several formations are integrated on a spherically-symmetric gravity field, considering the combination of several values of the formation parameters: along-track offset y_{off}, radial amplitude A_0, and cross-track amplitude B_0. The remaining formation parameters, i.e. radial phase α and horizontal phase β, are set to zero. These formation parameters are compared with the respective estimated formation parameters $\hat{y}_{\text{off}}$, $\hat{A}_0$ and $\hat{B}_0$, derived from the computed orbits.

The estimated formation parameters are geometrically derived from the relative motion between the orbits $\boldsymbol{o}^{(2)}$ and $\boldsymbol{o}^{(2)} + \boldsymbol{o}^{(12)}$, suitably represented in the Hill Reference Frame (HRF) by $\mathbf{x}^{(12)(\text{HRF})}$. The superscript (HRF) is omitted henceforth for the sake of simplicity. The complete time series of orbital positions $\mathbf{x}^{(12)}$ is divided into N segments with length equal to the orbital period. At the ith-segment, the amplitudes of $\mathbf{x}^{(12)}$ in each coordinate direction k are computed from the (local) minima $\min_i()$ and maxima $\max_i()$:

$$\Delta x_{k,i}^{(12)} = \max_i\left(x_k^{(12)}\right) - \min_i\left(x_k^{(12)}\right). \tag{B.3}$$

Equally important is to compute the location of the center of motion, along each coordinate direction k:

$$\Sigma x_{k,i}^{(12)} = \frac{\max_i\left(x_k^{(12)}\right) + \min_i\left(x_k^{(12)}\right)}{2}. \tag{B.4}$$

Having defined these quantities, the estimated formation parameters are the results of averaging the collection of N amplitudes and centers:

$$
\begin{aligned}
\hat{A}_0 &= \frac{1}{N}\sum_{i=1}^{N}\Delta x_{x,i}^{(12)} \\
\hat{B}_0 &= \frac{1}{N}\sum_{i=1}^{N}\Delta x_{z,i}^{(12)} \\
\hat{y}_{\text{off}} &= \frac{1}{N}\sqrt{\left(\Sigma x_{x,i}^{(12)}\right)^2 + \left(\Sigma x_{y,i}^{(12)}\right)^2 + \left(\Sigma x_{z,i}^{(12)}\right)^2}.
\end{aligned}
\tag{B.5}
$$

The estimated formation parameter's normalized errors $\Delta\left(y_{\text{off}}\right)$, $\Delta(A_0)$ and $\Delta(B_0)$ are defined as :

$$
\begin{aligned}
\Delta\big(\hat{A}_0\big) &= \big(\hat{A}_0 - A_0\big)/A_0 \\
\Delta\big(\hat{A}_0\big) &= \big(\hat{B}_0 - B_0\big)/B_0 \\
\Delta\big(\hat{y}_\text{off}\big) &= \big(\hat{y}_\text{off} - y_\text{off}\big)/y_\text{off}.
\end{aligned}
\tag{B.6}
$$

When the formation parameter is zero, the division by zero is avoided by replacing the respective denominator in Eq. (B.6) by $\sqrt{y_\text{off}^2 + A_0^2 + B_0^2}$.

Table B.1, summarizes the results of the numerical experiment for when $\boldsymbol{o}^{(2)}$ represents a circular orbit.

The vertical and cross-track amplitude are always within a few percent to the original formation, which is considered acceptable. Most errors are in the y_off formation parameter, which are particularly severe when in combination with non-zero and large vertical and cross-track amplitudes. The Hill theory, as described in Section 3.8.1, is a linearization of the orbital equations of motion and is only accurate for small inter-satellite distances, i.e. a few hundered meters in Low-Earth Orbit (LEO). Over large distances, the Hill Reference Frame can no longer be considered a cartesian system of coordinates and the Hill equations Eq. (3.4) are no longer accurate.

The same numerical experiment was repeated for the case of an orbit $\boldsymbol{o}^{(2)}$ with eccentricity equal to 0.01 (not shown). The difference between the original and estimated formation parameters were much larger, particularly at the largest values of original formation parameters or when two or more non-zero formation parameters were considered. This results is expected since the method described in this section is based on analytical formulas that are valid only for circular orbits.

y_{off}	A_0	B_0	$\hat{y}_{\text{off}}$	$\hat{A}_0$	$\hat{B}_0$	$\Delta(y_{\text{off}})\%$	$\Delta(A_0)\%$	$\Delta(B_0)\%$
0	0	200	1.47	1.47	199.93	0.74	0.73	-0.03
0	0	400	5.88	5.88	399.7	1.47	1.47	-0.08
0	0	1000	36.7	36.67	996.22	3.67	3.67	-0.38
0	200	0	0.00	199.96	0.00	0.00	-0.02	0.00
0	200	200	6.58	199.88	199.93	2.33	-0.06	-0.03
0	200	400	16.63	199.62	399.7	3.72	-0.19	-0.08
0	200	1000	79.01	197.8	996.22	7.75	-1.1	-0.38
0	400	0	0.01	399.93	0.00	0.00	-0.02	0.00
0	400	200	12.13	399.75	199.93	2.71	-0.06	-0.03
0	400	400	26.3	399.24	399.7	4.65	-0.19	-0.08
0	400	1000	93.93	395.61	996.21	8.72	-1.1	-0.38
0	1000	0	0.06	999.83	0.00	0.01	-0.02	0.00
0	1000	200	29.57	999.4	199.93	2.9	-0.06	-0.03
0	1000	400	59.99	998.1	399.69	5.57	-0.19	-0.08
0	1000	1000	163.95	989.03	996.21	11.59	-1.1	-0.38
200	0	0	199.99	0.00	0.00	0.00	0.00	0.00
200	0	200	199.98	1.47	199.94	-0.01	0.52	-0.03
200	0	400	199.99	5.88	399.71	0.00	1.31	-0.07
200	0	1000	202.8	36.67	996.26	1.4	3.6	-0.37
200	200	0	224.53	200.3	0.00	12.26	0.15	0.00
200	200	200	224.62	200.21	199.94	12.31	0.11	-0.03
200	200	400	225.14	199.95	399.7	12.57	-0.03	-0.07
200	200	1000	237.95	198.3	996.24	18.97	-0.85	-0.38
200	400	0	251.14	400.8	0.00	25.57	0.2	0.00
200	400	200	251.44	400.62	199.94	25.72	0.15	-0.03
200	400	400	252.52	400.09	399.7	26.26	0.02	-0.07
200	400	1000	268.12	396.46	996.23	34.06	-0.89	-0.38
200	1000	0	344.5	1005.19	0.00	72.25	0.52	0.00
200	1000	200	345.79	1004.72	199.94	72.9	0.47	-0.03
200	1000	400	349.77	1003.33	399.7	74.88	0.33	-0.08
200	1000	1000	381.87	993.75	996.22	90.93	-0.63	-0.38
400	0	0	399.94	0.00	0.00	-0.01	0.00	0.00
400	0	200	399.9	1.47	199.94	-0.02	0.33	-0.03
400	0	400	399.81	5.88	399.7	-0.05	1.04	-0.07
400	0	1000	400.55	36.68	996.24	0.14	3.41	-0.38
400	200	0	448.97	201.28	0.00	12.24	0.64	0.00
400	200	200	449.02	201.19	199.94	12.25	0.6	-0.03
400	200	400	449.27	200.93	399.7	12.32	0.46	-0.07
400	200	1000	455.69	199.73	996.23	13.92	-0.13	-0.38
400	400	0	502.16	403.34	0.00	25.54	0.84	0.00
400	400	200	502.31	403.16	199.94	25.58	0.79	-0.03
400	400	400	502.85	402.6	399.7	25.71	0.65	-0.07
400	400	1000	510.81	398.96	996.23	27.7	-0.26	-0.38
400	1000	0	688.99	1020.37	0.00	72.25	2.04	0.00
400	1000	200	689.66	1019.83	199.94	72.42	1.98	-0.03
400	1000	400	691.73	1018.22	399.7	72.93	1.82	-0.08
400	1000	1000	708.79	1007.41	996.22	77.2	0.74	-0.38
1000	0	0	999.1	0.00	0.00	-0.09	0.00	0.00
1000	0	200	998.99	1.47	199.94	-0.1	0.14	-0.03
1000	0	400	998.68	5.88	399.7	-0.13	0.55	-0.07
1000	0	1000	997.08	36.67	996.24	-0.29	2.59	-0.38
1000	200	0	1120.98	207.99	0.00	12.1	3.99	0.00
1000	200	200	1120.99	207.87	199.94	12.1	3.94	-0.03
1000	200	400	1121.04	207.58	399.7	12.1	3.79	-0.07
1000	200	1000	1122.99	208.46	996.24	12.3	4.23	-0.38
1000	400	0	1253.18	420.42	0.00	25.32	5.1	0.00
1000	400	200	1253.22	420.17	199.94	25.32	5.04	-0.03
1000	400	400	1253.39	419.45	399.7	25.34	4.86	-0.07
1000	400	1000	1256.1	415.81	996.23	25.61	3.95	-0.38
1000	1000	0	1719.62	1108.65	0.00	71.96	10.86	0.00
1000	1000	200	1719.87	1107.89	199.94	71.99	10.79	-0.03
1000	1000	400	1720.63	1105.64	399.7	72.06	10.56	-0.08
1000	1000	1000	1726.95	1090.89	996.22	72.7	9.09	-0.38

Table B.1 – Formation parameters along-track offset y_{off}, radial amplitude A_0 and cross-track amplitude B_0 compared to corresponding estimated formation parameters, in a circular orbit (units are km). The last three columns show the difference between the original and estimated formation parameters, normalized by the corresponding formation parameter or, in case it is zero, by $\sqrt{y_{\text{off}}^2 + A_0^2 + B_0^2}$.

B.2 Conclusion

The method based on the linearised Hill theory is accurate only when the reference orbit is circular and only two of the along-track offset y_{off}, radial amplitude A_0 and cross-track amplitude B_0 formation parameters are non-zero. If these three formation parameters are all non-zero, there is no assurance that the resulting formation with a circular mean orbit will have the required along-track offset, although the other two formation parameters only differ by a few percent.

In the thesis, the formations considered in Chapter 5, Section 6.3, and Chapters 7 and 8 are all derived from a circular reference orbit. Additionally, the considered cartwheel, pendulum and trailing formations have only one non-zero formation parameter, i.e. A_0, B_0 and y_{off}, respectively. The geometric formation parameters, i.e. those determined from the resulting orbits are, therefore, very close to the predefined values, as indicated in Table 7.3.

Validation of the simplistic noise model

<div style="text-align: right;">**C**</div>

The objective of the current chapter is to simulate the low-low Satellite-to-Satellite Tracking (ll-SST) errors at the level of the range combinations and gravity field parameters, following the simplistic noise model described in Section 4.3.3, and compare them with actual GRACE a posteriori residuals. This is done in a similar way to the validation of the advanced noise model, in Section 6.3. The motivation for this study is to complete the analysis of noise models considered in the thesis. The simulations described in this chapter assume a GRACE-like formation and error amplitudes comparable to those reported in literature, e.g. the references listed in Tables 2.5 and 2.6. Recall from Section 4.3.3 that the simplistic noise model only considers uncorrelated noise time series, which are solely described by their STandard Deviation (STD). In contrast, the advanced noise model assumes correlated errors, in addition to incorporating more noise types, such as the correction noise and the accelerometer noise.

Although the advanced noise model receives more attention in most of the thesis, the analysis of Chapter 5 was done considering the simplistic noise model. At the time this research was conducted, the advanced noise model was not yet developed and the results described in that chapter are seen as sufficiently relevant to be presented in spite of the outdated noise model.

Section C.1, C.2 and C.3 analyse the ranging noise, relative position noise and absolute position noise individually. These three noise types are then combined and compared with the GRACE a posteriori residuals in Section C.4. A summary of the results is presented in Section C.5 and Section C.6 concludes the analysis.
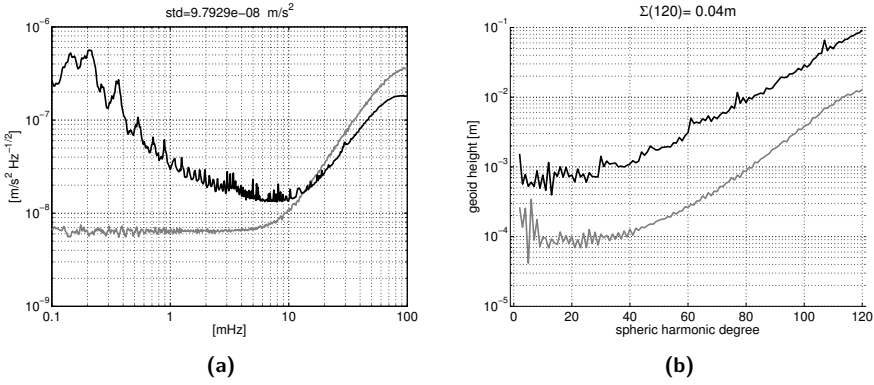
Figure C.1 – a) ASD of simulated ranging noise $\delta^{(R)}$, with $\delta^{(\rho)}=10^{-6}$ m.; b) DAS of the gravity field model error resulting from the propagation of the simulated ranging noise. The black curves in both plots represent the actual data and the grey curves represent the simulation results. The data period is 1 month for the simulation results. For the actual data, the data period of the ASD is the year of 2006. For the DAS, it is the month of February 2006.

C.1 Ranging noise

Figure C.1a presents the Amplitude Spectral Density (ASD) of the simulated ranging noise $\delta^{(R)}$, considering the measurement white noise of the ranging sensor with standard deviation equal to $\text{std}\left(\delta^{(\rho)}\right)=10^{-6}$ m (Biancale et al., 2005; Frommknecht et al., 2006). The resulting curve is well understood and results from the double differentiation of white noise. The analytical representation of this curve is given by Eq. (4.43), with the parameter σ equal to $\text{std}\left(\delta^{(\rho)}\right)$. The parameter τ is equal 19 s, as determined empirically by fitting Eq. (4.43) to the grey curve in Figure C.1a.

The reasons for the shape of the ranging noise $\delta^{(R)}$ are already discussed in Section 6.3.2.

The noise time series with ASDs shown in Figure C.1a, when propagated to the gravity field parameters, result in the error models with DAS shown in Figure C.1b.

The resulting gravity field model error amplitude spectrum is lower than the GRACE a posteriori residuals by a factor of 6.9. This happens because the low-frequency noise in GRACE a posteriori residuals, in addition to the low-degree coefficients, also propagates to the sectorial and near-sectorial high-degree coefficients; in

contrast, the simulated ranging noise are free from this problem. Furthermore, the stochastic model considered in the Frequency-Dependent Data Weighting (FDDW), built on the basis of the GRACE a posteriori residuals, is very similar to the ranging noise above 10 mHz. As a result, this bandwidth is effectively suppressed, resulting in an overall low geoid height error amplitude.

C.2 Relative position noise

It is assumed that modern Global Navigation Satellite Systems (GNSSs) and an appropriate Precise Orbit Determination (POD) technique exploiting a state-of-the-art dynamic model, are capable of providing orbits with a relative orbit position noise $\delta^{(\Delta \mathbf{x})}$ between the satellites in the formation equal to 10^{-3} m in all orthogonal components, or 1.7×10^{-3} m three-dimensional (3D) Root Mean Squared (RMS). Referring to Table 2.6 in Section 6.1, this assumption is reasonable. Figure C.2 presents the simulated relative position noise.

The shape of the ASD of the relative position noise in Figure C.2 is associated with the centred differentiation scheme. This is the differentiation scheme used in the numerical derivative of the noise in angle between the Line of Sight (LoS) vectors at successive epochs θ, cf. Eq. (4.23). In Eq. (C.1) to Eq. (C.3), the forward, centred and backwards differentiation schemes are described. In comparison to the centred differentiation scheme, the forward and backward schemes result in a ASD without the sudden drop close to the Nyquist frequency (not shown).

$$\left.\frac{\partial y}{\partial x}\right|_{\text{backward}} = \frac{y_i - y_{i-1}}{\Delta(x)}, \tag{C.1}$$

$$\left.\frac{\partial y}{\partial x}\right|_{\text{centred}} = \frac{y_{i+1} - y_{i-1}}{2\Delta(x)}, \tag{C.2}$$

$$\left.\frac{\partial y}{\partial x}\right|_{\text{forward}} = \frac{y_{i+1} - y_i}{\Delta(x)}. \tag{C.3}$$

Figure C.2 further shows that the amplitude of the relative position noise is between 5 to 30 times larger than the GRACE a posteriori residuals in the bandwidth 3 to 40 mHz. Additionally, between the frequencies of 0.2 and 6 mHz, the amplitude of the relative position noise increases with frequency while the amplitude of the GRACE a posteriori residuals decreases.

Propagating the relative position noise time series to the gravity field parameters results in the error per degree depicted in Figure C.2b. The amplitude of the relative
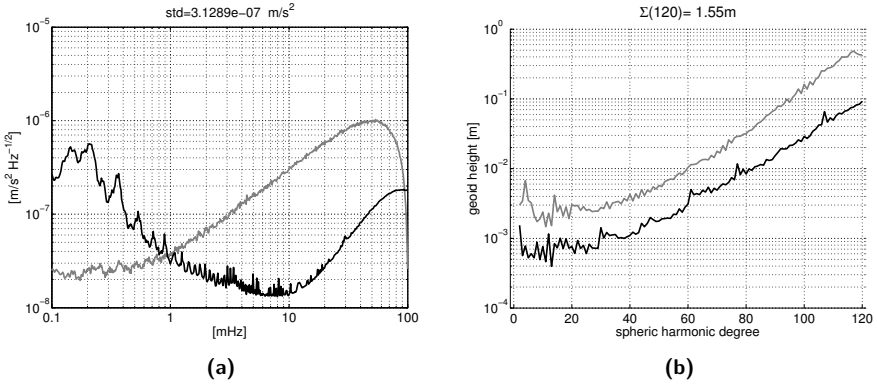
Figure C.2 – a) ASD of relative position noise $\delta^{(\mathrm{rP})}$ simulated with relative orbit position noise $\delta^{(\Delta\mathbf{x})}$ with magnitude $\mathrm{std}\left(\delta_x^{(\Delta\mathbf{x})}\right)=\mathrm{std}\left(\delta_y^{(\Delta\mathbf{x})}\right)=\mathrm{std}\left(\delta_z^{(\Delta\mathbf{x})}\right)=1\,\mathrm{mm}$; b) DAS of the gravity field model error resulting from the propagation of the simulated relative position noise. The black curves in both plots represent the actual data and the grey curves represent the simulation results. The data period is 1 month for the simulation results. For the actual data, the data period of the ASD is the year of 2006. For the DAS, it is the month of February 2006.

orbit position noise $\delta^{(\Delta\mathbf{x})}$ needs to be scaled by 0.18 in order to result in a gravity field model error similar to the propagated GRACE a posteriori residuals.

In an attempt to improve the agreement between the simulated relative position noise and the actual data noise, an alternative relative position noise $\delta^{(\mathrm{rP,alt})}$ is simulated. In that case, $\delta^{(\Delta\mathbf{x})}$ in Eq. (4.46) is not white noise with STD equal to 10^{-3} m but has the ASD shown in Figure 6.5, left-hand side plot (before scaling by the factor of 3 resulting from advances in positioning measurement and methodology), and STD equal to 2.2×10^{-3} m. The relative orbit position noise $\delta^{(\Delta\mathbf{x})}$ used in the computation of the alternative relative position noise $\delta^{(\mathrm{rP,alt})}$ is generated synthetically. The Fourier coefficients $\mathscr{F}(\delta)$ of a white-noise sequence with unit variance and of the appropriate length are multiplied by the Fourier coefficients associated with the ASD in Figure 6.5 left-hand side plot, $\mathscr{F}(\mathrm{ASD})$. The inverse Fourier transform $\mathscr{F}^{-1}$ is applied to the result:

$$\delta^{(\Delta\mathbf{x})} = \mathscr{F}^{-1}(\mathscr{F}(\delta)\,\mathscr{F}(\mathrm{ASD})). \tag{C.4}$$

In spite of these efforts, the resulting relative position noise is considerably different from the actual data noise, see Figure C.3.

The gravity field model error associated with the alternative relative position noise $\delta^{(\mathrm{rP,alt})}$, shown in Figure C.3b, is not particularly different from the original relative position noise in the gravity field parameters, compare with Figure C.2b. Nearly the same scale factor, 0.18, would have to be applied to the ASD shown in Figure 6.5 in order to match the propagated noise with the propagated GRACE a posteriori residuals.

In view of the added complexity of the alternative relative position noise $\delta^{(\mathrm{rP,alt})}$ and the associated negligible improvement in reproducing the GRACE a posteriori residuals, the simplistic noise model considers the relative position noise $\delta^{(\mathrm{rP})}$ computed on the basis of relative orbit position noise $\delta^{(\Delta\mathbf{x})}$ given by white noise, with STD $=$ 0.18 mm. Implied in this assumption is that, in the context of the simplistic noise model, the relative position noise is assumed to dominate the GRACE a posteriori residuals.
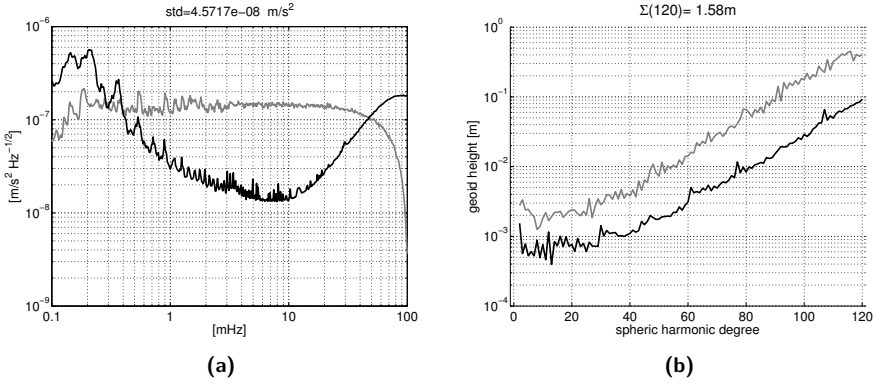
Figure C.3 – a) ASD of alternative relative position noise $\delta^{(\mathrm{rP,alt})}$ simulated with relative orbit position noise $\delta^{(\Delta\mathbf{x})}$ with ASD given by Figure 6.5, left-hand side plot; b) DAS of the gravity field model error resulting from the propagation of the simulated alternative relative position noise. The black curves in both plots represent the actual data and the grey curves represent the simulation results. The data period is 1 month for the simulation results. For the actual data, the data period of the ASD is the year of 2006. For the DAS, it is the month of February 2006.

C.3   Absolute position noise

It is assumed that the standard deviation of the absolute orbit position noise $\boldsymbol{\delta}^{(\mathbf{x})}$, for the purpose of simulating absolute position noise, is 0.010 m at all components, i.e. 0.017 m RMS in terms of magnitude. Table 2.5 confirms that the assumed noise level is consistent with literature.

Figure C.4 presents the simulated absolute position noise. The absolute position noise $\delta^{(\mathrm{aP})}$ is nearly constant at all frequencies. The slightly decreasing amplitude at the frequencies above 20 mHz is due to the averaging filter $\mathbf{w}$, see Eq. (4.50).

The propagated absolute position noise has a DAS shown in Figure C.4b and is a factor of 11 lower than the propagated GRACE a posteriori residuals. This is consistent with the fact that the amplitude of the absolute position noise is lower than the GRACE a posteriori residuals by at least the same factor. This noise type is not dominant in the simplistic noise model, considering that the gravitational acceleration changes in the order of $\sim 10^{-8}\,\mathrm{ms}^{-2}$ over the distances of a few centimetres. In the conducted simulation, the large number of data stochastically average this to the level of $8.57 \times 10^{-10}\,\mathrm{ms}^{-2}$. For that reason, there is no strong motivation to adjust the magnitude assumed for the absolute orbit position noise $\boldsymbol{\delta}^{(\mathbf{x})}$, as was the case for the relative position noise.
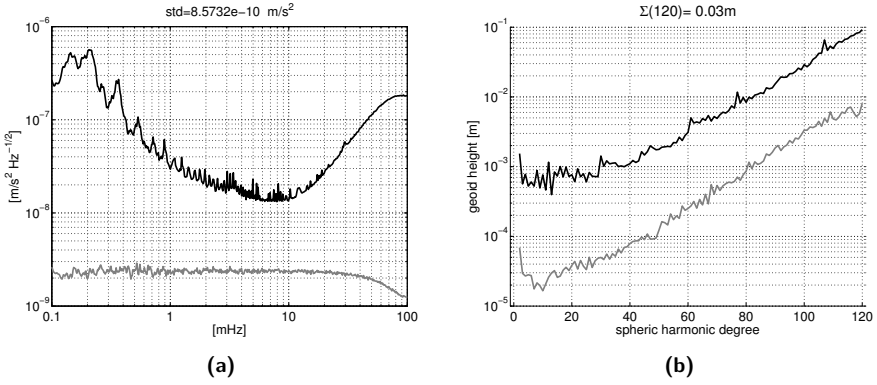
Figure C.4 – a) ASD of absolute position noise $\delta^{(aP)}$ simulated with absolute positioning noise with magnitude $\mathrm{std}\left(\delta_x{}^{(\mathbf{x})}\right)=\mathrm{std}\left(\delta_y{}^{(\mathbf{x})}\right)=\mathrm{std}\left(\delta_z{}^{(\mathbf{x})}\right)=0.010$ m and EIGEN-5C as background force model, $\overline{\boldsymbol{C}}^{(\mathrm{ref})}$ in Eq. (4.50); b) DAS of the gravity field model error resulting from the propagation of the simulated absolute position noise. The black curves in both plots represent the actual data and the grey curves represent the simulation results. The data period is 1 month for the simulation results. For the actual data, the data period of the ASD is the year of 2006. For the DAS, it is the month of February 2006.

C.4   Comparison with actual data

The errors associated with the simplistic noise model are plotted in Figure C.5. In Figure C.5a, the simplistic model noise types are shown in terms of range combinations and the respective error in the gravity field models is presented in Figure C.5b. The dark curves represent the actual GRACE data noise for the year of 2006.

Although the ASDs of the simplistic noise model time series do not match the actual data noise, propagating these quantities to the gravity field parameters produces a gravity field model error that is roughly representative and adequate as a conservative approximation.

Evidently, the resulting scaled-down relative orbit position noise can no longer be associated with the relative accuracy of the orbits; it only has meaning within the simplistic noise model as an empirically-determined quantity that sets the amplitude of the gravity field model error associated with the relative orbit position.
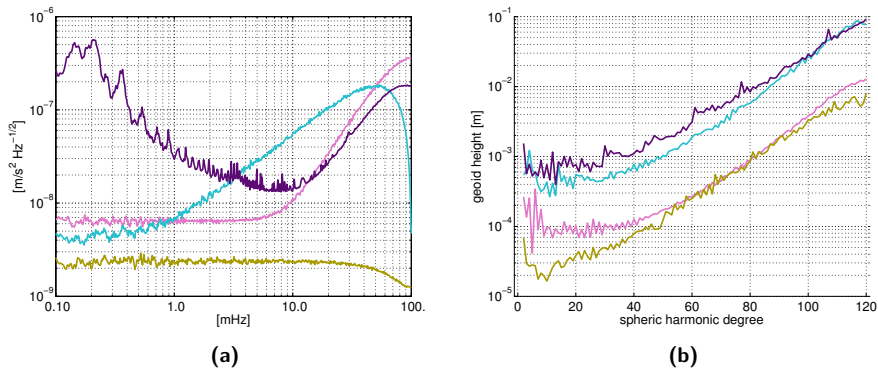
Figure C.5 – a) ASD of simulated simplistic noise types; b) DAS of the gravity field model error resulting from the propagation of the corresponding noise types. The dark-blue curves in both plots represent the actual GRACE data noise for the year of 2006. The data period is 1 month for the simulation results. For the actual data, the data period of the ASD is the year of 2006. For the DAS, it is the month of February 2006.

C.5   Summary

Table C.1 provides an overview of the assumptions made for the simulation of noise for the simplistic ll-SST noise model. Noteworthy is that the underlying time series of the simplistic noise types, i.e. ranging sensor noise $\delta^{(\rho)}$, relative orbit position noise $\delta^{(\Delta\mathbf{x})}$ and absolute orbit position noise $\boldsymbol{\delta}^{(\mathbf{x})}$, are realisations of white noise scaled to the specified STD.

name	symbol	assumptions	description	page nr.
ranging noise	$\delta^{(\mathrm{R})}$	$\mathrm{std}\big(\delta^{(\rho)}\big)= 10^{-6}\,\mathrm{m}$	error in the range measurements	100
relative position noise	$\delta^{(\mathrm{rP})}$	$\mathrm{std}\big(\delta^{(\Delta\mathbf{x})}\big)=$ 0.18 mm	error in the relative orbital positions	101
absolute position noise	$\delta^{(\mathrm{aP})}$	$\mathrm{std}\big(\delta^{(\mathbf{x})}\big)= 0.010\,\mathrm{m}$	error in the (absolute) orbital positions	102

Table C.1 – Summary of the assumptions considered for the simulation of the ll-SST noise type of the simplistic noise model.

To summarise, the STD of the range combination noise time series and the corresponding geoid heights error per degree at degrees 60 and 100 are presented in Table C.2. The relative position noise $\delta^{(\mathrm{rP})}$ has been scaled with the factor 0.18, as discussed in Section C.2.

| noise type | symbol | STD [m/s^2] | geoid error [mm] | | cumulative |
| | | | per degree | | |
			degree 60	degree 100	degree 120
simplistic noise model					
ranging noise	$\delta^{(\mathrm{R,spl})}$	9.8×10^{-8}	0.26	3.8	41
relative position noise[a]	$\delta^{(\mathrm{rP})}$	5.7×10^{-8}	1.9	29	280
absolute position noise	$\delta^{(\mathrm{aP})}$	8.6×10^{-10}	0.25	3.3	25
total		1.1×10^{-7}	1.9	30	290
actual data					
		5.6×10^{-8}	3.1	29	280

[a]Assuming white relative orbit position noise with $\mathrm{std}\!\left(\delta^{(\Delta \mathbf{x})}\right)\!=\!4.0 \times 10^{-4}$ m.

Table C.2 – Summary of the simplistic model, showing the STD of the time series of range combination error and the geoid height error per degree at degrees 60 and 100, as well as the cumulative geoid height error at degree 120. The statistics of the actual data noise refer to the year of 2006 in case of the STD and to the February 2006 in case of the geoid height errors.

C.6 Conclusion

The cumulative geoid error at degree 120 when using the simplistic noise model matches closely the value for the actual data. This agreement has been introduced artificially with the scaling of the relative position noise. If the scale factor is not applied, the resulting cumulative geoid error is 1.6×10^3 mm.

Within the simplistic noise model, the dominant relative position noise requires a scale factor 0.18, resulting in the amplitude in terms of orbit position error of 4.0×10^{-4} m. In view of the fact that this value is overly-optimistic regarding relative positioning noise (cf. Table 6.2), the scaled relative position noise should not be regarded as a physically relevant quantity but as an empirically-determined parameter of the simplistic noise model. The simulations done in the thesis considering the

simplistic ll-SST noise model, namely in Chapter 5, are not scaled; the result should therefore be interpreted as a conservative estimate.

Derivation of the ll-SST advanced noise model

<div style="text-align: right; font-size: 2em; font-weight: bold;">D</div>

This section describes the derivation of the formulas describing the noise types that compose the advanced noise model presented in Section 4.3.3. The derivations shown below are adapted from Ditmar (2009a).

D.1   Unified formulation for the range combinations

In the simulation environment, the range combinations can be computed from range data or from a force model (in contrast, the observed range combinations can only be computed from range data when processing actual data). This section introduces a common terminology that represents the aforementioned two procedures to compute the range combinations. This distinction is already described in Section 4.1.2, more specifically:

- in Eq. (4.18) that illustrates the estimation of range combinations from range data:

$$\bar{a}_i = \frac{\cos\theta_{i,-1}\cdot\rho_{i-1} - 2\rho_i + \cos\theta_{i,+1}\cdot\rho_{i+1}}{(\Delta t)^2}$$
$$\equiv \bar{a}\left(\rho, \mathbf{e}^{(\text{LoS})}\right),$$

- and Eq. (4.30) that represents the computation of range combinations on the basis of a force model (refer to Eq. (4.29) for the meaning of $*\mathbf{w}\cdot\mathbf{e}^{(\text{LoS})}$):

$$\bar{a} = \mathbf{a}^{(12)} * \mathbf{w} \cdot \mathbf{e}^{(\text{LoS})}$$
$$\equiv \bar{a}\left(\overline{\boldsymbol{C}}, \mathbf{x}, \mathbf{e}^{(\text{LoS})}\right).$$

Ditmar and Sluijs (2004) show that these two approaches are equivalent, as long as the force model used to integrate $\mathbf{x}$, from which θ and $\mathbf{e}^{(\text{LoS})}$ are computed, is described by the set of Stokes coefficients $\overline{\boldsymbol{C}}$.

D.1.1 Range combinations estimated from range data

As introduced in Eq. (4.18), the range combinations $\bar{a}$ are function of the range ρ according to:

$$\bar{a}_i = \frac{\cos\theta_{i,-1} \cdot \rho_{i-1} - 2\rho_i + \cos\theta_{i,+1} \cdot \rho_{i+1}}{(\Delta t)^2},$$

where, considering the k-th epoch before (k is negative) or after (k is positive) epoch i, the angle between the Line of Sight (LoS) vectors θ is, Eq. (4.22):

$$\theta_{i,k} = \cos^{-1} \frac{\mathbf{x}_{i+k}^{(\text{for})(1)} - \mathbf{x}_{i+k}^{(\text{for})(2)}}{\rho_{i+k}^{(\text{for})}} \cdot \frac{\mathbf{x}_i^{(\text{for})(2)} - \mathbf{x}_i^{(\text{for})(2)}}{\rho_i^{(\text{for})}}. \tag{D.1}$$

The previous equations can be formulated in terms of the unit vectors defining the LoS direction $\mathbf{e}^{(\text{LoS})}$ as:

$$\theta_{i,k} = \cos^{-1}\left(\mathbf{e}_{i+k}^{(\text{LoS})} \cdot \mathbf{e}_i^{(\text{LoS})}\right),$$

so that $\bar{a}$ can be defined as function of ρ and $\mathbf{e}^{(\text{LoS})}$:

$$\bar{a} = f\left(\rho, \mathbf{e}^{(\text{LoS})}\right) \equiv \bar{a}\left(\rho, \mathbf{e}^{(\text{LoS})}\right).$$

Although neither the orbit positions nor the force model appear explicitly, they are needed to determine the unit vectors defining the LoS direction $\mathbf{e}^{(\text{LoS})}$.

D.1.2 Range combinations computed from a force model

The range combinations $\bar{a}$ can also be computed from the point-wise inter-satellite accelerations $\mathbf{a}^{(12)}$ (see Eq. (4.10), Eq. (4.29) and Eq. (4.30)):

$$\bar{a}_i = \bar{\mathbf{a}}_i^{(12)} \cdot \mathbf{e}^{(\text{LoS})}{}_i$$
$$= \mathbf{a}_i^{(12)} * \mathbf{w} \cdot \mathbf{e}^{(\text{LoS})}{}_i$$
$$\equiv \left(\boldsymbol{R}_i^{(\text{TRF})\leftarrow(\text{CRF})} \left(\left(\boldsymbol{R}_i^{(\text{CRF})\leftarrow(\text{LHRF})} \mathbf{a}_i^{(12)} \right) * \mathbf{w} \right) \right) \cdot \mathbf{e}_i^{(\text{LoS})}.$$

The range combination can be interpreted as a weighted mean of point-wise accelerations. With that in mind, the averaging filter $\mathbf{w}$ is composed of a set of predefined coefficients.

The point-wise inter-satellite accelerations $\mathbf{a}^{(12)}$ are determined from the difference between the acceleration at the orbit positions of satellite 1 $\mathbf{x}^{(1)}$ and at the orbit positions of satellite 2 $\mathbf{x}^{(2)}$, considering the set of Stokes coefficients $\overline{C}$:

$$\mathbf{a}_i^{(12)} = \boldsymbol{\nabla} V \left(\mathbf{x}_i^{(1)}, \overline{C} \right) - \boldsymbol{\nabla} V \left(\mathbf{x}_i^{(2)}, \overline{C} \right).$$

The orbit positions $\mathbf{x}^{(1)}$ and $\mathbf{x}^{(2)}$ are integrated on the basis of $\overline{C}$.

To make it simpler to represent the range combinations computed from a force model, the following notation, already introduced in Section 4.3.1, Eq. (4.39), is used:

$$\bar{a}_i = \nabla' V \left(\mathbf{x}, \overline{C}, \mathbf{e}^{(\text{LoS})} \right).$$

As it can be seen from the previous equation, the ranges ρ are not considered explicitly, although they implicitly associated with $\mathbf{x}$.

D.2   Residual range combinations

If the knowledge of the gravitational field of the Earth (represented by the force model $\overline{C}$) was perfect (and assuming there are no other forces acting on the spacecrafts), the orbit positions $\mathbf{x}$ would describe accurately the actual motion of the satellites and $\mathbf{e}^{(\text{LoS})}$ would describe without error the LoS direction. Under these conditions and assuming that the ranges ρ were measured perfectly, the range combinations estimated from the range data would be equal to those computed from the force model:

$$\bar{a} \left(\rho, \mathbf{e}^{(\text{LoS})} \right) = \nabla' \left(\overline{C}, \mathbf{x}, \mathbf{e}^{(\text{LoS})} \right).$$

In reality, the force model $\overline{C}$ is given by a prediction of the gravitational field of the Earth, represented by $\overline{C}^{(\text{ref})}$, resulting in a discrepancy between the observed

range combinations (derived from the observed ranges $\rho^{\text{(obs)}}$ and the observed unit vectors defining the LoS direction $\mathbf{e}^{\text{(LoS)(obs)}}$) and the forecasted range combinations (computed from $\overline{\mathbf{C}}^{\text{(ref)}}$), originating the residual range combinations $\overline{a}^{\text{(res)}}$:

$$\overline{a}^{\text{(res)}} = \overline{a}\left(\rho^{\text{(obs)}}, \mathbf{e}^{\text{(LoS)(obs)}}\right) - \nabla'\left(\overline{\mathbf{C}}^{\text{(ref)}}, \mathbf{x}, \mathbf{e}^{\text{(LoS)(obs)}}\right).$$

With this modification, the orbit positions $\mathbf{x}$ do not describe perfectly the motion of the satellites, since they are integrated on the basis of $\overline{\mathbf{C}}^{\text{(ref)}}$. For this reason, they differ from the observed ones and are called forecasted orbit positions $\mathbf{x}^{\text{(for)}}$. The resulting difference in terms of range combinations is called the positioning noise $\delta^{\text{(P)}}$:

$$\begin{aligned} \overline{a}^{\text{(res)}} &= \overline{a}\left(\rho^{\text{(obs)}}, \mathbf{e}^{\text{(LoS)(obs)}}\right) - \nabla'\left(\overline{\mathbf{C}}^{\text{(ref)}}, \boxed{\mathbf{x}}, \mathbf{e}^{\text{(LoS)(obs)}}\right) \\ &= \overline{a}\left(\rho^{\text{(obs)}}, \mathbf{e}^{\text{(LoS)(obs)}}\right) - \nabla'\left(\overline{\mathbf{C}}^{\text{(ref)}}, \boxed{\mathbf{x}^{\text{(for)}}}, \mathbf{e}^{\text{(LoS)(obs)}}\right) - \boxed{\delta^{\text{(P)}}}. \end{aligned} \tag{D.2}$$

Likewise, the unit vectors describing the LoS direction $\mathbf{e}^{\text{(LoS)(obs)}}$ are not perfect, in view of that fact that they are computed from $\mathbf{x}^{\text{(for)}}$; for this reason they are represented as $\mathbf{e}^{\text{(LoS)(for)}}$. This modification introduces the orientation noise $\delta^{\text{(L)}}$:

$$\begin{aligned} \overline{a}^{\text{(res)}} &= \overline{a}\left(\rho^{\text{(obs)}}, \mathbf{e}^{\text{(LoS)(obs)}}\right) - \nabla'\left(\overline{\mathbf{C}}^{\text{(ref)}}, \mathbf{x}^{\text{(for)}}, \boxed{\mathbf{e}^{\text{(LoS)(obs)}}}\right) - \delta^{\text{(P)}} \\ &= \overline{a}\left(\rho^{\text{(obs)}}, \mathbf{e}^{\text{(LoS)(obs)}}\right) - \nabla'\left(\overline{\mathbf{C}}^{\text{(ref)}}, \mathbf{x}^{\text{(for)}}, \boxed{\mathbf{e}^{\text{(LoS)(for)}}}\right) - \delta^{\text{(P)}} - \boxed{\delta^{\text{(L)}}}. \end{aligned} \tag{D.3}$$

The same argument applies to the observed unit vectors defining the LoS direction used to compute the range combinations with range data, giving rise to the correction noise $\delta^{\text{(C)}}$:

$$\begin{aligned} \overline{a}^{\text{(res)}} &= \overline{a}\left(\rho^{\text{(obs)}}, \boxed{\mathbf{e}^{\text{(LoS)(obs)}}}\right) && - \nabla'\left(\overline{\mathbf{C}}^{\text{(ref)}}, \mathbf{x}^{\text{(for)}}, \mathbf{e}^{\text{(LoS)(for)}}\right) && - \delta^{\text{(P)}} - \delta^{\text{(L)}} \\ &= \overline{a}\left(\rho^{\text{(obs)}}, \boxed{\mathbf{e}^{\text{(LoS)(for)}}}\right) && + \boxed{\delta^{\text{(C)}}} - \nabla'\left(\overline{\mathbf{C}}^{\text{(ref)}}, \mathbf{x}^{\text{(for)}}, \mathbf{e}^{\text{(LoS)(for)}}\right) && - \delta^{\text{(P)}} - \delta^{\text{(L)}}. \end{aligned}$$

The ranges themselves are measured with a certain level of error, in the form of the estimated ranges $\hat{\rho}$, which translates into the ranging noise $\delta^{\text{(R)}}$ according to Eq. (4.45). Additionally, the measurements taken by the accelerometer remove the non-gravitational accelerations from the residual range combinations but leave the corresponding measurement errors, represented by the accelerometer noise $\delta^{\text{(acc)}}$. The inclusion of these observation errors dictates that the residual range combinations

are estimates of the actual values and are, therefore, represented by the symbol $\hat{\overline{a}}^{(\text{res})}$:

$$\overline{a}^{(\text{res})} = \overline{a}\left(\boxed{\rho^{(\text{obs})}}, \mathbf{e}^{(\text{LoS})(\text{for})}\right) \qquad\qquad + \delta^{(\text{C})}$$
$$-\nabla'\left(\overline{\boldsymbol{C}}^{(\text{ref})}, \mathbf{x}^{(\text{for})}, \mathbf{e}^{(\text{LoS})(\text{for})}\right) \qquad -\delta^{(\text{P})} - \delta^{(\text{L})}$$
$$\hat{\overline{a}}^{(\text{res})} + \boxed{\delta^{(\text{acc})}} = \overline{a}\left(\hat{\rho}, \mathbf{e}^{(\text{LoS})(\text{for})}\right) \qquad\qquad + \boxed{\delta^{(\text{R})}} + \delta^{(\text{C})}$$
$$-\nabla'\left(\overline{\boldsymbol{C}}^{(\text{ref})}, \mathbf{x}^{(\text{for})}, \mathbf{e}^{(\text{LoS})(\text{for})}\right) \qquad -\delta^{(\text{P})} - \delta^{(\text{L})}.$$

D.3 Forecasted noise types

In the following sections, the derivations of the positioning noise $\delta^{(\text{P})}$, orientation noise $\delta^{(\text{L})}$ and correction noise $\delta^{(\text{C})}$, represented by Eq. (4.59), Eq. (4.58) and Eq. (4.55), respectively, are presented.

D.3.1 Positioning noise

This section shows how to derive Eq. (4.59):

$$\boldsymbol{\delta}^{(\text{P})(\text{pw})} = \boldsymbol{\nabla} V\left(\mathbf{x}^{(\text{obs})}, \overline{\boldsymbol{C}}^{(\text{ref})}\right) - \boldsymbol{\nabla} V\left(\mathbf{x}^{(\text{for})}, \overline{\boldsymbol{C}}^{(\text{ref})}\right).$$

From Eq. (D.2), one sees that:

$$\nabla'\left(\overline{\boldsymbol{C}}^{(\text{ref})}, \boxed{\mathbf{x}^{(\text{obs})}}, \mathbf{e}^{(\text{LoS})(\text{obs})}\right) = \nabla'\left(\overline{\boldsymbol{C}}^{(\text{ref})}, \boxed{\mathbf{x}^{(\text{for})}}, \mathbf{e}^{(\text{LoS})(\text{obs})}\right) + \boxed{\delta^{(\text{P})}}.$$

In other words:

$$\delta^{(\text{P})} = \mathbf{a}^{(12)(\text{obs})} * \mathbf{w} \cdot \mathbf{e}^{(\text{LoS})(\text{obs})} - \mathbf{a}^{(12)(\text{for})} * \mathbf{w} \cdot \mathbf{e}^{(\text{LoS})(\text{obs})}.$$

The associative property of the inner product and the linearity of the convolution operation allow us to re-write the last equation as:

$$\delta^{(\text{P})} = \left(\mathbf{a}^{(12)(\text{obs})} - \mathbf{a}^{(12)(\text{for})}\right) * \mathbf{w} \cdot \mathbf{e}^{(\text{LoS})(\text{obs})}.$$

The observed unit vectors defining the LoS direction $\mathbf{e}^{(\text{LoS})(\text{obs})}$ are replaced by the forecasted equivalents $\mathbf{e}^{(\text{LoS})(\text{for})}$, since this noise type deals with errors in the orbit positions $\mathbf{x}$ and the corresponding second-order discrepancy (i.e. the influence of the errors of $\mathbf{e}^{(\text{LoS})}$ in $\delta^{(\text{P})}$) are negligible:

$$\delta^{(P)} = \left(\mathbf{a}^{(12)(\text{obs})} - \mathbf{a}^{(12)(\text{for})}\right) * \mathbf{w} \cdot \mathbf{e}^{(\text{LoS})(\text{for})}.$$

The point-wise positioning noise $\boldsymbol{\delta}^{(P)(\text{pw})}$ described by Eq. (4.59) can be seen in the equation above, before the projection along $\mathbf{e}^{(\text{LoS})(\text{for})}$ is done and the averaging filter $\mathbf{w}$ is applied:

$$\delta^{(P)} = \left(\boldsymbol{\nabla} V\left(\mathbf{x}^{(\text{obs})}, \overline{\boldsymbol{C}}^{(\text{ref})}\right) - \boldsymbol{\nabla} V\left(\mathbf{x}^{(\text{for})}, \overline{\boldsymbol{C}}^{(\text{ref})}\right)\right) * \mathbf{w} \cdot \mathbf{e}^{(\text{LoS})(\text{for})}$$
$$\equiv \boldsymbol{\delta}^{(P)(\text{pw})} * \mathbf{w} \cdot \mathbf{e}^{(\text{LoS})(\text{for})}.$$

D.3.2 Orientation noise

In this section, Eq. (4.58) is derived:

$$\delta^{(L)(\text{pw})} = \delta^{(L)(1)(\text{pw})} - \delta^{(L)(2)(\text{pw})}$$
$$\text{with} \quad \delta^{(L)(j)(\text{pw})} = \boldsymbol{\nabla} V\left(\mathbf{x}^{(j)}, \overline{\boldsymbol{C}}^{(\text{ref})}\right) \cdot \boldsymbol{\delta}^{(\text{LoS})} \quad \text{and} \quad j = 1, 2.$$

Eq. (D.3) hints that:

$$\nabla'\left(\overline{\boldsymbol{C}}^{(\text{ref})}, \mathbf{x}^{(\text{for})}, \mathbf{e}^{(\text{LoS})(\text{obs})}\right) = \nabla'\left(\overline{\boldsymbol{C}}^{(\text{ref})}, \mathbf{x}^{(\text{for})}, \mathbf{e}^{(\text{LoS})(\text{for})}\right) + \delta^{(L)}.$$

Rearranging and expanding the equation above:

$$\delta^{(L)} = \mathbf{a}^{(12)(\text{for})} * \mathbf{w} \cdot \mathbf{e}^{(\text{LoS})(\text{obs})} - \mathbf{a}^{(12)(\text{for})} * \mathbf{w} \cdot \mathbf{e}^{(\text{LoS})(\text{for})}.$$

Resorting to the associative property of the internal product:

$$\delta^{(L)} = \mathbf{a}^{(12)(\text{for})} * \mathbf{w} \cdot \left(\mathbf{e}^{(\text{LoS})(\text{obs})} - \mathbf{e}^{(\text{LoS})(\text{for})}\right) \tag{D.4}$$
$$\equiv \mathbf{a}^{(12)(\text{for})} * \mathbf{w} \cdot \boldsymbol{\delta}^{(\text{LoS})} \Rightarrow$$
$$\mathbf{e}^{(\text{LoS})(\text{obs})} = \mathbf{e}^{(\text{LoS})(\text{for})} + \boldsymbol{\delta}^{(\text{LoS})}. \tag{D.5}$$

Recalling that $\boldsymbol{\delta}^{(\Delta \mathbf{x})}$ is the relative orbit position noise, the term $\boldsymbol{\delta}^{(\text{LoS})}$ is represented by the contributions with magnitude $\boldsymbol{\delta}^{(\Delta \mathbf{x})}/\rho$ along the directions perpendicular to $\mathbf{e}^{(\text{LoS})(\text{obs})}$: the y-component and z-component in the Line-of-sight Reference Frame (LoSRF). Any small amplitude rotation of $\mathbf{e}^{(\text{LoS})(\text{obs})}$ does not change its magnitude significantly (i.e. $\cos\alpha \simeq 1$ if $\alpha \ll 1$), so the x-component of $\boldsymbol{\delta}^{(\text{LoS})(\text{LoSRF})}$

is approximately equal to zero. This means that, in the LoSRF, $\mathbf{e}^{\text{(LoS)(obs)}}$ is corrupted by:

$$\boldsymbol{\delta}^{\text{(LoS)(LoSRF)}} = \frac{1}{\rho^{\text{(for)}}} \begin{bmatrix} 0 \\ \delta_y^{(\Delta\mathbf{x})\text{(LoSRF)}} \\ \delta_z^{(\Delta\mathbf{x})\text{(LoSRF)}} \end{bmatrix}. \tag{D.6}$$

In any other reference frame the x-component is not necessarily zero and $\boldsymbol{\delta}^{\text{(LoS)}}$ is given by the more general expression:

$$\boldsymbol{\delta}^{\text{(LoS)}} = \frac{1}{\rho^{\text{(for)}}} \begin{bmatrix} \delta_x^{(\Delta\mathbf{x})} \\ \delta_y^{(\Delta\mathbf{x})} \\ \delta_z^{(\Delta\mathbf{x})} \end{bmatrix} = \frac{\boldsymbol{\delta}^{(\Delta\mathbf{x})\perp}}{\rho^{\text{(for)}}}. \tag{D.7}$$

considering that the relative orbit position noise $\boldsymbol{\delta}^{(\Delta\mathbf{x})}$ is defined in the same reference frame.

The sequence of operations in Eq. (D.4) can be inter-changed, owing to their linearity:

$$\delta^{\text{(L)}} = \left(\mathbf{a}^{(12)\text{(for)}} \cdot \boldsymbol{\delta}^{\text{(LoS)}} \right) * \mathbf{w}.$$

The point-wise orientation noise $\delta^{\text{(L)(pw)}}$ defined in Eq. (4.58) is given by:

$$\begin{aligned} \delta^{\text{(L)(pw)}} &= \mathbf{a}^{(12)\text{(for)}} \cdot \boldsymbol{\delta}^{\text{(LoS)}} \\ &= \left(\boldsymbol{\nabla} V \left(\mathbf{x}^{(1)}, \overline{\boldsymbol{C}}^{\text{(ref)}} \right) - \boldsymbol{\nabla} V \left(\mathbf{x}^{(2)}, \overline{\boldsymbol{C}}^{\text{(ref)}} \right) \right) \cdot \boldsymbol{\delta}^{\text{(LoS)}} \\ &= \boldsymbol{\nabla} V \left(\mathbf{x}^{(1)}, \overline{\boldsymbol{C}}^{\text{(ref)}} \right) \cdot \boldsymbol{\delta}^{\text{(LoS)}} - \boldsymbol{\nabla} V \left(\mathbf{x}^{(2)}, \overline{\boldsymbol{C}}^{\text{(ref)}} \right) \cdot \boldsymbol{\delta}^{\text{(LoS)}} \\ &= \delta^{\text{(L)(1)(pw)}} - \delta^{\text{(L)(2)(pw)}}. \end{aligned}$$

D.3.3   Correction noise

This section describes how Eq. (4.55) is derived:

$$\delta^{\text{(C)}} = -2 \frac{\dot{\mathbf{x}}^{(12)\perp}}{\rho} \delta^{\left(\dot{x}^{(12)\perp} \right)} + \left(\frac{\dot{\mathbf{x}}^{(12)\perp}}{\rho} \right)^2 \delta^{(\rho)}.$$

It is possible to use Eq. (4.55) to model the errors in the estimated centrifugal accelerations of the range combination approach without a significant loss of accuracy, in spite of that being a continuous function. In Ditmar et al. (2012, Section 2.2.4),

the range combinations are shown to approximate the finite difference of the along-track component of the point-wise inter-satellite acceleration considered in the classical acceleration approach. For this reason, the derivation of Eq. (4.55) starts from the classical point-wise inter-satellite acceleration (Rummel, 1979):

$$
\begin{aligned}
a^{(12)(\mathrm{LoS})} &= \ddot{\rho} - \frac{\left(\dot{\mathbf{x}}^{(12)\perp}\right)^2}{\rho} \\
&= \ddot{\rho} + a^{(12)(\mathrm{cent})}.
\end{aligned}
$$

The term $\ddot{\rho}$ describes the measured range accelerations and the term $a^{(12)(\mathrm{cent})}$ is associated with the point-wise inter-satellite centrifugal acceleration resulting from the rotation of the LoS vector, which is given by:

$$
a^{(12)(\mathrm{cent})} = -\frac{\left(\dot{\mathbf{x}}^{(12)\perp}\right)^2}{\rho}.
$$

Recall that $\dot{\mathbf{x}}^{(12)\perp}$ represents the orbit velocity of satellite 1 relatively to satellite 2 projected onto the plane perpendicular to the LoS direction and ρ is the inter-satellite range. The error in the $a^{(12)(\mathrm{cent})}$ terms is:

$$
\begin{aligned}
\delta^{(\mathrm{C})} &= \frac{\partial\, a^{(12)(\mathrm{cent})}}{\partial\, \dot{\mathbf{x}}^{(12)\perp}}\, \delta\!\left(\dot{x}^{(12)\perp}\right) + \frac{\partial\, a^{(12)(\mathrm{cent})}}{\partial\, \rho}\, \delta(\rho) \\
&= -2\frac{\dot{\mathbf{x}}^{(12)\perp}}{\rho}\, \delta\!\left(\dot{x}^{(12)\perp}\right) + \left(\frac{\dot{\mathbf{x}}^{(12)\perp}}{\rho}\right)^2 \delta(\rho),
\end{aligned}
$$

with $\delta(\rho)$ representing the ranging sensor noise and $\delta\!\left(\dot{x}^{(12)\perp}\right)$ describing the noise in the orbit velocity of satellite 1 relatively to satellite 2 projected onto the plane perpendicular to the LoS direction.

Omission signal and the mis-modelled static signal in the context of future satellite formations

E

In Section 4.3.1, the model errors are introduced as the mis-modelled time-variable signal, omission signal and mis-modelled static signal. Unlike the measurement errors, the model errors do not decrease as a function of the sensor accuracy, nor are they particular to the simplistic or advance noise models, refer to Section 4.3.3. Model errors reflect the accuracy of the knowledge of the Earth's gravitational field. The analysis conducted in Chapter 8 only considers the mis-modelled time-variable signal when quantifying the accuracy of future gravimetric missions. The reason for neglecting the omission signal and mis-modelled static signal is associated with the assumptions needed to simulate them. There is an arbitrary influence on the corresponding simulation results, depending on the underlying assumptions.

In the current section, the study of the omission signal and mis-modelled static signal is conducted, under a set of assumptions which is not realistic enough to be included in the noise budget of the formations analysed in Chapter 8. Furthermore, the effects of the omission signal and mis-modelled static signal are not expected to be significant in the data of future gravimetric missions. In the case of errors resulting from the omission signal, the reference gravitational field can be forecasted up to a sufficiently large degree, effectively eliminating this error. In what concerns the signals described by the coefficients above that degree, it is reasonable to assume that satellite formations for monitoring the temporal gravitational field variations are not sensitive to them. In case of the errors caused by the mis-modelled static signal, the Gravity field and steady-state Ocean Circulation Explorer (GOCE) mission has improved considerably the knowledge of the static field. For this reason, most research into future gravimetric formations ignores the effects of the mis-modelled static signal and omission signal, cf. Table 1.2. In spite of these issues, it is nonetheless

interesting to investigate the sensitivity of different formations to the omission signal and mis-modelled static signal.

In what concerns the mis-modelled static signal, it may even be the case that it is of significant magnitude for a future gravimetric mission, in particular if the formation is sensitive to signal at degrees higher than those covered by GOCE. In that case, as discussed in Section 6.2.2, long periods of data can be exploited to produce a tailored static gravity field model up to a high degree that, if included in the estimation of temporal gravitational field variations, absorbs all static gravity field signals. In this way, the contribution of the mis-modelled static signal is effectively mitigated. This procedure is not part of the conducted simulation study because its purpose is to determine the effect of mis-modelled static signal as function of the formation configuration, not to mitigate its effects.

The results of the analysis conducted in this chapter should be understood purely on relative terms, i.e. between the considered formations, not in absolute terms. The omission signal and mis-modelled static signal are studied only with the purpose of determining which formation is less sensitive to it.

E.1 Simulation particularities

In this section, the difficulties in predicting the amplitude of model errors are discussed for the omission signal and mis-modelled static signal. The simulation of model errors is characterised by a set of assumptions which may be arbitrary. The resulting error amplitudes from such assumptions are not necessarily compatible with the predicted measurement errors, which are derived from the characteristics of the instruments. These characteristics are studied in laboratory or with the help of numeric simulations and provide a much more reliable measure of accuracy, in particular when compared with predicted model errors.

E.1.1 Mis-modelled static signal

The mis-modelled static signal is usually represented as the difference between two gravity field models, the *newer* one estimated on the basis of incrementally larger amount and/or higher quality data than the *older* one (in here *new* and *old* are merely a way to distinguish between them). The choice of pair of models is largely arbitrary and its difference only depicts the deficiencies in the less accurate model, relative to the newer one. These deficiencies are already addressed in the newer model and, therefore, are a conservative description of the errors in the actual static gravitational field of the Earth. This is the case independently of the pair of models

that are considered. The difference between a recent pair of models is certainly lower than the difference between an older pair of models but even the former describes a conservative estimate of the mis-modelled static signal. As a consequence, the mis-modelled static signal simulated from any pair of gravity field model is too conservative, particularly when predicting future model errors.

Particular to the experiments described in this section is that the observed and forecasted orbits of the satellites differ as a result of the two different static gravity field models. Therefore, the positions of the two satellites are not the same and, consequently, there is the effect of the positioning noise affecting (mostly) the low frequencies. The set up of the simulations was chosen in this way because the effort of updating the static gravity field is necessarily connected with the necessity to deal with the positioning noise. The simulation of the mis-modelled static signal without the effect of the positioning noise would be associated with an extremely idealistic situation, which cannot ever become practical.

E.1.2 Omission signal

The usual procedure of simulating omission signal is to define a degree range above the maximum degree considered in the inversion of the observations. For example, this range could be defined between degrees 121 and 360, as is done in this section (considering GFZ/GRGS EIGEN, version 5 (EIGEN-5C), although the choice of model is not important). In actual data processing, the forecasted quantities are the result of the synthesis of the gravity field model of the Earth up to a degree much larger than 120, namely 180 in case of the computation of the Delft Mass Transport (DMT) model. The maximum degree considered when producing the forecasted quantities is determined empirically and can be raised to an arbitrarily high value, if needed (and computationally practical). In essence, the effects of mis-modelled high-frequency temporal gravitational field variations is mitigated if a sufficiently high number of Spherical Harmonic coefficients is used when computing the forecasted observation. It is practical to do so because i) the GOCE data provided unprecedented global high-degree static gravity field models and ii) the continued gathering of terrestrial data has reduced the number of location without gravimetric measurements considerably.

Evidently, there are still large areas of the globe which are only covered by GOCE data, which has limited spatial resolution compared to surface data. Therefore, the models omit the short wavelength gravitational variations in those areas. In the context of global gravity field recovery, these omission errors are sufficiently low to be considered marginal, particularly for satellites at altitudes similar to Gravity Recovery And Climate Experiment (GRACE). The effects of omission signal, in

those cases, are of much lower amplitude than those of other noise type, such as mis-modelled time-variable signal and/or those resulting from errors in the orbital positions.

E.2 Simulation set-up

The influence of the omission signal and mis-modelled static signal on the cartwheel, pendulum and trailing formation with maximum range equal to 200 km (the same as under analysis in Chapter 8) is studied. The simulations span a period of one month, with a sampling rate of 5 seconds. The simulation of the omission signal and mis-modelled static signal assumes different "true" and reference gravity field models, as described in Section 4.3.1. Table E.1 lists the assumptions considered in the simulation of these model errors.

name	symbol	assumptions
omission signal	$\delta^{(sp)}$	degrees 121 to 360 of EIGEN-5C
mis-modelled static signal	$\delta^{(st)}$	difference between EIGEN-5C and EIGEN-CG03C (degrees 2 - 120)

Table E.1 – Summary of the assumptions needed to simulate the model errors.

As indicated, the mis-modelled static signal is assumed to be the result of the difference between the EIGEN-5C and GFZ/GRGS EIGEN, version 3 (EIGEN-CG03C) models. In case of the simulation of the omission signal, the observed observations are restricted to degrees 121 to 360 since degrees 2 to 120 are accurately described by the forecasted observations. The analysis of the errors associated with the mis-modelled static signal at the level of the estimated gravity field parameters requires that the original residual static gravity field model is subtracted from the gravity field model estimated on the basis of the mis-modelled static signal.

E.3 Results

In a similar way to Section 8.2.1, this section compares the modelling errors in terms of range combinations and gravity field parameters for all formations with

Figure E.1 – a) ASD of the simulated omission signal $\delta^{(\mathrm{sp})}$ and b) the corresponding gravity field model error, for the cartwheel, pendulum and trailing formations with maximum range equal to 200 km.

200 km maximum range. The model errors under analysis are the omission signal in Section E.3.1 and the mis-modelled static signal in Section E.3.2.

E.3.1 Omission signal

When estimating the gravitational field of the Earth, the resulting model is distorted by the omission signal, i.e. the high-frequency signal which is not represented by the set of Stokes coefficients considered for the inversion. The purpose of the currently analysis is to quantify the sensitivity of the pendulum, cartwheel and trailing formations to the omission signal. The simulation results are shown in Figure E.1 and summarized in Table E.3.

In the cartwheel and trailing formations, the omission signal is dominated by the peak at 21 mHz, or 121 CPR, given that the orbital revolution period is 5679.3 s. This peak in the spectrum is a typical case of aliasing; it is the result of mapping the high frequency signal to the degrees below 120 and more intensively to those degrees closer to that value.

Exceptionally, the ASD of the data relative to the pendulum formation does not depict the peak at 21 mHz. It suggests that the wide variability of ranges in combination with the sampling of the gravitational field in the direction perpendicular to the direction of flight allow the higher frequencies of the omission signal to be more suppressed in the gravimetric data. In this way, the magnitude of the peak is

limited. On the other hand, the noise amplitude below 10 mHz is high, around 1 order of magnitude larger than the trailing formation. The power contained in the omission signal is still present in the observation and needs to go somewhere. Since the data is less sensitive to the high frequencies, the power of the signal is distributed over the low frequencies. In other words, the particular orientation and variability of the Line of Sight (LoS) direction of the pendulum formation, propagates the omission signal to a wider range of frequencies.

The noise amplitude propagated to the gravity field parameters, as shown in Figure E.1b, is proportional to the peak at 21 mHz of each formation. This suggests that the power of the omission signal concentrated at frequencies close to 21 mHz is distributed evenly to the coefficients at all degrees. Consequently, the trailing formation is most sensitive to the omission signal, the cartwheel formation is roughly a factor of 3 less sensitive (above degree 10) and the pendulum formation is less sensitive by one order of magnitude (between degrees 10 and 110). The larger variations in the range associated with the pendulum formation and, to a less extent, to the cartwheel formation, in combination with the respective orientation of the LoS direction, improve the sampling of the high-frequency features in the simulated gravitational signal.

The larger amplitude of the omission signal at low frequencies, below 8 mHz, only propagates to the gravity field parameters below degrees 10 and 20 for the cartwheel and pendulum formations, respectively, as seen by the local increase in the amplitude of those coefficients.

Recalling the results of Section 6.2.2, increasing the maximum degree of the static background model is an effective way of mitigating the omission signal. In other words, if the simulation of the omission signal is repeated considering the signal generated on the basis of a static gravity field model from, for example, degree 360 up to degree 600, the resulting omission signal would have a much lower amplitude.

formation	range combination error STD $[\,\text{m/s}^2]$	geoid height error [mm]		
		degree 60	degree 100	cum @ deg 120
cartwheel	2.6×10^{-9}	3.9	24	220
pendulum	3.5×10^{-9}	0.47	9.0	92
trailing	4.7×10^{-9}	12	94	720

Table E.2 – Summary of the omission signal, showing the STD of the time series of range combinations error and the resulting gravity field model error quantified in terms of the geoid height error at degrees 60 and 100 and cumulative geoid height error at degree 120.
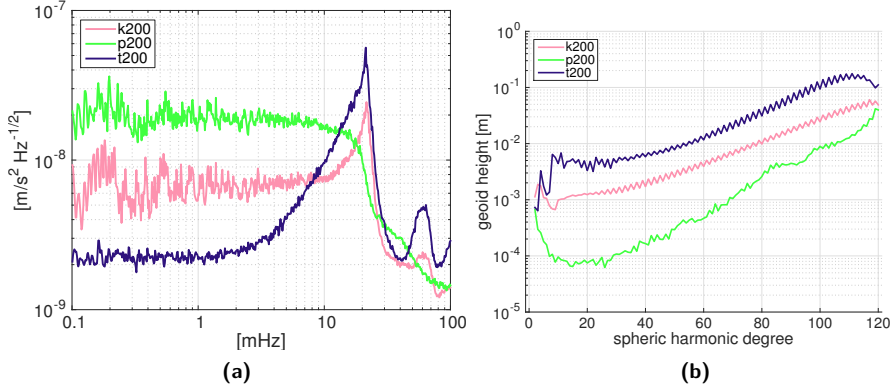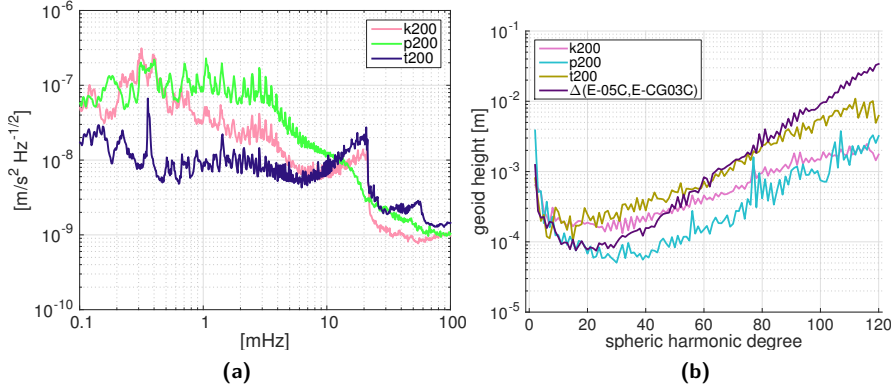
Figure E.2 – a) ASD of the simulated mis-modelled static signal $\delta^{(st)}$ and b) the corresponding gravity field model error, for the cartwheel, pendulum and trailing formations with maximum range equal to 200 km.

E.3.2 Mis-modelled static signal

The mis-modelled static signal results from the inaccurate knowledge of the static gravitational field. The observed range combinations and forecasted range combinations are simulated from different gravity field models so that the residual range combinations represent the mis-modelled static signal. Although not the focus of the thesis, the error in the mis-modelled static signal is a good way of determining the effectiveness of a formation in updating the static reference gravity field model (should it provide data that is sensitive to higher spherical harmonic degrees than GOCE). This error is computed as the difference between the original residual static gravity field model, i.e. the difference between the EIGEN-5C and EIGEN-CG03C models, and the propagated mis-modelled static signal. Included in this residual is the effect of the positioning noise, which cannot be separated from the fact that the observed and forecasted ($^{(for)}$) orbits follow different paths. Figure E.2 and Table E.3 summarise the results of the numerical study of the mis-modelled static signal.

Figure E.2a depicts similarities in comparison to the ASDs of the omission signal (Figure E.1), both in absolute terms and relatively between the formations:

- In absolute terms, the peak at 21 mHz is visible in the ASDs of both noise types – relevant to the cartwheel and trailing formations – although it has a lower amplitude in the mis-modelled static signal. The peak results from the increasing error amplitude with increasing degree of the difference between

the EIGEN-5C and EIGEN-CG03C models, labelled as "Δ(E-5C,E-CG03S)" in Figure E.2b. Since the residual range combinations are simulated from the model difference up to degree 120, the signal amplitude drops after 21 mHz, or roughly 120 CPR. In reality, it is not possible to truncate the Earth's gravitational field. However, the effect of the small spatial features that map onto the degrees larger to 120 is attributed to omission signal and not mis-modelled static signal, justifying the truncation of the residual gravity field model.

- In relative terms, the peak at 21 mHz is largest in the trailing formation, smaller in the cartwheel formation and non-existing in the pendulum formation.

These similarities suggest that the mechanism that drives the amplitude of the omission signal is the same as that of the mis-modelled static signal.

The effect of the positioning noise is clearly visible at the low frequencies when comparing the ASD with most amplitude for each formation in Figure 7.3 with Figure E.2a. Note that, unlike Chapter 7, the results if this section considers the predicted accuracy of future Global Navigation Satellite Systems (GNSSs) and, therefore, have the positioning noise downscaled by a factor of 3.

The errors resulting from mis-modelled static signal in the gravity field parameters, shown in Figure E.2b, differ by up to a factor of five between the considered formations. The data of the trailing formation contain the largest errors above degree 20. The pendulum formation shows the lowest error magnitude above degree 10. More importantly, the difference between the estimated mis-modelled static signal and the original residual static signal, i.e. the error associated with mis-modelled static signal, has a larger amplitude than the signal itself between degrees 10 and 50 for the cartwheel formation and between degrees 10 and 60 for trailing formation. This does not mean that these formations are unable to uniquely recover the simulated residual signal within these degree ranges. Recall that the simulation of the mis-modelled static signal considers the effect of the positioning noise. If much longer periods of data are considered and the effects of the positioning noise are removed by iteratively updating the reference gravity field model, the mis-modelled static signal magnitude decreases accordingly.

Thus, it is noted that the results of the mis-modelled static signal, particularly concerning the degree amplitudes, should be regarded as very conservative and mainly relevant for comparing in relative terms the sensitivity of the formations to mis-modelled static signal. Since the mis-modelled static signal is fully dominated by the deficient knowledge of the Earth's static gravitational field, it is safe to assume that as more data is gathered and the processing techniques are improved, the more

accurate the static gravity field models become and the less significant this error source is.

formation	range combination error STD $[\,\mathrm{m/s^2}]$	geoid height error [mm]		
		degree 60	degree 100	cum @ deg 120
cartwheel	5.0×10^{-9}	0.46	1.5	11
pendulum	9.1×10^{-9}	0.15	0.75	11
trailing	2.7×10^{-9}	0.72	5.5	38

Table E.3 – Summary of the mis-modelled static signal, showing the STD of the time series of range combinations error and the resulting gravity field model error quantified in terms of the geoid height error at degrees 60 and 100 and cumulative geoid height error at degree 120.

E.4   Error patterns of the mis-modelled static signal

The static gravitational field is not the focus of the dissertation. It's influence on time-varying gravity field models can be effectively mitigated, as discussed in Section 6.2.2, by averaging a large number of solutions and removing the corresponding signal from the measurements. On the other hand, one possible application for future gravimetric missions, in view of the desirable long period monitoring mass transport processes, is to model the static gravitational field. Even though the simulation of these errors in the conducted study are conservative, the spatial patterns of the corresponding error in the gravity field models provides insight into the geographical locations where the collected data are less accurate.

Figure E.3a, b and c shows spatial representation of the error in the gravity field models associated with the mis-modelled static signal, i.e. the difference between the propagated mis-modelled static signal and the assumed residual static gravity field model. For comparison, Figure E.3d shows the assumed residual static gravity field model, i.e. the difference between EIGEN-5C and EIGEN-CG03C.

The error spatial patterns of the propagated mis-modelled static signal are very different for the three formations, although all show that the largest errors are localized at the low latitudes:

- The **cartwheel formation** produces a spatial pattern characterised by long North-South stripes of similar amplitude at all the latitudes, with exception to the regions close the poles. These stripes appear homogeneously at all longitudes. The spatial pattern of the cartwheel formation does not become

more homogeneous at the equator, as one would expect from the radial attitude of the LoS vector, because the effects of the positioning noise dominate the solution.

- The **trailing formation** yields a spatial pattern showing strong North-South stripes at selected longitudes. Around the equator, the trailing formation measures the gravitational field strictly along the North-South direction and with the largest gaps between consecutive ground tracks. The resulting data contain insufficient information to allow the static residual gravitational signal to be reconstructed uniquely. As a consequence, strong and localized errors appear, becoming stretched in the North-South direction as a result of anisotropic sensitivity of the data.

- The spatial pattern resulting from the **pendulum formation** contains some North-South stripes of low amplitude at the equatorial band which are non-homogeneously distributed along longitude. The typical low-amplitude East-West stripes can be seen at higher latitudes.

(a) cartwheel

(b) pendulum

(c) trailing

(d) mis-modelled static signal
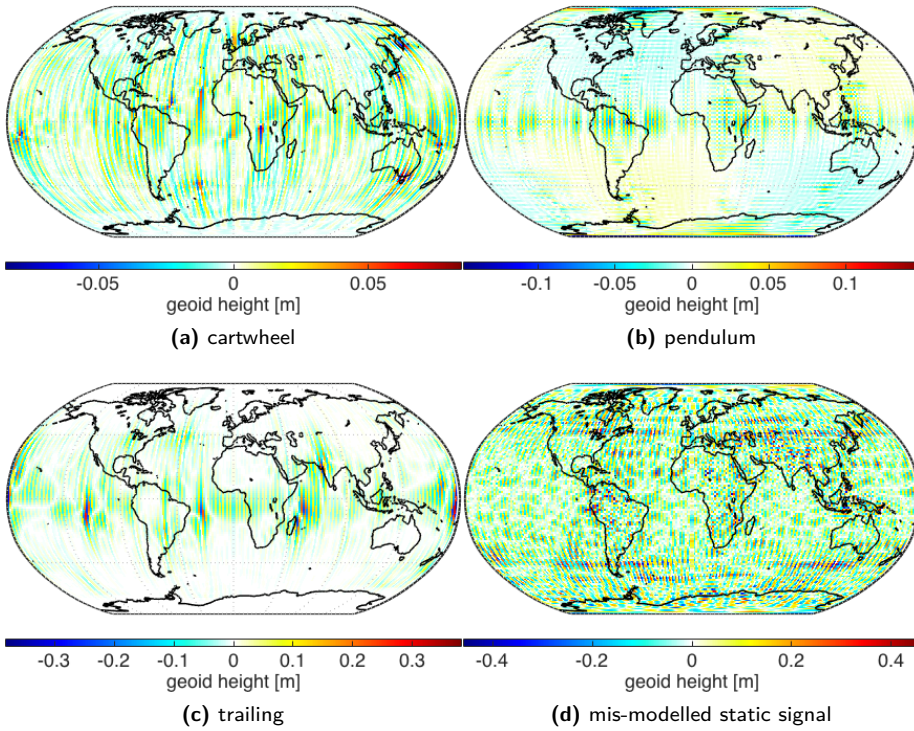
Figure E.3 – Spatial maps of the geoid height error of the mis-modelled static signal for the a) cartwheel, b) pendulum and c) trailing formations with maximum range equal to 200 km. Figure d) shows the spatial map of the difference between EIGEN-5C and EIGEN-CG03C, the residual gravity field model on the basis of which the mis-modelled static signal is computed.

E.5 Conclusions

The numerical study described in this section considered the following model errors:

- the error introduced by the omission signal, represented by degrees 121 to 360 of the EIGEN-5C model; and
- the wrongly quantified mis-modelled static signal, assumed to be equal to the difference between the EIGEN-5C and EIGEN-CG03C models.

Importantly, the effects of the positioning noise are included in the analysis of the mis-modelled static signal because the two types or noise are in practice mixed together.

It is shown that the trailing formation is most sensitive to the considered model errors. The omission signal in this formation is three times larger than in case of the cartwheel formation and eight times larger than in case of the pendulum formation. The trailing formations is four times more sensitive to mis-modelled static signal than the other formations.

The pendulum formation is the least sensitive to the omission signal and of comparable sensitivity to the mis-modelled static signal as the cartwheel formation.

Acronyms

F

cf.	*confer*, compare
e.g.	*exempli gratia*, for example
etc.	*et cetera*, and so forth
i.a.	*inter alia*, amongst others
i.e.	*id est*, that is
p.	page
pp.	pages
vs.	*versus*, against
1D	uni-dimensional
3D	three-dimensional
ACS	Attitude Control System
AIUB	Astronomical Institute of the University of Bern, Switzerland, `www.aiub.unibe.ch`
AIUB-GRACE03S	AIUB GRACE-only model, version 3, Jäggi et al. (2012)
AOCS	Attitude and Orbital Control System

AOD1B	Atmosphere and Ocean De-aliasing Level 1B product, Flechtner et al. (2006); Flechtner (2007, 2011)
ARMA	Auto-Regressive Moving-Average
ASD	Amplitude Spectral Density, equal to the square-root of the PSD
BDNSS	BeiDou/Compass Navigation Satellite System, Chengzhi (2013)
CAS	Chinese Academy of Sciences, China, `english.cas.cn`
CCR	Corner-Cube Retroreflector
CHAMP	CHallenging Mini-Satellite Payload, Reigber et al. (1996, 2002)
CIF	Conventional Inertial Frame
CNES	Centre National d'Études Spatiales, France, `cnes.fr`
CoM	Centre of Mass
CNES/GRGS-10d	CNES/GRGS 10-days gravity field models, Lemoine et al. (2007b); Bruinsma et al. (2010); Lemoine et al. (2013b)
COSMIC	Constellation Observing System for Meteorology, Ionosphere and Climate satellite mission (see also F3C)
COSMIC-2	2nd Constellation Observing System for Meteorology, Ionosphere and Climate satellite mission (see also F7C2)
CPR	Cycle Per Revolution
CPU	Central Processing Unit
CSR	Center for Space Research, The University of Texas at Austin, USA, `www.csr.utexas.edu`
CRF	Celestial Reference Frame, Section A.1
CTF	Conventional Terrestrial Frame

DAS	Degree Amplitude Spectrum
DD	Double-differenced
DFACS	Drag-Free Attitude Control Systems
DLR	Deutsches Zentrum für Luft- und Raumfahrt, Germany, `www.dlr.de`
DGM-1S	Delft Gravity Model, Farahani et al. (2013b)
DMT	Delft Mass Transport model, Liu et al. (2010); Ditmar et al. (2013)
DoF	Direction of Flight
DORIS	Doppler Orbit Determination and Radio-positioning Integrated on Satellite, Dorrer et al. (1991); Barlier (2005); Willis et al. (2006)
DOWR	Dual One-Way Ranging
DoY	Day of Year
DTU	Danish Technical University, Denmark, `www.dtu.dk`
DTU10	DTU Ocean wide Mean Sea Surface height model, 2010, Andersen (2010)
E2E	End-to-End
ECEF	Earth-Centred, Earth-Fixed reference frame, see TRF
ECF	Earth Centred Fixed reference frame, see TRF
ECI	Earth-Centred Inertial reference frame, see CRF
EFRF	Earth-Fixed Reference Frame reference frame, see TRF
ECMWF	European Centre for Medium-Range Weather Forecasts, UK, `www.ecmwf.int`
EGM2008	NGA's Earth Gravitational Model 2008, Pavlis et al. (2008)
EGM96	Joint NASA GSFC and NIMA Earth Gravitational Model 1996, Lemoine et al. (1998)

EIGEN	European Improved Gravity model of the Earth by New techniques
EIGEN-**CG03C**	GFZ/GRGS EIGEN, version 3, Förste et al. (2005)
EIGEN-**GL04C**	GFZ/GRGS EIGEN, version 4, Förste et al. (2008b)
EIGEN-**5C**	GFZ/GRGS EIGEN, version 5, Förste et al. (2008a)
EIGEN-**6C**	GFZ/GRGS EIGEN, version 6, Shako et al. (2014)
EIGEN-**6C2**	GFZ/GRGS EIGEN, version 6.2, Förste et al. (2012)
EIGEN-**6C4**	GFZ/GRGS EIGEN, version 6.4, Förste et al. (2014)
EOT08a	2008 Empirical Ocean Tide model derived from Altimeter data, Savcenko and Bosch (2008a,b)
EWH	Equivalent Water Height
EO	Earth Observation
ESA	European Space Agency, `www.esa.int`
ESTEC	European Space Research and Technology Centre, `www.esa.int/About_Us/ESTEC`
F3C	FORMOSAT-3/COSMIC, Kuo et al. (1999, 2005)
F7C2	FORMOSAT-7/COSMIC-2, Ector et al. (2010); Cook et al. (2013)
FDDW	Frequency-Dependent Data Weighting
FES	Finite Element Solution global tide model
FES2004	release 2004 of the Finite Element Solution global tide model, Lyard et al. (2006)
FORMOSAT-**3**	Taiwan's Formosa Satellite Mission-3 (see also F3C)
FORMOSAT-**7**	Taiwan's Formosa Satellite Mission-7 (see also F7C2)
GFO	GRACE Follow On, Sheard et al. (2012); Larkin (2012); Zaragoza (2013)

GFZ	Helmholtz-Zentrum Potsdam Deutsches GeoForschungsZentrum, Germany, `www.gfz-potsdam.de`
GGM02	GRACE Gravity Model 02, Tapley et al. (2005)
GGM03	GRACE Gravity Model 03, Tapley et al. (2007)
GIA	Glacial Isostatic Adjustment
GLDAS	Global Land Data Assimilation System, Rodell et al. (2004)
GloNaSS	Globalnaya Navigatsionnaya Sputnikovaya Sistema, Polischuk and Revnivykh (2004)
GNSS	Global Navigation Satellite System
GOCE	Gravity field and steady-state Ocean Circulation Explorer, Balmino et al. (1999); Floberghagen et al. (2011)
GOCO02S	Gravity Observation COmbination release 02 satellite-only gravity field model, Goiginger et al. (2011)
GOCO03S	Gravity Observation COmbination release 03 satellite-only gravity field model, Mayer-Gürr (2012)
GOT	Goddard Ocean Tide model, Ray (1999)
GPS	Global Positioning System
GRACE	Gravity Recovery And Climate Experiment, Tapley et al. (1996); Tapley (2004b)
GRAIL	Gravity Recovery and Interior Laboratory mission, Lehman et al. (2013)
GRF	Gradiometer Reference Frame, Section A.7
GRS	Geoscience and Remote Sensing, Faculty of Civil Engineering and Geosciences, Delft University of Technology (TU Delft)
GRGS	Groupe de Recherche de Géodésie Spatiale, France, `grgs.obs-mip.fr`

GSFC	Goddard Space Flight Center, United States of America (USA), `www.nasa.gov/centers/goddard`
HRF	Hill Reference Frame, Section A.8
hl-SST	high-low Satellite-to-Satellite Tracking
HPF	High-Level Processing Facility
IRF	Inertial Reference Frame
IST	Instituto Superior Técnico, `tecnico.ulisboa.pt`
ITG	Institut für Geodäsie und Geoinformation, Germany, `www.igg.uni-bonn.de`
ITG-GRACE2010	ITG GRACE-only model, 2010, Mayer-Gürr et al. (2010); Kurtenbach et al. (2009)
ITG-GRACE2010s	ITG GRACE-only static model, 2010, Mayer-Gürr et al. (2010)
JPL	Jet Propulsion Laboratory, USA, `www.jpl.nasa.gov`
KBR	K-Band Ranging
KO	Kinematic Orbit
L0	Level 0 data
L1A	Level 1A data
L1B	Level 1B data
L2	1227.60 mHz GPS carrier frequency
LaD	Land Dynamics hydrological model, Milly and Shmakin (2002)
LAGEOS	LAser GEOdynamics Satellite, Cohen and Smith (1985)
LASER	Light Amplification by the Stimulated Emission of Radiation

LEO	Low-Earth Orbit
LGM	Last Glacial Maximum
Lic. Eng.	Licenciatura em Engenharia (Licenciate in Engineering, pre-Bologna Accords), `en.wikipedia.org/wiki/Licentiate#Portugal`
LISA	Laser Interferometer Space Antenna, Merkowitz (2003)
LHRF	Local Horizontally-aligned Reference Frame, Section A.3
ll-SST	low-low Satellite-to-Satellite Tracking
LNOF	Local North-Oriented Frame
LORF	Local Orbital Reference Frame, Section A.4
LoS	Line of Sight
LoSRF	Line-of-sight Reference Frame, Section A.5
LS	Least-Squares
MasCon	Mass Concentration approach, Rowlands et al. (2005); Lemoine et al. (2007a)
MetOp	Meteorological Operational satellite programme, Edwards and Pawlak (2000)
MetOp-A	first satellite of the Meteorological Operational satellite programme
MOG2D-G	2D Gravity Waves model, Carrère (2003)
N/A	Not Applicable
NASA	National Aeronautics and Space Administration, USA
NCEP	National Centers for Environmental Prediction, USA, `www.ncep.noaa.gov`

NGA	National Geospatial-Intelligence Agency, USA (previously called NIMA), `www.nga.mil`
NIMA	National Imagery and Mapping Agency
OMCT	Ocean Model for Circulation and Tides, Thomas (2001)
PANDA	Position And Navigation Data Analyst software, Zhao (2004)
PCA	Principal Component Analisys
PCCG	Pre-Conditioned Conjugate Gradient method, Hestenes and Stiefel (1952)
PDO	Purely Dynamic Orbit
POD	Precise Orbit Determination
PPHA	Pacanowski, Ponte, Hirose and Ali barotropic ocean model, Hirose et al. (2001); Ali (2003)
PSD	Power Spectral Density, equal to the square of the ASD
PSO	Precise or Post-processed Science Orbit
RDO	Reduced Dynamic Orbit
RMS	Root Mean Squared
SAR	Synthetic Aperture Radar
SD	Single-Differenced
SD-E	Single-Differenced phase measurements between Epochs
SD-S	Single-Differenced phase measurements between GPS Satellites
SDR	Software Defined Radio
SGG	Satellite Gravity Gradient
SLR	Satellite Laser Ranging, Smith and Turcotte (1993); Combrinck (2010)

SNR	Signal-to-Noise Ratio
SRF	Satellite Reference Frame, Section A.6
SSO	Sun-Synchronous Orbit
SST-**AUX**-**2**	GOCE HPF non-tidal dealiasing product, Gruber et al. (2014)
STD	STandard Deviation
TPXO	ToPeX Ocean tidal model, Egbert et al. (1994); Egbert and Erofeeva (2002)
TRF	Terrestrial Reference Frame, Section A.2
TT	Terrestrial Time
TU Delft	Delft University of Technology, `www.tudelft.nl`
TUG	Technische Universität Graz, Austria, `www.tugraz.at`
TUM	Technische Universität München, Germany, `www.tum.de`
TWS	Terrestrial Water Storage
UK	United Kingdom
URL	Uniform Resource Locator
USA	United States of America
ZD	Zero-differenced

Symbols

<div style="text-align: right">**G**</div>

The following convention distinguishes between scalar, vector and tensor quantities:

- Scalar quantities are represented by lower-case or capital unformatted symbols, e.g.:
  - range: ρ;
  - co-latitude: ϑ;
  - gravitational potential: V.
- Vector quantities are represented by lower-case bold-face symbols, e.g.:
  - orbital elements: $\boldsymbol{o}$;
  - gravitational acceleration: $\mathbf{g}$;
  - unit vector: $\mathbf{e}$.
- Matrix quantities are represented by capital bold-face symbols, e.g.:
  - design matrix: $\mathbf{A}$;
  - a set of Stokes coefficients: $\overline{\boldsymbol{C}}$
  - gravity gradient: $\mathbf{G}$.

The superscripts described in Section G.2 add an additional meaning to the original symbol, associated with the context in which it is defined, such as:

- the forecasted orbit position of satellite 1, $\mathbf{x}^{(\mathrm{for})(1)}$;
- the reference gravitational potential, $V^{(\mathrm{ref})}$;
- the point-wise orientation noise of satellite 2, $\delta^{(\mathrm{L})(2)(\mathrm{pw})}$.

Subscripts, like superscripts, also add a contextual meaning but are restricted to either a component of a vector, such as:

- the x-component of the gravitational acceleration, g_x;
- the value of the (time-varying) range combination at epoch i, $\bar{a}_i$;
- the Stokes coefficient of degree ℓ and order m, $\overline{C}_{\ell m}$.

Notice that it is possible to refer to the y-component of the orbit velocity at epoch i with $\dot{\mathbf{x}}_{y,i}$ (which has the same meaning as $\dot{\mathbf{x}}_{i,y}$) but if the number of superscripts is low, it is preferable to move the component of the vector/tensor to superscript, e.g. $\dot{\mathbf{x}}_i^{(y)}$. The subscripts used in the thesis are presented in Section G.3.

As a general rule, all the quantities with index i are given with a constant sampling interval Δt. A quantity with the subscript i corresponds to the observation time $t_i := t_0 + (i-1)\Delta t$, where t_0 is an initial epoch ($i = 1, \dots N$ with N being the total number of data).

Regarding terminology, the term *synthetic* is used as a means to express that a certain measurement is generated numerically on the basis of an assumed model, rather than being the output of a real sensor.

A_0	radial amplitude
B_0	cross-track amplitude
α	radial phase
β	horizontal phase
x_{off}	radial offset
y_{off}	along-track offset
$\boldsymbol{o}$	orbital elements
a	semi-major axis
e	eccentricity
i	inclination
Ω	right ascension of the ascending node
ω	argument of perigee
M	mean anomaly
ν	true anomaly

$T^{(\mathrm{rev})}$	orbital revolution period
$T^{(\mathrm{revisit})}$	revisit period
m_j	model parameter j
$\mathbf{m}$	model parameters
$\hat{\mathbf{m}}^{(\mathrm{res})}$	model correction
$\mathbf{m}^{(\mathrm{ref})}$	reference model parameters
$\boldsymbol{\Phi}$	functional model
Φ_i	functional model element i
$\mathbf{A}$	design matrix
A_{ij}	design matrix element ij
$\mathbf{N}$	normal matrix
$\mathbf{C}^{(\mathrm{res})}$	data noise covariance matrix
$\mathbf{C}^{(\mathrm{ref})}$	reference model noise covariance matrix
$\mathbf{y}^{(\mathrm{obs})}$	observed data
$\mathbf{y}^{(\mathrm{for})}$	forecasted data
$\mathbf{y}^{(\mathrm{res})}$	residual data
ϑ	co-latitude
λ	longitude
r	radius
R	semi-major axis of a reference ellipsoid
G_0	universal gravitational constant
$M_\oplus$	mass of the Earth
$G_0 M_\oplus$	geocentric gravitational constant
t	time

Δt	sampling rate
f	frequency
$\mathbf{w}$	averaging filter
ℓ	degree
$L^{(\mathrm{max})}$	maximum degree
m	order
$|m|$	absolute value of order
$\overline{Y}$	4π-normalised surface spherical harmonic function
$\overline{Y}_{\ell m}$	spherical harmonic function of degree ℓ and order m
$\overline{C}$	Stokes coefficient
$\overline{C}_{\ell m}$	Stokes coefficient of degree ℓ and order m
V	gravitational potential
g	gravitational acceleration magnitude or component
$\mathbf{g}$	gravitational acceleration
$\bar{\mathbf{g}}$	average gravitational acceleration
$\mathbf{G}$	gravity gradient
$\mathbf{a}$	acceleration
$\bar{\mathbf{a}}$	averaged acceleration
$\mathbf{a}^{(\mathrm{ng})}$	non-gravitational acceleration
$\mathbf{a}^{(12)}$	inter-satellite acceleration
$a^{(12)(\mathrm{LoS})}$	point-wise inter-satellite acceleration projected onto the Line of Sight (LoS) direction
$a^{(12)(\mathrm{cent})}$	point-wise inter-satellite centrifugal acceleration
$\bar{\mathbf{a}}^{(12)}$	averaged inter-satellite acceleration

$\mathbf{e}$	unit vector
$\mathbf{e}^{(\mathrm{LoS})}$	unit vector defining the LoS direction
$\mathbf{d}$	LoS vector
θ	angle between the LoS vectors at successive epochs
ρ	range
$\dot{\rho}$	range-rate
$\ddot{\rho}$	range acceleration
$\bar{a}$	range combination
$\mathbf{x}$	orbit position
$\mathbf{x}^{(\mathrm{for})(\mathrm{adj})(\mathrm{LoS})}$	forecasted orbit positions adjusteds with range data along the LoS direction
$\mathbf{x}^{(\mathrm{for})(\mathrm{adj})(\mathrm{abs})}$	forecasted orbit positions adjusted to simulate absolute positioning noise
$\mathbf{x}^{(\mathrm{kpl})}$	Keplerian reference orbit
$\mathbf{x}^{(\mathrm{mod})}$	Modelled orbit
$\dot{\mathbf{x}}$	orbit velocity
δ	noise (scalar)
$\delta^{(\mathrm{obs})}$	observation noise
$\delta^{(\mathrm{for})}$	forecast noise
$\delta^{(\Delta\mathbf{x})}$	relative orbit position noise
$\delta^{(\Delta\dot{\mathbf{x}})}$	relative orbit velocity noise
$\delta^{(\mathbf{x})}$	absolute orbit position noise
$\delta^{(\mathrm{R})}$	ranging noise
$\delta^{(\mathrm{R,spl})}$	simplistic ranging noise

$\delta^{(\mathrm{rP})}$	relative position noise
$\delta^{(\mathrm{aP})}$	absolute position noise
$\delta^{(\mathrm{C})}$	correction noise
$\delta^{(\mathrm{acc})}$	accelerometer noise
$\delta^{(\mathrm{P})}$	positioning noise
$\delta^{(\mathrm{P})(\mathrm{pw})(\mathrm{rel})\parallel}$	relative point-wise positioning noise resulting from the relative orbit position noise parallel to the LoS direction
$\delta^{(\mathrm{P})(\mathrm{pw})(\mathrm{rel})\perp}$	relative point-wise positioning noise resulting from the relative orbit position noise perpendicular to the LoS direction
$\delta^{(\mathrm{P})(\mathrm{pw})(\mathrm{abs})}$	absolute point-wise positioning noise
$\delta^{(\mathrm{P})(\mathrm{LoS})}$	positioning noise resulting from the relative orbit position noise along the LoS direction
$\delta^{(\mathrm{P})(\mathrm{rel})\parallel}$	positioning noise resulting from the relative orbit position noise along the LoS direction
$\delta^{(\mathrm{P})(\mathrm{rel})\perp}$	positioning noise resulting from the relative orbit position noise perpendicular to the LoS direction
$\delta^{(\mathrm{L})}$	orientation noise
$\delta^{\left(\dot{x}^{(12)\perp}\right)}$	noise in the orbit velocity of satellite 1 relatively to satellite 2 projected onto the plane perpendicular to the LoS direction
$\boldsymbol{\delta}^{(\mathrm{LoS})}$	noise in the orientation of the LoS vector
$\delta^{(\mathrm{st})}$	mis-modelled static signal
$\delta^{(\mathrm{tv})}$	mis-modelled time-variable signal
$\delta^{(\mathrm{sp})}$	omission signal

G.1 Mathematical operations

$\boldsymbol{\nabla}$ gradient

$\boldsymbol{\nabla}\boldsymbol{\nabla}$ double gradient

∇^2 Laplace

$*$ convolution

$^{\mathrm{T}}$ transpose

$\mathscr{F}$ Fourier transform

$\boldsymbol{R}$ rotation matrix

$$\boldsymbol{\nabla} = \left[\frac{d}{d\,x_1}, ..., \frac{d}{d\,x_n}\right]^{\mathrm{T}}$$

$$\boldsymbol{\nabla}\boldsymbol{\nabla} = \boldsymbol{\nabla}\cdot\boldsymbol{\nabla}^{\mathrm{T}} = \begin{pmatrix} \frac{d^2}{d\,x_1^2} & \cdots & \frac{d^2}{d\,x_1\,d\,x_n} \\ \vdots & \ddots & \\ \frac{d^2}{d\,x_n\,d\,x_1} & & \frac{d^2}{d\,x_n^2} \end{pmatrix}$$

$$\nabla^2 = \boldsymbol{\nabla}^{\mathrm{T}}\cdot\boldsymbol{\nabla} = \frac{d^2}{d\,x_1^2} + ... + \frac{d^2}{d\,x_n^2}$$

G.2 Superscripts

Superscripts add an additional meaning to the original symbol, associated with the context in which it is defined, such as the forecasted orbit position of satellite 1 $\mathbf{x}^{(\mathrm{for})(1)}$, the reference gravitational potential $V^{(\mathrm{ref})}$, or the orbit position defined in the Line-of-sight Reference Frame (LoSRF, Section A.5) orbit position $\mathbf{x}^{(\mathrm{LoSRF})}$.

(cent)   centrifugal

(Cor)   Coriolis

(ref)   reference

(true)	"true"
(for)	forecasted
(obs)	observed
(res)	residual
(adj)	adjusted
(pw)	point-wise
(k)	noise type
(1)	satellite 1
(2)	satellite 2
(12)	satellite 1 relatively to satellite 2
(j)	satellite j
(CRF)	relative to the Celestial Reference Frame (CRF, Section A.1)
(TRF)	relative to the Terrestrial Reference Frame (TRF, Section A.2)
(LHRF)	relative to the Local Horizontally-aligned Reference Frame (LHRF, Section A.3)
(LoSRF)	relative to the Line-of-sight Reference Frame (LoSRF, Section A.5)
(HRF)	relative to the Hill Reference Frame (HRF, Section A.8)
(12)	inter-satellite
$(\mathbf{x})$	absolute orbit position
$(\Delta\mathbf{x})$	relative orbit position
$(\Delta\dot{\mathbf{x}})$	relative orbit velocity
(LoS)	LoS direction
(rel)	relative

(abs)	absolute
(max)	maximum
(min)	minimum
(avg)	average
(kpl)	Keplerian
(mod)	Modelled
(rev)	revolution
(revisit)	revisit
(**hl-SST**)	hl-SST
$\perp$	perpendicular

G.3   Subscript

Subscripts, like superscripts, also add a contextual meaning but are restricted to either a component of a vector, such as the x-component of the gravitational acceleration g_x, or the value of the (time-varying) range combination at epoch i, $\bar{a}_i$. Notice that it is possible to refer to the y-component of the orbit velocity at epoch i with $\dot{\mathbf{x}}_{y,i}$ (which has the same meaning as $\dot{\mathbf{x}}_{i,y}$) but if the number of superscripts is low, it is preferable to move the component of the vector/tensor to superscript, e.g. $\dot{\mathbf{x}}_i^{(y)}$.

i	epoch i
x	x-component
y	y-component
z	z-component
xx	xx-component
$\ell\|m\|$	degree and absolute value of order

Bibliography

Milton Abramowitz and Irene a. Stegun. **Handbook of Mathematical Functions With Formulas, Graphs and Mathematical Tables**. Applied mathematics series. National Bureau of Standards, Washington, D. C., 1964. ISBN 9780486612720. `http://people.math.sfu.ca/{~}cbm/aands/abramowitz{_}and{_}stegun.pdf`. Cited on page 132.

Ahmed Haider Ali. **Quality of wind stress fields measured by the skill of a barotropic ocean model: Importance of stability of the Marine Atmospheric Boundary Layer**. *Geophysical Research Letters*, 30(3):10–13, 2003. DOI 10.1029/2002GL016058. Cited on page 322.

O. B. Andersen. **The DTU10 Gravity field and Mean sea surface**. In *Second International Symposium of the Gravity Field of the Earth*, Fairbanks, Alaska, 2010. `http://www.space.dtu.dk/english/{~}/media/Institutter/Space/English/scientific{_}data{_}and{_}models/global{_}marine{_}gravity{_}field/dtu10.ashx`. Cited on pages 27 and 317.

A. Anselmi, S. Cesare, P.N.A.M. Visser, T. van Dam, N. Sneeuw, T. Gruber, B. Altés, F. Cossu, P. Ditmar, M. Murböck, M. Parisch, D. Renard, T. Reubelt, G. Sechi, and João Encarnação. **Assessment of a Next Generation Gravity Mission for monitoring the variations of earth's gravity field**. Technical report 22643/09/NL/AF, European Space Agency, Noordwijk, The Netherlands, 2010. Cited on pages 22, 46, and 271.

Donald F. Argus. **Uncertainty in the velocity between the mass center and surface of Earth**. *Journal of Geophysical Research*, 117(B10):1–15, oct 2012. DOI 10.1029/2012JB009196. Cited on page 30.

Daniel Arnold, Stefano Bertone, Adrian Jäggi, Gerhard Beutler, and Leos Mervart. **GRAIL Gravity Field Determination Using the Celestial Mechanics Approach**. *Icarus*, aug 2015. DOI 10.1016/j.icarus.2015.08.015. Cited on page 39.

G. Austen, E. W. Grafarend, and T. Reubelt. **Analysis of the Earth's Gravitational Field from Semi-Continuous Ephemeris of a Low Earth Orbiting GPS-Tracked Satellite of Type CHAMP, GRACE or GOCE**. In József Ádám and Klaus-Peter Schwarz, editors, *Vistas for Geodesy in the New Millennium*, pages 309–315. Springer Berlin Heidelberg, 2002. DOI 10.1007/978-3-662-04709-5_51. Cited on page 41.

J.L. Awange, E. Forootan, J. Kusche, J.B.K. Kiema, P.a. Omondi, B. Heck, K. Fleming, S.O. Ohanya, and R.M. Gonçalves. **Understanding the decline of water storage across the Ramser-Lake Naivasha using satellite-based methods**. *Advances in Water Resources*, 60:7–23, oct 2013. DOI 10.1016/j.advwatres.2013.07.002. Cited on page 29.

J.L. Awange, E. Forootan, M. Kuhn, J. Kusche, and B. Heck. **Water storage changes and climate variability within the Nile Basin between 2002 and 2011**. *Advances in Water Resources*, 73:1–15, nov 2014. DOI 10.1016/j.advwatres.2014.06.010. Cited on page 29.

T Badura, C Sakulin, C Gruber, and R Klostius. **Derivation of the CHAMP-only global gravity field model TUG-CHAMP04 applying the energy integral approach**. *Studia Geophysica et Geodaetica*, 50(1):59–74, jan 2006. DOI 10.1007/s11200-006-0002-3. Cited on page 40.

G. Balmino, R. Rummel, P. Visser, and P. Woodworth. **The Four Candidate Earth Explorer Core Missions - Gravity Field and Steady-State Ocean Circulation Mission**. Technical Report SP- 1233(1), European Space Agency, Noordwijk, The Netherlands, 1999. Cited on pages 96 and 319.

Tamara Bandikova and Jakob Flury. **Improvement of the GRACE star camera**

data based on the revision of the combination method. *Advances in Space Research*, 54(9):1818–1827, jul 2014. DOI 10.1016/j.asr.2014.07.004. Cited on pages 8, 265, and 269.

Tamara Bandikova, Jakob Flury, and Ung-Dai Ko. **Characteristics and accuracies of the GRACE inter-satellite pointing**. *Advances in Space Research*, 50(1):123–135, jul 2012. DOI 10.1016/j.asr.2012.03.011. Cited on pages 7, 8, and 98.

V. R. Barletta, R. Sabadini, and A. Bordoni. **Isolating the PGR signal in the GRACE data: impact on mass balance estimates in Antarctica and Greenland**. *Geophysical Journal International*, 172(1):18–30, jan 2008. DOI 10.1111/j.1365-246X.2007.03630.x. Cited on page 30.

François Barlier. **The DORIS system: a fully operational tracking system to get orbit determination at centimeter accuracy in support of Earth observations**. *Comptes Rendus Geoscience*, 337(14):1223–1224, oct 2005. DOI 10.1016/j.crte.2005.07.007. Cited on pages 19 and 317.

O Baur, M Kuhn, and W E Featherstone. **GRACE-derived ice-mass variations over Greenland by accounting for leakage effects**. *Journal of Geophysical Research*, 114(B6):B06407, jun 2009. DOI 10.1029/2008JB006239. Cited on page 30.

O. Baur, M. Kuhn, and W. E. Featherstone. **Continental mass change from GRACE over 2002–2011 and its impact on sea level**. *Journal of Geodesy*, 87(2):117–125, feb 2013. DOI 10.1007/s00190-012-0583-2. Cited on page 30.

O. Baur, H. Bock, E. Höck, A. Jäggi, S. Krauss, T. Mayer-Gürr, T. Reubelt, C. Siemes, and N. Zehentner. **Comparison of GOCE-GPS gravity fields derived by different approaches**. *Journal of Geodesy*, 88(10):959–973, oct 2014. DOI 10.1007/s00190-014-0736-6. Cited on page 39.

Oliver Baur, Michael Kuhn, and Will E Featherstone. **GRACE-Derived Linear and Nonlinear Secular Mass Variations Over Greenland**. In *VII Hotine-Marussi Symposium on Mathematical Geodesy*, pages 381–386. Springer Berlin Heidelberg, 2012. DOI 10.1007/978-3-642-22078-4_57. Cited on page 30.

Mélanie Becker, William LLovel, Anny Cazenave, Andreas Güntner, and Jean-François Crétaux. **Recent hydrological behavior of the East African great lakes region inferred from GRACE, satellite altimetry and rainfall observations**. *Comptes Rendus Geoscience*, 342(3):223–233, mar 2010. DOI 10.1016/j.crte.2009.12.010. Cited on page 29.

P. L. Bender, J. L. Hall, J Ye, and WM Klipstein. **Satellite-Satellite Laser Links for Future Gravity Missions**. *Space Science Reviews*, 108(1/2):377–384, 2003. DOI 10.1023/A:1026195913558. Cited on page 45.

Peter L. Bender, David N. Wiese, and R. Steven Nerem. **A Possible Dual-GRACE Mission with 90 degree and 63 degree Inclination Orbits**. In *3rd International Symposium on Formation Flying, Missions and Technologies (SP-654)*, Noordwijk, The Netherlands, 2008. ESA Communication Production Office. Cited on pages 7, 47, and 112.

Aleš Bezděk. **Calibration of accelerometers aboard GRACE satellites by comparison with POD-based nongravitational accelerations**. *Journal of Geodynamics*, 50(5):410–423, dec 2010. DOI 10.1016/j.jog.2010.05.001. Cited on page 23.

Aleš Bezděk, Josef Sebera, Jaroslav Klokočník, and Jan Kostelecký. **Gravity field models from kinematic orbits of CHAMP, GRACE and GOCE satellites**. *Advances in Space Research*, 53(3):412–429, feb 2014. DOI 10.1016/j.asr.2013.11.031. Cited on pages 21, 41, 44, and 55.

R. Biancale, G. Balmino, S. Bruinsma, J.-M. Lemoine, S Loyer, and F. Perosanz. **GRACE data processing in CNES/GRGS; results and discussion**. In *GRACE Science Team Meeting*, 2005. http://www.csr.utexas.edu/grace/GSTM/abstracts/abstract{_}submissions/biancale{_}1126766937.html. Cited on pages 24 and 284.

G Bianco, R Devoti, M Fermi, V Luceri, P. Rutigliano, and C Sciarretta. **Estimation of low degree geopotential coefficients using SLR data**. *Planetary and Space Science*, 46(11-12):1633–1638, nov 1998. DOI 10.1016/S0032-0633(97)00215-8. Cited on page 19.

B J Bloom, T L Nicholson, J R Williams, S L Campbell, M Bishof, X. Zhang, W Zhang, S L Bromley, and J Ye. **An optical lattice clock with accuracy and stability at the 10^{-18} level**. *Nature*, 506(7486):71–75, jan 2014. DOI 10.1038/nature12941. Cited on page 48.

H. Bock, U. Hugentobler, T.A. Springer, and G. Beutler. **Efficient precise orbit determination of LEO satellites using GPS**. *Advances in Space Research*, 30(2):295–300, jul 2002. DOI 10.1016/S0273-1177(02)00298-3. Cited on page 36.

Carmen Boening, Josh K. Willis, Felix W. Landerer, R. Steven Nerem, and John Fasullo. **The 2011 La Niña: So strong, the oceans fell**. *Geophysical Research Letters*, 39(19):1–5, oct 2012. DOI 10.1029/2012GL053055. Cited on page 30.

J Bouman, M Fuchs, E Ivins, W. van der Wal, E Schrama, P Visser, and M Horwath. **Antarctic outlet glacier mass change resolved at basin scale from satellite gravity gradiometry**. *Geophysical Research Letters*, 41(16):5919–5926, aug 2014. DOI 10.1002/2014GL060637. Cited on page 30.

S. Bruinsma, D. Tamagnan, and R. Biancale. **Atmospheric densities derived from CHAMP/STAR accelerometer observations**. *Planetary and Space Science*, 52(4):297–312,
mar 2004. DOI 10.1016/j.pss.2003.11.004. Cited on page 23.

Sean Bruinsma, Jean-Michel Lemoine, Richard Biancale, and Nicole Valès. **CNES/GRGS 10-day gravity field models (release 2) and their evaluation**. *Advances in Space Research*, 45(4):587–601, feb 2010. DOI 10.1016/j.asr.2009.10.012. Cited on pages 8, 28, 39, and 316.

Loren Carrère. **Modeling the barotropic response of the global ocean to atmospheric wind and pressure forcing - comparisons with observations**. *Geophysical Research Letters*, 30(6):1997–2000, 2003. DOI 10.1029/2002GL016473. Cited on page 321.

Kelley Case, Gerhard L.H. Kruizinga, and Sien-Chong Wu. **GRACE Level 1B Data Product User Handbook**. Technical Report JPL D-22027, Jet Propulsion Laboratory, California Institute of Technology, Pasadena, CA, USA, 2010. Cited on page 133.

A. Cazenave, K. Dominh, S. Guinehut, E. Berthier, W. Llovel, G. Ramillien, M. Ablain, and G. Larnicol. **Sea level budget over 2003-2008: A reevaluation from GRACE space gravimetry, satellite altimetry and Argo**. *Global and Planetary Change*, 65:83–88, 2009. DOI 10.1016/j.gloplacha.2008.10.004. Cited on page 30.

Anny Cazenave. **ATMOSPHERE: Enhanced: How Fast Are the Ice Sheets Melting?** *Science*, 314(5803):1250–1252, nov 2006. DOI 10.1126/science.1133325. Cited on page 30.

Stefano Cesare, Giorgio Biondetti, Sergio Mottini, Manlio Parisch, Gianfranco Sechi, Enrico Canuto, Marco Pisani, Miguel Aguirre, Bruno Leone, Luca Massotti, and Pierluigi Silvestrin. **Satellite-to-satellite laser tracking for a next generation gravity mission**. In *3rd International Symposium on Formation Flying, Missions and Technologies (SP-654)*, Noordwijk, The Netherlands, 2008. ESA Communication Production Office. Cited on pages 45, 218, and 219.

Stefano Cesare, Miguel Aguirre, Andrea Allasio, Bruno Leone, Luca Massotti, Danilo Muzi, and Pierluigi Silvestrin. **The measurement of Earth's gravity field after the GOCE mission**. *Acta Astronautica*, 67(7-8):702–712, oct 2010a. DOI 10.1016/j.actaastro.2010.06.021. Cited on pages 45 and 254.

Stefano Cesare, Sergio Mottini, Fabio Musso, Manlio Parisch, Gianfranco Sechi, Enrico Canuto, Miguel Aguirre, Bruno Leone, Luca Massotti, and Pierluigi Silvestrin. **Satellite Formation for a Next Generation Gravimetry Mission**. In Rainer Sandau, Hans-Peter Roeser, and Arnoldo Valenzuela, editors, *Small Satellite Missions for Earth Observation*, pages 125–133. Springer Berlin Heidelberg, Berlin, Heidelberg, 2010b. DOI 10.1007/978-3-642-03501-2_11. Cited on pages 8, 46, 247, and 265.

Don P Chambers and Jens Schröter. **Measuring ocean mass variability from satellite gravimetry**. *Journal of Geodynamics*, 52(5):333–343, 2011. DOI 10.1016/j.jog.2011.04.004. Cited on page 30.

J L Chen. **Spatial sensitivity of the Gravity Recovery and Climate Experiment (GRACE) time-variable gravity observations**. *Journal of Geophysical Research*, 110(B8):1–8, 2005. DOI 10.1029/2004JB003536. Cited on page 8.

J L Chen. **Satellite Gravity Measurements Confirm Accelerated Melting of Greenland Ice Sheet**. *Science*, 313(5795):1958–1960, sep 2006. DOI 10.1126/science.1129007. Cited on page 30.

J L Chen, C R Wilson, B D Tapley, D Blankenship, and D Young. **Antarctic regional ice loss rates from GRACE**. *Earth and Planetary Science Letters*, 266(1-2):140–148, 2008a. DOI 10.1016/j.epsl.2007.10.057. Cited on page 30.

J. L. Chen, C. R. Wilson, D. Blankenship, and B. D. Tapley. **Accelerated Antarctic ice loss from satellite gravity measurements**. *Nature Geoscience*, 2(12):859–862, dec 2009a. DOI 10.1038/ngeo694. Cited on page 30.

J L Chen, C R Wilson, B D Tapley, Z L Yang, and G Y Niu. **2005 drought event in the Amazon River basin as measured by GRACE and estimated by climate models**. *Journal of Geophysical Research*, 114(B5):B05404, may 2009b. DOI 10.1029/2008JB006056. Cited on page 29.

J. L. Chen, C. R. Wilson, and B. D. Tapley. **Interannual variability of Greenland ice losses from satellite gravimetry**. *Journal of Geophysical Research*, 116(B7):B07406, jul 2011. DOI 10.1029/2010JB007789. Cited on page 30.

Y Chen, B Schaffrin, and CK Shum. **Continental Water Storage Changes from GRACE Line-of-Sight Range Acceleration Measurements**. In *VI Hotine-Marussi Symposium on Theoretical and Computational Geodesy*, pages 62–66. Springer Berlin Heidelberg, Berlin, Heidelberg, 2008b. DOI 10.1007/978-3-540-74584-6_10. Cited on page 41.

Li Chengzhi. **The Chinese GNSS—System development and policy analysis**. *Space Policy*, 29(1):9–19, feb 2013. DOI 10.1016/j.spacepol.2012.11.001. Cited on pages 141 and 316.

B Christophe, JP Marque, and B Foulon. **In-orbit data verification of the accelerometers of the ESA GOCE mission**. In S. Boissier, M. Heydari-Malayeri, R. Samadi, and D. Valls-Gabaud, editors, *Socete Francaise d'Astronomie et d'astrophysique*, pages 2–5, 2010. http://sf2a.eu/semaine-sf2a/2010/proceedings/2010sf2a.conf..0113C.pdf. Cited on pages 23 and 219.

W.H. Clohessy and R.S. Wiltshire. **Terminal Guidance System for Satellite Rendezvous**. *Journal of the Aerospace Sciences*, 27(9):653–658, sep 1960. DOI 10.2514/8.8704. Cited on page 66.

Steven C. Cohen and David E. Smith. **LAGEOS Scientific Results: Introduction**. *Journal of Geophysical Research*, 90(B11):9217, 1985. DOI 10.1029/JB090iB11p09217. Cited on page 320.

Oscar L. Colombo and Scott B. Luthcke. **Kinematic Point Positioning of a LEO With Simultaneous Reduced-Dynamic Orbit Estimation**. In *17th International Technical Meeting of the Satellite Division of The Institute of Navigation (ION GNSS 2004)*, 2004. `http://bowie.gsfc.nasa.gov/697/staff/colombo/pdfs/jason.paper.ion.gnss.2004.pdf`. Cited on page 36.

Ludwig Combrinck. **Satellite Laser Ranging**. In Guochang Xu, editor, *Sciences of Geodesy - I*, chapter 9, pages 301–338. Springer Berlin Heidelberg, Berlin, Heidelberg, 2010. DOI 10.1007/978-3-642-11741-1_9. Cited on pages 18 and 322.

Kendra Cook, Chen-Joe Fong, Michael J Wenkel, Peter Wilczynski, Nick Yen, and G. S. Chang. **FORMOSAT-7/COSMIC-2 GNSS radio occultation constellation mission for global weather monitoring**. In *2013 IEEE Aerospace Conference*, pages 1–8, Big Sky, Montana, US, mar 2013. IEEE. DOI 10.1109/AERO.2013.6497317. Cited on pages 21, 113, 264, and 318.

C. Corbari, M. Mancini, Z. Su, and J. Li. **Evapotranspiration estimate from water balance closure using satellite data for the Upper Yangtze River basin**. *Hydrology Research*, 45(4-5):603, aug 2014. DOI 10.2166/nh.2013.016. Cited on page 29.

J. W. Cornelisse, H. F. R. Schoyer, and K. F. Wakker. **Rocket Propulsion and Spaceflight Dynamics**. Pitman Publishing Limited, 1979. ISBN 0273011413, 9780273011415. Cited on page 71.

C. M. Cox, B. F. Chao, and A. Au. **Inter-annual and annual variations in the geopotential observed using SLR**. In *14th International workshop on Laser Ranging*, 2004. `http://cddis.gsfc.nasa.gov/lw14/docs/papers/sci2b{_}ccm.pdf`. Cited on page 19.

Christoph Dahle, Frank Flechtner, Christian Gruber, Daniel König, Rolf König, and Grzegorz Michalak. **GFZ GRACE Level-2 Processing Standards Document for Level-2 Product Release 0005**. Technical report, Deutsches GeoForschungsZentrum, 2013. `ftp://podaac.jpl.nasa.gov/allData/grace/docs/ReleaseNotes{_}gfz{_}RL05.pdf`. Cited on pages 28 and 39.

Christoph Dahle, Frank Flechtner, Christian Gruber, Daniel König, Rolf König, Grzegorz Michalak, and Karl-hans Neumayer. **GFZ RL05: An Improved Time-Series of Monthly GRACE Gravity Field Solutions**. In Frank Flechtner, Nico Sneeuw, and Wolf-Dieter Schuh, editors, *Observation of the System Earth from Space - CHAMP, GRACE, GOCE and future missions*, Advanced Technologies in Earth Sciences, pages 29–39. Springer Berlin Heidelberg, Berlin, Heidelberg, 2014. DOI 10.1007/978-3-642-32135-1_4. Cited on page 6.

Mu Dapeng, Sun Zhongchang, and Guo Jinyun. **Estimating continental water storage variations in Central Asia area using GRACE data**. *IOP Conference Series: Earth and Environmental Science*, 17:012131, mar 2014. DOI 10.1088/1755-1315/17/1/012131. Cited on page 29.

Peter B. de Selding. **Iridium Next Deployment Delayed, Adding to SpaceX's 2017 Backlog**. *SpaceNews*, 2015. `http://spacenews.com/iridium-next-deployment-delayed-adding-to-spacexs-2017-backlog/`. Cited on page 113.

Marina Dehne, Felipe Guzmán Cervantes, Benjamin Sheard, Gerhard Heinzel, and Karsten Danzmann. **Laser interferometer for spaceborne mapping of the Earth's gravity field**. *Journal of Physics: Conference Series*, 154:

012023, mar 2009. DOI 10.1088/1742-6596/154/1/012023. Cited on pages 8 and 46.

P Ditmar. **Error budget of range combinations**. internal article, Delft, 2009a. Cited on page 295.

P. Ditmar. **Satellite Gravity and the Geosphere**. Faculty of Aerospace Engineering, T.U. Delft, AE4-E11 lecture notes, Delft, the Netherlands, 2009b. Cited on page 76.

P. Ditmar and R. Klees. **A Method to Compute the Earth's Gravity Field from SGG/SST Data to be Acquired by the GOCE Satellite**. Delft University Press, 2002. ISBN 9040722846 9789040722844. Cited on page 148.

P. Ditmar and a. a. Van Eck Van Der Sluijs. **A technique for modeling the Earth's gravity field on the basis of satellite accelerations**. *Journal of Geodesy*, 78(1-2):12–33, jun 2004. DOI 10.1007/s00190-003-0362-1. Cited on pages 39, 41, 78, 85, 165, and 296.

P. Ditmar, R. Klees, and X. Liu. **Frequency-dependent data weighting in global gravity field modeling from satellite data contaminated by non-stationary noise**. *Journal of Geodesy*, 81(1):81–96, jul 2007. DOI 10.1007/s00190-006-0074-4. Cited on pages 20, 44, 48, 79, 97, and 116.

P. Ditmar, A. Bezdek, X. Liu, and Q. Zhao. **On a Feasibility of Modeling Temporal Gravity Field Variations from Orbits of Non-dedicated Satellites**. In M.G. Sideris, editor, *Observing our Changing Earth*, volume 133 of *International Association of Geodesy Symposia*, pages 307–313. Springer Berlin Heidelberg, Berlin, Heidelberg, 2008. DOI 10.1007/978-3-540-85426-5_36. Cited on pages 20 and 48.

Pavel Ditmar, João Encarnação, and Hassan Hashemi Farahani. **Understanding data noise in gravity field recovery on the basis of inter-satellite ranging measurements acquired by the satellite gravimetry mission GRACE**. *Journal of Geodesy*, 86(6):441–465, nov 2012. DOI 10.1007/s00190-011-0531-6. Cited on pages 7, 14, 37, 41, 42, 43, 95, 102, 105, 144, 162, 165, 174, 175, 178, 192, 194, 196, 211, 261, and 301.

Pavel Ditmar, Hassan Hashemi Farahani, Pedro Inacio, Roland Klees, Qile Zhao, Jing Guo, Xianglin Liu, Yu Sun, Ricardo Riva, and Jiangjun Ran. **Delft Mass Transport model DMT-2**. In *EGU General Assembly*, 2013. http://adsabs.harvard.edu/abs/2013EGUGA..1510559D. Cited on pages 28, 42, 89, 211, and 317.

M Dorrer, B Laborde, and P Deschamps. **DORIS (Doppler orbitography and radiopositioning integrated from space): System assessment results with DORIS on SPOT 2**. *Acta Astronautica*, 25(8-9):497–504, aug 1991. DOI 10.1016/0094-5765(91)90032-Z. Cited on pages 19 and 317.

V. B. Dubovskoi, V. I. Leont'ev, a. V. Sbitnev, and V. G. Pshenyanik. **Technology of the construction of microaccelerometers for automatic spacecraft and the sphere of their application**. *Seismic Instruments*, 48(1):85–91, feb 2012. DOI 10.3103/S0747923912010045. Cited on pages 47 and 264.

Dave Ector, Lidia Cucurull, and Pete Wilczynski. **Plans for a 12 Satellite GNSS RO Constellation (COSMIC-2/FORMOSAT-7)**. In *International Workshop on Occultations for Probing Atmosphere and Climate*, Graz, Austria, 2010. http://www.uni-graz.at/opac2010/pdf{_}presentation/opac{_}2010{_}ector{_}dave{_}presentation08.pdf. Cited on pages 21, 113, 264, and 318.

P. G. Edwards and D. Pawlak. **Metop : The Space Segment for Eumetsat's Polar System**. Technical Report may, ESA Bulletin, No 102, 2000. http://www.esa.int/esapub/bulletin/bullet102/Edwards102.pdf. Cited on pages 21 and 321.

Gary D. Egbert and Svetlana Y. Erofeeva. **Efficient Inverse Modeling of Barotropic Ocean Tides**. *Journal of Atmospheric and Oceanic Technology*, 19(2): 183–204, feb 2002. DOI 10.1175/1520-0426(2002)019<0183:EIMOBO>2.0.CO;2. Cited on page 323.

Gary D. Egbert, Andrew F. Bennett, and Michael G. G. Foreman. **TOPEX/POSEIDON tides estimated using a global inverse model**. *Journal of Geophysical Research*, 99(C12): 24821, 1994. DOI 10.1029/94JC01894. Cited on page 323.

Basem Elsaka. **Sub-monthly gravity field recovery from simulated multi-GRACE mission type**. *Acta Geophysica*, 62(1):241–258, nov 2013. DOI 10.2478/s11600-013-0170-9. Cited on pages 11, 16, and 271.

Basem Elsaka, Juergen Kusche, and Karl-Heinz Ilk. **Recovery of the Earth's gravity field from formation-flying satellites: Temporal aliasing issues**. *Advances in Space Research*, 50(11):1534–1552, dec 2012. DOI 10.1016/j.asr.2012.07.016. Cited on pages 10 and 11.

Basem Elsaka, Jean-Claude Raimondo, Phillip Brieden, Tilo Reubelt, Jürgen Kusche, Frank Flechtner, Siavash Iran Pour, Nico Sneeuw, and Jürgen Müller. **Comparing seven candidate mission configurations for temporal gravity field retrieval through full-scale numerical simulation**. *Journal of Geodesy*, 88 (1):31–43, nov 2013. DOI 10.1007/s00190-013-0665-9. Cited on pages 11 and 57.

João Encarnação, Pavel Ditmar, and Xianglin Liu. **Analysis of Satellite Formations in the Context of Gravity Field Retrieval**. In *3rd International Symposium on Formation Flying, Missions and Technologies (SP-654)*, volume ESA SP-654, ESA Communication Production Office, 2008. ESA Communication Production Office. http://www.congrex.nl/08c01/abstracts/CXNL{_}08C01{_}187286.htm. Cited on pages 11, 16, 57, and 112.

O. Engels, E. Forootan, and J. Kusche. **Analysis of atmospheric data products for the reduction of satellite gravity measurements**. In *EGU General Assembly*, 2012. http://adsabs.harvard.edu/abs/2012EGUGA..14.2375E. Cited on page 17.

H. Hashemi Farahani, P. Ditmar, and R. Klees. **Assessment of the added value of data from the GOCE satellite mission to time-varying gravity field modelling**. *Journal of Geodesy*, nov 2013a. DOI 10.1007/s00190-013-0674-8. Cited on page 211.

H. Hashemi Farahani, P. Ditmar, R. Klees, X. Liu, Q. Zhao, and J. Guo. **The static gravity field model DGM-1S from GRACE and GOCE data: computation, validation and an analysis of GOCE mission's added value**. *Journal of Geodesy*, 150, jul 2013b. DOI 10.1007/s00190-013-0650-3. Cited on pages 27, 42, 44, and 317.

H.H. Farahani. **Modelling the Earth's static and time-varying gravity field using a combination of GRACE and GOCE data**. dissertation, Delft University of Technology, 2013. Cited on page 144.

Frank Flechtner. **Gravity Recovery and Climate Experiment AOD1B Product Description Document for product releases 01 to 04**. Technical report GR-GFZ-AOD-0001, GeoForschungszentrum Potsdam, 2007. ftp://podaac.jpl.nasa.gov/pub/grace/doc/AOD1B{_}20070413.pdf. Cited on pages 17, 88, 114, and 316.

Frank Flechtner. **GRACE AOD1B RL04 Quality Assurance**, 2011. http://op.gfz-potsdam.de/grace/results/grav/g007{_}aod1b{_}rl04.html. Cited on pages 17, 88, 114, and 316.

Frank Flechtner, Roland Schmidt, and Ulrich Meyer. **De-aliasing of Short-term Atmospheric and Oceanic Mass Variations for GRACE**. In J. Flury, R. Rummel, C. Reigber, M. Rothacher, G. Boedecker, and U. Schreiber, editors, *Observation of the Earth System from Space*, pages 83–97. Springer

Berlin Heidelberg, 2006. DOI 10.1007/3-540-29522-4_7. Cited on pages 17, 88, 114, and 316.

Rune Floberghagen, Michael Fehringer, Daniel Lamarre, Danilo Muzi, Björn Frommknecht, Christoph Steiger, Juan Piñeiro, and Andrea Costa. **Mission design, operation and exploitation of the gravity field and steady-state ocean circulation explorer mission**. *Journal of Geodesy*, 85(11):749–758, oct 2011. DOI 10.1007/s00190-011-0498-3. Cited on page 319.

Jakob Flury, Srinivas Bettadpur, and Byron D. Tapley. **Precise accelerometry onboard the GRACE gravity field satellite mission**. *Advances in Space Research*, 42(8):1414–1423, oct 2008. DOI 10.1016/j.asr.2008.05.004. Cited on pages 23, 98, 99, and 145.

L Földváry. **Mass-Change Acceleration in Antarctica from GRACE Monthly Gravity Field Solutions**. *Geodesy for Planet Earth*, 2012. DOI 10.1007/978-3-642-20338-1. Cited on page 30.

Lóránt Földváry, Dražen Švehla, Christian Gerlach, Martin Wermuth, Thomas Gruber, Reiner Rummel, Markus Rothacher, Björn Frommknecht, Thomas Peters, and Peter Steigenberger. **Gravity Model TUM-2Sp Based on the Energy Balance Approach and Kinematic CHAMP Orbits**. In *Earth Observation with CHAMP*, pages 13–18. Springer-Verlag, Berlin/Heidelberg, 2004. DOI 10.1007/3-540-26800-6_2. Cited on page 40.

Ehsan Forootan, Jürgen Kusche, Ina Loth, Wolf-Dieter Schuh, Annette Eicker, Joseph Awange, Laurent Longuevergne, Bernd Diekkrüger, Michael Schmidt, and C. K. Shum. **Multivariate Prediction of Total Water Storage Changes Over West Africa from Multi-Satellite Data**. *Surveys in Geophysics*, 35(4):913–940, may 2014. DOI 10.1007/s10712-014-9292-0. Cited on page 29.

C. Förste, F. Flechtner, R. Schmidt, U. Meyer, R. Stubenvoll, C. Förste, F. Barthelmes, R. König, K.H. Neumayer, M. Rothacher, C. Reigber, R. Biancale, S. Bruinsma, J.-M. Lemoine, and J.C. Raimondo. **A New High Resolution Global Gravity Field Model Derived From Combination of GRACE and CHAMP Mission and Altimetry/Gravimetry Surface Gravity Data**. In *European Geosciences Union*, Vienna, Austria, apr 2005. http://op.gfz-potsdam.de/grace/results/grav/g004{_}EGU05-A-04561.pdf. Cited on pages 27, 88, 118, and 318.

C. Förste, F. Flechtner, R. Schmidt, R. Stubenvoll, M. Rothacher, J. Kusche, K.H. Neumayer, R. Biancale, J.M. Lemoine, F. Barthelmes, S. Bruinsma, R. König, and U. Meyer. **EIGEN-GL05C - A new global combined high-resolution GRACE-based gravity field model of the GFZ-GRGS cooperation**. In *EGU General Assembly*, volume 10 of *EGU2008-A-03426*, 2008a. Cited on pages 27, 88, and 318.

Christoph Förste, Roland Schmidt, Richard Stubenvoll, Frank Flechtner, Ulrich Meyer, Rolf König, Hans Neumayer, Richard Biancale, Jean-Michel Lemoine, Sean Bruinsma, Sylvain Loyer, Franz Barthelmes, and Saskia Esselborn. **The GeoForschungsZentrum Potsdam/Groupe de Recherche de Gèodésie Spatiale satellite-only and combined gravity field models: EIGEN-GL04S1 and EIGEN-GL04C**. *Journal of Geodesy*, 82(6):331–346, oct 2008b. DOI 10.1007/s00190-007-0183-8. Cited on pages 27, 88, and 318.

Christoph Förste, Sean L. Bruinsma, Frank Flechtner, Jean-Charles Marty, Jean-Michel Lemoine, Christoph Dahle, Oleh Abrikosov, K.H. Neumayer, Richard Biancale, Franz Barthelmes, and Georges Balmino. **A preliminary update of the Direct Approach GOCE Processing and a new release of EIGEN-6C**. In *AGU Fall Meeting Abstracts*, San Francisco, CA, USA, dec 2012. http://icgem.gfz-potsdam.de/ICGEM/documents/Foerste-et-al-AGU{_}2012.pdf. Cited on pages 27 and 318.

Christoph Förste, Sean Bruinsma, Oleg Abrikosov, Frank Flechtner, Jean-Charles Marty, Jean-Michel Lemoine, Christoph Dahle, Hans Neumayer, Franz Barthelmes, Rolf König, Richard Biancale, Christoph Förste, Sean Bruinsma, Oleg Abrikosov, Frank Flechtner, and Jean-charles Marty. **EIGEN-6C4 - The latest combined global gravity field model including GOCE data up to degree and order 1949 of GFZ Potsdam and GRGS Toulouse**. In *EGU General Assembly*, volume 16, page 3707, 2014. `http://adsabs.harvard.edu/abs/2014EGUGA..16.3707F`. Cited on pages 27 and 318.

Jeff Foust. **The ups and downs of smallsat constellations**, 2015. `http://www.thespacereview.com/article/2776/1`. Cited on pages 113 and 264.

E. Friis-Christensen, H. Lühr, and G. Hulot. **Swarm: A constellation to study the Earth's magnetic field**. *Earth, Planets and Space*, 58(4):351–358, apr 2006. DOI 10.1186/BF03351933. Cited on page 46.

B. Frommknecht, H. Oberndorfer, Frank Flechtner, and Roland Schmidt. **Integrated sensor analysis for GRACE – development and validation**. *Advances in Geosciences*, 1:57–63, 2003. `http://hal.archives-ouvertes.fr/hal-00296763`. Cited on pages 98 and 169.

Bjorn Frommknecht. **Integrated Sensor Analysis of the GRACE Mission**. Dissertation, Technischen Universität München, 2007. Cited on page 132.

Björn Frommknecht, Ulrich Fackler, and Jakob Flury. **Integrated Sensor Analysis GRACE**. In J. Flury, R. Rummel, C. Reigber, M. Rothacher, G. Boedecker, and U. Schreiber, editors, *Observation of the Earth System from Space*, pages 99–113. Springer-Verlag, Berlin/Heidelberg, 2006. DOI 10.1007/3-540-29522-4_8. Cited on pages 23, 24, 98, 99, 132, 145, 146, 154, and 284.

Troy D. Fuchser and Phillip W. Ward. **Request for clarification in the paper: stability analysis of GPS carrier tracking loops by phase margin approach**. *GPS Solutions*, 17 (3):433–438, feb 2013. DOI 10.1007/s10291-012-0308-2. Cited on page 30.

A. S. Ganeshan, S. C. Rathnakara, R. Gupta, and Anup K. Jain. **Indian regional navigation satellite system (IRNSS) concept**. *Journal of Spacecraft Technology*, 15(2):19–23, 2005. ISSN 09711600. Cited on page 141.

D Garcia, G Ramillien, A Lombard, and A Cazenave. **Steric Sea-level Variations Inferred from Combined Topex/Poseidon Altimetry and GRACE Gravimetry**. *Pure and Applied Geophysics*, 164:721–731, 2007. DOI 10.1007/s00024-007-0182-y. Cited on page 30.

Ch. Gerlach. **A CHAMP-only gravity field model from kinematic orbits using the energy integral**. *Geophysical Research Letters*, 30(20):2037, 2003. DOI 10.1029/2003GL018025. Cited on page 39.

Ch. Gerlach, J. Flury, B. Frommknecht, F. Flechtner, and R. Rummel. **GRACE performance study and sensor analysis**. In *Joint CHAMP/GRACE Science Meeting*, 2004. `http://adsabs.harvard.edu/abs/2004cgsm.confE...6G`. Cited on pages 98 and 138.

Christian Gerlach, Nico Sneeuw, Pieter Visser, and Dražen Švehla. **CHAMP Gravity Field Recovery with the Energy Balance Approach: First Results**. In *First CHAMP Mission Results for Gravity, Magnetic and Atmospheric Studies*, volume 1, pages 134–139. Springer Berlin Heidelberg, Berlin, Heidelberg, 2003. DOI 10.1007/978-3-540-38366-6_20. Cited on page 39.

E. Gill, P. Sundaramoorthy, J. Bouwmeester, B. Zandbergen, and R. Reinhard. **Formation flying within a constellation of nanosatellites: The QB50 mission**. *Acta Astronautica*, 82(1):110–117, jan 2013. DOI

10.1016/j.actaastro.2012.04.029. Cited on page 47.

H. Goiginger, E. Höck, D. Rieser, T. Mayer-Gürr, A. Maier, S. Krauss, R. Pail, T. Fecher, T. Gruber, J.M. Brockmann, I. Krasbutter, W.-D. Schuh, A. Jäggi, L. Prange, W. Hausleitner, O. Baur, and J. Kusche. **The combined satellite-only global gravity field model GOCO02S**. In *EGU General Assembly*, volume 13, 2011. Cited on pages 27, 88, 151, and 319.

M. Götzelmann, W. Keller, and T. Reubelt. **Gross Error Compensation for Gravity Field Analysis Based on Kinematic Orbit Data**. *Journal of Geodesy*, 80(4):184–198, jun 2006. DOI 10.1007/s00190-006-0061-9. Cited on page 32.

a. Groh, H. Ewert, M. Scheinert, M. Fritsche, a. Rülke, a. Richter, R. Rosenau, and R. Dietrich. **An investigation of Glacial Isostatic Adjustment over the Amundsen Sea sector, West Antarctica**. *Global and Planetary Change*, 98-99:45–53, dec 2012. DOI 10.1016/j.gloplacha.2012.08.001. Cited on page 30.

A. Groh, H. Ewert, M. Fritsche, A. Rülke, R. Rosenau, M. Scheinert, and R. Dietrich. **Assessing the Current Evolution of the Greenland Ice Sheet by Means of Satellite and Ground-Based Observations**. *Surveys in Geophysics*, 35(6):1459–1480, nov 2014. DOI 10.1007/s10712-014-9287-x. Cited on page 30.

Th. Gruber, R. Rummel, O. Abrikosov, and R. van Hees. **GOCE High Level Processing Facility GOCE Level 2 Product Data Handbook**. Technical Report GO-MA-HPF-GS-0110, Issue 5, European Space Agency, 2014. https://earth.esa.int/documents/10174/1650485/GOCE{_}Product{_}Data{_}Handbook{_}Level-2. Cited on page 323.

Brian Gunter, John C. Ries, Srinivas Bettadpur, and Byron Tapley. **A simulation study of the errors of omission and commission for GRACE RL01 gravity fields**. *Journal of Geodesy*, 80(7):341–351, aug 2006. DOI 10.1007/s00190-006-0083-3. Cited on page 95.

Brian Gunter, T. Urban, R. Riva, M. Helsen, R. Harpold, S. Poole, P. Nagel, B. Schutz, and B. Tapley. **A comparison of coincident GRACE and ICESat data over Antarctica**. *Journal of Geodesy*, 83(11):1051–1060, jun 2009a. DOI 10.1007/s00190-009-0323-4. Cited on page 30.

Brian C Gunter, João Encarnação, Pavel Ditmar, and Roland Klees. **The use of satellite constellations and formations for future gravity field missions**. In *Advances in the Astronautical Sciences*, pages 1357–1368, Savannah, feb 2009b. http://www.univelt.com/book=1451. Cited on page 14.

Brian C Gunter, Pavel Ditmar, and João Encarnação. **The determination of time variable gravity from a constellation of non-dedicated satellites**. In *Advances in the Astronautical Sciences*, pages 1999–2007, Pittsburgh, aug 2010. http://www.univelt.com/book=1349. Cited on page 95.

J. Y. Guo, X. J. Duan, and C. K. Shum. **Non-isotropic Gaussian smoothing and leakage reduction for determining mass changes over land and ocean using GRACE data**. *Geophysical Journal International*, 181(1):290–302, apr 2010. DOI 10.1111/j.1365-246X.2010.04534.x. Cited on page 9.

Jinyun Guo, Dapeng Mu, Xin Liu, Haoming Yan, and Honglei Dai. **Equivalent water height extracted from GRACE gravity field model with robust independent component analysis**. *Acta Geophysica*, 62(4):953–972, may 2014. DOI 10.2478/s11600-014-0210-0. Cited on page 9.

Om P. Gupta. **Iridium NEXT partnership for Earth Observation: Exploiting Global Satellite Constellations for new Remote Sensing**

capabilities. In Philip E. Ardanuy and Jeffery J. Puschell, editors, *SPIE*. Royal Society London, Iridium Communications Inc., 2008. DOI 10.1117/12.800768. Cited on pages 21, 113, and 264.

S.-C. Han. **Crustal Dilatation Observed by GRACE After the 2004 Sumatra-Andaman Earthquake**. *Science*, 313(5787):658–662, aug 2006. DOI 10.1126/science.1128661. Cited on pages 4 and 30.

SC Han, C Jekeli, and C. K. Shum. **Static and temporal gravity field recovery using grace potential difference observables**. *Advances in Geosciences*, 1:19–26, jun 2003. DOI 10.5194/adgeo-1-19-2003. Cited on page 39.

Shin-Chan Han. **Time-variable aliasing effects of ocean tides, atmosphere, and continental water mass on monthly mean GRACE gravity field**. *Journal of Geophysical Research*, 109(B4):B04403, 2004a. DOI 10.1029/2003JB002501. Cited on pages 17, 156, and 269.

Shin-Chan Han. **Efficient Determination of Global Gravity Field from Satellite-to-satellite Tracking Mission**. *Celestial Mechanics and Dynamical Astronomy*, 88(1):69–102, jan 2004b. DOI 10.1023/B:CELE.0000009383.07092.1f. Cited on page 7.

Shin Chan Han, Jeanne Sauber, and Scott Luthcke. **Regional gravity decrease after the 2010 Maule (Chile) earthquake indicates large-scale mass redistribution**. *Geophysical Research Letters*, 37(23):1–5, 2010. DOI 10.1029/2010GL045449. Cited on page 30.

Christopher Harig and Frederik J Simons. **Mapping Greenland's mass loss in space and time**. *Proceedings of the National Academy of Sciences*, 109(49):19934–19937, dec 2012. DOI 10.1073/pnas.1206785109. Cited on page 30.

Ayman A. Hassan and Shuanggen Jin. **Water Cycle and Climate Signals in Africa Observed by Satellite Gravimetry**. *IOP Conference Series: Earth and Environmental Science*, 17:012149, mar 2014. DOI 10.1088/1755-1315/17/1/012149. Cited on page 29.

Kosuke Heki and Koji Matsuo. **Coseismic gravity changes of the 2010 earthquake in central Chile from satellite gravimetry**. *Geophysical Research Letters*, 37(24):1–4, 2010. DOI 10.1029/2010GL045335. Cited on page 30.

Tom Van Helleputte, Eelco Doornbos, and Pieter Visser. **CHAMP and GRACE accelerometer calibration by GPS-based orbit determination**. *Advances in Space Research*, 43(12):1890–1896, jun 2009. DOI 10.1016/j.asr.2009.02.017. Cited on page 23.

Chris M Henry, Diana M Allen, and Jianliang Huang. **Groundwater storage variability and annual recharge using well-hydrograph and GRACE satellite data**. *Hydrogeology Journal*, 19(4):741–755, 2011. DOI 10.1007/s10040-011-0724-3. Cited on page 29.

Magnus R. MR Hestenes and Eduard Stiefel. **Methods of Conjugate Gradients for Solving Linear Systems**. *Journal of Research of the National Bureau of Standards*, 49(6):409–436, 1952. http://nvlpubs.nist.gov/nistpubs/jres/049/jresv49n6p409{_}A1b.pdf. Cited on pages 148, 221, and 322.

G. W. Hill. **Researches in the Lunar Theory**. *American Journal of Mathematics*, 1(1):5, 1878. DOI 10.2307/2369430. Cited on page 66.

N Hinkley, J A Sherman, N B Phillips, M Schioppo, N D Lemke, K Beloy, M Pizzocaro, C W Oates, and A D Ludlow. **An Atomic Clock with 10-18 Instability**. *Science*, 341(6151):1215–1218, sep 2013. DOI 10.1126/science.1240420. Cited on page 48.

Naoki Hirose, Ichiro Fukumori, Victor Zlotnicki, and Rui M Ponte. **Modeling the high-frequency barotropic response of the ocean to atmospheric disturbances: Sensitivity to forcing, topography, and friction**, 2001. Cited on page 322.

Bernhard Hofmann-Wellenhof and Helmut Moritz. **Physical Geodesy**. Springer Vienna, 2006. DOI 10.1007/978-3-211-33545-1. Cited on page 86.

Martin Horwath and Reinhard Dietrich. **Signal and error in mass change inferences from GRACE: the case of Antarctica**. *Geophysical Journal International*, 177(3): 849–864, jun 2009. DOI 10.1111/j.1365-246X.2009.04139.x. Cited on page 30.

Martin Horwath, Jean-Michel Lemoine, Richard Biancale, and Stéphane Bourgogne. **Improved GRACE science results after adjustment of geometric biases in the Level-1B K-band ranging data**. *Journal of Geodesy*, 85(1):23–38, oct 2010. DOI 10.1007/s00190-010-0414-2. Cited on pages 7, 8, 98, and 166.

Rasmus Houborg, Matthew Rodell, Bailing Li, Rolf Reichle, and Benjamin F. Zaitchik. **Drought indicators based on model-assimilated Gravity Recovery and Climate Experiment (GRACE) terrestrial water storage observations**. *Water Resources Research*, 48(7):W07525, jul 2012. DOI 10.1029/2011WR011291. Cited on page 29.

Jeremy Hsu. **SpaceX Raises $ 1 Billion from Google and Fidelity for Satellite Internet Project**. *IEEE Spectrum*, 2015. http://spectrum.ieee.org/tech-talk/aerospace/satellites/spacex-raises-1-billion-from-google-fidelity-for-satellite-internet-project. Cited on pages 113 and 264.

J. Huang, J. Halpenny, W. van der Wal, C. Klatt, T. S. James, A. Rivera, and W Van Der Wal. **Detectability of groundwater storage change within the Great Lakes Water Basin using GRACE**. *Journal of Geophysical Research*, 117(8):1–26, aug 2012. DOI 10.1029/2011JB008876. Cited on page 29.

Cheinway Hwang, Ting-Jung Lin, Tzu-Pang Tseng, and Benjamin Fong Chao. **Modeling Orbit Dynamics of FORMOSAT-3/COSMIC Satellites for Recovery of Temporal Gravity Variations**. *IEEE Transactions on Geoscience and Remote Sensing*, 46(11):3412–3423, nov 2008a. DOI 10.1109/TGRS.2008.2004789. Cited on page 20.

Cheinway Hwang, Tzu-Pang Tseng, Tingjung Lin, Dražen Švehla, and Bill Schreiner. **Precise orbit determination for the FORMOSAT-3/COSMIC satellite mission using GPS**. *Journal of Geodesy*, 83(5): 477–489, aug 2008b. DOI 10.1007/s00190-008-0256-3. Cited on pages 35 and 36.

Cheinway Hwang, Tzu-Pang Tseng, Ting-Jung Lin, Dražen Švehla, Urs Hugentobler, and Benjamin Fong Chao. **Quality assessment of FORMOSAT-3/COSMIC and GRACE GPS observables: analysis of multipath, ionospheric delay and phase residual in orbit determination**. *GPS Solutions*, 14(1):121–131, nov 2009. DOI 10.1007/s10291-009-0145-0. Cited on pages 32, 34, 35, and 36.

K H Ilk. **A Validation Procedure for Satellite Orbits and Force Function Models Based on a New Balance Equation Approach**. In Paul Tregoning and Chris Rizos, editors, *Dynamic Planet*, pages 280–287. Springer Berlin Heidelberg, 2007. DOI 10.1007/978-3-540-49350-1_42. Cited on page 40.

K.H. Ilk and A. Löcher. **The Use of Energy Balance Relations for Validation of Gravity Field Models and Orbit Determination Results**. In Fernando Sansò, editor, *A Window on the Future of Geodesy*, pages 494–499. Springer-Verlag, Berlin/Heidelberg, 2005. DOI 10.1007/3-540-27432-4_84. Cited on page 39.

K.H. Ilk, J. Flury, R. Rummel, P. Schwintzer, W. Bosch, C. Haas, J. Schröter, D. Stammer, W. Zahel, H. Miller, R. Dietrich, P. Huybrechts, H. Schmeling, D. Wolf, H.J. Götze, J. Riegger, A. Bardossy, A. Güntner, and Th. Gruber. **Mass transport and mass distribution in the Earth system**. GeoForschungsZentrum Potsdam, Potsdam, 2nd edition, 2005. http://earth.esa.int/

workshops/goce04/participants/64/
paper{_}flury{_}mass{_}transport.pdf.
Cited on page 3.

KH Ilk, A Löcher, and T Mayer-Gürr. **Do We Need New Gravity Field Recovery Techniques for the New Gravity Field Satellites?** In *VI Hotine-Marussi Symposium on Theoretical and Computational Geodesy*, pages 3–9. Springer Berlin Heidelberg, Berlin, Heidelberg, 2008. DOI 10.1007/978-3-540-74584-6_1. Cited on page 42.

Noriyasu Inaba, Akihiro Matsumoto, Hidemi Hase, Satoshi Kogure, Mikio Sawabe, and Koji Terada. **Design concept of Quasi Zenith Satellite System**. *Acta Astronautica*, 65(7-8):1068–1075, oct 2009. DOI 10.1016/j.actaastro.2009.03.068. Cited on page 141.

Pedro Inácio, Pavel Ditmar, Hassan H Farahani, and Roland Klees. **Analysis of star-camera noise in GRACE data and its impact on monthly gravity field models**. *Journal of Geodesy*, 16, 2014. DOI 10.1007/s00190-015-0797-1. Cited on pages 8 and 265.

Erik R. Ivins, Thomas S. James, John Wahr, Ernst J. O. Schrama, Felix W. Landerer, and Karen M. Simon. **Antarctic contribution to sea level rise observed by GRACE with improved GIA correction**. *Journal of Geophysical Research: Solid Earth*, 118(6):3126–3141, jun 2013. DOI 10.1002/jgrb.50208. Cited on page 30.

Thomas Jacob, John Wahr, W Tad Pfeffer, and Sean Swenson. **Recent contributions of glaciers and ice caps to sea level rise.** *Nature*, 482(7386):514–8, mar 2012. DOI 10.1038/nature10847. Cited on page 30.

A. Jäggi, U. Hugentobler, H. Bock, and G. Beutler. **Precise orbit determination for GRACE using undifferenced or doubly differenced GPS data**. *Advances in Space Research*, 39(10):1612–1619, jan 2007. DOI 10.1016/j.asr.2007.03.012. Cited on pages 34, 35, 36, 37, 38, and 136.

A Jäggi, G Beutler, L Prange, R Dach, and L Mervart. **Assessment of GPS-only Observables for Gravity Field Recovery from GRACE**. In Michael G. Sideris, editor, *Observing our Changing Earth*, volume 133, pages 113–123. Springer Berlin Heidelberg, Berlin, Heidelberg, 2009. DOI 10.1007/978-3-540-85426-5_14. Cited on page 130.

A. Jäggi, U. Meyer, G. Beutler, L. Prange, R. Dach, and L. Mervart. **AIUB-GRACE03S: A static gravity field model computed with simultaneously solved-for time variations from 6 years of GRACE data using the Celestial Mechanics Approach**. *Paper in preparation*, 2011a. http://icgem.gfz-potsdam.de/ICGEM/shms/aiub-grace03s.gfc. Cited on page 27.

a. Jäggi, L. Prange, and U. Hugentobler. **Impact of covariance information of kinematic positions on orbit reconstruction and gravity field recovery**. *Advances in Space Research*, 47(9):1472–1479, may 2011b. DOI 10.1016/j.asr.2010.12.009. Cited on page 42.

A Jäggi, G Beutler, U Meyer, and L Prange. **AIUB-GRACE02S: status of GRACE gravity field recovery using the celestial mechanics approach**. In Steve Kenyon, Maria Christina Pacino, and Urs Marti, editors, *Geodesy for Planet Earth*, volume 136 of *International Association of Geodesy Symposia*, pages 161–169. Springer Berlin Heidelberg, Berlin, Heidelberg, 2012. DOI 10.1007/978-3-642-20338-1_20. Cited on pages 39 and 315.

Christopher Jekeli. **The determination of gravitational potential differences from satellite-to-satellite tracking**. *Celestial Mechanics and Dynamical Astronomy*, 75(2):85–101, 1999. DOI 10.1023/A:1008313405488. Cited on page 39.

Gholamreza Joodaki, John Wahr, and Sean Swenson. **Estimating the human contribution to groundwater depletion in the Middle East, from GRACE data, land surface models, and well observations**. *Water Resources*

Research, 50(3):2679–2692, mar 2014. DOI 10.1002/2013WR014633. Cited on page 29.

Zhigui Kang, Byron Tapley, Jianli Chen, John Ries, and Srinivas Bettadpur. **Geocenter variations derived from GPS tracking of the GRACE satellites**. *Journal of Geodesy*, 83 (10):895–901, 2009. DOI 10.1007/s00190-009-0307-4. Cited on page 30.

Jeongrae Kim. **Simulation study of a low-low satellite-to-satellite tracking mission**. Dissertation, The University of Texas at Austin, 2000. Cited on pages 7, 132, 145, 164, 165, 169, 170, and 173.

Jeongrae Kim and Seung Woo Lee. **Flight performance analysis of GRACE K-band ranging instrument with simulation data**. *Acta Astronautica*, 65(11-12):1571–1581, dec 2009. DOI 10.1016/j.actaastro.2009.04.010. Cited on pages 24, 132, 154, and 171.

Jeongrae Kim and Byron D. Tapley. **Error Analysis of a Low-Low Satellite-to-Satellite Tracking Mission**. *Journal of Guidance, Control, and Dynamics*, 25(6):1100–1106, nov 2002. DOI 10.2514/2.4989. Cited on pages 132 and 154.

R. Klees and P. Ditmar. **How to handle colored noise in large least-squares problems in the presence of data gaps?** In Fernando Sansò, editor, *V Hotine-Marussi Symposium on Mathematical Geodesy*, volume 127 of *International Association of Geodesy Symposia*, pages 39–48. Springer Berlin Heidelberg, Berlin, Heidelberg, 2004. DOI 10.1007/978-3-662-10735-5_6. Cited on pages 43 and 148.

R. Klees, P. Ditmar, and P. Broersen. **How to handle colored observation noise in large least-squares problems**. *Journal of Geodesy*, 76(11-12):629–640, mar 2003. DOI 10.1007/s00190-002-0291-4. Cited on pages 43, 148, and 221.

R Klees, E. A. Zapreeva, H. C. Winsemius, and H. H. G. Savenije. **Monthly mean water storage variations by the combination of GRACE and a regional hydrological model: application to the Zambezi River**. In *Dynamic Planet*, pages 488–495. Springer Berlin Heidelberg, Berlin, Heidelberg, 2007. DOI 10.1007/978-3-540-49350-1_71. Cited on page 29.

R. Klees, E. A. Revtova, B. C. Gunter, P. Ditmar, E. Oudman, H. C. Winsemius, and H. H. G. Savenije. **The design of an optimal filter for monthly GRACE gravity models**. *Geophysical Journal International*, 175 (2):417–432, nov 2008. DOI 10.1111/j.1365-246X.2008.03922.x. Cited on pages 9, 89, 211, and 249.

B. Klinger, O. Baur, and T. Mayer-Gürr. **GRAIL gravity field recovery based on the short-arc integral equation technique: simulation studies and first real data results**. *Planetary and Space Science*, 91:83–90, dec 2013. DOI 10.1016/j.pss.2013.12.001. Cited on page 40.

Alex S. Konopliv, Ryan S. Park, Dah-Ning Yuan, Sami W. Asmar, Michael M. Watkins, James G. Williams, Eugene Fahnestock, Gerhard Kruizinga, Meegyeong Paik, Dmitry Strekalov, Nate Harvey, David E. Smith, and Maria T. Zuber. **The JPL lunar gravity field to spherical harmonic degree 660 from the GRAIL Primary Mission**. *Journal of Geophysical Research: Planets*, 118(7):1415–1434, jul 2013. DOI 10.1002/jgre.20097. Cited on page 39.

R. Kroes. **Precise Relative Positioning of Formation Flying Spacecraft using GPS**. Dissertation, Delft University of Technology, 2006. `http://resolver.tudelft.nl/uuid:1a68ee94-3d55-44b9-9d8b-25fa44e96922`. Cited on page 37.

Remco Kroes, Oliver Montenbruck, William Bertiger, and Pieter N.A.M. Visser. **Precise GRACE baseline determination using GPS**. *GPS Solutions*, 9(1):21–31, feb 2005. DOI 10.1007/s10291-004-0123-5. Cited on pages 37 and 38.

Angelica Kruizinga. **CSR Release-05 GRACE Level-2 Data Products**, 2014. `http://www.csr.utexas.edu/grace/RL05.html`. Cited on pages 28 and 39.

U Ying-Hwa Kuo, C. Rocken, and Richard A. Anthes. **Constellation Observing System for Meteorology, Ionosphere and Climate (COSMIC): An Overview**. In *9th Symposium on Integrated Observing and Assimilation Systems For Atmosphere, Oceans, and Land Surface*, page 4, San Diego, CA, USA, 2005. `https://opensky.library.ucar.edu/collections/OSGC-000-000-001-230`. Cited on pages 21, 113, 264, and 318.

Y.H. Kuo, B. F. Chao, and L. C. Lee. **A constellation of microsatellites promises to help in a range of geoscience research**. *Eos, Transactions American Geophysical Union*, 80(40): 467, 1999. DOI 10.1029/EO080i040p00467-01. Cited on pages 21, 113, 264, and 318.

E. Kurtenbach, A. Eicker, T. Mayer-Gürr, M. Holschneider, M. Hayn, M. Fuhrmann, and J. Kusche. **Improved daily GRACE gravity field solutions using a Kalman smoother**. *Journal of Geodynamics*, 59-60:39–48, sep 2012. DOI 10.1016/j.jog.2012.02.006. Cited on pages 18 and 41.

Enrico Kurtenbach, Torsten Mayer-Gürr, and Annette Eicker. **Deriving daily snapshots of the Earth's gravity field from GRACE L1B data using Kalman filtering**. *Geophysical Research Letters*, 36(17):L17102, sep 2009. DOI 10.1029/2009GL039564. Cited on pages 18, 28, 40, 271, and 320.

Jürgen Kusche. **Approximate decorrelation and non-isotropic smoothing of time-variable GRACE-type gravity field models**. *Journal of Geodesy*, 81(11):733–749, feb 2007. DOI 10.1007/s00190-007-0143-3. Cited on page 9.

Philip Larkin. **ESTO :: News :: Laser System for GRACE Follow-On**, 2012. `http://esto.nasa.gov/news/news{_}gracefollowon.html`. Cited on pages 8, 45, 126, 219, 268, 271, and 318.

David H Lehman, Tom L Hoffman, and Glen G Havens. **The Gravity Recovery and Interior Laboratory mission**. In *2013 IEEE Aerospace Conference*, pages 1–11, Big Sky, Montana, US, mar 2013. IEEE. DOI 10.1109/AERO.2013.6496866. Cited on page 319.

F G Lemoine, S C Kenyon, J K Factor, R G Trimmer, N K Pavlis, D S Chinn, and C M Cox. **The Development of the Joint NASA GSFC and the NIMA Geopotential Model EGM96**. Technical Report NASA/TP—1998-206861, Goddard Space Flight Center, 1998. `http://bowie.gsfc.nasa.gov/697/staff/lemoine/EGM96{_}NASA-TP-1998-206861.pdf`. Cited on page 317.

F. G. Lemoine, S. B. Luthcke, D. D. Rowlands, D. S. Chinn, S. M. Klosko, and C. M. Cox. **The use of mascons to resolve time-variable gravity from GRACE**. In Paul Tregoning and Chris Rizos, editors, *Dynamic Planet*, pages 231–236. Springer Berlin Heidelberg, Berlin, Heidelberg, 2007a. DOI 10.1007/978-3-540-49350-1_35. Cited on pages 28 and 321.

Frank G. Lemoine, Sander Goossens, Terence J. Sabaka, Joseph B. Nicholas, Erwan Mazarico, David D. Rowlands, Bryant D. Loomis, Douglas S. Chinn, Douglas S. Caprette, Gregory a. Neumann, David E. Smith, and Maria T. Zuber. **High-degree gravity models from GRAIL primary mission data**. *Journal of Geophysical Research E: Planets*, 118(8): 1676–1698, 2013a. DOI 10.1002/jgre.20118. Cited on page 39.

Jean-Michel Lemoine, Sean Bruinsma, Sylvain Loyer, Richard Biancale, Jean-Charles Marty, Felix Perosanz, and Georges Balmino. **Temporal gravity field models inferred from GRACE data**. *Advances in Space Research*, 39(10):1620–1629, jan 2007b. DOI DOI:%2010.1016/j.asr.2007.03.062. Cited on pages 8, 28, 39, and 316.

Jean-Michel Lemoine, Sean Bruinsma, Pascal Gégout, Richard Biancale, Stéphane Bourgogne, and Jean-michel

Lemoine. **Release 3 of the GRACE gravity solutions from CNES/GRGS**. In *EGU General Assembly*, volume 15, 2013b. `http://adsabs.harvard.edu/abs/2013EGUGA..1511123L`. Cited on pages 8, 28, 39, and 316.

Onur Lenk. **Satellite based estimates of terrestrial water storage variations in Turkey**. *Journal of Geodynamics*, 67 (March 2003):106–110, jul 2013. DOI 10.1016/j.jog.2012.04.010. Cited on page 29.

Benjamin Lenoir, Bruno Christophe, and Serge Reynaud. **Experimental demonstration of bias rejection from electrostatic accelerometer measurements**. *Measurement*, 46(4):1411–1420, may 2013a. DOI 10.1016/j.measurement.2012.12.004. Cited on page 23.

Benjamin Lenoir, Bruno Christophe, and Serge Reynaud. **Unbiased acceleration measurements with an electrostatic accelerometer on a rotating platform**. *Advances in Space Research*, 51(1):188–197, jan 2013b. DOI 10.1016/j.asr.2012.08.012. Cited on page 23.

Bailing Li, Matthew Rodell, Benjamin F. Zaitchik, Rolf H. Reichle, Randal D. Koster, and Tonie M. van Dam. **Assimilation of GRACE terrestrial water storage into a land surface model: Evaluation and potential value for drought monitoring in western and central Europe**. *Journal of Hydrology*, 446-447:103–115, jun 2012. DOI 10.1016/j.jhydrol.2012.04.035. Cited on page 29.

Bofeng Li, Yunzhong Shen, and Xingfu Zhang. **Three frequency GNSS navigation prospect demonstrated with semi-simulated data**. *Advances in Space Research*, 51(7):1175–1185, apr 2013. DOI 10.1016/j.asr.2012.10.031. Cited on page 141.

Jin Li and Wenbin Shen. **GRACE detection of the medium- to far-field coseismic gravity changes caused by the 2004 M**

W9.3 Sumatra-Andaman earthquake. *Earthquake Science*, 25(3):235–240, jun 2012. DOI 10.1007/s11589-012-0849-z. Cited on page 30.

Tingjung Lin, Cheinway Hwang, Tzu-Pang Tseng, and B.F. Chao. **Low-degree gravity change from GPS data of COSMIC and GRACE satellite missions**. *Journal of Geodynamics*, 53(December 2007):34–42, jan 2012. DOI 10.1016/j.jog.2011.08.004. Cited on page 20.

X. Liu, P. Ditmar, C. Siemes, D. C. Slobbe, E. Revtova, R. Klees, R. Riva, and Q. Zhao. **DEOS Mass Transport model (DMT-1) based on GRACE satellite data: methodology and validation**. *Geophysical Journal International*, 181(2):769–788, mar 2010. DOI 10.1111/j.1365-246X.2010.04533.x. Cited on pages 28, 42, 44, 89, 112, 148, 149, 211, 221, and 317.

Xianglin Liu. **Global gravity field recovery from satellite-to-satellite tracking data with the acceleration approach**. Dissertation, Delft University of Technology, 2008. `http://www.ncg.knaw.nl/Publicaties/Geodesy/pdf/68Liu.pdf`. Cited on pages 41, 42, 131, and 132.

Xianglin Liu, Pavel Ditmar, and Qile Zhao. **A new variant of the acceleration approach for gravity field modeling from GRACE range measurements**. In *European Geosciences Union*, volume 9, 2007. `http://meetings.copernicus.org/www.cosis.net/abstracts/EGU2007/07315/EGU2007-J-07315.pdf`. Cited on page 81.

William Llovel, Stéphanie Guinehut, and Anny Cazenave. **Regional and interannual variability in sea level over 2002–2009 based on satellite altimetry, Argo float data and GRACE ocean mass**. *Ocean Dynamics*, 60(5):1193–1204, aug 2010. DOI 10.1007/s10236-010-0324-0. Cited on page 30.

A. Lombard, D. Garcia, G. Ramillien, A. Cazenave, R. Biancale, J.M. Lemoine,

F. Flechtner, R. Schmidt, and M. Ishii. **Estimation of steric sea level variations from combined GRACE and Jason-1 data**. *Earth and Planetary Science Letters*, 254(1-2):194–202, feb 2007. DOI 10.1016/j.epsl.2006.11.035. Cited on page 30.

Di Long, Bridget R. Scanlon, Laurent Longuevergne, Alexander Y. Sun, D. Nelun Fernando, and Himanshu Save. **GRACE satellite monitoring of large depletion in water storage in response to the 2011 drought in Texas**. *Geophysical Research Letters*, 40(13): 3395–3401, jul 2013. DOI 10.1002/grl.50655. Cited on page 29.

L. Longuevergne, C. R. Wilson, B. R. Scanlon, and J. F. Crétaux. **GRACE water storage estimates for the Middle East and other regions with significant reservoir and lake storage**. *Hydrology and Earth System Sciences*, 17 (12):4817–4830, dec 2013. DOI 10.5194/hess-17-4817-2013. Cited on page 29.

Laurent Longuevergne, Bridget R. Scanlon, and Clark R. Wilson. **GRACE Hydrological estimates for small basins: Evaluating processing approaches on the High Plains Aquifer, USA**. *Water Resources Research*, 46(11):1–15, nov 2010. DOI 10.1029/2009WR008564. Cited on page 29.

Bryant D. Loomis, R. S. Nerem, and S. B. Luthcke. **Simulation study of a follow-on gravity mission to GRACE**. *Journal of Geodesy*, 86 (5):319–335, oct 2011. DOI 10.1007/s00190-011-0521-8. Cited on pages 7 and 46.

S B Luthcke, N P Zelensky, D D Rowlands, F G Lemoine, and T A Williams. **The 1-Centimeter Orbit: Jason-1 Precision Orbit Determination Using GPS, SLR, DORIS, and Altimeter Data Special Issue: Jason-1 Calibration/Validation**. *Marine Geodesy*, 26(3):399–421, jul 2003. DOI 10.1080/714044529. Cited on page 34.

S. B. Luthcke, D. D. Rowlands, F. G. Lemoine, S. M. Klosko, D. S. Chinn, and J. J. Mc-Carthy. **Monthly spherical harmonic gravity field solutions determined from GRACE inter-satellite range-rate data alone**. *Geophysical Research Letters*, 33(2):10–13, jan 2006a. DOI 10.1029/2005GL024846. Cited on page 28.

S. B. Luthcke, H. J. Zwally, W. Abdalati, D. D. Rowlands, R. D. Ray, R. S. Nerem, F. G. Lemoine, J. J. McCarthy, and D. S. Chinn. **Recent Greenland Ice Mass Loss by Drainage System from Satellite Gravity Observations**. *Science*, 314(5803):1286–1289, nov 2006b. DOI 10.1126/science.1130776. Cited on page 30.

Florent Lyard, Fabien Lefevre, Thierry Letellier, and Olivier Francis. **Modelling the global ocean tides: modern insights from FES2004**. *Ocean Dynamics*, 56(5-6):394–415, sep 2006. DOI 10.1007/s10236-006-0086-x. Cited on pages 89 and 318.

JP Marque, B Christophe, and F Liorzou. **The ultra sensitive accelerometers of the ESA GOCE mission**. *International Astronautical Federation*, 08(B1.3.7):1–9, 2008. http://www.iafastro.net/iac/archive/browse/IAC-08/B1/3/1787/. Cited on pages 22 and 23.

Luca Massotti, Davina Di Cara, Jose del Amo, Roger Haagmans, Michael Jost, Christian Siemes, and Pierluigi Silvestrin. **The ESA Earth Observation Programmes Activities for the Preparation of the Next Generation Gravity Mission**. In *AIAA Guidance, Navigation, and Control (GNC) Conference*, pages 1–17, Reston, Virginia, aug 2013. American Institute of Aeronautics and Astronautics. DOI 10.2514/6.2013-4637. Cited on pages 10 and 57.

Torsten Mayer-Guerr, Martin Feuchtinger, and Juergen Kusche. **A Comparison of Various Procedures for Global Gravity Field Recovery from CHAMP Orbits**. In *Earth Observation with CHAMP*, pages 151–156. Springer-Verlag, Berlin/Heidelberg, 2005.

DOI 10.1007/3-540-26800-6_24. Cited on page 40.

T. Mayer-Gürr, K.H. Ilk, A. Eicker, and M. Feuchtinger. **ITG-CHAMP01: a CHAMP gravity field model from short kinematic arcs over a one-year observation period**. *Journal of Geodesy*, 78(7-8):462–480, feb 2005. DOI 10.1007/s00190-004-0413-2. Cited on page 40.

Torsten Mayer-Gürr. **Gravitationsfeldbestimmung aus der Analyse kurzer Bahnbögen am Beispiel der Satellitenmissionen CHAMP und GRACE**. Phd dissertation, Rheinischen Friedrich-Wilhelms Universität Bonn, 2006. `http://dgk.badw.de/fileadmin/docs/c-675.pdf`. Cited on page 40.

Torsten Mayer-Gürr. **The new combined satellite only model GOCO03S**. In *International Symposium on Gravity, Geoid and Height Systems*, Venice, Italy, 2012. `http://www.bernese.unibe.ch/publist/2012/pres/Pres{_}GGHS2012{_}mayer-guerr{_}etal.pdf`. Cited on pages 27 and 319.

Torsten Mayer-Gürr, Annette Eicker, and KH Karl-Heinz Ilk. **Gravity Field Recovery from GRACE-SST Data of Short Arcs**. In J. Flury, R. Rummel, C. Reigber, M. Rothacher, G. Boedecker, and U. Schreiber, editors, *Observation of the Earth System from Space*, pages 131–148. Springer Berlin Heidelberg, 2006. DOI 10.1007/3-540-29522-4_10. Cited on pages 41 and 43.

Torsten Mayer-Gürr, Annette Eicker, and Karl-Heinz Ilk. **ITG-Grace02s: a GRACE gravity field derived from range measurements of short arcs**. In *1st International Symposium of the International Gravity Field Service*, pages 193–198, 2007. Cited on page 40.

Torsten Mayer-Gürr, Enrico Kurtenbach, and Annette Eicker. **ITG-Grace2010: the new GRACE gravity field release computed in Bonn**. In *EGU General Assembly*, 2010. `http://www.igg.uni-bonn.de/apmg/index.php?id=itg-grace2010`. Cited on pages 27, 40, and 320.

Torsten Mayer-Gürr, Enrico Kurtenbach, and Annette Eicker. **Different Representations of the Time Variable Gravity Field to Reduce the Aliasing Problem in GRACE Data Analysis**. In Nico Sneeuw, Pavel Novák, Mattia Crespi, and Fernando Sansò, editors, *VII Hotine-Marussi Symposium on Mathematical Geodesy*, volume 137 of *International Association of Geodesy Symposia*, pages 285–290. Springer Berlin Heidelberg, Berlin, Heidelberg, 2012. DOI 10.1007/978-3-642-22078-4_43. Cited on page 18.

R Mayrhofer and R Pail. **Future Satellite Gravity Field Missions: Feasibility Study of Post-Newtonian Method**. In Steve Kenyon, Maria Christina Pacino, and Urs Marti, editors, *Geodesy for Planet Earth*, volume 136 of *International Association of Geodesy Symposia*, pages 231–238 LA – English. Springer Berlin Heidelberg, 2012. DOI 10.1007/978-3-642-20338-1_28. Cited on page 48.

Stephen M Merkowitz. **The LISA integrated model**. *Classical and Quantum Gravity*, 20(10):S255–S260, may 2003. DOI 10.1088/0264-9381/20/10/328. Cited on pages 46 and 321.

R. H. Merson and D. G. King-Hele. **Use of Artificial Satellites to Explore the Earth's Gravitational Field: Results from Sputnik 2 (1957β)**. *Nature*, 182(4636):640–641, sep 1958. DOI 10.1038/182640a0. Cited on page 18.

U. Meyer, A. Jäggi, and G. Beutler. **The impact of attitude control on GRACE accelerometry and Orbits**. In Steve Kenyon, Maria Christina Pacino, and Urs Marti, editors, *Geodesy for Planet Earth*, volume 136 of *International Association of Geodesy Symposia*, pages 139–146. Springer Berlin Heidelberg,

Berlin, Heidelberg, 2012a. DOI 10.1007/978-3-642-20338-1. Cited on page 98.

Ulrich Meyer, Adrian Jäggi, and Gerhard Beutler. **Monthly gravity field solutions based on GRACE observations generated with the Celestial Mechanics Approach**. *Earth and Planetary Science Letters*, 345-348:72–80, sep 2012b. DOI 10.1016/j.epsl.2012.06.026. Cited on pages 9 and 28.

P. C. D. Milly and A. B. Shmakin. **Global Modeling of Land Water and Energy Balances. Part I: The Land Dynamics (LaD) Model**. *Journal of Hydrometeorology*, 3 (3):283–299, jun 2002. DOI 10.1175/1525-7541(2002)003<0283:GMOLWA>2.0.CO;2. Cited on page 320.

Oliver Montenbruck, Yago Andres, Heike Bock, Tom van Helleputte, Jose van den Ijssel, Marc Loiselet, Christian Marquardt, Pierluigi Silvestrin, Pieter Visser, and Yoke Yoon. **Tracking and orbit determination performance of the GRAS instrument on MetOp-A**. *GPS Solutions*, 12(4):289–299, sep 2008. DOI 10.1007/s10291-008-0091-2. Cited on page 36.

Oliver Montenbruck, André Hauschild, Yago Andres, Axel Engeln, and Christian Marquardt. **(Near-)real-time orbit determination for GNSS radio occultation processing**. *GPS Solutions*, 17(2):199–209, jun 2012. DOI 10.1007/s10291-012-0271-y. Cited on page 20.

Malte Müller, Josef Y. Cherniawsky, Michael G. G. Foreman, and Jin-Song Storch. **Seasonal variation of the M 2 tide**. *Ocean Dynamics*, 64(2):159–177, jan 2014. DOI 10.1007/s10236-013-0679-0. Cited on pages 114, 214, and 270.

Michael Murböck and Roland Pail. **Reducing Non-tidal Aliasing Effects by Future Gravity Satellite Formations**. In Chris Rizos and Pascal Willis, editors, *Earth on the Edge: Science for a Sustainable Planet*, volume 139 of *International Association of Geodesy Symposia*, pages 407–412. Springer Berlin Heidelberg, 2014. DOI 10.1007/978-3-642-37222-3_54. Cited on pages 11 and 271.

Michael Murböck, Roland Pail, Ilias Daras, and Thomas Gruber. **Optimal orbits for temporal gravity recovery regarding temporal aliasing**. *Journal of Geodesy*, 88(2):113–126, nov 2013. DOI 10.1007/s00190-013-0671-y. Cited on page 270.

R.S. Nerem, P. Bender, B. Loomis, M.M. Watkins, W.M. Folkner, M. Stephens, T. Delker, J. Leitch, and R. Pierce. **Development of an Interferometric Laser Ranging System for a Follow-On Gravity Mission to GRACE**. In *American Geophysical Union Spring Meeting*, 2004. http://adsabs.harvard.edu/abs/2004AGUSM.G43C..02N. Cited on page 45.

John A. O'Keefe. **An application of Jacobi's integral to the motion of an earth satellite**. *The Astronomical Journal*, 62:265, oct 1957. DOI 10.1086/107530. Cited on page 39.

I. Panet, J. Flury, R. Biancale, T. Gruber, J. Johannessen, M. R. Broeke, T. Dam, P. Gegout, C. W. Hughes, G. Ramillien, I. Sasgen, L. Seoane, and M. Thomas. **Earth System Mass Transport Mission (e.motion): A Concept for Future Earth Gravity Field Measurements from Space**. *Surveys in Geophysics*, oct 2012. DOI 10.1007/s10712-012-9209-8. Cited on pages 3, 6, 10, 46, 212, and 254.

Fabrice Papa, Frederic Frappart, Andreas Güntner, Catherine Prigent, Filipe Aires, Augusto C. V. Getirana, and Raffael Maurer. **Surface freshwater storage and variability in the Amazon basin from multi-satellite observations, 1993-2007**. *Journal of Geophysical Research: Atmospheres*, 118(21):11,951–11,965, nov 2013. DOI 10.1002/2013JD020500. Cited on page 29.

Nikolaos K. Pavlis, Simon A. Holmes, Steve Kenyon, and John K. Factor. **An Earth Gravitational Model to Degree 2160: EGM2008**.

In *EGU General Assembly*, volume 10, apr 2008. Cited on pages 27 and 317.

Kenneth M Pesyna, Robert W Heath, and Todd E Humphreys. **Centimeter Positioning with a Smartphone-Quality GNSS Antenna**. In *ION GNSS+*, Tampa, USA, 2014. https://radionavlab.ae.utexas.edu/images/stories/files/papers/ion2014Pesyna.pdf. Cited on pages 47 and 264.

A Peters, KY Chung, and S Chu. **Measurement of gravitational acceleration by dropping atoms**. *Nature*, 400:849–852, 1999. DOI 10.1038/23655. Cited on page 45.

Nadja Peterseim, Anja Schlicht, Jakob Flury, and Christoph Dahle. **Identification and Reduction of Satellite-Induced Signals in GRACE Accelerometer Data**. In Frank Flechtner, Nico Sneeuw, and Wolf-Dieter Schuh, editors, *Observation of the System Earth from Space - CHAMP, GRACE, GOCE and future missions*, Advanced Technologies in Earth Sciences, pages 53–61. Springer Berlin Heidelberg, Berlin, Heidelberg, 2014. DOI 10.1007/978-3-642-32135-1_7. Cited on pages 8 and 265.

Christopher G. Piecuch, Katherine J. Quinn, and Rui M. Ponte. **Satellite-derived interannual ocean bottom pressure variability and its relation to sea level**. *Geophysical Research Letters*, 40(12):3106–3110, jun 2013. DOI 10.1002/grl.50549. Cited on page 30.

R. Pierce, J. Leitch, M. Stephens, P. Bender, and R.S. Nerem. **Intersatellite range monitoring using optical interferometry**. *Applied optics*, 47(27):5007–18, sep 2008. DOI 10.1364/AO.47.005007. Cited on pages 45, 218, 219, and 220.

Georgy M. Polischuk and Sergey G. Revnivykh. **Status and development of GLONASS**. *Acta Astronautica*, 54(11-12):949–955, jun 2004. DOI 10.1016/j.actaastro.2004.01.037. Cited on pages 140 and 319.

Siavash Iran Pour. **Sampling the Earth's Time-Variable Gravity Field from Satellite Orbit, Design of Future Gravity Satellite Missions**. Dissertation, Universität Stuttgart zur, 2013. http://dgk.badw.de/fileadmin/docs/c-721.pdf. Cited on page 16.

Zhao Qile, Liu Jingnan, and Ge Maorong. **High precision orbit determination of CHAMP satellite**. *Geo-spatial Information Science*, 9(3):180–186, jan 2006. DOI 10.1007/BF02826764. Cited on pages 35 and 36.

G Ramillien, F Frappart, A Cazenave, and A Guntner. **Time variations of land water storage from an inversion of 2 years of GRACE geoids**. *Earth and Planetary Science Letters*, 235(1-2):283–301, 2005. DOI 10.1016/j.epsl.2005.04.005. Cited on page 8.

G. Ramillien, A. Lombard, A. Cazenave, E.R. Ivins, M. Llubes, F. Remy, and R. Biancale. **Interannual variations of the mass balance of the Antarctica and Greenland ice sheets from GRACE**. *Global and Planetary Change*, 53(3):198–208, sep 2006. DOI 10.1016/j.gloplacha.2006.06.003. Cited on page 30.

G. L. Ramillien, L. Seoane, F. Frappart, R. Biancale, S. Gratton, X. Vasseur, and S. Bourgogne. **Constrained Regional Recovery of Continental Water Mass Time-variations from GRACE-based Geopotential Anomalies over South America**. *Surveys in Geophysics*, 33(5):887–905, feb 2012. DOI 10.1007/s10712-012-9177-z. Cited on page 29.

R. D. Ray and S. B. Luthcke. **Tide model errors and GRACE gravimetry: towards a more realistic assessment**. *Geophysical Journal International*, 167(3):1055–1059, dec 2006. DOI 10.1111/j.1365-246X.2006.03229.x. Cited on pages 7, 17, 114, and 214.

R. D. Ray, S. B. Luthcke, and J.-P. Boy. **Qualitative comparisons of global ocean tide models by analysis of intersatellite ranging data**.

Journal of Geophysical Research, 114(C9):1–11, sep 2009. DOI 10.1029/2009JC005362. Cited on pages 114, 214, and 270.

R.D. Ray. **A Global Ocean Tide Model From TOPEX/POSEIDON Altimetry: GOT99.2**. Technical report September 1999, Goddard Space Flight Center, 1999. `http://hdl.handle.net/2060/19990089548`. Cited on page 319.

C Reigber, P Schwintzer, and H Luehr. **CHAMP–a challenging mini-satellite payload for geoscientific research and application**. In *Erste Geodaetische Woche*, Stuttgart, 1996. Cited on pages 19 and 316.

Ch. Reigber, H. Lühr, and P Schwintzer. **CHAMP mission status**. *Advances in Space Research*, 30(2):129–134, jul 2002. DOI 10.1016/S0273-1177(02)00276-4. Cited on pages 19 and 316.

Christoph Reigber. **Gravity field recovery from satellite tracking data**. In Fernando Sansò and Reiner Rummel, editors, *Theory of Satellite Geodesy and Gravity Field Determination*, volume 25 of *Lecture Notes in Earth Sciences*, pages 197–234. Springer-Verlag, Berlin/Heidelberg, 1989. DOI 10.1007/BFb0010546. Cited on page 38.

Christoph Reigber, Roland Schmidt, Frank Flechtner, Rolf König, Ulrich Meyer, Karl-Hans Neumayer, Peter Schwintzer, and Sheng Yuan Zhu. **An Earth gravity field model complete to degree and order 150 from GRACE: EIGEN-GRACE02S**. *Journal of Geodynamics*, 39(1):1–10, jan 2005. DOI 10.1016/j.jog.2004.07.001. Cited on page 39.

T. Reubelt, G. Austen, and E.W. Grafarend. **Harmonic analysis of the Earth's gravitational field by means of semi-continuous ephemerides of a low Earth orbiting GPS-tracked satellite. Case study: CHAMP**. *Journal of Geodesy*, 77(5-6):257–278, aug 2003. DOI 10.1007/s00190-003-0322-9. Cited on page 41.

T Reubelt, N Sneeuw, and M A Sharifi. **Future Mission Design Options for Spatio-Temporal Geopotential Recovery**. In Stelios P. Mertikas, editor, *Gravity, Geoid and Earth Observation*, volume 135 of *International Association of Geodesy Symposia*, pages 163–170. Springer Berlin Heidelberg, Berlin, Heidelberg, 2010. DOI 10.1007/978-3-642-10634-7. Cited on pages 16 and 17.

T Reubelt, N Sneeuw, and E. W. Grafarend. **Comparison of Kinematic Orbit Analysis Methods for Gravity Field Recovery**. In Nico Sneeuw, Pavel Novák, Mattia Crespi, and Fernando Sansò, editors, *VII Hotine-Marussi Symposium on Mathematical Geodesy*, volume 137 of *International Association of Geodesy Symposia*, pages 259–265. Springer Berlin Heidelberg, Berlin, Heidelberg, 2012. DOI 10.1007/978-3-642-22078-4_39. Cited on page 39.

Tilo Reubelt, G Martin, and Erik W Grafarend. **Harmonic Analysis of the Earth's Gravitational Field from Kinematic CHAMP Orbits based on Numerically Derived Satellite Accelerations**. In J. Flury, R. Rummel, C. Reigber, M. Rothacher, G. Boedecker, and U. Schreiber, editors, *Observation of the Earth System from Space*, volume 2, pages 27–42. Springer-Verlag, Berlin/Heidelberg, 2006. DOI 10.1007/3-540-29522-4_3. Cited on page 42.

Tilo Reubelt, Nico Sneeuw, Siavash Iran Pour, Marc Hirth, Walter Fichter, Jürgen Müller, Phillip Brieden, Frank Flechtner, Jean-Claude Raimondo, Jürgen Kusche, Basem Elsaka, Thomas Gruber, Roland Pail, Michael Murböck, Bernhard Doll, Rolf Sand, Xinxing Wang, Volker Klein, Matthias Lezius, Karsten Danzmann, Gerhard Heinzel, Benjamin Sheard, Ernst Rasel, Michael Gilowski, Christian Schubert, Wolfgang Schäfer, Andreas Rathke, Hansjörg Dittus, and Ivanka Pelivan. **Future Gravity Field Satellite Missions**. In Frank Flechtner, Nico Sneeuw, and Wolf-Dieter Schuh, editors, *Observation of the System Earth from Space - CHAMP,*

GRACE, GOCE and future missions, pages 165–230. Springer Berlin Heidelberg, 2014. DOI 10.1007/978-3-642-32135-1_21. Cited on pages 6, 10, 11, 57, 95, 114, 214, and 270.

Jacques Richard, Yves Le Roy, Eric Thouvenot, Philippe Escudier, O M Gupta, and Iridium Com. **Altimetry Payload Specification for Iridium NEXT**. Technical report, Iridium Satellite LLC, 2008. Cited on pages 118 and 126.

Riccardo E. M. Riva, Jonathan L. Bamber, David a. Lavallée, and Bert Wouters. **Sea-level fingerprint of continental water and ice mass change from GRACE**. *Geophysical Research Letters*, 37(19):1–6, oct 2010. DOI 10.1029/2010GL044770. Cited on page 30.

M. Rodell, P. R. Houser, U. Jambor, J. Gottschalck, K. Mitchell, C.-J. C-J. Meng, K. Arsenault, B. Cosgrove, J. Radakovich, M. Bosilovich, J. K. Entin, J. P. Walker, D. Lohmann, and D. Toll. **The Global Land Data Assimilation System**. *Bulletin of the American Meteorological Society*, 85(3):381–394, mar 2004. DOI 10.1175/BAMS-85-3-381. Cited on page 319.

Matthew Rodell, Jianli Chen, Hiroko Kato, James S. Famiglietti, Joe Nigro, and Clark R. Wilson. **Estimating groundwater storage changes in the Mississippi River basin (USA) using GRACE**. *Hydrogeology Journal*, 15(1):159–166, sep 2006. DOI 10.1007/s10040-006-0103-7. Cited on page 29.

Matthew Rodell, Isabella Velicogna, and James S. Famiglietti. **Satellite-based estimates of groundwater depletion in India.** *Nature*, 460(7258):999–1002, aug 2009. DOI 10.1038/nature08238. Cited on page 29.

Josep Roselló, Pierluigi Silvestrin, Roland Weigand, Salvatore Addio, Alberto García, and Gustavo López Risueño. **Next generation of ESA's GNSS receivers for Earth Observation satellites**. In *6th ESA Workshop on Satellite Navigation Technologies*, volume 3, Noordwijk,

The Netherlands, 2012. ESA. `https://amstel.estec.esa.int/tecedm/website/biblio/RoselloNavitech2012.pdf`. Cited on page 141.

D. D. Rowlands, Dražen Švehla, and Óránt Földváry. **Resolving mass flux at high spatial and temporal resolution using GRACE intersatellite measurements**. *Geophysical Research Letters*, 32(4):L04310, feb 2005. DOI 10.1029/2004GL021908. Cited on pages 28 and 321.

Keven Roy and W. R. Peltier. **GRACE era secular trends in Earth rotation parameters: A global scale impact of the global warming process?** *Geophysical Research Letters*, 38(10):1–5, may 2011. DOI 10.1029/2011GL047282. Cited on page 30.

R. Rummel. **Determination of short-wavelength components of the gravity field from satellite-to-satellite tracking or satellite gradiometry**. *Manuscripta Geodaetica*, 4(2):107–148, 1979. Cited on pages 41, 81, 105, and 302.

R. Rummel. **Geoid and Gravity in Earth Sciences – An Overview**. *Earth, Moon, and Planets*, 94(1-2):3–11, nov 2005. DOI 10.1007/s11038-005-3755-8. Cited on page 3.

R Rummel, C Reigber, and K.~H. Ilk. **The use of satellite-to-satellite tracking for gravity parameter recovery**. In *ESA Special Publication*, volume 137 of *ESA Special Publication*, pages 153–161, apr 1978. Cited on page 60.

I Sasgen, Z Martinec, and K Fleming. **Regional ice-mass changes and glacial-isostatic adjustment in Antarctica from GRACE**. *Earth and Planetary Science Letters*, 264(3-4):391–401, dec 2007. DOI 10.1016/j.epsl.2007.09.029. Cited on page 30.

R. Savcenko and W. Bosch. **EOT08a - a new global ocean tide model derived by empirical analysis of multi-mission altimetry data .** In *EGU General Assembly*, volume 10, page 7962, 2008a. `http://meetings.copernicus.org/`

`www.cosis.net/abstracts/EGU2008/07470/` `EGU2008-A-07470.pdf`. Cited on page 318.

Roman Savcenko and Wolfgang Bosch. **EOT08a – empirical ocean tide model from multi-mission satellite altimetry**. Technical report, Geodätisches Deutsches Forschunsginstitut, Munich, Germany, 2008b. `ftp://ftp.dgfi.badw.de/pub/EOT08a/doc/` `EOT08a.pdf`. Cited on page 318.

J. D. Scargle. **Studies in astronomical time series analysis. II - Statistical aspects of spectral analysis of unevenly spaced data**. *The Astrophysical Journal*, 263:835, dec 1982. DOI 10.1086/160554. Cited on page 137.

Hanspeter Schaub and John L. Junkins. **Analytical Mechanics Of Space Systems**. American Institute of Aeronautics and Astronautics, Reston ,VA, jan 2003. DOI 10.2514/4.861550. Cited on pages 66, 68, 69, 70, and 278.

Hanspeter Schaub and John L. Junkins. **Errata List for the AIAA Education Series Text Book Analytical Mechanics of Space Systems**. American Institute of Aeronautics and Astronautics, 2009. `http://hanspeterschaub.info/` `Papers/errata2.pdf`. Cited on page 278.

R. Schmidt, F. Flechtner, U. Meyer, K.-H. Neumayer, Ch. Dahle, R. König, and J. Kusche. **Hydrological Signals Observed by the GRACE Satellites**. *Surveys in Geophysics*, 29(4-5):319–334, apr 2008a. DOI 10.1007/s10712-008-9033-3. Cited on pages 7, 112, and 173.

R. Schmidt, S. Petrovic, A. Güntner, F. Barthelmes, J. Wünsch, and J. Kusche. **Periodic components of water storage changes from GRACE and global hydrology models**. *Journal of Geophysical Research*, 113 (B8), 2008b. DOI 10.1029/2007JB005363. Cited on page 9.

E. Schrama, B. Wouters, and B. Vermeersen. **Present Day Regional Mass Loss of Greenland Observed with Satellite Gravimetry**. *Surveys in Geophysics*, 32(4-5):377–385, mar 2011. DOI 10.1007/s10712-011-9113-7. Cited on page 30.

E. J. O. Schrama and PNAM N. a. M. Visser. **Accuracy assessment of the monthly GRACE geoids based upon a simulation**. *Journal of Geodesy*, 81(1):67–80, aug 2006. DOI 10.1007/s00190-006-0085-1. Cited on pages 114, 214, and 270.

Ernst J. O. Schrama and Bert Wouters. **Revisiting Greenland ice sheet mass loss observed by GRACE**. *Journal of Geophysical Research*, 116(B2):B02407, feb 2011. DOI 10.1029/2009JB006847. Cited on page 30.

Ernst J. O. Schrama, Bert Wouters, and David a. Lavallée. **Signal and noise in Gravity Recovery and Climate Experiment (GRACE) observed surface mass variations**. *Journal of Geophysical Research*, 112(B8):B08407, aug 2007. DOI 10.1029/2006JB004882. Cited on pages 7 and 9.

Daniel Schültze, Gunnar Stede, Müller Vitali, Oliver Gerberding, Christoph Mahrdt, Benjamin Sheard, Gerhard Heinzel, and Karsten Danzmann. **LISA-like Laser Ranging for GRACE Follow-on LISA heritage : Laser Ranging Interferometer for GRACE follow-on**. In G. Auger, P. Binétruy, and E. Plagnol, editors, *9th LISA Symposium*, pages 285–290, Paris, 2012. Astronomical Society of the Pacific. `http://www.apc.univ-paris7.fr/` `{~}beckmann/Proceedings/Schutze.pdf`. Cited on page 46.

Günter Seeber. **Satellite Geodesy**. Walter de Gruyter, Berlin, New York, 2nd ed. edition, jan 2003. ISBN 3-11-017549-5. `http:` `//d-nb.info/967836875`. Cited on page 18.

Ki-Weon Seo, Clark R Wilson, Jianli Chen, and Duane E Waliser. **GRACE's spatial aliasing error**. *Geophysical Journal International*, 172(1):41–48, 2008. DOI 10.1111/j.1365-246X.2007.03611.x. Cited on page 17.

L. Seoane, G. Ramillien, F. Frappart, and M. Leblanc. **Regional GRACE-based estimates of water mass variations over Australia: validation and interpretation**. *Hydrology and Earth System Sciences*, 17(12):4925–4939, dec 2013. DOI 10.5194/hess-17-4925-2013. Cited on page 29.

Richard Shako, Oleh Abrikosov, Sean Bruinsma, Jean-charles Marty, Jean-michel Lemoine, Frank Flechtner, Hans Neumayer, and Christoph Dahle. **EIGEN-6C: A High-Resolution Global Gravity Combination Model Including GOCE Data**. In Frank Flechtner, Nico Sneeuw, and Wolf-Dieter Schuh, editors, *Observation of the System Earth from Space - CHAMP, GRACE, GOCE and future missions*, pages 155–161. Springer Berlin Heidelberg, 2014. DOI 10.1007/978-3-642-32135-1. Cited on pages 27 and 318.

M. Shamsudduha, R. G. Taylor, and L. Longuevergne. **Monitoring groundwater storage changes in the highly seasonal humid tropics: Validation of GRACE measurements in the Bengal Basin**. *Water Resources Research*, 48(2):W02508, feb 2012. DOI 10.1029/2011WR010993. Cited on page 29.

M.A. Sharifi, N. Sneeuw, and W. Keller. **Gravity recovery capability of four generic satellite formations**. In A Kilicoglu and R Forsberg, editors, *Gravity Field of the Earth. General Command of Mapping*, pages 211–216. 1st Int. Symp. of the International Gravity Field Service, Istanbul, Turkey, 2007. Cited on pages 10, 11, 55, 57, 69, and 112.

B. S. Sheard, G. Heinzel, K. Danzmann, D. a. Shaddock, W. M. Klipstein, and W. M. Folkner. **Intersatellite laser ranging instrument for the GRACE follow-on mission**. *Journal of Geodesy*, may 2012. DOI 10.1007/s00190-012-0566-3. Cited on pages 8, 24, 45, 46, 126, 219, 268, 271, and 318.

Christian Siemes, Roger Haagmans, Michael Kern, Gernot Plank, and Rune Floberghagen. **Monitoring GOCE gradiometer calibration parameters using accelerometer and star sensor data: methodology and first results**. *Journal of Geodesy*, 86(8):629–645, feb 2012. DOI 10.1007/s00190-012-0545-8. Cited on pages 23 and 30.

P Silvestrin, M Aguirre, L Massotti, B Leone, S Cesare, M Kern, and R Haagmans. **The future of the satellite gravimetry after the GOCE mission**. In Steve Kenyon, Maria Christina Pacino, and Urs Marti, editors, *Geodesy for Planet Earth*, volume 136 of *International Association of Geodesy Symposia*, pages 223–230. Springer Berlin Heidelberg, Berlin, Heidelberg, 2012. DOI 10.1007/978-3-642-20338-1_27. Cited on pages 10, 45, 218, 219, and 220.

Alka Singh, Florian Seitz, and Christian Schwatke. **Application of Multi-Sensor Satellite Data to Observe Water Storage Variations**. *IEEE Journal of Selected Topics in Applied Earth Observations and Remote Sensing*, 6(3):1502–1508, jun 2013. DOI 10.1109/JSTARS.2013.2258326. Cited on page 29.

D. C. Slobbe, P. Ditmar, and R. C. Lindenbergh. **Estimating the rates of mass change, ice volume change and snow volume change in Greenland from ICESat and GRACE data**. *Geophysical Journal International*, 176(1):95–106, jan 2009. DOI 10.1111/j.1365-246X.2008.03978.x. Cited on page 30.

David E. Smith and Donald L. Turcotte. **Millimeter Accuracy Satellite Laser Ranging: a Review**. In John J. Degnan, editor, *Contributions of Space Geodesy to Geodynamics: Technology*, volume 25 of *Geodynamics Series*. American Geophysical Union, Washington, D. C., 1993. DOI 10.1029/GD025p0133. Cited on pages 18 and 322.

Nico Sneeuw and Hanspeter Schaub. **Satellite clusters for future gravity field missions**. In *Gravity, Geoid and Space Missions*, pages 12–17. Springer-Verlag, Berlin/Heidelberg, 2005.

DOI 10.1007/3-540-26932-0_3. Cited on page 55.

Nico Sneeuw, Jakob Flury, and Reiner Rummel. **Science Requirements on Future Missions and Simulated Mission Scenarios**. *Earth, Moon, and Planets*, 94(1-2):113–142, nov 2005. DOI 10.1007/s11038-004-7605-x. Cited on pages 3, 60, 112, and 243.

Nicolaas Sneeuw. **A Semi-Analytical Approach to Gravity Field Analysis from Satellite Observations**. Dissertation, Technischen Universität München, 2000. http://tumb1.biblio.tu-muenchen.de/publ/diss/bv/2000/sneeuw.html. Cited on page 243.

G. Spada, J. L. Bamber, and R. T. W. L. Hurkmans. **The gravitationally consistent sea-level fingerprint of future terrestrial ice loss**. *Geophysical Research Letters*, 40(November 2012), feb 2013. DOI 10.1029/2012GL053000. Cited on page 30.

Giorgio Spada and Gaia Galassi. **New estimates of secular sea level rise from tide gauge data and GIA modelling**. *Geophysical Journal International*, 1, oct 2012. DOI 10.1111/j.1365-246X.2012.05663.x. Cited on page 30.

D. Stammer, R. D. Ray, O. B. Andersen, B. K. Arbic, W. Bosch, L. Carrère, Y. Cheng, D. S. Chinn, B. D. Dushaw, G. D. Egbert, S. Y. Erofeeva, H. S. Fok, J. A. M. Green, S. Griffiths, M. A. King, V. Lapin, F. G. Lemoine, S. B. Luthcke, F. Lyard, J. Morison, M. Müller, L. Padman, J. G. Richman, J. F. Shriver, C. K. Shum, E. Taguchi, and Y. Yi. **Accuracy assessment of global barotropic ocean tide models**. *Reviews of Geophysics*, 52(3):243–282, sep 2014. DOI 10.1002/2014RG000450. Cited on pages 114 and 214.

Holger Steffen, Heiner Denker, and Jürgen Müller. **Glacial isostatic adjustment in Fennoscandia from GRACE data and comparison with geodynamical models**. *Journal of Geodynamics*, 46(3-5):155–164, oct 2008.

DOI 10.1016/j.jog.2008.03.002. Cited on page 30.

Alexander Y. Sun. **Predicting groundwater level changes using GRACE data**. *Water Resources Research*, 49(9):5900–5912, sep 2013. DOI 10.1002/wrcr.20421. Cited on page 29.

D. Švehla and M. Rothacher. **Kinematic Precise Orbit Determination for Gravity Field Determination**. In F. Sansò, editor, *A Window on the Future of Geodesy*, volume 128 of *International Association of Geodesy Symposia*, pages 181–188. Springer-Verlag, Berlin/Heidelberg, 2005. DOI 10.1007/3-540-27432-4_32. Cited on pages 32, 34, 35, 36, and 42.

D Svehla, M. Rothacher, and D. Švehla. **Kinematic and reduced-dynamic precise orbit determination of low earth orbiters**. *Advances in Geosciences*, 1:47–56, 2003. DOI 10.5194/adgeo-1-47-2003. Cited on page 36.

Dražen Švehla and Lóránt Földváry. **From Kinematic Orbit Determination to Derivation of Satellite Velocity and Gravity Field**. In J. Flury, R. Rummel, C. Reigber, M. Rothacher, G. Boedecker, and U. Schreiber, editors, *Observation of the Earth System from Space*, book part (with own title) III, pages 177–192. Springer-Verlag, Berlin/Heidelberg, 2006. DOI 10.1007/3-540-29522-4_13. Cited on page 42.

P.L. Svendsen, O.B. Andersen, and A.a. Nielsen. **Acceleration of the Greenland ice sheet mass loss as observed by GRACE: Confidence and sensitivity**. *Earth and Planetary Science Letters*, 364:24–29, feb 2013. DOI 10.1016/j.epsl.2012.12.010. Cited on page 30.

Sean Swenson. **Estimated accuracies of regional water storage variations inferred from the Gravity Recovery and Climate Experiment (GRACE)**. *Water Resources Research*, 39(8):1223, 2003. DOI 10.1029/2002WR001808. Cited on page 29.

Bibliography

Sean Swenson and John Wahr. **Post-processing removal of correlated errors in GRACE data**. *Geophysical Research Letters*, 33(8):1–4, 2006. DOI 10.1029/2005GL025285. Cited on pages 6 and 249.

Sean Swenson, Don Chambers, and John Wahr. **Estimating geocenter variations from a combination of GRACE and ocean model output**. *Journal of Geophysical Research*, 113(B8):1–12, 2008. DOI 10.1029/2007JB005338. Cited on page 30.

M. E. Tamisiea, J. X. Mitrovica, and J. L. Davis. **GRACE Gravity Data Constrain Ancient Ice Geometries and Continental Dynamics over Laurentia**. *Science*, 316(5826):881–883, may 2007. DOI 10.1126/science.1137157. Cited on page 30.

Yusaku Tanaka and Kosuke Heki. **Long- and short-term postseismic gravity changes of megathrust earthquakes from satellite gravimetry**. *Geophysical Research Letters*, 41(15):5451–5456, aug 2014. DOI 10.1002/2014GL060559. Cited on pages 6 and 30.

Yusaku Tanaka, Kosuke Heki, Koji Matsuo, and Nikolay V Shestakov. **Crustal subsidence observed by GRACE after the 2013 Okhotsk deep-focus earthquake**. *Geophysical Research Letters*, 42(9):3204–3209, may 2015. DOI 10.1002/2015GL063838. Cited on page 30.

Jingshi Tang, Haowen Cheng, and Lin Liu. **Assessing the recent droughts in Southwestern China using satellite gravimetry**. *Water Resources Research*, 50(4):3030–3038, apr 2014. DOI 10.1002/2013WR014656. Cited on page 29.

B. Tapley, C. Reigber, and W Melbourne. **Gravity Recovery And Climate Experiment (GRACE) mission**, 1996. Cited on pages 6, 24, 26, 129, and 319.

B. Tapley, J.C. Ries, S. Bettadpur, D. Chambers, M. Cheng, F. Condi, B. Gunter, Z. Kang, P. Nagel, R. Pastor, T. Pekker, S. Poole, and F. Wang. **GGM02 – An improved Earth gravity field model from GRACE**. *Journal of Geodesy*, 79(8):467–478, sep 2005. DOI 10.1007/s00190-005-0480-z. Cited on pages 9, 27, and 319.

B. Tapley, J. Ries, S. Bettadpur, D. Chambers, M. Cheng, F. Condi, and S. Poole. **The GGM03 Mean Earth Gravity Model from GRACE**. In *AGU Fall Meeting Abstracts*, page 03, dec 2007. ftp://ftp.csr.utexas.edu/pub/grace/GGM03/GGM03{_}Tapley{_}2007{_}AGU.pdf. Cited on pages 27 and 319.

B. D. Tapley. **The gravity recovery and climate experiment: Mission overview and early results**. *Geophysical Research Letters*, 31(9):L09607, 2004a. DOI 10.1029/2004GL019920. Cited on pages 39 and 173.

Byron D Tapley. **GRACE Measurements of Mass Variability in the Earth System**. *Science*, 305(5683):503–505, jul 2004b. DOI 10.1126/science.1099192. Cited on pages 6, 24, 26, 129, and 319.

M Thomas. **Ozeanisch induzierte Erdrotationsschwankungen - Ergebnisse eines Simultanmodells für Zirkulation und Gezeiten im Weltozean**. Dissertation, Geowissenschaften, 2001. http://ediss.sub.uni-hamburg.de/volltexte/2002/608/. Cited on page 322.

P. F. Thompson, S. Bettadpur, and B. Tapley. **Impact of short period, non-tidal, temporal mass variability on GRACE gravity estimates**. *Geophysical Research Letters*, 31(6):L06619, mar 2004. DOI 10.1029/2003GL019285. Cited on pages 7, 114, 156, 214, and 269.

Xu Tianhe and Yang Yuanxi. **Calibration for CHAMP accelerometer data based on crossover points of the satellite**. *Geo-spatial Information Science*, 8(3):214–219, jan 2005. DOI 10.1007/BF02826824. Cited on page 23.

P. Touboul, B. Foulon, B. Christophe, and JP P. Marque. **CHAMP, GRACE, GOCE Instruments and Beyond**. In Steve Kenyon, Maria Christina Pacino, and Urs Marti, editors, *Geodesy for Planet Earth*, volume 136 of *International Association of Geodesy Symposia*, pages 215–221. Springer Berlin Heidelberg, 2012. DOI 10.1007/978-3-642-20338-1_26. Cited on pages 23 and 98.

J. H. van Angelen, M. R. van den Broeke, B. Wouters, and J. T. M. Lenaerts. **Contemporary (1960–2012) Evolution of the Climate and Surface Mass Balance of the Greenland Ice Sheet**. *Surveys in Geophysics*, 35(5):1155–1174, nov 2013. DOI 10.1007/s10712-013-9261-z. Cited on page 30.

Pieter Willem Lucas van Barneveld. **Orbit determination of satellite formations**. dissertation, Delft University of Technology, 2012. Cited on page 37.

T. van Dam, P.N.A.M. Visser, N. Sneeuw, T. Gruber, M. Losch, J. Bamber, M. King, M. Bierkens, M. Smit, M. Kern, R. Haagmans, T. Gruber, J. Bamber, M. Bierkens, M. King, and M. Smit. **Monitoring and modelling individual sources of mass distributions and transport in the Earth system by means of satellites**. Technical Report Contract 20403, European Space Agency, Noordwijk, The Netherlands, 2008. http://www.iapg.bgu.tum.de/mediadb/5746116/5746117/03{_}A07317{_}RD3{_}FinalReportESA-CONTRACT20403{_}opt.pdf. Cited on pages 11 and 95.

José van den IJssel and P Visser. **Performance of GPS-based accelerometry: CHAMP and GRACE**. *Advances in Space Research*, 39(10):1597–1603, 2007. DOI 10.1016/j.asr.2006.12.027. Cited on page 32.

Wouter van der Wal, Enrico Kurtenbach, Jürgen Kusche, and Bert Vermeersen. **Radial and tangential gravity rates from GRACE in areas of glacial isostatic adjustment**. *Geophysical Journal International*, 187(2): 797–812, nov 2011. DOI 10.1111/j.1365-246X.2011.05206.x. Cited on page 30.

I. Velicogna. **Increasing rates of ice mass loss from the Greenland and Antarctic ice sheets revealed by GRACE**. *Geophysical Research Letters*, 36(19):5–8, oct 2009. DOI 10.1029/2009GL040222. Cited on page 30.

I. Velicogna, T. C. Sutterley, and M. R. van den Broeke. **Regional acceleration in ice mass loss from Greenland and Antarctica using GRACE time-variable gravity data**. *Geophysical Research Letters*, 41(22):8130–8137, nov 2014. DOI 10.1002/2014GL061052. Cited on page 30.

Isabella Velicogna, John Wahr, and Huug Van den Dool. **Can surface pressure be used to remove atmospheric contributions from GRACE data with sufficient accuracy to recover hydrological signals?** *Journal of Geophysical Research*, 106(B8):16415, 2001. DOI 10.1029/2001JB000228. Cited on pages 7, 156, and 269.

G.S. Vergos, I.N. Tziavos, and M.G. Sideris. **On the Determination of Sea Level Changes by Combining Altimetric, Tide Gauge, Satellite Gravity and Atmospheric Observations**. In Steve Kenyon, Maria Christina Pacino, and Urs Marti, editors, *Geodesy for Planet Earth*, volume 136 of *International Association of Geodesy Symposia*, pages 123–130. Springer Berlin Heidelberg, Berlin, Heidelberg, 2012. DOI 10.1007/978-3-642-20338-1_15. Cited on page 30.

Sibylle Vey, Holger Steffen, Jürgen Müller, and Julia Boike. **Inter-annual water mass variations from GRACE in central Siberia**. *Journal of Geodesy*, oct 2012. DOI 10.1007/s00190-012-0597-9. Cited on page 29.

Josep Virgili and Peter C.E. Roberts. **Dsat, a QB50 CubeSat mission to study rarefied-gas drag modelling**. *Acta Astronautica*, 89:130–138, aug 2013. DOI

10.1016/j.actaastro.2013.04.006. Cited on pages 47 and 264.

P. N. A. M. Visser. **Designing Earth Gravity Field Missions for the Future: A Case Study**. In Stelios P. Mertikas, editor, *Gravity, Geoid and Earth Observation*, volume 135 of *International Association of Geodesy Symposia*, pages 131–138. Springer Berlin Heidelberg, Berlin, Heidelberg, 2010. DOI 10.1007/978-3-642-10634-7_18. Cited on pages 95, 114, 214, and 270.

P N A M Visser, N Sneeuw, T Reubelt, M Losch, and T Van Dam. **Space-borne gravimetric satellite constellations and ocean tides: aliasing effects**. *Geophysical Journal International*, pages 789–805, 2010. DOI 10.1111/j.1365-246X.2010.04557.x. Cited on pages 11, 46, 114, and 214.

P. N. A. M. Visser, EJO J O Schrama, N Sneeuw, and M Weigelt. **Dependency of Resolvable Gravitational Spatial Resolution on Space-Borne Observation Techniques**. In Steve Kenyon, Maria Christina Pacino, and Urs Marti, editors, *Geodesy for Planet Earth*, volume 136 of *International Association of Geodesy Symposia*, pages 373–379. Springer Berlin Heidelberg, 2012. DOI 10.1007/978-3-642-20338-1_45. Cited on pages 16 and 22.

P.N.A.M. Visser, J. van den IJssel, T. van Helleputte, H. Bock, A. Jäggi, G. Beutler, D. Svehla, U. Hugentobler, M. Heinze, and D. Švehla. **Orbit determination for the GOCE satellite**. *Advances in Space Research*, 43(5):760–768, mar 2009. DOI 10.1016/j.asr.2008.09.016. Cited on pages 34 and 36.

John Wahr, Mery Molenaar, and Frank Bryan. **Time variability of the Earth's gravity field: Hydrological and oceanic effects and their possible detection using GRACE**. *Journal of Geophysical Research*, 103(B12):30205, 1998. DOI 10.1029/98JB02844. Cited on page 9.

Hansheng Wang, Lulu Jia, Holger Steffen, Patrick Wu, Liming Jiang, Houtse Hsu, Long-wei Xiang, Zhiyong Wang, and Bo Hu. **Increased water storage in North America and Scandinavia from GRACE gravity data**. *Nature Geoscience*, 6(1):38–42, dec 2012a. DOI 10.1038/ngeo1652. Cited on page 29.

Lei Wang, C. K. Shum, and Christopher Jekeli. **Gravitational gradient changes following the 2004 December 26 Sumatra-Andaman Earthquake inferred from GRACE**. *Geophysical Journal International*, 1, oct 2012b. DOI 10.1111/j.1365-246X.2012.05674.x. Cited on page 30.

Qiuge Wang, Chao Chen, Bo Chen, Jianghai Xia, and Jinsong Du. **Feasibility of estimating groundwater storage changes in western Kansas using Gravity Recovery and Climate Experiment (GRACE) data**. *The Leading Edge*, 32(7):806–813, jul 2013. DOI 10.1190/tle32070806.1. Cited on page 29.

Xinxing Wang, Christian Gerlach, and Reiner Rummel. **Time-variable gravity field from satellite constellations using the energy integral**. *Geophysical Journal International*, 190(3):1507–1525, sep 2012c. DOI 10.1111/j.1365-246X.2012.05578.x. Cited on page 46.

Michael M. Watkins and Dah-Ning Yuan. **JPL Level-2 Processing Standards Document for Level-2 Product Release 05**. Technical report, Jet Propulsion Laboratory, NASA, Pasadena, CA, United States, 2012. `ftp://podaac.jpl.nasa.gov/allData/grace/docs/L2-JPL{_}ProcStds{_}v5.pdf`. Cited on pages 28 and 39.

M. Weigelt, T. van Dam, A. Jäggi, L. Prange, M. J. Tourian, W. Keller, and N. Sneeuw. **Time-variable gravity signal in Greenland revealed by high-low satellite-to-satellite tracking**. *Journal of Geophysical Research: Solid Earth*, 118(7):3848–3859, jul 2013a. DOI 10.1002/jgrb.50283. Cited on page 21.

Matthias Weigelt, Michael G. Sideris, and Nico Sneeuw. **On the influence of the ground track on the gravity field recovery from**

high–low satellite-to-satellite tracking missions: CHAMP monthly gravity field recovery using the energy balance approach revisited. *Journal of Geodesy*, 83(12):1131–1143, jul 2009. DOI 10.1007/s00190-009-0330-5. Cited on page 96.

Matthias Weigelt, Nico Sneeuw, E. J. O. Schrama, and Pieter N. A. M. Visser. **An improved sampling rule for mapping geopotential functions of a planet from a near polar orbit**. *Journal of Geodesy*, 87(2):127–142, feb 2013b. DOI 10.1007/s00190-012-0585-0. Cited on page 16.

Eric W. Weisstein. **Kepler's Equation**, 2015. http://mathworld.wolfram.com/KeplersEquation.html. Cited on page 70.

D. N. Wiese, W. M. Folkner, and R. S. Nerem. **Alternative mission architectures for a gravity recovery satellite mission**. *Journal of Geodesy*, 83(6):569–581, jun 2009. DOI 10.1007/s00190-008-0274-1. Cited on pages 7, 11, 45, 112, and 268.

D. N. Wiese, R. S. Nerem, and F. G. Lemoine. **Design considerations for a dedicated gravity recovery satellite mission consisting of two pairs of satellites**. *Journal of Geodesy*, 86(2):81–98, jun 2011a. DOI 10.1007/s00190-011-0493-8. Cited on pages 7, 11, and 47.

David N. Wiese, Robert S. Nerem, and Shin-Chan Han. **Expected improvements in determining continental hydrology, ice mass variations, ocean bottom pressure signals, and earthquakes using two pairs of dedicated satellites for temporal gravity recovery**. *Journal of Geophysical Research*, 116(B11):B11405, nov 2011b. DOI 10.1029/2011JB008375. Cited on pages 47 and 271.

David N. Wiese, Pieter Visser, and Robert S. Nerem. **Estimating low resolution gravity fields at short time intervals to reduce temporal aliasing errors**. *Advances in Space Research*, 48(6):1094–1107, sep 2011c. DOI

10.1016/j.asr.2011.05.027. Cited on pages 17, 18, 46, and 271.

Dudy D. Wijaya and Fritz K. Brunner. **Atmospheric range correction for two-frequency SLR measurements**. *Journal of Geodesy*, 85 (9):1–13, apr 2011. DOI 10.1007/s00190-011-0469-8. Cited on page 34.

Pascal Willis, Christian Jayles, and Yoaz Bar-Sever. **DORIS: From orbit determination for altimeter missions to geodesy**. *Comptes Rendus Geoscience*, 338(14-15):968–979, nov 2006. DOI 10.1016/j.crte.2005.11.013. Cited on pages 19 and 317.

H. C. Winsemius, H. H. G. Savenije, N. C. NC van de Giesen, BJJM J. J. M. van den Hurk, E. a. Zapreeva, and R. Klees. **Assessment of Gravity Recovery and Climate Experiment (GRACE) temporal signature over the upper Zambezi**. *Water Resources Research*, 42(12):1–8, dec 2006. DOI 10.1029/2006WR005192. Cited on page 29.

Philip L. Woodworth, Melisa Menéndez, and W. Roland Gehrels. **Evidence for Century-Timescale Acceleration in Mean Sea Levels and for Recent Changes in Extreme Sea Levels**. *Surveys in Geophysics*, 32(4-5):603–618, feb 2011. DOI 10.1007/s10712-011-9112-8. Cited on page 30.

B. Wouters and E. J. O. Schrama. **Improved accuracy of GRACE gravity solutions through empirical orthogonal function filtering of spherical harmonics**. *Geophysical Research Letters*, 34(23):L23711, dec 2007. DOI 10.1029/2007GL032098. Cited on page 9.

B. Wouters, D. Chambers, and E. J. O. Schrama. **GRACE observes small-scale mass loss in Greenland**. *Geophysical Research Letters*, 35(20):L20501, oct 2008. DOI 10.1029/2008GL034816. Cited on page 30.

B. Wouters, R. E. M. Riva, D. a. Lavallée, and J. L. Bamber. **Seasonal variations in sea level induced by continental water mass:**

First results from GRACE. *Geophysical Research Letters*, 38(3):L03303, feb 2011. DOI 10.1029/2010GL046128. Cited on page 30.

Patrick Wu and Hansheng Wang. **Postglacial isostatic adjustment in a self-gravitating spherical earth with power-law rheology**. *Journal of Geodynamics*, 46(3-5):118–130, oct 2008. DOI 10.1016/j.jog.2008.03.008. Cited on page 30.

Xiaoping Wu, Michael B. Heflin, Hugo Schotman, Bert L. a. Vermeersen, Danan Dong, Richard S. Gross, Erik R. Ivins, Angelyn W. Moore, and Susan E. Owen. **Simultaneous estimation of global present-day water transport and glacial isostatic adjustment**. *Nature Geoscience*, 3(9):642–646, aug 2010. DOI 10.1038/ngeo938. Cited on page 30.

S.H. Ye, J.S. Ping, X.G. Hu, X.H. Shen, H. Li, J.S. Wang, and Y. Wu. **A Plan for GRACE-type Satellite Gravity Mission**. In *Towards a Roadmap for Future Satellite Gravity Missions*, Graz, Austria, 2009. `http://www.igcp565.org/workshops/Graz/pdfs/P2b{_}06{_}Ping{_}GGOS2009-pjs.pdf`. Cited on page 271.

Zhang Yong-zhi, Xu Hai-jun, Wang Wei-Dong, Duan Hu-rong, and Zhang Ben-ping. **Gravity Anomaly From Satellite Gravity Gradiometry Data by GOCE in Japan Ms9.0 Strong Earthquake Region**. *Procedia Environmental Sciences*, 10(Esiat):529–534, jan 2011. DOI 10.1016/j.proenv.2011.09.086. Cited on page 30.

T. P. Yunck, W. I. Bertiger, S. C. Wu, Y. E. Bar-Sever, E. J. Christensen, B. J. Haines, S. M. Lichten, R. J. Muellerschoen, Y. Vigue, and P. Willis. **First assessment of GPS-based reduced dynamic orbit determination on TOPEX Poseidon**, 1994. Cited on page 32.

Sandra Zaragoza. **GRACE Follow-On Mission**, 2013. `https://www.ae.utexas.edu/news/features/grace-follow-on`. Cited on pages 8, 10, 45, 126, 219, 268, 271, and 318.

L. Zenner, T. Gruber, A. Jäggi, and G. Beutler. **Propagation of atmospheric model errors to gravity potential harmonics-impact on GRACE de-aliasing**. *Geophysical Journal International*, 182(2):797–807, jun 2010. DOI 10.1111/j.1365-246X.2010.04669.x. Cited on pages 7, 17, 116, 156, and 269.

L Zenner, T Gruber, G Beutler, A Jäggi, F Flechtner, T Schmidt, J Wickert, E Fagiolini, G Schwarz, and T Trautmann. **Using Atmospheric Uncertainties for GRACE De-aliasing: First Results**. In Steve Kenyon, Maria Christina Pacino, and Urs Marti, editors, *Geodesy for Planet Earth*, volume 136 of *International Association of Geodesy Symposia*, pages 147–152. Springer Berlin Heidelberg, 2012. DOI 10.1007/978-3-642-20338-1_18. Cited on pages 7 and 116.

T.Y. Zhang and S.G. S.R. Jin. **Estimate of glacial isostatic adjustment uplift rate in the Tibetan Plateau from GRACE and GIA models**. *Journal of Geodynamics*, 72:59–66, dec 2013. DOI 10.1016/j.jog.2013.05.002. Cited on page 30.

Qian Zhao, WeiPing Jiang, XinYu Xu, and XianCai Zou. **Feasibility study on application of satellite formations for eliminating the influence from aliasing error of ocean tide model**. *Science China Earth Sciences*, dec 2014. DOI 10.1007/s11430-014-5010-5. Cited on page 11.

Qile Zhao. **Research on precise orbit determination theory and software for both GPS navigation constellation and LEO satellites**. Dissertation, Wuhan University, China, 2004. Cited on pages 72, 131, and 322.

Qile Zhao, Zhigang Hu, Jing Guo, Min Li, and Maorong Ge. **Precise relative orbit determination of twin GRACE satellites**. *Geospatial Information Science*, 13(3):221–225, jan 2010a. DOI 10.1007/s11806-010-0362-2. Cited on pages 34, 36, 37, 38, 131, and 137.

QiLe Zhao, XiangLin Liu, P. Ditmar, Christian Siemes, Elena Revtova, Hassan Hashemi-Farahani, and Roland Klees. **Water storage**

variations of the Yangtze, Yellow, and Zhuji-ang river basins derived from the DEOS Mass Transport (DMT-1) model. *Science China Earth Sciences*, 54(5):667–677, dec 2010b. DOI 10.1007/s11430-010-4096-7. Cited on page 29.

S. Zhu, Ch. Reigber, and R. Konig. **Integrated adjustment of CHAMP, GRACE, and GPS data**. *Journal of Geodesy*, 78(1-2):103–108, jun 2004. DOI 10.1007/s00190-004-0379-0. Cited on pages 20, 35, and 36.

Bibliography

Curriculum Vitae

Name: João Gregório de Teixeira da Encarnação
Nationality: Portuguese
Date of birth: 1977

Higher education and work experience

2000	Lic. Eng. IST, Aerospace Engineering
2004	M.Sc. TU Delft, Aerospace Engineering
2007–2011	Ph.D. candidate, TU Delft, Geoscience and Remote Sensing (GRS)
2011–present	Researcher, TU Delft, Aerospace Engineering

Research interests, activities and project experience

2000–2004	Rocket Ascent Trajectories
2004–2007	Laser Propulsion
2007–2015	Ph.D. thesis work on Next-generation satellite gravimetry for measuring mass transport in the Earth system
2008	Monitoring and Modelling Individual Sources of Mass Distribution and Transport in the Earth System by Means of Satellites (ESA contract 20403)
2010	Assessment of a Next Generation Gravity Mission for Monitoring the Variations of Earth's Gravity Field (ESTEC contract 22643/09/NL/AF)

2011–present	Research in Accelerometer calibration and thermosphere neutral density and winds
2011–present	Development of the Swarm Level 2 Algorithms and Associated Level 2 Processing Facility (ESA Contract 4000102140/10/NL/JA)
2013	GOCE+ Theme 3: Air density and wind retrieval using Gravity field and steady-state Ocean Circulation Explorer (GOCE) data (European Space Agency (ESA) contract 400010284/11/NL/EL)
2013–2015	Assessment of Satellite Constellations for Monitoring the Variations in Earth's Gravity Field (ESA contract 4000108663/13/NL/MV)